

Therapeutic Solutions

by MicroVention®



HydroFrame®
HydroCoil® Embolic System



HydroFill®
HydroCoil® Embolic System



HydroSoft®
HydroCoil® Embolic System

HYDROGEL ADVANCED COILS

The clinical benefits of **hydrogel** NOW engineered with the softness of bare platinum on the **V-Trak® Advanced Coil System**.

- CLINICALLY STUDIED HYDROGEL
- EFFECTIVE^{1,2,3}
- ESTABLISHED SAFETY PROFILE⁴
- SOFTER DESIGN⁵

For more information or a product demonstration, contact your local MicroVention representative:



MicroVention, Inc.

Worldwide Headquarters

1311 Valencia Avenue
Tustin, CA 92780 USA

PH +1.714.247.8000

MicroVention UK Limited

MicroVention Europe, S.A.R.L.

MicroVention Deutschland GmbH

PH +44 (0) 191 258 6777

PH +33 (1) 39 21 77 46

PH +49 211 210 798-0

microvention.com

References

1. Speirs, Burke, Lee, and Ala. The next generation HydroCoil: initial clinical experience with the HydroFill embolic coil. J NeuroIntervent Surg, 2013.
2. Brinjikiji et al. Abstract 112. Presented at: International Stroke Conference 2015, Nashville, Tennessee, February 11-13, 2015.
3. Lee, Seo, Less, Cho, Kang and Han. Mid-term outcome of intracranial aneurysms treated with HydroSoft coils compared to historical controls treated with bare platinum coils: a single-center experience. Acta Neurochir, 156:1687-1694, 2014.
4. Laymond et al. Patients prone to recurrence after endovascular treatment: periprocedural results of the PRET randomized trial on large and recurrent aneurysms, AJNR AM J Neuroradiol, 2014.
5. Data on file at MicroVention, Inc.

COILING OPTIMIZED



NOW AVAILABLE

**BARRICADE COMPLEX
FINISHING COIL**

- ◆ Extremely soft profile of The Barricade Finishing coil now in a complex shape
- ◆ Excellent microcatheter stability for confident coil placement
- ◆ Available in a size range of 1mm-5mm

BARRICADE™ COIL SYSTEM



MADE IN AMERICA

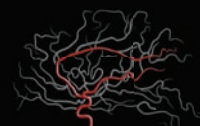
The Barricade Coil System is intended for the endovascular embolization of intracranial aneurysms and other neurovascular abnormalities such as arteriovenous malformations and arteriovenous fistulae. The System is also intended for vascular occlusion of blood vessels within the neurovascular system to permanently obstruct blood flow to an aneurysm or other vascular malformation and for arterial and venous embolizations in the peripheral vasculature. Refer to the instructions for use for complete product information.

18 TECHNOLOGY DRIVE #169, IRVINE CA 92618

p: 949.788.1443 | f: 949.788.1444

WWW.BLOCKADEMEDICAL.COM

MKTG-031 Rev. A



BLOCKADE
M E D I C A L

66%

of Patients in MR CLEAN
Were Treated with a
Trevo[®] Stent Retriever

stryker[®]
Neurovascular

Trevo[®]
PROVUE RETRIEVER

MR CLEAN¹

First clinical evidence for intra-arterial
treatment with stent retrievers

- **Largest** of the randomized AIS trials², with over 500 patients enrolled
- The Trevo Retriever was the **#1** device used in the **MR CLEAN** Trial

¹ O.A. Berkhemer et al. A Randomized Trial for Intra-arterial Treatment for Acute Ischemic Stroke. *N Eng J Med* December 2014.

² MR CLEAN is the largest AIS Trial in which stent retrievers were used.
<http://www.mrclean-trial.org/>



From cervical to sacral
we've got you covered.

Introducing the first PMMA indicated for treating pathological fractures of the sacrum.

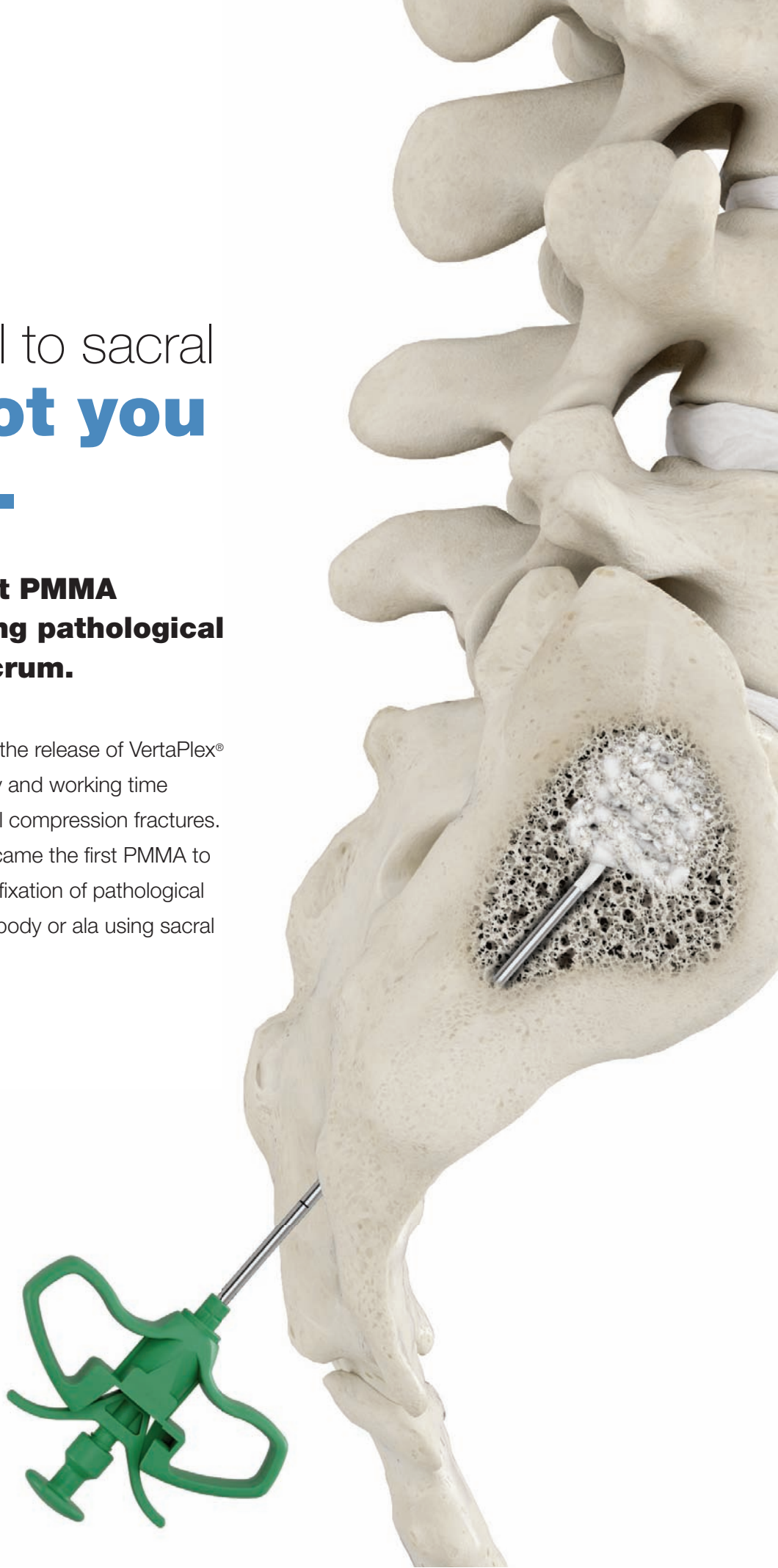
Stryker set the bar in 2008 with the release of VertaPlex® HV, addressing specific viscosity and working time preferences for treating vertebral compression fractures. Now in 2015, VertaPlex® HV became the first PMMA to receive 510(k) clearance for the fixation of pathological fractures of the sacral vertebral body or ala using sacral vertebroplasty or sacroplasty.

strykerIVS.com

Products referenced with TM designation are trademarks of Stryker. Products referenced with ® designation are registered trademarks of Stryker.

The information presented in this overview is intended to demonstrate the breadth of Stryker product offerings. Always refer to the package insert, product label and/or user instructions before using any Stryker product. Products may not be available in all markets. Product availability is subject to the regulatory or medical practices that govern individual markets. Please contact your Stryker representative if you have questions about the availability of Stryker products in your area.

1000-000-008 Rev None





THE FOUNDATION OF THE ASNR



THE FOUNDATION OF THE ASNR SYMPOSIUM 2016: EMERGENCY NEURORADIOLOGY MAY 21-22

ASNR 54TH ANNUAL MEETING MAY 23-26



Howard A. Rowley, MD, ASNR 2016 Program Chair/President-Elect
Programming developed in cooperation with ...

American Society of Functional Neuroradiology (ASFNR)
Christopher G. Filippi, MD

American Society of Head and Neck Radiology (ASHNR)
Lindell R. Gentry, MD

American Society of Pediatric Neuroradiology (ASPNR)
Erin Simon Schwartz, MD

American Society of Spine Radiology (ASSR)
Gregory J. Lawler, MD

Society of NeuroInterventional Surgery (SNIS)
Charles J. Prestigiacomo, MD

American Society of Neuroradiology (ASNR) Health Policy Committee
Robert M. Barr, MD, FACR

Computer Science and Informatics (CSI) Committee
John L. Go, MD

Research Scientists Committee
Dikoma C. Shungu, PhD

ABSTRACT DEADLINE:
Friday, December 11, 2015

Please visit www.asnr.org/2016
for more information

ASNR 54TH ANNUAL MEETING
c/o American Society of Neuroradiology
800 Enterprise Drive, Suite 205
Oak Brook, Illinois 60523-4216
Phone: 630-574-0220
Fax: 630 574-0661
www.asnr.org/2016

SCAN NOW
TO VISIT
OUR WEBSITE



SAVE THE DATE... MAY 21-26, 2016
WASHINGTON MARRIOTT WARDMAN PARK • WASHINGTON DC

Official Journal:

American Society of Neuroradiology
 American Society of Functional Neuroradiology
 American Society of Head and Neck Radiology
 American Society of Pediatric Neuroradiology
 American Society of Spine Radiology

EDITOR-IN-CHIEF

Jeffrey S. Ross, MD

Professor of Radiology, Department of Radiology,
 Mayo Clinic College of Medicine, Phoenix, Arizona

SENIOR EDITORS

Harry J. Cloft, MD, PhD

Professor of Radiology and Neurosurgery,
 Department of Radiology, Mayo Clinic College of
 Medicine, Rochester, Minnesota

Thierry A.G.M. Huisman, MD

Professor of Radiology, Pediatrics, Neurology, and
 Neurosurgery, Chairman, Department of Imaging
 and Imaging Science, Johns Hopkins Bayview,
 Director, Pediatric Radiology and Pediatric
 Neuroradiology, Johns Hopkins Hospital,
 Baltimore, Maryland

C.D. Phillips, MD, FACR

Professor of Radiology, Weill Cornell Medical
 College, Director of Head and Neck Imaging,
 New York-Presbyterian Hospital, New York,
 New York

Pamela W. Schaefer, MD

Clinical Director of MRI and Associate Director of
 Neuroradiology, Massachusetts General Hospital,
 Boston, Massachusetts, Associate Professor,
 Radiology, Harvard Medical School, Cambridge,
 Massachusetts

Charles M. Strother, MD

Professor of Radiology, Emeritus, University of
 Wisconsin, Madison, Wisconsin

Jody Tanabe, MD

Professor of Radiology and Psychiatry,
 Chief of Neuroradiology,
 University of Colorado, Denver, Colorado

STATISTICAL SENIOR EDITOR

Bryan A. Comstock, MS

Senior Biostatistician,
 Department of Biostatistics,
 University of Washington, Seattle, Washington

EDITORIAL BOARD

Ashley H. Aiken, *Atlanta, Georgia*
 A. James Barkovich, *San Francisco, California*
 Walter S. Bartynski, *Charleston, South Carolina*
 Barton F. Branstetter IV, *Pittsburgh, Pennsylvania*
 Jonathan L. Brisman, *Lake Success, New York*
 Julie Bykowski, *San Diego, California*
 Donald W. Chakeres, *Columbus, Ohio*
 Asim F. Choudhri, *Memphis, Tennessee*
 Alessandro Cianfoni, *Lugano, Switzerland*
 Colin Derdeyn, *St. Louis, Missouri*
 Rahul S. Desikan, *San Diego, California*
 Richard du Mesnil de Rochemont, *Frankfurt,
 Germany*
 Clifford J. Eskey, *Hanover, New Hampshire*
 Massimo Filippi, *Milan, Italy*
 David Fiorella, *Cleveland, Ohio*
 Allan J. Fox, *Toronto, Ontario, Canada*
 Christine M. Glastonbury, *San Francisco,
 California*
 John L. Go, *Los Angeles, California*
 Wan-Yuo Guo, *Taipei, Taiwan*
 Rakesh K. Gupta, *Lucknow, India*
 Lotfi Hacin-Bey, *Sacramento, California*
 David B. Hackney, *Boston, Massachusetts*
 Christopher P. Hess, *San Francisco, California*
 Andrei Holodny, *New York, New York*
 Benjamin Huang, *Chapel Hill, North Carolina*
 George J. Hunter, *Boston, Massachusetts*
 Mahesh V. Jayaraman, *Providence, Rhode Island*
 Valerie Jewells, *Chapel Hill, North Carolina*
 Timothy J. Kaufmann, *Rochester, Minnesota*
 Kenneth F. Layton, *Dallas, Texas*
 Ting-Yim Lee, *London, Ontario, Canada*
 Michael M. Lell, *Erlangen, Germany*
 Michael Lev, *Boston, Massachusetts*
 Karl-Olof Lovblad, *Geneva, Switzerland*
 Franklin A. Marden, *Chicago, Illinois*
 M. Gisele Matheus, *Charleston, South Carolina*
 Joseph C. McGowan, *Merion Station,
 Pennsylvania*
 Kevin R. Moore, *Salt Lake City, Utah*
 Christopher J. Moran, *St. Louis, Missouri*
 Takahisa Mori, *Kamakura City, Japan*
 Suresh Mukherji, *Ann Arbor, Michigan*
 Amanda Murphy, *Toronto, Ontario, Canada*
 Alexander J. Nemeth, *Chicago, Illinois*
 Laurent Pierot, *Reims, France*
 Jay J. Pillai, *Baltimore, Maryland*
 Whitney B. Pope, *Los Angeles, California*
 M. Judith Donovan Post, *Miami, Florida*
 Tina Young Poussaint, *Boston, Massachusetts*
 Joana Ramalho, *Lisbon, Portugal*

Otto Rapalino, *Boston, Massachusetts*
 Àlex Rovira-Cañellas, *Barcelona, Spain*
 Paul M. Ruggieri, *Cleveland, Ohio*
 Zoran Rumboldt, *Rijeka, Croatia*
 Amit M. Saindane, *Atlanta, Georgia*
 Erin Simon Schwartz, *Philadelphia, Pennsylvania*
 Aseem Sharma, *St. Louis, Missouri*
 J. Keith Smith, *Chapel Hill, North Carolina*
 Maria Vittoria Spampinato, *Charleston, South
 Carolina*
 Gordon K. Sze, *New Haven, Connecticut*
 Krishnamoorthy Thamburaj, *Hershey, Pennsylvania*
 Kent R. Thielen, *Rochester, Minnesota*
 Cheng Hong Toh, *Taipei, Taiwan*
 Thomas A. Tomsick, *Cincinnati, Ohio*
 Aquilla S. Turk, *Charleston, South Carolina*
 Willem Jan van Rooij, *Tilburg, Netherlands*
 Arastoo Vossough, *Philadelphia, Pennsylvania*
 Elysa Widjaja, *Toronto, Ontario, Canada*
 Max Wintermark, *Charlottesville, Virginia*
 Ronald L. Wolf, *Philadelphia, Pennsylvania*
 Kei Yamada, *Kyoto, Japan*

EDITORIAL FELLOW

Hillary R. Kelly, *Boston, Massachusetts*

SPECIAL CONSULTANTS TO THE EDITOR

AJNR Blog Editor

Neil Lall, *Denver, Colorado*

Case of the Month Editor

Nicholas Stence, *Aurora, Colorado*

Case of the Week Editors

Juan Pablo Cruz, *Santiago, Chile*

Sapna Rawal, *Toronto, Ontario, Canada*

Classic Case Editor

Sandy Cheng-Yu Chen, *Taipei, Taiwan*

Clinical Correlation Editor

Christine M. Glastonbury, *San Francisco, California*

Facebook Editor

Peter Yi Shen, *Sacramento, California*

Health Care and Socioeconomics Editor

Pina C. Sanelli, *New York, New York*

Physics Editor

Greg Zaharchuk, *Stanford, California*

Podcast Editor

Yvonne Lui, *New York, New York*

Twitter Editor

Ryan Fitzgerald, *Little Rock, Arkansas*

YOUNG PROFESSIONALS ADVISORY COMMITTEE

Asim K. Bag, *Birmingham, Alabama*

Anna E. Nidecker, *Sacramento, California*

Peter Yi Shen, *Sacramento, California*

Founding Editor

Juan M. Taveras

Editors Emeriti

Mauricio Castillo, Robert I. Grossman,

Michael S. Huckman, Robert M. Quencer

Managing Editor

Karen Halm

Electronic Publications Manager

Jason Gantenberg

Executive Director, ASNR

James B. Gantenberg

Director of Communications, ASNR

Angelo Artemakis

AJNR (Am J Neuroradiol ISSN 0195-6108) is a journal published monthly, owned and published by the American Society of Neuroradiology (ASNR), 800 Enterprise Drive, Suite 205, Oak Brook, IL 60523. Annual dues for the ASNR include \$170.00 for journal subscription. The journal is printed by Cadmus Journal Services, 5457 Twin Knolls Road, Suite 200, Columbia, MD 21045; Periodicals postage paid at Oak Brook, IL and additional mailing offices. Printed in the U.S.A. POSTMASTER: Please send address changes to American Journal of Neuroradiology, P.O. Box 3000, Denville, NJ 07834, U.S.A. Subscription rates: nonmember \$380 (\$450 foreign) print and online, \$305 online only; institutions \$440 (\$510 foreign) print and basic online, \$875 (\$940 foreign) print and extended online, \$365 online only (basic), extended online \$790; single copies are \$35 each (\$40 foreign). Indexed by PubMed/Medline, BIOSIS Previews, Current Contents (Clinical Medicine and Life Sciences), EMBASE, Google Scholar, HighWire Press, Q-Sensei, RefSeek, Science Citation Index, and SCI Expanded. Copyright © American Society of Neuroradiology.

CALL FOR AJNR EDITORIAL FELLOWSHIP CANDIDATES

ASNR and AJNR are pleased once again to join efforts with other imaging-related journals that have training programs on editorial aspects of publishing for trainees or junior staff (3–5 years after training), including Radiology (Olmsted fellowship), AJR (Figley and Rogers fellowships), and Radiologia.

2016 Candidate Information and Requirements

GOALS

- Increase interest in “editorial” and publication-related activities in younger individuals.
- Increase understanding and participation in the AJNR review process.
- Incorporate into AJNR’s Editorial Board younger individuals who have previous experience in the review and publication process.
- Fill a specific need in neuroradiology not offered by other similar fellowships.
- Increase the relationship between “new” generation of neuroradiologists and more established individuals.
- Increase visibility of AJNR among younger neuroradiologists.

ACTIVITIES OF THE FELLOWSHIP

- Serve as Editorial Fellow for one year. This individual will be listed on the masthead as such.
- Review at least one manuscript per month for 12 months. Evaluate all review articles submitted to AJNR.
- Access to our electronic manuscript review system will be granted so that the candidate can learn how these systems work.
- Be involved in the final decision of selected manuscripts together with the Editor-in-Chief.
- Participate in all monthly Senior Editor telephone conference calls.
- Participate in all meetings of the Editors and Publications Committee during the annual meetings of ASNR and RSNA as per candidate’s availability. The Foundation of the ASNR will provide \$2000 funding for this activity.
- Evaluate progress and adjust program to specific needs in biannual meeting or telephone conference with the Editor-in-Chief.
- Write at least one editorial for AJNR.
- Embark on an editorial scientific or bibliometric project that will lead to the submission of an article to AJNR or another appropriate journal as determined by the Editor-in-Chief. This project will be presented by the Editorial Fellow at the ASNR annual meeting.
- Serve as liaison between AJNR and ASNR’s Young Professionals Network and the 3 YPs appointed to AJNR as special consultants. Participate in meetings and telephone calls with this group. Design one electronic survey/year polling the group regarding readership attitudes and wishes.
- Recruit trainees as reviewers as determined by the Editor-in-Chief.
- Participate in Web improvement projects.
- Invite Guest Editors for AJNR’s News Digest to cover a variety of timely topics.

QUALIFICATIONS

- Be a fellow in neuroradiology from North America, including Canada (this may be extended to include other countries).
- Be a junior faculty neuroradiology member (< 3 years) in either an academic and private environment.
- Be an “in-training” or member of ASNR in any other category.

APPLICATION

- Include a short letter of intent with statement of goals and desired research project. CV must be included.
- Include a letter of recommendation from the Division Chief or fellowship program director. A statement of protected time to perform the functions outlined is desirable.
- Applications will be evaluated by AJNR’s Senior Editors and the Chair of the Publications Committee prior to the ASNR meeting. The name of the selected individual will be announced at the meeting.
- Applications should be received by March 4, 2016 and sent to Ms. Karen Halm, AJNR Managing Editor, electronically at khalm@asnr.org.



CALL FOR
APPLICATIONS

ARRS/ASNR Scholarship in Neuroradiology

Applications are being accepted in any area of research related to neuroradiology. Applications should describe the unique nature of the research effort independent of existing research efforts, and should have well-defined goals for the funding period of the grant. The two-year scholarship will provide \$150,000 (\$75,000 per year); it requires a minimum fifty percent time commitment.

Eligibility

- Applicant must be a member of both ARRS and ASNR at the time of application and for the duration of the award.
- Applicant must hold a full-time faculty position in a department of radiology, radiation oncology, or nuclear medicine within a North American educational institution at the time of application.
- Applicant must be within 5 years of initial faculty appointment with an academic rank of instructor or assistant professor (or equivalent).
- Applicant must have completed advanced training and be certified by the American Board of Radiology (ABR) or on track for certification.
- Applicant must have completed neuroradiology training in an accredited ACGME neuroradiology fellowship program.

The deadline for receipt of applications is **November 23, 2015**.

Log onto www.arrs.org/RoentgenFund/Scholarships/ARRS_ASNR.aspx or foundation.asnr.org for more information.

This scholarship is funded by The Roentgen Fund® in conjunction with The Foundation of the American Society of Neuroradiology. To support this and other important scholarships with a generous tax-deductible contribution, visit roentgenfund.arrs.org.

Application
Deadline:
**November
23**

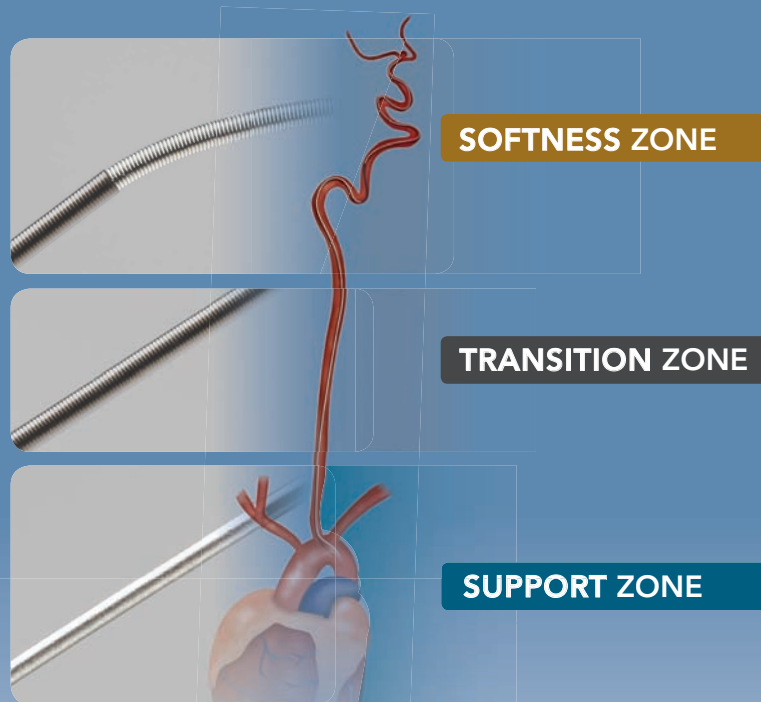
ARRS
Your Medical Imaging Society
CONNECT • LEARN • ADVANCE

www.arrs.org

THE FOUNDATION OF THE ASNR



Aneurysm The



ENHANCED CONTROL TO MAXIMIZE COIL PERFORMANCE

The **V-Trak® Advanced Coil System**, the next generation to power the performance of our most technically advanced line of coils. Offering the optimal combination of support and flexibility.

INDICATIONS FOR USE:

The HydroCoil® Embolic System (HES) is intended for the endovascular embolization of intracranial aneurysms and other neurovascular abnormalities such as arteriovenous malformations and arteriovenous fistulae. The HES is also intended for vascular occlusion of blood vessels within the neurovascular system to permanently obstruct blood flow to an aneurysm or other vascular malformation and for arterial and venous embolizations in the peripheral vasculature. The device should only be used by physicians who have undergone pre-clinical training in all aspects of HES procedures as prescribed by MicroVention.

MICROVENTION, V-Trak, HydroCoil, HydroFrame, HydroFill and HydroSoft are registered trademarks of MicroVention, Inc. Scientific and clinical data related to this document are on file at MicroVention, Inc. Refer to Instructions for Use, contraindications and warnings for additional information. Federal (USA) law restricts this device for sale by or on the order of a physician. © 2015 MicroVention, Inc. 9/15



Target® Detachable Coil

See package insert for complete indications, contraindications, warnings and instructions for use.

INTENDED USE / INDICATIONS FOR USE

Target Detachable Coils are intended to endovascularly obstruct or occlude blood flow in vascular abnormalities of the neurovascular and peripheral vessels.

Target Detachable Coils are indicated for endovascular embolization of:

- Intracranial aneurysms
- Other neurovascular abnormalities such as arteriovenous malformations and arteriovenous fistulae
- Arterial and venous embolizations in the peripheral vasculature

CONTRAINDICATIONS

None known.

POTENTIAL ADVERSE EVENTS

Potential complications include, but are not limited to: allergic reaction, aneurysm perforation and rupture, arrhythmia, death, edema, embolus, headache, hemorrhage, infection, ischemia, neurological/intracranial sequelae, post-embolization syndrome (fever, increased white blood cell count, discomfort), TIA/stroke, vasospasm, vessel occlusion or closure, vessel perforation, dissection, trauma or damage, vessel rupture, vessel thrombosis. Other procedural complications including but not limited to: anesthetic and contrast media risks, hypotension, hypertension, access site complications.

WARNINGS

- Contents supplied STERILE using an ethylene oxide (EO) process. Do not use if sterile barrier is damaged. If damage is found, call your Stryker Neurovascular representative.
- For single use only. Do not reuse, reprocess or resterilize. Reuse, reprocessing or resterilization may compromise the structural integrity of the device and/or lead to device failure which, in turn, may result in patient injury, illness or death. Reuse, reprocessing or resterilization may also create a risk of contamination of the device and/or cause patient infection or cross-infection, including, but not limited to, the transmission of infectious disease(s) from one patient to another. Contamination of the device may lead to injury, illness or death of the patient.
- After use, dispose of product and packaging in accordance with hospital, administrative and/or local government policy.
- **This device should only be used by physicians who have received appropriate training in interventional neuroradiology or interventional radiology and preclinical training on the use of this device as established by Stryker Neurovascular.**
- Patients with hypersensitivity to 316LVM stainless steel may suffer an allergic reaction to this implant.
- MR temperature testing was not conducted in peripheral vasculature, arteriovenous malformations or fistulae models.
- The safety and performance characteristics of the Target Detachable Coil System (Target Detachable Coils, InZone Detachment Systems,

delivery systems and accessories) have not been demonstrated with other manufacturer's devices (whether coils, coil delivery devices, coil detachment systems, catheters, guidewires, and/or other accessories). Due to the potential incompatibility of non Stryker Neurovascular devices with the Target Detachable Coil System, the use of other manufacturer's device(s) with the Target Detachable Coil System is not recommended.

- To reduce risk of coil migration, the diameter of the first and second coil should never be less than the width of the ostium.
- In order to achieve optimal performance of the Target Detachable Coil System and to reduce the risk of thromboembolic complications, it is critical that a continuous infusion of appropriate flush solution be maintained between a) the femoral sheath and guiding catheter, b) the 2-tip microcatheter and guiding catheters, and c) the 2-tip microcatheter and Stryker Neurovascular guidewire and delivery wire. Continuous flush also reduces the potential for thrombus formation on, and crystallization of infusate around, the detachment zone of the Target Detachable Coil.
- Do not use the product after the "Use By" date specified on the package.
- Reuse of the flush port/dispenser coil or use with any coil other than the original coil may result in contamination of, or damage to, the coil.
- Utilization of damaged coils may affect coil delivery to, and stability inside, the vessel or aneurysm, possibly resulting in coil migration and/or stretching.
- The fluoro-saver marker is designed for use with a Rotating Hemostatic Valve (RHV). If used without an RHV, the distal end of the coil may be beyond the alignment marker when the fluoro-saver marker reaches the microcatheter hub.
- If the fluoro-saver marker is not visible, do not advance the coil without fluoroscopy.
- Do not rotate delivery wire during or after delivery of the coil. Rotating the Target Detachable Coil delivery wire may result in a stretched coil or premature detachment of the coil from the delivery wire, which could result in coil migration.
- Verify there is no coil loop protrusion into the parent vessel after coil placement and prior to coil detachment. Coil loop protrusion after coil placement may result in thromboembolic events if the coil is detached.
- Verify there is no movement of the coil after coil placement and prior to coil detachment. Movement of the coil after coil placement may indicate that the coil could migrate once it is detached.
- Failure to properly close the RHV compression fitting over the delivery wire before attaching the InZone® Detachment System could result in coil movement, aneurysm rupture or vessel perforation.
- Verify repeatedly that the distal shaft of the catheter is not under stress before detaching the Target Detachable Coil. Axial compression or tension forces could be stored in the 2-tip microcatheter causing the tip to move during coil delivery. Microcatheter tip movement could cause the aneurysm or vessel to rupture.
- Advancing the delivery wire beyond the microcatheter tip once the coil has been detached involves risk of aneurysm or vessel perforation.
- The long term effect of this product on extravascular tissues has not been established so care should be taken to retain this device in the intravascular space.

Damaged delivery wires may cause detachment failures, vessel injury or unpredictable distal tip response during coil deployment. If a delivery wire is damaged at any point during the procedure, do not attempt to straighten or otherwise repair it. Do not proceed with deployment or detachment. Remove the entire coil and replace with undamaged product.

- After use, dispose of product and packaging in accordance with hospital, administrative and/or local government policy.

CAUTIONS / PRECAUTIONS

- Federal Law (USA) restricts this device to sale by or on the order of a physician.
- Besides the number of InZone Detachment System units needed to complete the case, there must be an extra InZone Detachment System unit as back up.
- Removing the delivery wire without grasping the introducer sheath and delivery wire together may result in the detachable coil sliding out of the introducer sheath.
- Failure to remove the introducer sheath after inserting the delivery wire into the RHV of the microcatheter will interrupt normal infusion of flush solution and allow back flow of blood into the microcatheter.
- Some low level overhead light near or adjacent to the patient is required to visualize the fluoro-saver marker; monitor light alone will not allow sufficient visualization of the fluoro-saver marker.
- Advance and retract the Target Detachable Coil carefully and smoothly without excessive force. If unusual friction is noticed, slowly withdraw the Target Detachable Coil and examine for damage. If damage is present, remove and use a new Target Detachable Coil. If friction or resistance is still noted, carefully remove the Target Detachable Coil and microcatheter and examine the microcatheter for damage.
- If it is necessary to reposition the Target Detachable Coil, verify under fluoroscopy that the coil moves with a one-to-one motion. If the coil does not move with a one-to-one motion or movement is difficult, the coil may have stretched and could possibly migrate or break. Gently remove both the coil and microcatheter and replace with new devices.
- Increased detachment times may occur when:
 - Other embolic agents are present.
 - Delivery wire and microcatheter markers are not properly aligned.
 - Thrombus is present on the coil detachment zone.
- Do not use detachment systems other than the InZone Detachment System.
- Increased detachment times may occur when delivery wire and microcatheter markers are not properly aligned.
- Do not use detachment systems other than the InZone Detachment System.

Copyright © 2014 Stryker
NV00006677.AA

Trevo® XP ProVue Retrievers

See package insert for complete indications, complications, warnings, and instructions for use.

INDICATIONS FOR USE

The Trevo Retriever is intended to restore blood flow in the neurovasculature by removing thrombus in patients experiencing ischemic stroke within 8 hours of symptom onset. Patients who are ineligible for intravenous tissue plasminogen activator (IV t-PA) or who fail IV t-PA therapy are candidates for treatment.

COMPLICATIONS

Procedures requiring percutaneous catheter introduction should not be attempted by physicians unfamiliar with possible complications which may occur during or after the procedure. Possible complications include, but are not limited to, the following: air embolism; hematoma or hemorrhage at puncture site; infection; distal embolization; pain/headache; vessel spasm, thrombosis, dissection, or perforation; emboli; acute occlusion; ischemia; intracranial hemorrhage; false aneurysm formation; neurological deficits including stroke; and death.

COMPATIBILITY

3x20 mm retrievers are compatible with Trevo® Pro 14 Microcatheters (REF 90231) and Trevo® Pro 18 Microcatheters (REF 90238). 4x20 mm retrievers are compatible with Trevo® Pro 18 Microcatheters (REF 90238). Compatibility of the Retriever with other microcatheters has not been established. Performance of the Retriever device may be impacted if a different microcatheter is used. The Merci® Balloon Guide Catheters are recommended for use during thrombus removal procedures. Retrievers are compatible with the Abbott Vascular DOC® Guide Wire Extension (REF 22260).

WARNINGS

- Contents supplied STERILE, using an ethylene oxide (EO) process. Nonpyrogenic.
- To reduce risk of vessel damage, adhere to the following recommendations:
 - Take care to appropriately size Retriever to vessel diameter at

intended site of deployment.

- Do not perform more than six (6) retrieval attempts in same vessel using Retriever devices.
- Maintain Retriever position in vessel when removing or exchanging Microcatheter.
- To reduce risk of kinking/fracture, adhere to the following recommendations:
 - Immediately after unsheathing Retriever, position Microcatheter tip marker just proximal to shaped section of Retriever during manipulation and withdrawal.
 - Do not rotate or torque Retriever.
 - Use caution when passing Retriever through stented arteries.
- Do not resterilize and reuse. Structural integrity and/or function may be impaired by reuse or cleaning.
- The Retriever is a delicate instrument and should be handled carefully. Before use and when possible during procedure, inspect device carefully for damage. Do not use a device that shows signs of damage. Damage may prevent device from functioning and may cause complications.
- Do not advance or withdraw Retriever against resistance or significant vasospasm. Moving or torquing device against resistance or significant vasospasm may result in damage to vessel or device. Assess cause of resistance using fluoroscopy and if needed reshape the device to withdraw.
- If Retriever is difficult to withdraw from the vessel, do not torque Retriever. Advance Microcatheter distally, gently pull Retriever back into Microcatheter, and remove Retriever and Microcatheter as a unit. If undue resistance is met when withdrawing the Retriever into the Microcatheter, consider extending the Retriever using the Abbott Vascular DOC guidewire extension (REF 22260) so that the Microcatheter can be exchanged for a larger diameter catheter such as a DAC® catheter. Gently withdraw the Retriever into the larger diameter catheter.
- Administer anti-coagulation and anti-platelet medications per standard institutional guidelines.

PRECAUTIONS

- Prescription only – device restricted to use by or on order of a physician.
- Store in cool, dry, dark place.
- Do not use open or damaged packages.
- Use by "Use By" date.
- Exposure to temperatures above 54°C (130°F) may damage device and accessories. Do not autoclave.
- Do not expose Retriever to solvents.
- Use Retriever in conjunction with fluoroscopic visualization and proper anti-coagulation agents.
- To prevent thrombus formation and contrast media crystal formation, maintain a constant infusion of appropriate flush solution between guide catheter and Microcatheter and between Microcatheter and Retriever or guidewire.
- Do not attach a torque device to the shaped proximal end of DOC® Compatible Retriever. Damage may occur, preventing ability to attach DOC® Guide Wire Extension.



Concentric Medical
301 East Evelyn
Mountain View, CA 94041



EMERGO Europe
Molenstraat 15
2513 BH, The Hague
The Netherlands



0459



Stryker Neurovascular
47900 Bayside Parkway
Fremont, CA 94538-6515

stryker.com/neurovascular

Date of Release: FEB/2014

EX_EN_US

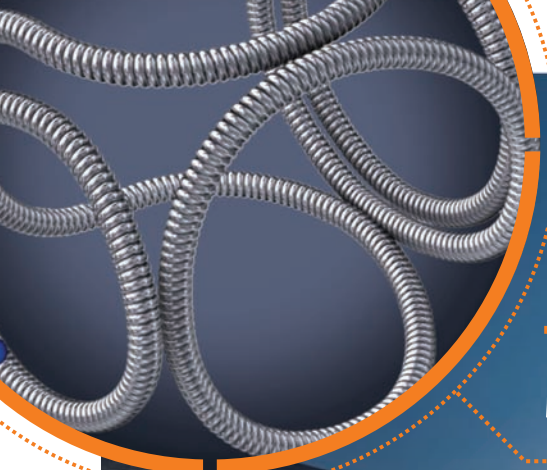
Stryker Neurovascular
47900 Bayside Parkway
Fremont, CA 94538-6515

stryker.com/neurovascular
stryker.com/emea/neurovascular

Date of Release: JUN/2014

EX_EN_GL

Copyright © 2014 Stryker
NV00009028.AA



Target[®] DETACHABLE COILS



Smooth and Stable

Whether you are framing, filling or finishing, Target Detachable Coils deliver consistently smooth deployment and exceptional microcatheter stability. Focused on design, Target Coils feature a host of advantages to ensure the high-powered performance you demand.

For more information, please visit www.strykerneurovascular.com/Target or contact your local Stryker Neurovascular sales representative.

stryker[®]
Neurovascular

OCTOBER 2015

AJNR

VOLUME 36 • PP 1793-1993

AJNR

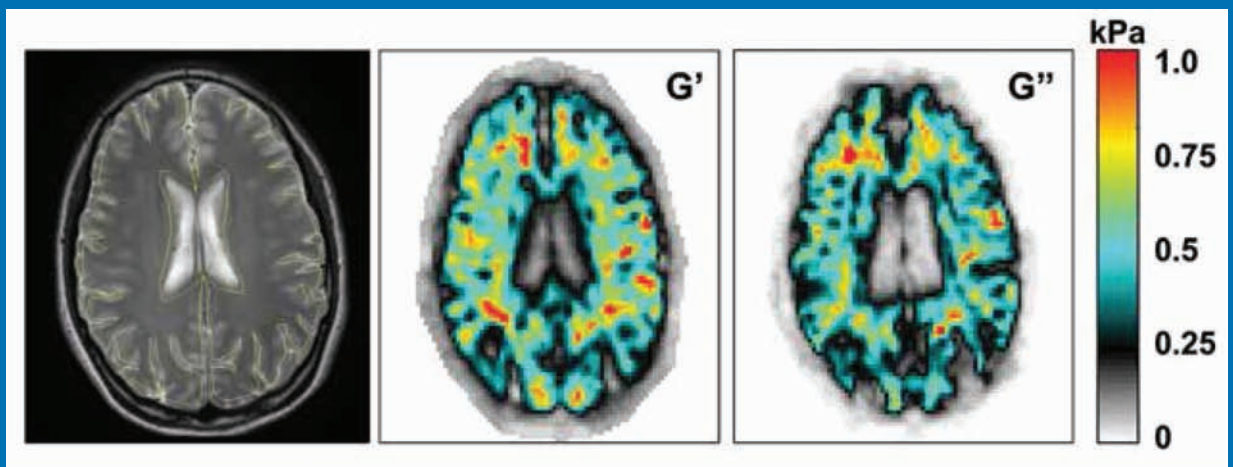
AMERICAN JOURNAL OF NEURORADIOLOGY

OCTOBER 2015
VOLUME 36
NUMBER 10
WWW.AJNR.ORG

THE JOURNAL OF DIAGNOSTIC AND
INTERVENTIONAL NEURORADIOLOGY

Cystic pituitary adenomas vs. Rathke cleft cysts
Hyperintense dentate and repeat gadolinium administration
Intrasaccular flow disrupters for aneurysm treatment

Official Journal ASNR • ASFNR • ASHNR • ASPNR • ASSR



AJNR

AMERICAN JOURNAL OF NEURORADIOLOGY

OCTOBER 2015
VOLUME 36
NUMBER 10
WWW.AJNR.ORG

Publication Preview at www.ajnr.org features articles released in advance of print. Visit www.ajnrblog.org to comment on AJNR content and chat with colleagues and AJNR's News Digest at <http://ajnrdigest.org> to read the stories behind the latest research in neuroimaging.

1793 **PERSPECTIVES** *S. Mukherjee*

EDITORIAL

1794 **We Are Not Alone** *S. Mirbagheri, et al.*

REVIEW ARTICLE

 1796 **Intracranial Aneurysms: Wall Motion Analysis for Prediction of Rupture** **INTERVENTIONAL**
A.E. Vanrossomme, et al.

RESEARCH PERSPECTIVES

 1803 **Hot Topics in Research: Preventive Neuroradiology in Brain Aging and Cognitive Decline** **ADULT BRAIN**
C.A. Raji, et al.

EDITORIAL PERSPECTIVES

1810 **Subspecialty Virtual Impact Factors within a Dedicated Neuroimaging Journal** *A.F. Choudhri, et al.*

SOCIAL MEDIA VIGNETTE

1814 **Social Media in Medical Education** *R.T. Fitzgerald, et al.*

GENERAL CONTENTS

  1816 **Accuracy of Parenchymal Cerebral Blood Flow Measurements Using Pseudocontinuous Arterial Spin-Labeling in Healthy Volunteers** **ADULT BRAIN**
K. Ambarki, et al.

  1822 **Gray Matter Volume Reduction Is Associated with Cognitive Impairment in Neuromyelitis Optica** **ADULT BRAIN**
Q. Wang, et al.

1830 **CTP in Transient Global Amnesia: A Single-Center Experience of 30 Patients** **ADULT BRAIN**
I.A. Meyer, et al.

 1834 **Timing-Invariant CT Angiography Derived from CT Perfusion Imaging in Acute Stroke: A Diagnostic Performance Study** **ADULT BRAIN**
INTERVENTIONAL *E.J. Smit, et al.*

 1839 **Significance of Development and Reversion of Collaterals on MRI in Early Neurologic Improvement and Long-Term Functional Outcome after Intravenous Thrombolysis for Ischemic Stroke** **ADULT BRAIN**
INTERVENTIONAL *M. Ichijo, et al.*

  1846 **Independent Poor Prognostic Factors for True Progression after Radiation Therapy and Concomitant Temozolomide in Patients with Glioblastoma: Subependymal Enhancement and Low ADC Value** **ADULT BRAIN**
R.-E. Yoo, et al.

-  1853 **MRI Tractography of Corticospinal Tract and Arcuate Fasciculus in High-Grade Gliomas Performed by Constrained Spherical Deconvolution: Qualitative and Quantitative Analysis** *E. Mormina, et al.* **ADULT BRAIN**
-  1859 **Hyperintense Dentate Nuclei on T1-Weighted MRI: Relation to Repeat Gadolinium Administration** *M.E. Adin, et al.* **ADULT BRAIN**
-  1866 **Differentiation between Cystic Pituitary Adenomas and Rathke Cleft Cysts: A Diagnostic Model Using MRI** *M. Park, et al.* **ADULT BRAIN**
-  1874 **Cognitive and White Matter Tract Differences in MS and Diffuse Neuropsychiatric Systemic Lupus Erythematosus** *B. Cesar, et al.* **ADULT BRAIN**
-  1884 **Cytotoxic Edema in Posterior Reversible Encephalopathy Syndrome: Correlation of MRI Features with Serum Albumin Levels** *B. Gao, et al.* **ADULT BRAIN**
-   1890 **Seizure Frequency Can Alter Brain Connectivity: Evidence from Resting-State fMRI** *R.D. Bharath, et al.* **FUNCTIONAL**
-    1899 **Meta-Analysis of CSF Diversion Procedures and Dural Venous Sinus Stenting in the Setting of Medically Refractory Idiopathic Intracranial Hypertension** *S.R. Satti, et al.* **INTERVENTIONAL**
-   1905 **Changing Clinical and Therapeutic Trends in Tentorial Dural Arteriovenous Fistulas: A Systematic Review** *D. Cannizzaro, et al.* **INTERVENTIONAL**
-   1912 **Progressive versus Nonprogressive Intracranial Dural Arteriovenous Fistulas: Characteristics and Outcomes** *S.W. Hetts, et al.* **INTERVENTIONAL**
-    1920 **Additional Value of Intra-Aneurysmal Hemodynamics in Discriminating Ruptured versus Unruptured Intracranial Aneurysms** *J.J. Schneiders, et al.* **INTERVENTIONAL**
-    1927 **Hemodynamic Differences in Intracranial Aneurysms before and after Rupture** *B.M.W. Cornelissen, et al.* **INTERVENTIONAL**
-  1934 **Stent-Assisted Coiling of Wide-Neck Intracranial Aneurysms Using Low-Profile LEO Baby Stents: Initial and Midterm Results** *K. Aydin, et al.* **INTERVENTIONAL**
-  1942 **Single-Layer WEBs: Intrasaccular Flow Disrupters for Aneurysm Treatment—Feasibility Results from a European Study** *J. Caroff, et al.* **INTERVENTIONAL**
-  1947 **Combined Use of Mechanical Thrombectomy with Angioplasty and Stenting for Acute Basilar Occlusions with Underlying Severe Intracranial Vertebrobasilar Stenosis: Preliminary Experience from a Single Chinese Center** *F. Gao, et al.* **INTERVENTIONAL**
- 1953 **Clopidogrel Resistance in Neurovascular Stenting: Correlations between Light Transmission Aggregometry, VerifyNow, and the Multiplate** *N. Flechtenmacher, et al.* **INTERVENTIONAL**
-  1959 **A Comparison of 4D DSA with 2D and 3D DSA in the Analysis of Normal Vascular Structures in a Canine Model** *C. Sandoval-Garcia, et al.* **INTERVENTIONAL**
- 1964 **Dynamic Angiography and Perfusion Imaging Using Flat Detector CT in the Angiography Suite: A Pilot Study in Patients with Acute Middle Cerebral Artery Occlusions** *T. Struffert, et al.* **INTERVENTIONAL**
-   1971 **MR Elastography Can Be Used to Measure Brain Stiffness Changes as a Result of Altered Cranial Venous Drainage During Jugular Compression** *A. Hatt, et al.* **EXTRACRANIAL VASCULAR
ADULT BRAIN**
-   1978 **Diagnostic Accuracy of 4 Commercially Available Semiautomatic Packages for Carotid Artery Stenosis Measurement on CTA** *J. Borst, et al.* **EXTRACRANIAL VASCULAR**
- 1988 **Improved Image Quality in Head and Neck CT Using a 3D Iterative Approach to Reduce Metal Artifact** *W. Wuest, et al.* **HEAD & NECK**

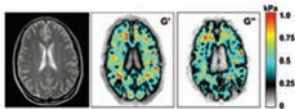
ONLINE FEATURES

LETTERS

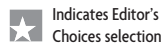
E65 Standardized Brain Tumor Imaging Protocol for Clinical Trials

G.V. Goldmacher, et al.

E67 ERRATUM



Region of interest outlined on the left in yellow, with the viscoelastic property maps for G' and G'' shown at the right, in kilopascals. Stiffer tissues are shown in warmer colors.



Indicates Editor's Choices selection



Indicates Fellows' Journal Club selection



Indicates open access to non-subscribers at www.ajnr.org



Indicates article with supplemental on-line table



Indicates article with supplemental on-line photo



Indicates article with supplemental on-line video



Evidence-Based Medicine Level 1



Evidence-Based Medicine Level 2



Title: *Otherworldly*

The word "alien" is frequently used to describe the amazing and unusual geologic landscape at Trona Pinnacles in California. One can recognize the pinnacles from numerous Hollywood movies that have been shot here including *Star Trek V: The Final Frontier* and *Planet of the Apes*. This landscape is dominated by numerous tufas (made of calcium carbonate), which were formed underwater 10,000 to 100,000 years ago in the Searles lake bed basin. This long-exposure image gives the streaky effect to the clouds over the tufas that enhances the unreal appearance of the surreal landscape.

Sugoto Mukherjee, Assistant Professor of Neuroradiology, Department of Radiology and Medical Imaging, University of Virginia Health System, Charlottesville, Virginia

We Are Not Alone

 S. Mirbagheri, K. Yousem, and  D.M. Yousem

While numerous recent US studies indicate a decline in medical malpractice suits across many medical specialties in the past decade, medicolegal concerns facing radiologists have conversely increased.¹⁻⁴ A 2013 report on diagnostic radiologists indicated that 30.9% (2600 of 8401) of all US radiologists have been sued.⁴ A subsequent 2014 study of neuroradiologists found that 449/904 (49.7%) American Society of Neuroradiology members had been sued, and of these, nearly 50% were sued multiple times.³ The level of concern over malpractice suits was reported as moderate in severity by practicing neuroradiologists in the United States, and most respondents, despite substantial contradictory evidence on the outcomes of malpractice trials favoring defendants, thought that the medicolegal system was weighted against them.³ We are scared.

Have we exported malpractice suits as readily as we have exported Kentucky Fried Chicken and Subway outlets across the globe? With the exception of the European Union, few countries outside the United States report malpractice lawsuit rates. We, therefore, created an informal survey, which was sent via e-mail to 96 neuroradiologists worldwide, representing 49 countries, to gain a sense of whether the American experience and anxiety over being sued are unique or universal. The survey results were sent to 60 officers of those national radiology society boards to confirm the data.

The data from this informal survey are presented in the Table.

<http://dx.doi.org/10.3174/ajnr.A4531>

The following are the 8 countries with the highest rates of radiologic malpractice suits, shown with average radiologist salaries and annual malpractice premium rates (presented respectively in parentheses):

- United States, government and private (46%, \$340,000, \$21,000)³
- Italy, government (50%, \$300,000, \$3000)
- Ireland, government (35%, \$235,000, \$8000)
- Germany, government and private (30%, \$300,000, \$1670)
- Spain, government (10%, \$65,000, \$550)
- Sweden, government (10%, \$130,000, \$550)
- Saudi Arabia, government (10%, \$300,000, \$8500)
- Chile, government (10%, \$120,000, \$1000).

The responses generally revealed a moderate level of concern about malpractice that is a global phenomenon. The impact on our collective practice of medicine varies from mild to moderate across countries. As to Americans' fear of malpractice lawyers, WE ARE NOT ALONE.

REFERENCES

1. Jena AB, Seabury S, Lakdawalla D, et al. **Malpractice risk according to physician specialty.** *N Engl J Med* 2011;365:629–36 CrossRef Medline
2. Mello MM, Studdert DM, Kachalia A. **The medical liability climate and prospects for reform.** *JAMA* 2014;312:2146–55 CrossRef Medline
3. Pereira NP, Lewin JS, Yousem KP, et al. **Attitudes about medical malpractice: an American Society of Neuroradiology survey.** *AJNR Am J Neuroradiol* 2014;35:638–43 CrossRef Medline
4. Baker SR, Whang JS, Luk L, et al. **The demography of medical malpractice suits against radiologists.** *Radiology* 2013;266:539–47 CrossRef Medline

Survey research data collected

Country	Average Radiologist Salary	Radiologist/ Practice Pays for Insurance	Average Insurance Premium	Radiology Malpractice Rate	Representative Radiologist Sued for Malpractice	Fear of Being Sued ^a	Practices Defensive Medicine ^a	Malpractice Affects Practice ^a
Africa								
Egypt	\$50,000	No	Null	5%	No	3	4	2
Americas								
Argentina	\$37,000	Yes	\$1200	5%	Yes	1	2	2
Brazil	\$130,000	Yes	\$560	1%	No	1	1	2
Canada	\$300,000	No	\$3000	5%	Yes	2	2	2
Chile	\$120,000	Yes	\$1000	10%	Yes	3	3	4
Guatemala	\$35,000	No	Null	1%	No	1	1	1
United States	\$340,000	Yes	\$21,000	46%	No	4	4	Null
Asia								
Indonesia	\$60,000	Yes	\$300	0%	Yes	5	5	4
Japan	\$100,000	Yes	\$70	1%	Yes	2	4	4
Malaysia	\$190,000	Yes	\$8400	0%	No	2	2	2
Philippines	\$21,000	No	Null	2%	No	2	1	2
Singapore	\$200,000	Yes	\$1750	5%	Yes	3	3	3
South Korea	\$200,000	Yes	\$5000	3%	Yes	2	1	2
Sri Lanka	\$12,000	No	Null	0%	No	2	3	2
Taiwan	\$120,000	Yes	\$600	3%	Yes	4	4	4
Australia/Oceania								
Australia	\$450,000	Yes	\$5000	5%	No	2	2	2
New Zealand	\$240,000	Yes	\$1300	0.1%	No	2	2	2
Europe								
Belgium	\$300,000	No	Null	1%	No	3	3	3
Bosnia/Herzegovina	\$17,000	No	Null	2%	No	3	2	2
Croatia	\$25,000	No	Null	2%	Null	2	3	2
Cyprus	\$84,000	Yes	Null	5%	Yes	2	2	3
Denmark	\$100,000	No	Null	10%	Yes	2	2	1
Finland	\$100,000	No	Null	1%	No	1	2	2
France	\$180,000	Yes	\$1360	5%	Yes	3	5	4
Germany	\$300,000	Yes	\$1670	30%	Yes	2	3	2
Greece	\$30,000	No	\$750	1%	No	2	3	2
Ireland	\$235,000	Yes	\$8000	35%	No	4	3	4
Italy	\$300,000	Yes	\$3000	50%	Yes	3	3	4
Lithuania	\$14,000	No	Null	3%	No	3	4	4
The Netherlands	\$165,000	No	Null	1%	No	2	1	2
Norway	\$200,000	Yes	\$70	1%	Yes	1	1	1
Portugal	\$150,000	Yes	\$2000	1%	Yes	2	3	3
Spain	\$65,000	Yes	\$550	10%	Yes	2	2	3
Sweden	\$130,000	No	\$550	10%	Yes	2	2	1
Turkey	\$40,000	Yes	\$300	3%	No	3	3.2	3.4
United Kingdom	\$175,000	Yes	\$1700	2%	No	2	2	2
Middle East								
Iran	\$36,000	Yes	\$400	4%	Yes	4	4	3
Iraq	\$19,200	No	Null	0%	Yes	3	4	5
Israel	\$12,000	Yes	\$330	2%	No	2	2	2
Lebanon	\$120,000	Yes	\$200	1%	Yes	4	4	3
Saudi Arabia	\$300,000	Yes	\$8500	10%	Yes	5	4	3

Note:—Null indicates no response/not applicable.

^a1 = never, 2 = rarely, 3 = sometimes, 4 = often, 5 = always.

Intracranial Aneurysms: Wall Motion Analysis for Prediction of Rupture

A.E. Vanrossomme, O.F. Eker, J.-P. Thiran, G.P. Courbebaisse, and K. Zouaoui Boudjeltia



ABSTRACT

SUMMARY: Intracranial aneurysms are a common pathologic condition with a potential severe complication: rupture. Effective treatment options exist, neurosurgical clipping and endovascular techniques, but guidelines for treatment are unclear and focus mainly on patient age, aneurysm size, and localization. New criteria to define the risk of rupture are needed to refine these guidelines. One potential candidate is aneurysm wall motion, known to be associated with rupture but difficult to detect and quantify. We review what is known about the association between aneurysm wall motion and rupture, which structural changes may explain wall motion patterns, and available imaging techniques able to analyze wall motion.

Intracranial aneurysms are abnormal focal dilations of the cerebral vasculature with a prevalence approximating 2%–5%.^{1–3} Complications associated with intracranial aneurysms include mass effect on adjacent structures—cranial nerves, brain stem, and so forth^{4,5}—and rupture, the most severe and frequent complication. The estimated incidence of this latter complication is approximately 1% per aneurysm and per year.^{3,6} With short-term mortality from rupture ranging from 35% to 50% and with almost half of survivors having moderate-to-severe long-term disability,^{6–8} neurosurgical and endovascular treatment could potentially be advocated for all unruptured intracranial aneurysms. However, these treatments are associated with approximate mortality rates of 3% and 2% and long-term disability rates of 15% and 5%,^{8–10} respectively, so their use remains controversial. Current guidelines for recommending treatment are based on aneu-

rysm size, location, and patient age.^{11,12} The Unruptured Cerebral Aneurysm Study suggests treating small aneurysms in locations associated with high risk of rupture and observing larger ones, up to 10 mm, in locations associated with a low risk of rupture (internal carotid, middle cerebral arteries).⁶ The Population, Hypertension, Age, Size of Aneurysm, Earlier Subarachnoid Hemorrhage from Another Aneurysm, and Site of Aneurysm (PHASES) score allows the calculation of a 5-year rupture risk, depending on multiple factors.¹³ This score allows a better assessment of the benefits versus risks of treatment in daily practice. However, for aneurysms considered at low risk of rupture, additional criteria are needed to discriminate those that may rupture and therefore should be treated and those that just require surveillance.

Aneurysm wall motion has been suggested to potentially provide predictive information on the risk of rupture. Numerous studies reported the detection of wall motion through different imaging techniques, such as phase-contrast MRA, transcranial power Doppler ultrasonography, 4D-CTA, and 3D rotational angiography (Table).^{14–33} Among these studies, some have reported an association between rupture status and wall motion.

Structurally speaking, the heterogeneous thickness of the aneurysm wall and its infiltration by inflammatory cells have also been reported³⁴; whether and how these factors can modify wall motion is not understood.

This article reviews the current knowledge of the association between aneurysm wall motion and rupture, the structural changes that could explain the wall motion patterns, and imaging techniques able to analyze wall motion.

From the Laboratory of Experimental Medicine (A.E.V., K.Z.B.), Université Libre de Bruxelles, Bruxelles, Belgium; Department of Interventional Neuroradiology (O.F.E.), Gui de Chaulliac Hospital, Centre Hospitalier Régional Universitaire Montpellier, Montpellier, France; Signal Processing Laboratory (J.-P.T.), Swiss Federal Institute of Technology Lausanne, Lausanne, Switzerland; Department of Radiology (J.-P.T.), University Hospital Center and University of Lausanne, Lausanne, Switzerland; and Centre de Recherche en Acquisition et Traitement de l'Image pour la Santé – Centre National de Recherche Scientifique – Unité Mixte de Recherche 5220 (G.P.C.), Institut National des Sciences Appliquées Lyon, Université de Lyon, Lyon, France.

A.E.V. is supported by the Fonds Erasme pour la Recherche Médicale, Université Libre de Bruxelles, Brussels, Belgium. This research received funding from the Thrombus Project (European Commission, 7th Framework Project) under grant agreement reference 269966.

Please address correspondence to Axel Vanrossomme, MD, Laboratoire de Médecine Expérimentale, Centre Hospitalier Universitaire André Vésale, Rue de Gozée 706, 6110 Montigny-le-Tilleul, Belgium; e-mail: avrossom@ulb.ac.be

Indicates open access to non-subscribers at www.ajnr.org

<http://dx.doi.org/10.3174/ajnr.A4310>

Previous work on aneurysm wall motion

Authors and Year of Publication	Imaging Modality	Study Object	No.	Aneurysms and Rupture Status	Frequency of Wall Motion Detection	Wall Motion Quantification
Wardlaw and Cannon (1996) ¹⁴	PD-US	In vivo	40	6U/31R	Not reported	Yes
Wardlaw et al (1998) ¹⁵	PD-US	In vivo	9	3U/9R	Not reported	Yes
Hoskins et al (1998) ¹⁶	PD-US	Phantom	NA	NA	NA	Yes
Kato et al (2004) ¹⁷	4D-CTA	In vivo	15	15U	10/15 ^a	No
Hayakawa et al (2005) ¹⁸	4D-CTA	In vivo	23	23R	4/23	No
Ishida et al (2005) ¹⁹	4D-CTA	In vivo	30	29U/5R	13/34	No
Yaghai et al (2007) ²⁰	4D-CTA	Phantom	NA	NA	NA	No
Krings et al (2009) ²¹	4D-CTA	In vivo	1	1U	1/1	Yes
Hayakawa et al (2011) ²²	4D-CTA	In vivo	51	53U/12R	24/65	No
Kuroda et al (2012) ²³	4D-CTA	In vivo	18	22U	Not reported	Yes
Firouzian et al (2013) ²⁴	4D-CTA	In vivo	14	19U	19/19	Yes
Hayakawa et al (2014) ²⁵	4D-CTA	In vivo	37	56U	20/56	No
Meyer et al (1993) ²⁶	PC-MRA	In vivo	15	10U/6R	15/16	Yes
Karmonik et al (2010) ²⁷	PC-MRA	In vivo	7	7U	7/7	Yes
Dempere-Marco et al (2006) ²⁸	3D RA	In vivo	3	3U	2/3	Yes
Oubel et al (2007) ²⁹	3D RA	In vivo	4	4U	4/4	Yes
Zhang et al (2009) ³⁰	3D RA	Phantom	NA	NA	NA	Yes
Zhang et al (2009) ³¹	3D RA	Phantom	NA	NA	NA	Yes
Oubel et al (2010) ³²	3D RA	In vivo	18	11U/7R	10/18	Yes
Zhang et al (2011) ³³	3D RA	Phantom + in vivo	2	2U	1/2	Yes

Note:—No. indicates number of patients; PD-US, power Doppler ultrasonography; PC-MRA, phase-contrast MR angiography; 3D RA, 3D rotational angiography; U, unruptured; R, ruptured; NA, not applicable.

^a Authors focused on bleb detection only. Pulsating bleb was found in 10 of the 15 cases.

ASSOCIATION BETWEEN WALL MOTION AND RUPTURE

Meyer et al²⁶ first suggested a possible association between wall motion patterns and aneurysm rupture. These authors retrospectively compared the flow dynamics of 6 ruptured and 10 unruptured aneurysms by using cine phase-contrast MRA. They observed that the volume of ruptured aneurysms increased more from diastole to systole than did the volume of unruptured aneurysms ($51.0 \pm 10.0\%$ versus $17.6 \pm 8.9\%$, $P < .005$), independent of aneurysm size. This study, however, is limited in its conclusions. First, it is outdated, because MR imaging has improved considerably during these past 2 decades, and cine phase-contrast MRA would not be the technique of choice today. Moreover the postprocessing technique is also outdated with regard to current standards. Second, phase-contrast techniques are prone to flow artifacts and might, therefore, mistake slow flow for wall motion. Third, this study was based on a small number of patients and was retrospective with regard to rupture status. Therefore, caution is needed in the interpretation of its results.

Using 4D-CTA, Hayakawa et al¹⁸ observed aneurysm wall motion in 4 of 23 patients with ruptured aneurysms. During surgical clipping performed in 2 of these 4 patients, they observed that the rupture site matched the position of the wall motion detected by 4D-CTA. Ishida et al¹⁹ studied 30 patients by using the same 4D-CTA technique and observed a pulsating bleb in 7 of 29 unruptured aneurysms and in 2 of 5 ruptured ones. Again, during surgical clipping performed in these 2 ruptured aneurysms, these authors observed that the rupture site matched the position of the pulsating bleb. These 2 studies are interesting but focused on the detection of blebs and their motion. They showed some ability to detect the rupture site when blebs ruptured but did not investigate the relation between motion and rupture. Other limitations include the following: the limited number of patients, especially in the ruptured group of the study of Ishida et al¹⁹; the subjective

assessment of the rupture point by the neurosurgeon not relying on precise spatial correlation; and apparent motion artifacts of immobile bone structures, possibly due to gantry rotation as emphasized by Matsumoto et al³⁵ in a letter to the authors. Ishida et al replied that more work was needed to validate 4D-CTA for aneurysm dynamics visualization and that this work was just a step along the path.

Oubel et al³² introduced the concept of differential pulsation, defined as the aneurysm wall motion corrected for the wall motion of the parent artery and its diameter. Using high-frame-rate DSA, these authors measured aneurysm wall motion in 18 patients with 7 ruptured aneurysms and reported a statistically significant association between this differential pulsation and the rupture status. Kuroda et al²³ found no significant difference in cardiac cycle-related volume changes between unruptured aneurysms and normal arteries assessed by 4D-CTA in 18 patients, suggesting that the differential pulsation may be a more useful indicator than the wall motion magnitude or the cardiac cycle-related volume changes to discriminate aneurysms at high-versus-low risk of rupture.

These studies suggest a possible association between aneurysm wall motion and rupture, but they share 2 limitations: the small numbers of patients studied and the aneurysms being considered retrospectively after rupture instead of prospectively considering those likely to rupture. A recent study indeed showed that aneurysm characteristics can be different before and after rupture and suggests caution with the interpretation of such results.³⁶ These limitations support the need for a larger study, prospective with regard to rupture status, to test whether the outcome (rupture, growth of the aneurysm, and so forth) depends on the type of wall motion. Ideally, unruptured aneurysms should be followed without treatment until they rupture, but this plan would be unethical except with patients who refuse treatment.

ASSOCIATION BETWEEN ANEURYSM WALL CHANGES AND RUPTURE

The differences in wall motion between ruptured and unruptured aneurysms suggest differences in wall architecture or composition, including inflammatory and atherosclerotic changes and structural matrix proteins.

Wall Architecture

The aneurysm wall is histologically characterized by a loss or disruption of internal elastic lamina, intimal hyperplasia, disorganization of smooth-muscle fibers, loss of cell components, and infiltration by inflammatory cells.^{34,37-41} Disruption of the internal elastic lamina seems to occur early during aneurysm formation,⁴²⁻⁴⁶ whereas other changes (eg, de-endothelialization, luminal thrombosis, smooth-muscle cell proliferation, T-cell and macrophage infiltration) are associated with rupture.³⁴ Frösen et al³⁴ identified 4 wall types associated with rupture: type A with an endothelialized wall with linearly organized smooth-muscle cells; type B with a thickened wall with disorganized smooth-muscle cells; type C with a hypocellular wall with either intimal hyperplasia or organizing luminal thrombus; and type D with an extremely thin, thrombosis-lined hypocellular wall. The rupture rate increased from type A to D. These authors suggested that these 4 types are most likely consecutive stages of wall degeneration leading to rupture. In addition, there was usually a type A-to-D gradient from the neck to the fundus.³⁴ This illustrates the heterogeneity of the wall, which can be seen as a global vascular disease with focal progression leading to rupture. Whether these wall types relate to wall motion modification is not fully understood. However, Costalat et al⁴⁷ described 3 kinds of aneurysm wall biomechanical properties—rigid, intermediate, and soft—the latter was only seen in ruptured or pruruptured aneurysms. This latter study supports the hypothesis of a motion of greater magnitude in ruptured and pruruptured aneurysms. Moreover, the elastic modulus at the aneurysm fundus being 30%–50% lower than that at the neck has been described; the fundus wall is therefore more distensible.⁴⁸

Inflammatory and Atherosclerotic Changes in the Aneurysm Wall

Inflammatory changes in the aneurysm wall are characterized by leukocyte infiltration, leading to smooth-muscle cell proliferation and fibrosis.^{34,39} Smooth-muscle cells and macrophages produce matrix metalloproteinases, mostly matrix metalloproteinase-1, -2, and -9, which degrade extracellular matrix components. Early on, matrix metalloproteinases are balanced by tissue inhibitor of metalloproteinase-1 and -2, but not in late-stage aneurysms, in which the expression of matrix metalloproteinases is increased; this change leads to extracellular matrix damage, growth of the aneurysm, and rupture.⁴⁹⁻⁵¹

Atherosclerotic changes seem to be present in most aneurysms, and their extent correlates with aneurysm growth. Small aneurysms have atherosclerotic lesions characterized by intimal thickening due to proliferating smooth-muscle cells with few macrophages and lymphocytes, whereas large aneurysms have more advanced lesions with more cellular infiltrates and mature smooth-muscle cells.^{52,53} In addition, aneurysm smooth-muscle cells acquire a dedifferentiated

phenotype similar to that in smooth-muscle cells in atherosclerotic plaques.⁵⁴ Most interesting, atherosclerosis is associated with chronic inflammation, which might explain, at least in part, the inflammatory changes.⁵⁵⁻⁵⁷

Structural Matrix Proteins

Collagen. Collagen content is lower in aneurysm walls than in normal arteries. In addition, the number of cross-links between collagen fibers is lower, and collagenase and elastase activities are higher in ruptured aneurysms than in unruptured ones. These comparisons raise the hypothesis that elevated collagenolytic and elastolytic activities could be predisposing factors for rupture.⁵⁸ Additionally, while expression of collagen III and IV is lower in all (unruptured and ruptured) aneurysms than in normal arteries, collagen IV expression is lower in ruptured aneurysms than in unruptured ones.³⁸

Laminin and Fibronectin. Laminin and fibronectin are thought to maintain the structural integrity of the vessel wall by anchoring endothelial cells to the internal elastic lamina and smooth-muscle layers. Laminin is more cohesive than fibronectin and is predominant in mature vessels, whereas fibronectin is predominant in immature ones. While the expression of laminin is lower in both unruptured and ruptured aneurysms than in normal arteries, the expression of fibronectin is only higher in ruptured aneurysms, raising the hypothesis that an increased fibronectin-to-laminin ratio might contribute to rupture.³⁸

Alpha-Smooth-Muscle Actin. Alpha-smooth-muscle actin expression is lower in aneurysm walls than in normal arteries and even lower in ruptured aneurysms than in unruptured ones. In addition, and in contrast to normal arteries and unruptured aneurysms, the myocytes in ruptured aneurysms are loose and no longer arranged in tightly compacted functional bands.³⁸

Changes in structural matrix proteins raise the hypothesis that collagen III, collagen IV, and α -smooth-muscle actin are involved in aneurysm formation and that an increase in the fibronectin-to-laminin ratio could contribute to rupture. Because the expression of collagen IV and laminin is maximal in mature vessels whereas fibronectin is usually found in immature ones, aneurysm formation and rupture seem to be associated with an angiogenically immature vessel wall.³⁸ It was hypothesized that an increase in immature collagen, lower collagen content, or a less structured wall could lead to a more distensible behavior.⁴⁸

IMAGING ANEURYSM WALL MOTION

The imaging of wall motion has multiple challenges. First, the motion itself is 3-fold: the global pulsation of the aneurysm, potential movements of focal parts of the wall (eg, blebs), and global cerebral vasculature motion during the cardiac cycle.^{18,19,59,60} Second, the magnitude of motion is small, and the timeframe is short; thus, techniques with high spatial and temporal resolutions are needed. Third, depending on the technique, artifacts can impair the results and they must be kept to a minimum. The radiation dose must also be considered when using dynamic x-ray-based imaging modalities. Six imaging techniques can detect aneurysm wall motion, but only 4 (Table) are used in living humans. The other 2 are based on laser displacement sensor and flat

panel volumetric CT. Laser displacement sensor has been used to detect aneurysm wall motion of an ex vivo animal model and a silicone phantom in 2 studies.^{61,62} Flat panel volumetric CT has been used to image posttreatment rabbit aneurysm pulsation, but though promising, this tool has never been used to image aneurysm wall motion in humans.^{63,64}

The 4 techniques applied in living humans are transcranial power Doppler ultrasonography, phase-contrast MRA, 3D rotational angiography, and 4D-CTA.

Transcranial Power Doppler Ultrasonography

Transcranial power Doppler ultrasonography was developed as a tool to image blood flow in intracranial vessels. With a higher sensitivity to blood flow than color Doppler, power Doppler is more appropriate for small-vessel imaging. This technique was used by the same group of investigators to detect aneurysm pulsation in 2 in vivo studies and 1 in vitro study. The pulsation was quantified by comparing the aneurysm cross-sectional area between systole and diastole, measured by using the sonography device algorithm.¹⁴⁻¹⁶ Aneurysm pulsation was detected in both in vivo studies, but its magnitude was much larger than that usually seen with other techniques and during neurosurgery. The in vitro study revealed that pulsation as seen on power Doppler depended on the device settings, introducing dependency on the operator and raising concerns about its reproducibility.¹⁶ Moreover, some of the observed pulsation may be related to very slow intra-aneurysmal blood flow during part of the cardiac cycle, leading to the absence of a Doppler signal and hence exaggerating apparent wall motion.

Other limitations of transcranial power Doppler ultrasonography are limited acoustic windows due to bone structures; additionally, 20% of patients have poor or absent acoustic windows⁶⁵ and limited spatial resolution, especially with low-frequency transducers that are required to image deep arteries. Temporal and spatial resolutions are indeed dependent on the frequency of the transducer and the depth of the structure of interest. Axial resolution is half the spatial pulse length, which is the product of the number of cycles in a pulse and the wavelength. Lateral resolution depends on the wavelength and the width of the transducer and can be improved by focusing ultrasounds; temporal resolution of Doppler depends on the pulse length, the depth of the structure of interest, and the size of the color box.⁶⁶ Since these studies were published, progress has been made in transcranial Doppler imaging, which now shows good agreement with CTA as demonstrated for intracranial vessel localization.⁶⁷ Transcranial power Doppler ultrasonography could, therefore, be re-evaluated for intracranial aneurysm imaging.

Cine Phase-Contrast MRA

Phase-contrast MRA is based on the measurement of the phase shift of blood flowing through a magnetic field gradient; the sign of the phase shift is determined by the direction of the flow. Because phase-contrast sequences are only sensitive to a given range of blood velocities that must be determined a priori, the optimal sequence must be tuned for each patient. Nevertheless, even with optimal velocity-encoding, the signal within the aneurysm could be impaired because of the highly heterogeneous

intracranial flow. Although this technique has the advantage of not exposing the patient to ionizing radiation or contrast material, it is limited by a low sensitivity for motion depiction. Coupled with gadolinium-enhanced MRA, this technique provides information on morphologic and flow characteristics, while the temporal resolution of MRA alone is insufficient to assess aneurysm wall motion.⁶⁸ Two studies showed that aneurysm wall motion could be detected and quantified with this technique. Quantification of motion was achieved either by volume quantification for each phase²⁶ or by measuring the distance between the aneurysm wall and the center of the aneurysm to avoid taking global artery motion into account.²⁷ Meyer et al²⁶ showed that volume modification during the cardiac cycle was larger in ruptured aneurysms than in unruptured ones. Focusing on unruptured aneurysms, Karmonik et al²⁷ showed that in addition to outward and inward wall displacement during the cardiac cycle, there was local heterogeneity within the aneurysm wall, consisting of out-of-phase movements of some parts compared with others.

Phase-contrast MRA has several limitations. First, because of the lack of standardized blood-velocity values, acquisition time is too long for clinical use. Second, its spatial resolution is low but could be improved with high-field MR imaging scanners.²⁷ Third, motion (of cerebral arteries during the cardiac cycle or of the patient) and flow artifacts from out-of-range velocities can decrease image quality. The current best techniques are probably conventional gradient echo-based cine imaging sequences (eg, gradient-recalled acquisition in steady state [GRASS], true fast imaging with steady-state precession [trueFISP], true spin tagging with alternating radiofrequency [trueSTAR]).^{69,70} These methods have high spatial resolution (up to 1 mm³ voxels or 0.86 × 0.86 × 2 mm³ voxels) and high temporal resolution (50–100) and have a higher SNR than phase-contrast sequences, making them promising tools to image wall motion. Moreover, increasing the magnetic field strength from 1.5T to 3T or using a gadolinium-based contrast agent could enhance SNR as reported for cardiac investigations.⁷¹ Usual dynamic contrast-enhanced MRA techniques that rely on parallel imaging, partial *k*-space sampling, or half-Fourier would not be appropriate for wall motion imaging because the temporal resolutions are not sufficient (500–1500 ms).⁷²

3D Rotational Angiography

3D rotational angiography is an x-ray-based projection imaging technique in which both the source and the detector rotate around approximately 200°. In a clinical setting, this technique is based on acquisition of a sequence of 2D images that are used to reconstruct an isotropic 3D image, but 2D images can also be used to retrieve dynamic information and detect wall motion. Using this technique, several authors succeeded in detecting and quantifying wall motion.²⁸⁻³³ Quantification was achieved through either an optical flow method for image registration or, later, free-form deformations with B-spline interpolation.^{29,31,32} In 3 articles reporting the data from 18 patients, Dempere-Marco et al²⁸ and Oubel et al,^{29,32} demonstrated the ability to detect and quantify wall motion with this technique. During the same period, Zhang et al^{30,31,33} applied this technique on in silico models,

on in vitro samples, and in vivo, but only in 2 patients. This technique has high spatial and temporal resolutions (respectively, 0.2 mm and from 35 to 165 ms, depending on vessel configuration).⁷³ However, this technique is invasive, exposes the patient to ionizing radiation, and requires injection of iodinated contrast material. It is also challenging to ensure homogeneous contrast distribution inside the aneurysm during the acquisition. Because 3D rotational angiography is the most invasive technique among the 4 discussed in this review, it should probably be reserved for a subset of selected patients that still needs to be defined (eg, patients already programmed for a catheter-injected angiography could benefit from this dynamic technique).

4D-CTA

Faster gantry rotation and multidetector rows are major developments in CT technology, which have led to increased spatial and temporal resolutions. In addition, with an effective scan width of >20 and ≤160 mm, scanners with ≥64 detector rows allow continuous acquisition without table movement and subsequent 4D reconstructions. Several studies used 4D-CTA and reported successful detection of aneurysm wall motion in phantoms and in patients. Although most studies were based on electrocardiogram-gated 4D-CTA,^{17-19,22-25} some reported that pulsatility imaging was also possible without gating.^{20,21} The analysis of wall motion was either qualitative with visual assessment by multiple readers or quantitative. For quantitative analysis, some authors chose to convert the original matrix into an easier-to-process “black and white” matrix. Hounsfield units that were out of a predetermined range (approximately 100–900 HU) were substituted for zero, whereas Hounsfield units within the range were substituted for 1. This matrix could then be analyzed through segmentation of the aneurysm sac and the calculation of the aneurysm volume for each frame.²³ Other authors used nonrigid B-spline registration to obtain a motion-compensated multiphase 3D image and a deformation field for each phase. The deformation field could then be combined with aneurysm segmentation to determine wall deformation.²⁴ Two studies investigated the motion of cerebral arteries and showed their 2-type motion: pulsation consisting of changes in vessel volume and a positional change of the whole vessel during the cardiac cycle.^{59,60} Moreover, the direction and the amplitude of these movements differed from one artery to another in the same subject.⁵⁹

4D-CTA has several advantages. First, scanners are available in almost all hospitals in developed countries. Second, the duration of the examination is very short because its acquisition lasts just a few seconds. Third, while of the same order of magnitude as the analyzed motion, its spatial resolution is high (0.25 mm for high-resolution CT scans and from 0.60 to 0.80 mm for standard CT scans)⁷⁴ and its temporal resolution ranges between 75 and 150 ms.⁷⁵ Nevertheless, this technique has limitations. First, although rarely addressed in the clinical studies discussed here, the radiation dose for dynamic acquisitions can be very high. Second, intravenous iodine contrast injection is needed. Third, images can be impaired by reconstruction artifacts that are reduced with multidetector row CT scanners.

To reduce these reconstruction artifacts, one could analyze wall motion by using the raw data (ie, the sinogram). The

registration technique used with 3D rotational angiography is extended and adapted to 4D-CTA.^{32,33} Using the sinogram instead of reconstructed images would improve both spatial and temporal resolution appropriate for detecting small-amplitude motion.^{76,77}

CONCLUSIONS

Guidelines for treatment of intracranial aneurysms need to include better tools to appropriately predict aneurysm rupture. The PHASES score provides useful information about the outcome, but other tools might help refine the rupture risk. The analysis of aneurysm wall motion seems promising for this purpose. Multiple retrospective clinical studies have shown an association between wall motion and rupture status, but there is a lack of prospective studies to assess this relationship. The hypothesis that a difference in wall motion patterns is associated with an increased risk of rupture is also theoretically supported by the demonstration of histologic alterations of the aneurysm wall, most notably thinning and loss of mural cells in the most advanced stages leading to a more distensible behavior predominantly at the fundus. This could explain why the largest motion amplitude is usually seen at the fundus. Up to now, no study has investigated the relationship between histologic changes and biomechanical properties of the wall.

With regard to imaging modalities, there is no consensus on the best available technique, but 3D rotational angiography and 4D-CTA seem the most promising because they are the least subject to flow artifacts; however, the radiation dose should not be neglected, especially in young patients.⁷⁸ For patients who need conventional angiography anyway, dynamic 3D rotational angiography would be the best available technique. Finally, the lack of standardization in imaging protocols and reconstruction algorithms should be resolved to ensure that research data are comparable.

ACKNOWLEDGMENTS

The authors thank Pierre Alain Gevenois, MD, PhD, for his invaluable assistance in preparing the manuscript and Nathalie Nagy, MD, for her valuable advice on the histology of intracranial aneurysms.

Disclosures: Axel Vanrussomme—RELATED: Grant: My research activities are supported entirely by the “Fonds Erasme pour le recherche médicale” from October 2013 to September 2015. Jean-Philippe Thiran—RELATED: Grant: European Union-funded Thrombus Project financed this work.* Karim Zouaoui Boudjeltia—RELATED: Grant: European PF7 Grant: Thrombus Project.* *Money paid to the institution.

REFERENCES

1. Vlak MH, Algra A, Brandenburg R, et al. **Prevalence of unruptured intracranial aneurysms, with emphasis on sex, age, comorbidity, country, and time period: a systematic review and meta-analysis.** *Lancet Neurol* 2011;10:626–36
2. Vega C, Kwoon JV, Lavine SD. **Intracranial aneurysms: current evidence and clinical practice.** *Am Fam Physician* 2002;66:601–08
3. Rinkel GJ, Djibuti M, Algra A, et al. **Prevalence and risk of rupture of intracranial aneurysms: a systematic review.** *Stroke* 1998;29:251–56
4. Hassan T, Hamimi A. **Successful endovascular management of brain aneurysms presenting with mass effect and cranial nerve palsy.** *Neurosurg Rev* 2013;36:87–97; discussion 97
5. van Rooij WJ, Sluzewski M. **Unruptured large and giant carotid ar-**

- tery aneurysms presenting with cranial nerve palsy: comparison of clinical recovery after selective aneurysm coiling and therapeutic carotid artery occlusion. *AJNR Am J Neuroradiol* 2008;29:997–1002
6. Morita A, Kirino T, Hashi K, et al. The natural course of unruptured cerebral aneurysms in a Japanese cohort. *N Engl J Med* 2012;366:2474–82
 7. Morita A, Fujiwara S, Hashi K, et al. Risk of rupture associated with intact cerebral aneurysms in the Japanese population: a systematic review of the literature from Japan. *J Neurosurg* 2005;102:601–06
 8. International Study of Unruptured Intracranial Aneurysms Investigators. Unruptured intracranial aneurysms: risk of rupture and risks of surgical intervention. *N Engl J Med* 1998;339:1725–33
 9. Pierot L, Barbe C, Spelle L; ATENA investigators. Endovascular treatment of very small unruptured aneurysms: rate of procedural complications, clinical outcome, and anatomical results. *Stroke* 2010;41:2855–59
 10. McDonald JS, McDonald RJ, Fan J, et al. Comparative effectiveness of unruptured cerebral aneurysm therapies: propensity score analysis of clipping versus coiling. *Stroke* 2013;44:988–94
 11. Komotar RJ, Mocco J, Solomon RA. Guidelines for the surgical treatment of unruptured intracranial aneurysms: the first annual J Lawrence Pool Memorial Research Symposium—controversies in the management of cerebral aneurysms. *Neurosurgery* 2008;62:183–93; discussion 193–94
 12. Steiner T, Juvela S, Unterberg A, et al; European Stroke Organization. European Stroke Organization guidelines for the management of intracranial aneurysms and subarachnoid haemorrhage. *Cerebrovasc Dis* 2013;35:93–112
 13. Greving JP, Wermer MJ, Brown RD Jr, et al. Development of the PHASES score for prediction of risk of rupture of intracranial aneurysms: a pooled analysis of six prospective cohort studies. *Lancet Neurol* 2014;13:59–66
 14. Wardlaw JM, Cannon JC. Color transcranial “power” Doppler ultrasound of intracranial aneurysms. *J Neurosurg* 1996;84:459–61
 15. Wardlaw JM, Cannon J, Statham PF, et al. Does the size of intracranial aneurysms change with intracranial pressure? Observations based on color “power” transcranial Doppler ultrasound. *J Neurosurg* 1998;88:846–50
 16. Hoskins PR, Pratts J, Wardlaw J. A flow model of cerebral aneurysms for use with power Doppler studies. *Br J Radiol* 1998;71:76–80
 17. Kato Y, Hayakawa M, Sano H, et al. Prediction of impending rupture in aneurysms using 4D-CTA: histopathological verification of a real-time minimally invasive tool in unruptured aneurysms. *Minim Invasive Neurosurg* 2004;47:131–35
 18. Hayakawa M, Katada K, Anno H, et al. CT angiography with electrocardiographically gated reconstruction for visualizing pulsation of intracranial aneurysms: identification of aneurysmal protuberance presumably associated with wall thinning. *AJNR Am J Neuroradiol* 2005;26:1366–69
 19. Ishida F, Ogawa H, Simizu T, et al. Visualizing the dynamics of cerebral aneurysms with four-dimensional computed tomographic angiography. *Neurosurgery* 2005;57:460–71; discussion 460–71
 20. Yaghmai V, Rohany M, Shaibani A, et al. Pulsatility imaging of saccular aneurysm model by 64-slice CT with dynamic multiscan technique. *J Vasc Interv Radiol* 2007;18:785–88
 21. Krings T, Willems P, Barfett J, et al. Pulsatility of an intracavernous aneurysm demonstrated by dynamic 320-detector row CTA at high temporal resolution. *Cent Eur Neurosurg* 2009;70:214–18
 22. Hayakawa M, Maeda S, Sadato A, et al. Detection of pulsation in ruptured and unruptured cerebral aneurysms by electrocardiographically gated 3-dimensional computed tomographic angiography with a 320-row area detector computed tomography and evaluation of its clinical usefulness. *Neurosurgery* 2011;69:843–51; discussion 851
 23. Kuroda J, Kinoshita M, Tanaka H, et al. Cardiac cycle-related volume change in unruptured cerebral aneurysms: a detailed volume quantification study using 4-dimensional CT angiography. *Stroke* 2012;43:61–66
 24. Firouzian A, Manniesing R, Metz CT, et al. Quantification of intracranial aneurysm morphodynamics from ECG-gated CT angiography. *Acad Radiol* 2013;20:52–58
 25. Hayakawa M, Tanaka T, Sadato A, et al. Detection of pulsation in unruptured cerebral aneurysms by ECG-gated 3D-CT angiography (4D-CTA) with 320-row area detector CT (ADCT) and follow-up evaluation results: assessment based on heart rate at the time of scanning. *Clin Neuroradiol* 2014;24:145–50
 26. Meyer FB, Huston J 3rd, Riederer SS. Pulsatile increases in aneurysm size determined by cine phase-contrast MR angiography. *J Neurosurg* 1993;78:879–83
 27. Karmonik C, Diaz O, Grossman R, et al. In-vivo quantification of wall motion in cerebral aneurysms from 2D cine phase contrast magnetic resonance images. *Rofa* 2010;182:140–50
 28. Dempere-Marco L, Oubel E, Castro M, et al. CFD analysis incorporating the influence of wall motion: application to intracranial aneurysms. In: *Proceedings of the 9th International Conference of the Medical Image Computing and Computer-Assisted Intervention Society*, Copenhagen, Denmark. October 1–6, 2006
 29. Oubel E, De Craene M, Putman CM, et al. Analysis of intracranial aneurysm wall motion and its effects on hemodynamic patterns. In: *Proceedings of the Society of Photo-Optical Instrumentation Engineers, Medical Imaging: Physiology, Function, and Structure from Medical Images*, San Diego, California. February 17–22, 2007
 30. Zhang C, De Craene M, Villa-Uriol MC, et al. Estimating continuous 4D wall motion of cerebral aneurysms from 3D rotational angiography. In: *Proceedings of the 12th International Conference of the Medical Image Computing and Computer-Assisted Society*, London, United Kingdom. September 20–24, 2009
 31. Zhang C, Villa-Uriol MC, De Craene M, et al. Morphodynamic analysis of cerebral aneurysm pulsation from time-resolved rotational angiography. *IEEE Trans Med Imaging* 2009;28:1105–16
 32. Oubel E, Cebral JR, De Craene M, et al. Wall motion estimation in intracranial aneurysms. *Physiol Meas* 2010;31:1119–35
 33. Zhang C, Villa-Uriol MC, De Craene M, et al. Dynamic estimation of three-dimensional cerebrovascular deformation from rotational angiography. *Med Phys* 2011;38:1294–306
 34. Frösen J, Piippo A, Paetau A, et al. Remodeling of saccular cerebral artery aneurysm wall is associated with rupture: histological analysis of 24 unruptured and 42 ruptured cases. *Stroke* 2004;35:2287–93
 35. Matsumoto M, Sasaki T, Suzuki K, et al. Visualizing the dynamics of cerebral aneurysms with four-dimensional computed tomographic angiography. *Neurosurgery* 2006;58:E1003; author reply E1003
 36. Schneiders JJ, Marquering HA, van den Berg R, et al. Rupture-associated changes of cerebral aneurysm geometry: high-resolution 3D imaging before and after rupture. *AJNR Am J Neuroradiol* 2014;35:1358–62
 37. Abruzzo T, Shengelaia GG, Dawson RC 3rd, et al. Histologic and morphologic comparison of experimental aneurysms with human intracranial aneurysms. *AJNR Am J Neuroradiol* 1998;19:1309–14
 38. Kilic T, Sohrabifar M, Kurtkaya O, et al. Expression of structural proteins and angiogenic factors in normal arterial and unruptured and ruptured aneurysm walls. *Neurosurgery* 2005;57:997–1007; discussion 997–1007
 39. Chyatte D, Bruno G, Desai S, et al. Inflammation and intracranial aneurysms. *Neurosurgery* 1999;45:1137–46; discussion 1146–47
 40. Scanarini M, Mingrino S, Giordano R, et al. Histological and ultrastructural study of intracranial saccular aneurysmal wall. *Acta Neurochir (Wien)* 1978;43:171–82
 41. Schlote W, Gaus C. Histologic aspects from ruptured and nonruptured aneurysms. *Neurol Res* 1994;16:59–62
 42. Kim C, Cervós-Navarro J, Kikuchi H, et al. Degenerative changes in the internal elastic lamina relating to the development of saccular cerebral aneurysms in rats. *Acta Neurochir (Wien)* 1993;121:76–81
 43. Kim C, Kikuchi H, Hashimoto N, et al. Involvement of internal elas-

- tic lamina in development of induced cerebral aneurysms in rats. *Stroke* 1988;19:507–11
44. Hazama F, Hashimoto N. An animal model of cerebral aneurysms. *Neuropathol Appl Neurobiol* 1987;13:77–90
 45. Yamazoe N, Hashimoto N, Kikuchi H, et al. Elastic skeleton of intracranial cerebral aneurysms in rats. *Stroke* 1990;21:1722–26
 46. Cawley CM, Dawson RC, Shengelaia G, et al. Arterial saccular aneurysm model in the rabbit. *AJNR Am J Neuroradiol* 1996;17:1761–66
 47. Costalat V, Sanchez M, Ambard D, et al. Biomechanical wall properties of human intracranial aneurysms resected following surgical clipping (IRRA Project). *J Biomech* 2011;44:2685–91
 48. Steiger HJ, Aaslid R, Keller S, et al. Strength, elasticity and viscoelastic properties of cerebral aneurysms. *Heart Vessels* 1989;5:41–46
 49. Aoki T, Kataoka H, Moriwaki T, et al. Role of TIMP-1 and TIMP-2 in the progression of cerebral aneurysms. *Stroke* 2007;38:2337–45
 50. Aoki T, Kataoka H, Morimoto M, et al. Macrophage-derived matrix metalloproteinase-2 and -9 promote the progression of cerebral aneurysms in rats. *Stroke* 2007;38:162–69
 51. Ishibashi R, Aoki T, Nishimura M, et al. Contribution of mast cells to cerebral aneurysm formation. *Curr Neurovasc Res* 2010;7:113–24
 52. Killer-Oberpfalzer M, Aichholzer M, Weis S, et al. Histological analysis of clipped human intracranial aneurysms and parent arteries with short-term follow-up. *Cardiovasc Pathol* 2012;21:299–306
 53. Kosierkiewicz TA, Factor SM, Dickson DW. Immunocytochemical studies of atherosclerotic lesions of cerebral berry aneurysms. *J Neuropathol Exp Neurol* 1994;53:399–406
 54. Coen M, Burkhardt K, Bijlenga P, et al. Smooth muscle cells of human intracranial aneurysms assume phenotypic features similar to those of the atherosclerotic plaque. *Cardiovasc Pathol* 2013;22:339–44
 55. Ross R. Atherosclerosis—an inflammatory disease. *N Engl J Med* 1999;340:115–26
 56. Dessi M, Noce A, Bertucci P, et al. Atherosclerosis, dyslipidemia, and inflammation: the significant role of polyunsaturated fatty acids. *ISRN Inflammation* 2013; <http://dx.doi.org/10.1155/2013/191823>. Accessed October 3, 2013
 57. Krychtiuk KA, Kastl SP, Speidl WS, et al. Inflammation and coagulation in atherosclerosis. *Hamostaseologie* 2013;33:269–82
 58. Gaetani P, Tartara F, Grazioli V, et al. Collagen cross-linkage, elastolytic and collagenolytic activities in cerebral aneurysms: a preliminary investigation. *Life Sci* 1998;63:285–92
 59. Umeda Y, Ishida F, Hamada K, et al. Novel dynamic four-dimensional CT angiography revealing 2-type motions of cerebral arteries. *Stroke* 2011;42:815–18
 60. Nishida T, Kinoshita M, Tanaka H, et al. Quantification of cerebral artery motion during the cardiac cycle. *AJNR Am J Neuroradiol* 2011;32:E206–08
 61. Boecher-Schwarz HG, Ringel K, Kopacz L, et al. Ex vivo study of the physical effect of coils on pressure and flow dynamics in experimental aneurysms. *AJNR Am J Neuroradiol* 2000;21:1532–36
 62. Ueno J, Matsuo T, Sugiyama K, et al. Mechanism underlying the prevention of aneurysmal rupture by coil embolization. *J Med Dent Sci* 2002;49:135–41
 63. Mitha AP, Reichardt B, Grasruck M, et al. Dynamic imaging of a model of intracranial saccular aneurysms using ultra-high-resolution flat-panel volumetric computed tomography: laboratory investigation. *J Neurosurg* 2009;111:947–57
 64. Gupta R, Cheung AC, Bartling SH, et al. Flat-panel volume CT: fundamental principles, technology, and applications. *Radiographics* 2008;28:2009–22
 65. Topcuoglu MA. Transcranial Doppler ultrasound in neurovascular diseases: diagnostic and therapeutic aspects. *J Neurochem* 2012; 123(suppl 2):39–51
 66. Ng A, Swanevelde J. Resolution in ultrasound imaging. *Contin Educ Anaesth Crit Care Pain* 2011;11:186–92
 67. Barlinn K, Zivanovic Z, Zhao L, et al. Intracranial vessel localization with power motion Doppler (PMD-TCD) compared with CT angiography in patients with acute ischaemic stroke. *Int J Stroke* 2013;8:398–402
 68. Weishaupt D, Koechli VD, Marincek B. *How does MRI work? An Introduction to the Physics and Function of Magnetic Resonance Imaging*. 2nd ed. Berlin: Springer-Verlag; 2006:78–81
 69. Tsuruda JS, Halbach VV, Higashida RT, et al. MR evaluation of large intracranial aneurysms using cine low flip angle gradient-refocused imaging. *AJR Am J Roentgenol* 1988;151:153–62
 70. Yan L, Wang S, Zhuo Y, et al. Unenhanced dynamic MR angiography: high spatial and temporal resolution by using true FISP-based spin tagging with alternating radiofrequency. *Radiology* 2010;256:270–79
 71. Gerretsen SC, Versluis B, Bekkers SC, et al. Cardiac cine MRI: comparison of 1.5 T, non-enhanced 3.0 T and blood pool enhanced 3.0 T imaging. *Eur J Radiol* 2008;65:80–85
 72. Hadizadeh DR, Marx C, Gieseke J, et al. High temporal and high spatial resolution MR angiography (4D-MRA). *Rofa* 2014;186:847–59
 73. Davis B, Royalty K, Kowarschik M, et al. 4D digital subtraction angiography: implementation and demonstration of feasibility. *AJNR Am J Neuroradiol* 2013;34:1914–21
 74. Pontone G, Bertella E, Mushtaq S, et al. Coronary artery disease: diagnostic accuracy of CT coronary angiography—a comparison of high and standard spatial resolution scanning. *Radiology* 2014;271:688–94
 75. Sabarudin A, Sun Z. Coronary CT angiography: diagnostic value and clinical challenges. *World J Cardiol* 2013;5:473–83
 76. Sepehri S, Zouaoui K, Thiran J-P. A realistic computed tomography simulator for small motion analysis of cerebral aneurysms. In: *Proceedings of the 35th Annual International Conference of the IEEE Engineering in Medicine and Biology Society*, Osaka, Japan. July 3–7, 2013
 77. Thiran JP, Sepehri S. Direct detection of small motion from dynamic tomography images. In: *Proceedings of the 21st European Signal Processing Conference*, Marrakech, Morocco. September 9–13, 2013
 78. Mathews JD, Forsythe AV, Brady Z, et al. Cancer risk in 680,000 people exposed to computed tomography scans in childhood or adolescence: data linkage study of 11 million Australians. *BMJ* 2013;346:f2360

Hot Topics in Research: Preventive Neuroradiology in Brain Aging and Cognitive Decline

C.A. Raji, H. Eyre, S.H. Wei, D.E. Bredesen, S. Moylan, M. Law, G. Small, P.M. Thompson, R.M. Friedlander, D.H. Silverman, B.T. Baune, T.A. Hoang, N. Salamon, A.W. Toga, and M.W. Vernooij



SUMMARY: Preventive neuroradiology is a new concept supported by growing literature. The main rationale of preventive neuroradiology is the application of multimodal brain imaging toward early and subclinical detection of brain disease and subsequent preventive actions through identification of modifiable risk factors. An insightful example of this is in the area of age-related cognitive decline, mild cognitive impairment, and dementia with potentially modifiable risk factors such as obesity, diet, sleep, hypertension, diabetes, depression, supplementation, smoking, and physical activity. In studying this link between lifestyle and cognitive decline, brain imaging markers may be instrumental as quantitative measures or even indicators of early disease. The purpose of this article is to provide an overview of the major studies reflecting how lifestyle factors affect the brain and cognition aging. In this hot topics review, we will specifically focus on obesity and physical activity.

ABBREVIATIONS: AD = Alzheimer disease; APOE = Apolipoprotein E; BMI = body mass index; MCI = mild cognitive impairment

Preventive neuroradiology is an emerging discipline that has the potential to contribute substantially to human health. Preventive neuroradiology is the application of multimodal brain imaging toward early identification of subclinical brain disease prevention through the influence of modifiable risk factors. Positioned at the intersection of neurology and psychiatry, it has applications in a multitude of diseases including age-related cognitive decline, mood and psychotic disorders, and a variety of other neuropsychiatric conditions. Preventive neuroradiology also has application to the recently proposed field of health neuroscience,¹ a concept that studies the interplay between the brain and physical health during the life span.¹

A specific area where preventive neuroradiology is having an

impact is in the area of age-related cognitive decline. As populations age, the burden of age-related cognitive decline is rising. Globally, the number of older individuals (60 years of age or older) is expected to more than double, from 841 million in 2013 to >2 billion in 2050,² with rates of dementia expected to increase from an estimated 44 million worldwide in 2013³ to an estimated 75.6 million in 2030, and 136 million in 2050.

The expected precipitous rise in rates of age-related cognitive decline has not, to date, been met with a substantial expansion in treatment options. In fact, current pharmacologic therapies for the most common form of dementia, Alzheimer disease (AD), appear to provide some symptomatic relief but do not influence the underlying pathophysiology.⁴ This problem signifies the need to focus on increasing our understanding of preventive lifestyle modifications and their neurobiologic underpinnings of the disease. For example, with AD, a recent study has highlighted the important role of risk-factor reduction for decreasing prevalence.⁵ Barnes and Yaffe⁵ explored the role of 7 potentially modifiable AD risk factors: diabetes, midlife hypertension, midlife obesity, smoking, depression, low educational attainment, and physical inactivity. They determined that these factors contributed to up to half of AD cases globally (17.2 million), and a 10%–25% reduction in all risk factors could potentially prevent as many as 1.1–3.0 million cases. An emerging literature currently explores the effect of these risk factors on neurobiology factors. Other lifestyle factors that have been found to reduce the risk of AD include mind-body exercise (eg, yoga, tai chi, qi gong⁶), conventional physical activity (eg, aerobic, strength training⁶), nutritional supplements (eg, ω -3 fatty acids, flavonols⁷), stress-reduction techniques (eg, Mindfulness-Based Stress Reduction⁸),

Received February 15, 2015; accepted after revision February 23.

From the Departments of Radiology (C.A.R., S.H.W., T.A.H., N.S.), Psychiatry (H.E., G.S.), Neurology (D.E.B.), and Nuclear Medicine (D.H.S.), University of California at Los Angeles Medical Center, University of California at Los Angeles, Los Angeles, California; Discipline of Psychiatry (H.E., B.T.B.), University of Adelaide, Adelaide, South Australia, Australia; School of Medicine (S.M.), Deakin University, Geelong, Victoria, Australia; Department of Radiology (M.L.) and Laboratory of Neuroimaging (P.M.T., A.W.T.), University of Southern California, Los Angeles, California; Department of Neurosurgery (R.M.F.), University of Pittsburgh, Pittsburgh, Pennsylvania; and Departments of Radiology and Epidemiology (M.W.V.), Erasmus University Medical Center, Rotterdam, the Netherlands.

This work was supported by the National Institute of Biomedical Imaging and Bioengineering (grant P41EB015922) and the National Institutes of Health (grant U01AG024904).

Please address correspondence to Cyrus A. Raji, MD, PhD, Department of Radiology, UCLA Medical Center, 757 Westwood Blvd, Los Angeles, CA 90095; e-mail: cyrusraji@gmail.com; @cyrusrjai

Indicates open access to non-subscribers at www.ajnr.org

<http://dx.doi.org/10.3174/ajnr.A4409>

sleep-modification strategies,⁹ and dietary interventions (eg, fish consumption, Mediterranean diet).¹⁰

Classic risk-factor studies in dementia are hampered by the difficult phenotyping of the disease with large heterogeneity in severity and presentation, and by the fact that once symptomatic, irreversible brain damage is already present. The paradigm shift in medicine from cure toward prevention calls for identification of potentially modifiable factors that affect disease in an earlier stage. During the past decades, brain imaging has proved instrumental as a means of studying brain changes in aging and age-related cognitive decline.^{11–14} Many new imaging markers have been identified that either serve as quantifiable intermediate factors in the pathway of lifestyle and age-related cognitive decline or could even indicate disease in an early stage. For example, the hippocampal structure has been shown to be affected both positively and negatively by lifestyle factors by using structural, functional, and molecular forms of neuroimaging.^{15,16} Neuroradiology as a discipline is hence highly important in better understanding the role of these lifestyle factors in positively or negatively affecting structural, functional, and molecular radiologic correlates.

In this hot topics in research review, we explore the potential role for “preventive neuroradiology” in the risk reduction of neuropsychiatric disorders, by using age-related cognitive decline as an example.

OBESITY AND AGE-RELATED COGNITIVE DECLINE

Insights from Clinical Trials and Epidemiology

There is evidence of an association between midlife obesity and increased risk of dementia. The Barnes and Yaffe model⁵ suggests a pooled relative risk estimate of 1.60 (95% CI, 1.34–1.92) and approximately 2% (677,000) of AD cases worldwide are potentially attributable to midlife obesity. A recent systematic review¹⁷ identified 10 prospective studies that examined the association between various measures of body weight and dementia, of which 7 were suitable for inclusion in a meta-analysis. Three of 4 studies found that body mass index (BMI) (as a continuous measure) was associated with an increased risk of all-cause dementia; 2 of 5 studies indicated that obesity (BMI \geq 30) was associated with an increased risk of all-cause dementia; and 2 of 5 studies found that obesity was associated with an increased risk for AD.

Insights from Neurobiology

Commonly proposed mediators for the relationship between higher body tissue adiposity and brain structure at any age include hypercortisolemia, reduced exercise, impaired respiratory function, inflammation, oxidative stress, cardiovascular disease, hypertension and/or hyperlipidemia, and type 2 diabetes mellitus.^{18,19} The co-occurrence of at least 3 of the following cardiovascular factors including large waist circumference (or adiposity), increased triglycerides, elevated blood pressure, and fasting hyperglycemia has been referred to as “the metabolic syndrome.”²⁰ Adiposity is also associated with insulin resistance and subsequent type 2 diabetes, hypertension, dyslipidemia, cardiovascular disease, degenerative joint disease, cancer, and lung disease.²¹ Moreover, an elevated BMI is significantly correlated with a reduction in neuronal fiber bundle length, which is believed to contribute to brain atro-

phy. Finally, greater brain atrophy may occur in people with central leptin insufficiency, a marker of obesity.¹⁸

Insights from Neuroradiology: Structural Imaging

Volumetric MR Imaging. Several studies have investigated the relationship between BMI and brain atrophy. In an early study,¹⁸ tensor-based morphometry was used to examine gray matter and white matter volume differences in 94 elderly subjects who remained cognitively healthy for at least 5 years after their scan. When controlling for age, sex, and race, subjects with obesity with a high BMI (BMI of $>$ 30) showed atrophy in the frontal lobes, anterior cingulate gyrus, hippocampus, and thalamus compared with individuals with a normal BMI (18.5–25). Overweight subjects (BMI of 25–30) had atrophy in the basal ganglia and corona radiata of the WM. Overall brain volume did not differ between overweight and obese persons. In a similar study, Bobb et al²² explored 5-year longitudinal associations between change in BMI and gray matter with time, in a cohort of 247 former heavy-metal workers and community controls. Higher baseline BMI was associated with greater decline in temporal and occipital GM ROI volumes. Change in BMI during the 5-year period was only associated with a change in hippocampal volume and not other ROIs. Overall, higher BMI was associated with declines in volume in temporal and occipital GM with time.

A recent study²³ explored the associations among physical activity, BMI, and brain structure in normal aging, mild cognitive impairment (MCI), and AD dementia. This study included 963 participants from the multisite Cardiovascular Health Study including healthy controls ($n = 724$), patients with Alzheimer dementia ($n = 104$), and individuals with MCI ($n = 135$). Physical activity was independently associated with greater whole-brain and regional brain volumes and reduced ventricular dilation. Those with higher BMI had lower whole-brain and regional brain volumes. A physical activity–BMI conjunction analysis showed brain preservation with physical activity and volume loss with increased BMI in overlapping brain regions (Fig 1).

A study by Driscoll et al²⁴ explored the influence of midlife obesity on brain atrophy. In this study, associations between global (BMI) and central (waist circumference) midlife obesity and subsequent trajectories of regional brain atrophy in 152 individuals [M (age) = 69 ± 7.8 years] were examined. After follow-up, 21 individuals became cognitively impaired. Results suggest that midlife obesity may be an important modifier of brain atrophy in individuals who are developing cognitive impairment and dementia, while it has little effect on structural brain integrity in older adults without dementia.

Brain Tissue Integrity. MR imaging advancements such as diffusion tensor imaging have more recently been used to quantify subtle changes in WM tract microstructure and connectivity in senescent and developing adolescent brains. Furthermore, the use of tractography and diffusion pattern statistical analyses is instrumental in determining the spatial definition of individual tracts. Research has shown that cerebral WM integrity is decreased in the aging brain, particularly affecting the prefrontal regions.²⁵

A recent study by Stanek et al²⁶ examined the association between BMI and WM integrity. The authors used a diffusion

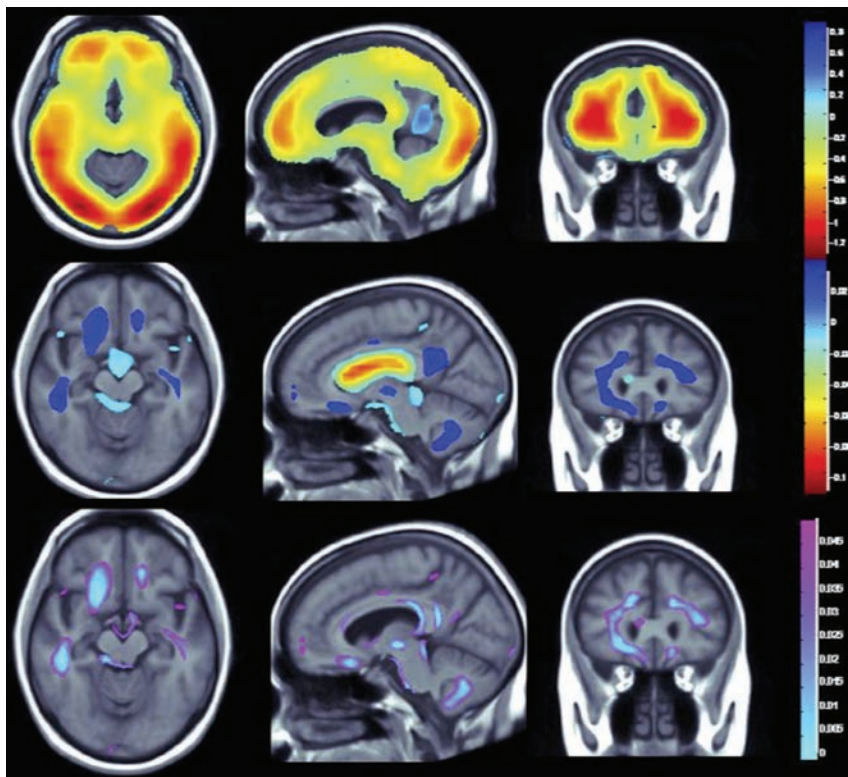


FIG 1. Relationship between obesity and physical activity on brain structure (adapted with permission from Boyle et al²³). The top panel shows whole-brain 3D maps in which regional brain volumes are inversely correlated with BMI. The middle panel shows where regional brain volumes positively correlate with physical activity. The lower panel shows regions of significant brain volume differences from both higher BMI and physical activity in a conjunction analysis that identifies brain areas that are independently influenced by these factors.

tensor imaging index of tract coherence—fractional anisotropy to examine the structure of the corpus callosum and fornix. This study classified 103 adult participants between 21 and 86 years of age without a history of neurologic, medical, or psychiatric illness according to BMI. Individuals with obesity demonstrated lower fractional anisotropy than healthy and overweight persons for all WM indexes, but no fractional anisotropy differences emerged between overweight and healthy individuals.

Functional Imaging. Functional MR imaging may provide an efficacious method for assessing the impact of adiposity in cognitively intact middle-aged adults because it can identify altered brain activation patterns indicative of cognitive vulnerability.²⁷ Prior work has identified changes in brain activation during cognition in association with elevated BMI.^{28–30} One recent study explored how a centralized distribution of adiposity relates to brain activation during a working memory task in a cognitively intact middle-aged sample.³¹ Seventy-three adults, 40–60 years of age, completed a verbal working memory task during fMRI. Central adiposity was assessed with waist circumference. Larger waist circumference was associated with a diminished working memory–related blood oxygen level–dependent response in the right superior frontal gyrus and left middle frontal gyrus. Reduced task-related activation in the right superior frontal gyrus and left middle frontal gyrus was related to slower reaction time on the task, controlling for age and education.

PHYSICAL ACTIVITY AND AGE-RELATED COGNITIVE DECLINE

Insights from Clinical Trials and Epidemiology

Conventional physical activity is one of the most promising therapies for the treatment and prevention of age-related cognitive decline and dementia.⁴ Most important, there are a variety of subtypes of physical activity, from aerobic activity, to resistance, to stretching and toning. A recent randomized controlled trial³² examined the efficacy of resistance and aerobic training in the improvement of cognitive functions in subjects with subjective MCI. The study occurred during 6 months and involved 86 community-dwelling women 70–80 years of age. Physical activity protocols included twice-weekly resistance training, twice-weekly aerobic training, or twice-weekly balance and toning training (ie, control). Resistance training improved selective attention/conflict resolution and associated memory compared with balance and toning training. In contrast, aerobic physical activity improved general balance and mobility and cardiovascular capacity. The study also found that aerobic physical activity improved verbal memory

and both resistance and aerobic physical activity improved spatial memory.

A recent meta-analysis³³ examined the efficacy of exercise on cognition in older adults with MCI. MCI was diagnosed based on documented criteria or via the Mini-Mental State Examination. Fourteen randomized controlled trials with 1695 participants 65–95 years of age were used. These studies had a duration of 6–52 weeks. Overall, 42% of effect sizes were potentially clinically relevant (effect size of >0.20) with only 8% of cognitive outcomes statistically significant. The meta-analysis revealed negligible but significant effects of exercise on verbal fluency (effect size: 0.17 [range, 0.04–0.30]). No significant benefit was found for additional executive measures, memory, or information processing. The authors critically appraised randomized controlled trial methods and concluded that they had moderate quality, with most trial samples being too small for sufficient power. They suggested that there is clearly some effect of exercise at moderate-to-high levels of exertion.

Physical activity is on a continuum with physical inactivity. Worldwide, approximately 13% (nearly 4.3 million) of AD cases may be attributable to physical inactivity.⁵ A recent systematic review and meta-analysis identified 16 prospective studies on the association between physical activity and dementia that included 163,797 older adults without dementia at baseline and 3219 individuals with dementia at follow-up.³⁴ The combined relative risk in the highest-versus-lowest physical activity groups was 0.72 for

all-cause dementia and 0.55 for AD. The previously mentioned Barnes and Yaffe⁵ model suggests a relative risk of 1.82 for AD.

Insights from Neurobiology

The biologic mechanisms by which cognition is enhanced through physical exercise remain to be completely elucidated, though the number of studies that have tried to identify these mechanisms has increased in the past 10 years. For the most part, the studies that support the notion that physical exercise has an impact on brain functions have focused on the direct biologic effects of exercise by using both animal and human models.⁶ However, exercise may enhance cognition indirectly by improving health conditions (ie, stress, sleep), reducing chronic diseases (ie, coronary heart disease) that impact neurocognitive functions, and offering psychological and social effects.³⁵ The molecular mechanisms by which exercise induces angiogenesis, neurogenesis, and synaptogenesis have received growing attention in recent years.⁶

From a mechanistic perspective, sedentary behaviors may contribute to the risk of AD and dementia by 2 main factors.^{5,36} First, they are associated with an increased risk of cardiometabolic risk factors—diabetes, hypertension, obesity³⁷—that are associated with an increased risk of dementia.^{38,39} Second, sedentary behaviors appear to have direct effects on neurobiologic processes. A recent review⁴⁰ outlines evidence to suggest that sedentary behaviors may have detrimental effects on the brain via reducing neurogenesis, synaptic plasticity, neurotrophin production, and angiogenesis and by increasing inflammation. Most important however, no studies have integrated objective measurements of both sedentary behavior and physical activity with measures of cognition or potential mechanistic outcomes such as neurogenesis and synaptic plasticity, regional fat deposits including visceral fat and pericardial fat, disrupted glucose metabolism, and/or inflammation.⁴⁰

Insights from Neuroradiology: Structural Brain Imaging

Volumetric MR Imaging. Imaging studies corroborate the findings of the beneficial effects of exercise on brain structure and function. Higher gray and white matter cortical volumes were present on MR volumetric imaging in individuals with and without dementia with better aerobic fitness (maximal oxygen consumption, maximal oxygen uptake, peak oxygen uptake, or maximal aerobic capacity).^{41,42} MR imaging studies in elderly populations without dementia also found that bilateral hippocampal volumes are better maintained in fit individuals, with resultant superior performance in tasks related to spatial memory.⁴³ A cross-sectional study by Makizako et al⁴⁴ examined associations between light- and moderate-intensity physical activity (measured with accelerometers), total duration of physical activity, hippocampal volume, and memory in older adults with MCI. Moderate physical activity was associated with hippocampal volume after controlling for age, but light and total physical activity were not. Both light and moderate physical activity groups were not associated with memory performance. Structural equation modeling demonstrated that moderate physical activity was not directly associated with memory but significantly contributed to hippocampal volume; hippocampal volume loss was significantly

and directly associated with poor memory performance. This finding suggests that the benefits of moderate physical activity on memory among older adults with MCI may be mediated by hippocampal volume. Most intriguing, reversal of age-related hippocampal volume loss by 2%, equivalent to 1–2 years of volume loss, was observed after exercise training during late adulthood; this finding was accompanied by a concomitant increased serum brain-derived neurotrophic factor and improved memory function.⁴⁵

Randomized controlled trials have demonstrated the neuroprotective effects of exercise on brain aging in elderly populations, including in those with dementia, leading to positive effects on brain structure and cognitive performance. Some studies also suggested that these effects may be dependent on the duration, quality, and variety of exercise.⁴⁶

No studies have examined the relationship between sedentary behavior and brain structure.⁴⁰ We hypothesize that sedentary behaviors are associated with atrophy of numerous brain regions, particularly the hippocampus. Faster rates of hippocampal volume decay are associated with MCI and AD.^{47,48}

Functional Imaging. We are aware of 1 study exploring hippocampal physiology (blood flow) in sedentary older adults.⁴⁹ In this study, investigators used resting hippocampal cerebral blood flow measures (via arterial spin-labeling MR imaging) and sedentary time/physical activity (via accelerometry) on 33 cognitively healthy adults (52–81 years of age), 9 of whom were *Apolipoprotein E (APOE) ε4* carriers. Results indicated that the relationship between sedentary time and cerebral blood flow in the left hippocampus differs by *APOE* status, whereby *APOE ε4* carriers show higher cerebral blood flow as a function of longer sedentary time compared with noncarriers, possibly suggesting a cerebral blood flow regulatory response to compensate for metabolic alterations in dementia risk. These data suggest that the relationship between cerebral blood flow and sedentary time is different in *APOE ε4* carriers and noncarriers and that sedentary time may act as a behavioral risk factor for cerebral blood flow dysregulation in those at genetic risk for developing AD.

Types of physical activity other than cardiovascular have also been shown to help improve cognitive function. Strength training frequency of at least once per week was associated with greater cerebrovascular perfusion in older women compared with those who did not engage in strength-training activities.⁵⁰ A 12-month long, twice-weekly resistance training program in elderly women found functional changes in the regions of the cerebral cortex, most strikingly in the left middle temporal gyrus and the left anterior insula to the lateral orbital frontal cortex, associated with improved hemodynamics and response inhibition based on the Flanker test performance.⁵¹ In addition, a 12-month randomized trial of exercise, including both cardiovascular and coordination training, in older adults showed that improved motor fitness was associated with retained or improved hippocampal volumes.⁵²

Brain Tissue Integrity. Life-long aerobic fitness in a small number of elderly athletes was also associated with findings of reduced white matter hyperintensities by 83% compared with sedentary individuals and higher fractional anisotropy within multiple

white matter tracts related to motor control and coordination.⁵³ White matter hyperintensities are a marker of vascular damage. Active exercise in the elderly is associated with lower mean diffusivity in the cingulate cortex and medial temporal lobe, suggestive of improved microstructural integrity within memory and executive function networks.⁵⁴ A 1-year exercise program showed a promising association between improved fitness and increased white matter integrity in the frontal and temporal lobes and improved short-term memory, though the cognitive improvements were not independently associated with imaging findings.⁵⁵ Improvements in temporal lobe connectivity are associated with changes in levels of serum growth factors such as brain-derived neurotrophic factor, vascular endothelial growth factor, and insulin-like growth factor-1; these molecules may serve as biomarkers for neurologic function and may underlie the biochemical regulation of white matter plasticity.^{46,56}

Molecular Imaging

Emerging evidence suggests that higher levels of physical exercise/fitness are associated with reduced amyloid A β burden⁵⁷⁻⁵⁹ and potentially lowered intracellular τ protein⁵⁸; however, there are some null findings.^{60,61} A recent study⁵⁹ aimed to see if plasma A β and A β brain deposition were associated with physical activity levels and whether these associations differed between carriers and noncarriers of the *APOE* $\epsilon 4$ allele. Five-hundred forty-six cognitively intact participants (60–95 years of age) were included in these analyses, with physical activity assessed by questionnaire. A subgroup ($n = 116$) underwent ¹¹C Pittsburgh compound-B positron-emission tomography scanning to quantify brain amyloid load. After stratification of the cohort based on *APOE* $\epsilon 4$ allele carriage, it was evident that only noncarriers received the benefit of reduced plasma A β from physical activity. Conversely, lower levels of Pittsburgh compound-B were observed in higher exercising *APOE* $\epsilon 4$ carriers. Lower plasma A β 1–42/1–40 and brain amyloid were observed in those reporting higher levels of physical activity.

Another recent study⁶² explored whether engagement in physical activity might favorably alter the age-dependent evolution of AD-related brain and cognitive changes in a cohort of at-risk, late-middle-aged adults. In this study, 317 enrollees underwent an MR imaging acquisition; a subset also underwent ¹¹C Pittsburgh compound-B PET ($n = 186$) and [¹⁸F] fluorodeoxyglucose PET ($n = 152$). There were significant age \times physical activity interactions for A β burden, glucose metabolism, and hippocampus volume. This finding suggested that with advancing age, physically active individuals exhibited a lesser degree of biomarker alterations compared with the physically inactive ones.

DISCUSSION

Summary

Overall, the results from this work highly suggest that the effects of lifestyle factors on cognitive function in aging act through impact on brain structure and function. Neuroimaging studies increasingly reveal structural and functional brain changes in relation to lifestyle factors that translate to measurable cognitive differences. This finding implies that these quantitative neuroimaging metrics

may be effective surrogate markers that can be utilized in trials or can help identify novel pathways for intervention.

Clinical and Public Health Implications

There are some more immediate clinical implications for this field. Two relevant areas include rapid, automated quantitation of brain volume.⁶³ This provides a relatively inexpensive means to track brain atrophy and the effects of lifestyle interventions; the lower cost compared with analysis by neuroradiologists may make this more available to the community. Additionally, the need for lifestyle modification advice and interventions for adult and late-life individuals is highly relevant to this field, given their noted effects on the brain. The global mental health implications of neuroscience were more broadly outlined recently.⁶⁴

Future Directions

In this review, we have focused on obesity and physical activity and their effects on the brain. We are aware of a number of other lifestyle factors that require investigation across the neuroimaging modalities. For example, more recent studies have begun to parse out the potential effects of aerobic, resistance, and coordinative exercises and dual-task interventions in improving structural, functional, and cognitive aspects of aging.⁶⁵ Other lifestyle factors that may positively affect the brain include mind-body therapies (eg, yoga, qi gong, tai chi⁶), supplements (eg, ω -3 fatty acids,⁶⁶ flavonols⁶⁷), stress-reduction techniques (eg, Mindfulness-Based Stress Reduction⁶), sleep-modification strategies,⁹ and dietary interventions (eg, fish consumption,¹⁵ Mediterranean diet⁶⁸). Other lifestyle factors that impact the brain include smoking, alcohol consumption, sleep, and hypertension. Continuing this work is critical for the development of treatment plans and may affect health care policy and personal philosophies on preventive and therapeutic lifestyle modification. By taking a multifaceted approach to lifestyle modification, one may reap additive or synergistic benefits, even at an early age.

Future studies may help elucidate the mechanism underlying cognitive improvements and identify target populations in which a longitudinal regimen of nonpharmacologic lifestyle modifications may yield significant health benefits. Furthermore, the lifestyle modification may be tailored to individuals with specific illnesses or genetic predispositions with a feasible, preventive goal in mind. Most important, there are coexisting lifestyle factors and a relative lack of premorbid conditions associated with a healthy lifestyle that may act as confounds. These must be carefully considered in future studies.

Developing literature is exploring the role of preventive neuroradiology in other psychiatric disorders. In depression, a meta-analysis confirmed a direct correlation between increasing depressive episode numbers and decreased hippocampal volume.⁶⁹ The hippocampus is, therefore, a potential target for preventive interventions. In schizophrenia, a group of ultra-high-risk subjects was followed longitudinally with structural MR imaging.⁷⁰ This study found both groups of subjects who subsequently developed psychosis (schizophrenia and affective psychosis) showed reductions in the frontal cortex relative to ultra-high-risk subjects who did not develop psychosis. The subgroup that subsequently developed schizophrenia also showed smaller volumes in the pa-

rietal cortex and, at trend level, in the temporal cortex, whereas those who developed an affective psychosis had significantly smaller subgenual cingulate volumes. This finding also raises targets for preventive interventions.

In preventive neuroradiology, imaging doctors act as actionable information consultants to both referring physicians and their patients in delivering the added value of quantitative neuroimaging. For example, if a neuroradiologist can provide quantitative measurements of hippocampal volume to a geriatric psychiatrist, thereby identifying significant hippocampal volume decrease in a patient with subtle memory loss, it gives that referring physician improved confidence as to the potential etiology of patient symptoms and subsequent management. Such actionable information can also be used to engage patients in brain-directed lifestyle programs that can then be reassessed with a combination of clinical evaluations and follow-up quantitative neuroimaging.⁷¹ In such a new clinic model, neuroradiologists can act as visible team members for improving patient outcomes. This aspect of preventive neuroradiology is also an illustrative example of value-based imaging that is promoted as important for the future of radiology.⁷²

Disclosures: Cyrus A. Raji—UNRELATED: Consultancy: Brainreader ApS, Change Your Brain Change Your Life Foundation. Dale E. Bredsen—UNRELATED: Employment: Muses Labs. Steven Moylan—UNRELATED: Employment: Barwon Health (clinical psychiatrist work); Other: Deakin University, Comments: employed as a clinical lecturer. Meng Law—RELATED: Grant: Toshiba*; Consulting Fee or Honorarium: Guebert; Consultancy: Bracco.* Gary Small—UNRELATED: Consultancy: Forum Pharmaceuticals,* Herbalife,* Novartis,* Lilly,* Pfizer,* Janssen*; Grants/Grants Pending: Pom Wonderful*; Payment for Lectures (including service on Speakers Bureaus): Novartis*; Patents (planned, pending or issued): FDDNP-PET; Royalties: HarperCollins, Workman Publishing Company, NewsMax Media; Stock/Stock Options: TauMark. Paul M. Thompson—RELATED: Grant: National Institutes of Health grants.* Dan H. Silverman—OTHER RELATIONSHIPS: Dr Dan Silverman is the inventor of NeuroQ, which is now licensed and sold separately by SynterMed (<http://www.syntermed.com/>). Bernhard T. Baune—UNRELATED: Board Membership: Lundbeck; Employment: University of Adelaide; Grants/Grants Pending: National Health and Medical Research Council Australia; Payment for Lectures (including service on Speakers Bureaus): Lundbeck. Arthur W. Toga—RELATED: Grant: National Institute of Biomedical Imaging and Bioengineering.* National Institutes of Health.* Comments: Laboratory of Neuro Imaging-Resource, Award No. P41EB015922; The Alzheimer's Disease Neuroimaging Initiative, Award No. U01AG024904. *Money paid to the institution.

REFERENCES

- Erickson KI, Creswell JD, Verstynen TD, et al. **Health neuroscience: defining a new field.** *Curr Dir Psychol Sci* 2014;23:446–53
- United Nations, Department of Economic and Social Affairs, Population Division. *World Population Ageing 2013.* ST/ESA/SER.A/348. New York: United Nations; 2013
- Prince M, Prina M, Guerchet M; Alzheimer's Disease International. *World Alzheimer Report 2013: Journey of Caring—An Analysis of Long-Term Care for Dementia.* London: Alzheimer's Disease International; 2013
- Selkoe DJ. **Preventing Alzheimer's disease.** *Science* 2012;337:1488–92
- Barnes DE, Yaffe K. **The projected effect of risk factor reduction on Alzheimer's disease prevalence.** *Lancet Neurol* 2011;10:819–28
- Eyre HA, Baune BT. **Assessing for unique immunomodulatory and neuroplastic profiles of physical activity subtypes: a focus on psychiatric disorders.** *Brain Behav Immun* 2014;39:42–55
- Varteresian T, Lavretsky H. **Natural products and supplements for geriatric depression and cognitive disorders: an evaluation of the research.** *Curr Psychiatry Rep* 2014;16:456
- Wells RE, Kerr CE, Wolkin J, et al. **Meditation for adults with mild**

- cognitive impairment: a pilot randomized trial.** *J Am Geriatr Soc* 2013;61:642–45
- Coogan AN, Schutová B, Husung S, et al. **The circadian system in Alzheimer's disease: disturbances, mechanisms, and opportunities.** *Biol Psychiatry* 2013;74:333–39
- Di Marco LY, Marzo A, Muñoz-Ruiz M, et al. **Modifiable lifestyle factors in dementia: a systematic review of longitudinal observational cohort studies.** *J Alzheimers Dis* 2014;42:119–35
- Hua X, Leow AD, Parikshak N, et al; Alzheimer's Disease Neuroimaging Initiative. **Tensor-based morphometry as a neuroimaging biomarker for Alzheimer's disease: an MRI study of 676 AD, MCI, and normal subjects.** *Neuroimage* 2008;43:458–69
- Mueller SG, Weiner MW, Thal LJ, et al. **The Alzheimer's Disease Neuroimaging Initiative.** *Neuroimaging Clin N Am* 2005;15:869–77, xi–xii
- DeCarli C, Mungas D, Harvey D, et al. **Memory impairment, but not cerebrovascular disease, predicts progression of MCI to dementia.** *Neurology* 2004;63:220–27
- Morra JH, Tu Z, Apostolova LG, et al; Alzheimer's Disease Neuroimaging Initiative. **Automated mapping of hippocampal atrophy in 1-year repeat MRI data from 490 subjects with Alzheimer's disease, mild cognitive impairment, and elderly controls.** *Neuroimage* 2009;45:S3–15
- Raji CA, Erickson KI, Lopez OL, et al. **Regular fish consumption and age-related brain gray matter loss.** *Am J Prev Med* 2014;47:444–51
- Ho AJ, Raji CA, Becker JT, et al. **The effects of physical activity, education, and body mass index on the aging brain.** *Hum Brain Mapp* 2011;32:1371–82
- Beydoun MA, Beydoun HA, Wang Y. **Obesity and central obesity as risk factors for incident dementia and its subtypes: a systematic review and meta-analysis.** *Obes Rev* 2008;9:204–18
- Raji CA, Ho AJ, Parikshak NN, et al. **Brain structure and obesity.** *Hum Brain Mapp* 2010;31:353–64
- Moylan S, Berk M, Dean OM, et al. **Oxidative & nitrosative stress in depression: why so much stress?** *Neurosci Biobehav Rev* 2014;45:46–62
- Yaffe K, Haan M, Blackwell T, et al. **Metabolic syndrome and cognitive decline in elderly Latinos: findings from the Sacramento Area Latino Study of Aging study.** *J Am Geriatr Soc* 2007;55:758–62
- Poirier P, Després JP, Bertrand OF. **Identifying which patients with diabetes should be tested for the presence of coronary artery disease—the importance of baseline electrocardiogram and exercise testing.** *Can J Cardiol* 2006;22(suppl A):9A–15A
- Bobb JF, Schwartz BS, Davatzikos C, et al. **Cross-sectional and longitudinal association of body mass index and brain volume.** *Hum Brain Mapp* 2014;35:75–88
- Boyle CP, Raji CA, Erickson KI, et al. **Physical activity, body mass index, and brain atrophy in Alzheimer's disease.** *Neurobiol Aging* 2015;36(suppl 1):S194–202
- Driscoll I, Beydoun MA, An Y, et al. **Midlife obesity and trajectories of brain volume changes in older adults.** *Hum Brain Mapp* 2012;33:2204–10
- Marks BL, Madden DJ, Bucur B, et al. **Role of aerobic fitness and aging on cerebral white matter integrity.** *Ann N Y Acad Sci* 2007;1097:171–74
- Stanek KM, Griever SM, Brickman AM, et al. **Obesity is associated with reduced white matter integrity in otherwise healthy adults.** *Obesity* 2011;19:500–04
- Bondi MW, Houston WS, Eyler LT, et al. **fMRI evidence of compensatory mechanisms in older adults at genetic risk for Alzheimer disease.** *Neurology* 2005;64:501–08
- Braskie MN, Small GW, Bookheimer SY. **Vascular health risks and fMRI activation during a memory task in older adults.** *Neurobiol Aging* 2010;31:1532–42
- Gonzales MM, Tarumi T, Miles SC, et al. **Insulin sensitivity as a mediator of the relationship between BMI and working memory-related brain activation.** *Obesity* 2010;18:2131–37
- Volkow ND, Wang GJ, Telang F, et al. **Inverse association between**

- BMI and prefrontal metabolic activity in healthy adults. *Obesity* 2009;17:60–65
31. Gonzales MM, Kaur S, Eagan DE, et al. **Central adiposity and the functional magnetic resonance imaging response to cognitive challenge.** *Int J Obes (Lond)* 2014;38:1193–99
 32. Nagamatsu LS, Handy TC, Hsu CL, et al. **Resistance training promotes cognitive and functional brain plasticity in seniors with probable mild cognitive impairment.** *Arch Intern Med* 2012;172:666–68
 33. Gates N, Fiatarone Singh MA, Sachdev PS, et al. **The effect of exercise training on cognitive function in older adults with mild cognitive impairment: a meta-analysis of randomized controlled trials.** *Am J Geriatr Psychiatry* 2013;21:1086–97
 34. Hamer M, Chida Y. **Physical activity and risk of neurodegenerative disease: a systematic review of prospective evidence.** *Psychol Med* 2009;39:3–11
 35. Bherer L, Erickson KI, Liu-Ambrose T. **A review of the effects of physical activity and exercise on cognitive and brain functions in older adults.** *J Aging Res* 2013;2013:657508
 36. Barnes DE, Whitmer RA, Yaffe K. **Physical activity and dementia: the need for prevention trials.** *Exerc Sport Sci Rev* 2007;35:24–29
 37. de Rezende LF, Rey-López JP, Matsudo VK, et al. **Sedentary behavior and health outcomes among older adults: a systematic review.** *BMC Public Health* 2014;14:333
 38. Profenno LA, Porsteinsson AP, Faraone SV. **Meta-analysis of Alzheimer's disease risk with obesity, diabetes, and related disorders.** *Biol Psychiatry* 2010;67:505–12
 39. Kennelly SP, Lawlor BA, Kenny RA. **Blood pressure and the risk for dementia: a double edged sword.** *Ageing Res Rev* 2009;8:61–70
 40. Voss MW, Carr LJ, Clark R, et al. **Revenge of the "sit" II: does lifestyle impact neuronal and cognitive health through distinct mechanisms associated with sedentary behavior and physical activity?** *Ment Health Physical Act* 2014;7:9–24
 41. Colcombe SJ, Kramer AF, McAuley E, et al. **Neurocognitive aging and cardiovascular fitness: recent findings and future directions.** *J Mol Neurosci* 2004;24:9–14
 42. Colcombe SJ, Erickson KI, Scalf PE, et al. **Aerobic exercise training increases brain volume in aging humans.** *J Gerontol A Biol Sci Med Sci* 2006;61:1166–70
 43. Erickson KI, Prakash RS, Voss MW, et al. **Aerobic fitness is associated with hippocampal volume in elderly humans.** *Hippocampus* 2009;19:1030–39
 44. Makizako H, Liu-Ambrose T, Shimada H, et al. **Moderate-intensity physical activity, hippocampal volume, and memory in older adults with mild cognitive impairment.** *J Gerontol A Biol Sci Med Sci* 2015;70:480–86
 45. Erickson KI, Voss MW, Prakash RS, et al. **Exercise training increases size of hippocampus and improves memory.** *Proc Natl Acad Sci U S A* 2011;108:3017–22
 46. Kirk-Sanchez NJ, McGough EL. **Physical exercise and cognitive performance in the elderly: current perspectives.** *Clin Interv Aging* 2014;9:51–62
 47. Fein G, Di Sclafani V, Tanabe J, et al. **Hippocampal and cortical atrophy predict dementia in subcortical ischemic vascular disease.** *Neurology* 2000;55:1626–35
 48. Mueller SG, Schuff N, Yaffe K, et al. **Hippocampal atrophy patterns in mild cognitive impairment and Alzheimer's disease.** *Hum Brain Mapp* 2010;31:1339–47
 49. Zlatar ZZ, Wierenga CE, Bangen KJ, et al. **Increased hippocampal blood flow in sedentary older adults at genetic risk for Alzheimer's disease.** *J Alzheimers Dis* 2014;41:809–17
 50. Xu X, Jerskey BA, Cote DM, et al. **Cerebrovascular perfusion among older adults is moderated by strength training and gender.** *Neurosci Lett* 2014;560:26–30
 51. Liu-Ambrose T, Nagamatsu LS, Voss MW, et al. **Resistance training and functional plasticity of the aging brain: a 12-month randomized controlled trial.** *Neurobiol Aging* 2012;33:1690–98
 52. Niemann C, Godde B, Voelcker-Rehage C. **Not only cardiovascular, but also coordinative exercise increases hippocampal volume in older adults.** *Front Aging Neurosci* 2014;6:170
 53. Tseng BY, Gundapuneedi T, Khan MA, et al. **White matter integrity in physically fit older adults.** *Neuroimage* 2013;82:510–16
 54. Tian Q, Erickson KI, Simonsick EM, et al. **Physical activity predicts microstructural integrity in memory-related networks in very old adults.** *J Gerontol A Biol Sci Med Sci* 2014;69:1284–90
 55. Voss MW, Heo S, Prakash RS, et al. **The influence of aerobic fitness on cerebral white matter integrity and cognitive function in older adults: results of a one-year exercise intervention.** *Hum Brain Mapp* 2013;34:2972–85
 56. Voss MW, Erickson KI, Prakash RS, et al. **Neurobiological markers of exercise-related brain plasticity in older adults.** *Brain Behav Immun* 2013;28:90–99
 57. Eder D, Bugg JM, Goate AM, et al. **Exercise engagement as a moderator of the effects of APOE genotype on amyloid deposition.** *Arch Neurol* 2012;69:636–43
 58. Liang KY, Mintun MA, Fagan AM, et al. **Exercise and Alzheimer's disease biomarkers in cognitively normal older adults.** *Ann Neurol* 2010;68:311–18
 59. Brown BM, Peiffer JJ, Taddei K, et al. **Physical activity and amyloid- β plasma and brain levels: results from the Australian Imaging, Biomarkers and Lifestyle Study of Ageing.** *Mol Psychiatry* 2013;18:875–81
 60. Vemuri P, Lesnick TG, Przybelski SA, et al. **Effect of lifestyle activities on Alzheimer disease biomarkers and cognition.** *Ann Neurol* 2012;72:730–38
 61. Bugg JM, Head D. **Exercise moderates age-related atrophy of the medial temporal lobe.** *Neurobiol Aging* 2011;32:506–14
 62. Okonkwo OC, Schultz SA, Oh JM, et al. **Physical activity attenuates age-related biomarker alterations in preclinical AD.** *Neurology* 2014;83:1753–60
 63. Rathakrishnan BG, Doraiswamy PM, Petrella JR. **Science to practice: translating automated brain MRI volumetry in Alzheimer's disease from research to routine diagnostic use in the work-up of dementia.** *Front Neurol* 2014;4:216
 64. Stein DJ, He Y, Phillips A, et al. **Global mental health and neuroscience: potential synergies.** *Lancet Psychiatry* 2015;2:178–85
 65. Gregory MA, Gill DP, Petrella RJ. **Brain health and exercise in older adults.** *Curr Sports Med Rep* 2013;12:256–71
 66. Cederholm T, Salem N Jr, Palmblad J. **ω -3 fatty acids in the prevention of cognitive decline in humans.** *Adv Nutr* 2013;4:672–76
 67. Brickman AM, Khan UA, Provenzano FA, et al. **Enhancing dentate gyrus function with dietary flavanols improves cognition in older adults.** *Nat Neurosci* 2014;17:1798–803
 68. Mosconi L, Murray J, Tsui WH, et al. **Mediterranean diet and magnetic resonance imaging-assessed brain atrophy in cognitively normal individuals at risk for Alzheimer's disease.** *J Prev of Alzheimers Dis* 2014;1:23–32
 69. Videbech P, Ravnkilde B. **Hippocampal volume and depression: a meta-analysis of MRI studies.** *Am J Psychiatry* 2004;161:1957–66
 70. Dazzan P, Soulsby B, Mechelli A, et al. **Volumetric abnormalities predating the onset of schizophrenia and affective psychoses: an MRI study in subjects at ultrahigh risk of psychosis.** *Schizophr Bull* 2012;38:1083–91
 71. MacIntosh BJ, Swardfager W, Crane DE, et al. **Cardiopulmonary fitness correlates with regional cerebral grey matter perfusion and density in men with coronary artery disease.** *PLoS One* 2014;9:e91251
 72. Norbash A, Bluth E, Lee CI, et al. **Radiologist manpower considerations and Imaging 3.0: effort planning for value-based imaging.** *J Am Coll Radiol* 2014;11:953–58

Subspecialty Virtual Impact Factors within a Dedicated Neuroimaging Journal

 A.F. Choudhri and  M. Castillo

ABSTRACT

BACKGROUND AND PURPOSE: The growing number of subspecialties within neuroradiology compete for pages in neuroradiology journals. We performed a bibliometric analysis of the *American Journal of Neuroradiology* to identify the virtual Impact Factor of different journal subsections and article topics.

MATERIALS AND METHODS: Original Research and Review Articles published in *American Journal of Neuroradiology* during 2010–2012 were evaluated. The journal section for each article was recorded, and the number of citations was evaluated by using the Web of Science database. Numbers of citations within the first 2 years after publication were evaluated, normalized to the 2013 journal Impact Factor (for *American Journal of Neuroradiology*, 3.675), and used to calculate a virtual Impact Factor for different journal subsections.

RESULTS: One thousand forty-nine Original Research and Review Articles were published during this time, which obtained an average of 6.59 citations each within their first 2 years after publication; 91.8% of articles obtained at least 1 citation. Expedited Publications had the greatest number of citations, averaging 43.7 citations each (virtual Impact Factor, 24.39), followed by Review Articles averaging 9.39 citations each (virtual Impact Factor 5.23). Virtual Impact Factors for other sections were the following: Interventional, 4.54; Brain, 3.70; Pediatrics, 2.91; Functional, 2.74; Head & Neck, 2.24; and Spine, 1.86. Virtual Impact Factors for article topics were the following: interventional, 4.75; functional/advanced, 3.79; brain, 3.66; pediatrics, 2.99; head and neck, 2.46; and spine, 2.32.

CONCLUSIONS: Citation patterns of Original Research and Review Articles in *American Journal of Neuroradiology* varied widely on the basis of subsections. Understanding the citation patterns of specific topics and subsections of a journal may aid authors and editors in evaluating the appropriate balance among various topics and allow authors to determine whether their articles are being cited at a level expected for similar ones in a journal.

ABBREVIATIONS: JIF = journal Impact Factor; VIF = virtual Impact Factor

Citation analysis is an important means of evaluating the performance of journals and of authors, with implications regarding promotions, grant funding, advertising sales, and library selections.^{1–3} The growing number of subspecialties within neuroradiology compete for journal pages, and citation profiles of

these different subsections have not been evaluated. We performed a bibliometric analysis of *American Journal of Neuroradiology* (*AJNR*) to identify citation patterns based on subsections and article topics.

Neuroradiology encompasses evaluation of the brain, head and neck, spine, and peripheral nervous system, including minimally invasive diagnostic and therapeutic techniques in these areas. Several journals dedicated to neuroradiology exist; however, neuroradiologic articles are also included in general radiology journals and in radiology subspecialty journals such as those dedicated to pediatric radiology. While there is a growing body of bibliometric analyses in the radiology literature,^{4–7} few studies have focused on neuroradiology topics to date.^{8–10}

We hypothesized that the citation characteristics of a journal are heterogeneous among journal subsections and varying topics. We undertook a bibliometric analysis to evaluate the citation characteristics of neuroradiology articles within a neuroradiology

Received February 4, 2015; accepted after revision March 19.

From the Departments of Radiology (A.F.C.), Neurosurgery (A.F.C.), and Ophthalmology (A.F.C.), University of Tennessee Health Science Center, Memphis, Tennessee; Department of Radiology (A.F.C.), Le Bonheur Children's Hospital, Memphis, Tennessee; and Department of Radiology (M.C.) University of North Carolina, Chapel Hill, North Carolina.

This work was supported by an *AJNR* Editorial Fellowship to A.F.C.

Paper previously presented at: American Society of Neuroradiology Annual Meeting and the Foundation of the ASNR Symposium, April 25–30, 2015; Chicago, Illinois.

Please address correspondence to Asim F. Choudhri, MD, Department of Radiology, Le Bonheur Children's Hospital, 848 Adams Ave-G216, Memphis, TN 38103; e-mail: achoudhri@uthsc.edu; @AsimChoudhriMD

<http://dx.doi.org/10.3174/ajnr.A4380>

Table 1: Citation characteristics of journal sections (2010–2012) based on the first 2 years of citations

Journal Category	No.	Mean	SD	Minimum	Maximum	Median	% with Citations in First 2 Years	VIF
Expedited Pub Review	11	43.73	31.94	13	116	36	1.000	24.38
Interventional	53	9.38	7.95	0	38	7	0.981	5.23
Brain	232	8.13	9.91	0	83	5	0.948	4.54
Extracranial	321	6.64	6.18	0	61	5	0.941	3.70
Vascular	9	6.33	5.96	0	19	5	0.889	3.53
Pediatrics	98	5.22	4.99	0	36	4	0.949	2.91
Other ^a	68	5.12	6.18	0	31	3	0.868	2.85
Functional	34	4.91	3.75	0	17	4	0.941	2.74
Head & Neck	131	4.02	4.63	0	34	3	0.824	2.24
Spine	92	3.33	3.13	0	15	3	0.848	1.85
Noncategorized ^b	77	1.91	3.92	0	19	0	0.403	1.06

Note:—Pub indicates Publication.

^a Other includes Patient Safety ($n = 3$), Pharmacology Vignette ($n = 10$), Research Perspectives ($n = 9$), Practice Perspectives ($n = 7$), Health Care Reform Vignette ($n = 6$), and Methodologic Perspective ($n = 5$).

^b While the citation characteristics for these noncategorized items (editorials, letters to the editor, and so forth) are presented here, they were not considered in the formula for determining the VIF correction factor.

journal. We additionally sought to determine the citation characteristics of neuroradiology articles pertaining to specific subtopics.

MATERIALS AND METHODS

Article Selection

Only Original Research and Review Articles published in *AJNR* from 2010 to 2012 were evaluated. Full-text versions of all articles were obtained as PDF downloads and reviewed for topic. This study did not directly involve patient information and met the criteria for institutional review board exemption.

Journal Section Categorization

The journal section for each article (eg, Brain, Head & Neck, Pediatrics, Spine, Functional) was recorded. Additional journal subcategorizations, such as “Fellows’ Journal Club” or “Editor’s Choice” were also recorded.

Article Topic Categorization

The PDF of each article was evaluated to identify included topics, regardless of the initial categorization by the journal. While an article has only 1 category, as designated in the journal, there may be more than 1 topic that applies. For example, an article in the Pediatrics section of the journal on a head and neck topic will be assigned a topic of both pediatrics and head and neck, and a spine intervention article in the Interventional section would be assigned to the spine and interventional topics.

Citation Analysis

Each selected article was evaluated by using the Web of Science (Thompson Reuters, New York, New York) database for its number of citations. The number of citations within the first 2 calendar years after their publication was recorded and normalized to the 2013 *AJNR* journal Impact Factor (JIF, 3.675). This ratio was used to calculate a virtual Impact Factor (VIF) for each journal subsection. For instance, if a journal has a JIF of 5, and the articles received, on average, 8 citations, then a journal subsection that received an average of 4 citations would have a VIF of 2.5.

Citations from noncategorized items, including letters to the editor, editorials, and errata, were not included in the VIF calculation. Each article selected for analysis was reviewed in the Web of Science database to determine how many citations it received. While we could find no existing bibliometric reports formally documenting this methodology, we believe that using the average number of citations for each journal subsection is a valid extension of the reported methodology of the JIF.^{11–14}

Statistics

Data were collected in a spreadsheet (Excel; Microsoft, Redmond, Washington), and statistics were calculated by using SPSS Version 21 (IBM, Armonk, New York) and Excel. Discrete variables

(number of articles with zero versus greater than 1 citation) were compared using the Fisher exact test. Continuous variables (number of citations, VIF) were compared with a Student *t* test when there was a Gaussian distribution of data and otherwise with the nonparametric Wilcoxon rank sum test. *P* values < .05 were considered significant.

RESULTS

One thousand forty-nine Original Research and Review Articles were published in *AJNR* during the 3 years evaluated. An additional 77 uncategorized items, including editorials, letters to the editor, and errata, were excluded from analysis. The 1049 categorized articles accumulated 6.59 ± 8.53 (range, 0–116; median, 4) citations within their first 2 years after publication, and 91.8% of articles had at least 1 citation. On the basis of a JIF of 3.675, the VIF for a given section was determined as (Number of Citations / (6.59 / 3.675)).

Citations by Journal Section

Expedited Publications had the most citations with 11 articles averaging 43.7 ± 31.9 (range, 13–116; median, 36) citations each (VIF, 24.39). Review Articles had the next highest number of citations, with 53 articles averaging 9.38 ± 7.95 (range, 0–38; median, 7) citations each (VIF, 5.23), and 52 (98.1%) of these articles received at least 1 citation within 2 years of publication. VIFs for other sections ranged from 4.54 for Interventional (the highest) to 1.86 for Spine (the lowest) (Table 1). Articles selected as “Editor’s Choices” had a VIF of 5.14, and those selected for the “Fellows’ Journal Club” had a VIF of 3.83.

Citations by Article Topic

When we evaluated the citation characteristics by article topic as opposed to journal-assigned categories, interventional articles had the highest citation numbers, averaging 8.52 ± 12.54 (range, 0–116; median, 5) citations with a VIF of 4.75, which was similar to the journal category of Interventional ($P = .69$) (Table 2). Articles related to the spine were cited 4.16 ± 3.69 (range, 0–19;

Table 2: Citation characteristics by topic and other designations

Topic	No.	Mean	SD	Minimum	Maximum	Median	% with Citations in First 2 Years	VIF
Interventional	317	8.52	12.54	0	116	5	0.927	4.753
Functional/advanced	199	6.80	5.49	0	36	6	0.965	3.791
Brain	484	6.57	6.28	0	61	5	0.940	3.663
Pediatrics	115	5.36	5.12	0	36	4	0.930	2.987
Head and neck	189	4.42	4.46	0	34	3	0.868	2.463
Spine	145	4.16	3.69	0	19	3	0.883	2.319
Editor's Choice ^a	83	9.22	9.75	0	61	6	0.976	5.139
Fellows' Journal Club ^a	82	6.87	5.72	0	31	6	0.902	3.828
Nonvascular interventional	122	6.07	5.78	0	34	4.5	0.918	3.387
Peds head and neck	17	4.94	3.42	0	11	4	0.941	2.755
Spine interventional	64	4.14	3.37	0	15	7	0.891	2.309

Note:—Peds indicates Pediatrics.

^a“Fellows' Journal Club” and “Editor's Choices” are journal designations that are independent of the journal-selection category.

median, 3) times, with a VIF of 2.32, which was higher than the Spine category of the journal ($P = .074$). The percentage of articles having at least 1 citation within 2 years of publication ranged from 82.4% for Head & Neck articles (108 of 131) to 100% for Expedited Publication (11 of 11).

Number of Articles Receiving at Least 1 Citation

The number of publications receiving at least 1 citation within 2 years was statistically lower for the Head & Neck category compared with Review Articles ($P = .003$), Interventional ($P = .0003$), Brain ($P = .0003$), and Pediatrics ($P = .0042$). The number of publications receiving at least 1 citation within 2 years was statistically lower for the Spine category than Review Articles ($P = .0103$), Interventional ($P = .0053$), Brain ($P = .0075$), and Pediatrics ($P = .028$).

DISCUSSION

Citation patterns of Original Research and Review Articles in *AJNR* varied widely on the basis of subsections, with Review Articles accumulating the greatest number of citations within the first 2 years after publication. Understanding these citation patterns for specific topics and subsections of a journal may aid editors in evaluating the appropriate balance between topics and allow authors to determine whether their articles are being cited at levels expected for similar topics in a journal.

The highest number of citations was for articles classified as “Expedited Publication,” which is not unexpected because these are presumably important and timely topics. Thus, encouraging the submission of such articles has the potential to influence the Impact Factor of a journal. Expedited peer review and waived fees, such as those for color figures or article length, may be ways to encourage such submissions as *AJNR* does.

Articles that received the designation of “Editor's Choice” and “Fellows' Journal Club” were cited more often than others in their given journal categories. These designations are chosen by the Editor-in-Chief, and it is possible that the assigned designations improved recognition of the articles and resulted in increased citations. In addition, the articles chosen for these categories are usually those with state-of-the-art topics, clinically important, and of higher evidence-based levels, which may also contribute to

their increased citations. Articles related to spine intervention trended toward a higher number of citations than diagnostic spine articles overall, probably because they are viewed and cited by specialists outside of just imaging.

Limitations in our study include the inability to determine the exact parameters that compose the official JIF because this is a proprietary algorithm that is modified with time. Additionally, the JIF changes with time, and we only used a single JIF for this investigation, the 2013 JIF, which was the most recent one available at the time of analysis. As with all citations, it is not possible to determine citations when the original article

serves as a foundation for future work or when it is criticized or refuted. Many articles are well-received by readers, becoming popular reading but are not cited. One of the reasons many journals have decreased or eliminated case reports, despite their popularity among readers, is the negative effect on the JIF. We created our VIF on the basis of citations in the first 2 years after publication, mirroring the methodology of the JIF. The JIF also can be calculated for other periods of citations, in particular the 5-year JIF, which may give additional information about the longevity of impact of an article; however, we chose to perform a 2-year analysis because the 2-year JIF is the most commonly used metric.

The resultant quality of articles in a journal is a factor of the quality of work being performed in a given area, the alternative outlets for publication that a given author may choose, and the quality of the editorial review process. It is possible that areas such as interventional, in which many reviewers practice for a large percentage of their careers, receive higher quality reviews because the reviewers want to simultaneously select the best articles and provide the best feedback to the authors during the review process to improve the articles. In contrast, a smaller number of radiologists have most of their practice in head and neck and likely even fewer have their practice and academic interests primarily in spine.

Beyond neuroradiology journals, there are spine-focused journals in neurosurgery and orthopaedic surgery (eg, *Journal of Neurosurgery–Spine*, and *Spine*). These 2 journals have JIFs of 2.355 and 2.447, respectively, very similar to the 2.319 VIF for articles with a spine topic in *AJNR*. Comparisons such as this may help determine whether subsections and/or topics are being cited like those in journals with a potentially overlapping focus.

Knowledge of subsection VIF may allow prediction of the influence on the JIF, with reallocation of journal pages between sections. Page allotment limitations from print journals may be mitigated as they shift toward on-line publications.

Because the financial and logistic barriers for creating larger new journals has decreased, it may be tempting for physicians with a narrow area of interest to contemplate creation of a focused journal on a given topic, and understanding citation trends may provide evidence that a narrowly focused journal may or may not have the ability to survive. For example, it is clear from our investigation that for subspecialties such as spine and head and neck

imaging, creating their own freestanding journals may be difficult and physicians are better served by remaining within a larger journal with a higher JIF than they would in independent journals dedicated to their specialty. In addition, authors of articles with a given topic may be able to better recognize the expected citations of their article and whether submitting to a specific journal such as *AJNR* is best for them. For instance, the author of a diagnostic spine imaging article in *AJNR*, which will have fewer citations than the average article in the journal, may be less discouraged if they know their article has been cited more than other diagnostic spine articles in the same or other journals. Thus, encouraging all journals to calculate and publish their virtual JIF by sections may be useful to prospective authors.

CONCLUSIONS

Understanding the citation expectations of specific topics and subsections of a journal may aid editors in evaluating the appropriate balance among various topics and allow authors to determine whether their article is being cited at a level expected for similar topics in a journal.

REFERENCES

1. Chew FS, Relyea-Chew A. **How research becomes knowledge in radiology: an analysis of citations to published papers.** *AJR Am J Roentgenol* 1988;150:31–37
2. Chew FS. **The scientific literature in diagnostic radiology for American readers: a survey and analysis of journals, papers, and authors.** *AJR Am J Roentgenol* 1986;147:1055–61
3. Choudhri AF, Siddiqui A, Khan NR, et al. **Understanding bibliometric parameters and analysis.** *Radiographics* 2015;35:736–46
4. Yoon DY, Yun EJ, Ku YJ, et al. **Citation classics in radiology journals: the 100 top-cited articles, 1945–2012.** *AJR Am J Roentgenol* 2013;201:471–81
5. Brinjikji W, Klunder A, Kallmes DF. **The 100 most-cited articles in the imaging literature.** *Radiology* 2013;269:272–76
6. Pagni M, Khan NR, Cohen HL, et al. **Highly cited works in radiology: the top 100 cited articles in radiologic journals.** *Acad Radiol* 2014;21:1056–66
7. Yun EJ, Yoon DY, Kim BY. **Where do radiologists publish their work? A comparative analysis of publications by radiologists in nonradiology journals in 2000 and 2010.** *AJR Am J Roentgenol* 2013;200:W560–65
8. McDonald RJ, Cloft HJ, Kallmes DF. **Fate of manuscripts previously rejected by the American Journal of Neuroradiology: a follow-up analysis.** *AJNR Am J Neuroradiol* 2009;30:253–56
9. Khosla A, McDonald RJ, Bornmann L, et al. **Getting to yes: the fate of neuroradiology manuscripts rejected by Radiology over a 2-year period.** *Radiology* 2011;260:3–5
10. Lee JY, Yoon DY, Yoon SD, et al. **Neurointerventional research between 2003 and 2012: slow growth, high interdisciplinary collaboration, and a low level of funding.** *AJNR Am J Neuroradiol* 2014;35:1877–82
11. Garfield E. **The history and meaning of the journal Impact Factor.** *JAMA* 2006;295:90–93
12. Garfield E. **Citation analysis as a tool in journal evaluation.** *Science* 1972;178:471–79
13. Garfield E, Cawkell AE. **Citation analysis studies.** *Science* 1975;189:397
14. Garfield E. **Citation indexes for science; a new dimension in documentation through association of ideas.** *Science* 1955;122:108–11

Social Media in Medical Education

R.T. Fitzgerald, A. Radmanesh, and C.M. Hawkins

According to a 2011 survey, 94% of medical students and 79.4% of residents in the United States are active on-line social media users.¹ Social media represent a relatively simple technique to provide educational material in a format that is adapted to the learning styles preferred by the “millennial” generation. Evidence suggests that most incoming medical students are receptive to on-line learning tools even in the absence of prior exposure to such methods for educational purposes.² However, despite all of the attention social media have received in medical education circles, it remains unclear how social media use can be optimized to educate communities of learners through information sharing and knowledge dissemination.³

Those of us engaged in the education of medical students, residents, and fellows have witnessed a transition in recent years from print textbooks, journals, and syllabi to predominantly electronic media. At many medical schools across the country, learning experience has in part shifted from classrooms into on-line platforms, commonly accessed through mobile devices. For instance, Stanford Medical School saw an increase in class attendance from 30% to 80% after transitioning much of the traditionally didactic classroom lessons into concise on-line sessions, and reserving classroom time for interactive discussions and problem solving.⁴ Similarly, many radiology programs, such as the program at the University of Arkansas for Medical Sciences, now use Web-based educational activities as an adjuvant to traditional didactic lectures. Advantages of electronic educational resources, or e-learning, include ease of access and physical transport, searchability, and the potential for interaction among trainees as well as between trainees and educators.³ Dissemination of electronic educational resources via social media leverages one of this format’s strengths: information flow is based largely on relative value as judged by users. For example, popular or particularly valuable

resources will be posted, “liked,” retweeted, and “favorited” more often, thus gaining a wider audience than resources that are deemed less valuable.

As of 2011, most health professional students prefer to receive educational material on-line.⁵ Even beyond formal training, practicing physicians now have access to an increasing array of on-line sources for continuing medical education (CME) such as the American Society of Neuroradiology’s eCME course catalog (<http://members.asnr.org/ecme/>) and American Academy of Neurology’s on-line CME site (<https://cme.neurology.org/s/catalog>). Social media represent an ideal way for professional organizations to disseminate new or updated on-line CME material to their members. Furthermore, social media also allow professional organizations to meaningfully interact with their members, collect feedback, and respond purposefully in a way that was not possible with traditional methods of member-organization communication.

In their review of social media use in medical education, Cheston et al³ report that the introduction of social media-based content favorably impacts learner satisfaction and knowledge. Social media succeed in accomplishing this in a number of ways. For educators, links to reading assignments or “case of the week” installments can be efficiently distributed to a group of followers using platforms such as Twitter. Hashtags can serve to archive current and past assignments, and to manage on-line group discussions on a particular topic. Tweet chats during and after lectures and journal clubs offer trainees the opportunity to ask questions and have discussions, or provide the group with links to related material in real time. Through such interactivity, social media channels promote knowledge sharing, rather than consumption of the material that is “pushed” to target audiences. In addition, participants in social media forums often have a variety of experiences and abilities, thus diversifying and enriching conversations.

The potentials of social media for medical education are only recently being realized, and robust evidenced-based data on this subject are lacking. In the coming years with the anticipated continuing shift of student preferences toward on-line content, increased interconnectivity, and peer-to-peer knowledge sharing, social media have the potential to substantially impact and dis-

From the Department of Radiology (R.T.F.), Neuroradiology Division, University of Arkansas for Medical Sciences, Little Rock, Arkansas; Department of Radiology and Biomedical Imaging (A.R.), University of California, San Francisco, San Francisco, California; and Emory University School of Medicine (C.M.H.), Atlanta, Georgia.

Please address correspondence to Ryan T. Fitzgerald, MD, Department of Radiology, Neuroradiology Division, University of Arkansas for Medical Sciences, 4301 W Markham St, Little Rock, AR 72205; e-mail: fitzgeraldryant@uams.edu; @ryantfitzgerald

<http://dx.doi.org/10.3174/ajnr.A4136>

rupt medical education. The radiology community would be well served by leading this charge.

REFERENCES

1. Bosslet GT, Torke AM, Hickman SE, et al. **The patient-doctor relationship and online social networks: results of a national survey.** *J Gen Intern Med* 2011;26:1168–74
2. Sandars J, Morrison C. **What is the net generation? The challenge for future medical education.** *Med Teach* 2007;29:85–88
3. Cheston CC, Flickinger TE, Chisolm MS. **Social media use in medical education.** *Acad Med* 2013;88:893–901
4. Prober CG, Heath C. **Lecture halls without lectures—a proposal for medical education.** *N Engl J Med* 2012;366:1657–59
5. Giordano C, Giordano C. **Health professions students' use of social media.** *J Allied Health* 2011;40:78–81

Accuracy of Parenchymal Cerebral Blood Flow Measurements Using Pseudocontinuous Arterial Spin-Labeling in Healthy Volunteers

K. Ambarki, A. Wåhlin, L. Zarrinkoob, R. Wirestam, J. Petr, J. Malm, and A. Eklund



ABSTRACT

BACKGROUND AND PURPOSE: The arterial spin-labeling method for CBF assessment is widely available, but its accuracy is not fully established. We investigated the accuracy of a whole-brain arterial spin-labeling technique for assessing the mean parenchymal CBF and the effect of aging in healthy volunteers. Phase-contrast MR imaging was used as the reference method.

MATERIALS AND METHODS: Ninety-two healthy volunteers were included: 49 young (age range, 20–30 years) and 43 elderly (age range, 65–80 years). Arterial spin-labeling parenchymal CBF values were averaged over the whole brain to quantify the mean $pCBF_{ASL}$ value. Total CBF was assessed with phase-contrast MR imaging as the sum of flows in the internal carotid and vertebral arteries, and subsequent division by brain volume returned the $pCBF_{PCMRI}$ value. Accuracy was considered as good as that of the reference method if the systematic difference was less than 5 mL/min/100 g of brain tissue and if the 95% confidence intervals were equal to or better than ± 10 mL/min/100 g.

RESULTS: $pCBF_{ASL}$ correlated to $pCBF_{PCMRI}$ ($r = 0.73$; $P < .001$). Significant differences were observed between the $pCBF_{ASL}$ and $pCBF_{PCMRI}$ values in the young ($P = .001$) and the elderly ($P < .001$) volunteers. The systematic differences (mean ± 2 standard deviations) were -4 ± 14 mL/min/100 g in the young subjects and 6 ± 12 mL/min/100 g in the elderly subjects. Young subjects showed higher values than the elderly subjects for $pCBF_{PCMRI}$ (young, 57 ± 8 mL/min/100 g; elderly, 54 ± 7 mL/min/100 g; $P = .05$) and $pCBF_{ASL}$ (young, 61 ± 10 mL/min/100 g; elderly, 48 ± 10 mL/min/100 g; $P < .001$).

CONCLUSIONS: The limits of agreement were too wide for the arterial spin-labeling method to be considered satisfactorily accurate, whereas the systematic overestimation in the young subjects and underestimation in the elderly subjects were close to acceptable. The age-related decrease in parenchymal CBF was augmented in arterial spin-labeling compared with phase-contrast MR imaging.

ABBREVIATIONS: ASL = arterial spin-labeling; HE = healthy elderly; HY = healthy young; pCASL = pseudocontinuous ASL; pCBF = parenchymal CBF; PCMRI = phase-contrast MRI; VA = vertebral artery

Using well-established perfusion imaging techniques, such as PET, SPECT, or other techniques such as perfusion CT, cerebral blood flow can be quantified within parenchymal tissue and ex-

pressed in milliliters per minute per 100 g of brain tissue (mL/min/100 g). These methods require injection of a contrast agent or a radioactive tracer. However, radiotracers are associated with exposure to ionizing radiation, CT contrast agents are nephrotoxic, and perfusion studies of this kind cannot be repeated until the contrast medium or tracer disappears. Using arterial spin-labeling (ASL) MR imaging,¹ it is possible to assess parenchymal CBF (pCBF) noninvasively. Recent developments have enabled quantitative assessment of whole-brain perfusion with ASL within a few minutes.^{2,3} The accuracy of pCBF estimates obtained by using ASL, however, is still a subject of discussion.⁴ Age- and sex-related differences in pCBF have been found by using ASL, PET, and SPECT.^{5–10} However, these effects are still not fully understood, and no consensus has been established from previously published data.^{11,12}

Total CBF is defined by the 4 arteries that supply the brain (ie, the internal carotid arteries and the vertebral arteries [VAs]). The blood flow of these arteries, and thus the total CBF, can be measured with good accuracy at the level of the foramen magnum by

Received December 20, 2014; accepted after revision February 16, 2015.

From the Department of Radiation Sciences (K.A., A.W., A.E.), Centre for Biomedical Engineering and Physics (K.A., A.E.), Center for Functional Brain Imaging (A.W., A.E.), and Department of Clinical Neuroscience (L.Z., J.M.), Umeå University, Umeå, Sweden; Department of Medical Radiation Physics (R.W.), Lund University, Lund, Sweden; and PET Center (J.P.), Institute of Radiopharmaceutical Cancer Research, Helmholtz-Zentrum Dresden-Rossendorf, Dresden, Germany.

This work was supported by Swedish Research Council (grants 621-2011-5216 and 13514), European Union Objective 2 Norra Norrland (project 148273 CMTF), County Council of Västerbotten and Swedish Heart and Lung Foundation (grant 20110383), and the Swedish Brain Foundation.

Please address correspondence to K. Ambarki, PhD, Umeå Hospital, Department of Radiation Sciences, S-901 87 Umeå, Sweden; e-mail: khalid.ambarki@vll.se

Indicates open access to non-subscribers at www.ajnr.org

Indicates article with supplemental on-line photo.

Evidence-Based Medicine Level 2.

<http://dx.doi.org/10.3174/ajnr.A4367>

using 2D phase-contrast MR imaging (PCMRI).^{13,14} Using high-resolution morphologic MR imaging data and postprocessing software, the total volume of the brain parenchymal tissue can be assessed. Total CBF can be obtained accurately with PCMRI (shown here as $pCBF_{PCMRI}$ values),¹⁴ and brain parenchymal volume can be measured accurately¹⁵ from the T1 sequence. By dividing flow by volume, $pCBF_{PCMRI}$ can be estimated with expected good accuracy and used as a reference to evaluate the accuracy of $pCBF$ obtained via ASL ($pCBF_{ASL}$).

The aim of this study was to investigate the accuracy of a clinically implemented pseudocontinuous ASL method for assessing $pCBF$ in 92 healthy individuals by using PCMRI as the reference method. The effects of aging and sex on $pCBF$ were assessed by using both methods, and the results were compared.

MATERIALS AND METHODS

Subjects

A total of 111 subjects, recruited by advertisement in a daily newspaper, were included in this prospective study. The subjects were defined as healthy if they had no neurologic or cardiac disease, hypertension, peripheral vascular disease, or renal disease. Eleven subjects were excluded after the physical examination because of a Mini-Mental State Examination score of <28 points ($n = 3$),¹⁶ electrocardiogram changes ($n = 1$), a blood pressure of $>160/90$ mm Hg ($n = 1$), or neurologic issues ($n = 6$). After the MR imaging examination, 8 subjects were excluded because of claustrophobia ($n = 3$) or technical problems or missing MR imaging data ($n = 5$). The remaining 92 healthy subjects were categorized in 1 of 2 different age groups (ie, 49 subjects in the healthy young [HY] group [age range, 20–30 years; mean age \pm standard deviation, 25 ± 2 years; 27 women] and 43 subjects in the healthy elderly [HE] group [age range, 65–80 years; mean age \pm standard deviation, 71 ± 4 years; 23 women]). In addition, the 92 subjects were classified according to sex (ie, the study group included 50 healthy women and 42 healthy men). The research protocol used in this study was approved by the ethical review board of Umeå University. Each patient provided oral and written informed consent.

MR Imaging

Each subject was scanned by using a 3T MR imaging unit (Discovery MR 750; GE Healthcare, Milwaukee, Wisconsin) supplied with a 32-channel head coil.

Three-dimensional time-of-flight angiography was performed to visualize the ICAs and the VAs. TOF angiography was used to position a perpendicular PCMRI plane at the cervical (C1–C2) level. The 2D PCMRI data were acquired with the following parameters: TR, 9 ms; TE, 5 ms; section thickness, 5 mm; flip angle, 15°; FOV, 180×180 mm²; acquisition matrix, 512×512 ; in-plane resolution, 0.35×0.35 mm²; views per segment, 6; velocity encoding, 70 cm/s; and NEX, 2. Thirty-two velocity-coded and magnitude images throughout the entire cardiac cycle were collected. A peripheral pulse signal was used for retrospective cardiac gating. The acquisition time of the PCMRI was approximately 2 minutes 30 seconds, depending on the subject's heart rate.

Whole-brain perfusion data were obtained by using a 3D pseudocontinuous ASL (pCASL) method implemented by the manufacturer (Appendix). In summary, the pCASL was applied,

followed by an interleaved 3D stack of spiral fast spin-echo readout with background suppression.³ The pCASL parameters were as follows: sampling points on 8 spirals, 512; FOV, 240×240 mm²; true in-plane resolution, 3.75 mm^{17–19}; reconstructed matrix, 128×128 ; TR, 4674 ms; TE, 10 ms; NEX, 3; section thickness, 4 mm; labeling plane positioned at the base of the cerebellum; labeling duration, 1500 ms; postlabeling delay, 1525 ms²⁰; sections covering the whole brain, 40–44; control/label pairs, 30; and acquisition time, 4 minutes 31 seconds.

High-resolution T1-weighted data for assessing brain parenchymal volume were collected by using a sagittal 3D fast-spoiled gradient-echo sequence to image the whole brain with 176 sections, a section thickness of 1 mm, a TR of 7 ms, a TE of 2 ms, a flip angle of 10°, a FOV of 250×250 mm, an acquisition matrix of 256×256 , and an acquisition time of 5 minutes 20 seconds.

MR Imaging Data Postprocessing and Analysis

Brain Parenchymal Tissue Segmentation. The T1-weighted data were processed by using the VBM8 toolbox (<http://dbm.neuro.uni-jena.de/vbm.html>) and default parameters of SPM8 software (<http://www.fil.ion.ucl.ac.uk/spm/>) by using Matlab R2013b (MathWorks, Natick, Massachusetts). The segmentation method of VBM8 is based on an adaptive maximum a posteriori approach,²¹ and tissue compartments were classified into gray matter, white matter, and CSF. GM and WM segmentations were inspected visually to ensure quality of the segmentation. No severe missegmentation of brain parenchymal tissue was observed, and therefore no data were omitted from the analysis. However, in a few of the elderly subjects, the periventricular WM was misclassified as GM, but the segmentation did not alter the whole-brain segmentation, and no manual correction had to be performed.

ASL Measurement of Parenchymal Cerebral Blood Flow. The pCASL $pCBF$ maps (in mL/min/100 g) were computed by the postprocessing FuncTool software (version 10.4.04; GE Healthcare) that was based on a general kinetic model for ASL.²² The details of the manufacturer's implementation method to quantify the $pCBF$ maps are shown in the Appendix.

Using the SPM8 software, GM and WM masks were co-registered to the ASL data and down-sampled to the same pixel size as that of the reconstructed ASL data. The GM and WM masks were then smoothed in-plane with a Gaussian kernel (3.25×3.25 mm² full width at half maximum) to create a resolution identical to the true spatial resolution of ASL (On-line Fig 1). Erosion was applied to exclude the 2 outer pixel layers from the brain mask (GM and WM) to avoid ASL artifacts and inclusion of the skull. Each pixel in the brain mask contains the volume fractions of GM (F_{GM}) and WM (F_{WM}). The brain parenchymal volume was calculated as the sum of the GM and WM volumes. The mean $pCBF$ from the ASL data ($pCBF_{ASL}$) was estimated by using equation 1:

$$pCBF_{ASL} = \frac{\sum_{i=1}^{i=n} CBF(i)}{\sum_{i=1}^{i=n} (F_{GM}(i) + F_{WM}(i))}$$

where F_{GM} and F_{WM} are the volume fractions of GM and WM, respectively, $CBF(i)$ is the cerebral blood flow (mL/min/100 g of brain tissue) within the i th ASL pixel, and n is the number of pixels that contain brain tissue ($F_{GM} + F_{WM} > 0\%$). Our aim was to estimate the perfusion in the entire parenchymal tissue. No partial volume correction was thus necessary to separate perfusion signal from individual WM and GM voxels.

PCMRI Measurement of Vessel Velocity and Parenchymal Cerebral Blood Flow. PCMRI data were analyzed by using Segment software version 1.8 (Medviso, Lund, Sweden). The magnitude images were used to delineate manually the cross-section areas of the ICAs and VAs. The positions and sizes of the cross-section areas were kept constant during the cardiac cycle. For each vessel, the flow rate was computed as the mean velocity multiplied by the cross-section area.

The blood flow rates of the bilateral ICAs and VAs were summed, and the derived blood flow rate was averaged over the cardiac cycle to estimate the total CBF (reported in milliliters per minute). Thereafter, the parenchymal cerebral blood flow from PCMRI ($pCBF_{PCMRI}$) was calculated in milliliters per minute per 100 g of brain tissue by using equation 2:

$$pCBF_{PCMRI} = \frac{tCBF}{\rho \times BPV} \times 100,$$

where tCBF is total CBF, BPV is brain parenchymal volume, and ρ is the brain tissue density (1.05 g/mL).²³

Furthermore, the velocity of blood in the labeling plane directly affects the labeling efficiency of the pCASL and thus also the pCBF quantification.^{3,13} To investigate the effect of the mean velocity of the bilateral ICAs and VAs on the ASL data, mean velocities were computed and correlated to the difference between $pCBF_{PCMRI}$ and $pCBF_{ASL}$.

Comparison of $pCBF_{PCMRI}$ and $pCBF_{ASL}$ with respect to age and sex

Subjects	$pCBF_{PCMRI}$ (Mean \pm SD) (mL/min/100 g)	$pCBF_{ASL}$ (Mean \pm SD) (mL/min/100 g)	P Value
HY ($n = 49$)	57 \pm 8	61 \pm 10	<.05 ^a
HE ($n = 43$)	54 \pm 7	48 \pm 10	<.001 ^a
HW ($n = 50$)	58 \pm 8	58 \pm 12	.94
HM ($n = 42$)	53 \pm 6	51 \pm 11	.16
All ($n = 92$)	56 \pm 8	55 \pm 12	.34

Note:—HW indicates healthy women; HM, healthy men.

^a Value is significant.

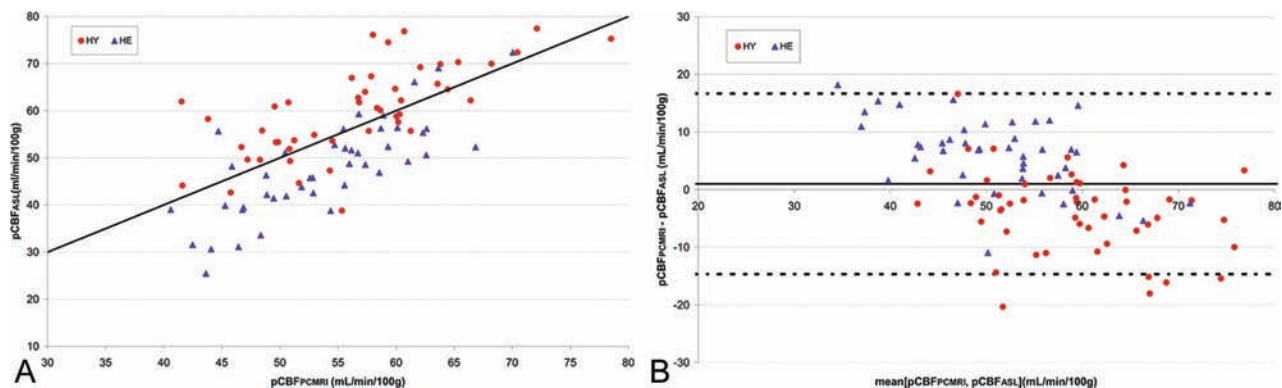


FIGURE. A, Scatterplot of parenchymal cerebral blood flow determined by ASL ($pCBF_{ASL}$) versus PCMRI-determined parenchymal cerebral blood flow ($pCBF_{PCMRI}$). The solid black line is the identity line. The correlation coefficient r is 0.73 ($P < .001$). B, Corresponding Bland-Altman plot. The horizontal dashed lines represent the 95% confidence intervals of the difference between $pCBF_{PCMRI}$ and $pCBF_{ASL}$.

Statistical Analysis

SPSS Statistics version 18 (IBM, Armonk, New York) was used to perform statistical analysis. Variables were expressed as means \pm standard deviation. The Shapiro-Wilk test was used to test the normal distribution of the measured parameters. Differences between the groups were investigated by using the unpaired Student t test. For the comparison between $pCBF_{ASL}$ and $pCBF_{PCMRI}$ values, linear regression analysis and Bland-Altman plots were used.²⁴ Differences between the $pCBF_{PCMRI}$ and $pCBF_{ASL}$ values were tested by using the paired Student t test. The accuracy was defined as the systematic bias and the random difference (mean difference \pm 2 standard deviations) between the 2 methods. We considered the accuracy of ASL-based pCBF measurement to be good if the systematic difference against the reference method was <5 mL/min/100 g and if the randomized difference was less than or equal to ± 10 mL/min/100 g, which corresponds to the limits of agreement previously shown for repeated measurements with PCMRI¹⁴ and for repeated measurements with ASL.¹⁹ A P value of $<.05$ was considered statistically significant.

RESULTS

Comparison of PCMRI and ASL

The pCBF values obtained by PCMRI and ASL are shown in the Table, and a comparison between the $pCBF_{PCMRI}$ and $pCBF_{ASL}$ values is displayed in the Figure. There was a significant correlation between $pCBF_{PCMRI}$ and $pCBF_{ASL}$ values ($r = 0.73$; $P < .001$). Corresponding correlation coefficients (r) when the HY and HE groups were compared separately were 0.73 ($P < .001$) and 0.78 ($P < .001$), respectively. As shown in the Table, there was a significant difference between $pCBF_{ASL}$ and $pCBF_{PCMRI}$ for HE ($P < .001$) and HY ($P = .001$) subjects but not for the whole group ($P = .34$). For all subjects, the mean bias and the limits of agreement between the 2 methods were 1 ± 16 mL/min/100 g (mean \pm 2 standard deviations). The mean bias ($pCBF_{PCMRI} - pCBF_{ASL}$) showed an underestimation by ASL in HE subjects (6 ± 12 mL/min/100 g) and an overestimation in HY subjects (-4 ± 14 mL/min/100 g), whereas it was similar for healthy men and women (2 ± 19 and 0 ± 16 mL/min/100 g, respectively; $P = .256$). The difference between $pCBF_{PCMRI}$ and $pCBF_{ASL}$ showed significant corre-

lation with the mean velocities of the VAs ($r = -0.47$; $P < .001$; On-line Fig 2) and ICAs ($r = -0.35$; $P = .001$).

Dependence of pCBF_{ASL} and pCBF_{PCMRI} on Age and Sex

pCBF_{ASL} values were significantly higher in HY than in HE subjects ($P < .001$; Table). A similar pattern emerged for pCBF_{PCMRI} values, but the difference was less evident ($P = .05$; Table). Therefore, the percent decrease of the mean pCBF with aging was lower in pCBF_{PCMRI} (-5%) than in pCBF_{ASL} (-21%). The pCBF_{PCMRI} and pCBF_{ASL} values were significantly higher in women (pCBF_{PCMRI} 9% [$P = 4 \times 10^{-4}$]; pCBF_{ASL} 12% [$P = .002$]).

DISCUSSION

Methods for assessing cerebral perfusion by using ASL are available on most modern MR imaging scanners, but their accuracy is still not fully established. Using high-spatial-resolution PCMRI as the reference method, the accuracy of ASL was investigated in this study, and the dependencies on age and sex were quantified and compared. A good correlation was found between the reference method and ASL, but a significant difference between the mean values was observed for both HE (approximately -11%) and HY (5%) subjects. Consequently, the observed effect of aging on pCBF was estimated as much lower in values obtained from PCMRI than in those from ASL (5% vs 21%). Because of ASL overestimation in HY subjects and underestimation in HE subjects, no significant difference between pCBF_{PCMRI} and pCBF_{ASL} values was observed in the group as a whole (Table).

In this study, high-resolution PCMRI with an in-plane resolution of 0.35 mm was used, which represents >8 pixels per diameter for the internal carotid and vertebral arteries. With high spatial resolution (>4 pixels per diameter) and by using similar MR imaging parameters (velocity encoding, TE, TR, and section thickness) as in the present study, it was shown previously that PCMRI can accurately (<10% error) measure the blood flow in ICAs and VAs and thus can be considered a criterion-standard technique for measuring total CBF.¹⁴

The ASL sequence used in this study had a short MR imaging acquisition time (<5 minutes for whole-brain coverage), and we used a pseudocontinuous arterial-labeling scheme with 3D segmented readout and background suppression, which is considered one of the best ASL approaches for assessing pCBF.² It is important to emphasize that in this study, the ASL data were obtained with a commercially available ASL sequence, and the CBF estimates were quantified by using the manufacturer's postprocessing software without any additional corrections, as was also done in previous studies.^{19,25} It should be mentioned that the CBF quantification model used in this study was slightly different than the model proposed in a recent consensus article concerning ASL for clinical applications (Appendix).²

Jain et al²⁶ reported results from a group of children that were similar to ours (ie, a significant correlation of pCBF values determined by PCMRI and ASL). Other studies have found moderate to good correlations ($r = 0.4-0.8$) between pseudocontinuous ASL and PET imaging for pCBF measurements.^{4,27,28} On the contrary, Henriksen et al²⁹ showed a large underestimation of ASL-based pCBF (75%) compared with the estimation by PCMRI and no correlation between the 2 methods. One explanation for this result might be that they used a model-free pulsed-ASL method.

The results of our study further support the use of pseudocontinuous ASL. PET is most likely a good method for comparison with ASL, because it is possible to perform intermodal comparisons of global and regional brain perfusion measurements. A recent study found a relatively low correlation between ASL and PET for measuring pCBF in GM at resting state,⁴ but it is not feasible to repeat such a study with a large number of volunteers.

In accordance with the results of our study, previous ASL studies found a difference of mean pCBF (17%) or perfusion in GM (20%-30%) between HY and HE subjects.^{5,6} In these previous ASL studies, no age-specific postlabeling delay was used, and the postlabeling delays that were used ranged from 800 to 1700 ms. PET and SPECT studies have revealed similar results.^{9,10} Our findings confirm that pCBF decreases with age in healthy adults. However, the magnitude of the decline in pCBF as determined by ASL was approximately 4 times larger than that determined by PCMRI, and these results bring into question previous observations regarding the magnitude of decrease in ASL-derived pCBF that is associated with healthy aging. Aging causes general brain atrophy and cortical thinning, which may increase the partial volume effects,^{30,31} and aging also leads to increased arterial transit time.³² Potentially, such changes influence the accuracy of ASL.⁵ Increasing the postlabeling delay for elderly subjects could remedy some ASL inaccuracies.² Furthermore, the CBF quantification model used in our study (see Appendix and equation 3) assumes that the longitudinal relaxation time of gray matter (T_{1GM}) and the brain-to-blood partition coefficient (λ) are constant. However, previous studies have provided no real consensus with regard to a possible effect of aging on T_{1GM} .^{33,34} Furthermore, it is known that λ values are higher in the neonatal brain than in the adult brain.³⁵ Hence, we cannot rule out the possibility that the brain-to-blood partition coefficient varies over a life span between 25 and 71 years of age.

Women had higher pCBF_{PCMRI} (9%) and pCBF_{ASL} (12%) values than the men in this study. Similar results have been reported, with pCBF values being 9%-15% higher in women.^{5,10,36} Because various imaging modalities have indicated the same relative difference, it can be regarded as reliable, and it indicates that the accuracy of the ASL method was not affected by differences related to sex. The T_1 relaxation of blood (T_{1b}) can influence the accuracy of ASL perfusion measurements.^{26,37} Previous studies have shown higher mean T_{1b} values (6%-9%) in women than in men, and the lower blood hematocrit level in women than in men may explain this observed sex difference in mean T_{1b} .³⁸⁻⁴⁰ In a previous study, Piechnik et al⁴⁰ found significantly higher mean T_{1b} values in women than in men (1577 vs 1491 ms, respectively). Using equation 3 in the Appendix and T_{1b} for men and for women, we estimated that the relative sex difference in pCBF_{ASL} values in our data decreased from 12% to approximately 4%, which then is less than the PCMRI findings. In the same study, Piechnik et al⁴⁰ found no differences in T_{1b} values between HY (20-30 years) and HE (60-70 years) subjects, which indicates that the T_{1b} effect is not the dominating factor in explaining the large effect of aging on pCBF_{ASL}.

Motion artifacts during the ASL scan were not corrected, which might be a source of error in the pCBF_{ASL} estimates. Another factor that might influence the ASL perfusion accuracy is the location of the labeling plane. In the present study, the labeling plane was located at the base of the cerebellum and should be

oriented perpendicularly to the cerebral feeding arteries. This placement was difficult to achieve; manually placing the labeling plane for ASL was not possible, because the current commercial implementation of pCASL does not allow it. Furthermore, the tortuosity of cerebral arteries increases with age, which may partly explain the underestimation of pCBF_{ASL} in HE subjects.⁴¹ For 5 HE subjects, pCBF_{ASL} values were unreasonably low (ie, of the order of 20–30 mL/min/100 g; Fig 1A). When we excluded these HE subjects from the analysis, we observed a minor increase (from 46 to 48 mL/min/100 g) in the mean pCBF_{ASL} in HE subjects, which did not change our main conclusions. Furthermore, we visually inspected the labeling-plane position in these 5 HE subjects with respect to the geometry of the feeding cerebral arteries by using TOF angiography. In 3 subjects, the labeling plane was close to parallel with the VAs, and ASL data showed a very low CBF_{ASL} in the posterior region (see example in On-line Fig 3). However, on 2 other HE subjects with a low pCBF_{ASL}, the labeling plane was close to perpendicular to both ICAs and VAs, and thus its position should not cause the low CBF_{ASL} that we observed in the posterior regions (On-line Fig 3). In future studies, it will be important to investigate in detail how the tortuosity of ICAs and VAs can alter the estimation of pCBF values with ASL.

The tortuosity of ICAs and VAs is also challenging for the PCMRI method, in which misalignment of the PCMRI plane can cause an underestimation of the total cerebral blood flow.⁴² In our study, this potential problem was partially avoided by careful manual placement of the PCMRI planes in the TOF angiogram. A potential source of pCBF overestimation in PCMRI is the inclusion of extracerebral blood flow of the anterior spinal artery and ophthalmic arteries. The lumen of the spinal artery has been reported to be small (diameter, <1 mm), and the total blood flow rate of the slightly larger ophthalmic artery is approximately 22 mL/min in healthy adults.^{43,44} Hence, we estimated that the total blood flow of these extracerebral arteries could represent 3%–4% of potential pCBF overestimation by using our reference PCMRI method.

Finally, pCBF quantification in white matter by ASL is problematic because of the low signal-to-noise ratio⁴⁵ and its long and nonuniform arterial transit time.^{46,47} If white matter pCBF shows a systematic bias, it would affect the mean whole-brain value.

CONCLUSIONS

For mean parenchymal cerebral blood flow, a high degree of correlation was found between the ASL and PCMRI (reference) methods. For HY adults, the accuracy of pCBF assessment determined by ASL was good with regard to the systematic difference, though the randomized difference against the PCMRI method was outside of the limits according to our criteria. There were both systematic underestimation and a similarly large randomized difference in results for the HE subjects. Consequently, age-related reductions in pCBF became augmented with ASL compared with the reference method.

APPENDIX

The true in-plane spatial resolution of the pCASL sequence was 3.75 mm.^{17–19} Background suppression pulses were achieved by saturating the imaged volume before labeling and by applying 4 nonselective inversion pulses at 1500 ms, 680 ms, 248 ms, and 57

ms before readout.⁴⁸ A reference image was obtained 2000 ms after saturation in the same sequence as the rest of the ASL data.

The following description of the CBF quantification method was provided by the manufacturer of the MR imaging scanner:

$$\text{CBF} = 6000\lambda(1 - e^{-T_{\text{sat}}/T_{1\text{GM}}}) \frac{e^{\text{PLD}/T_{1\text{b}}} \Delta S}{2\alpha T_{1\text{b}}(1 - e^{-\tau/T_{1\text{b}}}) S_0},$$

where PLD is the postlabeling delay time (1525 ms); τ is the labeling duration (1500 ms); α is a combination of inversion efficiency (0.8) and background suppression efficiency (0.75)⁴⁸ resulting in an overall labeling efficiency of 0.6; λ is the tissue-to-blood partition coefficient (0.9 mL/g)³⁵; $T_{1\text{b}}$ and $T_{1\text{GM}}$ are the longitudinal relaxation times of blood (1600 ms) and GM (1200 ms), respectively; T_{sat} is the saturation time (2000 ms)¹⁸; S_0 is the reference image signal (obtained voxelwise); and ΔS is the ASL difference image signal. The scaling factor 6000 was used to convert to CBF units (mL/min/100 g). In our study, it was assumed that WM perfusion can be calculated by using the model described above and setting parameters. Compared with the quantification proposed by Alsop et al,² a term for compensation of the imperfect relaxation in the reference image is added.

Disclosures: Ronnie Wirestam—RELATED: Grant: Swedish Research Council.* Comments: Government funding for part of my salary as university professor. Anders Eklund—RELATED: Grant: Swedish Research Council.* *Money paid to institution.

REFERENCES

- Williams DS, Detre JA, Leigh JS, et al. **Magnetic resonance imaging of perfusion using spin inversion of arterial water.** *Proc Natl Acad Sci U S A* 1992;89:212–16 CrossRef Medline
- Alsop DC, Detre JA, Golay X, et al. **Recommended implementation of arterial spin-labeled perfusion MRI for clinical applications: a consensus of the ISMRM perfusion study group and the European consortium for ASL in dementia.** *Magn Reson Med* 2014 Apr 8. [Epub ahead of print] CrossRef Medline
- Dai W, Garcia D, de Bazelaire C, et al. **Continuous flow-driven inversion for arterial spin labeling using pulsed radio frequency and gradient fields.** *Magn Reson Med* 2008;60:1488–97 CrossRef Medline
- Heijtel DF, Mutsaerts HJ, Bakker E, et al. **Accuracy and precision of pseudo-continuous arterial spin labeling perfusion during baseline and hypercapnia: a head-to-head comparison with ¹⁵O H₂O positron emission tomography.** *Neuroimage* 2014;92:182–92 CrossRef Medline
- Parkes LM, Rashid W, Chard DT, et al. **Normal cerebral perfusion measurements using arterial spin labeling: reproducibility, stability, and age and gender effects.** *Magn Reson Med* 2004;51:736–43 CrossRef Medline
- Asllani I, Habeck C, Borogovac A, et al. **Separating function from structure in perfusion imaging of the aging brain.** *Hum Brain Mapp* 2009;30:2927–35 CrossRef Medline
- Biagi L, Abbruzzese A, Bianchi MC, et al. **Age dependence of cerebral perfusion assessed by magnetic resonance continuous arterial spin labeling.** *J Magn Reson Imaging* 2007;25:696–702 CrossRef Medline
- Chen JJ, Rosas HD, Salat DH. **Age-associated reductions in cerebral blood flow are independent from regional atrophy.** *Neuroimage* 2011;55:468–78 CrossRef Medline
- Leenders KL, Perani D, Lammertsma AA, et al. **Cerebral blood flow, blood volume and oxygen utilization. Normal values and effect of age.** *Brain* 1990;113:27–47 CrossRef Medline
- Slosman DO, Chicherio C, Ludwig C, et al. **(133)Xe SPECT cerebral blood flow study in a healthy population: determination of T-scores.** *J Nucl Med* 2001;42:864–70 Medline
- Meltzer CC, Cantwell MN, Greer PJ, et al. **Does cerebral blood flow decline in healthy aging? A PET study with partial-volume correction.** *J Nucl Med* 2000;41:1842–48 Medline

12. Aanerud J, Borghammer P, Chakravarty MM, et al. **Brain energy metabolism and blood flow differences in healthy aging.** *J Cereb Blood Flow Metab* 2012;32:1177–87 CrossRef Medline
13. Aslan S, Xu F, Wang PL, et al. **Estimation of labeling efficiency in pseudocontinuous arterial spin labeling.** *Magn Reson Med* 2010;63:765–71 CrossRef Medline
14. Wählin A, Ambarki K, Hauksson J, et al. **Phase contrast MRI quantification of pulsatile volumes of brain arteries, veins, and cerebrospinal fluids compartments: repeatability and physiological interactions.** *J Magn Reson Imaging* 2012;35:1055–62 CrossRef Medline
15. Valverde S, Oliver A, Cabezas M, et al. **Comparison of 10 brain tissue segmentation methods using revisited IBSR annotations.** *J Magn Reson Imaging* 2015;41:93–101 CrossRef Medline
16. Folstein MF, Folstein SE, McHugh PR. **“Mini-mental state.” A practical method for grading the cognitive state of patients for the clinician.** *J Psychiatr Res* 1975;12:189–98 CrossRef Medline
17. Pienaar R, Paldino MJ, Madan N, et al. **A quantitative method for correlating observations of decreased apparent diffusion coefficient with elevated cerebral blood perfusion in newborns presenting cerebral ischemic insults.** *Neuroimage* 2012;63:1510–18 CrossRef Medline
18. Järnum H, Steffensen EG, Knutsson L, et al. **Perfusion MRI of brain tumours: a comparative study of pseudo-continuous arterial spin labelling and dynamic susceptibility contrast imaging.** *Neuroradiology* 2010;52:307–17 CrossRef Medline
19. Mutsaerts HJ, Steketee RM, Heijtel DF, et al. **Inter-vendor reproducibility of pseudo-continuous arterial spin labeling at 3 Tesla.** *PLoS One* 2014;9:e104108 CrossRef Medline
20. Melzer TR, Watts R, MacAskill MR, et al. **Arterial spin labelling reveals an abnormal cerebral perfusion pattern in Parkinson’s disease.** *Brain* 2011;134:845–55 CrossRef Medline
21. Rajapakse JC, Giedd JN, Rapoport JL. **Statistical approach to segmentation of single-channel cerebral MR images.** *IEEE Trans Med Imaging* 1997;16:176–86 CrossRef Medline
22. Buxton RB, Frank LR, Wong EC, et al. **A general kinetic model for quantitative perfusion imaging with arterial spin labeling.** *Magn Reson Med* 1998;40:383–96 CrossRef Medline
23. Torack RM, Alcalá H, Gado M, et al. **Correlative assay of computerized cranial tomography CCT, water content and specific gravity in normal and pathological postmortem brain.** *J Neuropathol Exp Neurol* 1976;35:385–92 CrossRef Medline
24. Bland JM, Altman DG. **Statistical methods for assessing agreement between two methods of clinical measurement.** *Lancet* 1986;1:307–10 Medline
25. Bron EE, Steketee RM, Houston GC, et al; Alzheimer’s Disease Neuroimaging Initiative. **Diagnostic classification of arterial spin labeling and structural MRI in presenile early stage dementia.** *Hum Brain Mapp* 2014;35:4916–31 CrossRef Medline
26. Jain V, Duda J, Avants B, et al. **Longitudinal reproducibility and accuracy of pseudo-continuous arterial spin-labeled perfusion MR imaging in typically developing children.** *Radiology* 2012;263:527–36 CrossRef Medline
27. van Golen LW, Kuijter JP, Huisman MC, et al. **Quantification of cerebral blood flow in healthy volunteers and type 1 diabetic patients: comparison of MRI arterial spin labeling and [(15)O]H₂O positron emission tomography (PET).** *J Magn Reson Imaging* 2014;40:1300–09 CrossRef Medline
28. Zhang K, Herzog H, Mauler J, et al. **Comparison of cerebral blood flow acquired by simultaneous [15O]water positron emission tomography and arterial spin labeling magnetic resonance imaging.** *J Cereb Blood Flow Metab* 2014;34:1373–80 CrossRef Medline
29. Henriksen OM, Larsson HB, Hansen AE, et al. **Estimation of inter-subject variability of cerebral blood flow measurements using MRI and positron emission tomography.** *J Magn Reson Imaging* 2012;35:1290–99 CrossRef Medline
30. Kety SS. **Human cerebral blood flow and oxygen consumption as related to aging.** *J Chronic Dis* 1956;3:478–86 CrossRef Medline
31. Good CD, Johnsrude IS, Ashburner J, et al. **A voxel-based morphometric study of ageing in 465 normal adult human brains.** *Neuroimage* 2001;14:21–36 CrossRef Medline
32. Scheel P, Ruge C, Schöning M. **Flow velocity and flow volume measurements in the extracranial carotid and vertebral arteries in healthy adults: reference data and the effects of age.** *Ultrasound Med Biol* 2000;26:1261–66 CrossRef Medline
33. Cho S, Jones D, Reddick WE, et al. **Establishing norms for age-related changes in proton T1 of human brain tissue in vivo.** *Magn Reson Imaging* 1997;15:1133–43 CrossRef Medline
34. Breger RK, Yetkin FZ, Fischer ME, et al. **T1 and T2 in the cerebrum: correlation with age, gender, and demographic factors.** *Radiology* 1991;181:545–47 CrossRef Medline
35. Herscovitch P, Raichle ME. **What is the correct value for the brain-blood partition coefficient for water?** *J Cereb Blood Flow Metab* 1985;5:65–69 CrossRef Medline
36. Esposito G, Van Horn JD, Weinberger DR, et al. **Gender differences in cerebral blood flow as a function of cognitive state with PET.** *J Nucl Med* 1996;37:559–64 Medline
37. Varela M, Hajnal JV, Petersen ET, et al. **A method for rapid in vivo measurement of blood T1.** *NMR Biomed* 2011;24:80–88 CrossRef Medline
38. Wu WC, Jain V, Li C, et al. **In vivo venous blood T1 measurement using inversion recovery true-FISP in children and adults.** *Magn Reson Med* 2010;64:1140–47 CrossRef Medline
39. Qin Q, Strouse JJ, van Zijl PC. **Fast measurement of blood T1 in the human jugular vein at 3 Tesla.** *Magn Reson Med* 2011;65:1297–304 CrossRef Medline
40. Piechnik SK, Ferreira VM, Lewandowski AJ, et al. **Normal variation of magnetic resonance T1 relaxation times in the human population at 1.5 T using ShMOLLI.** *J Cardiovasc Magn Reson* 2013;15:13 CrossRef Medline
41. Bullitt E, Zeng D, Mortamet B, et al. **The effects of healthy aging on intracerebral blood vessels visualized by magnetic resonance angiography.** *Neurobiol Aging* 2010;31:290–300 CrossRef Medline
42. Zhao M, Charbel FT, Alperin N, et al. **Improved phase-contrast flow quantification by three-dimensional vessel localization.** *Magn Reson Imaging* 2000;18:697–706 CrossRef Medline
43. Sheehy NP, Boyle GE, Meaney JF. **Normal anterior spinal arteries within the cervical region: high-spatial-resolution contrast-enhanced three-dimensional MR angiography.** *Radiology* 2005;236:637–41 CrossRef Medline
44. Ambarki K, Hallberg P, Jóhannesson G, et al. **Blood flow of ophthalmic artery in healthy individuals determined by phase-contrast magnetic resonance imaging.** *Invest Ophthalmol Vis Sci* 2013;54:2738–45 CrossRef Medline
45. van Osch MJ, Teeuwisse WM, van Walderveen MA, et al. **Can arterial spin labeling detect white matter perfusion signal?** *Magn Reson Med* 2009;62:165–73 CrossRef Medline
46. Pohmann R. **Accurate, localized quantification of white matter perfusion with single-voxel ASL.** *Magn Reson Med* 2010;64:1109–13 CrossRef Medline
47. Lu K, Liu T, Wong EC, et al. **Regional white matter perfusion measurement using an optimized pseudo-continuous ASL MRI.** In: *Proceedings of the 17th Annual Meeting of the International Society of Magnetic Resonance in Medicine [abstract 4401]*. Honolulu, Hawaii. April 18–24, 2009
48. Garcia DM, Duhamel G, Alsop DC. **Efficiency of inversion pulses for background suppressed arterial spin labeling.** *Magn Reson Med* 2005;54:366–72 CrossRef Medline

Gray Matter Volume Reduction Is Associated with Cognitive Impairment in Neuromyelitis Optica

Q. Wang, N. Zhang, W. Qin, Y. Li, Y. Fu, T. Li, J. Shao, L. Yang, F.-D. Shi, and C. Yu



ABSTRACT

BACKGROUND AND PURPOSE: Whether gray matter impairment occurs in neuromyelitis optica is a matter of ongoing debate, and the association of gray matter impairment with cognitive deficits remains largely unknown. The purpose of this study was to investigate gray matter volume reductions and their association with cognitive decline in patients with neuromyelitis optica.

MATERIALS AND METHODS: This study included 50 patients with neuromyelitis optica and 50 sex-, age-, handedness-, and education-matched healthy subjects who underwent high-resolution structural MR imaging examinations and a battery of cognitive assessments. Gray matter volume and cognitive differences were compared between the 2 groups. The correlations of the regional gray matter volume with cognitive scores and clinical variables were explored in the patients with neuromyelitis optica.

RESULTS: Compared with healthy controls (635.9 ± 51.18 mL), patients with neuromyelitis optica (602.8 ± 51.03 mL) had a 5.21% decrease in the mean gray matter volume of the whole brain ($P < .001$). The significant gray matter volume reduction in neuromyelitis optica affected the frontal and temporal cortices and the right thalamus (false discovery rate correction, $P < .05$). The regional gray matter volumes in the frontal and temporal cortices were negatively correlated with disease severity in patients with neuromyelitis optica (Alphasim correction, $P < .05$). Patients with neuromyelitis optica had impairments in memory, information processing speed, and verbal fluency ($P < .05$), which were correlated with gray matter volume reductions in the medial prefrontal cortex and thalamus (Alphasim correction, $P < .05$).

CONCLUSIONS: Gray matter volume reduction is present in patients with neuromyelitis optica and is associated with cognitive impairment and disease severity in this group.

ABBREVIATIONS: BLV = brain lesion volume; EDSS = Expanded Disability Status Scale; GMV = gray matter volume; HC = healthy control; NMO = neuromyelitis optica; NMO-IgG = neuromyelitis optica immunoglobulin G; r = partial correlation coefficient

Neuromyelitis optica (NMO) is an idiopathic, severe, demyelinating disease of the central nervous system that is characterized by optic neuritis and myelitis.^{1,2} Although the brain is

traditionally considered to be spared in NMO,³ recent studies have identified brain lesions in 60% of patients with this condition.⁴ In 10% of patients with NMO, the site of brain lesions on MR imaging coincides with high concentrations of the water channel aquaporin 4,^{5,6} the target of NMO immunoglobulin G (NMO-IgG).

Although several investigations have revealed gray matter impairment in NMO by comparing intergroup differences in the regional homogeneity,⁷ amplitude of low-frequency fluctuation,⁸ diffusivity,⁹⁻¹¹ perfusion,¹² and magnetization transfer ratio,¹³ whether GM structural impairment is a feature of NMO is an ongoing debate. Several studies have identified reductions in GM volume (GMV)¹⁴⁻¹⁶ or cortical thickness¹⁷ in patients with NMO; however, 3 additional studies have failed to demonstrate reductions in the GMV^{18,19} or cortical thickness in patients.²⁰ These conflicting outcomes may result from the low statistical power of the relatively small sample sizes (15–30 patients with NMO in previous studies). Studies with a large sample of patients with NMO may help clarify this issue.

Received January 8, 2015; accepted after revision March 14.

From the Department of Radiology and Tianjin Key Laboratory of Functional Imaging (Q.W., N.Z., W.Q., C.Y.) and Department of Neurology and Tianjin Neurological Institute (Y.L., Y.F., T.L., J.S., L.Y., F.-D.S.), Tianjin Medical University General Hospital, Tianjin, China; and Department of Neurology (F.-D.S.), Barrow Neurological Institute, St. Joseph's Hospital and Medical Center, Phoenix, Arizona.

This study was supported by the Tianjin Key Technology Research and Development Program (14ZCZDSY00018), the National Basic Research Program of China 2013CB966900, and the National Natural Science Foundation of China (No. 81425013).

Please address correspondence to Chunshui Yu, MD, Department of Radiology, Tianjin Medical University General Hospital, No. 154, Anshan Rd, Heping District, Tianjin 300052, China; e-mail: chunshuiyu@tjmu.edu.cn

Indicates open access to non-subscribers at www.ajnr.org

Indicates article with supplemental on-line tables.

Indicates article with supplemental on-line photos.

Evidence-Based Medicine Level 2.

<http://dx.doi.org/10.3174/ajnr.A4403>

Table 1: Demographic and clinical characteristics of the subjects^a

Subjects	Patients with		P Value
	NMO	HCs	
No. of subjects	50	50	NA
Sex (female/male)	42:8	43:7	.779
Age (yr)	47.4 (13.4)	49.8 (8.9)	.294
Education (yr)	11.2 (3.4)	12.1 (3.1)	.192
NMO-IgG (\pm)	32/18	NA	NA
Brain lesion volumes (cm ³) ^b	3.3 (5.1)	NA	NA
Onset age (yr)	41.6 (14.1)	NA	NA
Relapsing frequency (times/yr)	0.8 (0.7)	NA	NA
No. of attacks (times)	4.5 (5.1)	NA	NA
Disease duration (yr)	6.6 (6.7)	NA	NA
EDSS score	3.8 (2.3)	NA	NA

Note:—NA indicates not applicable.

^a All values are expressed as mean (SD).

^b Thirty-seven patients had visible brain lesions.

Cognitive impairment has been repeatedly reported in patients with NMO^{10,17,18,21–24} and is characterized by deficits in multiple cognitive domains, including memory, attention, and speed of information processing. The neural correlates of the cognitive impairment in NMO have been attributed to focal reductions in white matter volume and integrity.^{10,18} A recent study found no correlation between cognitive impairment and cortical thinning in 23 patients with NMO.¹⁷ However, it remains unknown whether GMV reduction is associated with cognitive impairment in these patients.

By recruiting a large sample of patients with NMO ($n = 50$), we aimed to clarify the GMV changes in NMO and the correlations of GMV changes with cognitive impairment and clinical variables in these patients.

MATERIALS AND METHODS

Subjects

Fifty right-handed patients with NMO and 50 sex-, age-, handedness-, and education-matched healthy controls (HCs) were included (Table 1). All patients were enrolled from a single center (Department of Neurology, Tianjin Medical University General Hospital) by using a data base for patients with NMO who had visited our hospital for treatment during the past 5 years. During the recruitment phase, we invited these patients to return to our hospital to participate in this experiment. On accepting the invitation, they would be subjected to a series of screening procedures to confirm whether they met the inclusion criteria. The healthy controls were recruited by advertisements from the local community. The inclusion criteria for both patients and controls were age (18–70 years) and right-handedness. All patients also fulfilled the revised Wingerchuk diagnostic criteria for NMO,¹ including the 2 absolute criteria of optic neuritis and acute myelitis and at least 2 of the following 3 supportive criteria: brain MR imaging findings negative or nondiagnostic for multiple sclerosis at onset, MR imaging evidence of a spinal cord lesion involving ≥ 3 vertebral segments, and a positive serologic test for NMO-IgG. The diagnostic basis for each patient with NMO is shown in On-line Table 1. The exclusion criteria for both patients and controls were the following: 1) contraindications against MR imaging; 2) serious visual, auditory, or motor impairment that would influence cognitive tests; 3) history of head trauma or other neuropsychiatric diseases; and 4) poor imaging quality (visible artifacts). Serum NMO-IgG

was tested by using a cell-based assay with quantitative flow cytometry.²⁵ The disease severity was assessed by the Expanded Disability Status Scale (EDSS) scores. All of the participants provided written informed consent that met the approval of the local Medical Research Ethics Committee, and the study was approved by the institutional review board.

Cognitive Assessment

A battery of cognitive tests was administered to all subjects by a professional psychologist within 1 month after the MR imaging examinations. The California Verbal Learning Test–Second Edition was used to assess verbal learning and memory function.²⁶ In this test, immediate verbal memory was assessed by the Immediate Recall of Trial 2; short-delayed verbal memory was measured by the Short-Delay Free and Cued Recalls; and long-delayed verbal memory was evaluated by the Long-Delay Free and Cued Recalls. The Paced Auditory Serial Addition Tests were used to assess auditory processing speed and working memory.²¹ The Symbol Digit Technique Test was administered to measure visual spatial processing speed and working memory.²¹ The Controlled Oral Word Association Test was used to assess phonemic verbal fluency. The Wisconsin Card Sorting Test was used to evaluate executive function. A few subjects were excluded due to failure to complete some items of these cognitive tests, and the number of patients with NMO and HCs finally included in the cognitive-related analyses is displayed in On-line Tables 2–6.

MR Imaging Acquisition

MR imaging data were acquired by using a 3T MR imaging system (Discovery MR750; GE Healthcare, Milwaukee, Wisconsin). Tight but comfortable foam padding was used to minimize head motion; earplugs were used to reduce scanner noise. The T2-weighted images were acquired by using a fast spin-echo sequence with the following parameters: TR = 6816 ms; TE = 103 ms; flip angle = 142°; FOV = 240 × 240 mm; matrix = 512 × 512; section thickness = 6 mm; section gap = 1.5 mm; and 20 axial sections. Sagittal 3D T1-weighted images were acquired by a brain volume sequence with the following parameters: TR = 8.2 ms; TE = 3.2 ms; TI = 450 ms; flip angle = 12°; FOV = 256 × 256 mm; matrix = 256 × 256; section thickness = 1 mm; no gap; and 188 sagittal sections.

Analysis of Brain Lesions

Each brain lesion was identified by consensus of 2 neuroradiologists. According to the criteria of a prior study,⁴ the brain MR imaging presentation of each patient was classified into 4 categories: normal, nonspecific lesions, MS-like lesions, and atypical lesions. “MS-like lesions” were those that fulfilled the criteria of Barkhof et al²⁷ for the diagnosis of multiple sclerosis. “Nonspecific lesions” were defined as deep white matter lesions with the following features: not ovoid, neither abutted nor perpendicular to the ventricles, or too few to fulfill the criteria of Barkhof et al for multiple sclerosis.⁴ “Atypical lesions” were defined as large confluent cerebral hemisphere lesions (>3 cm) and confluent diencephalic lesions (involving the thalamus and hypothalamus).⁴ The brain lesion volumes (BLVs) were independently measured by 2 neuroradiologists. For each patient, each brain lesion was

manually outlined section by section on T2-weighted images by using the MRICro software program (<http://www.mccauslandcenter.sc.edu/mricro/mricron/index.html>). The BLV of the patient was then automatically estimated by the product of the lesion area and section thickness. The mean value of the BLV of each patient from the 2 investigators was considered the BLV of this patient.

GMV Calculation

The GMV was calculated by using the Statistical Parametric Mapping package (SPM8; <http://www.fil.ion.ucl.ac.uk/spm/software/spm8>). The structural MR images were segmented into GM, white matter, and CSF by using the standard unified segmentation model. After an initial affine registration of the GM concentration map into the Montreal Neurological Institute space, the GM concentration images were nonlinearly warped by using the Diffeomorphic Anatomical Registration Through Exponentiated Lie Algebra technique²⁸ and then were resampled to a voxel size of $1.5 \times 1.5 \times 1.5 \text{ mm}^3$. The GMV of each voxel was obtained by multiplying the GM concentration map by the nonlinear determinants derived from the spatial normalization step. Finally, the GMV images were smoothed with a Gaussian kernel of $6 \times 6 \times 6 \text{ mm}^3$ full width at half maximum. After spatial preprocessing, the normalized, modulated, and smoothed GMV maps were used for statistical analysis.

Statistical Analysis

First, a general linear model was implemented to compare differences in the cognitive scores between the NMO and HC groups by using SPSS 18.0 (IBM, Armonk, New York) ($P < .05$). Second, voxel-based comparisons were performed to identify the brain regions with significant group differences in GMV by using a 2-sample 2-tailed t test, and the multiple comparisons were corrected by using the false discovery rate method ($P < .05$). Third, voxel-based partial correlation analysis was performed to test the relationships of the GMV with clinical parameters and cognitive scores within brain regions that exhibited significant group differences in GMV in the patients with NMO, and the correlation between GMV and BLV was investigated in 37 patients with NMO with abnormal brain MR imaging findings. For these voxel-based correlation analyses, multiple comparisons were corrected by the Alphasim method (single voxel $P = .01$, 5000 simulations, full width at half maximum = 6 mm, cluster connection radius = 2.5 mm, within a significant GM mask, which resulted in a corrected threshold of $P < .05$ and a cluster size threshold of >33 voxels). Age, sex, and years of education were entered as covariates of no interest. BLV was also added as an additional nuisance covariate to explore whether it would affect the correlation between GMV and the cognitive test results.

RESULTS

Demographic and Clinical Data of Subjects

Our sample included 50 patients with NMO (42 women and 8 men) and 50 HCs (43 women and 7 men) (Table 1). The mean age of the patients at the time of the study was 47.4 ± 13.4 years (range, 19–68 years). No significant differences were found in sex ($\chi^2 = 0.078$, $P = .779$), age ($t = -1.055$, $P = .294$), and years of education ($t = -1.312$, $P = 0.192$) between the 2 groups. Thirty-

Table 2: Neuropsychological tests for patients with NMO and healthy controls^a

Neuropsychological Tests	Patients with NMO	HCs	P Value
CVLT-II			
IR2	8.7 (2.2) ($n = 44$)	9.6 (2.5) ($n = 45$)	.075
SDFR	11.1 (2.6) ($n = 44$)	11.8 (2.3) ($n = 45$)	.176
SDCR	11.0 (2.2) ($n = 44$)	12.0 (2.2) ($n = 45$)	.030 ^b
LDFR	10.9 (2.9) ($n = 44$)	12.2 (2.2) ($n = 45$)	.017 ^b
LDCR	10.5 (3.1) ($n = 44$)	12.1 (2.2) ($n = 45$)	.007 ^b
PASAT	34.4 (12.3) ($n = 43$)	37.6 (7.7) ($n = 45$)	.152
SDMT	42.1 (12.2) ($n = 39$)	49.5 (15.1) ($n = 45$)	.018 ^b
WCST	8.8 (3.9) ($n = 34$)	10.0 (5.2) ($n = 44$)	.245
COWAT (semantic)	17.5 (4.7) ($n = 43$)	19.5 (4.0) ($n = 44$)	.035 ^b

Note:—CVLT-II indicates California Verbal Learning Test—Second Edition; COWAT, Controlled Oral Word Association Test; IR2, Immediate Recall of Trail 2; LDCR, Long-Delay Cued Recall; LDFR, Long-Delay Free Recall; PASAT, Paced Auditory Serial Addition Test; SDCR, Short-Delay Cued Recall; SDFR, Short-Delay Free Recall; SDMT, Symbol Digit Modalities Test; WCST, Wisconsin Card Sorting Test.

^a Data are shown as mean (SD).

^b Significant.

two of the 50 patients (64%) were seropositive for NMO-IgG. The mean onset age of the patients was 41.6 ± 14.1 years (range, 15–66 years). The mean number of relapses per year was 0.8 ± 0.7 (range, 0–4). The mean EDSS score was 3.8 ± 2.3 (range, 0–9). Neuromyelitis optica was monophasic in 4 cases and multiphasic in the other 46 cases, with a mean number of relapses of 4.5 ± 5.1 (range, 1–30). Five patients had other autoimmune diseases (Sjogren syndrome, $n = 1$; rheumatoid arthritis, $n = 2$; desmosis, $n = 2$), 6 patients had endocrinopathy (diabetes mellitus, $n = 3$; hypothyroidism, $n = 2$; hyperthyroidism, $n = 1$), and 1 patient had hyperthyroidism with scleroderma.

Thirty-seven (74%) of these 50 patients with NMO had abnormal brain MRI findings. Brain MRI was categorized into 4 subgroups according to the criteria of a prior study⁴: normal (13 patients, 26%), nonspecific lesions (6 patients, 12%), MS-like lesions (23 patients, 46%), and atypical lesions (8 patients, 16%). The mean BLV was $3.3 \pm 5.1 \text{ cm}^3$ (range, 0.02–18.67 cm^3). Spinal cord MRI was collected at the initial diagnosis of the disease, and the results showed longitudinally extensive lesions (≥ 3 vertebral segments) on T2-weighted images in 47 of 50 patients (94%). The other 3 patients had a spinal cord lesion that involved fewer than 3 vertebral segments.

For each cognitive test, the sex, age, and years of education were matched ($P > .05$) between the patient and control groups (On-line Tables 2–6).

Group Differences in Cognitive Tests

The performance of neuropsychological tests is summarized in Table 2. Patients with NMO performed significantly worse on the Short-Delay Cued Recall ($P = .030$), Long-Delay Free ($P = .017$), and Cued ($P = .007$) Recalls of the California Verbal Learning Test—Second Edition, the Symbol Digit Technique Test ($P = .018$), and the Controlled Oral Word Association Test ($P = .035$) compared with the performance of the HCs. However, none of these differences was significant according to the Bonferroni correction ($P < .05$) for multiple comparisons. There were no significant differences in the Immediate Recall of Trial 2 ($P = .075$) and Short-Delay Free Recall ($P = .176$) of the California Verbal Learning Test—Second Edition, the Paced Auditory Serial Addition

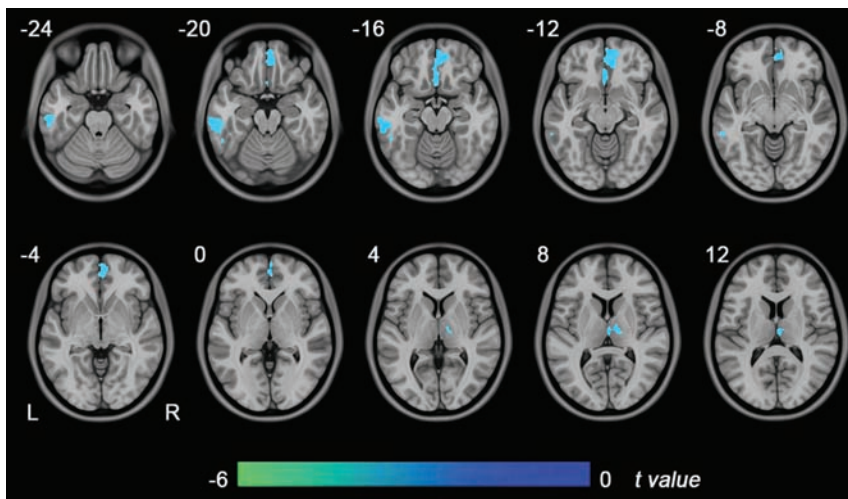


FIG 1. Brain regions with GMV differences between patients with NMO and healthy controls ($P < .05$, false discovery rate correction). Blue represents significant GMV reductions in the patients with NMO. L indicates left; R, right.

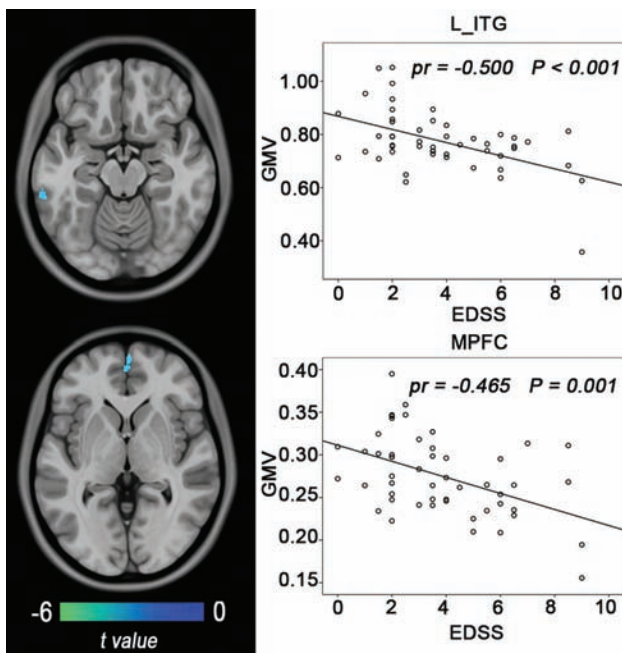


FIG 2. Correlations between the GMV and clinical variables in patients with NMO. The *left column* shows brain regions where the GMV is correlated with EDSS scores (Alphasim correction, $P < .05$). The *right column* shows scatter diagrams of these correlations. ITG indicates inferior temporal gyrus; MPFC, medial prefrontal cortex.

Tests ($P = .152$), and the Wisconsin Card Sorting Test ($P = .245$) between the 2 groups.

Group Differences in the GMV

The GMV of the whole brain of patients with NMO (602.8 ± 51.03 mL) was significantly reduced compared with that of HCs (635.9 ± 51.18 mL) ($P = .002$). Compared with the HCs, patients with NMO had reduced GMV in the medial prefrontal cortex, the left inferior temporal gyrus, and the right thalamus (false discovery rate correction, $P < .05$) (Fig 1). No significantly increased GMV was found in patients with NMO.

Subgroup Differences in the GMV

On the basis of the combination of the 3 supportive criteria (NMO-IgG, brain MR imaging, and spinal MR imaging) for NMO, we further divided patients into 4 diagnostic subgroups: NMO-IgG + spinal MR imaging ($n = 21$); brain MR imaging + spinal MR imaging ($n = 18$); NMO-IgG + brain MR imaging ($n = 3$); and NMO-IgG + brain MR imaging + spinal MR imaging ($n = 8$). Because the sample sizes of the latter 2 groups were too small to perform intergroup comparisons, we only investigated voxel-based GMV differences between each of the first 2 subgroups and the HC group. Compared with the HC group, only the first NMO subgroup (NMO-IgG + spinal MR imaging) had a significantly reduced false discovery rate

correction ($P < .05$). The distribution of brain regions with GMV reductions in this subgroup (On-line Fig 1) was similar in the total patient population (Fig 1). However, we did not find any significant GMV differences between the second NMO subgroup (brain MR imaging + spinal MR imaging) and the HC group.

For each patient with NMO, we also extracted GMV values of brain regions that exhibited significant GMV reductions in the total patient population (Fig 1). Then, we used a 2-sample t test to compare the GMV differences in these regions between each NMO subgroup and the HC group. We found that both NMO subgroups (NMO-IgG + spinal MR imaging and brain MR imaging + spinal MR imaging) exhibited significantly reduced GMVs in all of these regions (Bonferroni correction, $P < .05$) (On-line Fig 2).

Correlation between the GMV and Clinical Parameters

Correlations between the GMV and clinical variables in the patients with NMO are shown in Fig 2. In the patients with NMO, the EDSS scores had a negative correlation (Alphasim correction, $P < .05$) with the GMV in the left inferior temporal gyrus (partial correlation coefficient [pr] = -0.500 , $P < .001$) and the right medial prefrontal cortex ($pr = -0.465$, $P = 0.001$). No significant positive correlation between the GMV and EDSS scores was found in the patients with NMO. No significant correlations were observed for the relapsing frequency, disease duration, onset age, and GMV.

Correlation between the GMV and Cognitive Scores

Correlations between the GMV and cognitive scores are shown in Fig 3. Voxel-based analysis revealed that the patients with NMO had a significantly positive correlation (Alphasim correction, $P < .05$) between the Immediate Recall of Trial 2 and the GMV of the medial prefrontal cortex ($pr = 0.563$, $P < .001$). The Long-Delay ($pr = 0.420$, $P = 0.005$) and Short-Delay ($pr = 0.401$, $P = .007$) Free Recalls also had positive correlations with the GMV of the right thalamus. These cognitive scores did not show any negative correlations with the

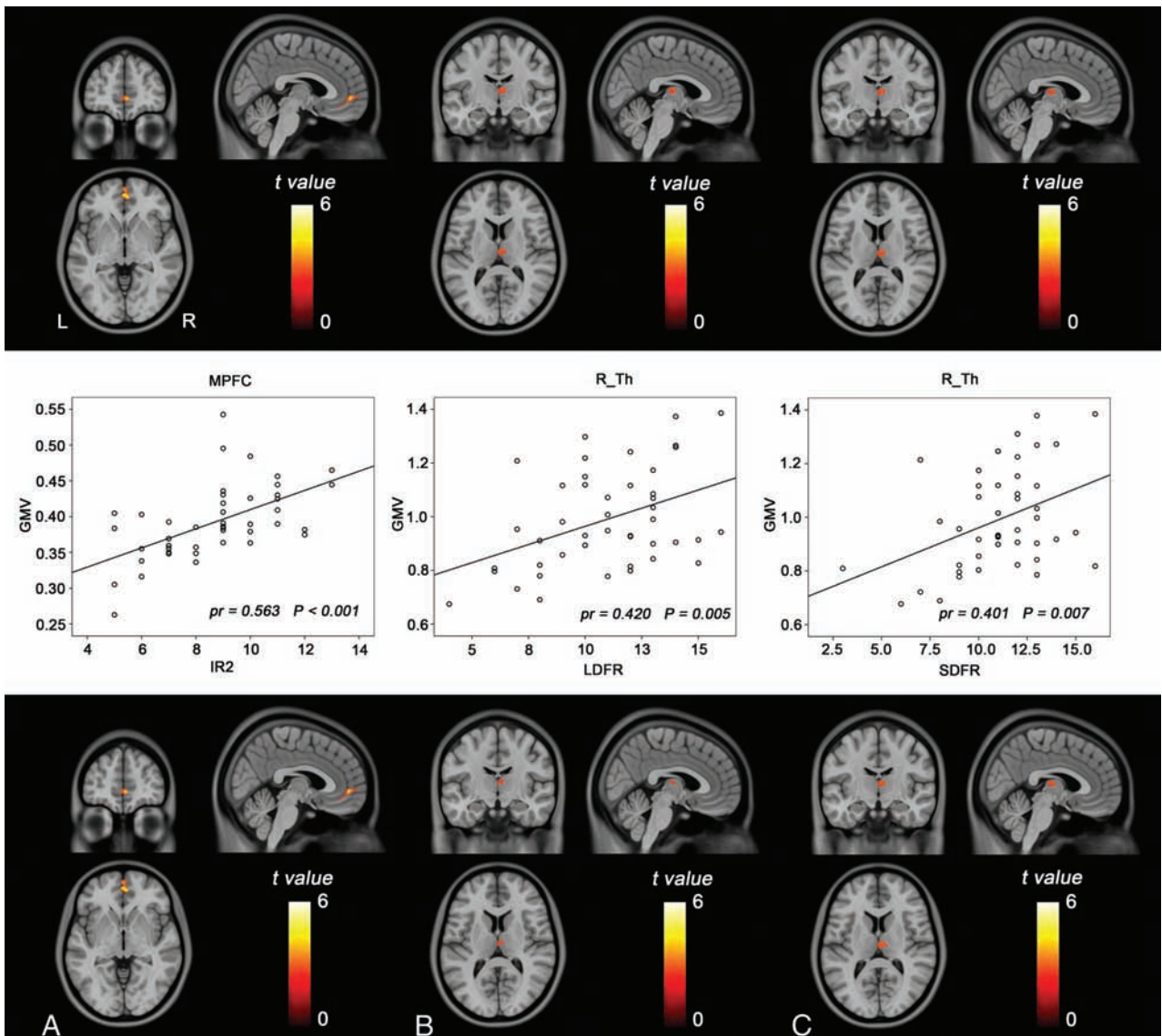


FIG 3. Correlations between the GMV and cognitive scores in patients with NMO. The upper row shows brain regions where the GMV is correlated with cognitive scores (Alphasim correction, $P < .05$). The middle row shows scatter diagrams of these correlations. The lower row shows brain regions where the GMV is correlated with cognitive scores after further controlling for the brain lesion volume. Immediate recall of Trial 2 (A), long-delay free recall (B), and short-delay free recall (C). MPFC indicates medial prefrontal cortex; R_Th, right thalamus.

regional GMV in patients with NMO. No significant correlations were observed between other cognitive scores and the GMV. Even after further controlling for the effect of BLV, these correlations remained significant (Fig 3).

Correlation between the GMV and BLV

Correlations between the GMV and BLV are demonstrated in Fig 4. Voxel-based analysis revealed that the patients with NMO exhibited significant negative correlations (Alphasim correction, $P < .05$) between BLV and GMV in the right thalamus ($pr = -0.376$, $P = .022$) and left inferior temporal gyrus ($pr = -0.510$, $P = .001$). When we excluded the 2 patients with visible lesions in these 2 regions, the correlations between BLV and GMV in the right thalamus ($pr = -0.380$, $P = .024$) and left inferior temporal gyrus ($pr = -0.499$, $P = .002$) remained significant. No positive correlations were found in the patients with NMO.

DISCUSSION

In a large sample of patients with NMO, we found GMV reductions in the frontal and temporal cortices and the right thalamus. Moreover, the frontal and temporal GMV reductions were associated with disease severity in the patients with NMO. Finally, we identified significant correlations between GMV reductions and cognitive reductions in the patients with NMO, suggesting that GM pathology is associated with cognitive impairment in NMO.

In this study, the diagnosis of NMO was strictly according to the Wingerchuk diagnostic criteria for NMO.¹ All patients fulfilled the absolute criteria (optic neuritis and acute myelitis) and at least 2 of the 3 supportive criteria (contiguous spinal cord MR imaging lesion extending over ≥ 3 vertebral segments, brain MR imaging that did not meet the diagnostic criteria for multiple sclerosis, and NMO-IgG seropositive status). Only 64% of our

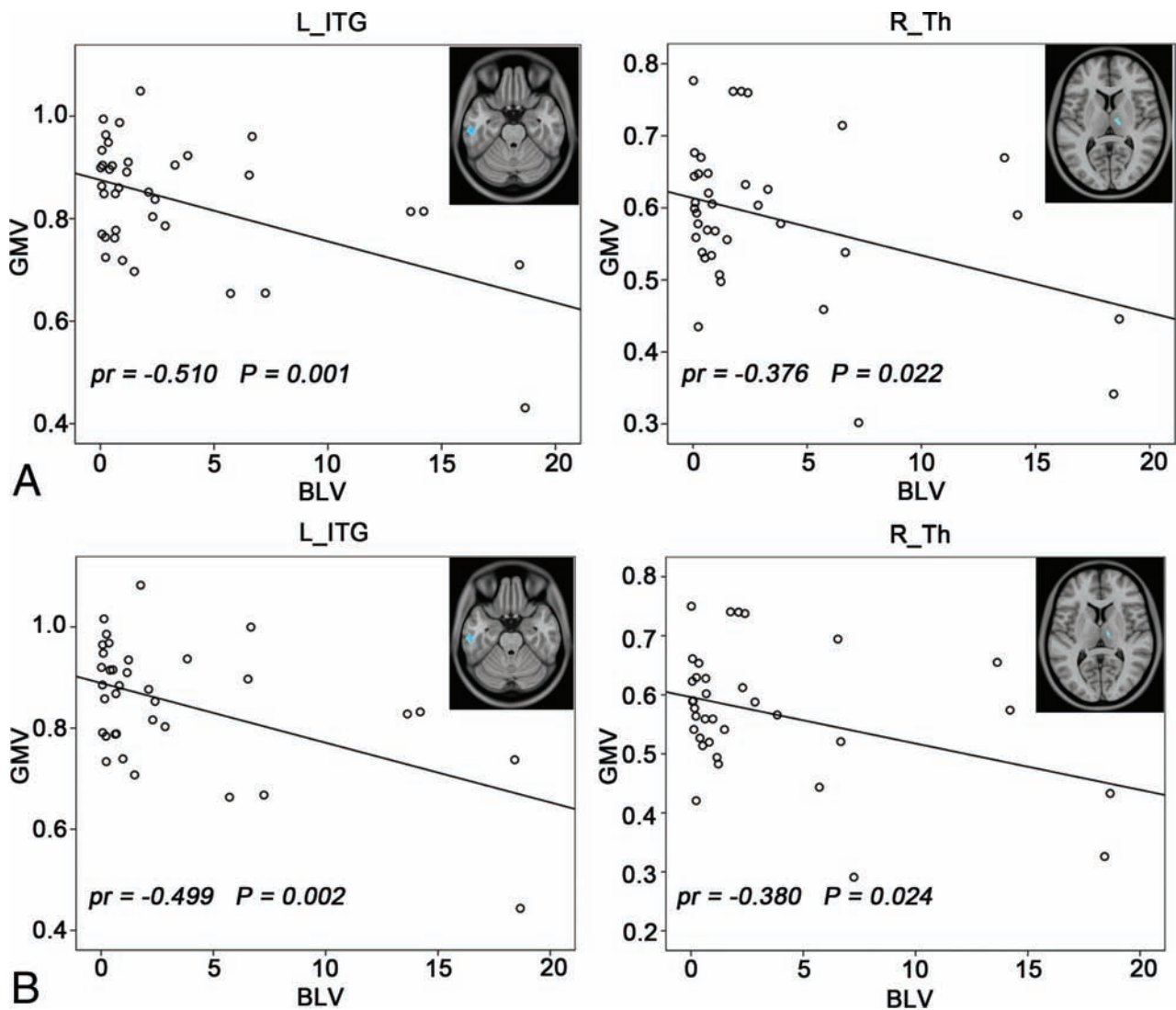


FIG 4. Correlations between the GMV and BLV in patients with NMO (Alphasim correction, $P < .05$). *A*, Before removing 2 patients with thalamic and inferior temporal gyrus (ITG) lesions. *B*, After removing 2 patients with thalamic and ITG lesions.

patients were seropositive for NMO-IgG, which is a lower incidence than those reported in previous studies.^{25,29} However, all patients with seronegative NMO-IgG fulfilled the other 2 supportive criteria for NMO (brain MR imaging that did not meet the diagnostic criteria for multiple sclerosis and a contiguous spinal cord MR imaging lesion extending over ≥ 3 vertebral segments). Although 3 patients had a spinal cord lesion that involved fewer than 3 vertebral segments, they fulfilled the other 2 supportive criteria (NMO-IgG + and brain MR imaging that did not meet the diagnostic criteria for multiple sclerosis). Consistent with previous studies reporting the presence of other autoimmune diseases in a subset of patients with NMO,^{30,31} 6 of the patients with NMO in this study presented with autoimmune diseases. Although they fulfilled the diagnostic criteria for NMO, we cannot exclude the effects of comorbidities on the intergroup GMV differences. To reduce this possibility, we excluded the 6 patients and re-performed GMV comparisons. We found that the intergroup GMV differences were similar before and after excluding these patients (On-line Fig 3), suggesting that the impact of comorbidities on the intergroup GMV comparisons was not significant.

Consistent with prior findings,^{10,17,18,21-24} we also found cognitive impairment in the patients with NMO. The cognitive impairments in NMO were deficits in short- and long-term memory, speed of information processing, and verbal fluency on semantic stimuli. These impaired cognitive domains have frequently been reported in patients with NMO.^{10,18,21-24} However, inconsistent with previous studies that reported deficits in immediate memory, attention, and executive abilities,^{10,17,18,21,23,24} we did not find any significant changes in these 3 cognitive domains in the patients with NMO. This discrepancy may be related to variations in the sample size, demographic and clinical features, and cognitive scales used.

There is an ongoing debate on the abnormality of GM in NMO, especially for structural impairments.¹⁴⁻¹⁶ We found GMV reductions in the frontal and temporal lobes and thalamus, the range of which largely surpassed the brain regions connected to the spinal cord and optic nerves. Therefore, the mechanism of axonal degeneration secondary to the damage of the spinal cord and optic nerves cannot fully explain these extensive reductions in the GMV.¹⁵ We also found negative correlations between the

GMVs of the right thalamus and left inferior temporal gyrus and the BLV, even after excluding patients with visible lesions in these regions. This finding suggests that the GMV reductions in these regions are secondary to brain lesions, which may be mediated by a mechanism of axonal degeneration. This inference is also supported by our subgroup analyses of the GMV differences. The subgroup (NMO-IgG + spinal MR imaging) that presented with an increased incidence of brain lesions also exhibited more significant GMV reductions than those in the subgroup (brain MR imaging + spinal MR imaging) that exhibited fewer brain lesions. However, the GMV reduction in the medial prefrontal cortex was not correlated with the brain lesion volume, indicating that the axonal degeneration mechanism cannot explain the medial prefrontal cortex reduction observed in NMO. This assertion is consistent with the findings of a pathologic study that failed to detect cortical changes that reflected axonal degeneration in patients with NMO.³² Consequently, the primary neurodegenerative processes (neuronal loss) may at least partially account for the GMV reductions in patients with NMO. This hypothesis is confirmed by the results of a pathologic study that revealed a substantial cortical neuronal loss in NMO spectrum disorders.²⁴

The frontal cortex and thalamus are closely associated with cognitive function.^{10,15,18,33-35} The GMV reductions in these regions may affect cognitive performance.^{33,35} In our study, a GMV reduction in the thalamus was correlated with deficits in delayed memory; this correlation was consistent with prior findings in multiple sclerosis in which a GMV reduction in the thalamus predicted many cognitive deficits.³⁶ The positive association between several prefrontal regions and immediate memory supported prior findings that the prefrontal cortex played an important role in cognitive function.^{18,37} Taken together, our findings suggest that GMV reductions in the frontal cortex and thalamus are associated with cognitive impairment in patients with NMO.

We also found significant negative correlations between regional GMV reductions in the frontal and temporal cortices and EDSS scores. These findings suggest that reductions in the GMV are an important pathologic process in NMO, which may be related to disease severity. Our findings also suggest a potential role of GMV reductions in predicting the severity of the disorder.^{7,38,39}

A limitation of this study is that a few of the subjects who underwent GMV analysis were excluded in the correlation analysis with cognitive scores because they did not successfully complete the cognitive assessments due to biliousness or other private reasons. However, we believe that our findings for these correlations are robust because the smallest group still included 34 patients with NMO. Another limitation is the cross-sectional design of our study. Further studies with a longitudinal design should be performed to determine the evolution of GMV changes in NMO.

CONCLUSIONS

We used a combination of structural brain MR imaging and neuropsychological tests to investigate GMV reductions and their association with cognitive impairment in a large sample of patients with NMO. We confirmed that GMV reductions are associated with NMO, and we revealed the distribution of re-

gional GMV reductions in NMO. By investigating correlations between GMV reductions and BLV, we suggest that both neurodegeneration and axonal degeneration mechanisms may contribute to GMV reductions in NMO. We also found significant correlations between GMV reductions and cognitive impairments, indicating a role of GM structural impairment in cognitive deficits in NMO.

ACKNOWLEDGMENTS

The authors thank the Tianjin Neuroimmunology laboratory team for conducting the detection of NMO-IgG and other autoantibodies.

Disclosures: Fu-Dong Shi—RELATED: Grant: National Basic Research Program of China (Grant 2013CB966900), the National Science Foundation of China (grant 81230028), the National Key Clinical Specialty Construction Program of China.* *Money paid to the institution.

REFERENCES

1. Wingerchuk DM, Lennon VA, Pittock SJ, et al. **Revised diagnostic criteria for neuromyelitis optica.** *Neurology* 2006;66:1485–89 CrossRef Medline
2. Wingerchuk DM, Lennon VA, Lucchinetti CF, et al. **The spectrum of neuromyelitis optica.** *Lancet Neurol* 2007;6:805–15 CrossRef Medline
3. Wingerchuk DM, Hogancamp WF, O'Brien PC, et al. **The clinical course of neuromyelitis optica (Devic's syndrome).** *Neurology* 1999; 53:1107–14 CrossRef Medline
4. Pittock SJ, Lennon VA, Krecke K, et al. **Brain abnormalities in neuromyelitis optica.** *Arch Neurol* 2006;63:390–96 CrossRef Medline
5. Pittock SJ, Weinshenker BG, Lucchinetti CF, et al. **Neuromyelitis optica brain lesions localized at sites of high aquaporin 4 expression.** *Arch Neurol* 2006;63:964–68 CrossRef Medline
6. Barnett Y, Sutton IJ, Ghadiri M, et al. **Conventional and advanced imaging in neuromyelitis optica.** *AJNR Am J Neuroradiol* 2014;35: 1458–66 CrossRef Medline
7. Liang P, Liu Y, Jia X, et al. **Regional homogeneity changes in patients with neuromyelitis optica revealed by resting-state functional MRI.** *Clin Neurophysiol* 2011;122:121–27 CrossRef Medline
8. Liu Y, Liang P, Duan Y, et al. **Abnormal baseline brain activity in patients with neuromyelitis optica: a resting-state fMRI study.** *Eur J Radiol* 2011;80:407–11 CrossRef Medline
9. Yu CS, Lin FC, Li KC, et al. **Diffusion tensor imaging in the assessment of normal-appearing brain tissue damage in relapsing neuromyelitis optica.** *AJNR Am J Neuroradiol* 2006;27:1009–15 Medline
10. He D, Wu Q, Chen X, et al. **Cognitive impairment and whole brain diffusion in patients with neuromyelitis optica after acute relapse.** *Brain Cogn* 2011;77:80–88 CrossRef Medline
11. Zhao DD, Zhou HY, Wu QZ, et al. **Diffusion tensor imaging characterization of occult brain damage in relapsing neuromyelitis optica using 3.0T magnetic resonance imaging techniques.** *Neuroimage* 2012;59:3173–77 CrossRef Medline
12. Sánchez-Catasús CA, Cabrera-Gomez J, Almaguer Melian W, et al. **Brain tissue volumes and perfusion change with the number of optic neuritis attacks in relapsing neuromyelitis optica: a voxel-based correlation study.** *PLoS One* 2013;8:e66271 CrossRef Medline
13. Rocca MA, Agosta F, Mezzapesa DM, et al. **Magnetization transfer and diffusion tensor MRI show gray matter damage in neuromyelitis optica.** *Neurology* 2004;62:476–78 CrossRef Medline
14. Chansue JB, Lamy J, Rousseau F, et al. **White matter volume is decreased in the brain of patients with neuromyelitis optica.** *Eur J Neurol* 2013;20:361–67 CrossRef Medline
15. Duan Y, Liu Y, Liang P, et al. **Comparison of grey matter atrophy between patients with neuromyelitis optica and multiple sclerosis: a voxel-based morphometry study.** *Eur J Radiol* 2012;81:e110–14 CrossRef Medline

16. von Glehn F, Jarius S, Cavalcanti Lira RP, et al. **Structural brain abnormalities are related to retinal nerve fiber layer thinning and disease duration in neuromyelitis optica spectrum disorders.** *Mult Scler* 2014;Jan 29. [Epub ahead of print] CrossRef Medline
17. Liu Y, Xie T, He Y, et al. **Cortical thinning correlates with cognitive change in multiple sclerosis but not in neuromyelitis optica.** *Eur Radiol* 2014;24:2334–43 CrossRef Medline
18. Blanc F, Noblet V, Jung B, et al. **White matter atrophy and cognitive dysfunctions in neuromyelitis optica.** *PLoS One* 2012;7:e33878 CrossRef Medline
19. Duan Y, Liu Y, Liang P, et al. **White matter atrophy in brain of neuromyelitis optica: a voxel-based morphometry study.** *Acta Radiol* 2014;55:589–93 CrossRef Medline
20. Calabrese M, Oh MS, Favaretto A, et al. **No MRI evidence of cortical lesions in neuromyelitis optica.** *Neurology* 2012;79:1671–76 CrossRef Medline
21. Blanc F, Zéphir H, Lebrun C, et al. **Cognitive functions in neuromyelitis optica.** *Arch Neurol* 2008;65:84–88 Medline CrossRef
22. He D, Chen X, Zhao D, et al. **Cognitive function, depression, fatigue, and activities of daily living in patients with neuromyelitis optica after acute relapse.** *Int J Neurosci* 2011;121:677–83 CrossRef Medline
23. Vanotti S, Cores EV, Eizaguirre B, et al. **Cognitive performance of neuromyelitis optica patients: comparison with multiple sclerosis.** *Arq Neuropsiquiatr* 2013;71:357–61 CrossRef Medline
24. Saji E, Arakawa M, Yanagawa K, et al. **Cognitive impairment and cortical degeneration in neuromyelitis optica.** *Ann Neurol* 2013;73:65–76 CrossRef Medline
25. Yang CS, Zhang DQ, Wang JH, et al. **Clinical features and sera anti-aquaporin 4 antibody positivity in patients with demyelinating disorders of the central nervous system from Tianjin, China.** *CNS Neurosci Ther* 2014;20:32–39 CrossRef Medline
26. Blanco-Rojas L, Arboix A, Canovas D, et al. **Cognitive profile in patients with a first-ever lacunar infarct with and without silent lacunes: a comparative study.** *BMC Neurol* 2013;13:203 CrossRef Medline
27. Barkhof F, Filippi M, Miller DH, et al. **Comparison of MRI criteria at first presentation to predict conversion to clinically definite multiple sclerosis.** *Brain* 1997;120(pt 11):2059–69 CrossRef Medline
28. Ashburner J. **A fast diffeomorphic image registration algorithm.** *Neuroimage* 2007;38:95–113 CrossRef Medline
29. Papadopoulos MC, Verkman AS. **Aquaporin 4 and neuromyelitis optica.** *Lancet Neurol* 2012;11:535–44 CrossRef Medline
30. Wingerchuk DM, Weinshenker BG. **The emerging relationship between neuromyelitis optica and systemic rheumatologic autoimmune disease.** *Mult Scler* 2012;18:5–10 CrossRef Medline
31. Freitas E, Guimarães J. **Neuromyelitis optica spectrum disorders associated with other autoimmune diseases.** *Rheumatol Int* 2015;35:243–53 CrossRef Medline
32. Popescu BF, Parisi JE, Cabrera-Gómez JA, et al. **Absence of cortical demyelination in neuromyelitis optica.** *Neurology* 2010;75:2103–09 CrossRef Medline
33. Llufriu S, Martínez-Heras E, Fortea J, et al. **Cognitive functions in multiple sclerosis: impact of gray matter integrity.** *Mult Scler* 2014;20:424–32. CrossRef Medline
34. Tona F, Petsas N, Sbardella E, et al. **Multiple sclerosis: altered thalamic resting-state functional connectivity and its effect on cognitive function.** *Radiology* 2014;271:814–21 CrossRef Medline
35. Calabrese M, Agosta F, Rinaldi F, et al. **Cortical lesions and atrophy associated with cognitive impairment in relapsing-remitting multiple sclerosis.** *Arch Neurol* 2009;66:1144–50 CrossRef Medline
36. Štecková T, Hlušík P, Sládková V, et al. **Thalamic atrophy and cognitive impairment in clinically isolated syndrome and multiple sclerosis.** *J Neurol Sci* 2014;342:62–68 CrossRef Medline
37. Morgen K, Sammer G, Courtney SM, et al. **Evidence for a direct association between cortical atrophy and cognitive impairment in relapsing-remitting MS.** *Neuroimage* 2006;30:891–98 CrossRef Medline
38. De Stefano N, Matthews PM, Filippi M, et al. **Evidence of early cortical atrophy in MS: relevance to white matter changes and disability.** *Neurology* 2003;60:1157–62 CrossRef Medline
39. Mesaros S, Rovaris M, Pagani E, et al. **A magnetic resonance imaging voxel-based morphometry study of regional gray matter atrophy in patients with benign multiple sclerosis.** *Arch Neurol* 2008;65:1223–30 CrossRef Medline

CTP in Transient Global Amnesia: A Single-Center Experience of 30 Patients

I.A. Meyer, M. Wintermark, J.-F. Démonet, and P. Michel

ABSTRACT

BACKGROUND AND PURPOSE: Medial temporal lobe abnormalities on DWI and functional imaging are occasionally observed in patients with transient global amnesia. We used CTP to study these patients during or briefly after resolution of their amnesic syndrome.

MATERIALS AND METHODS: From 2002 onward, patients satisfying clinical criteria for transient global amnesia who underwent CTP were included. Patients with additional clinical features suggesting transient ischemic attack or stroke and those with an ischemic lesion on subsequent DWI were excluded. If deemed necessary by the clinician, DWI was performed within 10 days.

RESULTS: Thirty patients with transient global amnesia underwent CTP at a median latency of 5.9 hours (interquartile range, 4.3–9.7 hours) after symptom onset. All findings, except for those in 1 patient, were normal, including those in the 14 patients with well-imaged hippocampi. In the patient with abnormal findings, CTP and PWI showed hypoperfusion in both lentiform nuclei extending into the insulae, with normalization on the repeat CTP 6 days later. In 10 patients, DWI was performed at a median latency of 2 days (interquartile range, 0–9 days). Of these, 2 showed punctate hippocampal lesions, often seen in transient global amnesia. In 2 patients excluded because of mildly atypical transient global amnesia and ischemic lesions on subsequent DWI, acute CTP findings were also normal.

CONCLUSIONS: Patients with transient global amnesia had normal CTP findings in the acute phase with the exception of 1 patient with transient hypoperfusion in both basal ganglia. If imaging is performed for typical and atypical transient global amnesia, DWI should be the preferred method.

ABBREVIATION: TGA = transient global amnesia

Transient global amnesia (TGA) is characterized by the sudden onset of antero- and retrograde amnesia that is often triggered by an acute emotional or physical event and spontaneously resolves within 24 hours. Repetitive questioning and anxiety are often present, but other focal neurologic disturbances are usually absent.^{1,2}

Functional brain imaging with SPECT and PET shows local disturbances in regional blood flow (usually hypoperfusion, rarely hyperperfusion) and in oxygen/glucose metabolism, most frequently in 1 or both medial temporal lobes.^{3–5} Punctate signal hyperintensities appearing in 1 or both hippocampi on DWI were first described by Matsui et al⁶ in a classic TGA case in 2002 and then more systematically by Sedlaczek et al.⁷ Although the specific

sites of impairment have been identified, the underlying etiology of TGA remains elusive.²

Images in a case series of patients with TGA who underwent PWI within 24 hours of symptom onset showed unilateral perfusion abnormalities in 4 of the 28 patients (1 in the anterior, 1 in the posterior, and 2 in the middle cerebral artery territory).⁸ However, the authors did not specify whether structures relevant for memory were involved.

CTP is widely used for the early diagnosis of acute ischemic stroke and TIA, though its true value remains to be established by appropriate research.⁹ To our knowledge, results using CTP for acute TGA diagnosis have not been published. We, therefore, aimed to determine the frequency and localization of perfusion abnormalities in patients with acute TGA by using CTP to investigate its potential diagnostic value and to better elucidate the pathogenesis of this disorder.

MATERIALS AND METHODS

We included and retrospectively analyzed those patients admitted to the emergency department of the University Hospital of Laus-

Received January 20, 2015; accepted after revision March 2.

From the Neurology Service (I.A.M., P.M.) and the Leenaards Memory Center (J.-F.D.), Centre Hospitalier Universitaire Vaudois, Lausanne, Switzerland; and Department of Radiology (M.W.), Stanford University School of Medicine, Stanford, California.

Please address correspondence to Ivo A. Meyer, MD, Centre Hospitalier Universitaire Vaudois, Rue du Bugnon 46, 1011 Lausanne, Switzerland; e-mail: ivo.meyer@chuv.ch; @ivo_meyer

<http://dx.doi.org/10.3174/ajnr.A4370>

anne from June 2002 to April 2014 who had a final diagnosis of TGA and underwent CTP within 24 hours of admission. CTP was part of the standard diagnostic protocol of the hospital to detect cerebral ischemia from June 2002 until April 2006 and has been performed at the discretion of the treating physician since April 2006. All patients underwent neurologic evaluation, and the diagnosis of TGA was made if the criteria of Hodges and Warlow¹⁰ were met. Additional examinations such as electroencephalography and DWI were performed as considered necessary by the treating physician. Exclusion criteria were poor-quality CTP and a proved ischemic lesion on DWI after an initial TGA diagnosis.

We collected the following parameters: demographics (age, sex); cerebrovascular risk factors, including hypertension, hyperlipidemia, diabetes mellitus, smoking history, atrial fibrillation, previous cerebrovascular event (stroke or transient ischemic attack) or TGA; high-risk alcohol consumption defined as exceeding 24 g/day; and the presence of a triggering event (emotional or physical). The duration of amnesia was determined by serial bedside testing of the capability to retain at least 4 words of a standardized 5-word list.^{11,12} Formal neuropsychological testing was performed, depending on the treating physician's judgment.

CTP was performed on a LightSpeed 16 Advantage (16 detectors; GE Healthcare, Milwaukee, Wisconsin) until November 2005 and a LightSpeed VCT (64 detectors; GE Healthcare) thereafter, by using their commercially available software. The parameters for cerebral perfusion imaging were the following: 80 kV, 240 mA, and 0.4-second gantry rotation time; acquisition delay was 7 seconds after injection of 50 mL of iohexol, 300 mg/mL of iodine (Accupaque 300; Amersham, Oslo, Norway) with an injection rate of 5 mL per second into an antecubital vein by using a power injector (Stellant D CT Injection System; Medrad, Indianapolis, Pennsylvania). Two injections with acquisition of 8 or sixteen 5-mm sections each (four 10-mm sections before October 2005) were performed. The lowest CTP section level usually cut through the thalami before October 2005 and the midbrain thereafter; temporal lobes were therefore variably included. CTP data were transferred to a workstation and analyzed by using different versions of Philips Brain Perfusion software (Philips Medical Systems, Cleveland, Ohio) to create parametric maps of MTT, CBF, and CBV.

For MR imaging, we used both 1.5T ($n = 6$) and 3T ($n = 1$) MR imaging systems from different companies and with different acquisition systems. Patients who underwent MR imaging outside our clinic were analyzed either by 0.2T ($n = 1$) or 1.5T ($n = 2$) MR imaging systems.

This study was conducted under the auspices of the legislation of the Canton de Vaud, Switzerland, which does not require informed consent for the retrospective scientific analysis of data collected during routine clinical care. In addition, the President of the Ethics Commission for Research on Humans of the Canton and the Medical Director of the institution have granted the right to access medical records to coauthors not directly involved in the care of these patients.

RESULTS

Of 157 patients presenting with clinical symptoms compatible with a diagnosis of TGA between June 2002 and March 2014,

Patient characteristics and diagnostic tests performed^a

Characteristic	
Women (%)	18 (60.0)
Age (yr)	64 (57–70)
Cerebrovascular risk factor, none (%)	13 (43.3)
Current smokers (%) ^b	2 (6.7)
Hypertension, treated (%)	10 (33.3)
Hyperlipidemia, treated (%)	5 (16.7)
Impaired glucose tolerance (%)	1 (3.3)
History of atrial fibrillation (%)	5 (16.7)
High-risk alcohol consumption (%)	2 (6.7)
Previous cerebrovascular event (%)	3 (10.0)
Approximate duration of anterograde amnesia (hr)	12 (4–17)
Previous episode of TGA (%)	3 (10.0)
Documented triggering event, any (%)	16 (53.3)
Emotional (%)	9 (30.0)
Physical (%)	7 (23.3)
CTP	
Delay from TGA onset (hr)	6 (4–10)
Anterograde amnesia still present (%)	20 (66.7)
Hippocampi well-visualized on CTP (%)	14 (46.7)
EEG (%)	23 (76.7)
Delay from onset (hr)	21 (7–27)
Abnormalities (all nonspecific)	10 (33.3)
DWI (%)	10 (33.3)
Delay from onset (days)	2 (1–3)
Punctate hippocampal lesions (%)	2 (6.7)

Note:—EEG indicates electroencephalography.

^a Data are shown as No. (%) for categoric variables and median \pm interquartile range for continuous variables.

^b Four additional patients (13.3%) did smoke in the past.

32 (20%) underwent CTP. All examinations were of good quality. Two patients were excluded because of acute ischemic lesions later shown on DWI. Of the remaining 30 patients with a final diagnosis of TGA, 60% were women and the median age was 64 years (interquartile range, 57–70 years). A triggering event (emotional or physical) was documented in 53% of patients. In 77% of the patients who underwent electroencephalography, transient epileptic amnesia was ruled out. In the remaining 23%, there was no clinical suspicion for this diagnosis. Other patient characteristics and the diagnostic tools used are summarized in the Table.

In all except 1 patient, CTP findings were normal, including those of 47% of patients with well-visualized hippocampi. Perfusion abnormalities were observed in a 43-year-old healthy patient with typical TGA presentation. The patient had anterograde and retrograde amnesia spanning several years, accompanied by repetitive questions and moderate anxiety but without identity loss. No triggering event was recorded in this patient. CTP performed at 2.5 hours after symptom onset showed decreased CBF, decreased CBV, and increased MTT in both lentiform nuclei, extending into the insulae but not into the hippocampi. PWI performed 4.0 hours after symptom onset showed findings similar to those of CTP (Fig 1). Acute electroencephalography findings obtained between CTP and MR imaging examinations were normal. When the patient woke up the next morning in the hospital 18 hours after symptom onset, all symptoms had disappeared and no headache, fever, or other symptoms emerged. A neuropsychological assessment performed at approximately 24 hours still showed mild amnesic features (recall difficulties) and a borderline

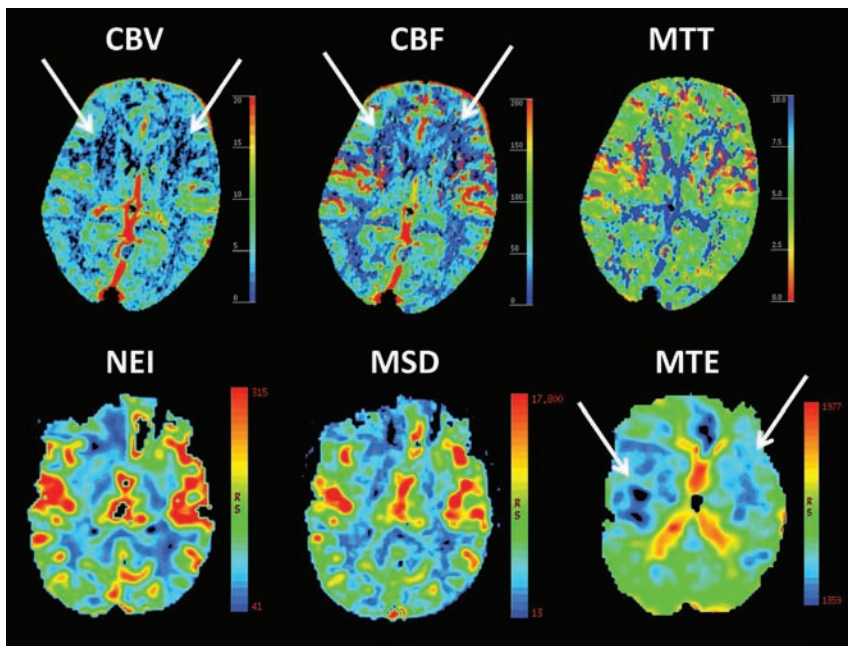


FIG 1. Upper row: CTP shows abnormalities in the lentiform nuclei bilaterally (*white arrows*) in a 43-year-old patient with transient global amnesia at 2.5 hours from symptom onset. Bottom row: PWI shows abnormalities (*white arrows*) at 4.0 hours from symptom onset. NEI indicates negative enhancement integral (CBV equivalent); MSD, maximum slope of decrease (CBF equivalent); MTE, mean time to enhance (MTT equivalent).

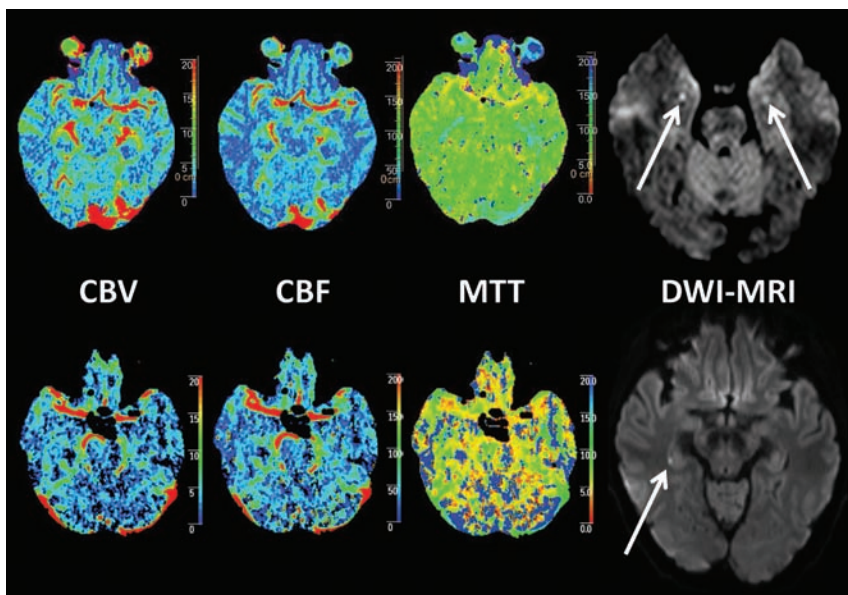


FIG 2. Acute CTP and subacute DWI in 2 female patients presenting with classic TGA symptoms. All CTP map findings for both patients were normal, while punctate DWI lesions were detected in the lateral hippocampus, bilaterally at 45 hours (62-year-old patient, upper row), and unilaterally at 64 hours (61-year-old patient, lower row) after symptom onset, respectively.

executive dysfunction. The patient was not reassessed with a neuropsychological examination. DWI performed at 4 days did not show any lesions, and repeat CTP findings at 6 days were normal.

Overall, the frequency of abnormalities found by CTP was 3% in this case series. Low-resolution DWI was performed in 10 of our patients at a median delay of 2 days after symptom onset (interquartile range, 1–3 days). Three of these patients

were examined between approximately day 2 and 3, and punctate lesions in the medial hippocampus were observed on DWI in 2 of them 45 and 64 hours after symptom onset, respectively (Fig 2). In the remaining 7 patients outside this time interval, no punctate lesions were detected.

DISCUSSION

We found that CTP investigation findings during or immediately after TGA were normal in all except 1 patient in this single-center case series. These results strongly suggest that CTP is not a suitable diagnostic tool to confirm TGA. This finding is also supported by the fact that 2 patients who fulfilled the TGA criteria but had ischemic lesions on MR imaging did not show perfusion abnormalities on CTP.¹³

Our data do not support widespread hypoperfusion in the mesiotemporal area or elsewhere as a cause of TGA in most patients or of the punctate hippocampal DWI lesions.^{2,7} Our single patient with CTP perfusion abnormalities showed an unexpected pattern involving both lentiform nuclei and extending into the insulae. We excluded an artifactual finding by confirming the hypoperfusion with an additional PWI within 2 hours and by validating normalization of the CTP 6 days later. These findings are important because on a clinical level, this patient's symptoms were equivalent to those observed in the other patients who lacked perfusion abnormalities.

We do not know whether the CTP flow abnormalities observed could have triggered a punctate lesion in the mesial temporal structures because the hippocampi did not seem to be directly involved and DWI was not performed within the ideal time interval of 48–72 hours after symptom onset.^{1,2,14} We hypothesize that disruption of the corticohippocampal circuitry without direct involvement of the mesiotemporal region may have caused a clinical syndrome indistinguishable from classic TGA.

In both SPECT and PET studies, perfusion abnormalities in the basal ganglia have been reported for TGA but were associated with concomitant medial temporal lobe hypoperfusion.^{4,11} Analogous to this study, the case series of patients with TGA examined by using PWI by Toledo et al⁸ did not show a correlation between perfusion abnormalities and hippocampal DWI lesions on subacute imaging. Hypotheses for such abnormalities temporally re-

lated to TGA but lying outside of the limbic system include cortical spreading depression (migraine) or hitherto unexplained mechanisms.

Our study has limitations due to its retrospective nature and the nonconsecutive performance of CTP on the patients with TGA. Furthermore, CTP imaging included the entire hippocampi in only 14 patients, which may have lowered the detection rate of perfusion abnormalities in this region. Only 2 of 10 patients showed typical DWI punctate hippocampal lesions. This result was probably due to the low resolution of our examinations, the use of different MR imaging machines and measurement specifications, and image acquisition outside of the optimal timeframe.

CONCLUSIONS

Our data suggest that CTP does not offer additional diagnostic information in the work-up of typical TGA and is therefore not recommended on a routine basis. If imaging is performed in typical or atypical TGA, DWI is the preferred mode of imaging.¹⁵

Disclosures: Jean-François Démonet—UNRELATED: Board Membership: Eli Lilly,* Novartis*; Grants/Grants Pending: Leenards Foundation,* European Union Horizon 2020 Small and Medium-sized Enterprises Instrument Phase 2 Alzheimer's Disease Diagnosis by Amoneta Diagnostics project (pending)* project Eurostars Alzheimer's Disease bioCHIP (pending)*; Royalties: Oxford University Press; Travel/Accommodations/Meeting Expenses Unrelated to Activities Listed: Schwabe Pharmaceuticals.* Patrik Michel—RELATED: Grant: Swiss Heart Foundation*; UNRELATED: Board Membership: Boehringer-Ingelheim,* Bayer,* Pfizer*; Consultancy: Amgen,* Pierre-Fabre*; Grants/Grants Pending: Swiss National Science Foundation*; Payment for Lectures (including service on Speakers Bureaus): Boehringer-Ingelheim,* Bayer,* Pfizer,* Covidien,* St. Jude Medical*; Travel/Accommodations/Meeting Expenses Unrelated to Activities Listed: Boehringer-Ingelheim,* Bayer.* *Money paid to the institution.

REFERENCES

1. Szabo K. **Transient global amnesia.** *Front Neurol Neurosci* 2014; 34:143–49
2. Bartsch T, Butler C. **Transient amnesic syndromes.** *Nat Rev Neurol* 2013;9:86–97
3. Bettermann K. **Transient global amnesia: the continuing quest for a source.** *Arch Neurol* 2006;63:1336–38
4. Quinette P, Guillery-Girard B, Dayan J, et al. **What does transient global amnesia really mean? Review of the literature and thorough study of 142 cases.** *Brain* 2006;129:1640–58
5. Gonzalez-Martinez V, Comte F, de Verbizier D, et al. **Transient global amnesia: concordant hippocampal abnormalities on positron emission tomography and magnetic resonance imaging.** *Arch Neurol* 2010;67:510
6. Matsui M, Imamura T, Sakamoto S, et al. **Transient global amnesia: increased signal intensity in the right hippocampus on diffusion-weighted magnetic resonance imaging.** *Neuroradiology* 2002;44:235–38
7. Sedlaczek O, Hirsch JG, Grips E, et al. **Detection of delayed focal MR changes in the lateral hippocampus in transient global amnesia.** *Neurology* 2004;62:2165–70
8. Toledo M, Pujadas F, Grivé E, et al. **Lack of evidence for arterial ischemia in transient global amnesia.** *Stroke* 2008;39:476–79
9. Zhu G, Michel P, Jovin T, et al. **Prediction of recanalization in acute stroke patients receiving intravenous and endovascular revascularization therapy.** *Int J Stroke* 2015;10:28–36
10. Hodges R, Warlow P. **Syndromes of transient amnesia: towards a classification—a study of 153 cases.** *J Neurol Neurosurg Psychiatry* 1990;53:834–43
11. Bartsch T, Deuschl G. **Transient global amnesia: functional anatomy and clinical implications.** *Lancet Neurol* 2010;9:205–14
12. Croisile B, Astier JL, Beaumont C. **Standardization of the 5-word test in a group of 191 normal subjects aged 50 to 90 years [in French].** *Rev Neurol* 2007;163:323–33
13. Eskiolglou E, Beaud V, Maeder P, et al. **Amnesic strokes and TIAs are rare and frequently missed: a 12.5 year single center experience.** In: *Proceedings of the International Stroke Conference*, Nashville, Tennessee. February 16–19, 2015
14. Weon YC, Kim JH, Lee JS, et al. **Optimal diffusion-weighted imaging protocol for lesion detection in transient global amnesia.** *AJNR Am J Neuroradiol* 2008;29:1324–28
15. Schellinger PD, Bryan RN, Caplan LR, et al; Therapeutics and Technology Assessment Subcommittee of the American Academy of Neurology. **Evidence-based guideline: the role of diffusion and perfusion MRI for the diagnosis of acute ischemic stroke—report of the Therapeutics and Technology Assessment Subcommittee of the American Academy of Neurology.** *Neurology* 2010;75:177–85

Timing-Invariant CT Angiography Derived from CT Perfusion Imaging in Acute Stroke: A Diagnostic Performance Study

E.J. Smit, E.-j. Vonken,  F.J.A. Meijer, J.W. Dankbaar, A.D. Horsch, B. van Ginneken, B. Velthuis, I. van der Schaaf, and M. Prokop



ABSTRACT

BACKGROUND AND PURPOSE: Timing-invariant (or delay-insensitive) CT angiography derived from CT perfusion data may obviate a separate cranial CTA in acute stroke, thus enhancing patient safety by reducing total examination time, radiation dose, and volume of contrast material. We assessed the diagnostic accuracy of timing-invariant CTA for detecting intracranial artery occlusion in acute ischemic stroke, to examine whether standard CTA can be omitted.

MATERIALS AND METHODS: Patients with suspected ischemic stroke were prospectively enrolled and underwent CTA and CTP imaging at admission. Timing-invariant CTA was derived from the CTP data. Five neuroradiologic observers assessed all images for the presence and location of intracranial artery occlusion in a blinded and randomized manner. Sensitivity and specificity of timing-invariant CTA and standard CTA were calculated by using an independent expert panel as the reference standard. Interrater agreement was determined by using κ statistics.

RESULTS: We included 108 patients with 47 vessel occlusions. Overall, standard CTA and timing-invariant CTA provided similar high diagnostic accuracy for occlusion detection with a sensitivity of 96% (95% CI, 90%–100%) and a specificity of 100% (99%–100%) for standard CTA and a sensitivity of 98% (95% CI, 94%–100%) and a specificity of 100% (95% CI, 100%–100%) for timing-invariant CTA. For proximal large-vessel occlusions, defined as occlusions of the ICA, basilar artery, and M1, the sensitivity and specificity were 100% (95% CI, 100%–100%) for both techniques. Interrater agreement was good for both techniques (mean κ value, 0.75 and 0.76).

CONCLUSIONS: Timing-invariant CTA derived from CTP data provides diagnostic accuracy similar to that of standard CTA for the detection of artery occlusions in acute stroke.

Stroke imaging research currently focuses on prediction of patient outcome and identifying patients who are suitable for neurointerventional treatment.^{1,2} For these purposes, advanced stroke imaging protocols typically add CT perfusion imaging or diffusion-weighted MR imaging to the traditional work-up, consisting of noncontrast CT and CT angiography.^{2,3} Noncontrast CT is used to differentiate hemorrhagic stroke from ischemic stroke and to assess early signs of ischemia. CTA is used to localize arterial occlusions and to identify proximal large-vessel occlusions that may be suitable for endovascular treatment. CT perfu-

sion imaging and DWI are used to assess the extent and severity of hypoperfusion and particularly increase the sensitivity of imaging in the early stages of ischemic stroke.⁴ The practical advantages of CT perfusion imaging are that it is widely available and does not delay treatment decisions because it is fast and most patients already undergo CT scanning.³

Currently, CTA can be derived from CT perfusion data. Such an approach allows the enhancement of patient safety by reducing the total scanning time, radiation dose, and amount of contrast material needed.⁵ In CT perfusion imaging, multiple scans after intravenous injection of contrast material are obtained with time, generating a 4D dataset, which is used to derive cerebral perfusion maps such as the cerebral blood flow, cerebral blood volume, and arrival times. When imaging is performed on a CT scanner with large spatial coverage, however, this 4D data can also be used to provide CT angiographic information, referred to as 4D-CTA or dynamic CTA. Previous studies have assessed whether 4D-CTA can be used for detection of vascular occlusion in a stroke setting but found that image quality was moderate and diagnostic performance for stroke assessment was limited because large-vessel

Received December 4, 2014; accepted after revision February 22, 2015.

From the Department of Radiology (E.J.S., E.-j.V., J.W.D., A.D.H., B.V., I.v.d.S.), University Medical Center Utrecht, Utrecht, the Netherlands; and Department of Radiology (E.J.S., F.J.A.M., B.v.G., M.P.), Radboud University Medical Center Nijmegen, Nijmegen, the Netherlands.

Please address correspondence to E.J. Smit, MD, University Medical Center Utrecht, Department of Radiology (E01.132), PO Box 85500, 3508 GA Utrecht, the Netherlands; e-mail: ewoudsmit@gmail.com

 Indicates open access to non-subscribers at www.ajnr.org

<http://dx.doi.org/10.3174/ajnr.A4376>

occlusions may be missed.⁵⁻⁸ Recently, a different approach to obtain CTA from CT perfusion source data was presented that combines the whole 4D-CTA dataset into 1 high-quality 3D-CTA dataset by displaying maximum contrast enhancement with time.⁵ This technique is referred to as “timing-invariant CTA” because it is insensitive to delayed contrast arrival and was shown to provide similar-to-superior image quality compared with standard CTA.⁵

The aim of our study was to test the diagnostic performance of timing-invariant CTA for stroke evaluation, to assess whether standard CTA can be omitted when CT perfusion imaging has been performed.

MATERIALS AND METHODS

Patients

Institution review board approval and informed consent were obtained. Consecutive patients admitted to our hospital with suspected ischemic stroke were prospectively enrolled. They underwent standard CTA and CT perfusion imaging if they fulfilled the following criteria: 1) admission at <9 hours after onset of neurologic deficit (including patients who woke up with stroke symptoms if the time between going to sleep and admission was <9 hours), 2) NIHSS score of at least 2, 3) no signs of hemorrhage on noncontrast CT, and 4) no known contrast allergy or kidney failure. For this study, we selected all patients who were scanned on our 256-section CT scanner (iCT; Philips Healthcare, Best, the Netherlands). Scans were performed according to a previously reported protocol: CT perfusion imaging was performed by using 40 mL of intravenous contrast material, 80 kV(peak), and 150 mAs every 2 seconds during 48 seconds (volume CT dose index = 5.8 mGy per acquisition, dose-length product = 1157 mGy × cm), and CT angiography was performed by using 50 mL of intravenous contrast material, 120 kVp, and 150 mAs (volume CT dose index = 19.5 mGy, dose-length product = 775 mGy cm).⁵ CT perfusion imaging and CTA were performed subsequently, and both, before tPA administration. For the purpose of this study, the volume covered by standard CTA was manually clipped to correspond with the volume of CT perfusion. For all imaging studies, the intracranial arteries being included in the CT perfusion volume were verified.

Timing-invariant CTA was automatically derived from the CT perfusion data on a scientific workstation (iX Viewer; ISI, Utrecht, the Netherlands). Timing-invariant CTA provides angiographic images by displaying maximal enhancement with time (temporal maximum intensity projection) with a prior noise-reducing filter in the temporal domain.^{5,9} This temporal noise-reducing filter improves image quality without loss of spatial resolution. Due to the choice of the temporal maximum, this technique is timing-invariant (ie, the maximal enhancement of a vessel is displayed independent of its contrast arrival time).⁹ In this study, timing-invariant CTA was implemented as a 1D Gaussian low-pass filter across all time points of the CTP sequence (parameters: SD = 1.5 seconds, kernel size = 5) followed by determining the maximal CT number with time (temporal MIP), which is the output CT number displayed on the timing-invariant CTA.

Procedures

Timing-invariant CTA and standard CTA were assessed for the presence and location of arterial occlusion.

All scans were assessed by 5 experienced radiologic observers (2 neuroradiologists, 1 radiologist, and 2 radiology residents, with 9 [I.v.d.S.], 7 [F.J.A.M.], 7 [A.D.H.], 5 [J.W.D.] and 3 [E.J.S.] years of experience in evaluating cerebral CTA examinations, respectively). These observers were individually presented with a random sequence of scans and were blinded to patient information and imaging technique. To reduce potential sources of bias, we presented all sequences with different randomization.

Images were scored for the presence of occlusion in the following arteries: 1) intracranial part of the internal carotid artery, 2) middle cerebral artery segment 1 (M1), 3) distal MCA segment 2 (M2+), 3) anterior cerebral artery segment 1 (A1), 4) anterior cerebral artery segment 2 (A2), 5) basilar artery, and 6) posterior cerebral artery. Arteries were separately scored for both hemispheres. Scans were presented with equal display settings, and observers could change these settings in accordance with clinical practice (arbitrary planes, slab thickness, and window leveling).

The final diagnosis (reference standard) was made by an independent expert panel consisting of a neurointerventional radiologist and a neuroradiologist (with >15 and 10 years of experience in evaluating cerebral CTA examinations, respectively) who were provided with all available imaging and relevant clinical information (including follow-up). This expert panel was blinded to the observer scores and reviewed all cases in which differences were found between the observer scores on standard CTA and timing-invariant CTA.

Statistical Analysis

To assess diagnostic accuracy, we determined the sensitivity and specificity of standard CTA and timing-invariant CTA with the diagnosis of the expert panel serving as the reference test. The diagnosis per CTA technique was the one made by the majority of the observers. The sensitivity and specificity were calculated per artery segment separately and for the major cerebral arteries combined. These values were expressed with their 95% confidence intervals.

To assess reproducibility, we determined interobserver agreement by using κ statistics for both timing-invariant CTA and standard CTA. These parameters were expressed as average values together with their range among observers.

RESULTS

From October 2009 to October 2011, 167 consecutive patients underwent imaging at our hospital for suspected ischemic stroke. One hundred fifteen patients were eligible for this diagnostic study because they were scanned on a 256-section CT scanner and CT perfusion source data were available for analysis. Of these, 6 patients were excluded because imaging was unsuccessful due to severe patient motion (4 on CT perfusion imaging and 2 on standard CTA), and 1 patient was excluded because the CT perfusion images did not include the circle of Willis. The final analysis included 108 patients (58 women; mean age, 68 ± 13 years). The median NIHSS score at admission was 6 (interquartile range,

Diagnostic performance of standard CTA and timing-invariant CTA for assessment of artery occlusion in the various territories^a

Territory	Occlusions	Standard CTA		Timing-Invariant CTA	
		Sensitivity	Specificity	Sensitivity	Specificity
Overall	47	96% (90–100)	100% (99–100)	98% (94–100)	100% (100–100)
Internal carotid artery	9	100% (100–100)	100% (100–100)	100% (100–100)	100% (100–100)
Anterior cerebral artery	2	100% (100–100)	99% (98–100)	100% (100–100)	99% (98–100)
Middle cerebral artery	33	94% (86–100)	100% (100–100)	100% (100–100)	99% (98–100)
Segment 1 (M1)	25	100% (100–100)	100% (100–100)	100% (100–100)	100% (100–100)
Segment 2+ (M2+)	8	75% (45–100)	100% (100–100)	100% (100–100)	100% (100–100)
Basilar artery	1	100% (100–100)	100% (100–100)	100% (100–100)	100% (100–100)
Posterior cerebral artery	2	100% (100–100)	99% (98–100)	50% (0–100)	100% (100–100)

^a Data in parentheses are 95% confidence intervals.

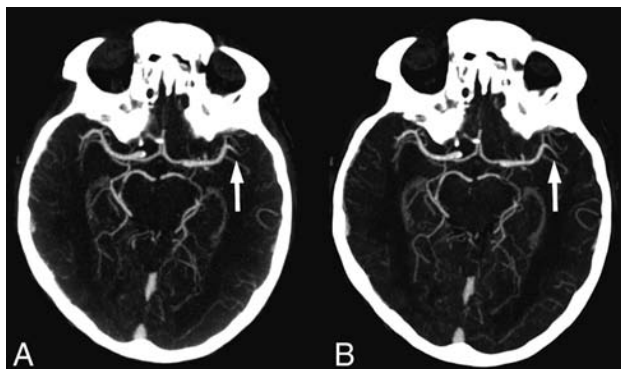


FIG 1. Standard CT angiography (A) and timing-invariant CT angiography (B) images in a patient with a left-sided middle cerebral artery occlusion in the M2 segment. The occlusion was detected on both CT angiography techniques.

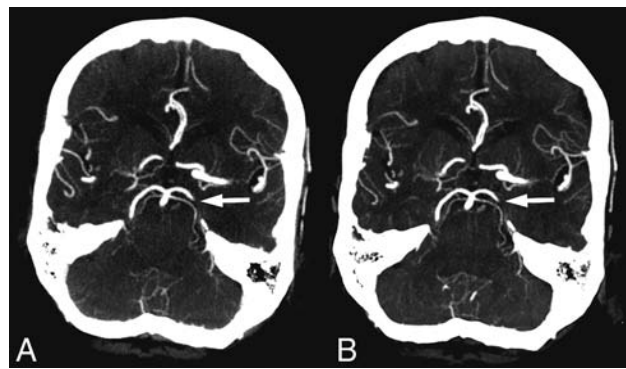


FIG 2. Standard CT angiography (A) and timing-invariant CT angiography (B) images in a patient with a left-sided posterior cerebral artery occlusion. This was the only occlusion missed on timing-invariant CTA and was considered a result of observer variation because it was scored as a false-negative finding by 3 observers on timing-invariant CTA and by 2 observers on standard CTA.

3–13), and the median time from onset of symptoms to CT was 107 minutes (interquartile range, 40–200 minutes).

Thirty-five patients (32%) had an arterial occlusion, in which 9 occlusions were located in the internal carotid artery, 33 in the middle cerebral artery (25 in the M1 segment and 8 in M2+ segment), 2 in the anterior cerebral artery (both in segment A1), 1 in the basilar artery, and 2 in the posterior cerebral artery.

An overview of the results is presented in the Table. Overall, standard CT angiography and timing-invariant CT angiography provided similar high diagnostic accuracy for occlusion detection in acute ischemic stroke with a sensitivity of 96% (95% CI, 90%–100%) and a specificity of 100% (95% CI, 99%–100%) for standard CTA and a sensitivity of 98% (95% CI, 94%–100%) and a specificity of 100% (95% CI, 100%–100%) for timing-invariant CTA. For proximal large-vessel occlusions, defined as occlusions of the ICA, basilar artery, and M1, the sensitivity and specificity were 100% (95% CI, 100%–100%) for both techniques. For distal middle cerebral artery occlusions (M2+), standard CTA provided a sensitivity of 75% (95% CI, 45%–100%) and a specificity of 100% (95% CI, 100%–100%) compared with a sensitivity and specificity of 100% (95% CI, 100%–100%) for timing-invariant CTA (not significant). An example of a M2 occlusion that was detected on both techniques is shown in Fig 1.

For the posterior cerebral artery, 1 of 2 occlusions was missed on timing-invariant CTA, while both were diagnosed on standard CTA. Overall, only this 1 occlusion was missed on timing-invariant CTA (missed by 3 observers on timing-invariant CTA but also by 2 observers on standard CTA), shown in Fig 2.

In 8 patients, differences were found between the observer

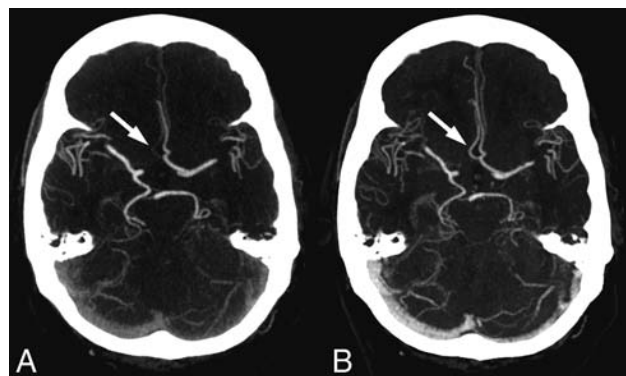


FIG 3. Images show the effect of delayed contrast material arrival in a patient with right-sided hemiparesis. A, On standard CT angiography, the right-sided anterior cerebral artery was considered occluded in both segments A1 and A2. B, On timing-invariant CTA, the right-sided anterior cerebral artery was considered hypoplastic in segment A1 and patent in segment A2. Standard CTA shows only faint enhancement in the right-sided A2 segment (arrow) because the bulk of contrast material arrived after the standard CTA acquisition. Timing-invariant CT shows strong A2 enhancement (arrow) because it is delay-insensitive and displays maximal contrast enhancement with time.

scores on standard CTA and timing-invariant CTA, and these cases were presented to the expert panel. In all cases, the expert panel found that the standard CTA and timing-invariant CTA images provided the same diagnosis. In 4 cases, however, standard CTA showed faint enhancement in an artery segment, whereas timing-invariant CTA showed high enhancement. Figure 3 shows an example of these differences in a patient with a hypoplastic A1

segment that was scored as a false-positive finding on standard CTA as a combined A1 and A2 occlusion, resulting from only faint A2 enhancement, while on timing-invariant CTA, the segment was scored as a true-negative finding because it showed clear A2 enhancement. In the remaining 4 cases, the differences in observer scores between standard CTA and timing-invariant CTA could only be explained by observer variation because there was mostly 1 observer difference and the images were virtually identical (Figs 1 and 2).

Overall interrater agreement was good for both timing-invariant CTA (mean κ value = 0.76; range observers, 0.69–0.83; mean agreement = 97%; range observers, 96%–98%), and standard CTA (mean κ value = 0.75; range observers, 0.63–0.85; mean agreement = 97%; range observers, 96%–98%).

DISCUSSION

In acute stroke, CT angiography is performed to identify proximal large-vessel occlusions suitable for endovascular treatment. In this study, we found that CTA derived from CT perfusion data can successfully detect such occlusions; this feature makes it unnecessary to perform a separate CTA acquisition of the brain. Timing-invariant CTA integrates information across the whole time sequence of the CT perfusion acquisition and is, therefore, less susceptible to delays in regional enhancement, which may hamper standard CTA.⁵ Our results imply that standard CTA for the evaluation of intracranial occlusions can be omitted if CT perfusion imaging has been performed. The advantage of such an approach lies in improvement of patient safety: Because 1 scan can be performed instead of 2 separate ones, total scanning time, contrast material usage, and radiation dose will be reduced.⁵ The exact benefits will depend on the scan protocol, but the approach will typically allow a combined CTA and CT perfusion imaging protocol that can be performed within 60 to 90 seconds, reduces the radiation dose by 0.5–1.0 mSv, and requires only 40–50 mL of intravenous contrast material.^{4,5,10,11} Within this time, tPA can be prepared for administration; therefore, advanced imaging need not delay thrombolytic therapy.⁴

In our study, we found a few differences in occlusion detection between standard CTA and timing-invariant CTA. We analyzed these cases and found that most of these differences could be explained only by observer variation because the images were virtually identical. In some cases however, we found that segments that seemed occluded on standard CTA actually showed contrast enhancement on timing-invariant CTA. This difference implies that these segments cannot be occluded because they fill with contrast material, albeit at a later point in time than that used for acquiring the standard CTA. Our results imply that standard CTA may not be able to differentiate delayed enhancement of a vascular segment from vessel occlusion. Standard CTA is delay-sensitive because it is performed at 1 moment in time: Vessels will not be visible if contrast material has not yet arrived at the time of acquisition. Timing-invariant CTA, on the other hand, is delay-insensitive because it displays the maximum contrast during the total time of the CT perfusion acquisition, typically some 60 seconds. Timing-invariant CTA is, therefore, less susceptible to suboptimal contrast enhancement resulting from variations in cardiac output or delayed arrival due to vascular pathology.^{5,9,12,13} A

strength of the suggested approach is that CT perfusion images and 4D-CTA images are simultaneously available for side-by-side comparison. This combined information can resolve discrepancies and helps differentiate hypoplastic vessel segments, vessel stenosis, and occlusions with good collateralization.^{5,9,12,13}

Our study has limitations. First, our scanner could not cover the whole brain during CT perfusion but only a 5- to 6-cm range around the circle of Willis. We could, therefore, evaluate the main cerebral arteries that are relevant for endovascular treatment but not the distal pericallosal and cortical branches. In this comparison study, we focused on the question of whether occlusions can be reliably detected on the CTA images that are derived from the CT perfusion data. To make sure that the results were not biased by the greater coverage of standard CTA, we cropped the CTA data so that identical volumes could be evaluated and compared. Most manufactures now have scanners that provide whole-brain coverage during CT perfusion imaging. With this equipment, no additional brain CTA is necessary if timing-invariant CTA is calculated from the CT perfusion acquisition. For assessing the extracranial portions of the carotid artery, cervical CTA, MR angiography, or sonography may be performed.^{14–16} Cervical imaging remains important for assessing the extracranial extent of ICA occlusion for neurointerventional planning or detecting carotid plaques as a source of emboli. Second, timing-invariant CTA is currently not commercially available but can be easily implemented in commercial or research software, and 1 major vendor has announced the implementation on its CT workstation.⁵

CONCLUSIONS

Timing-invariant CTA derived from CT perfusion data provides diagnostic performance similar to that of standard CTA for the detection of artery occlusions in acute stroke.

Disclosures: Ewoud J. Smit—UNRELATED: Payment for Lectures (including service on Speakers Bureaus); Toshiba Medical Systems. Frederick J.A. Meijer—UNRELATED: Payment for Lectures (including service on Speakers Bureaus); Toshiba Medical Systems (Speakers Bureau). Jan W. Dankbaar—RELATED: Grant: Dutch Heart Foundation (2012T061). Birgitta Velthuis—UNRELATED: Grants/Grants Pending: Netherlands Heart Foundation (grant number 2008 T034) Dutch Acute Stroke Trial*; Payment for Lectures (including service on Speakers Bureaus); Philips Healthcare.* Mathias Prokop—RELATED: Grant: Philips Healthcare*; UNRELATED: Grants/Grants Pending: Philips Healthcare,* Toshiba Medical Systems*; Payment for Lectures (including service on Speakers Bureaus): Bracco, Toshiba Medical Systems, Bayer-Schering, CME Science; Travel/Accommodations/Meeting Expenses Unrelated to Activities Listed: Toshiba Medical Systems, Philips Healthcare, European School of Radiology, CME Science. *Money paid to the institution.

REFERENCES

1. Shuaib A, Butcher K, Mohammad AA, et al. **Collateral blood vessels in acute ischaemic stroke: a potential therapeutic target.** *Lancet Neurol* 2011;10:909–21
2. Schellinger PD, Bryan RN, Caplan LR, et al; Therapeutics and Technology Assessment Subcommittee of the American Academy of Neurology. **Evidence-based guideline: the role of diffusion and perfusion MRI for the diagnosis of acute ischemic stroke—report of the Therapeutics and Technology Assessment Subcommittee of the American Academy of Neurology.** *Neurology* 2010;75:177–85
3. Wintermark M, Rowley HA, Lev MH. **Acute stroke triage to intravenous thrombolysis and other therapies with advanced CT or MR imaging: pro CT.** *Radiology* 2009;251:619–926
4. Lev MH. **Acute stroke imaging: what is sufficient for triage to endovascular therapies?** *AJNR Am J Neuroradiol* 2012;33:790–92
5. Smit EJ, Vonken E-J, van der Schaaf IC, et al. **Timing-invariant re-**

- construction for deriving high-quality CT angiographic data from cerebral CT perfusion data. *Radiology* 2012;263:216–25
6. Yang CY, Chen YF, Lee CW, et al. **Multiphase CT angiography versus single-phase CT angiography: comparison of image quality and radiation dose.** *AJNR Am J Neuroradiol* 2008;29:1288–95
 7. Willems PW, Brouwer PA, Barfett JJ, et al. **Detection and classification of cranial dural arteriovenous fistulas using 4D-CT angiography: initial experience.** *AJNR Am J Neuroradiol* 2010;32:49–53
 8. Frölich AM, Psychogios MN, Klotz E, et al. **Angiographic reconstructions from whole-brain perfusion CT for the detection of large vessel occlusion in acute stroke.** *Stroke* 2012;43:97–102
 9. Smit EJ, Vonken EJ, van Seeters T, et al. **Timing-invariant imaging of collateral vessels in acute ischemic stroke.** *Stroke* 2013;44:2194–99
 10. Balemans CE, Reichert LJM, van Schelven BI, et al. **Epidemiology of contrast material-induced nephropathy in the era of hydration.** *Radiology* 2012;263:706–13
 11. Huda W, Ogden KM, Khorasani MR. **Converting dose-length product to effective dose at CT.** *Radiology* 2008;248:995–1003
 12. Bae KT. **Intravenous contrast medium administration and scan timing at CT: considerations and approaches.** *Radiology* 2010;256:32–61
 13. Frölich AM, Wolff SL, Psychogios MN, et al. **Time-resolved assessment of collateral flow using 4D CT angiography in large-vessel occlusion stroke.** *Eur Radiol* 2014;24:390–96
 14. Chappell FM, Wardlaw JM, Young GR, et al. **Carotid artery stenosis: accuracy of noninvasive tests—individual patient data meta-analysis.** *Radiology* 2009;251:493–502
 15. El-Saden SM, Grant EG, Hathout GM, et al. **Imaging of the internal carotid artery: the dilemma of total versus near total occlusion.** *Radiology* 2001;221:301–08
 16. Corti R, Fuster V. **Imaging of atherosclerosis: magnetic resonance imaging.** *Eur Heart J* 2011;32:1709–19b

Significance of Development and Reversion of Collaterals on MRI in Early Neurologic Improvement and Long-Term Functional Outcome after Intravenous Thrombolysis for Ischemic Stroke

M. Ichijo, E. Iwasawa, Y. Numasawa, K. Miki, S. Ishibashi, M. Tomita, H. Tomimitsu, T. Kamata, H. Fujigasaki, S. Shintani, and H. Mizusawa

ABSTRACT

BACKGROUND AND PURPOSE: Predicting response to rtPA is essential in the era of endovascular therapy for stroke. The purpose of this study was to elucidate prognostic factors of early neurologic improvement and long-term outcome with respect to the development and reversion of leptomeningeal collaterals in recanalization therapy after acute ischemic stroke.

MATERIALS AND METHODS: We analyzed consecutive patients with proximal MCA occlusion treated with rtPA from 2007 to 2012 at 2 hospital stroke centers. All patients routinely underwent brain MR imaging before rtPA. To assess the reversion of collateral signs, we included patients who underwent follow-up MR imaging. We assessed the development and reversion of collaterals by using a combination of 2 MR imaging collateral markers, the hyperintense vessel sign and the posterior cerebral artery laterality sign. Early neurologic improvement was defined as a decrease in the NIHSS score of ≥ 10 or a score of ≤ 2 at 24 hours of treatment.

RESULTS: Early neurologic improvement was observed in 22 of 48 eligible patients. The development of collaterals at arrival (15/22 versus 9/26, $P = .042$) was significantly associated with early neurologic improvement. Multivariate analysis adjusting for other variables showed that the development of collaterals at arrival (OR, 4.82; 95% CI, 1.34–19.98; $P = .015$) was independently associated with early neurologic improvement. Reversion of collaterals was significantly associated with successful recanalization ($P < .001$), and multivariate analysis showed that the reversion of collaterals was an independent prognostic factor of long-term functional outcome (OR, 5.07; 95% CI, 1.38–22.09; $P = .013$).

CONCLUSIONS: Our results indicate that the development of leptomeningeal collaterals plays a crucial role in achieving early neurologic improvement, and reversion of collaterals predicts a favorable outcome via arterial recanalization after rtPA treatment for acute stroke.

ABBREVIATIONS: ENI = early neurologic improvement; HV = hyperintense vessel; IQR = interquartile range; MCA = middle cerebral artery; PCA = posterior cerebral artery; TIMI = Thrombolysis in Myocardial Infarction

Proximal intracranial arterial occlusion is associated with poor functional outcome, and salvaging brain tissue at risk of infarction is of great interest. Intravenous administration of recombinant tissue plasminogen activator to recanalize the occluded artery has significantly reduced mortality and improved long-term outcomes after ischemic stroke, as shown in large clinical trials.^{1,2} Approximately 25% of patients who received IV rtPA

experienced neurologic improvement within 24 hours after administration (early neurologic improvement [ENI]),^{3–7} and the long-term functional outcome at 3 months was better than that of patients who did not experience ENI.^{6,8} Identifying factors predicting neurologic improvement shortly after reperfusion therapy with rtPA in clinical practice may help select patients who are likely to respond to IV rtPA and improve the selection of patients for more aggressive therapies, including endovascular intervention. ENI has been associated with lower baseline NIHSS scores⁷ and younger age,^{4,6,7} but not with time from onset to treatment.^{4,7,8} Although the theory of thrombolysis predicts that early recanalization should contribute to ENI, a proportion of patients with early recanalization did not experience ENI in some studies,^{9,10} suggesting that other unspecified factors also play a role.

At the acute phase of proximal MCA occlusion, the primary collateral circulation is occasionally established via leptomeningeal anastomoses from the anterior cerebral artery and posterior cerebral artery (PCA). Hyperintense vessels (HVs) on FLAIR MR

Received October 8, 2014; accepted after revision March 3, 2015.

From the Department of Neurology and Neurological Science (M.I., E.I., Y.N., S.I., and H.M.), Department of Endovascular Surgery (K.M.), and Clinical Research Center (M.T.), Tokyo Medical and Dental University, Tokyo, Japan; Department of Neurology, JA Toride Medical Center (H.T., S.S.), Ibaraki, Japan; Department of Neurology, Musashino Red Cross Hospital (M.I., T.K.), Tokyo, Japan; and Department of Internal Medicine (H.F.), Metropolitan Bokutoh Hospital, Tokyo, Japan.

Please address correspondence to S. Ishibashi, MD, PhD, Department of Neurology and Neurological Science, Tokyo Medical and Dental University, 1-5-45, Yushima, Bunkyo-ku, Tokyo 113-0034; e-mail: t-ishibashi.nuro@tmd.ac.jp

 Indicates article with supplemental on-line appendix and table.

<http://dx.doi.org/10.3174/ajnr.A4384>

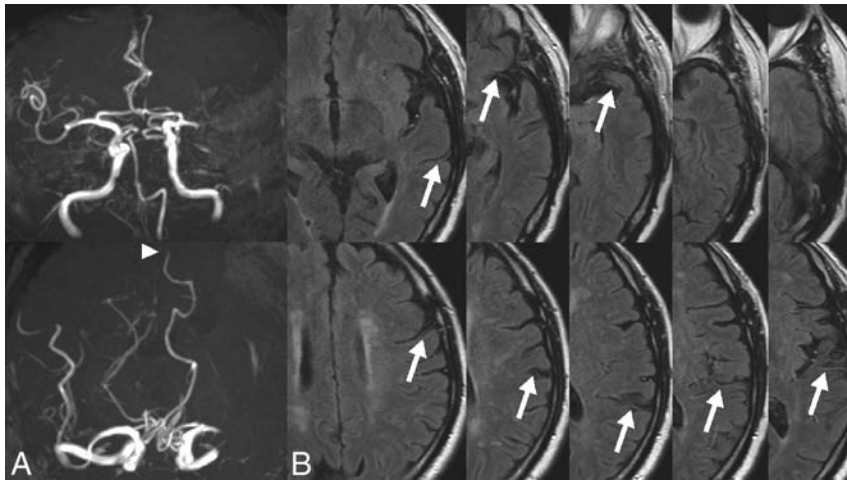


FIG 1. PCA laterality sign and hyperintense vessels on MR images. A, MRA shows an occlusion of the M1 portion of the left MCA and signal extent of the ipsilateral PCA (arrowhead). B, FLAIR MR imaging shows hyperintense vessels (arrows) in 8 of 10 axial sections.

imaging¹¹⁻¹⁴ and prominent PCA laterality on 3D-TOF MRA^{15,16} were reported as MR imaging radiologic markers of collateral flow. The presence of good collateral circulation before recanalization therapy is correlated with smaller infarct volume and better long-term neurologic outcome in patients with acute ischemic stroke caused by proximal MCA occlusion¹⁷ as well as with a prolonged therapeutic time window.¹⁸ Recently, the disappearance of collateral perfusion signs (collateral signs) on MR imaging was reported in patients with internal carotid artery occlusion in whom a high TICI flow grade was restored after immediate endovascular therapy.¹⁹ This finding indicates that the reversion of collateral signs may be a marker of hemodynamic improvement after recanalization.¹⁹ In this study, we focused on the development and reversion of leptomeningeal collateral circulation in acute proximal MCA occlusion and investigated their relationship with ENI and long-term outcome in the setting of thrombolytic therapy.

MATERIALS AND METHODS

For detailed methods, see the On-line Appendix. This retrospective case control study was performed on all patients admitted to 2 hospital stroke centers from April 2007 to November 2012. We selected patients with acute proximal MCA occlusion (M1 or M2 segment) who were treated with IV rtPA according to Japanese guidelines.²⁰ All patients routinely underwent brain MR imaging (Signa HDxt 1.5T Optima Edition; GE Healthcare, Milwaukee, Wisconsin; Magnetom Avanto; Siemens, Erlangen, Germany; or Symphony; Siemens) before rtPA and follow-up brain CT after stroke (median, 9 days; interquartile range [IQR], 6–12 days). To assess the reversion of collateral signs, we included patients who underwent follow-up MR imaging. In accordance with the standard protocol of our institutions for patients with ischemic stroke, demographic data and information on cardiovascular risk factors and medical history, the results of diagnostic tests, NIHSS scores, and modified Rankin Scale scores at 3 months after stroke were collected. We assessed ENI, defined as a decrease in NIHSS score of ≥ 10 or an NIHSS score ≤ 2 at 24 hours after rtPA treatment.⁴⁻⁸

Readers (E.I. and M.I.) blinded to all clinical information as-

essed the presence of PCA laterality and HVs on FLAIR. PCA laterality was considered present if ≥ 1 segmental extent was observable on axial stereoscopic images (Fig 1A), as described in previous studies.^{15,16} If signal from both PCAs ended in the same segment, laterality was defined as negative. HVs were defined as linear or serpentine hyperintense signals relative to gray matter distal to the Sylvian fissure.¹² To quantify the degree of HV, 10 FLAIR MR imaging sections were analyzed, from 2 sections below to 7 sections above the first M1 segment in which the MCA appeared (Fig 1B).¹⁴ The resulting HV score ranged from 0 to 10. A large reduction in the HV score was defined as a decrease of ≥ 5 on follow-up MR imaging. The “de-

velopment of collaterals” was defined as positive PCA laterality and an HV score of ≥ 5 on initial MR imaging. The disappearance of PCA laterality or the reduction of the HV score by ≥ 5 on follow-up MR imaging or both was defined as the “reversion of collaterals.” Interrater reliability for the presence of PCA laterality and HV score grading between 2 observers were estimated; in the event of discrepancies between readers, the final result was reached by consensus. Recanalization status after IV rtPA was assessed with a modified grading system based on the Thrombolysis in Myocardial Infarction (TIMI) grade.²¹ Successful recanalization was defined as TIMI 3 on follow-up MRA, and the percentage of successful recanalization was used as the recanalization rate. The Alberta Stroke Program Early CT Score²² was used to evaluate the initial DWI hyperintensity and final infarct extent on follow-up CT scans. Initial DWI volume was measured by using NIH Image (<http://rsb.info.nih.gov/nih-image/>). Univariable parametric and nonparametric comparisons of clinical characteristics were performed as appropriate. To identify independent predictors of ENI and long-term functional outcome, we performed multivariate logistic regression analyses as shown in the On-line Appendix.

RESULTS

Baseline Clinical and Radiologic Characteristics in Patients with Collateral Development and Reversion

From April 2007 to November 2012, 57 patients were examined for inclusion in this study; 5 were excluded for motion artifacts on MR imaging and 4 were excluded because they did not provide informed consent. Among 48 patients who met the inclusion criteria, the median age was 79 years (IQR, 70–83 years), 46% were women, and the median initial NIHSS score was 16 (IQR, 11–23). The location of the arterial occlusion was the M1 MCA in 35 patients and the M2 MCA in 13 patients. Development of collaterals (positive PCA laterality and HV score ≥ 5 at arrival) was observed in 24 (50%) of 48 patients. Twenty-five patients had PCA laterality at arrival. The signal extent of PCA in all these patients was confined to the ipsilateral side of the ischemic hemisphere (Fig 2A). Thirty-nine patients had HV scores of ≥ 5 , and

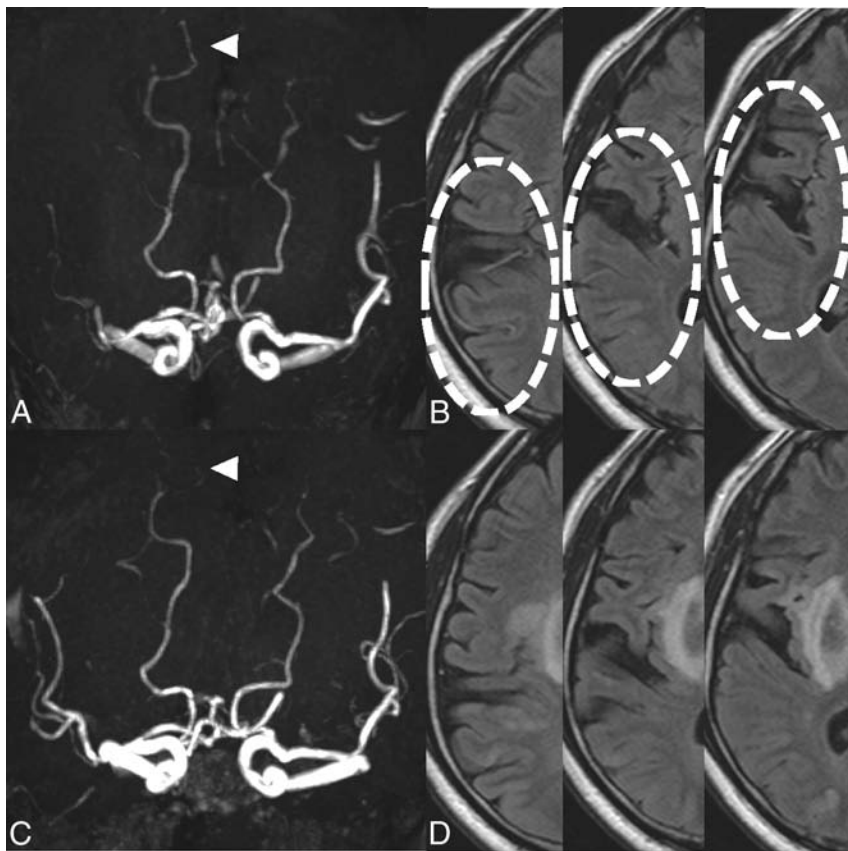


FIG 2. Reversion of collateral signs on MR images. MRA (A and C) and FLAIR MR imaging (B and D) of a representative patient who experienced early neurologic improvement after IV rtPA. PCA laterality (arrowheads) and hyperintense vessels (dotted circles) were observed before treatment (A and B) but disappeared after thrombolysis (C and D), indicating the reversion of collaterals.

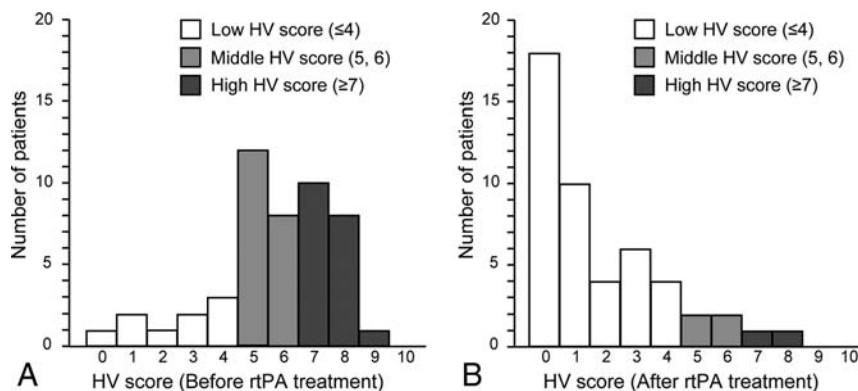


FIG 3. Distribution of the hyperintense vessel (HV) score before and after rtPA treatment. Most patients (39 of 48, 81%) were initially classified in the middle and high HV score group before treatment (A); however, the number of patients with a middle or high HV score dramatically decreased after thrombolysis (B).

the distribution of HV scores before IV rtPA is shown in Fig 3A. The κ coefficient for interobserver agreement was 0.917 for PCA laterality and 0.772 for the grading as low, medium, or high HV score by the 2 observers, which indicated good agreement. Reversion of collaterals (disappearance of PCA laterality and/or a large reduction in the HV score) was observed in 25 (52%) of 48 patients. The collateral reversion was observed in approximately 50% of patients in each collateral marker. PCA laterality had disappeared in 13 (52%) of 25 patients (Fig 2C), and 22 (56%) of 39

patients showed a large reduction in the HV score (≥ 5) after IV rtPA (Fig 2B, -D). The HV score was significantly lower after IV rtPA than before IV rtPA (1 versus 6; IQR, 0–3 versus 5–7; $P < .0001$; Fig 3B).

The groups with and without reversion of collaterals were equivalent in age, NIHSS score at arrival, cardiovascular risk factors, stroke etiology, and past medication (Table 1). Both groups were equivalent in the duration between the 2 MR imaging scans. The initial NIHSS score, DWI ASPECTS, and DWI volume did not differ significantly between the groups. The NIHSS score obtained 24 hours and 7 days after admission was significantly lower in patients with reversion of collaterals than in those without it (24 hours, 7 versus 11; IQR, 2–12 versus 6–17; $P = .022$; 7 days, 4 versus 8; IQR, 1–8 versus 3–14; $P = .008$). The successful recanalization rate (TIMI 3) assessed by follow-up MR imaging was significantly higher in patients with reversion of collaterals than in those without it (23 of 25 patients versus 8 of 23 patients; $P < .001$). The follow-up CT ASPECTS was significantly higher in patients with reversion of collaterals than in those without it (8 versus 6; IQR, 6.5–9 versus 4–8; $P = .017$), indicating a smaller infarct extent (Table 1). Significantly more patients with reversion of collaterals had a favorable long-term functional outcome (mRS, 0–1 at 3 months) than those without it (16 of 25 patients versus 8 of 23 patients; $P = .043$).

Prognostic Factors of ENI and Long-Term Functional Outcome after IV rtPA in Patients with Proximal MCA Occlusion

ENI was observed in 22 (46%) of 48 patients. The group with ENI and the group without ENI were equivalent in age, NIHSS score at arrival, cardiovascular risk factors, stroke etiology, and past medication (Table 2). DWI ASPECTS at arrival (8 versus 8; IQR, 6.75–9 versus 6.75–8; $P = .33$) and the arterial occlusion site ($P = .33$) did not differ between groups. Consistent with previous research,^{3-5,7} the rate of good long-term functional outcome (modified Rankin Scale score of 0–1 at 3 months) was significantly higher in the ENI-positive group than the ENI-negative group (16 of 22 patients versus 8 of 26 patients; $P = .008$). The development of collateral signs was detected in a significantly greater number of patients in

Table 1: Characteristics of patients with and without reversion of collaterals^a

	Reversion of Collaterals		P Value
	Yes (n = 25)	No (n = 23)	
Age (median) (IQR)	78 (71–81)	79 (68–86)	.52
Male sex (No.) (%)	13 (52)	13 (57)	.78
mRS 0–1 before stroke (No.) (%)	25 (100)	22 (96)	.48
Cardiovascular risk factors (No.) (%)			
Hypertension	15 (60)	13 (57)	1
Diabetes mellitus	7 (28)	3 (13)	.29
Hyperlipidemia	4 (16)	7 (30)	.31
Atrial fibrillation	21 (84)	13 (57)	.057
Congestive heart failure	5 (20)	4 (17)	1
Previous stroke	6 (24)	6 (26)	1
Smoking	9 (36)	9 (41)	.77
Past medication at stroke onset (No.) (%)			
Antiplatelet therapy	7 (28)	8 (35)	.76
Anticoagulant therapy	5 (20)	4 (17)	1
Antihypertensive therapy	13 (52)	10 (44)	.58
Statin therapy	2 (8)	4 (17)	.41
Stroke etiology (No.) (%)			
Cardioembolism	19 (76)	11 (48)	.07
Atherosclerosis	4 (16)	8 (35)	.19
Other or undetermined	2 (8)	4 (17)	.41
Severity of stroke at arrival (median) (IQR)			
Initial GCS	13 (11–14)	12 (10–14)	.62
Initial DWI volume (mL)	21.6 (13.8–42.5)	22.9 (10.6–41.1)	.63
DWI ASPECTS at arrival	8 (7–9)	8 (6–8)	.72
Initial NIHSS score	17 (14–24)	16 (11–21)	.35
Duration between 2 MRI scans (days)	7 (5–9)	6 (3–8)	.2
Neurologic and radiologic outcome after rtPA (median) (IQR)			
24-hr NIHSS	7 (2–12)	11 (6–17)	.022 ^b
7-day NIHSS	4 (1–8)	8 (3–14)	.008 ^c
Hemorrhagic transformation	6 (24)	10 (43)	.22
Successful recanalization	23 (92)	8 (35)	<.001 ^d
Follow-up CT ASPECTS	8 (6.5–9)	6 (4–8)	.017 ^b
M1 to M6 area in ASPECTS	5 (4–6)	3 (2–6)	.021 ^b
C, I, L, IC area in ASPECTS	3 (2.5–4)	3 (2–3)	.12
mRS 0–1 at 3 mo (No.) (%)	16 (64)	8 (35)	.043 ^b

Note:—GCS indicates Glasgow Coma Scale; C, caudate nucleus; I, insular cortex; L, lenticular nucleus; IL, internal capsule.

^a For continuous variables, the median and *P* values (Mann-Whitney *U* test) are shown. The resulting proportions and the *P* values (Fisher exact test with Yates correction, when appropriate) are shown.

^b *P* < .05.

^c *P* < .01.

^d *P* < .001 was considered significant.

the group with ENI than in the group without ENI (15 of 22 patients versus 9 of 26 patients, *P* = .042).

Univariate analysis revealed that the history of atrial fibrillation and the development of collaterals at arrival were significantly associated with ENI (Table 3). Multivariate logistic regression analysis was performed to further evaluate the independent predictors of ENI after adjusting for age, history of atrial fibrillation, NIHSS score at arrival, and time to rtPA administration as covariates. The development of collaterals at arrival (OR, 4.82; 95% CI, 1.34–19.98; *P* = .015) and history of atrial fibrillation (OR, 5.32; 95% CI, 1.16–32.1; *P* = .031) were independently associated with ENI after adjustment for other variables (Table 3). Univariate and multivariate analyses were performed to evaluate the prognostic factors for long-term functional outcome. In a univariate analysis, initial DWI volume and reversion of collaterals were predictive of long-term functional outcome. Multivariate logistic regression analysis was performed to further evaluate independent predictors of clinical outcome. Reversion of collaterals

(OR, 5.07; 95% CI, 1.38–22.09; *P* = .013) was independently associated with favorable outcome, after adjustment for other variables (On-line Table).

DISCUSSION

We showed that the development of leptomeningeal collaterals, assessed by PCA laterality on MRA and HV score on FLAIR, was significantly associated with ENI in patients with proximal MCA occlusion treated with IV rtPA. Because the principal purpose of thrombolytic therapy is to open obstructed vessels and to reperfuse the ischemic penumbra,²³ early recanalization after IV rtPA should contribute to ENI. However, 37%–46% of patients with recanalization performed within 2 hours after IV rtPA, as assessed by transcranial Doppler,⁹ or after endovascular treatment¹⁰ showed no immediate clinical improvement or may have even worsened. In our study, the positive association observed between the development of collateral signs on MR imaging and ENI indicates that leptomeningeal collateral development may be an important factor for achieving ENI after recanalization therapy.

Several factors may explain why well-developed collaterals lead to ENI. First, the leptomeningeal collateral circulation plays an important role in preserving cerebral blood flow in the territory of the occluded artery.^{24,25} Well-developed leptomeningeal collateral circulation is associated with maintaining the perfusion of penumbral regions, as evaluated by using CT perfusion or MR imaging perfusion methods,^{26,27} resulting

in the protection of distal brain tissues. Consistently, our recent study showed that patients with PCA laterality had a significantly smaller infarct volume, particularly in the cortical region, on follow-up CT than those without this sign who were treated with rtPA after acute MCA occlusion.¹⁶ Second, retrograde collateral filling may allow the access of thrombolytic agents to distal clots,²⁸ which may minimize the ischemic damage to the structure of the distal vessels themselves. Because cerebral arteries and capillaries in the brain are impaired early and in a progressive fashion after focal cerebral ischemia,^{29,30} the degree of ischemic vascular injury can be minimized by collateral blood supply to vessels and brain tissue located within the territory of the occluded artery. These possible effects of collateral circulation may protect brain tissue and/or vessel structures from ischemic damage until MCA recanalization.

Another important finding of our study was that the collateral signs observed on MR imaging were diminished in almost half of

Table 2: Comparison of the presence and absence of early neurologic improvement after IV rtPA in patients with proximal middle cerebral artery occlusion^a

	Early Neurologic Improvement		
	Yes (n = 22)	No (n = 26)	P Value
Age (yr) (median) (IQR)	78.5 (74–81)	78.5 (68–84)	.92
Male sex (No.) (%)	10 (45)	16 (62)	.38
mRS 0–1 before stroke (No.) (%)	22 (100)	25 (96)	1
NIHSS score at arrival (median) (mean)	17.9 ± 8.1	16.0 ± 5.7	.29
Systolic blood pressure (mean)	161.3 ± 29.6	155.0 ± 30.8	.91
Diastolic blood pressure (mean)	88.5 ± 26.1	78.3 ± 21.9	.19
Temperature (°C) (mean)	36.3 ± 0.4	36.2 ± 0.7	.75
Cardiovascular risk factors (No.) (%)			
Hypertension	14 (64)	14 (54)	.57
Diabetes mellitus	7 (27)	4 (15)	.48
Hyperlipidemia	5 (23)	6 (23)	1
Atrial fibrillation	19 (86)	15 (58)	.054
Congestive heart failure	4 (18)	5 (19)	1
Previous stroke	5 (23)	7 (27)	1
Smoking	6 (27)	12 (48)	.23
Past medication at stroke onset (No.) (%)			
Antiplatelet therapy	8 (36)	7 (27)	.54
Anticoagulant therapy	4 (18)	5 (19)	1
Antihypertensive therapy	14 (64)	9 (35)	.08
Statin therapy	2 (9)	4 (15)	.67
Stroke etiology (No.) (%)			
Cardioembolism	17 (77)	13 (50)	.074
Atherosclerosis	4 (18)	8 (31)	.5
Other or undetermined	1 (5)	5 (19)	.2
Imaging analysis			
Initial DWI volume (mL) (median) (IQR)	19.8 (11.5–42.3)	22.7 (13.9–41.2)	.26
DWI ASPECTS at arrival (median) (IQR)	8 (6.75–9)	8 (6.75–8)	.33
MCA MI occlusion (No.) (%)	18 (82)	17 (65)	.33
Development of collaterals at arrival (No.) (%) ^c	15 (68)	9 (35)	.042 ^b
Stroke outcome			
Follow-up CT ASPECTS (median) (IQR)	8 (6–9.25)	6 (4.75–8)	.004 ^d
mRS 0–1 at 3 mo (No.) (%)	16 (73)	8 (31)	.008 ^d

^a For continuous variables, the median and *P* values (Mann-Whitney *U* test) are shown. The resulting proportions and the *P* values (Fisher exact test with Yates correction, when appropriate) are shown.

^b *P* < .05.

^c The development of collaterals was defined as positive in the presence of PCA laterality and an HV score of ≥5 on initial MRI.

^d *P* < .01 was considered significant.

Table 3: Univariate analyses and multivariate logistic regression analysis for the association of early neurologic improvement after IV rtPA in patients with proximal middle cerebral artery occlusion

	Crude OR		Adjusted OR	
	(95% CI)	<i>P</i> Value	(95% CI)	<i>P</i> Value
Age (yr)	0.99 (0.95–1.06)	.91	1.00 (0.94–1.06)	.95
Male sex	0.52 (0.16–1.63)	.26		
History of atrial fibrillation	4.64 (1.20–23.36)	.025 ^a	5.32 (1.16–32.1)	.031 ^a
NIHSS score at arrival	1.04 (0.88–1.04)	.34	1.02 (0.89–1.09)	.72
DWI ASPECTS at arrival	1.16 (0.80–1.73)	.44		
Time to rtPA administration	0.99 (0.97–1.02)	.49	1.00 (0.97–1.03)	.84
Development of collaterals at arrival ^b	4.0 (1.25–14.27)	.019 ^a	4.82 (1.34–19.98)	.015 ^a

^a *P* < .05 was considered significant.

^b The development of collaterals was defined as positive in the presence of PCA laterality positivity and an HV score of ≥5 on initial MRI.

^c Adjusted for age, history of atrial fibrillation, NIHSS score at arrival, and time to rtPA administration.

patients with well-developed collateral signs before rtPA administration; we found a significant association between the reversion of collateral signs and long-term functional outcome. A previous study reported that HVs were observed on FLAIR in all patients with MCA occlusion within 24 hours of stroke onset and the percentage of HV-positive patients subsequently decreased in a time-dependent manner, though HVs were still observed in some cases

of successful recanalization on follow-up MR imaging. Thus, according to these findings, collateral reversion may indicate improvement in cerebral hemodynamic status. Indeed, the extent of infarction in the cortical regions (M1–M6 in ASPECTS; total score, 6) was significantly smaller in patients with collateral reversion than in those without it (median ASPECTS, 5 versus 3; *P* = .021), but no significant differences were observed in other

for up to 2 weeks.³¹ However, the mechanism underlying these changes in collateral signs has not been well-documented. In the course of ischemic stroke, collateral blood flow should play an important role in providing blood to cerebral tissues at risk of infarction in the territory of the occluded artery.^{24–27} Therefore, a failure or reduction of collateral circulation may cause infarct growth in the occluded territory. In a recent study that evaluated the temporal profile of collateral flow by using modified perfusion MR imaging in patients with acute ischemic stroke, compared with initial MR imaging, the leptomeningeal collateral flow reduced 3–5 days after stroke onset in approximately one-third of patients without spontaneous recanalization.³² In the no-recanalization group, the decrease in collateral flow was associated with infarct growth within 5 days.³² Therefore, maintaining collateral flow may help prevent infarct growth during the acute phase of ischemic stroke if recanalization is not achieved.

We observed reversion of collaterals after thrombolysis in approximately 50% of patients with initially well-developed collaterals and significant association with favorable long-term functional outcome. Because early collateral development via leptomeningeal anastomoses after MCA occlusion is induced by a pressure gradient between the anterior cerebral artery or PCA territory and a territory distal to the MCA occlusion site,^{24,25} leptomeningeal collaterals may decrease or disappear after the occluded MCA reopens at an optimal timing because of normalization of the pressure gradient. Several studies in patients with acute internal carotid or MCA occlusion reported that HV collateral signs on initial FLAIR MR imaging disappeared within several days after early spontaneous recanalization³¹ or successful vascularization via endovascular therapy.¹⁹ In this study, reversion of collaterals was significantly associated with a high rate

ASPECTS regions, such as the insular cortex, basal ganglia, and internal capsule (median ASPECTS, 3 versus 3, $P = .12$) (Table 1). Because leptomeningeal collaterals, which are upstream of the penetrating cortical vessels, play a major role in compensating for low blood flow in the cerebral cortex after ischemic stroke, collateral reversion may exhibit the recovery of effective “cortical” blood flow after the optimal timing of recanalization, contributing to prevention of infarct extent.

This study has several limitations. First, it was retrospective and limited by a small sample size and a nonrandomized population; and the timing for initial and follow-up MR imaging was heterogeneous. The timing of the development and reversion of collateral circulation is not well-elucidated. The timing and duration of MR imaging may influence the existence of collateral signs, though there was no significant association between the timing of the MR imaging scan and the collateral development or reversion in our study. Second, MR imaging acquisitions before and after rtPA therapy during acute ischemic stroke may be challenging in a clinical setting. The greatest benefit of rtPA therapy comes from earlier treatment, and MR imaging screening before rtPA may cause a time delay. Generalizing our results to all hospitals may be a problem because the delay in MR imaging screening might be greater in centers less specialized for emergency stroke MR imaging.

CONCLUSIONS

Recently, the Multicenter Randomized Clinical Trial of Endovascular Treatment for Acute Ischemic Stroke in the Netherlands (MR CLEAN) study reported that endovascular therapy within 6 hours of stroke onset in addition to rtPA improved functional independence at 3 months.³³ Leptomeningeal collaterals contribute to ENI after acute ischemic stroke, and the development of collateral signs on MR imaging can help identify patients more likely to show ENI in the setting of thrombolysis and help us select patients for additional endovascular therapy. Considering the results, reversion of collaterals is associated with more favorable outcome in patients with acute proximal MCA occlusion after administration of rtPA, which may be due to improved hemodynamic status. Reversion of collaterals may help us to examine the risk of recurrent stroke or infarct extent, to achieve an appropriate prevention after proximal cerebral artery occlusion.

ACKNOWLEDGMENTS

The authors would like to thank Enago (www.enago.jp) for the English language review.

Disclosures: Tomoyuki Kamata—UNRELATED: Payment for Lectures (including service on Speakers Bureaus); Otsuka Pharmaceutical, Eisai, AstraZeneca, Ono Pharmaceutical, Novartis Pharma, Bayer, Shionogi.

REFERENCES

- National Institute of Neurological Disorders and Stroke rt-PA Stroke Study Group. **Tissue plasminogen activator for acute ischemic stroke.** *N Engl J Med* 1995;333:1581–87
- Hacke W, Kaste M, Fieschi C, et al; Second European-Australasian Acute Stroke Study Investigators. **Randomised double-blind placebo-controlled trial of thrombolytic therapy with intravenous alteplase in acute ischaemic stroke (ECASS II).** *Lancet* 1998;352:1245–51
- Felberg RA, Okon NJ, El-Mitwalli A, et al. **Early dramatic recovery during intravenous tissue plasminogen activator infusion: clinical pattern and outcome in acute middle cerebral artery stroke.** *Stroke* 2002;33:1301–07
- Brown DL, Johnston KC, Wagner DP, et al. **Predicting major neurological improvement with intravenous recombinant tissue plasminogen activator treatment of stroke.** *Stroke* 2004;35:147–50
- Saposnik G, Di Legge S, Webster F, et al. **Predictors of major neurologic improvement after thrombolysis in acute stroke.** *Neurology* 2005;65:1169–74
- Blinzler C, Breuer L, Huttner HB, et al. **Characteristics and outcome of patients with early complete neurological recovery after thrombolysis for acute ischemic stroke.** *Cerebrovasc Dis* 2011;31:185–90
- Machumpurath B, Davis SM, Yan B. **Rapid neurological recovery after intravenous tissue plasminogen activator in stroke: prognostic factors and outcome.** *Cerebrovasc Dis* 2011;31:278–83
- Muresan IP, Favrole P, Levy P, et al. **Very early neurologic improvement after intravenous thrombolysis.** *Arch Neurol* 2010;67:1323–28
- Alexandrov AV, Hall CE, Labiche LA, et al. **Ischemic stunning of the brain: early recanalization without immediate clinical improvement in acute ischemic stroke.** *Stroke* 2004;35:449–52
- Penumbra Pivotal Stroke Trial Investigators. **The Penumbra Pivotal Stroke Trial: safety and effectiveness of a new generation of mechanical devices for clot removal in intracranial large vessel occlusive disease.** *Stroke* 2009;40:2761–68
- Schellinger PD, Chalela JA, Kang DW, et al. **Diagnostic and prognostic value of early MR imaging vessel signs in hyperacute stroke patients imaged <3 hours and treated with recombinant tissue plasminogen activator.** *AJNR Am J Neuroradiol* 2005;26:618–24
- Lee KY, Latour LL, Luby M, et al. **Distal hyperintense vessels on FLAIR: an MRI marker for collateral circulation in acute stroke?** *Neurology* 2009;72:1134–39
- Liu W, Xu G, Yue X, et al. **Hyperintense vessels on FLAIR: a useful non-invasive method for assessing intracerebral collaterals.** *Eur J Radiol* 2011;80:786–91
- Olindo S, Chausson N, Joux J, et al. **Fluid-attenuated inversion recovery vascular hyperintensity: an early predictor of clinical outcome in proximal middle cerebral artery occlusion.** *Arch Neurol* 2012;69:1462–68
- Uemura A, O’uchi T, Kikuchi Y, et al. **Prominent laterality of the posterior cerebral artery at three-dimensional time-of-flight MR angiography in M1-segment middle cerebral artery occlusion.** *AJNR Am J Neuroradiol* 2004;25:88–91
- Ichijo M, Miki K, Ishibashi S, et al. **Posterior cerebral artery laterality on magnetic resonance angiography predicts long-term functional outcome in middle cerebral artery occlusion.** *Stroke* 2013;44:512–15
- Bang OY, Saver JL, Kim SJ, et al. **Collateral flow predicts response to endovascular therapy for acute ischemic stroke.** *Stroke* 2011;42:693–99
- Ribo M, Flores A, Rubiera M, et al. **Extending the time window for endovascular procedures according to collateral pial circulation.** *Stroke* 2011;42:3465–69
- Liu W, Yin Q, Yao L, et al. **Decreased hyperintense vessels on FLAIR images after endovascular recanalization of symptomatic internal carotid artery occlusion.** *Eur J Radiol* 2012;81:1595–600
- Shinohara Y, Yamaguchi T. **Outline of the Japanese Guidelines for the Management of Stroke 2004 and subsequent revision.** *Int J Stroke* 2008;3:55–62
- TIMI Study Group. **The Thrombolysis in Myocardial Infarction (TIMI) trial—phase I findings.** *N Engl J Med* 1985;312:932–36
- Barber PA, Demchuk AM, Zhang J, et al; ASPECTS Study Group. **Validity and reliability of a quantitative computed tomography score in predicting outcome of hyperacute stroke before thrombolytic therapy.** *Lancet* 2000;355:1670–74
- De Silva DA, Fink JN, Christensen S, et al; Echoplanar Imaging Thrombolytic Evaluation Trial (EPITHET) Investigators. **Assessing reperfusion and recanalization as markers of clinical outcomes af-**

- ter intravenous thrombolysis in the Echoplanar Imaging Thrombolytic Evaluation Trial (EPITHET).** *Stroke* 2009;40:2872–74
24. Shuaib A, Butcher K, Mohammad AA, et al. **Collateral blood vessels in acute ischaemic stroke: a potential therapeutic target.** *Lancet Neurol* 2011;10:909–21
 25. Liebeskind DS. **Collateral circulation.** *Stroke* 2003;34:2279–84
 26. Miteff F, Levi CR, Bateman GA, et al. **The independent predictive utility of computed tomography angiographic collateral status in acute ischaemic stroke.** *Brain* 2009;132:2231–38
 27. Bang OY, Saver JL, Buck BH, et al; UCLA Collateral Investigators. **Impact of collateral flow on tissue fate in acute ischaemic stroke.** *J Neurol Neurosurg Psychiatry* 2008;79:625–29
 28. Caplan LR, Hennerici M. **Impaired clearance of emboli (washout) is an important link between hypoperfusion, embolism, and ischemic stroke.** *Arch Neurol* 1998;55:1475–82
 29. Cipolla MJ, McCall AL, Lessov N, et al. **Reperfusion decreases myogenic reactivity and alters middle cerebral artery function after focal cerebral ischemia in rats.** *Stroke* 1997;28:176–80
 30. del Zoppo GJ, Mabuchi T. **Cerebral microvessel responses to focal ischemia.** *J Cereb Blood Flow Metab* 2003;23:879–94
 31. Maeda M, Koshimoto Y, Uematsu H, et al. **Time course of arterial hyperintensity with fast fluid-attenuated inversion-recovery imaging in acute and subacute middle cerebral arterial infarction.** *J Magn Reson Imaging* 2001;13:987–90
 32. Campbell BC, Christensen S, Tress BM, et al; EPITHET Investigators. **Failure of collateral blood flow is associated with infarct growth in ischemic stroke.** *J Cereb Blood Flow Metab* 2013;33:1168–72
 33. Berkhemer OA, Fransen PS, Beumer D, et al; MR CLEAN Investigators. **A randomized trial of intraarterial treatment for acute ischemic stroke.** *N Engl J Med* 2015;372:11–20

Independent Poor Prognostic Factors for True Progression after Radiation Therapy and Concomitant Temozolomide in Patients with Glioblastoma: Subependymal Enhancement and Low ADC Value

R.-E. Yoo, S.H. Choi, T.M. Kim, S.-H. Lee, C.-K. Park, S.-H. Park, I.H. Kim, T.J. Yun, J.-H. Kim, and C.H. Sohn



ABSTRACT

BACKGROUND AND PURPOSE: Subependymal enhancement and DWI have been reported to be useful MR imaging markers for identifying true progression. Our aim was to determine whether the subependymal enhancement pattern and ADC can differentiate true progression from pseudoprogression in patients with glioblastoma multiforme treated with concurrent chemoradiotherapy by using temozolomide.

MATERIALS AND METHODS: Forty-two patients with glioblastoma multiforme with newly developed or enlarged enhancing lesions on the first follow-up MR images obtained within 2 months of concurrent chemoradiotherapy completion were included. Subependymal enhancement was analyzed for the presence, location, and pattern (local or distant relative to enhancing lesions). The mean ADC value and the fifth percentile of the cumulative ADC histogram were determined. A multiple logistic regression analysis was performed to identify independent factors associated with true progression.

RESULTS: Distant subependymal enhancement (ie, extending >1 cm or isolated from the enhancing lesion) was significantly more common in true progression ($n = 24$) than in pseudoprogression ($n = 18$) ($P = .042$). The fifth percentile of the cumulative ADC histogram was significantly lower in true progression than in pseudoprogression ($P = .014$). Both the distant subependymal enhancement and the fifth percentile of the cumulative ADC histogram were independent factors associated with true progression ($P = .041$ and $P = .033$, respectively). Sensitivity and specificity for the diagnosis of true progression were 83% and 67%, respectively, by using both factors.

CONCLUSIONS: Both the distant subependymal enhancement and the fifth percentile of the cumulative ADC histogram were significant independent factors predictive of true progression.

ABBREVIATIONS: CCRT = concurrent chemoradiotherapy; GBM = glioblastoma multiforme; TMZ = temozolomide; RANO = Response Assessment in Neuro-Oncology

Glioblastoma multiforme (GBM) is the most common form of malignant primary brain tumor in adults,¹ which is notorious for its intrinsic aggressiveness and a dismal prognosis.^{2,3} The

current standard treatment for GBM is maximal safe tumor resection followed by radiation therapy with concurrent temozolomide (TMZ) and adjuvant TMZ.⁴

Recently, the criteria for assessing therapeutic responses in high-grade gliomas have been updated by the Response Assessment in Neuro-Oncology (RANO) Working Group to address the limitations of the previous guideline.⁵ For instance, contrast enhancement, which has been regarded as a surrogate marker for tumor progression, has been reassessed as a nonspecific finding merely reflecting the passage of contrast material across a disrupted blood-tumor barrier.⁶⁻¹¹ In particular, radiologists and clinicians have increasingly recognized the occurrence of progressive MR imaging lesions immediately after completion of concurrent chemoradiotherapy (CCRT) with TMZ, which spontaneously improved without further treatment other than the adjuvant TMZ.¹²⁻¹⁴ The treatment-related reaction is termed pseudoprogression and has received attention as a potential pitfall in the response evaluation. At present, owing to the lack of established findings in conventional contrast-enhanced MR imaging for the differential diagnosis of true

Received December 20, 2014; accepted after revision March 2, 2015.

From the Departments of Radiology (R.-E.Y., S.H.C., T.J.Y., J.-H.K., C.H.S) and Pathology (S.-H.P.); Departments of Internal Medicine (S.-H.L., T.M.K.) and Radiation Oncology (C.H.S., I.H.K.), Cancer Research Institute; and Department of Neurosurgery (C.-K.P.), Biomedical Research Institute; Seoul National University College of Medicine, Seoul, Korea; and Center for Nanoparticle Research (R.-E.Y., S.H.C.), Institute for Basic Science and School of Chemical and Biological Engineering (R.-E.Y., S.H.C.), Seoul National University, Seoul, Korea.

This study was supported by a grant from the Korea Healthcare Technology R&D Projects, Ministry for Health, Welfare and Family Affairs (HI13C0015), and the Research Center Program of Institute for Basic Science in Korea.

Please address correspondence to Seung Hong Choi, MD, PhD, Department of Radiology, Seoul National University College of Medicine, 28, Yongon-dong, Chongno-gu, 110-744, Seoul, Korea; Center for Nanoparticle Research, Institute for Basic Science and School of Chemical and Biological Engineering, Seoul National University, 1 Gwanak-ro, Gwanak-gu, 151-742, Seoul, Korea; e-mail: verocay@snuh.org

 Indicates open access to non-subscribers at www.ajnr.org

 Indicates article with supplemental on-line photo.

<http://dx.doi.org/10.3174/ajnr.A4401>

progression from pseudoprogession,^{9,10} RANO stresses that the diagnosis of true progression can be made within the first 12 weeks after completion of radiation therapy only if most of the new enhancement is located outside the radiation field or if there is pathologic confirmation of progressive disease.⁵

During the past few decades, there has been extensive effort to identify imaging biomarkers for tumor progression. Among the many parameters derived from advanced MR imaging techniques, DWI has been consistently reported to be helpful in differentiating tumor progression from treatment-related changes or necrosis.¹⁵⁻²² Meanwhile, most previous studies pertaining to the role of conventional MR imaging have not shown promising results.^{9,23} Nevertheless, a recent study focusing on the conventional MR imaging findings has proposed subependymal enhancement as a useful MR imaging marker for differentiating true progression from pseudoprogession.²⁴ To our knowledge, however, no previous studies have conducted in-depth analysis of the subependymal enhancement, and its potential as an independent predictor for true progression remains elusive.

The purpose of the present study was to determine whether the subependymal enhancement pattern and ADC can differentiate true progression from pseudoprogession in patients with GBM treated with radiation therapy and concomitant TMZ.

MATERIALS AND METHODS

This retrospective study was approved by our institutional review board, and informed consent was waived.

Patient Selection

One hundred thirty-two patients with newly diagnosed GBM, who had undergone surgical resection or stereotactic biopsy at our institution between June 2008 and March 2013 were selected from our radiology report data base. The inclusion criteria were patients with the following: 1) histopathologic diagnosis of GBM according to the World Health Organization criteria; 2) CCRT with TMZ and 6 cycles of adjuvant TMZ performed after surgical resection or biopsy; 3) baseline contrast-enhanced MR imaging performed within 24–48 hours after surgery before CCRT with TMZ; 4) the first follow-up 3T MR imaging including DWI ($b=1000 \text{ s/mm}^2$) performed within 2 months (mean, 28 days; range, 12–62 days) after the end of CCRT; 5) newly developed or enlarged measurable contrast-enhancing lesions inside the radiation field on the first follow-up MR images; and 6) follow-up contrast-enhanced MR imaging after 6 cycles of adjuvant TMZ to confirm true progression or pseudoprogession. The measurable contrast-enhancing lesions were defined as bidimensional contrast-enhancing lesions with 2 perpendicular diameters of at least 10 mm.⁵ We excluded 88 patients for the following reasons: 1) poor quality of the MR images, 2) no newly visible enhancing lesions on the first follow-up MR images, 3) definite disease progression according to the RANO criteria, and 4) the presence of subependymal enhancement on the baseline MR images.⁵ Two additional patients were excluded because of follow-up loss in one and a switch to bevacizumab in the other (Fig 1).

Therefore, 42 patients (27 men, 15 women; mean age, 56 years; age range, 28–80 years) were included in this study. After adjuvant TMZ, true progression and pseudoprogession were con-

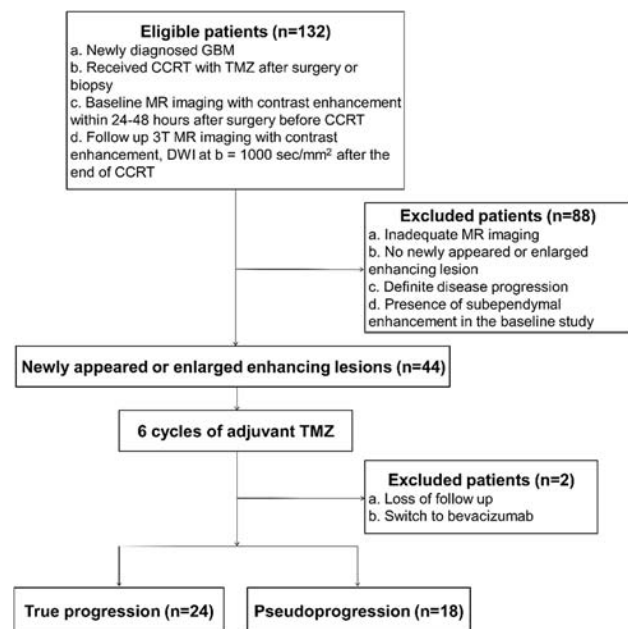


FIG 1. Flow diagram of patient selection, with inclusion and exclusion criteria.

firmed in 24 and 18 patients, respectively, by our neuro-oncology team (consisting of radiologists, neurosurgeons, neuro-oncologists, and radiation oncologists) according to the RANO criteria (Fig 1).⁵ Clinical characteristics of the patients, including age, sex, Karnofsky performance score (at the time of the first follow-up MR imaging), methylation status of O6-methylguanine DNA methyltransferase promoter of the tumor, surgical method, and radiation dose of the CCRT, were documented.

Image Acquisition

For all cases, the first follow-up MR imaging studies after the completion of CCRT with TMZ were performed with 1 of two 3T MR imaging scanners (Signa Excite; GE Healthcare, Milwaukee, Wisconsin [true progression, $n = 6$; pseudoprogession, $n = 3$]; Magnetom Verio; Siemens, Erlangen, Germany [true progression, $n = 18$; pseudoprogession, $n = 15$]) with an 8-channel head coil.

The imaging protocol included 3D magnetization-prepared rapid acquisition of gradient echo, axial TSE T2WI, axial FLAIR imaging, and DWI. Echo-planar DWI was performed in the axial plane before contrast material injection. Diffusion-weighted images were acquired in 3 orthogonal directions and combined into a trace image. By using these data, we calculated ADC maps at b -values of 0 and 1000 s/mm^2 on a voxel-by-voxel basis with software incorporated into the MR imaging unit. Axial spin-echo T1WI was repeated after intravenous administration of a single dose (0.1 mmol per kilogram of body weight) of gadobutrol (Gadovist; Bayer Schering Pharma, Berlin, Germany). A standard dose of 0.1 mmol/kg body weight of a gadolinium-based contrast agent (Gadovist) was injected intravenously at a rate of 5 mL/s, followed by a 20-mL bolus of saline at a rate of 5 mL/s by using a power injector (Optistar; Mallinckrodt, St Louis, Missouri). A fat-suppression pulse was added to the axial T1WI after administration of the contrast agent. Specific imaging parameters for the sequences are provided in Table 1.

Table 1: MR imaging parameters

Parameters	3D MPRAGE	Axial TSE T2WI	FLAIR	DWI
TR (ms)	1500	4500–5160	9000–9902	6900–10,000
TE (ms)	1.9	91–106	97–163	55–67
T1 (ms)	900	NA	2500	NA
Echo-train length	1	16–19	0–11	1
Flip angle (degree)	9	90–130	90–130	90
Section thickness (mm)	1	5	5	3–5
Intersection gap (mm)	0	1	1	0.9–1
FOV (mm)	250 × 250	199–220 × 220	199–220 × 220	240 × 240
Matrix	256 × 256	448–640 × 256–290	320–384 × 192–209	160 × 160
No. of signals acquired	1	0–2	0–1	0–3
No. of sections	192	25	25	50–70

Note:—NA indicates not available.

Qualitative Image Analysis for Subependymal Enhancement

Two neuroradiologists (S.H.C. and J.-H.K. with 7 and 15 years of experience, respectively, in the interpretation of MR imaging studies), who were blinded as to whether the patients had true progression or pseudoprogession, analyzed the first follow-up MR images together and reached a consensus reading for subependymal enhancement in terms of the following: 1) the presence or absence, 2) location, and 3) pattern of enhancement. Regarding the pattern, the subependymal enhancement was categorized into 1 of the following, according to the positional relationship between the subependymal enhancement and an enhancing lesion: 1) type I: enhancement at the ependymal lining abutting the newly developed or enlarged measurable contrast-enhancing lesion; 2) type II: enhancement extending along the ventricular margin with the distance of extension (ie, distance from the margin of the enhancing lesion to the farthest end of the subependymal enhancement) measuring ≤ 1 cm; 3) type III: enhancement extending along the ventricular margin with the distance of extension measuring > 1 cm; and 4) type IV: enhancement at the ependymal lining isolated from the enhancing lesion. Type I and II patterns were classified as local, whereas type III and IV patterns were classified as distant (On-line Fig 1).

Quantitative Image Analysis for ADC Maps

The MR imaging data for ADC maps were digitally transferred from the PACS workstation to a personal computer. ROIs that contained the entire measurable contrast-enhancing lesions, excluding the areas of necrosis or cysts, were manually drawn in each section of the ADC maps by 1 neuroradiologist (R.-E.Y. with 5 years of experience in the interpretation of MR imaging studies) by using ImageJ software (National Institutes of Health, Bethesda, Maryland). The data acquired from each section were summated to derive voxel-by-voxel ADC values for the entire contrast-enhancing lesions by using software developed in house.

Subsequently, the mean ADC values were calculated. For further quantitative analysis, the fifth percentiles (the point at which 5% of the voxel values that form the cumulative ADC histogram are found to the left) were calculated on the basis of the previous finding that the fifth percentile of the cumulative ADC histogram was a significant predictor for the differential diagnosis between true progression and pseudoprogession.^{17,21}

Statistical Analysis

All statistical analyses were performed by using the statistical software MedCalc for Windows, Version 11.1.1.0 (MedCalc Software, Mariakerke, Belgium). The data for each parameter were assessed for normality with the Kolmogorov-Smirnov test. In all tests, P values $< .05$ were considered statistically significant.

Clinical characteristics of the patients in the 2 groups were compared by using either the Fisher exact test or the unpaired Student t test. The Fisher exact test was performed to assess whether the incidence of the subependymal enhancement significantly differed between the true progression and pseudoprogession groups. The unpaired Student t test was used to compare the mean ADC values and the fifth percentiles of the cumulative ADC histograms between the 2 groups. Variables showing a univariate association with true progression (at $P < .10$) were included in a multivariable stepwise logistic regression analysis to identify independent predictors of true progression.

Sensitivity and specificity of the imaging parameters for the diagnosis of true progression were calculated. To determine an optimal cutoff value that provided a balance between sensitivity and specificity, a receiver operating characteristic curve was constructed for the ADC values. In addition, a leave-one-out cross-validation method was used to test the effects of outliers.²⁵

RESULTS

Clinical Characteristics of the Patients

There was a significant difference in age between the true progression and pseudoprogession groups ($P = .002$). Other clinical characteristics did not significantly differ between the 2 groups (Table 2).

Qualitative Image Analysis for Subependymal Enhancement

Subependymal enhancement was significantly more common in the true progression group (19 of 24) than in the pseudoprogession group (8 of 18) ($P = .027$). Anatomic locations of the subependymal enhancement were as follows: unilateral lateral ventricle ($n = 25$), bilateral lateral ventricles ($n = 1$), and fourth ventricle ($n = 1$). With regard to the pattern, the incidence of distant subependymal enhancement was significantly higher in the true progression group than in the pseudoprogession group ($P = .042$), whereas that of local subependymal enhancement did not significantly differ between the 2 groups ($P > .99$) (Table 3 and Fig 2).

Quantitative Image Analysis for ADC Maps

The fifth percentile of the cumulative ADC histogram was significantly lower in the true progression group than in the pseudopro-

gression group ($895 \times 10^{-6} \text{ mm}^2/\text{s}$ versus $998 \times 10^{-6} \text{ mm}^2/\text{s}$, $P = .014$). In contrast, the mean ADC value was not significantly different between the 2 groups ($1247 \times 10^{-6} \text{ mm}^2/\text{s}$ versus $1310 \times 10^{-6} \text{ mm}^2/\text{s}$, $P = .298$) (Table 3).

Table 2. Clinical characteristics of the patients

Characteristic	True Progression (n = 24)	Pseudoprogession (n = 18)	P Value
Age (yr)	60.50 ± 11.58	48.22 ± 12.54	.002
Sex			.347
Male	17	10	
Female	7	8	
Karnofsky performance score			.371
<70	4	1	
≥70	20	17	
Surgery			.623
Biopsy	3	1	
Resection	21	17	
Radiation dose (Gy)	55.52 ± 8.17	57.83 ± 7.52	.376
Methylated MGMT promoter ^a			1.000
Negative	6	5	
Positive	15	13	

Note:—MGMT indicates O6-methylguanine DNA methyltransferase.

^a The promoter methylation status of MGMT, which was investigated by using the methylation-specific polymerase chain reaction technique, was documented whenever available.

Table 3: Qualitative and quantitative image analyses^a

	True Progression (n = 24)	Pseudoprogession (n = 18)	P Value
Subependymal enhancement	19 (79)	8 (44)	.027
Local	9 (38)	6 (33)	>.99
Type I	8 (33)	4 (22)	
Type II	1 (4)	2 (11)	
Distant	10 (42)	2 (11)	.042
Type III	5 (21)	0 (0)	
Type IV	5 (21)	2 (11)	
ADC ($\times 10^{-6} \text{ mm}^2/\text{s}$)			
Mean	1247 ± 197	1310 ± 182	.298
Fifth percentile	895 ± 136	998 ± 120	.014

^a Numbers in parentheses are percentages.

Multiple Logistic Regression Analysis for Independent Variables

The multiple logistic regression analysis revealed that age, the distant subependymal enhancement, and the fifth percentile of the cumulative ADC histogram were independent predictors of true progression (OR, 1.08; 95% CI, 1.01–1.17; $P = .026$ for the age; OR, 8.30; 95% CI, 1.09–63.16; $P = .041$ for the distant subependymal enhancement; and OR, 0.99; 95% CI, 0.98–1.00; $P = .033$ for the fifth percentile of the cumulative ADC histogram) (Fig 3).

Sensitivity and Specificity for the Diagnosis of True Progression with Imaging Parameters

Sensitivity and specificity for the diagnosis of true progression were 42% (95% CI, 24–61) and 89% (95% CI, 67–97), respectively, when considering only distant subependymal enhancement. Sensitivity and specificity were 67% (95% CI, 45–84) and 78% (95% CI, 52–94), respectively, when using only the optimal cutoff ADC value (fifth percentile of the cumulative ADC histogram) of $915 \times 10^{-6} \text{ mm}^2/\text{s}$.

The predictive equation was calculated with the 2 logistic regression parameters as

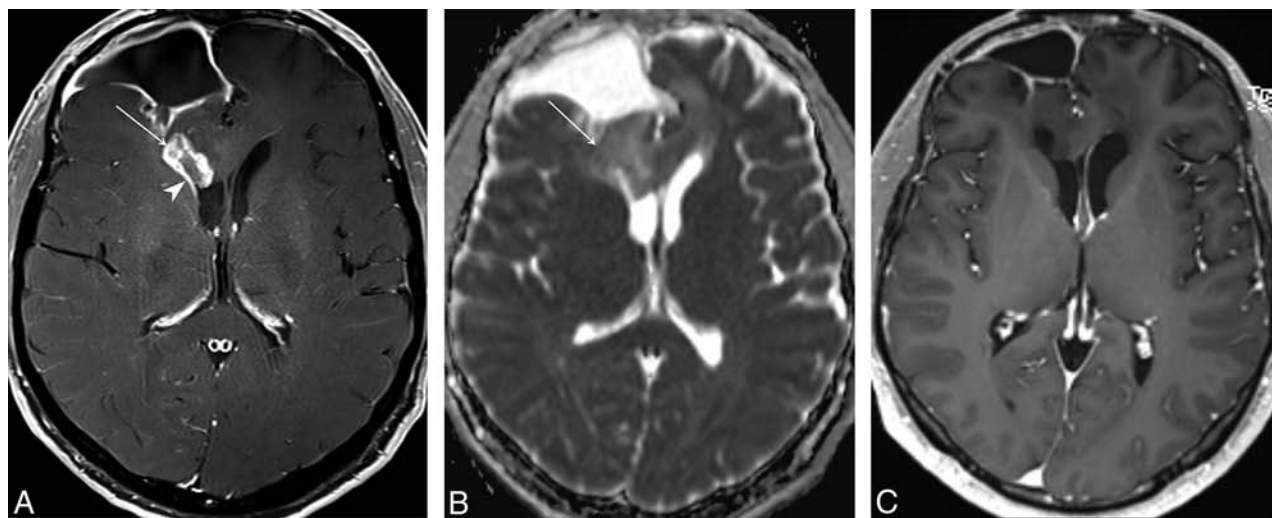


FIG 2. Pseudoprogession in a 40-year-old man with glioblastoma who had undergone surgical resection. A, Axial contrast-enhanced T1-weighted MR image obtained within 1 month after the end of concurrent chemotherapy and radiation therapy shows a newly developed enhancing lesion (arrow) in the right frontal periventricular white matter. The ventricular margin adjacent to the enhancing lesion (arrowhead) also shows linear enhancement (arrowhead), with the distance of extension measuring ≤ 1 cm. B, On the ADC map, a decrease in ADC value is not apparent at the lesion (arrow) (mean, $1264 \times 10^{-6} \text{ mm}^2/\text{s}$; fifth percentile, $1059 \times 10^{-6} \text{ mm}^2/\text{s}$). C, Follow-up MR image after a 6-month continuation of temozolomide reveals resolution of the enhancing lesion.

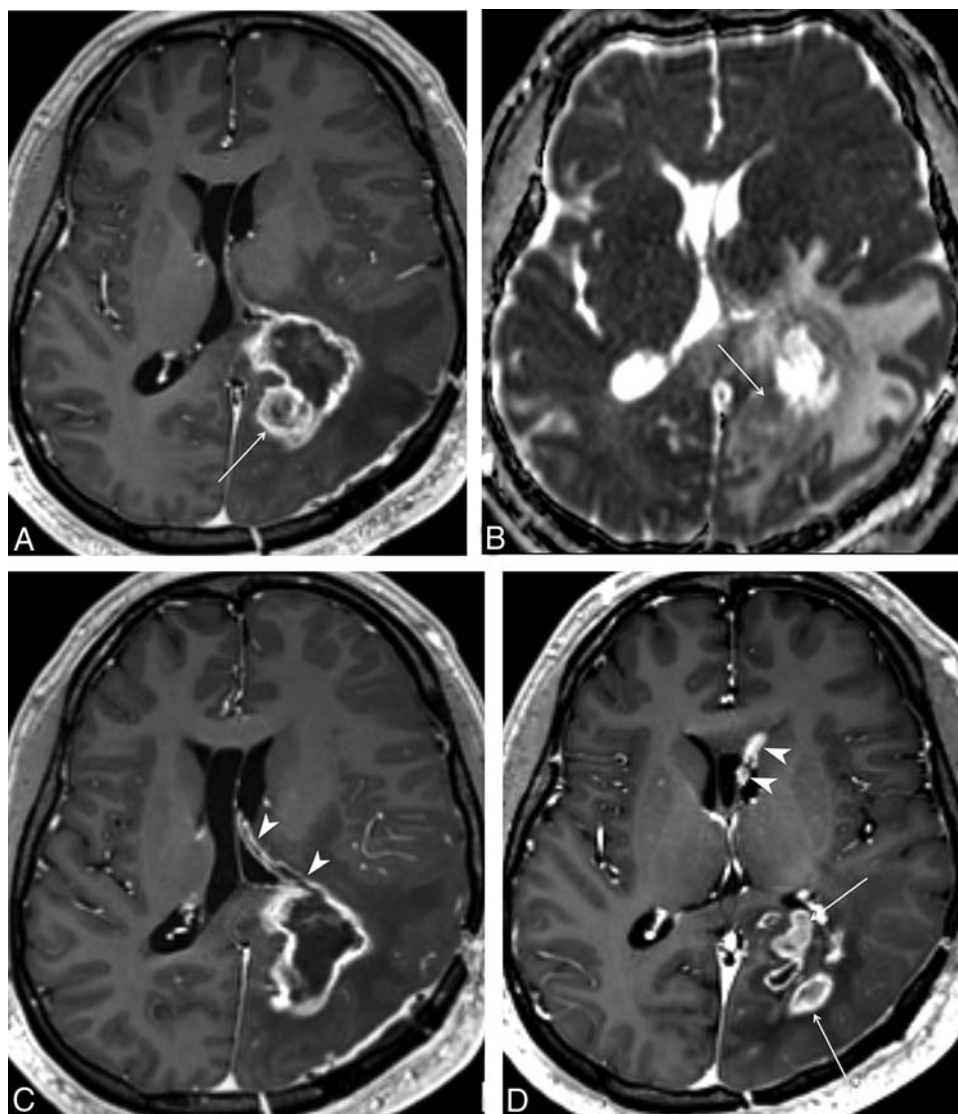


FIG 3. True progression in a 36-year-old man with glioblastoma who had undergone surgical resection. *A*, On the axial contrast-enhanced T1-weighted MR image obtained within 1 month after the end of concurrent chemotherapy and radiation therapy, a newly developed enhancing lesion (*arrow*) is noted in the left occipital lobe. *B*, On the ADC map, the ADC value is decreased in some portion of the lesion (*arrow*) (mean, $1292 \times 10^{-6} \text{ mm}^2/\text{s}$; fifth percentile, $991 \times 10^{-6} \text{ mm}^2/\text{s}$). *C*, Axial contrast-enhanced T1-weighted MR image at a higher level reveals linear enhancement (*arrowheads*) along the ventricular margin, with the distance of extension measuring $>1 \text{ cm}$. *D*, Follow-up MR image after a 6-month continuation of temozolomide demonstrates aggravation of both the left occipital lobe lesion (*arrows*) and subependymal enhancement (*arrowheads*) in the left lateral ventricle.

follows: $P = e^{\chi} / (1 + e^{\chi})$, where $\chi = -0.0085 \times (\text{fifth percentile of the cumulative ADC histogram}) + 2.2808 \times (\text{distant subependymal enhancement}) + 7.8108$. The cutoff point for the diagnosis of true progression was defined as a probability value $\geq .50$. The sensitivity, specificity, and accuracy of the equation were 83% (20 of 24), 67% (12 of 18), and 76% (32 of 42), respectively. Leave-one-out cross-validation revealed a sensitivity of 79% (19 of 24), a specificity of 61% (11 of 18), and an accuracy of 71% (30 of 42).

DISCUSSION

Our results demonstrated the value of using the subependymal enhancement pattern and DWI to differentiate true progression from pseudoprogession in patients with GBM treated with CCRT by using TMZ.

Along with the increasing recognition of pseudoprogession, there has been a growing interest in ADC values as surrogate markers for differentiating true progression from pseudoprogres-

sion.¹⁵⁻²² Previous studies found that the fifth percentile of the cumulative ADC histogram based on the entire newly developed or enlarged enhancing lesion could be used to accurately differentiate them.^{17,21} Specifically, Chu et al¹⁷ reported a sensitivity of 73% and a specificity of 73% for diagnosing true progression, by using a cutoff ADC value of $929 \times 10^{-6} \text{ mm}^2/\text{s}$. Our results showed that the fifth percentile value was significantly lower in the true progression group than in the pseudoprogession group ($P = .014$), while the mean value was not significantly different between the 2 groups—findings in keeping with those of the previous study. With a cutoff ADC value of $915 \times 10^{-6} \text{ mm}^2/\text{s}$, sensitivity and specificity for the diagnosis of true progression were 67% and 78%, respectively.

With the advent of various advanced MR imaging techniques, conventional MR imaging has been thought to have a

limited role in the differential diagnosis of true progression from pseudoprogression.^{9,23} Nonetheless, some authors have suggested that certain conventional MR imaging findings may be helpful for differentiating them. Mullins et al²³ reported that though individual enhancement patterns such as subependymal enhancement did not show a statistically significant difference between tumor recurrence and radiation necrosis, their combinations—specifically, corpus callosum involvement in conjunction with multiple enhancing lesions with or without crossing of the midline and subependymal spread—favored predominant glioma progression.

More recently, Young et al²⁴ investigated the potential utility of various conventional MR imaging signs in a larger patient population. The study, unlike that by Mullins et al,²³ included those with worsening (new or increased) enhancing lesions on the initial postradiotherapy MR imaging (usually 2–4 weeks after completion of radiotherapy) and found that the incidence of subependymal enhancement was significantly higher in the early progression group than in the pseudoprogression group ($P = .001$). In agreement with the previous findings, the present study found subependymal enhancement significantly more common in the true progression group than in the pseudoprogression group ($P = .027$). Subependymal spread of tumor, albeit less common than local progression, is a known pattern of glioma failure, with reported rates ranging from 0% to 24%.^{26,27} According to previous studies, even though the recurrence pattern of GBM after CCRT was predominantly central at first, distant recurrences, including subependymal spread, often developed during the patient's clinical course.^{28,29} It has been speculated that the infiltration of the ventricular margin may occur either by direct spread of tumor cells in the subependymal space or by deposits transferred by the CSF.³⁰

Unlike the study by Young et al,²⁴ we further analyzed the subependymal enhancement in terms of its pattern and found that only the distant subependymal enhancement was significantly more common in the true progression group than in the pseudoprogression group ($P = .042$). The occurrence of local subependymal enhancement in pseudoprogression may be attributed to treatment-related necrosis. The periventricular region is known to be supplied by long medullary arteries with no collateral vessels. It has been suggested that the relatively poor vascularity may predispose the periventricular region to radiation-induced vasculopathy.⁹ Furthermore, the periventricular region close to a newly developed contrast-enhancing lesion may be more prone to radiation necrosis because the radiation dose delivered to a specific region during intensity-modulated radiation therapy decreases with increasing distance from the center of the enhancing lesion.^{31,32} On the basis of the findings, we infer that the local subependymal enhancement is more likely to reflect radiation necrosis, compared with the distant subependymal enhancement.

Sensitivity and specificity for the diagnosis of true progression were 42% and 89%, respectively, by using only the distant subependymal enhancement. Although the specificity is relatively high, the clinical utility of the imaging findings may be limited due to its low sensitivity. However, our results suggest that the distant subependymal enhancement, when present, can be an early clue to the diagnosis of true progression.

Moreover, the multiple logistic regression analysis revealed that the distant subependymal enhancement and the fifth percentile of the cumulative ADC histogram were independently predictive of true progression (OR, 8.30; $P = .041$; OR, 0.99; $P = .033$, respectively). Given that the enhancing portion presumably represents a wide spectrum of histologic features comprising normal brain tissue, radiation necrosis, and highly cellular recurrent tumor, we infer that the enhancing lesion with the high fifth percentile value may also contain small foci of viable tumor with low ADC values. Hence, we speculate that the incidence of distant subependymal enhancement is likely to be influenced by multiple factors, including the anatomic location of the viable tumor portion within the enhancing lesion (ie, whether it is close to the ventricular margin), not just by the fifth percentile value itself. The sensitivity and specificity for the diagnosis of true progression were 83% and 67%, respectively, by using both independent factors.

Apart from the intrinsic limits of any retrospective study, several other limitations should be mentioned. First, MR imaging was performed on 2 different 3T MR imaging units. However, MR images were optimized to maintain the image quality and to minimize differences between the 2 units. Second, although any discernible necrotic or cystic area was excluded from ROI measurements, it was difficult to eliminate the possibility of including small necrotic or cystic areas. Nonetheless, the contamination was presumed to have had a negligible effect on our results because we used the fifth percentile of the cumulative ADC histogram as the main parameter, rather than the mean value. Third, the present study included a relatively small patient population, in which we could not find any statistically significant difference in the methylation status of O6-methylguanine DNA methyltransferase promoter between the true progression and pseudoprogression groups. On the other hand, the age of the patients was unexpectedly found to be an independent predictor of true progression. A further study with a larger population is warranted to strengthen the statistical power. Fourth, given the possibilities of the occurrence of pseudoprogression later than 3 months after the end of CCRT and coexistence of the 2 entities, some ambiguity may be inevitably present in the final diagnosis of true progression or pseudoprogression because the diagnosis was made on the basis of the follow-up MR images rather than pathologic confirmation. Fifth, there may have been false-negative results for subtle subependymal enhancement because high-resolution volumetric T1-weighted images were not available in some patients from the early study period.

CONCLUSIONS

Both the distant subependymal enhancement (ie, extending >1 cm or isolated from the enhancing lesion) and the fifth percentile of the cumulative ADC histogram of enhancing lesions were significant independent predictors for true progression in patients with GBM. Compared with the histogram analysis of ADC values, the visual assessment of subependymal enhancement is relatively straightforward and less time-consuming. In clinical practice, despite the inherent difficulty of differentiating true progression from pseudoprogression, the diagnostic accuracy may be im-

proved by taking into account both the subependymal enhancement pattern and ADC values.

Disclosures: Seung Hong Choi—RELATED: Grant: Korea Healthcare Technology R&D Projects, Ministry for Health, Welfare and Family Affairs (H113C0015), and the Research Center Program of Institute for Basic Science in Korea.* *Money paid to the institution.

REFERENCES

1. Wen PY, Kesari S. **Malignant gliomas in adults.** *N Engl J Med* 2008;359:492–507
2. Brandes AA, Tosoni A, Spagnoli F, et al. **Disease progression or pseudoprogression after concomitant radiochemotherapy treatment: pitfalls in neurooncology.** *Neuro Oncol* 2008;10:361–67
3. Jeon HJ, Kong DS, Park KB, et al. **Clinical outcome of concomitant chemoradiotherapy followed by adjuvant temozolomide therapy for glioblastomas: single-center experience.** *Clin Neurol Neurosurg* 2009;111:679–82
4. Stupp R, Mason WP, van den Bent MJ, et al; European Organisation for Research and Treatment of Cancer Brain Tumor and Radiotherapy Groups, National Cancer Institute of Canada Clinical Trials Group. **Radiotherapy plus concomitant and adjuvant temozolomide for glioblastoma.** *N Engl J Med* 2005;352:987–96
5. Wen PY, Macdonald DR, Reardon DA, et al. **Updated response assessment criteria for high-grade gliomas: Response Assessment in Neuro-Oncology Working Group.** *J Clin Oncol* 2010;28:1963–72
6. Cairncross JG, Macdonald DR, Pexman JH, et al. **Steroid-induced CT changes in patients with recurrent malignant glioma.** *Neurology* 1988;38:724–26
7. Finn MA, Blumenthal DT, Salzman KL, et al. **Transient postictal MRI changes in patients with brain tumors may mimic disease progression.** *Surg Neurol* 2007;67:246–50; discussion 250
8. Henegar MM, Moran CJ, Silbergeld DL. **Early postoperative magnetic resonance imaging following nonneoplastic cortical resection.** *J Neurosurg* 1996;84:174–79
9. Kumar AJ, Leeds NE, Fuller GN, et al. **Malignant gliomas: MR imaging spectrum of radiation therapy- and chemotherapy-induced necrosis of the brain after treatment.** *Radiology* 2000;217:377–84
10. Ulmer S, Braga TA, Barker FG 2nd, et al. **Clinical and radiographic features of peritumoral infarction following resection of glioblastoma.** *Neurology* 2006;67:1668–70
11. Watling CJ, Lee DH, Macdonald DR, et al. **Corticosteroid-induced magnetic resonance imaging changes in patients with recurrent malignant glioma.** *J Clin Oncol* 1994;12:1886–89
12. Brandsma D, Stalpers L, Taal W, et al. **Clinical features, mechanisms, and management of pseudoprogression in malignant gliomas.** *Lancet Oncol* 2008;9:453–61
13. Chaskis C, Neyns B, Michotte A, et al. **Pseudoprogression after radiotherapy with concurrent temozolomide for high-grade glioma: clinical observations and working recommendations.** *Surg Neurol* 2009;72:423–28
14. Taal W, Brandsma D, de Bruin HG, et al. **Incidence of early pseudoprogression in a cohort of malignant glioma patients treated with chemoradiation with temozolomide.** *Cancer* 2008;113:405–10
15. Abdel Razek AA, Kandeel AY, Soliman N, et al. **Role of diffusion-weighted echo-planar MR imaging in differentiation of residual or recurrent head and neck tumors and posttreatment changes.** *AJNR Am J Neuroradiol* 2007;28:1146–52
16. Asao C, Korogi Y, Kitajima M, et al. **Diffusion-weighted imaging of radiation-induced brain injury for differentiation from tumor recurrence.** *AJNR Am J Neuroradiol* 2005;26:1455–60
17. Chu HH, Choi SH, Ryoo I, et al. **Differentiation of true progression from pseudoprogression in glioblastoma treated with radiation therapy and concomitant temozolomide: comparison study of standard and high-b-value diffusion-weighted imaging.** *Radiology* 2013;269:831–40
18. Hein PA, Eskey CJ, Dunn JF, et al. **Diffusion-weighted imaging in the follow-up of treated high-grade gliomas: tumor recurrence versus radiation injury.** *AJNR Am J Neuroradiol* 2004;25:201–09
19. Lee WJ, Choi SH, Park CK, et al. **Diffusion-weighted MR imaging for the differentiation of true progression from pseudoprogression following concomitant radiotherapy with temozolomide in patients with newly diagnosed high-grade glioma.** *Acad Radiol* 2012;19:1353–61
20. Matsusue E, Fink JR, Rockhill JK, et al. **Distinction between glioma progression and post-radiation change by combined physiologic MR imaging.** *Neuroradiology* 2010;52:297–306
21. Song YS, Choi SH, Park CK, et al. **True progression versus pseudoprogression in the treatment of glioblastomas: a comparison study of normalized cerebral blood volume and apparent diffusion coefficient by histogram analysis.** *Korean J Radiol* 2013;14:662–72
22. Cha J, Kim ST, Kim HJ, et al. **Differentiation of tumor progression from pseudoprogression in patients with posttreatment glioblastoma using multiparametric histogram analysis.** *AJNR Am J Neuroradiol* 2014;35:1309–17
23. Mullins ME, Barest GD, Schaefer PW, et al. **Radiation necrosis versus glioma recurrence: conventional MR imaging clues to diagnosis.** *AJNR Am J Neuroradiol* 2005;26:1967–72
24. Young RJ, Gupta A, Shah AD, et al. **Potential utility of conventional MRI signs in diagnosing pseudoprogression in glioblastoma.** *Neurology* 2011;76:1918–24
25. Man MZ, Dyson G, Johnson K, et al. **Evaluating methods for classifying expression data.** *J Biopharm Stat* 2004;14:1065–84
26. Kyritsis AP, Levin VA, Yung WK, et al. **Imaging patterns of multifocal gliomas.** *Eur J Radiol* 1993;16:163–70
27. Sneed PK, Gutin PH, Larson DA, et al. **Patterns of recurrence of glioblastoma multiforme after external irradiation followed by implant boost.** *Int J Radiat Oncol Biol Phys* 1994;29:719–27
28. Milano MT, Okunieff P, Donatello RS, et al. **Patterns and timing of recurrence after temozolomide-based chemoradiation for glioblastoma.** *Int J Radiat Oncol Biol Phys* 2010;78:1147–55
29. Ogura K, Mizowaki T, Arakawa Y, et al. **Initial and cumulative recurrence patterns of glioblastoma after temozolomide-based chemoradiotherapy and salvage treatment: a retrospective cohort study in a single institution.** *Radiat Oncol* 2013;8:97
30. McGeachie RE, Gold LH, Latchaw RE. **Periventricular spread of tumor demonstrated by computed tomography.** *Radiology* 1977;125:407–10
31. Ammirati M, Chotai S, Newton H, et al. **Hypofractionated intensity modulated radiotherapy with temozolomide in newly diagnosed glioblastoma multiforme.** *J Clin Neurosci* 2014;21:633–37
32. Burnet NG, Jena R, Burton KE, et al. **Clinical and practical considerations for the use of intensity-modulated radiotherapy and image guidance in neuro-oncology.** *Clin Oncol (R Coll Radiol)* 2014;26:395–406

MRI Tractography of Corticospinal Tract and Arcuate Fasciculus in High-Grade Gliomas Performed by Constrained Spherical Deconvolution: Qualitative and Quantitative Analysis

E. Mormina, M. Longo, A. Arrigo, C. Alafaci, F. Tomasello, A. Calamuneri, S. Marino, M. Gaeta, S.L. Vinci, and F. Granata



ABSTRACT

BACKGROUND AND PURPOSE: MR imaging tractography is increasingly used to perform noninvasive presurgical planning for brain gliomas. Recently, constrained spherical deconvolution tractography was shown to overcome several limitations of commonly used DTI tractography. The purpose of our study was to evaluate WM tract alterations of both the corticospinal tract and arcuate fasciculus in patients with high-grade gliomas, through qualitative and quantitative analysis of probabilistic constrained spherical deconvolution tractography, to perform reliable presurgical planning.

MATERIALS AND METHODS: Twenty patients with frontoparietal high-grade gliomas were recruited and evaluated by using a 3T MR imaging scanner with both morphologic and diffusion sequences (60 diffusion directions). We performed probabilistic constrained spherical deconvolution tractography and tract quantification following diffusion tensor parameters: fractional anisotropy; mean diffusivity; linear, planar, and spherical coefficients.

RESULTS: In all patients, we obtained tractographic reconstructions of the medial and lateral portions of the corticospinal tract and arcuate fasciculus, both on the glioma-affected and nonaffected sides of the brain. The affected lateral corticospinal tract and the arcuate fasciculus showed decreased fractional anisotropy ($z = 2.51, n = 20, P = .006$; $z = 2.52, n = 20, P = .006$) and linear coefficient ($z = 2.51, n = 20, P = .006$; $z = 2.52, n = 20, P = .006$) along with increased spherical coefficient ($z = -2.51, n = 20, P = .006$; $z = -2.52, n = 20, P = .006$). Mean diffusivity values were increased only in the lateral corticospinal tract ($z = -2.53, n = 20, P = .006$).

CONCLUSIONS: In this study, we demonstrated that probabilistic constrained spherical deconvolution can provide essential qualitative and quantitative information in presurgical planning, which was not otherwise achievable with DTI. These findings can have important implications for the surgical approach and postoperative outcome in patients with glioma.

ABBREVIATIONS: AF = arcuate fasciculus; Cl = linear coefficient; Cp = planar coefficient; Cs = spherical coefficient; CSD = constrained spherical deconvolution; CST = corticospinal tract; FA = fractional anisotropy; HGG = high-grade glioma; MD = mean diffusivity

Gliomas are the most common type of WM-involved invasive cerebral primary neoplasm in adults. These brain tumors represent approximately 80% of primary malignant brain tumors and almost 3% of all types of cancer, and patient prognosis is poor.

In recent years, the use of noninvasive study techniques, such as cortical mapping and fMRI, has improved presurgical planning

for brain neoplasms. However, these methods alone are considered inadequate to achieve the primary neurosurgical aim, obtaining the most radical tumor resection with the minimum of postoperative deficits, because they do not provide good anatomic representation of the spatial location of WM tracts affected by the tumor.¹ Tractography is the most common neuroimaging technique used to reveal WM structure by analysis of DWI signals dependent on anisotropic water diffusion.² From DWI gradient directions, it is possible to generate an anisotropic map showing WM bundles and their orientations; this information is adapted by tractographic algorithms to yield a 3D representation of WM tracts. DTI-based tractography is widely used for presurgical planning and is a powerful tool in the evaluation of major WM fiber bundles; it has also a positive impact on neurosurgical resection, disease prognosis, and preservation of brain function.³ Although widely used and histologically validated,⁴ DTI approaches have several limitations, such as partial volume effects or lack of

Received December 30, 2014; accepted after revision March 10, 2015.

From the Departments of Biomedical Science and Morphological and Functional Images (E.M., F.G., A.A., M.G., S.L.V., M.L.) and Neurosciences (C.A., F.T., A.C.), University of Messina, Messina, Italy; and Scientific Institute for Recovery and Care Centro Neurolesi Bonino Pulejo (S.M.), Messina, Italy.

Please address correspondence to A. Arrigo, MD, Department of Biomedical Science and Morphological and Functional Images, University of Messina, via Consolare Valeria, one c/o A.O.U. Policlinico "G. Martino", 98125 Messina, Italy; e-mail: alessandro.arrigo@hotmail.com

Indicates open access to non-subscribers at www.ajnr.org

<http://dx.doi.org/10.3174/ajnr.A4368>

tensor estimation in voxels characterized by low fractional anisotropy (FA) values.⁵ Recent tractographic algorithms, such as probabilistic constrained spherical deconvolution (CSD), have overcome these limitations.⁶

The corticospinal tract (CST) and arcuate fasciculus (AF) are 2 of the WM pathways most commonly investigated by tractography because of their important roles in voluntary movement control and language, respectively.⁷ Probabilistic CSD improves tractographic reconstruction of the lateral portion of the CST, corresponding to the somatotopic representation of hand, face, tongue, and voluntary swallow muscles, which is not detectable by DTI-based approaches.⁸ In addition, this technique allows better evaluation of all AF components, including projections to the Geschwind area and other cortical regions, compared with other tractographic methods.⁹ The main aim of this study was to evaluate WM tract alterations of both the CST and AF in patients with frontoparietal high-grade gliomas (HGGs), through a qualitative and quantitative analysis by using probabilistic CSD tractography, to obtain reliable presurgical planning.

MATERIALS AND METHODS

Participants

In our study, we recruited 20 patients (9 women and 11 men; mean age, 47.4 ± 14.2 years; age range, 20–67 years), all affected by HGG, which involved mainly the lateral part of the frontoparietal lobes. After MR imaging evaluation, all patients underwent surgery, and all diagnoses were confirmed histologically.

The study was approved by our institution review board, and written informed consent was obtained from all subjects.

Data Acquisition and Preprocessing

The study was performed with an Achieva 3T MR imaging scanner (Philips Healthcare, Best, the Netherlands) by using a 32-channel coil. We performed the following sequences:

- A T1-weighted fast-field echo 3D high-resolution sequence with TR, 8.1 ms; TE, 3.7 ms; flip angle, 8°; reconstruction matrix, 240 × 240; voxel size, 1 mm³ without an intersection gap;
- A FLAIR volume isotropic turbo spin-echo acquisition sensitivity encoding 3D sequence with TR, 8000 ms; TE, 360 ms; TI, 2400 ms; reconstruction matrix, 240 × 240; voxel size, 1 mm³ without an intersection gap;
- Diffusion-weighted MR imaging acquired with a dual-phase encoded pulsed gradient spin-echo sequence with TR, 15,120 ms; TE, 54 ms; scan matrix, 160 × 160; section thickness, 2 mm without an intersection gap; 60 gradient directions; b-value, 1000 s/mm². We corrected the diffusion-weighted dataset for eddy current distortions and motion artifacts and adjusted the diffusion gradients with proper rotation of the b-matrix.¹⁰

Data Processing and Fiber Tracking

To avoid possible coregistration errors between morphologic and diffusion images caused by HGGs,⁸ we did not normalize patient data to a common template space as usual. Seed ROIs were also selected directly in the native space of each subject. Fiber tracking was obtained with a probabilistic CSD algorithm (MRtrix software package; <http://software.incf.org/software/mrtrix/mrtrix-package>)⁹ with manually selected ROIs. Fiber tracking was

stopped when 10,000 tracts reached the selected ROI or when 100,000 total tracts were generated. The 3D segmentation of each HGG and the 3D visualization of tracts were performed by using 3D Slicer software (www.slicer.org)¹¹ with T1-weighted images set as an overlay.

Qualitative Analysis

Qualitative analysis was performed by a radiologist with 20 years of experience who evaluated reconstructed tracts on superimposed 3D T1-weighted images. We verified the anatomic course of each fiber bundle section by section, in axial, coronal, and sagittal planes, comparing the neoplasm-affected side with the healthy one. During this step, the reader could detect any macroscopic WM tract dislocation or disruption in the affected side. Moreover, neoplasm 3D segmentation was used to depict the spatial relationship between tracts and gliomas.

Quantitative and Statistical Analysis

Quantitative analysis of reconstructed tracts, both in healthy and affected hemispheres, was performed by using the output data of MRtrix. Diffusion tensors were sampled along fiber tracts, and the mean values of FA, mean diffusivity (MD), linear coefficient (Cl), planar coefficient (Cp), and spherical coefficient (Cs) were considered for each bundle. All parameters were calculated with in-house scripts built with the Matlab software package (MathWorks, Natick, Massachusetts), based on the eigenvalues obtained from MRtrix output data.

As previously described,^{12–14} we used a combined approach of diffusion tensor parameters and probabilistic CSD tractography to overcome the well-known limitations of DTI in voxels containing crossing fibers and to increase the sensitivity of diffusion tensor metric changes in these regions.

Statistical analysis was performed by the nonparametric Wilcoxon signed rank test for paired measures of bundles in the healthy-versus-affected sides. Furthermore, Šidák correction was performed to account for multiple comparisons. The significance threshold was set to an α value of .05, resulting in an effective threshold of .0102 after correction.

RESULTS

All recruited patients were symptomatic with different degrees of motor and/or speech impairment, from mild to severe. All patients had both CST and AF involved by HGGs, which were located in the lateral frontoparietal lobes. There was a prevalence of left-sided involvement (11 left side, 9 right side). After surgery, the histologic analysis of resected neoplasms confirmed each lesion as III or IV World Health Organization grade: grade III ($n = 15$) and grade IV ($n = 5$). We were able to obtain tractographic reconstructions of the medial portion of the CST and the lateral portion of the CST and AF, both in the healthy and neoplasm-affected sides in all 20 patients.

Qualitative Analysis

Qualitative analysis revealed the anatomic course of each reconstructed fiber bundle, morphologic alterations of WM tracts on affected sides, and the spatial relationship between those tracts and the HGG.

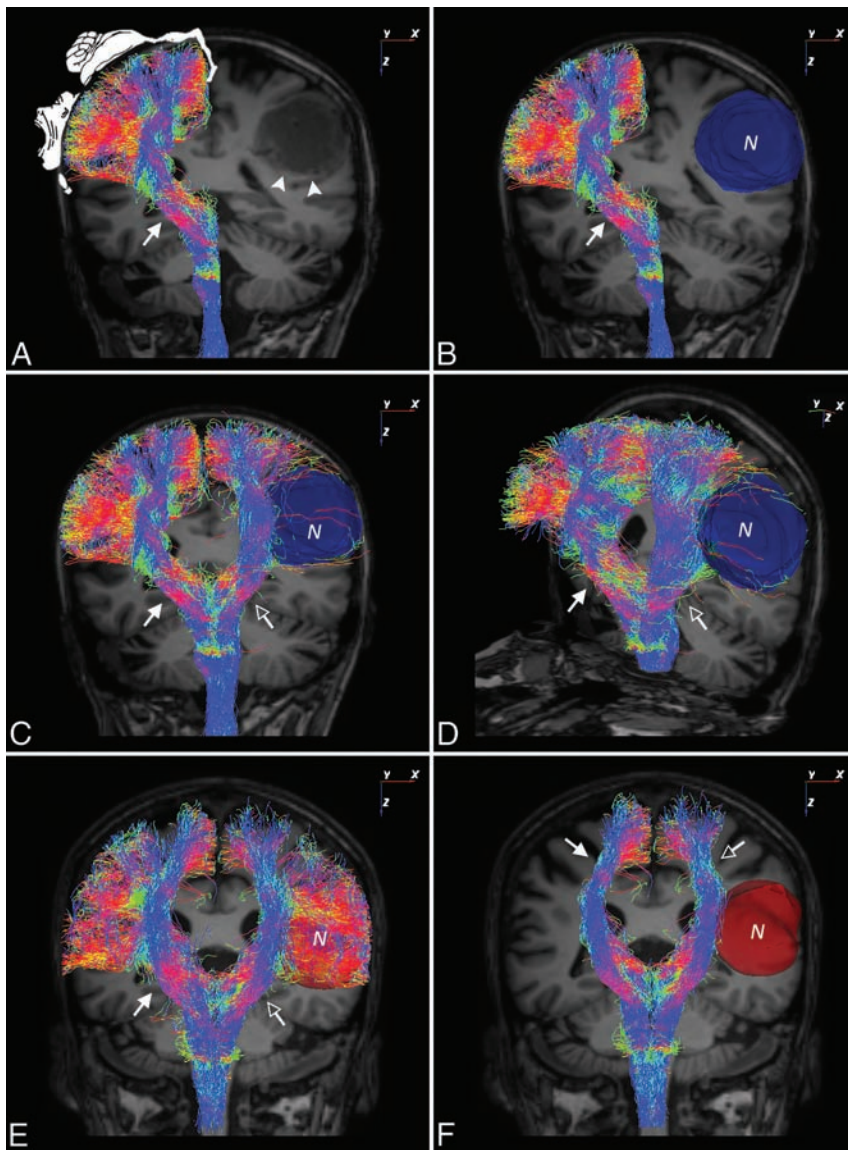


FIG 1. Tractographic reconstruction of corticospinal tracts in patients with high-grade gliomas. Coronal T1-weighted MR image (A) shows the corticospinal tract (arrow) on the healthy side with overlay of the Pensfield motor homunculus (arrowheads indicate neoplasm margins) and the neoplasm volume segmentation (B) (blue volume). Coronal (C) and sagittal (D) rotated images show tractographic reconstruction of CSTs on both healthy (arrow) and neoplasm-affected sides (empty arrow) of the brain. In this patient, the lateral portion of the CST on the affected side is poorly represented due to neoplasm disruption. E, Coronal T1-weighted MR image shows CSTs, both on healthy (arrow) and neoplasm-affected sides (empty arrow) of another patient (neoplasm segmentation is depicted by red volume). In this case, on the affected side, the lateral portion of the CST passes through the neoplasm and is poorly involved. F, Coronal T1-weighted MR image shows the medial portion of CSTs on the healthy side (arrow) and the absence of their involvement in the neoplasm-affected one (empty arrow). N indicates neoplasm.

Probabilistic CSD tractography of the CST yielded streamlines of both the medial and lateral portions of the CST on each side of the brain. Qualitative analysis for the healthy side showed a reliable representation of all components of the Pensfield homunculus (Fig 1A). In the neoplasm-affected side, all evaluated tracts showed a strict spatial relationship with HGGs. In 6/20 patients, the lateral portion of the CST was disrupted by the neoplasm, with consequent poor representation of streamlines (Fig 1B–D). In the other 14 patients, the lateral portion of the CST passed through the neoplasm and was, therefore, less compromised than expected

on the basis of morphologic MR imaging evaluation of the neoplasms (Fig 1E). In all patients, the medial portion of the CST was not affected by the neoplasm (Fig 1F).

Probabilistic CSD tractographic reconstructions also allowed reliable recognition of the anatomic course for all AF segments, such as Broca, Wernicke, and Geschwind projections (Fig 2) on both sides. Qualitative analysis showed that the AF was involved by the neoplasm on the affected side of all subjects (Fig 2D–F), with different degrees of morphologic impairment.

Quantitative Analysis

Quantitative analysis showed that FA was significantly decreased in the lateral portion of the CST ($z = 2.51$, $n = 20$, $P = .006$) and in the AF ($z = 2.52$, $n = 20$, $P = .006$) of the side affected by the neoplasm; furthermore, no significant difference was found for FA ($P > .0102$) in the medial portion of the CST. Although MD was increased in all affected tracts, only the lateral portion of the CST reached significance ($z = -2.53$, $n = 20$, $P = .006$). CI was significantly decreased in the affected bundles for the lateral portion of the CST ($z = 2.51$, $n = 20$, $P = .006$) and the AF ($z = 2.52$, $n = 20$, $P = .006$). Cs was significantly increased for the affected lateral CST ($z = -2.51$, $n = 20$, $P = .006$) and for the AF ($z = -2.52$, $n = 20$, $P = .006$). No differences were observed when measuring Cp. Quantitative results are summarized in Fig 3.

DISCUSSION

In this study we evaluated 20 patients with HGGs centered in the lateral frontoparietal lobes. Each patient underwent glioma surgical resection after presurgical evaluation of the main WM fiber bundles involved by MR imaging tractography. Because the main

goal of the surgical approach was to remove neoplasms while preserving brain function, accurate presurgical planning was essential to granting the best possible quality of life after surgery.

Presurgical tractographic analysis, performed by a probabilistic CSD-based tractographic approach, revealed involvement of the CST and AF in each patient. These 2 WM fiber bundles have clinically relevant roles in voluntary motion control and speech and language, respectively. Common DTI approaches cannot depict the entire motor tract, allowing only reconstruction of the

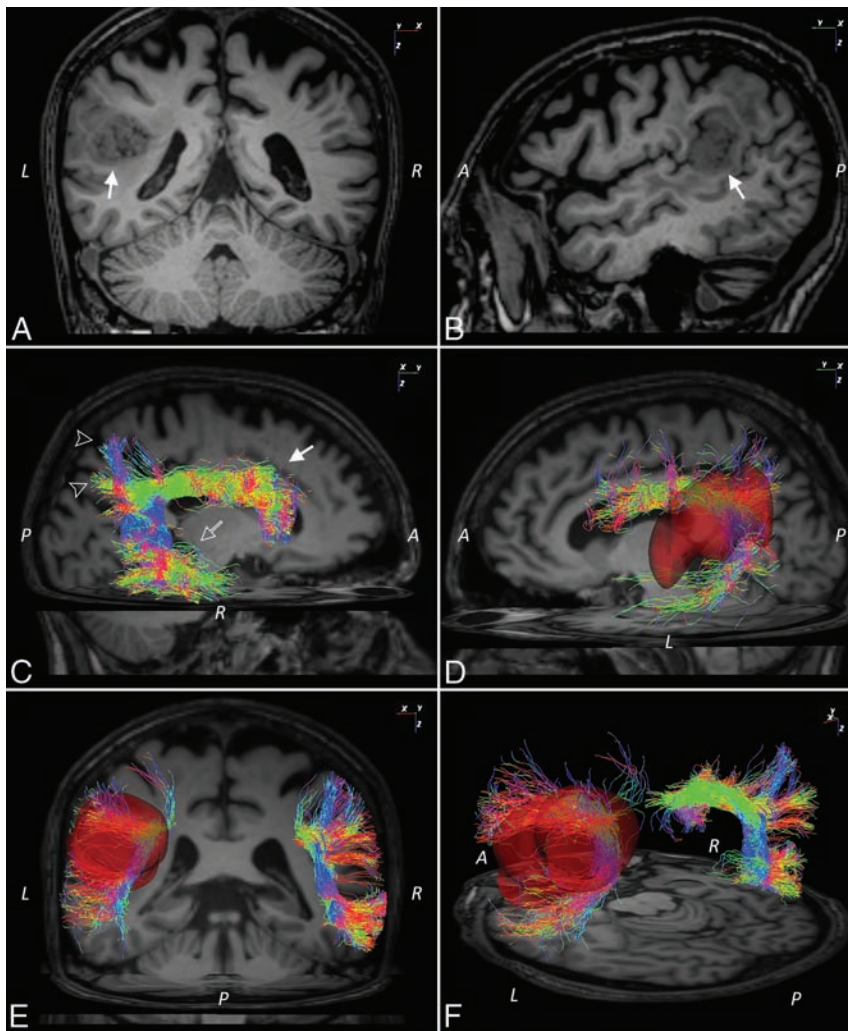


FIG 2. Tractographic reconstruction of arcuate fasciculi in a patient with a high-grade glioma. Coronal (A) and sagittal (B) T1-weighted MR images show a frontoparietal high-grade glioma on the left side (arrow). C, Sagittal T1-weighted MR image shows tractographic reconstruction of the right arcuate fasciculus on the healthy side with the depiction of Broca (arrow), Wernicke (empty arrow), and Geschwind projections (empty arrowheads). D, The left AF on the affected side passes through the neoplasm (neoplasm segmentation is depicted by a red volume). Coronal (E) and axial (F) tilted T1-weighted MR images show the AFs on both affected and healthy sides (neoplasm segmentation is depicted by a red volume). A indicates anterior; P, posterior; R, right; L, left.

medial portion of the CST, corresponding to a somatotopic depiction of the lower limbs, trunk, and upper limbs without the hand. Conversely, these techniques could not represent the lateral portion of the CST, which corresponds to a somatotopic depiction of the hand, face, tongue, and voluntary swallow muscles,¹⁵ due to the inherent limitations of DTI approaches to resolve complex fiber configurations,⁶ which were estimated to represent approximately 90% of WM voxels of the entire brain.¹⁶ By overcoming these limitations, probabilistic CSD-based tractography allowed a reconstruction of the entire CST (medial and lateral parts),⁸ with a marked match between tracts and all somatotopic parts of the Penfield motor homunculus. It also demonstrated that brain neoplasms can involve different WM modifications, resulting in DTI parameter changes and alterations of the average WM fiber bundle morphology represented with tractography. In particular, Witwer et al¹⁷ described deviated, infiltrated, edema-

tous, and disrupted WM patterns, depending on tumor type and location.

Different DTI-based studies reported that high-grade gliomas mainly cause complete tract disruption,¹⁸ whereas low-grade gliomas infiltrate tracts along myelinated fibers.¹⁹ All these patterns of tumors cause DTI parameter changes, in particular FA decrease, in involved regions.²⁰ Furthermore, the presence of voxels with FA values lower than the DTI threshold (commonly set to 0.2) causes an interruption of reconstructed WM tracts,²¹ and the use of an FA threshold lower than 0.2 results in poor accuracy of major eigenvector-direction estimation.¹ These limitations can produce 3 negative effects on tractographic presurgical planning, particularly in CST evaluation. First, the reconstructed CST tract could show a false interruption, for example, in the lateral portion of the CST.²⁰ Second, DTI findings could suggest a false safe resection margin around the lesion.⁸ Last, the lack of reconstruction of the lateral portion of the CST fails to provide any qualitative or quantitative information about this part of the tract and its relationship to neoplasms. These combined effects make presurgical planning inaccurate and may contribute to unexpected postoperative functional deficits.

Use of the CSD technique allowed reconstruction of fibers in voxels with low anisotropy and characterization of voxels in tumoral and peritumoral areas¹ and voxels with complex axonal spatial configurations. In addition, it was demonstrated that edema-affected and infiltrated tracts could reduce their anisotropy, while preserving sufficient directional information for tractographic depiction.¹

In our study, we could reconstruct the medial and lateral portions of the CST of 20 patients in both the healthy and neoplasm-affected sides of the brain by using probabilistic CSD tractography.

This approach allowed reliable reconstruction of these pathways with an accurate representation of the entire Penfield motor homunculus on the healthy side, avoiding well-known reconstruction problems from crossing fibers. Moreover, on the involved side, we detected differing degrees of involvement for the lateral portion of the CST, from deviation to disruption, with no alterations of the medial portion.

AF depiction in presurgical planning is clinically relevant to avoid aphasic syndromes induced by surgical lesions or stroke.^{21,22} This WM bundle connects to Broca, Wernicke, and Geschwind areas and other brain regions involved in language

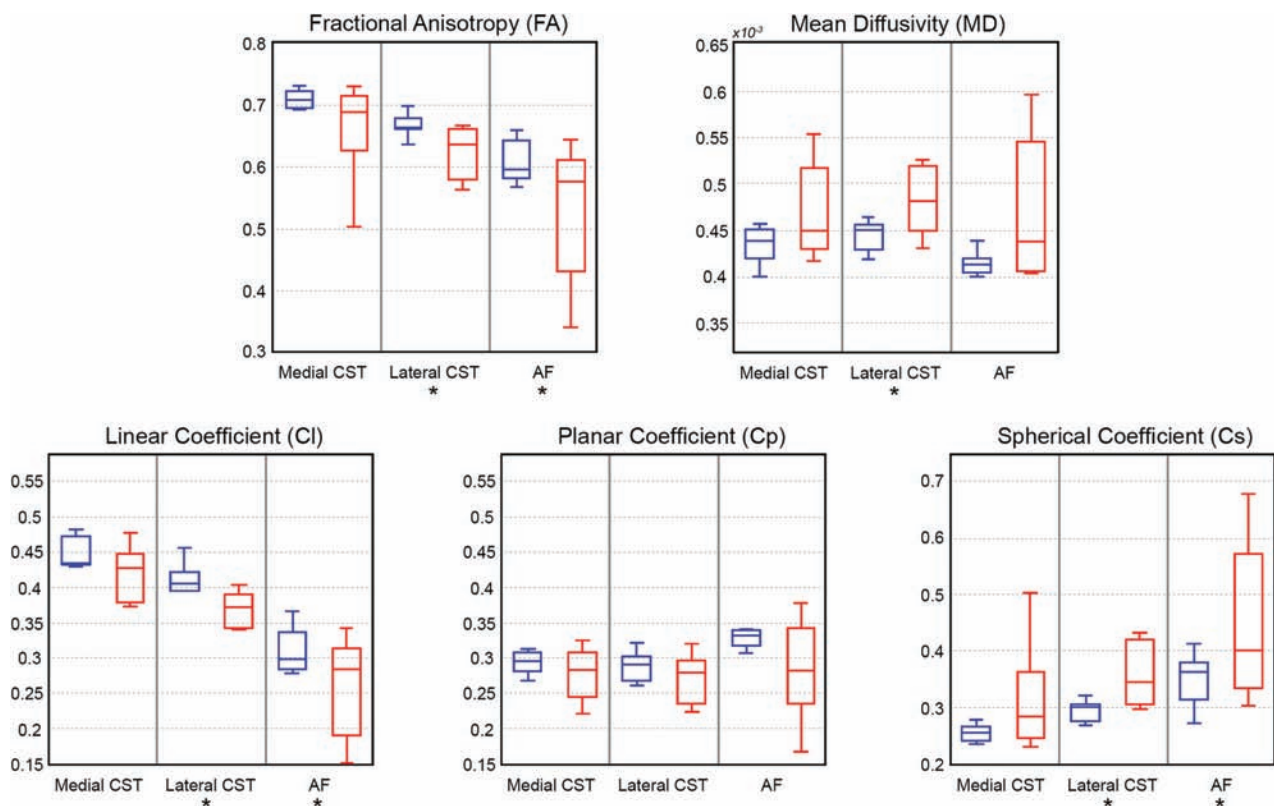


FIG 3. Diffusion tensor parameter distributions of the medial and lateral corticospinal portions and arcuate fasciculi. Blue and red boxplots represent DTI parameter distributions in the healthy and neoplasm-affected sides, respectively. Asterisks indicate statistical significance ($P < .05$ corrected for multiple comparisons).

and speech.²³ Because brain stimulation techniques are less effective for WM tracts than for GM, evaluating the morphologic localization of the AF is essential for appropriate presurgical planning.²⁴⁻²⁷ DTI-based tractographic studies revealed incomplete AF reconstructions, in particular of the anterior portion.²⁴ The evaluation of this AF segment is considered an important predictor of postoperative outcome because a lesion in the anterior portion of AF could cause negative effects on speech fluency.²⁸ DTI approaches have tractographic reconstruction limitations in the centrum semiovale, due to the presence of crossing fibers.²⁴ In addition, DTI tractography of AFs in patients with brain neoplasms resulted in incomplete correspondence with intracortical stimulation, suggesting that this technique is not optimal for mapping language areas.²⁹ Finally, the same negative effects of DTI techniques discussed above for CST are also relevant to AFs involved by gliomas during presurgical planning. Thus, the use of probabilistic CSD, which includes voxels not considered by DTI tractography, could provide advantages in the evaluation of DTI metrics in aphasic syndromes as well.

In this cohort of patients, we found that probabilistic CSD-based tractography allowed reliable representation of AFs both in glioma-involved and noninvolved sides of the brain, even in arduous regions for conventional DTI tractography. Qualitative analysis showed that all affected AFs were dislocated, infiltrated, or disrupted by the neoplasm.

From probabilistic CSD tractography, we extrapolated a quantitative analysis based on the main DTI parameters (FA, MD, Cp, Cl, and Cs). FA and MD are well-known values measuring axonal

integrity and anisotropic water diffusivity, respectively. Cl measures the intravoxel uniformity of tract direction and fiber tract organization, Cs estimates the intravoxel diffusivity,³⁰ and Cp estimates voxels in which there are crossing or kissing fibers.¹² No statistically significant changes were found for the medial CST both in healthy and affected sides of the brain, suggesting that in our group of patients, these bundles are not involved with HGGs. In all patients, we found statistically significant differences in both the lateral CST and AF between the involved and noninvolved sides. In particular, we detected decreased FA and Cl and increased Cs in the involved side. MD was increased in all affected tracts, reaching significance only in the lateral portion of CST, probably due to the low number of subjects. The significant FA decrease could reflect a remarkable change in WM microstructure, induced by tract deviation, infiltration, or disruption or influenced by edema.³⁰ MD increase could be associated with loss of WM integrity with a consequent increase in free tissue water.³¹ Cl and Cs are 2 known shape-oriented anisotropy measures, indexes of anisotropic and isotropic diffusion changes, respectively.³⁰ In our study, neoplasms changed the intravoxel uniformity and diffusivity of affected tracts, causing Cl decrease and Cs increase. These parameters, combined with the use of FA and MD, could provide a powerful quantitative estimation of WM tracts involved by HGGs. Finally, we evaluated Cp for all tracts, which is another shape-oriented parameter reflecting the intravoxel presence of crossing fibers.³⁰ In our study, the Cp value was not significantly different between the healthy and affected side. This result could

be due to a lack of sensitivity in cases of >2 crossing fibers inside the same voxel.¹²

The major limitation of this study is the relatively small patient cohort, which might influence the statistical power of our findings. In addition, it was not possible to perform follow-up MR imaging tractography after surgical neoplasm resections. This lack of MR imaging follow-up prohibited us from providing an evaluation of the postoperative outcome after CSD-based presurgery planning.

CONCLUSIONS

The results presented here demonstrated that probabilistic CSD tractography provides useful qualitative and quantitative analysis in presurgical planning for HGGs. Our qualitative analysis showed that probabilistic CSD allowed reliable reconstruction of tracts not detected with other DTI techniques, such as those involved by neoplasms or with complex fiber configurations. We also demonstrated that quantitative analysis based on CSD tractography can characterize the involvement of the tracts by the neoplasms, overcoming the well-known quantitative underestimation related to DTI reconstruction. Furthermore, because postoperative quantitative measurements are also important for the prediction of brain-function recovery,³² further studies performed with probabilistic CSD could provide noteworthy results on surgical-outcome evaluation.

REFERENCES

1. Jellison BJ, Field AS, Medow J, et al. **Diffusion tensor imaging of cerebral white matter: a pictorial review of physics, fiber tract anatomy, and tumor imaging patterns.** *AJNR Am J Neuroradiol* 2004; 25:356–69
2. Basser PJ, Pajevic S, Pierpaoli C, et al. **In vivo fiber tractography using DT-MRI data.** *Magn Reson Med* 2000;44:625–32
3. Romano A, D'Andrea G, Minniti G, et al. **Pre-surgical planning and MR-tractography utility in brain tumour resection.** *Eur Radiol* 2009;19:2798–808
4. Dyrby TB, Søgaard LV, Parker GJ, et al. **Validation of in vitro probabilistic tractography.** *Neuroimage* 2007;37:1267–77
5. Jones DK, Cercignani M. **Twenty-five pitfalls in the analysis of diffusion MRI data.** *NMR Biomed* 2010;23:803–20
6. Tournier JD, Calamante F, Connelly A. **Robust determination of the fibre orientation distribution in diffusion MRI: non-negativity constrained super-resolved spherical deconvolution.** *Neuroimage* 2007;35:1459–72
7. Kristo G, Leemans A, Raemaekers M, et al. **Reliability of two clinically relevant fiber pathways reconstructed with constrained spherical deconvolution.** *Magn Reson Med* 2013;70:1544–56
8. Farquharson S, Tournier JD, Calamante F, et al. **White matter fiber tractography: why we need to move beyond DTI.** *J Neurosurg* 2013;118:1367–77
9. Tournier JD, Calamante F, Connelly A. **MRtrix: diffusion tractography in crossing fiber regions.** *International Journal of Imaging Systems and Technology* 2012;22:53–66
10. Leemans A, Jones DK. **The B-matrix must be rotated when correcting for subject motion in DTI data.** *Magn Reson Med* 2009; 61:1336–49
11. Fedorov A, Beichel R, Kalpathy-Cramer J, et al. **3D Slicer as an image computing platform for the Quantitative Imaging Network.** *Magn Reson Imaging* 2012;30:1323–41
12. Reijmer YD, Leemans A, Heringa SM, et al. **Improved sensitivity to cerebral white matter abnormalities in Alzheimer's disease with spherical deconvolution based tractography.** *PLoS One* 2012; 7:e44074
13. Arrigo A, Mormina E, Anastasi GP, et al. **Constrained spherical deconvolution analysis of the limbic network in human, with emphasis on a direct cerebello-limbic pathway.** *Front Hum Neurosci* 2014;8:987
14. Mormina E, Arrigo A, Calamuneri A, et al. **Diffusion tensor imaging parameters' changes of cerebellar hemispheres in Parkinson's disease.** *Neuroradiology* 2015;57:327–34
15. Kinoshita M, Yamada K, Hashimoto N, et al. **Fiber-tracking does not accurately estimate size of fiber bundle in pathological condition: initial neurosurgical experience using neuronavigation and subcortical white matter stimulation.** *Neuroimage* 2005;25:424–29
16. Jeurissen B, Leemans A, Tournier JD, et al. **Investigating the prevalence of complex fiber configurations in white matter tissue with diffusion magnetic resonance imaging.** *Hum Brain Mapp* 2013; 34:2747–66
17. Witwer BP, Moftakhar R, Hasan KM, et al. **Diffusion-tensor imaging of white matter tracts in patients with cerebral neoplasm.** *J Neurosurg* 2002;97:568–75
18. Chen F, Zhang X, Li M, et al. **Axial diffusivity and tensor shape as early markers to assess cerebral white matter damage caused by brain tumors using quantitative diffusion tensor tractography.** *CNS Neurosci Ther* 2012;18:667–73
19. Duffau H, Khalil I, Gatignol P, et al. **Surgical removal of corpus callosum infiltrated by low-grade glioma: functional outcome and oncological considerations.** *J Neurosurg* 2004;100:431–37
20. Min ZG, Rana N, Niu C, et al. **Does diffusion tensor tractography of the corticospinal tract correctly reflect motor function?** *Med Princ Pract* 2014;23:174–76
21. Kim SH, Jang SH. **Prediction of aphasia outcome using diffusion tensor tractography for arcuate fasciculus in stroke.** *AJNR Am J Neuroradiol* 2013;34:785–90
22. Hayashi Y, Kinoshita M, Nakada M, et al. **Correlation between language function and the left arcuate fasciculus detected by diffusion tensor imaging tractography after brain tumor surgery.** *J Neurosurg* 2012;117:839–43
23. Henning Stieglitz L, Seidel K, Wiest R, et al. **Localization of primary language areas by arcuate fascicle fiber tracking.** *Neurosurgery* 2012; 70:56–64; discussion 64–65
24. Li Z, Peck KK, Brennan NP, et al. **Diffusion tensor tractography of the arcuate fasciculus in patients with brain tumors: comparison between deterministic and probabilistic models.** *J Biomed Sci Eng* 2013;6:192–200
25. Roux FE, Boulanaour K, Ranjeva JP, et al. **Cortical intraoperative stimulation in brain tumors as a tool to evaluate spatial data from motor functional MRI.** *Invest Radiol* 1999;34:225–29
26. Cosgrove GR, Buchbinder BR, Jiang H. **Functional magnetic resonance imaging for intracranial navigation.** *Neurosurg Clin N Am* 1996;7:313–22
27. Mueller WM, Yetkin FZ, Hammeke TA, et al. **Functional magnetic resonance imaging mapping of the motor cortex in patients with cerebral tumors.** *Neurosurgery* 1996;39:515–20; discussion 520–21
28. Fridriksson J, Guo D, Fillmore P, et al. **Damage to the anterior arcuate fasciculus predicts non-fluent speech production in aphasia.** *Brain* 2013;136:3451–60
29. Leclercq D, Duffau H, Delmaire C, et al. **Comparison of diffusion tensor imaging tractography of language tracts and intraoperative subcortical stimulations.** *J Neurosurg* 2010;112:503–11
30. Westin CF, Maier SE, Mamata H, et al. **Processing and visualization for diffusion tensor MRI.** *Med Image Anal* 2002;6:93–108
31. Sternberg EJ, Lipton ML, Burns J. **Utility of diffusion tensor imaging in evaluation of the peritumoral region in patients with primary and metastatic brain tumors.** *AJNR Am J Neuroradiol* 2014; 35:439–44
32. Kinoshita M, Nakada M, Okita H, et al. **Predictive value of fractional anisotropy of the arcuate fasciculus for the functional recovery of language after brain tumor resection: a preliminary study.** *Clin Neurol Neurosurg* 2014;117:45–50

Hyperintense Dentate Nuclei on T1-Weighted MRI: Relation to Repeat Gadolinium Administration

M.E. Adin, L. Kleinberg, D. Vaidya, E. Zan,  S. Mirbagheri, and  D.M. Yousem

ABSTRACT

BACKGROUND AND PURPOSE: A hyperintense appearance of the dentate nucleus on T1-weighted MR images has been related to various clinical conditions, but the etiology remains indeterminate. We aimed to investigate the possible associations between a hyperintense appearance of the dentate nucleus on T1-weighted MR images in patients exposed to radiation and factors including, but not limited to, the cumulative number of contrast-enhanced MR images, amount of gadolinium administration, dosage of ionizing radiation, and patient demographics.

MATERIALS AND METHODS: The medical records of 706 consecutive patients who were treated with brain irradiation at The Johns Hopkins Medical Institutions between 1995 and 2010 were blindly reviewed by 2 readers.

RESULTS: One hundred eighty-four subjects were included for dentate nuclei analysis. Among the 184 subjects who cumulatively underwent 2677 MR imaging studies following intravenous gadolinium administration, 103 patients had hyperintense dentate nuclei on precontrast T1-weighted MR images. The average number of gadolinium-enhanced MR imaging studies performed in the group with normal dentate nuclei was significantly lower than that of the group with hyperintense dentate nuclei. The average follow-up time was 62.5 months. No significant difference was observed between hyperintense and normal dentate nuclei groups in terms of exposed radiation dose, serum creatinine and calcium/phosphate levels, patient demographics, history of chemotherapy, and strength of the scanner. No dentate nuclei abnormalities were found on the corresponding CT scans of patients with hyperintense dentate nuclei ($n = 44$). No dentate nuclei abnormalities were found in 53 healthy volunteers.

CONCLUSIONS: Repeat performance of gadolinium-enhanced studies likely contributes to a long-standing hyperintense appearance of dentate nuclei on precontrast T1-weighted-MR images.

ABBREVIATIONS: CEMRI = contrast-enhanced MRI; DN = dentate nucleus; HDN = hyperintense appearance of the dentate nucleus; NDN = normal dentate nucleus; MFS = magnetic field strength of the scanner; p 25 = 25th percentile; p75 = 75th percentile; RD = radiation dose; RT = radiation therapy

A hyperintense appearance of the dentate nucleus (HDN) on precontrast T1-weighted MR imaging has been reported to be related to various clinical conditions. There is no consensus about the underlying etiology, and the mechanism and clinical implications remain poorly understood. A number of variables may have direct or indirect effect on the dentate nucleus (DN). Among those factors, radiation therapy (RT) has well-known short-term and long-term effects on the CNS.¹ RT is reported to

cause calcification in brain tissue.^{2,3} A retrospective study conducted on pediatric patients suggested that the DN is particularly sensitive to the effects of brain irradiation, leading to structural changes on DTI.⁴

Few studies in the English literature have investigated HDN on T1WI.⁵⁻⁸ The possible etiologies of HDN remain indeterminate. The appearance has been attributed to radiation therapy, the secondary-progressive subtype of MS, and, most recently, to cumulative numbers of gadolinium-enhanced MR imaging scans.^{5,6} No long-term longitudinal radiologic studies have been completed defining the radiologic course of HDN, to our knowledge. The frequency of HDN in the healthy population has not been determined because none of the existing studies included a healthy control group to provide a comparison.

The purpose of our study was to explore associations of HDN in irradiated patients with long-term follow-up MRI studies. We examined various factors including the cumulative number of

Received December 20, 2014; accepted after revision February 19, 2015.

From the Division of Neuroradiology (M.E.A., E.Z., S.M., D.M.Y.), The Russell H. Morgan Department of Radiology and Radiological Science; Department of Radiation Oncology and Radiation Molecular Sciences (L.K.); and Johns Hopkins Bloomberg School of Public Health (D.V.), The Johns Hopkins Medical Institutions, Baltimore, Maryland.

Please address correspondence to Mehmet Emin Adin, MD, Johns Hopkins Medical Institutions, 600 N. Wolfe St. Phipps B100, Baltimore, MD 21287; e-mail: emin.adin@gmail.com

<http://dx.doi.org/10.3174/ajnr.A4378>

gadolinium-enhanced MR images, total amount of gadolinium administration, different commercial gadolinium agents, dosage of therapeutic ionizing radiation, histology of underlying brain neoplasm, calcium/phosphate level, creatinine levels, magnetic field strength of the scanner (MFS), patient demographics, and chemotherapy exposure, by using a large cohort with retrospective evaluation of long-term longitudinal follow-up brain MR imaging studies.

MATERIALS AND METHODS

We retrospectively reviewed the medical records of 706 consecutive patients who were treated with brain irradiation for primary brain neoplasms at The Johns Hopkins Medical Institutions between June 1995 and January 2010. The institutional review board approved our study in compliance with the Health Insurance Portability and Accountability Act and waived informed consent. We reviewed clinical notes, discharge summaries, operative notes, radiologic studies, RT summaries, and prior studies performed at outside institutions, when available. In a subset group, we investigated whether there was a threshold value of gadolinium administration before HDN is evident and whether there is a significant difference among gadolinium agents used during the follow-up. We excluded all cases that lacked the exact dosage and gadolinium agent information. In this group, for the same reason, we excluded cases with outside studies for which such information was not available.

Radiologic interpretations for all available MR images for all subjects were made independently by 2 radiologists who were blinded to clinical diagnoses and treatment protocols. A determination of HDN was made on the basis of the qualitative comparison of the signal intensity of the middle cerebellar peduncle versus the DN on T1WI, because white matter tracts (middle cerebellar peduncle) are typically brighter than gray matter nuclei in the normal state on T1WI. Once HDN was determined for a subject, comparative assessment of prior studies was done to detect the first appearance of HDN, and follow-up studies were reviewed to look for its disappearance with time. Any disagreement between readers regarding final conclusions was resolved by discussion and consensus. The senior author (D.M.Y.), who has 25 years' experience, was used as the tiebreaker when there were ambiguities as to the signal intensity of the DN. No κ tests were performed because there were only 9 scans of all MR imaging studies that required such a review for signal intensity. CT scans of patients demonstrating HDN were also reviewed by using the same methodology ($n = 54$). CT studies with severe artifactual degradation in the posterior fossa and those that were performed only after iodine enhancement were excluded ($n = 10$).

The MFS was noted for each study to investigate its influence on the bright appearance of the DN. RT was classified according to site, dose, and number of fractions applied in each individual. Approximate radiation exposure to the DN for each subject was quantitatively calculated and depicted by color isodose lines applied to multiplanar CT and MR imaging of each individual's RT therapy plan. The treatment plans were created by using the Pinnacle³ Planning system (Philips Healthcare, Best, the Netherlands), Leksell GammaPlan (Elekta Instruments, Stockholm, Sweden), Brainlab (Brainlab, Feldkirchen, Germany), or Multi-

plan (Accuray, Sunnyvale, California). The radiation dose (RD) and techniques were specific to the patients' illnesses and included stereotactic single treatment or hypofractionated radiosurgery plans for acoustic neuroma or meningioma of 1200–1600 cGy in a single fraction or 2500 cGy hypofractionated for 5 days, delivered with a dose distribution tightly conforming to the abnormality. Patients with meningiomas or gliomas were treated to wider areas of normal-appearing brain, and for larger or infiltrating tumors, 4500–6000 cGy was delivered during 25–33 treatment days by 3D and intensity-modulated treatment approaches. The radiation treatment plan, containing isodose lines pictorially demonstrating the radiation dose distributed throughout the brain, was used to determine a quantitative value of the dose delivered to the DN. In general, there was not specific quantification or depiction of the RD for areas of the brain receiving <20% of the dose prescribed to the tumor, and this region was considered outside the radiated brain. If the DN was out of the region of the brain receiving >20% of the dose targeted at the tumor, an approximate value according to the total RD was recorded. These values were accepted as negligible in amplitude and were censored in statistical analyses.

Underlying brain tumors were classified according to their histologic type. Patient demographics and serum calcium phosphate levels at the time of detection of HDN were also detailed. Chemotherapy regimen, if any, was also investigated.

We excluded the following: patients with no MR images available in the radiology archive ($n = 458$), MR imaging studies degraded with severe artifacts, a surgical cavity, or any type of posterior fossa lesion that obscured thorough examination of the DN ($n = 23$; 21 adult and 2 pediatric cases), patients with hepatic dysfunction ($n = 1$), patients with a history of total parenteral nutrition and/or manganese intake ($n = 3$), and patients who did not have MR imaging available after brain irradiation ($n = 37$). All studies were performed by using either 1.5T (Magnetom Avanto and Magnetom Espree; Siemens, Erlangen, Germany; Intera and Achieva; Philips Healthcare; and Signa; GE Healthcare, Milwaukee, Wisconsin) or 3T (Verio and Skyra; Siemens; and Achieva; Philips Healthcare) MR imaging machines. The T1WI used one of the following: 1) an MPRAGE pulse sequence with 8°–9° flip angle and TR, 1900–2200 ms; TE, 2–5 ms; 2) a spin-echo pulse sequence with TR, 400–600 ms; TE, 2–20 ms; or 3) a T1-weighted FLAIR sequence with TR, 2000 ms; TI, 860 ms; and TE, 8–12 ms. No specific methodology was used to enroll subjects for either 1.5T or 3T scanners; however, the number of 1.5T studies exceeded that of 3T scans because the institution did not purchase 3T scanners until the most recent 10 years and the study spanned 1995–2010. In our institution, and thus in the present study, we used almost exclusively Magnevist (gadopentetate dimeglumine; Bayer HealthCare Pharmaceuticals, Wayne, New Jersey) for contrast-enhanced MR imaging (CEMRI) in subjects with normal renal function and without known Magnevist contrast reactions. Omniscan (gadodiamide; GE Healthcare, Piscataway, New Jersey), MultiHance (gadobenate dimeglumine; Bracco Diagnostics, Princeton, New Jersey), ProHance (gadoteridol; Bracco Diagnostics), OptiMARK (gadoversetamide; Mallinckrodt, St. Louis, Missouri), and Gadavist (gadobutrol; Bayer Schering Pharma, Berlin, Germany) were other agents used in a small proportion of the

CEMRI scans. In 113 cases, all individual consecutive studies were performed by using Magnevist (gadopentetate dimeglumine). In most of the remaining cases, different combinations of gadolinium molecules were injected with an unevenly distributed dosage. The renal function of subjects was evaluated by using the most recent serum creatinine levels at the time of the relevant MR imaging scan, and the estimated glomerular filtration rate was calculated when possible.

To investigate the incidence of HDN on T1WI in the general population and justify the qualitative methodology, we recruited a control group consisting of 53 healthy volunteers (age range, 22–75; mean age, 41.9 ± 11.8 years; 15 women and 38 men). None of the control group participants underwent prior CEMRI scanning of any body part. The total number of MR imaging scans in the control group was 133 (mean, 2.5 ± 2.3). MPRAGE (either 1.5T Magnetom Avanto and Magnetom Espree [Siemens] or 3T Verio and Skyra [Siemens]) was used in evaluating the DN in 52 control subjects, and 3D fast echo-spoiled gradient echo (1.5T Signa; GE Healthcare) was used in 1 control subject. We qualitatively compared the signal intensities of the DN and middle cerebellar peduncle by using ROI measurement in this group. None of the control group participants underwent cranial CT imaging.

For statistical analyses, demographic, clinical, laboratory, and outcome measures were tabulated in 2 groups: those with normal

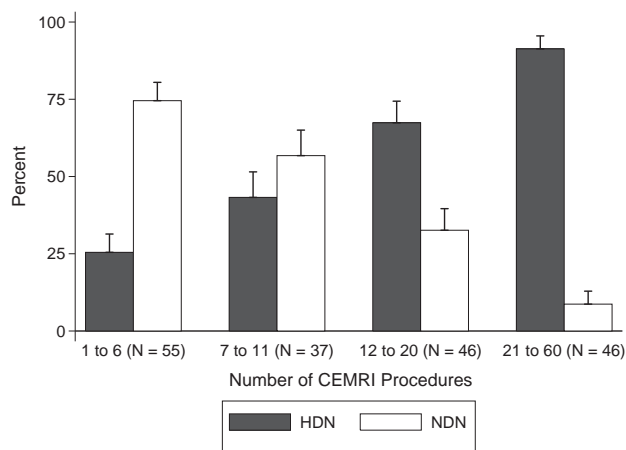


FIG 1. Graph shows the number of contrast-enhanced MR imaging scans divided into 4 subgroups for both the HDN and NDN groups. The likelihood of developing HDN significantly increases in those with a history of >6 CEMRI scans.

Table 1: Demographics and diagnoses of the pediatric age group tabulated as NDN versus HDN^a

Variable/Group	NDN (n = 5) (%)	HDN (n = 15) (%)
Race (white versus nonwhite)	3 W (100)	11 W (73), 4 NW (27)
Sex (female vs male)	3 F (60), 2 M (40)	5 F (33), 10 M (67)
Total RT dose mean (SD) (cGy)	5628 (222)	5196 (680)
Anaplastic astrocytoma	1 (20.0)	1 (6.7)
Astrocytoma	0 (0.0)	3 (20.0)
Astrocytoma, pilocytic	1 (20.0)	2 (13.3)
Desmoplastic nodular medulloblastoma	0 (0.0)	1 (6.7)
Ependymoma	1 (20.0)	2 (13.3)
Glioma, malignant	1 (20.0)	0 (0.0)
Medulloblastoma	1 (20.0)	5 (33.3)
Primitive neuroectodermal tumor	0 (0.0)	1 (6.7)

Note:—W indicates white; NW, nonwhite.

^aNote a significantly higher HDN percentage compared with the adult population.

dentate nuclei (NDN) and those with HDN. Categorical variables were tabulated as number (percentage within group), and continuous variables were tabulated as median (25th percentile [p25] to 75th percentile [p75]). Group differences were tested by using χ^2 or Fisher exact tests (if cell counts were low) for categorical variables and nonparametric rank sum tests for continuous variables. The variable specific dose was left-censored at 500 U when the DN was located beyond the outer dose lines representing the lowest amount of radiation, generally <20% of the RD prescribed to the tumor, which is considered to have a minimal risk of causing toxicity or tissue injury/side effects. Rank sum statistics were conservative for this variable because the median in both groups lay in the censored range. We plotted the percentage of individuals with HDN versus quartiles of the CEMRI number as a bar chart along with their 95% confidence intervals (Fig 1). We performed logistic regression analyses for HDN versus NDN as the dependent variable with the number of CEMRIs as the independent variable adjusted for age, sex, and race (classified as white versus nonwhite). The variable “total number of CEMRI” was highly skewed and not normally distributed. Because a few individuals received high numbers of CEMRIs, we logarithmically transformed this variable to limit the undue influence of these high numeric values on the regression results.

RESULTS

We evaluated 184 subjects in this study (83 females, 101 males). The ages of subjects ranged from 3 to 73 years (mean, 43.3 ± 16.8 years). Twenty subjects were younger than 18 years of age (Table 1). Among the 184 subjects who altogether underwent 2677 MR imaging studies (mean, 14.55; range, 1–60) following IV gadolinium administration, 103 (55.9%) patients showed HDN on T1WI. The estimated glomerular filtration rate was measured in 84 subjects and was 60 mL/min per 1.73 m² in all subjects. Of these, 25 had NDN, and 59, HDN. The upper normal limit of the creatinine value was accepted as 1.1 mg/dL. In only 3 cases was the creatinine value >1.1 mg/dL (range, 0.2–1.4 mg/dL). The median (p25 to p75) serum creatinine value was 0.7 (0.5–0.8) for NDN (56 individuals) and 0.65 (0.–0.8) for HDN (92 individuals). The rank sum test *P* value for the difference between groups was .99.

Strong Impact of the Number of CEMRIs and Volume of Gadolinium Administered

The average number of CEMRIs for the NDN group was significantly lower than that of HDN group (median [p25 to p75] for NDN, 6 [4.0–11.0]; range, 1–25; and median [p25 to p75] for HDN, 18 [10.0–26.0]; range, 2–60; *P* < .001). The logistic regression model was used to assess the impact of factors that may relate to HDN on T1WI. A strong association was found between the total number of contrast-enhanced MR imaging studies and the existence of HDN on T1WI. After we adjusted for age, sex, nonwhite race, and follow-up time in logistic regression, doubling the number

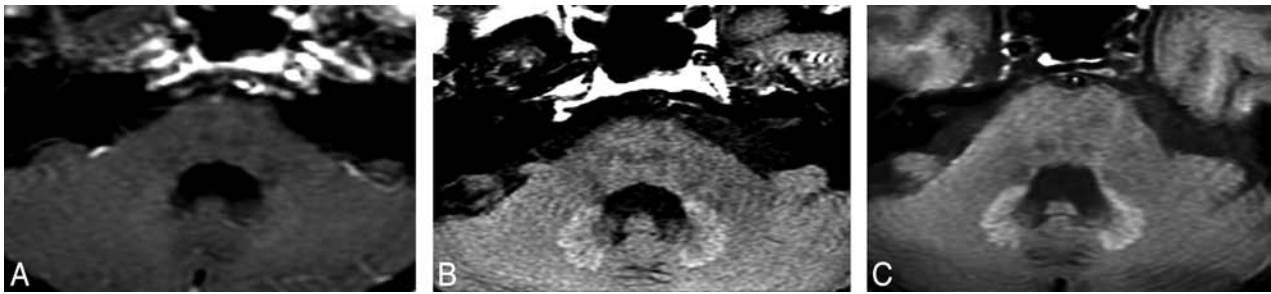


FIG 2. HDN on axial T1WI of a subject who underwent 25 CEMRI scans and 5400-cGy RT for pilocytic astrocytoma originating from the optic nerve. DN was unremarkable on the CT scan (not shown here) of this particular case. Initial HDN (A) becomes more obvious on follow-up studies performed 5 (B) and 8 (C) years after the first study with positive findings. Images A and B were obtained from 1.5T and C was obtained from 3T scanners. This individual underwent 12 CEMRIs during the follow-up.

of contrast-enhanced studies was associated with a 2.92-fold odds of having HDN ($P < .001$). The adjusted odds of HDN were estimated to be 12.3 times higher in subjects who underwent >20 enhanced MR imaging scans compared with patients undergoing ≤ 20 scans (95% CI, 4.1–37.0).

The rank sum test was used to investigate the difference between the total volume of gadolinium administration in the HDN and NDN groups. In the HDN group, the average total amount of gadolinium administration was significantly higher than that of NDN group (NDN group: median (p25 to p75), 40.0 mL (20.0–83.0); HDN group: median (p25 to p75), 76.0 mL (31.5–120.0); P value = .032). Accordingly, the average total number of CEMRI scans before HDN become evident was significantly higher than the total number of CEMRI scans in the NDN group (NDN group: median [p25 to p75], 2.0 [1.0–5.0]; HDN group: median [p25 to p75], 5.0 [2.0–8.0]; P value = .004). We performed logistic regression with the presence of HDN as the dependent variable and (1 at a time) the log-transformed number of CEMRIs or the log-transformed total gadolinium volume as predictor variables. Every doubling of the number of CEMRIs was associated with 1.51 times higher odds of HDN (95% CI, 1.14–2.01; $P = .004$). Every doubling of the total gadolinium volume was associated with 1.33 times higher odds of HDN (95% CI, 1.02–1.73; $P = .038$). In multiple logistic regression analyses when both (log-transformed number of CEMRIs and log-transformed total gadolinium volume) were added as predictors, the log-transformed number of CEMRI scans remained statistically significant ($P = .016$). The diagnostic efficiency of the number of CEMRIs and total gadolinium dose was determined by using receiver operating characteristic analysis. After ≥ 4 CEMRI scans ($n = 137$, ROC area = 0.642, standard error = 0.046, [95% CI, 0.556–0.722]) or a total dose of 77 mL of gadolinium ($n = 137$ receiver operating characteristic area = 0.6076, standard error = 0.0485, [95% CI, 0.519–0.688]), there was a significant increase in the likelihood of developing HDN. The best averages of sensitivity and specificity were found at the thresholds of 4 and 6 CEMRIs, with the threshold of 4 having higher sensitivity but lower specificity (sensitivity, 62.5%; specificity, 61.4%) and the threshold of 6 having lower sensitivity but higher specificity (sensitivity, 46.3%; specificity, 77.2%). In sensitivity analyses, we also stratified analyses by younger than 18 years of age and equal to or older than 18 years. The point estimate of the association of the number of CEMRI

studies with HDN was similar in both children and adults. However, because of the small sample size of children ($n = 20$), this did not reach statistical significance ($P = .11$).

Follow-Up Impact

The average time interval between completion of RT and the first detection of HDN was 63 months (median [p25 to p75], 54 months [3.0–54.0 months], range, 3–324 months). The average radiologic follow-up time was 62.5 months for all subjects (median [p25 to p75] for NDN, 14 months [5.5–48.5 months]; and for HDN, 82 months [41.0–109.0 months]; range, 1–356 months, $P < .001$). For those with HDN, the mean follow-up time after the first study with positive findings was 35 months (median [p25 to p75], 23 months [9.0–60.0 months]; range, 1–139 months). Twelve cases did not have follow-up studies after the first month of detection of HDN. On follow-up, 2 cases (2.2%) reverted to a normal DN signal after being bright (after 5 and 36 months). All cases with HDN had bilateral hyperintensity initially. However, in 2 cases, the hyperintensity of 1 DN disappeared and left only a unilateral HDN at the 122nd and 134th months of follow-up. The longest follow-up of a patient who developed HDN that persisted was 11.5 years after initial detection (Fig 2).

Impact of Diagnosis Relates to Number of CEMRIs and Follow-Up Period

Various pathologic diagnoses in both the NDN and HDN groups had a distinct distribution (Table 2). The incidence of World Health Organization grades III and IV malignant tumors in the group with NDN was higher than that of the group with HDN, and this difference was statistically significant ($P < .001$). Sixty-one percent of patients were diagnosed with glioblastoma multiforme in the group with NDN, whereas this rate was only 16% in the group with HDN. Eighty percent of the patients in the group negative for HDN died during the follow-up as opposed to 58% mortality in the HDN group ($P = .002$).

No Impact of Demographic Variables

Race was classified as white versus nonwhite because of the lower representation of some races. The race of 146 subjects was white, while 38 subjects were nonwhite. The nonwhite group included 23 African Americans, 2 Asians, 2 Hispanics, and 11 other (multiracial) subjects. The race and age demographic between the NDN and HDN groups was not statistically significant ($P = .4$).

Table 2: Diagnoses of brain tumors in the group with NDN and those with HDN^a

Histology	NDN (n = 81) (%)	HDN (n = 103) (%)
Anaplastic astrocytoma	8 (9.9)	19 (18.4)
Astroblastoma	0 (0.0)	1 (1.0)
Astrocytoma	4 (4.9)	14 (13.6)
Astrocytoma, pilocytic	2 (2.5)	4 (3.9)
Desmoplastic nodular medulloblastoma	0 (0.0)	1 (1.0)
Ependymoma	4 (4.9)	5 (4.9)
Fibrillary astrocytoma	1 (1.2)	4 (3.9)
Gemistocytic astrocytoma	1 (1.2)	0 (0.0)
Giant cell glioblastoma	1 (1.2)	0 (0.0)
Glioblastoma	50 (61.7)	16 (15.5)
Glioma, malignant	4 (4.9)	7 (6.8)
Medulloblastoma	3 (3.7)	7 (6.8)
Medulloblastoma	0 (0.0)	1 (1.0)
Mixed glioma	0 (0.0)	3 (2.9)
Myxopapillary ependymoma	0 (0.0)	2 (1.9)
Oligodendroglioma	2 (2.5)	10 (9.7)
Oligodendroglioma, anaplastic	1 (1.2)	7 (6.8)
Pleomorphic xanthoastrocytoma	0 (0.0)	1 (1.0)
Primitive neuroectodermal tumor	0 (0.0)	1 (1.0)

^a Note the high percentages of glioblastoma multiforme in the NDN group.

Statistical analyses showed no relationship between HDN and variables such as sex, radiation site, creatinine levels, calcium/phosphate levels, and history of chemotherapy. Of all included cases, 84 (45.6%) subjects received chemotherapy, and there was no significant difference between the NDN and HDN groups in terms of a history of chemotherapy (46.9% for the NDN and 44.6% for the HDN group).

No Impact of MFS

The possible impact of MFS was evaluated by interpreting repeat studies on different MFSs when available. The total number of MR images investigated was 733. The MFS was 1.5T for 690 studies and 3T in the remaining 43 studies. The effect of the MFS was analyzed by the following: whether any 3T scan was performed, by the number of 3T scans performed, and by the percentage of 3T scans performed per individual. There was no statistically significant difference between the HDN and NDN groups for all 3 parameters ($P = .46, .50, \text{ and } .36$, respectively). One reader also qualitatively evaluated whether the MFS changed his final assessment of DN intensity in serial MR images with both 1.5T and 3T magnets. The MFS did not change the reader's final decision in any of the cases.

Impact of Gadolinium Agent Used

For further reliable analyses of gadolinium agents, we excluded cases that had at least 1 outside MR image and those lacking technique and dosage information in at least 1 CEMRI scan during the follow-up period ($n = 47$). One hundred thirty-seven (female, 54; male, 83) cases were therefore included in our core subset analysis. In 113 of 137 individuals who were included for subset analysis, every CEMRI study was performed using a Magnevist (gadopentetate dimeglumine) injection. In all except 1 of the remaining cases ($n = 23$), at least 1 different gadolinium molecule including Magnevist was injected during the follow-up (Table 3). Given the preponderance of Magnevist administration, we collapsed the group with "any kind of non-Magnevist usage" during the fol-

Table 3: Number of CEMRI scans, total gadolinium doses, and commercial agents one-by-one in the group with HDN and NDN with doses collapsed

Contrast Medium	NDN (n = 57)	HDN (n = 80)
No. of CEMRIs (p25 to p75) (median)	2.0 (1.0–5.0), 57	5.0 (2.0–8.0), 80
Total gadolinium (p25 to p75) (median)	40.0 (20.0–83.0), 57	76.0 (31.5–120.0), 80
Magnevist	51 (89.5)	62 (77.5)
Any non-Magnevist agent used		
No	51 (89.5)	62 (77.5)
Yes	6 (10.5)	18 (22.5)
Omniscan		
No	53 (93.0)	70 (87.5)
Yes	4 (7.0)	10 (12.5)
MultiHance		
No	53 (93.0)	75 (93.8)
Yes	4 (7.0)	5 (6.3)
ProHance		
No	57 (100.0)	78 (97.5)
Yes	0 (0.0)	2 (2.5)
OptiMARK		
No	57 (100.0)	79 (98.8)
Yes	0 (0.0)	1 (1.3)
Gadavist		
No	57 (100.0)	79 (98.8)
Yes	0 (0.0)	1 (1.3)

low-up into a single category. The Fisher exact test showed no statistically significant difference between Magnevist and non-Magnevist usage ($P = .109$).

No Impact of RT

Data records of total RDs were available for 129 (NDN: $n = 58$; HDN: $n = 71$) subjects. Of this group, specific RD exposures of the DN were retrieved for 109 subjects (NDN: $n = 52$; HDN: $n = 57$). Total RT duration and fraction data were available for 108 subjects (NDN: $n = 52$; HDN: $n = 56$). The median value of total RD exposure of the brain was higher in the NDN group than in the HDN group (median [p25 to p75] for NDN, 5940.0 cGy [5375.0–6000.0 cGy]; for the HDN group: 5400.0 cGy [5040.0–5940.0 cGy], $P = .017$). The DN was located outside the outermost circles (indicating the lowest radiation exposure) on all 3 imaging planes in 23 subjects with NDN and 25 subjects with HDN. Those cases were considered to have received a negligible amount of radiation exposure and were censored in the statistical analysis because RD could not be numerically quantified when the DN was located outside the RF (ie, the lowest circle). In cases with DN located within the colored isodose lines (ie, within the RF), the mean RDs were 3181 and 3261 cGy, respectively, for the groups with NDN and HDN (NDN: $n = 29$; HDN: $n = 32$). The mean number of fractions during RT was 31 (NDN) and 29 (HDN) days for the 2 groups. There was no statistically significant difference between 2 groups (those with NDN and HDN) on the χ^2 test for total RD, specific RD, and therapy duration ($P = .12, .86, \text{ and } .30$, respectively).

No Confounders of Calcification or Hemorrhage

The CT studies of 44 of the subjects with HDN who had CTs performed were unremarkable in terms of the appearance of the DN. Calcification and hemorrhage, common causes of T1WI hyperintensity, were excluded by these CT scans.

No HDN in Control Group

The healthy control group underwent MR imaging without contrast agent administration. None of the control group had HDN. In quantitative signal-intensity analyses, the median (p25 to p75) of the ROI value was 380.4 (354.4–407.5) for average DN intensity and 384.7 (364.9–409.9) for average middle cerebellar peduncle intensity. The rank sum test for the difference between the 2 did not reach statistical significance ($P = .46$).

DISCUSSION

In this study, analyses of multiple longitudinal MR images with long follow-up periods revealed that once HDN was evident, it was most likely to remain permanently, as long as 139 months after onset. Among various variables we investigated, our data suggest a statistically significant association between HDN and repeat CEMRI scans in patients who underwent various amounts of brain irradiation. An increase in the total number of CEMRI scans and thus total amount of gadolinium administration significantly increased the risk for developing HDN. After ≥ 4 CEMRI scans and a total dose of 77 mL of gadolinium, there was a significant increase in the likelihood of developing HDN. No significant association was found between doses of radiation exposure to DN and HDN on T1WI. Although the radiation dosing schema used differed in potential biologic impact because the total dose and number and size of fractions varied by diagnosis and tumor size, no relationship was encountered between whether a significant dose was given to the dentate nucleus and HDN. While it cannot be excluded that a subgroup of patients treated with a particular regimen might be vulnerable to such an effect, the absence of any observed association suggests that this is not the case. We also showed that the number of the subjects whose DNs were located outside the outermost RF did not significantly differ between subjects with HDN and those with NDN. Thus, the DNs do not necessarily need to be within the RF to become hyperintense on T1WI.

Gadolinium, a molecule known to induce cell damage, has been shown to deposit in normal and pathologic human tissue in different studies.⁹⁻¹² There is evidence that in individuals with a history of multiple CEMRI scans, gadolinium-based MR imaging contrast agents can deposit for up to 3 years in structures such as kidney, skin, muscle, and bone after becoming insoluble free gadolinium⁺³ as a result of transmetalation and dissociation processes.¹³ We have verified that HDN on T1WI possibly results from gadolinium deposits that can persist longer than 11 years. Different gadolinium molecules have different kinetics and thus different propensities for dechelation.¹⁴ Omniscan (gadodiamide) and Magnevist (gadopentetate dimeglumine) were used in the very first studies in the literature conducted on subjects with HDN on T1WI.^{7,8} In the present retrospective study, we primarily used Magnevist (gadopentetate dimeglumine) for CEMRI scans in subjects with normal renal function during the time of this study. Statistical analyses yielded no significant association between serum creatinine level and the development of HDN. Omniscan (gadodiamide), MultiHance (gadobenate dimeglumine), ProHance (gadoteridol), OptiMARK (gadoxetamide), and Gadavist (gadobutrol) were also used in some cases. The sample sizes of other commercial gadolinium agents were too small compared with Magnevist to make a reliable sta-

tistical analysis for individual gadolinium agents. Nevertheless, there was no statistically significant difference between the HDN incidences by using Magnevist and a combination of different gadolinium agents. We recommend further evaluation.

In the present study, we investigated the associations between an HDN and the components of RT such as total RD to brain, specific RD to the DN, and the number of fractions during RT. No statistically significant association was found between any of these variables and HDN on T1WI. These findings were contrary to what was suggested by Kasahara et al,⁷ who found a correlation between the brightness of the DN and the amount of radiation exposure. In terms of underlying brain pathologies, we found a significant difference in dispersion of histopathologic diagnoses of brain neoplasms between the group with NDN and that with HDN. Malignant tumors with low survival rates such as glioblastoma multiforme were more likely to be in the NDN group but also underwent fewer enhanced scans because of that shorter life span. During the follow-up period, the death rate was significantly higher in the NDN group compared with the HDN group. We speculate that the early death of subjects with high-grade tumors led to a decreased total number of follow-up MR imaging studies, thus the total amount of gadolinium exposure and a lower rate of HDN.

Hyperintensity on T1WI in the basal ganglia has been shown to be caused by various entities. Total parenteral nutrition supplemented with manganese has proved to cause abnormal high signal intensity at the globus pallidus on T1WI.¹⁵⁻¹⁷ It has been speculated that a hyperintense globus pallidus in patients with liver failure and significant liver collaterals is also related to the manganese accumulation in the basal ganglia by virtue of bypass conduits that skip the hepatic clearance.¹⁸ In light of these studies, we excluded patients on total parenteral nutrition therapy and those with liver failure. Iron is one of the best-known causes of T1 shortening on MR imaging along with several other substances.¹⁵⁻¹⁹ Calcium deposition in cortical and deep gray matter has also been associated with paradoxical T1 shortening on MR imaging.²⁰ None of our patients had a history of iron metabolism disorder. We did not find a statistically significant relationship between serum calcium or phosphate levels and HDN on T1WI. RT is reported to cause calcification in brain tissue.^{2,3} However, there was no radiologic evidence of DN calcium accumulation on CT examinations of subjects included in our study.

Prior studies showed that the MFS may contribute to contrast differences between brain structures, which could have affected the appreciation of signal alteration.²¹ In the present study, we found no significant difference among the scanners with different MFSs in qualitatively evaluating the appearances of DN on T1WI. There was also no statistically significant difference between scanner strengths (1.5T and 3T) in terms of HDN incidence. Most of our patients underwent CEMRI with a 1.5T scanner because the present study extended back to 1995.

In the English literature, few studies have investigated HDN on T1WI, and each drew different conclusions for possible etiologies.⁵⁻⁸ Roccaglitia et al⁸ reported a higher incidence of HDN on T1WI in a subset of patients with secondary-progressive MS compared with 2 other groups comprising patients with relapsing-remitting and primary-progressive MS subtypes. In a study conducted on 362 adult patients, Kasahara et al⁷ considered the

relationship between T1 hyperintensity in DN and variables such as brain irradiation, multiple sclerosis, and liver dysfunction. They found a significant association between brain irradiation history and T1 hyperintensity in DN. However, details about interaction or correlation between whole- and partial-brain irradiation, if any, were not discussed in these studies, and they did not look at the number of gadolinium-enhanced MR imaging examinations as a variable. Kanda et al⁶ compared subjects who underwent at least 6 CEMRI scans with subjects who underwent at least 6 unenhanced MR imaging scans and found a significant association between T1 hyperintensity of GP and DN and the total number of CEMRIs. Most recently Errante et al⁵ replicated the same technique with Kanda et al, excluding the globus pallidus, and reinforced the findings of Kanda et al. They supported the idea of a strong association of the total number of gadolinium administrations with increased T1 shortening in the human DN by showing a linear regression model in cases with repeat CEMRI scans in their retrospective study.⁷

The lack of a histologic examination and thus a molecular investigation of DN was the main limitation of our observational study. Although in receiver operating characteristic analyses, 4 CEMRI scans were significantly associated with a higher percentage of HDN, we did not detect an absolute threshold for the number of CEMRI scans resulting in HDN. Magnevist was administered in all scans in a vast majority of our subjects. A combination of different agents was used during the follow-up scans in the remainder of the subjects. Therefore, further studies with evenly distributed commercial gadolinium molecules are needed to reliably compare the association of HDN and other gadolinium molecules. Given the retrospective design of our study, the time intervals between studies and the time interval between the last day of RT and the first MR imaging scan and/or first detection of HDN could not be adjusted. This situation resulted in different follow-up times and thus variable timing of the detection of HDN. Because the follow-up period was longer than a decade for some instances, body mass index was not evaluated to prevent the potential interactions of body weight fluctuations in run-time. Because this was a retrospective, observational, radiologic study, we did not seek the clinical consequences of HDN. Our goal was to elucidate an imaging finding, not its clinical significance.

CONCLUSIONS

Our study revealed that repeat performance of CEMRI studies in irradiated subjects contributes to a hyperintense appearance of the DN on T1WI. This appearance may be related to the accumulation of gadolinium in the DN. Other variables that could be associated with HDN demonstrated no significant effect on the DN appearance in this retrospective study.

Disclosures: Dhananjay Vaidya—UNRELATED: Consultancy: Consumable Science, Comments: included consultancy regarding the filing of a pending patent; Grants/Grants Pending: National Institutes of Health.* David M. Yousem—UNRELATED: Expert Testimony: consultations on medicolegal cases; Payment for Lectures (including service on Speakers Bureaus): American College of Radiology Education Center*; Royalties: Elsevier for 3 books; Payment for Development of Educational Presentations: CMEInfo.com for Continuing Medical Education.* *Money paid to the institution.

REFERENCES

- Jain R, Robertson PL, Gandhi D, et al. Radiation-induced cavernomas of the brain. *AJNR Am J Neuroradiol* 2005;26:1158–62
- Lee KF, Suh JH. CT evidence of grey matter calcification secondary to radiation therapy. *Comput Tomogr* 1977;1:103–10
- Valk PE, Dillon WP. Radiation injury of the brain. *AJNR Am J Neuroradiol* 1991;12:45–62
- Perreault S, Lober RM, Cheshier S, et al. Time-dependent structural changes of the dentatohalamic pathway in children treated for posterior fossa tumor. *AJNR Am J Neuroradiol* 2014;35:803–07
- Errante Y, Cirimele V, Mallio CA, et al. Progressive increase of T1 signal intensity of the dentate nucleus on unenhanced magnetic resonance images is associated with cumulative doses of intravenously administered gadodiamide in patients with normal renal function, suggesting dechelation. *Invest Radiol* 2014;49:685–90
- Kanda T, Ishii K, Kawaguchi H, et al. High signal intensity in the dentate nucleus and globus pallidus on unenhanced T1-weighted MR images: relationship with increasing cumulative dose of a gadolinium-based contrast material. *Radiology* 2014;270:834–41
- Kasahara S, Miki Y, Kanagaki M, et al. Hyperintense dentate nucleus on unenhanced T1-weighted MR images is associated with a history of brain irradiation. *Radiology* 2011;258:222–28
- Roccatagliata L, Vuolo L, Bonzano L, et al. Multiple sclerosis: hyperintense dentate nucleus on unenhanced T1-weighted MR images is associated with the secondary progressive subtype. *Radiology* 2009;251:503–10
- Zhao J, Zhou ZQ, Jin JC, et al. Mitochondrial dysfunction induced by different concentrations of gadolinium ion. *Chemosphere* 2014;100:194–99
- Ray DE, Cavanagh JB, Nolan CC, et al. Neurotoxic effects of gadopentetate dimeglumine: behavioral disturbance and morphology after intracerebroventricular injection in rats. *AJNR Am J Neuroradiol* 1996;17:365–73
- Abraham JL, Thakral C. Tissue distribution and kinetics of gadolinium and nephrogenic systemic fibrosis. *Eur J Radiol* 2008;66:200–07
- Thakral C, Abraham JL. Nephrogenic systemic fibrosis: histology and gadolinium detection. *Radiol Clin North Am* 2009;47:841–53, vi–vii
- Thakral C, Alhariri J, Abraham JL. Long-term retention of gadolinium in tissues from nephrogenic systemic fibrosis patient after multiple gadolinium-enhanced MRI scans: case report and implications. *Contrast Media Mol Imaging* 2007;2:199–205
- Sieber MA, Lengsfeld P, Frenzel T, et al. Preclinical investigation to compare different gadolinium-based contrast agents regarding their propensity to release gadolinium in vivo and to trigger nephrogenic systemic fibrosis-like lesions. *Eur Radiol* 2008;18:2164–73
- Boyko OB, Burger PC, Shelburne JD, et al. Non-heme mechanisms for T1 shortening: pathologic, CT, and MR elucidation. *AJNR Am J Neuroradiol* 1992;13:1439–45
- Mirowski SA, Sartor K, Gado M. High-intensity basal ganglia lesions on T1-weighted MR images in neurofibromatosis. *AJR Am J Roentgenol* 1990;154:369–73
- Moore DF, Ye F, Schiffmann R, et al. Increased signal intensity in the pulvinar on T1-weighted images: a pathognomonic MR imaging sign of Fabry disease. *AJNR Am J Neuroradiol* 2003;24:1096–101
- Inoue E, Hori S, Narumi Y, et al. Portal-systemic encephalopathy: presence of basal ganglia lesions with high signal intensity on MR images. *Radiology* 1991;179:551–55
- Vymazal J, Righini A, Brooks RA, et al. T1 and T2 in the brain of healthy subjects, patients with Parkinson disease, and patients with multiple system atrophy: relation to iron content. *Radiology* 1999;211:489–95
- Suzuki S, Nishio S, Takata K, et al. Radiation-induced brain calcification: paradoxical high signal intensity in T1-weighted MR images. *Acta Neurochir (Wien)* 2000;142:801–04
- Fushimi Y, Miki Y, Urayama S, et al. Gray matter-white matter contrast on spin-echo T1-weighted images at 3 T and 1.5 T: a quantitative comparison study. *Eur Radiol* 2007;17:2921–25

Differentiation between Cystic Pituitary Adenomas and Rathke Cleft Cysts: A Diagnostic Model Using MRI

M. Park, S.-K. Lee, J. Choi, S.-H. Kim, S.H. Kim, N.-Y. Shin, J. Kim, and S.S. Ahn



ABSTRACT

BACKGROUND AND PURPOSE: Cystic pituitary adenomas may mimic Rathke cleft cysts when there is no solid enhancing component found on MR imaging, and preoperative differentiation may enable a more appropriate selection of treatment strategies. We investigated the diagnostic potential of MR imaging features to differentiate cystic pituitary adenomas from Rathke cleft cysts and to develop a diagnostic model.

MATERIALS AND METHODS: This retrospective study included 54 patients with a cystic pituitary adenoma (40 women; mean age, 37.7 years) and 28 with a Rathke cleft cyst (18 women; mean age, 31.5 years) who underwent MR imaging followed by surgery. The following imaging features were assessed: the presence or absence of a fluid-fluid level, a hypointense rim on T2-weighted images, septation, an off-midline location, the presence or absence of an intracystic nodule, size change, and signal change. On the basis of the results of logistic regression analysis, a diagnostic tree model was developed to differentiate between cystic pituitary adenomas and Rathke cleft cysts. External validation was performed for an additional 16 patients with a cystic pituitary adenoma and 8 patients with a Rathke cleft cyst.

RESULTS: The presence of a fluid-fluid level, a hypointense rim on T2-weighted images, septation, and an off-midline location were more common with pituitary adenomas, whereas the presence of an intracystic nodule was more common with Rathke cleft cysts. Multiple logistic regression analysis showed that cystic pituitary adenomas and Rathke cleft cysts can be distinguished on the basis of the presence of a fluid-fluid level, septation, an off-midline location, and the presence of an intracystic nodule ($P = .006, .032, .001, \text{ and } .023$, respectively). Among 24 patients in the external validation population, 22 were classified correctly on the basis of the diagnostic tree model used in this study.

CONCLUSIONS: A systematic approach using this diagnostic tree model can be helpful in distinguishing cystic pituitary adenomas from Rathke cleft cysts.

ABBREVIATIONS: AUC = area under the curve; RCC = Rathke cleft cyst

Pituitary adenoma is a benign neoplasm that arises from the adenohypophysis and is the most common intrasellar pathology, accounting for 10%–15% of all intracranial neoplasms.^{1,2} Typical imaging findings of an uncomplicated pituitary adenoma include slow enhancement compared with that of the pituitary gland, lateral deviation of the infundibulum, and isointense signal intensity relative to gray matter on T1-weighted imaging.³ Intratumoral hem-

orrhage and ischemic infarction are common with larger pituitary adenomas, which may result in hemorrhagic or cystic changes or both, leading to various signal intensities on MR imaging.⁴⁻⁸

Rathke cleft cyst (RCC) is a benign epithelial cyst believed to originate from the remnants of the Rathke pouch.⁹ Typical imaging findings include a nonenhancing, noncalcified, intrasellar/suprasellar cyst with an intracystic nodule.⁹⁻¹² Depending on its cystic content and the presence of an associated intracystic nodule, an RCC may show various signal intensities on both T1- and T2-weighted images.¹³⁻¹⁵ More specifically, T1 hyperintensity and T2 hypointensity of an RCC associated with a high intracystic protein content can mimic cystic pituitary adenoma with hemorrhage, which makes imaging diagnosis of a cystic pituitary adenoma or an RCC a challenge.

Preoperative differentiation between a cystic pituitary adenoma and an RCC is important for treatment planning.¹⁶⁻¹⁸ Par-

Received December 2, 2014; accepted after revision February 24, 2015.

From the Department of Radiology, Research Institute of Radiological Science (M.P., S.-K.L., J.K., S.S.A.), Biostatistics Collaboration Unit, Medical Research Center (J.C.), and Departments of Neurosurgery (S.-H.K.) and Pathology (S.H.K.), Yonsei University College of Medicine, Seoul, South Korea; and Department of Radiology (N.-Y.S.), Ewha Womans University School of Medicine, Seoul, South Korea.

Please address correspondence to S.S. Ahn, MD, PhD, Department of Radiology, Research Institute of Radiological Science, Yonsei University College of Medicine, 50 Yonsei-ro, Seodaemun-gu, 120–752 Seoul, South Korea; e-mail: sungsoo@yuhs.ac

<http://dx.doi.org/10.3174/ajnr.A4387>

Table 1: Demographic and clinical data of patients with a cystic pituitary adenoma or Rathke cleft cyst

Patient Data	Cystic Pituitary Adenomas (n = 54)	Rathke Cleft Cysts (n = 28)	P Value ^a
Age (mean ± SD), y	37.7 ± 11.4	31.5 ± 12.7	.026
Sex, male/female ratio	14:40	10:18	.362
Size of tumor/cyst (mean ± SD), mm	18.4 ± 7.9	19.2 ± 5.5	.644
Suprasellar extension, n (%)	31 (57.4)	19 (67.8)	.358
Abnormal hormone level, n (%)	49 (90.7)	25 (89.3)	.833
Symptoms, n (%)			
Local mass effect	11 (20.4)	13 (46.3)	.014
Hormonal symptoms	18 (33.3)	8 (28.6)	.660
Headache	14 (25.9)	7 (25.0)	.927

Note.—SD indicates standard deviation.

^a From the χ^2 test.

tial resection of the wall and evacuation of cyst contents are sufficient for an RCC, whereas a cystic pituitary adenoma may require total resection, not only to relieve mass effect but also to correct hormone excess.^{9,19-21} Unnecessary surgical excision of an RCC may lead to serious complications, such as CSF leaks, infection, and hypothalamic injury, though the incidences thereof are very low.^{21,22} Thus, obtaining the correct preoperative diagnosis with which to determine the proper surgical indication and to plan the optimal surgical procedure is a major concern for neurosurgeons.⁹ To date, several characteristic MR imaging appearances of pituitary adenomas and RCCs have been reported,^{2,9,12,20,23-25} but there are some cases for which the diagnoses are inconclusive when 1 or 2 imaging findings are used, and none of the studies has systemically analyzed the MR imaging appearances of cystic pituitary adenomas to differentiate them from RCCs. Therefore, we evaluated the diagnostic potential of a multifactor analysis of MR imaging findings and developed a diagnostic tree model to increase the diagnostic accuracy in differentiating cystic pituitary adenomas and RCCs before surgery.

MATERIALS AND METHODS

Study Population

This retrospective study was approved by the Yonsei University Health System institutional review board, and the requirement for informed consent was waived. We retrospectively reviewed preoperative MR imaging and electronic medical records. Among 891 patients with a sellar mass who underwent surgery between August 2007 and July 2013, we identified 82 patients (24 men and 58 women; mean [± standard deviation] age, 35.6 ± 12.1 years) with a lack of solid enhancement or thin-rim enhancement (<2 mm) on preoperative MR imaging. Among them, 54 patients (14 men and 40 women; mean age, 37.7 ± 11.4 years) were diagnosed with a pituitary adenoma and 28 patients (10 men and 18 women; mean age, 31.5 ± 12.7 years) were diagnosed with an RCC on the basis of histopathology reports. None of the included pituitary adenomas involved the cavernous sinus. Craniopharyngioma was not included for analysis, because only 3 patients presented with a cystic mass without a solid enhancing portion during the same period, and 2 of them had typical imaging findings of craniopharyngioma. Those 54 patients with a pituitary adenoma underwent surgery because of medication treatment failure (n = 10), local mass effect (n = 11), hormonal symptoms (n = 18), headache (n = 14), or rapid size increase (n = 1). Twenty-eight patients with an RCC underwent surgery because of local mass effect (n =

13), hormonal symptoms (n = 8), or headache (n = 7). Laboratory and immunohistochemical findings (available for 26 patients) revealed that 46 patients had a hormonally functioning adenoma with prolactin (32 cases), growth hormone (8 cases), adrenocorticotrophic hormone (5 cases), or thyroid-stimulating hormone (1 case). In the other 8 patients, the adenoma was nonfunctioning, with or without hypopituitarism. The characteristics of the 82 patients are shown in Table 1.

Validation Population

For validation, an additional 24 patients (10 men and 14 women; mean age, 38.8 ± 15.8 years) with a cystic pituitary adenoma (n = 16) or an RCC (n = 8) histopathologically confirmed between August 2013 and August 2014 were subsequently included in the study.

Data Acquisition

Each of the preoperative MR imaging examinations of the sella was performed with a 3T MR unit using an 8-channel head coil (Achieva; Philips Healthcare, Best, the Netherlands). The following pulse sequences were acquired: sagittal T2-weighted imaging (TE, 3000 ms; TR, 80 ms; section thickness, 3 mm; matrix, 400 × 316; and FOV, 23 × 23 cm), sagittal T1-weighted imaging (TR, 2000 ms; TE, 10 ms; section thickness, 2–3 mm; matrix, 256 × 200; and FOV, 23 × 23 cm), axial T2-weighted imaging (TR, 3000 ms; TE, 80 ms; section thickness, 5 mm; matrix 400 × 309; and FOV, 23 × 23 cm), and coronal T2-weighted imaging (TR, 2129.8 ms; TE, 90 ms; section thickness, 1–2 mm; matrix, 368 × 368; and FOV, 18 × 18 cm). Five coronal T1-weighted dynamic images (TR, 230 ms; TE, 15 ms; section thickness, 2–3 mm; matrix, 352 × 351; and FOV, 20 × 20 cm) were obtained every 25–30 seconds after an intravenous bolus injection (0.2 mL/kg) of gadolinium-based contrast (gadoterate meglumine [Dotarem; Guerbet, Aulnay-sous-Bois, France]), followed by coronal T1-weighted imaging (TR, 2000 ms; TE, 10 ms; section thickness, 2 mm; matrix, 320 × 240; and FOV, 20 × 20 cm) and sagittal T1-weighted imaging (TR, 2000 ms; TE, 10 ms; section thickness, 2 mm; matrix, 320 × 250; and FOV, 20 × 20 cm).

Image Analysis

Two radiologists (one with 5 years and one with 1 year of experience in neuroradiology) who were blinded to the final histologic diagnosis independently analyzed the imaging of each patient to document the following findings: presence of a fluid-fluid level, hypointense rim on T2-weighted images, septation, off-midline location, presence of an intracystic nodule, change in size, and change in signal intensity (Fig 1).^{2,9,12,20,23-25} The presence or absence of a fluid-fluid level was evaluated on either axial or sagittal T2-weighted images. A peripheral hypointense rim was regarded as present if the peripheral portion of a sellar lesion was lower than the signal intensity of white matter on T2-weighted images. Septation was identified on axial or coronal T2-weighted images and/or on contrast-enhanced T1-weighted images. Off-midline location was defined as lateralization of the lesion in the

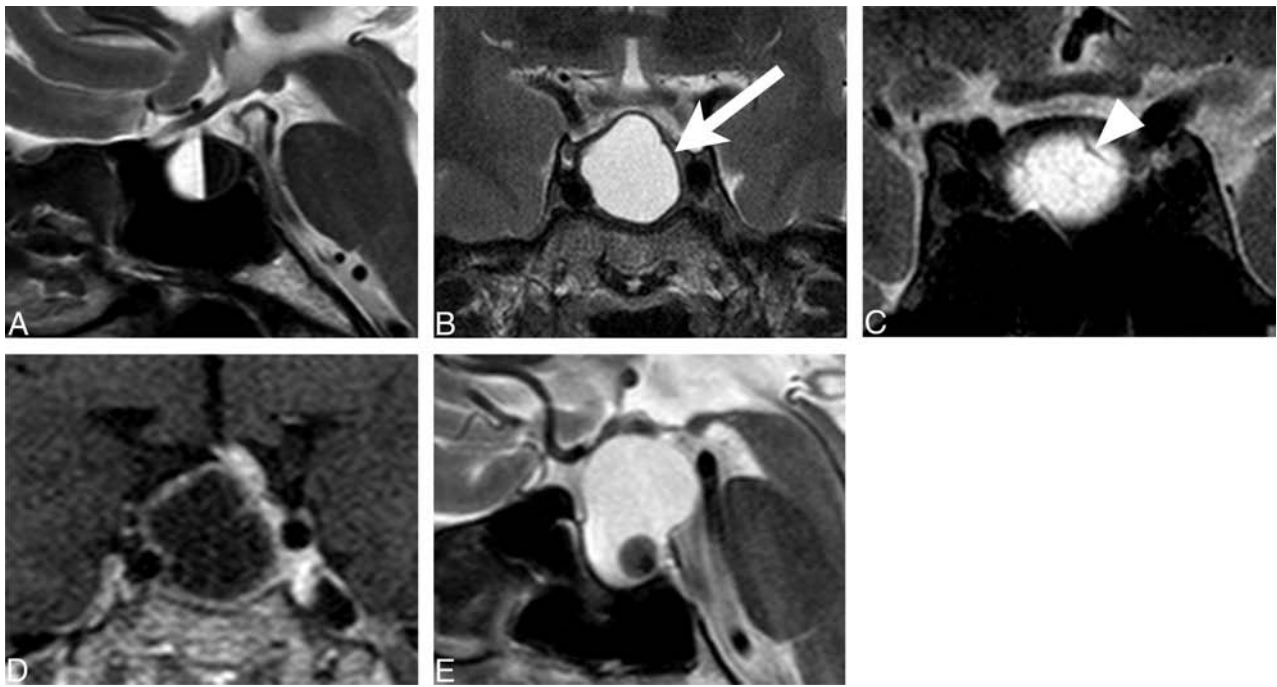


FIG 1. Typical MR features for image analysis: A, fluid-fluid level (sagittal T2-weighted image); B, peripheral hypointense rim (*arrow*) (coronal T2-weighted image); C, septation (*arrowhead*) (coronal T2-weighted image); D, off-midline location, deviating pituitary stalk (coronal contrast-enhanced T1-weighted image); and E, intracystic nodule (sagittal T2-weighted image).

sella turcica or stalk deviation by the lesion. An intracystic nodule was defined as a nodule showing various signal intensities on T1- and T2-weighted images without enhancement after contrast-medium administration. A size change (either increase or decrease) or signal change was defined as present if there was any change in size or signal intensities on T1- and T2-weighted images between the 2 preoperative MR imaging examinations, when previous MR imaging examinations were performed ($n = 78$). The median follow-up interval for all the cases was 59 days (interquartile range, 26–126 days), for adenomas ($n = 55$) it was 58 days (interquartile range, 26–154 days), and for RCCs ($n = 23$) it was 62 days (interquartile range, 27–98 days). Interobserver agreement for the imaging findings was assessed, and discordant interpretations were resolved by consensus.

For the validation group, the significant MR imaging findings in the study group were evaluated for differentiation. Two radiologists (one with 5 years and one with 1 year of experience in neuroradiology) who were blinded to the final histopathologic diagnoses performed imaging analyses on the basis of the diagnostic tree model.

Review of Imaging Reports

Each official radiologic report had been written by several neuro-radiologists with >5 years' experience in neuroradiology and was reviewed retrospectively. Final impressions of the radiologic reports were recorded to compare them with those of the diagnostic tree model in terms of diagnostic accuracy. When there were several differential diagnoses on the reports, only the first impression was used for analysis.

Statistical Analysis

Statistical analyses were performed by using the software package R version 3.0.2 (<http://www.R-project.org>) and MedCalc version 9.3.6.0 (MedCalc Software, Mariakerke, Belgium). The interobserver agreement for each imaging feature was calculated by using the κ statistic. A κ value of 0.81–1.0 indicated excellent agreement between the 2 observers, 0.61–0.80 indicated good agreement, 0.41–0.60 indicated moderate agreement, 0.21–0.40 indicated fair agreement, and 0–0.20 indicated only slight agreement. The frequencies of imaging features of cystic pituitary adenomas and those of RCCs were compared with χ^2 tests. The contribution of each imaging feature was evaluated by univariate logistic regression and a multivariable logistic regression model after a stepwise procedure was performed to differentiate cystic pituitary adenomas and RCCs. On the basis of the results of logistic regression analysis, a recursive-partitioning-tree classification algorithm was used to suggest a diagnostic tree model. Finally, the discriminatory powers of the diagnostic tree model and radiologic reports were assessed by receiver operating characteristic analysis, and the areas under the curve (AUCs) for receiver operating characteristic analysis were compared. A P value of <.05 was considered statistically significant.

RESULTS

Interobserver agreements for imaging features were good to excellent, with κ values of 0.780 for the presence of a fluid-fluid level, 0.677 for a hypointense rim on T2-weighted images (Fig 2), 1.0 for septation, 0.926 for an off-midline location, and 0.892 for the presence of an intracystic nodule.

The frequencies of MR imaging findings were significantly different between pituitary adenomas and RCCs. The presence of a fluid-fluid level, a hypointense rim on T2-weighted images, an

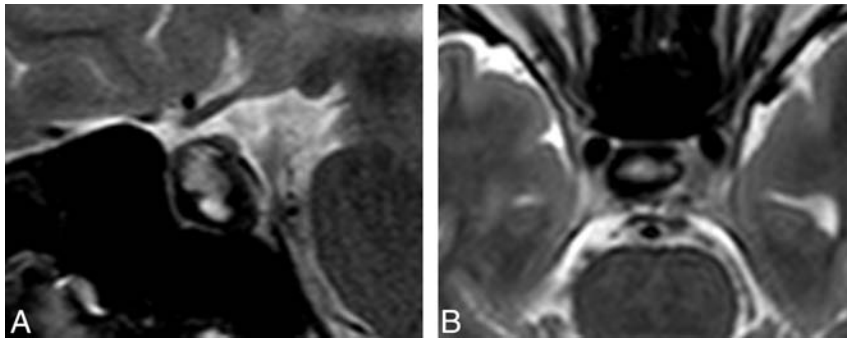


FIG 2. Representative case of discordant interpretation. A, A hypointense rim on a T2-weighted image of a 27-year-old woman with a pituitary adenoma, which was misinterpreted as a fluid-fluid level on axial T2-weighted images by one reader. B, Later, a hypointense rim on a T2-weighted image was agreed on consensually.

Table 2: MR imaging features of cystic pituitary adenomas and Rathke cleft cysts

Variable	Cystic Pituitary Adenomas (n = 54) (n [%])	Rathke Cleft Cysts (n = 28) (n [%])	P Value ^a
Fluid-fluid level	37 (68.5)	1 (3.6)	<.001
Hypointense rim on T2	41 (75.9)	6 (21.4)	<.001
Septation	21 (38.9)	1 (3.6)	.002
Off-midline location	45 (83.3)	2 (7.1)	<.001
Intracystic nodule	9 (16.7)	19 (67.9)	<.001
Size change	24 (44.4)	8 (28.6)	.212
Increase	20 (37.0)	3 (10.7)	.012
Decrease	4 (7.4)	5 (17.9)	.151
Signal change	20 (37.0)	4 (14.3)	.05

^aFrom the χ^2 test.

off-midline location, septation, and signal change of the lesion were more common with pituitary adenomas than with RCCs (Table 2). An intracystic nodule in the lesion was observed significantly more often in RCCs than in pituitary adenomas.

Receiver operating characteristic curve analyses were performed, and the following 3 variables exhibited good performances in diagnosing cystic pituitary adenomas: the presence of a fluid-fluid level (sensitivity, 68.5%; specificity, 96.4%; AUC value, 0.825), a hypointense rim on T2-weighted images (sensitivity, 75.9%; specificity, 78.6%; AUC value, 0.773), and an off-midline location (sensitivity, 83.3%; specificity, 92.9%; AUC value, 0.881). The presence of an intracystic nodule also exhibited good performance in diagnosing RCCs (sensitivity, 83.3%; specificity, 67.9%; AUC value, 0.756).

The ORs from the univariate logistic regression analysis of MR imaging variables for predicting cystic pituitary adenomas are listed in Table 3. Multiple logistic regression analysis with a stepwise procedure was performed to identify the MR imaging variables that contributed to the differentiation of cystic pituitary adenomas from RCCs. The presence of a fluid-fluid level, septation, and an off-midline location were selected as independent factors associated with cystic pituitary adenomas and the presence of an intracystic nodule as associated with RCCs. These variables and their adjusted ORs are listed in Table 3.

Using the recursive-partitioning analysis based on the classification and regression tree method,²⁶ we were able to establish a diagnostic tree model (Fig 3). The diagnostic tree model was able to correctly classify 79 (96.3%) of 82 cases in the study population

(Figs 5 and 6). In terms of diagnosing pituitary adenomas, the sensitivity and specificity of the diagnostic tree model were 98.1% and 92.9% and those of the official radiologic reports were 77.8% and 92.9%, respectively. Receiver operating characteristic curve analyses were performed to compare the AUCs between the diagnostic tree model and those of the official radiologic reports. The AUC values were 0.991 for the diagnostic tree model and 0.853 for the radiologic reports, and the difference was statistically significant ($P < .001$) (Fig 4).

The proposed diagnostic tree model was then validated on subsequent data from the 24 patients in the external-validation group. There were no significant differences between the study group and the validation group in terms of age, sex, or histopathology results ($P = .252$, $P = .119$, and $P = .762$, respectively). The imaging diagnoses made by 2 radiologists on the basis of the diagnostic tree model agreed for all the patients. Twenty-two of these 24 cases were classified correctly (91.7%) (Figs 5 and 6). One RCC was misclassified as a cystic pituitary adenoma because of septation (Fig 7), and one cystic pituitary adenoma was misclassified as an RCC because of its midline location and the absence of a fluid-fluid level and septation.

DISCUSSION

We first evaluated the diagnostic value of imaging findings for differentiating cystic pituitary adenomas and RCCs. Consistent with previous reports,^{3,8,20,27} we found that the presence of a fluid-fluid level, septation, and an off-midline location strongly favored a diagnosis of cystic pituitary adenoma over that of RCC. Conversely, the presence of an intracystic nodule was associated significantly with RCCs. On the basis of these results, we established a diagnostic tree model that increased the diagnostic accuracy for differentiating cystic pituitary adenomas from RCCs by using preoperative MR imaging. The use of this model with MR imaging findings resulted in the correct classification of >95% of the study cases and 91.7% of the validation cases. Given its availability and simplicity, we believe that this method has important clinical implications for making correct preoperative diagnoses and determining the proper treatment planning.

RCCs are sometimes indistinguishable from cystic pituitary adenomas on MR imaging, and a previous study reported that 50% of surgically proven RCCs were misdiagnosed as pituitary adenomas preoperatively because of their various signal intensities, which ranged from hypointense to hyperintense on both T1- and T2-weighted images.¹⁵ These various MR signal intensities depend on the composition of the cyst, including protein, mucopolysaccharides, and cholesterol.^{15,28} Another study reported that wall enhancement of cystic lesions may play a role in differentiating neoplastic from nonneoplastic cysts.²⁹ However, RCCs are often surrounded by the enhancing normal pituitary gland, thus mimicking wall enhancement, especially when there is a partial volume-averaging effect.¹¹ In addition, RCCs may show patchy or

Table 3: Potential predicting variables for pituitary adenomas on MR imaging using logistic regression analysis

Variable	Univariate Analysis		Multivariate Analysis ^a	
	Crude OR (95% CI)	P Value	Adjusted OR (95% CI)	P Value
Fluid-fluid level	58.76 (7.36–468.94)	<.001	165.42 (4.42–6190.89)	.006
Hypointense rim on T2	11.56 (3.86–34.65)	<.001		
Septation	17.18 (2.17–136.08)	.007	48.00 (1.39–1653.33)	.032
Off-midline location	65.0 (13.04–323.97)	<.001	71.73 (5.55–926.93)	.001
Intracystic nodule	0.09 (0.03–0.28)	<.001	0.037 (0.002–0.63)	.023
Suprasellar extension	1.63 (0.6–4.09)	.449		
Size change	2.00 (0.75–5.33)	.170		
Increase	4.52 (1.21–16.96)	.025		
Decrease	2.717 (0.67–11.07)	.163		
Signal change	3.53 (1.07–11.65)	.038		

^a Multivariate analysis after stepwise procedure.

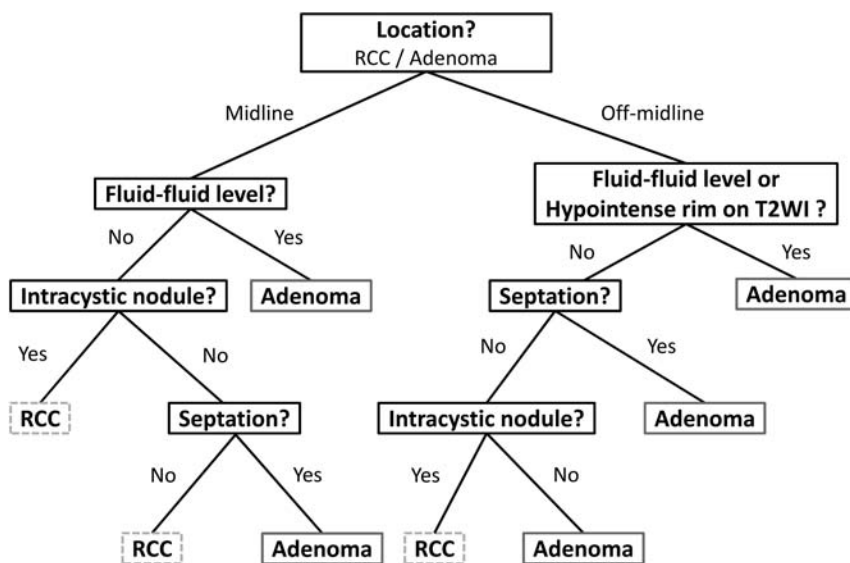


FIG 3. Diagnostic decision tree for the differentiation of cystic pituitary adenomas and Rathke cleft cysts using MR imaging.

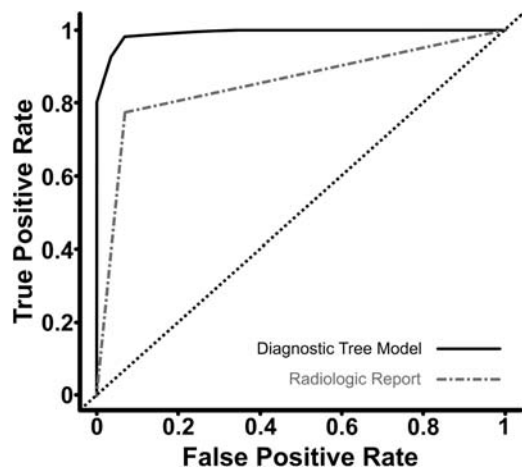


FIG 4. Receiver operating characteristic curve comparison between the diagnostic decision tree model and official radiologic report for the differentiation of cystic pituitary adenomas and Rathke cleft cysts.

ring enhancement, which can be attributed to inflammation and/or squamous metaplasia in the cyst wall.¹⁵ The presence of an intracystic nodule has been suggested as a characteristic MR imaging feature of RCCs, with an incidence of 37.5%–45%.^{9,13}

Although intracystic nodules were more common in RCCs than in cystic pituitary adenomas, we also observed intracystic nodules in pituitary adenomas (67.9% vs 16.7%, respectively). Moreover, these nodules can easily be mistaken for hemorrhage and vice versa, which makes the preoperative differentiation between RCCs and cystic pituitary adenomas problematic.³⁰

The presence of a fluid-fluid level, presumably related to intracystic hemorrhage, was significantly more common in, and had high predictive value for, cystic pituitary adenomas. Intratumoral hemorrhage in pituitary adenomas is common even without clinical symptoms.^{7,31,32} Thus, clinical symptoms themselves are not always sufficient to make a correct diagnosis of hemorrhagic adenoma. Furthermore, hemorrhagic pituitary adenomas can exhibit various signal intensities on both T1- and T2-weighted MR imaging, which makes imaging diagnoses difficult. More accurate diagnoses can be achieved by considering other imaging parameters collectively.

An off-midline location was the most important imaging finding for distinguishing pituitary adenomas from RCCs on the basis of multivariate logistic regression analysis in our study, which may be explained by their different origins.

RCCs are believed to originate from the remnants of the Rathke pouch and are located mainly in the midline of the pituitary gland.⁹ Conversely, adenomas arise from the adenohypophysis, and the 2 most common pituitary adenomas, prolactinomas and growth hormone–secreting adenomas, tend to arise laterally in the sella turcica.^{10,33} Thus, lateral bulging of the gland and displacement of the infundibulum were considered characteristic findings of pituitary adenomas.^{3,27} However, adrenocorticotropic hormone–secreting adenomas are often located at the midline, which may overlap with the location of RCCs.³³ In our study, an off-midline location alone showed high diagnostic value, but that value could be improved when combined with other imaging parameters via a diagnostic tree model.

In this study, cystic pituitary adenomas and RCCs did not have a significant size change difference. Several reports have indicated that some RCCs undergo reduction without treatment and even resolve spontaneously, which suggests that simple RCCs may be dynamic in nature.^{18,30,34} Although growth rates are variable, pituitary adenomas usually enlarge slowly over years and may also exhibit size change, even regression, accompanied by intratumoral hemorrhage and resorption.^{4,10,31} We also observed that size increases were more frequent in cystic pituitary adenomas than in RCCs, but on the basis of multivariate analysis, size in-



FIG 5. A 71-year-old female patient presented with a 21.2-mm nonenhancing intrasellar cystic lesion. The lesion was located in the midline on a coronal contrast-enhanced T1-weighted image (A), and a fluid-fluid level (B) and septation (C) were seen on sagittal and coronal T2-weighted images. This lesion was classified as a cystic pituitary adenoma on the basis of the diagnostic tree model and was finally diagnosed by histopathology as a pituitary adenoma.

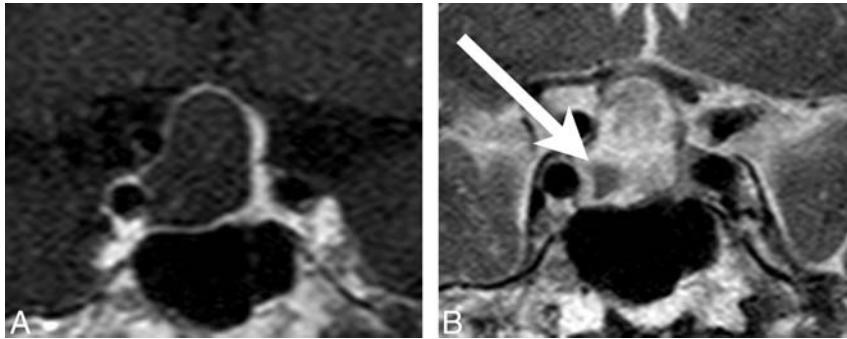


FIG 6. A 42-year-old male patient presented with a 23.8-mm nonenhancing sellar and suprasellar lesion. The cystic lesion had an off-midline location on contrast-enhanced T1-weighted imaging (A) and an intracystic nodule (arrow) showing hypointensity on coronal T2-weighted imaging (B). There was no identified fluid-fluid level or septation. Therefore, this lesion was classified as a Rathke cleft cyst on the basis of the diagnostic tree model and was diagnosed through histopathology as a Rathke cleft cyst.

creases did not have predictive value for diagnosing cystic pituitary adenomas.

Clinical findings could be important clues for making a preoperative diagnosis. However, preoperative endocrine dysfunction was reported in up to 80% of patients with an RCC, which makes diagnosis with clinical findings alone difficult.^{9,35} In our study, the incidence of hormonal symptoms was 28.6%, which was less common than in previous studies but not significantly different than that of cystic pituitary adenomas (33.3%), which supports the idea that radiologic findings are important when making a preoperative diagnosis.

Previously, T2*-weighted imaging was proposed as a potential way to detect intratumoral hemorrhage in pituitary adenomas.⁷ Another study in which diffusion-weighted MR imaging was used revealed that the ADC values of RCCs were significantly higher than those of other cystic lesions, including cystic or hemorrhagic pituitary adenomas; therefore, diffusion-weighted MR imaging may be useful for differentiating cystic lesions in the pituitary fossa.³⁶ However, these sequences are not routinely performed for standard sellar MR imaging because of susceptibility artifacts related to the skull base and, thus, were not performed in our patients. In this study, features of conventional T1- and T2-weighted MR imaging were evaluated without the need for any additional advanced imaging techniques. Our proposed diagnostic tree model with a combination of imaging features (ie, an off-midline

location, the presence of a fluid-fluid level or a hypointense rim on T2-weighted MR imaging, septation, and the presence of an intracystic nodule) is easy to use and can achieve high diagnostic performance (AUC value, 0.991), which is significantly superior to that of the original radiologic reports (AUC value, 0.853). Furthermore, it can suggest which imaging features should be considered more important than the others in differentiating cystic pituitary adenomas and RCCs. In addition, the diagnostic tree model showed high diagnostic performance in the validation group by the radiologists with 5 years or 1 year of experience, which suggests that

radiologists with less experience may also benefit from the systematic approach for differentiating cystic pituitary adenomas and RCCs.

Our study had several limitations. It was a retrospective study with a possible selection bias. We excluded pituitary adenomas with an enhancing solid portion, which may indicate that these results cannot be generalized to all pituitary adenomas and RCCs that show typical imaging features. However, the purpose of this study was to differentiate pituitary adenomas that present as cystic lesions from RCCs. Therefore, we proposed a diagnostic tree model that is easily applicable in clinical situations when a cystic mass without solid enhancement in the sella is observed and surgical treatment is considered because of the patient's symptoms. Because this study was retrospective, we were not able to correlate the findings of each image with pathology results. In addition, we did not include craniopharyngioma, another common pathology in this region. RCCs and craniopharyngiomas have been suggested to be on a histologic continuum, and the differentiation of these lesions is often difficult, even at the microscopic and molecular levels.³⁷ However, in the study period, there were only 3 cases of craniopharyngiomas that presented as cystic masses without a solid enhancing portion, and 2 of them showed imaging findings typical of craniopharyngioma. The number of patients in this study was relatively small, but significant differences in MR imaging findings were found between the cystic pituitary adenomas and

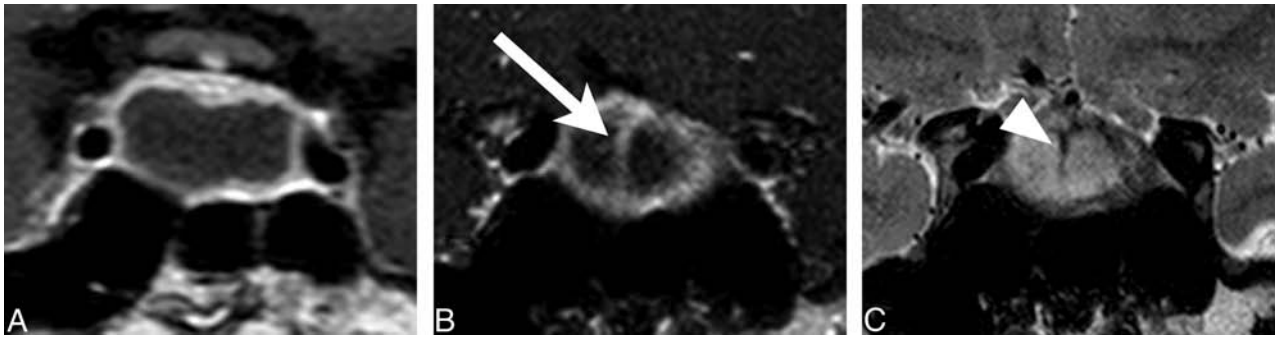


FIG 7. A 19-year-old man presented with a nonenhancing intrasellar lesion with a midline location (A) and internal septation (B [arrow] and C [arrowhead]) on coronal contrast-enhanced T1-weighted imaging (A and B) and coronal T2-weighted imaging (C). There was no visible fluid-fluid level or intracystic nodule, so this lesion was classified as a cystic pituitary adenoma based of the diagnostic tree model; however, it was finally diagnosed as a Rathke cleft cyst.

RCCs. Our diagnostic tree model exhibited good performance in both the study population and the external validation group; however, further study with a large number of patients may be needed to investigate the quality of the developed classifier.

CONCLUSIONS

We found that the presence of a fluid-fluid level, septation, an off-midline location, and the absence of an intracystic nodule were important imaging features for differentiating cystic pituitary adenomas from RCCs. The proposed diagnostic tree model using preoperative MR imaging increases the diagnostic accuracy for differentiating cystic pituitary adenomas from RCCs and may serve as a helpful tool for guiding disease management.

REFERENCES

- Gutenberg A, Larsen J, Lupi I, et al. **A radiologic score to distinguish autoimmune hypophysitis from nonsecreting pituitary adenoma preoperatively.** *AJNR Am J Neuroradiol* 2009;30:1766–72 CrossRef Medline
- Rennert J, Doerfler A. **Imaging of sellar and parasellar lesions.** *Clin Neurol Neurosurg* 2007;109:111–24 CrossRef Medline
- Johnsen DE, Woodruff WW, Allen IS, et al. **MR imaging of the sellar and juxtaseellar regions.** *Radiographics* 1991;11:727–58 CrossRef Medline
- Zhang X, Zhang W, Fu LA, et al. **Hemorrhagic pituitary macroadenoma: characteristics, endoscopic endonasal transsphenoidal surgery, and outcomes.** *Ann Surg Oncol* 2011;18:246–52 CrossRef Medline
- Semple PL, Webb MK, de Villiers JC, et al. **Pituitary apoplexy.** *Neurosurgery* 2005;56:65–72; discussion 72–73 Medline
- Piotin M, Tampieri D, Rüfenacht DA, et al. **The various MRI patterns of pituitary apoplexy.** *Eur Radiol* 1999;9:918–23 CrossRef Medline
- Tosaka M, Sato N, Hirato J, et al. **Assessment of hemorrhage in pituitary macroadenoma by T2*-weighted gradient-echo MR imaging.** *AJNR Am J Neuroradiol* 2007;28:2023–29 CrossRef Medline
- Kurihara N, Takahashi S, Higano S, et al. **Hemorrhage in pituitary adenoma: correlation of MR imaging with operative findings.** *Eur Radiol* 1998;8:971–76 CrossRef Medline
- Wang SS, Xiao DY, Yu YH, et al. **Diagnostic significance of intracystic nodules on MRI in Rathke's cleft cyst.** *Int J Endocrinol* 2012;2012:958732 Medline
- Osborn AG. *Osborn's Brain: Imaging, Pathology, and Anatomy.* Salt Lake City, Utah: Amirsys Publishing; 2013
- Byun WM, Kim OL, Kim D. **MR imaging findings of Rathke's cleft cysts: significance of intracystic nodules.** *AJNR Am J Neuroradiol* 2000;21:485–88 Medline
- Choi SH, Kwon BJ, Na DG, et al. **Pituitary adenoma, craniopharyngioma, and Rathke cleft cyst involving both intrasellar and suprasellar regions: differentiation using MRI.** *Clin Radiol* 2007;62:453–62 CrossRef Medline
- Binning MJ, Gottfried ON, Osborn AG, et al. **Rathke cleft cyst intracystic nodule: a characteristic magnetic resonance imaging finding.** *J Neurosurg* 2005;103:837–40 CrossRef Medline
- Brassier G, Morandi X, Tayiar E, et al. **Rathke's cleft cysts: surgical-MRI correlation in 16 symptomatic cases.** *J Neuroradiol* 1999;26:162–71 Medline
- Wen L, Hu L-b, Feng X-y, et al. **Rathke's cleft cyst: clinicopathological and MRI findings in 22 patients.** *Clin Radiol* 2010;65:47–55 CrossRef Medline
- Mehta GU, Jane JA Jr. **Pituitary tumors.** *Curr Opin Neurol* 2012;25:751–55 CrossRef Medline
- Nishioka H, Haraoka J, Izawa H, et al. **Magnetic resonance imaging, clinical manifestations, and management of Rathke's cleft cyst.** *Clin Endocrinol* 2006;64:184–88 CrossRef Medline
- Saeki N, Sunami K, Sugaya Y, et al. **MRI findings and clinical manifestations in Rathke's cleft cyst.** *Acta Neurochir (Wien)* 1999;141:1055–61 CrossRef Medline
- Roelfsema F, Biermasz NR, Pereira AM. **Clinical factors involved in the recurrence of pituitary adenomas after surgical remission: a structured review and meta-analysis.** *Pituitary* 2012;15:71–83 CrossRef Medline
- Goel A, Shah A, Jhavar SS, et al. **Fluid-fluid level in pituitary tumors: analysis of management of 106 cases.** *J Neurosurg* 2010;112:1341–46 CrossRef Medline
- Buchfelder M, Schlaffer S. **Surgical treatment of pituitary tumours.** *Best Pract Res Clin Endocrinol Metab* 2009;23:677–92 CrossRef Medline
- Barker FG 2nd, Klibanski A, Swearingen B, et al. **Transsphenoidal surgery for pituitary tumors in the United States, 1996–2000: mortality, morbidity, and the effects of hospital and surgeon volume.** *J Clin Endocrinol Metab* 2003;88:4709–19 CrossRef Medline
- Connor SE, Penney CC. **MRI in the differential diagnosis of a sellar mass.** *Clin Radiol* 2003;58:20–31 CrossRef Medline
- Bonneville F, Cattin F, Marsot-Dupuch K, et al. **T1 signal hyperintensity in the sellar region: spectrum of findings.** *Radiographics* 2006;26:93–113 CrossRef Medline
- Jassal DS, McGinn G, Embil JM. **Pituitary apoplexy masquerading as meningoencephalitis.** *Headache* 2004;44:75–78 CrossRef Medline
- Breiman L, Friedman J, Stone CJ, et al. *Classification and Regression Trees.* Belmont, California: Wadsworth International Group; 1984
- Kucharczyk W, Davis DO, Kelly WM, et al. **Pituitary adenomas: high-resolution MR imaging at 1.5 T.** *Radiology* 1986;161:761–65 CrossRef Medline
- Asari S, Ito T, Tsuchida S, et al. **MR appearance and cyst content of Rathke cleft cysts.** *J Comput Assist Tomogr* 1990;14:532–35 CrossRef Medline
- Hua F, Asato R, Miki Y, et al. **Differentiation of suprasellar nonneoplasms.** *Acta Neurochir (Wien)* 1999;141:1055–61 CrossRef Medline

- plastic cysts from cystic neoplasms by Gd-DTPA MRI. *J Comput Assist Tomogr* 1992;16:744–49 CrossRef Medline
30. Binning MJ, Liu JK, Gannon J, et al. **Hemorrhagic and nonhemorrhagic Rathke cleft cysts mimicking pituitary apoplexy.** *J Neurosurg* 2008;108:3–8 CrossRef Medline
 31. Mohr G, Hardy J. **Hemorrhage, necrosis, and apoplexy in pituitary adenomas.** *Surg Neurol* 1982;18:181–89 CrossRef Medline
 32. Poussaint TY, Barnes PD, Anthony DC, et al. **Hemorrhagic pituitary adenomas of adolescence.** *AJNR Am J Neuroradiol* 1996;17:1907–12 Medline
 33. Bonneville JF, Bonneville F, Cattin F. **Magnetic resonance imaging of pituitary adenomas.** *Eur Radiol* 2005;15:543–48 CrossRef Medline
 34. Amhaz HH, Chamoun RB, Waguespack SG, et al. **Spontaneous involution of Rathke cleft cysts: is it rare or just underreported?** *J Neurosurg* 2010;112:1327–32 CrossRef Medline
 35. Shin JL, Asa SL, Woodhouse LJ, et al. **Cystic lesions of the pituitary: clinicopathological features distinguishing craniopharyngioma, Rathke's cleft cyst, and arachnoid cyst.** *J Clin Endocrinol Metab* 1999;84:3972–82 CrossRef Medline
 36. Kunii N, Abe T, Kawamo M, et al. **Rathke's cleft cysts: differentiation from other cystic lesions in the pituitary fossa by use of single-shot fast spin-echo diffusion-weighted MR imaging.** *Acta Neurochir (Wien)* 2007;149:759–69 CrossRef Medline
 37. Zada G, Lin N, Ojerholm E, et al. **Craniopharyngioma and other cystic epithelial lesions of the sellar region: a review of clinical, imaging, and histopathological relationships.** *Neurosurg Focus* 2010;28:E4 CrossRef Medline

Cognitive and White Matter Tract Differences in MS and Diffuse Neuropsychiatric Systemic Lupus Erythematosus

B. Cesar, M.G. Dwyer, J.L. Shucard, P. Polak,  N. Bergsland, R.H.B. Benedict, B. Weinstock-Guttman, D.W. Shucard, and R. Zivadinov



ABSTRACT

BACKGROUND AND PURPOSE: Multiple sclerosis and neuropsychiatric systemic lupus erythematosus are autoimmune diseases with similar CNS inflammatory and neurodegenerative characteristics. Our aim was to investigate white matter tract changes and their association with cognitive function in patients with MS and those with neuropsychiatric systemic lupus erythematosus compared with healthy controls by using diffusion tensor imaging.

MATERIALS AND METHODS: Thirty patients with relapsing-remitting MS and 23 patients with neuropsychiatric systemic lupus erythematosus matched for disease severity and duration and 43 healthy controls were scanned with 3T MR imaging. The DTI was postprocessed, corrected for lesions, and analyzed with tract-based spatial statistics. Cognitive assessment included examination of processing speed; visual, auditory/verbal, and visual-spatial memory; and sustained attention and executive function. Differences were considered significant at $P < .05$.

RESULTS: Tract-based spatial statistics analysis revealed significantly decreased fractional anisotropy and increased mean diffusivity in patients with MS compared with healthy controls, decreased fractional anisotropy in patients with MS compared with those with neuropsychiatric systemic lupus erythematosus, and an increased mean diffusivity in patients with neuropsychiatric systemic lupus erythematosus compared with healthy controls. Patients with MS showed decreased fractional anisotropy throughout central WM pathways, including the corpus callosum and the inferior longitudinal and fronto-occipital fasciculi compared with those with neuropsychiatric systemic lupus erythematosus. Altered cognitive scores in patients with MS were significantly associated with decreased fractional anisotropy and increased mean diffusivity in all examined domains, while in patients with diffuse neuropsychiatric systemic lupus erythematosus, only decreased fractional anisotropy in the superior WM pathways showed significant association with executive function.

CONCLUSIONS: Patients with MS and neuropsychiatric systemic lupus erythematosus showed widespread WM tract alterations outside overt lesions, though more severe changes were identified in patients with MS. The WM tract changes were associated with cognitive dysfunction in all explored domains only in patients with MS.

ABBREVIATIONS: AD = axial diffusivity; FA = fractional anisotropy; HC = healthy control; MD = mean diffusivity; NPSLE = neuropsychiatric systemic lupus erythematosus; PASAT = Paced Auditory Serial Addition Task; RD = radial diffusivity; SLE = systemic lupus erythematosus; TBSS = tract-based spatial statistics

Multiple sclerosis and systemic lupus erythematosus (SLE) are both chronic inflammatory autoimmune diseases that adversely affect the CNS.¹ MS is characterized by both focal and diffuse damage in the brain and spinal cord due to demyelination, leading to axonopathy and tissue atrophy. While the pathology of MS is pri-

marily restricted to the CNS, SLE can involve multiple organ systems. CNS involvement in SLE is mainly attributed to autoantibody attack on small vessels, resulting in diffuse ischemic damage. However, axonal loss and demyelination may also result from direct antibody attack on neuronal cells, either on neuronal bodies or in the WM tracts.²

Although SLE and MS have notable differences in etiology, there is a marked overlap concerning the CNS inflammatory and neurodegenerative nature of these 2 diseases.³ In 1972, Fulford et

Received December 24, 2014; accepted after revision February 13, 2015.

From the Buffalo Neuroimaging Analysis Center, Department of Neurology (B.C., M.G.D., P.P., N.B., R.Z.), Department of Neurology (M.G.D., J.L.S., R.H.B.B., B.W.-G., D.W.S.), Division of Cognitive and Behavioral Neurosciences (B.C., J.L.S., D.W.S.), Neuroscience Program (J.L.S., D.W.S.), and MRI Clinical Translational Research Center (R.Z.), School of Medicine and Biomedical Sciences, University at Buffalo, State University of New York, Buffalo, New York; and Magnetic Resonance Laboratory (N.B.), IRCCS Don Gnocchi Foundation, Milan, Italy.

This work was supported in part by National Institutes of Health Grant NS049111 to J.L.S.

Please address correspondence to Robert Zivadinov, MD, PhD, FAAN, Department of Neurology, School of Medicine and Biomedical Sciences, 100 High St, Buffalo, NY 14203; e-mail: rzivadinov@bnac.net

 Indicates open access to non-subscribers at www.ajnr.org

<http://dx.doi.org/10.3174/ajnr.A4354>

al⁴ first coined the term “lupoid sclerosis” when referring to patients with SLE who presented with symptoms similar to those in MS. Additionally, neuropsychological and cognitive testing revealed similarities in cognitive profiles of patients with MS and those with SLE that may be the result of similar dysfunctional CNS structures.^{5,6} These neuropsychological findings included deficits in working memory and processing speed and general lower cognitive scores, even in the absence of a diagnosed neurologic or psychiatric condition.^{7,8} It is possible that these cognitive disturbances may be attributed to decreased WM integrity, the presence and extent of WM lesions, or GM damage, all of which are present in patients with MS and those with SLE.^{2,3,8-10}

Unlike in MS, the relationship between cerebral pathology and resulting neuropsychiatric disorders in SLE is not well-established. Neuropsychiatric symptoms range from transient to chronic and are heterogeneous among patients.^{3,6} The American College of Rheumatology has identified 19 different syndromes of neuropsychiatric systemic lupus erythematosus (NPSLE). NPSLE includes focal syndromes such as seizures, strokes, and transient ischemic attacks and also diffuse syndromes such as anxiety disorders, mood disorders, headache, and cognitive impairment.¹¹ Since the establishment of a separate NPSLE diagnosis, more studies have concentrated on using the NPSLE population for further inquiry into neurocognitive dysfunction. In a 1-year longitudinal study, subjects with NPSLE were found to have cognitive impairment associated with GM and WM dysfunction.¹² Several other studies have associated cognitive impairment with WM abnormalities in patients with NPSLE.¹³

The present study investigated the integrity of WM tracts adjusted for lesions by comparing DTI anisotropy in patients with NPSLE with diffuse syndromes, excluding patients with the defined focal syndromes, versus a group of patients with MS and a healthy control (HC) group. We used the voxel-based DTI tract-based spatial statistics (TBSS) (fMRI of the Brain Software Library [FSL]; <http://fsl.fmrib.ox.ac.uk/fsl/fslwiki/TBSS>)¹⁴ method to reveal subtle changes along WM tracts. We also derived global WM measures to show an averaged measure of diffusivity in the brain. Because the MS disease process involves predominantly demyelination of the WM tracts, we hypothesized that patients with MS would have significantly lower DTI fractional anisotropy (FA) values and increased mean diffusivity (MD) values (measures of WM tract integrity) compared with patients with NPSLE and that patients with MS and those with NPSLE would have significantly lower FA and higher MD compared with HCs. We also explored the association between WM tract changes and cognitive function within study groups. We hypothesized that decreased WM tract integrity, indicated by increased MD and decreased FA, would be associated with poorer cognitive function.

MATERIALS AND METHODS

Subjects

Participants were 30 patients with relapsing-remitting MS, 23 patients with NPSLE with diffuse syndromes, and 43 HCs. The outpatient groups were matched for disease duration (MS, mean of 11.7 years; NPSLE, mean of 15 years), and all patients had mild-to-moderate disease severity. Patients with NPSLE and those with MS were recruited from the specialty centers in a local hospital

and rheumatologists in the area. The diagnosis of SLE was independently confirmed by a rheumatology specialist and clinical routine laboratory testing obtained from medical records, whereas the MS diagnosis was confirmed by a neurology specialist. HC participants were recruited from advertisements in a local newspaper. All participants were screened for general exclusion criteria. The participants were then tested further for other exclusionary criteria such as a history of head trauma, learning disability, alcohol and drug use, notable hearing loss, visual problems, or other medical conditions unrelated to MS and SLE that could affect cognition. HC participants were excluded if they had a *Diagnostic and Statistical Manual of Mental Disorders, 4th ed* Axis I psychiatric disorder or if they were on psychotropic or any other medications that could affect cognition.

All subjects met the criteria for MR imaging testing based on a health-screening interview and an MR imaging questionnaire containing information about medical history (medications, surgeries, pregnancy, illness, and so forth). The Expanded Disability Status Scale was used to measure disease severity in patients with MS and was obtained at a 30-day interval from cognitive testing. Disease activity at the time of testing was measured for patients with NPSLE with a checklist based on the Systemic Lupus Activity Measure,¹⁵ with scores ranging from 0 to 19, and was calculated as the sum of positive responses on a checklist of current symptoms (including fever, hair loss, joint pain, and so forth). The determination of cognitive impairment was based on the American College of Rheumatology guidelines established by the cognition subcommittee of the Ad Hoc Committee on Lupus Response Criteria.¹¹ Patients with SLE were determined to have NPSLE with diffuse syndromes on the basis of a review of their medical records and on the data obtained from the neuropsychological, psychological, and other medical components of the study. Those patients diagnosed with a mood disorder all had major depression (mild to moderate), defined as related to the underlying NPSLE.

Neuropsychological testing was overseen by a board-certified clinical neuropsychologist. The battery of neuropsychological tests assessed cognitive function in the domains of processing speed; visual, auditory/verbal, and visual-spatial memory; sustained attention; and executive function. Processing speed and visual working memory were assessed with the oral Rao adaptation of the Symbol Digit Modalities Test.^{16,17} Attention and verbal working memory were assessed with the Rao adaptation of the Paced Auditory Serial Addition Task (PASAT) by using 3-second interstimulus interval conditions.^{17,18} Auditory/verbal memory was assessed with the California Verbal Learning Test, 2nd ed.¹⁹ Visual-spatial memory was assessed with the Brief Visuospatial Memory Test–Revised.²⁰ Executive function was assessed with the Delis-Kaplan Executive Function System Test.²¹

The study was approved by an internal institutional review board, and written informed consent was obtained from all participants. All participants were compensated for their time.

MR Imaging Acquisition

All subjects were scanned on a 3T whole-body MR imaging system (Signa Excite HD; GE Healthcare, Milwaukee, Wisconsin), with a maximum slew rate of 150 T/m/s and maximum gradient amplitude in each orthogonal plane of 40 mT/m (zoom mode) by

using an 8-channel head and neck coil. All scans were prescribed parallel to the subcallosal line in an axial-oblique orientation. The subjects were scanned with FLAIR (TR = 8500 ms, TE = 120 ms, TI = 2100 ms, voxel size = $0.94 \times 0.94 \times 3$ mm), 3D gradient recalled-echo T1WI (TR = 24 ms, TE = 7 ms, voxel size = $0.94 \times 0.94 \times 1.5$ mm), and DTI sequences (TR = 8600 ms, TE = 85 ms, $b = 1000$, 39 diffusion directions, voxel size = $1.1 \times 1.1 \times 3$ mm).

MR Imaging Analysis

Volumetric data were obtained by using 3D T1WI. Scans were adjusted by using an in-house-developed inpainting technique to avoid tissue misclassification. Structural Image Evaluation by using Normalization of Atrophy Cross-Sectional (SIENAX, Version 2.6; <http://fsl.fmrib.ox.ac.uk/fslwiki/SIENA>) was used to acquire measures of normalized whole-brain and GM and WM volumes, with actual segmentation performed by the FMRIB Automated Segmentation Tool (FAST; <http://fsl.fmrib.ox.ac.uk/fsl/wiki/fast>).^{22,23}

Lesions were evaluated on FLAIR images with reference to T2/proton-attenuation images. A semiautomated edge-detection contouring-thresholding technique was used to create subject-specific binary lesion masks, also used in Zivadinov et al.²⁴

The DTI was corrected for motion and eddy current distortion by using the FMRIB Diffusion Toolbox (<http://www.fmrib.ox.ac.uk/fsl/fdt/index.html>).²⁵ To eliminate all nonbrain tissue, we extracted and desklulled the original $b = 0$ images (with no diffusion-weighting) by using the FSL Brain Extraction Tool (<http://fsl.fmrib.ox.ac.uk/fsl/wiki/BET>).²⁶ On the basis of the Matlab (MathWorks, Natick, Massachusetts) code provided by the original authors,²⁷ we applied a bi-tensor fitting to account for the partial voluming effects of free water. The FA, MD, radial diffusivity (RD), and axial diffusivity (AD) maps were calculated in Matlab by using the corrected tissue diffusion tensor as estimated by the free water elimination technique.²⁸ Because field maps were not acquired in this study, a 2-step process was used to reduce the inherent susceptibility-induced spatial distortions in EPI-based acquisitions. First, the $b = 0$ images were linearly coregistered into the same geometric space as the FLAIR images by using the FMRIB Linear Image Registration Tool (FLIRT; <http://fsl.fmrib.ox.ac.uk/fsl/wiki/FLIRT>). The images were then nonlinearly coregistered by using the Advanced Normalization Tools package (<http://stnava.github.io/ANTS/>).²⁹ These 2 transformations were then applied to each of the DTI outputs so that all scalar measurements were resampled into the native FLAIR geometric space.^{14,29} Specific tissue compartment masks of WM (see above) were used to obtain global WM diffusion measures.

Voxelwise intergroup statistical analysis of the DTI data was performed by using TBSS.¹⁴ First, subjects' FA data were aligned into a common space by using the FMRIB Nonlinear Registration Tool (FNIRT; <http://fsl.fmrib.ox.ac.uk/fsl/wiki/FNIRT>), which uses a b-spline representation of the registration warp field. Next, the mean FA image was created and thinned to create a mean FA skeleton, which represented the centers of all tracts common to the group. Each subject's aligned FA data were then projected onto this skeleton. The same transformations and skeletonization were also applied to the other DTI metric maps, as well as to the individual subject lesion maps.

Statistical Analysis

Analyses were performed by using SPSS, Version 20.0 (IBM, Armonk, New York). Due to non-normality, the T2 lesion number and volume differences between the groups were evaluated with the Mann-Whitney *U* test. Whole-brain and tissue-specific volume differences were evaluated by using 1-way ANOVA with post hoc Tukey correction. Parametric 1-way ANCOVAs, adjusted for age and sex, were performed to assess differences in global WM diffusion characteristics among the groups. One-way ANCOVA, adjusted for age and sex, was performed to compare the neuropsychological tests among the 3 groups, while the Bonferroni post hoc *t* test was used to assess differences between the individual groups.

For both global WM and voxelwise TBSS analyses, the specific DTI parameters investigated were FA and MD. In the event that either was found significantly different between group comparisons ($P < .05$), additional diffusion metrics, RD and AD, were also reported. For TBSS analysis, lesions maps were also taken into consideration as voxelwise covariates, to model out their effect and focus on changes in WM in these groups. Additionally, we directly compared lesion attenuation between patients with MS and those with NPSLE along TBSS-derived tracts ($P < .05$).

Age and sex were also used as covariates in both the TBSS and global WM analyses. For TBSS analysis, ANCOVA was performed to compare the 3 groups, with additional post hoc *t* tests to investigate regional differences between HCs and patients with MS, HCs and patients with NPSLE, and patients with MS and NPSLE. Inference was performed by using the nonparametric FSL Randomise permutation testing tool (<http://fsl.fmrib.ox.ac.uk/fsl/wiki/Randomise>) with 5000 permutations for each test.³⁰ The Randomise command using the FSL General Linear Model function (<http://fsl.fmrib.ox.ac.uk/fsl/wiki/GLM>) allows the comparison of diffusion metrics among the study groups in a voxelwise fashion. The tracts were dilated by using the `tbss_fill` command in FSL to enhance visualization of the results. Within-group comparisons of neuropsychological test scores with diffusion metrics (FA and MD) were performed for each subject group. Using the FSL General Linear Model function, we created matrices, including neuropsychological test scores as voxelwise covariates, in the TBSS comparisons. The subjects' lesion data were also incorporated as voxelwise covariates in all analyses. All TBSS results were corrected for family-wise error at $P < .05$ by using threshold-free cluster enhancement to account for spatially correlated changes.³¹

RESULTS

General Demographic and Clinical Characteristics

Table 1 shows demographic and clinical characteristics of the 3 study groups. There were no significant differences among the study groups for age and sex. On the basis of the disease-severity scores, both subjects with NPSLE and those with MS were determined to have mild-to-moderate disease severity. The median Expanded Disability Status Scale score, used for quantifying disability in MS, was 3.3 for the patients with MS,³² while the mean Systemic Lupus Activity Measure, used for quantifying disability in SLE, was 9.9 for patients with NPSLE.¹⁵ No significant differences in disease duration were seen between the 2 patient groups. Medications taken by the study subjects are listed in Table 1. None of the HCs were on prescribed medications.

Of the 23 patients with NPSLE, 6 had migraine, mood disorder, and cognitive impairment; 6 had migraine and mood disorder; 5 had migraine and cognitive impairment; 2 had mood disorder and cognitive impairment; and 4 had migraine. In addition to CNS-related NPSLE syndromes, 14 of the 23 patients had peripheral involvement (8 had peripheral neuropathy and cranial neuropathy and 6 had peripheral neuropathy).

Neuropsychological Characteristics

Table 2 shows the neuropsychological measures of the 3 groups. Significant ANCOVA differences among the 3 groups were found for the California Verbal Learning Test, 2nd ed ($P = .001$); the Brief Visuospatial Memory Test–Revised; ($P = .005$), and the Delis-Kaplan Executive Function System ($P = .011$). There was also a trend toward significance for the PASAT ($P = .061$).

There were no significant differences in cognitive performance between the subjects with MS and those with NPSLE on any of the neuropsychological measures. Patients with MS performed significantly worse than HCs on the California Verbal Learning Test,

2nd ed ($P = .003$); the Brief Visuospatial Memory Test–Revised ($P = .004$); and the Delis-Kaplan Executive Function System ($P = .010$). There were no significant differences in performance between patients with MS and HCs on the Symbol Digit Modalities Test or the PASAT. Subjects with NPSLE performed significantly worse than HCs on the California Verbal Learning Test, 2nd ed ($P = .009$). In general, there was a clear trend of cognitive dysfunction in patients with NPSLE compared with HCs.

General Conventional MR Imaging Characteristics

Table 3 shows lesion and brain volumetry outcomes in the 3 study groups.

Patients with MS showed a significantly higher T2 lesion number and volume compared with HCs ($P < .0001$ for both). Patients with MS also had an increased T2 lesion number and volume compared with patients with NPSLE ($P < .0001$ for both). There were no significant T2 lesion number differences between patients with NPSLE and HCs. Patients with NPSLE showed significantly increased T2 lesion volume compared with HCs ($P = .023$). Figure 1 shows areas where patients with MS had significantly greater lesion attenuation than patients with NPSLE, including the left superior corona radiata and a small portion of the right posterior corona radiata.

Patients with MS showed significantly decreased whole-brain volume compared with HCs ($P < .0001$) and also compared with patients with NPSLE ($P = .003$). No significant whole-brain volume differences were found between patients with NPSLE and HCs.

Table 1: Demographic and clinical characteristics of the study groups^a

	MS (n = 30)	dNPSLE (n = 23)	HC (n = 43)	P Value ^b
Female sex (No.) (%)	23 (76.5%)	22 (95.7)	37 (86.0)	.150
Age (yr) (mean) (SD)	43.8 (8.6)	48.9 (12.5)	44.7 (9.8)	.170
Disease duration (yr) (mean) (SD)	11.7 (8)	15 (9.6)	NA	.237
SLAM checklist (mean) (SD)	NA	9.9 (4.9)	NA	NA
EDSS (median) (IQR)	3.3 (2.1–6.0)	NA	NA	NA

Note:—NA indicates not applicable; dNPSLE, neuropsychiatric systemic lupus erythematosus with diffuse syndromes; SLAM, systemic lupus activity measure; EDSS, Expanded Disability Status Scale; IQR, interquartile range.

^a Disease-modifying medications for treatment of MS included interferon β ($n = 18$), natalizumab ($n = 8$), and glatiramer acetate ($n = 4$). Other treatment included antianxiety (dNPSLE, $n = 2$; MS, $n = 0$), antiepileptic (dNPSLE, $n = 0$; MS, $n = 5$), antidepressants (dNPSLE, $n = 10$; MS, $n = 11$), antifatigue (dNPSLE, $n = 0$; MS, $n = 4$), antispastic (dNPSLE, $n = 0$; MS, $n = 8$), antiparesthesia (dNPSLE, $n = 0$; MS, $n = 8$), hydroxychloroquine (Plaquenil) (dNPSLE, $n = 21$), imuran (dNPSLE, $n = 4$), immunosuppressive (dNPSLE, $n = 2$; MS, $n = 5$), steroids or nonsteroidal antiinflammatory drugs (dNPSLE, $n = 17$; MS, $n = 1$).

^b The χ^2 test was used to evaluate significant differences in sex distribution among the groups, and analysis of variance was used to evaluate significant differences in age and disease duration.

Table 2: Comparison of subject groups on neuropsychological measures^a

	MS (Mean) (SD)	dNPSLE (Mean) (SD)	HC (Mean) (SD)	ANOVA (P Value)	MS vs HC (P Value)	dNPSLE vs HC (P Value)	MS vs dNPSLE (P Value)
SDMT	54.6 (16.1)	54.8 (10.3)	60.7 (10.4)	.091	.137	.373	1.0
CVLT2	49.3 (12.3)	50.35 (9.7)	57.9 (7.9)	.001	.003	.009	1.0
BVMT-R	21.7 (7.4)	24.3 (6.9)	26.9 (5.7)	.005	.004	.571	.359
D-KEFS	9.2 (2.8)	10.3 (2.6)	119 (2.2)	.011	.010	.252	.722
PASAT	41.6 (16)	42 (12.3)	48.3 (12.3)	.061	.111	.226	1.0

Note:—CVLT2 indicates California Verbal Learning Test, 2nd ed; BVMT-R, Brief Visuospatial Memory Test–Revised; D-KEFS, Delis-Kaplan Executive Function System; SDMT, Symbol Digit Modalities Test; dNPSLE, neuropsychiatric systemic lupus erythematosus with diffuse syndromes.

^a Reported measures are raw scores. The statistical analysis among the groups was performed using 1-way analysis of covariance, adjusted for age and sex. Post hoc tests between the individual groups were performed using a Bonferroni correction.

Table 3: Comparison of conventional MRI characteristics among the study groups^a

	MS (n = 30)	dNPSLE (n = 23)	HC (n = 43)	MS vs HCs ^b (P Value)	dNPSLE vs HCs ^c (P Value)	MS vs dNPSLE ^d (P Value)
T2 lesion number (mean) (SD)	31.1 (19.2)	11.7 (9.3)	7.9 (4.8)	<.0001	.06	<.0001
T2 lesion volume (mean) (SD)	15.2 (3.1)	1.9 (1.3)	1.6 (4)	<.0001	.023	<.0001
Normalized WB volume (mean) (SD)	1490.4 (113.5)	1570.3 (79)	1596.5 (64.2)	<.0001	.465	.003
Normalized WM volume (mean) (SD)	784.5 (58.0)	829.3 (45.1)	849.0 (40.8)	<.0001	.285	.005
Normalized GM volume (mean) (SD)	704.0 (63.9)	751.5 (58.8)	755.3 (42)	.001	.964	.008

Note:—WB indicates whole-brain; dNPSLE, neuropsychiatric systemic lupus erythematosus with diffuse syndromes.

^a The statistical analysis among the groups was performed using 1-way analysis of variance with post hoc Tukey correction, except for the T2 lesion number and volume, which were analyzed using the Mann-Whitney U test. All volumes are given in milliliters.

^b P value for MS vs HCs.

^c P value for SLE vs HCs.

^d P value for MS vs SLE.

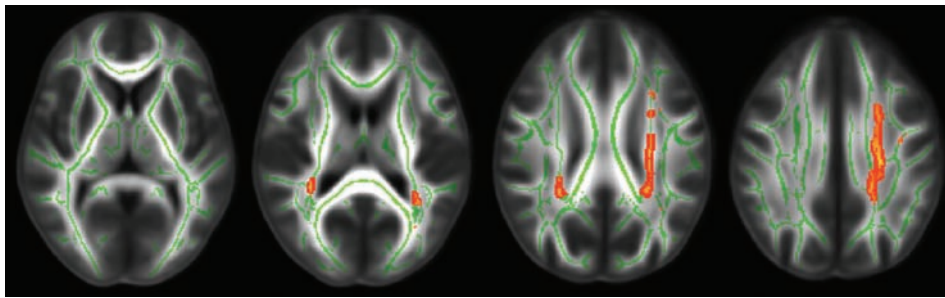


FIG 1. A comparison of lesion attenuation along WM tracts in patients with MS and those with NPSLE by using TBSS analysis. Red-highlighted areas show where patients with MS had significantly greater lesion attenuation than patients with NPSLE ($P < .05$). Patients with MS have significant lesion attenuation as shown in the left superior corona radiata and a small portion of the right posterior corona radiata.

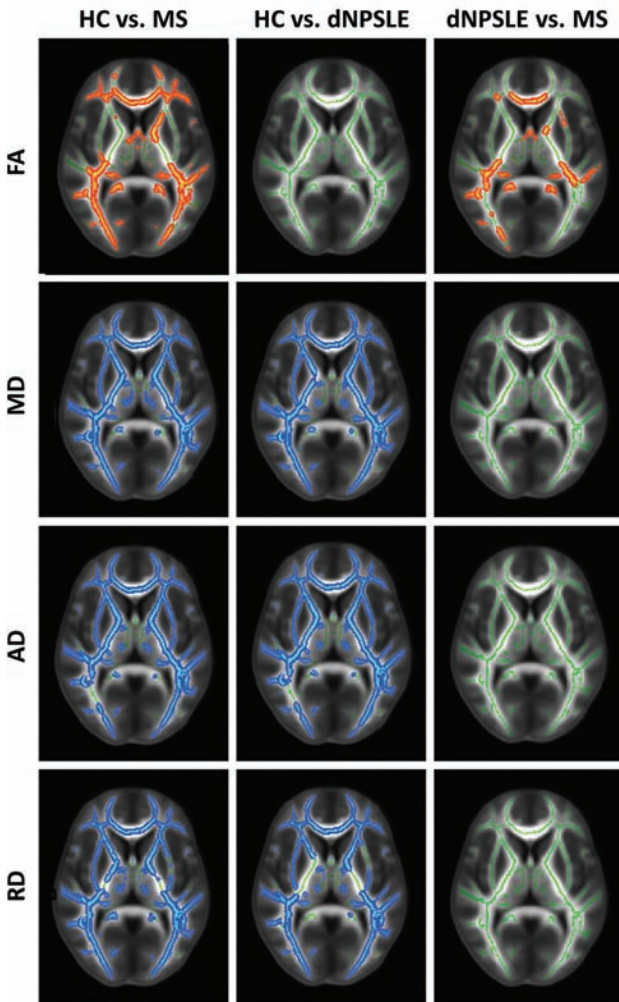


FIG 2. Diffusion tensor imaging TBSS differences among patients with MS, patients with NPSLE with diffuse syndromes, and HCs, controlling for age and sex. The results are shown for FA, MD, RD, and AD differences between the studied groups ($P < .05$). Red-highlighted areas show where significantly lower FA was found in the second reported group, indicating less anisotropic diffusion. Blue-highlighted areas show significantly increased diffusivity in the second reported group, indicating more diffuse WM damage.

Patients with MS showed significantly decreased WM volume compared with HCs ($P < .0001$). The patients with MS also showed significantly decreased WM volume compared with patients with NPSLE ($P = .005$). No significant WM volume differences were found between patients with NPSLE and HCs.

Patients with MS showed significantly decreased GM volume compared with patients with NPSLE ($P = .008$) and also compared with HCs ($P = .001$). No significant GM volume differences were found when comparing patients with NPSLE and HCs.

Diffusion Tensor Imaging White Matter Characteristics among the Study Groups

Figure 2 summarizes the results of WM tract differences by using the TBSS analysis. Highlighted areas represent significant diffusivity differences among the 3 study groups corrected for multiple comparisons at the family-wise $P < .05$ level on the threshold-free cluster-enhanced images. Table 4 shows the global WM differences among the study groups.

In the TBSS analysis comparing patients with MS and HCs, patients with MS showed significant widespread damage throughout WM tracts across all diffusion metrics without any specific regional predilection for FA, MD, AD, and RD (Fig 2, left column). Global WM measures also revealed significantly different diffusivity characteristics across all diffusivity metrics (FA, $P = .001$; MD, $P < .0001$; AD, $P = .006$; and RD, $P < .0001$; Table 4).

TBSS contrasts between patients with NPSLE and HCs also revealed widespread differences in WM tract diffusivity in MD, RD, and AD measures; however, no significant differences were found for FA (Fig 2, middle column). Global WM measures also revealed significant differences for MD ($P = .001$), AD ($P = .003$), and RD ($P < .0001$), but not for FA (Table 4).

TBSS contrasts between patients with MS and those with NPSLE showed prevalent FA differences throughout central WM pathways, including the corpus callosum; the inferior longitudinal and fronto-occipital fasciculi; and also parts of the forceps major, forceps minor, cingulum, and thalamic radiation (Fig 2, right column). Figure 3 provides additional sagittal and coronal views of decreased FA in patients with MS compared with patients with NPSLE. There were no significant differences in TBSS analysis between patients with MS and those with NPSLE for MD, AD, and RD measures. Global WM measures showed no significant differences between patients with MS and those with NPSLE for any diffusion metrics.

White Matter Tract Integrity and Cognitive Function Associations among the Study Groups

Figure 4 shows the results of within-group comparisons of cognitive performance and WM tract integrity diffusion metrics for each subject group.

Table 4: Comparison of global white matter diffusion tensor imaging characteristics among the study groups^a

	MS	dNPSLE	HC	MS vs HCs ^b	dNPSLE vs HCs ^c	MS vs dNPSLE ^d
FA (mean) (SD)	.398 (.006)	.411 (.004)	.418 (.002)	.001	.112	.310
MD × 10 ⁻³ (mean) (SD)	.786 (.009)	.775 (.008)	.734 (.008)	<.0001	.001	.780
AD × 10 ⁻³ (mean) (SD)	1.149 (.010)	1.150 (.012)	1.096 (.013)	.006	.003	.784
RD × 10 ⁻³ (mean) (SD)	.604 (.01)	.587 (.006)	.553 (.006)	<.0001	<.0001	.528

Note:—dNPSLE indicates neuropsychiatric systemic lupus erythematosus with diffuse syndromes.

^a The statistical analysis between the groups was performed using 1-way analysis of variance controlling for age and sex. FA is a dimensionless measure. Diffusivity is given in square millimeters second⁻¹.

^b P value for MS vs HCs.

^c P value for SLE vs HCs.

^d P value for MS vs SLE.

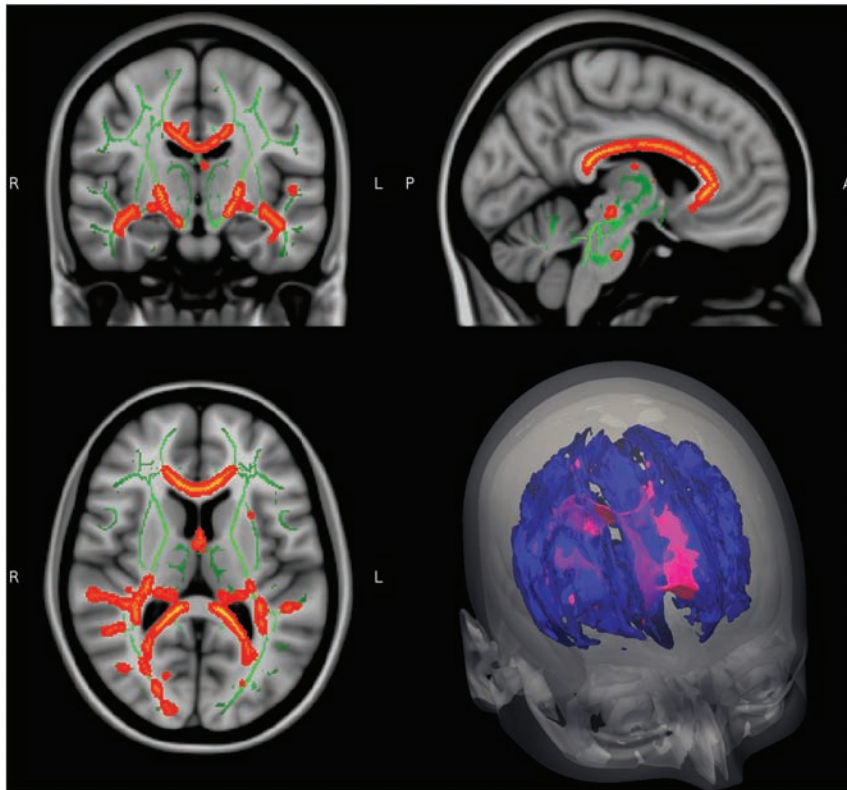


FIG 3. Details of TBSS FA comparison between patients with MS and those with NPSLE with diffuse syndromes. Red areas show where FA is significantly lower in patients with MS compared with patients with NPSLE in central white matter pathways, including the corpus callosum, inferior longitudinal fasciculus, and fronto-occipital fasciculus ($P < .05$).

Lower cognitive scores in patients with MS were significantly associated with decreased FA and MD for all examined domains, while in patients with NPSLE, only decreased FA in the superior WM pathways was significantly associated with executive functioning (Delis-Kaplan Executive Function System). Lower PASAT scores were significantly associated with increased MD in the HC group.

DISCUSSION

While the full extent of NPSLE and MS pathology is not completely understood, both diseases involve inflammatory autoimmune processes that lead to axonal loss with consequent neurologic impairment and deficits in cognitive performance.^{33,34} Numerous studies have also revealed WM abnormalities in patients with NPSLE,^{35,36} including the presence of WM lesions³⁷ and increased WM tract diffusivity.³⁸ The pathogenesis of CNS

involvement in SLE is likely related to an inflammatory response secondary to auto-antibody-mediated vasculitis.³⁵

The increased sensitivity in DTI has proved useful for detecting WM tract deterioration.³⁹⁻⁴¹ DTI allows quantitative measurements of diffusion anisotropy along WM tracts. FA is a widely used measure that reflects the degree of directionality of water diffusion. For example, the myelin within intact WM tracts generally is uniformly oriented parallel to the overall tracts, and molecular water movement is much greater parallel to the tracts than perpendicular to the tracts. This myelin orientation results in highly directional, anisotropic diffusion and therefore high FA values. However, as tracts become damaged due to demyelination or other pathologic processes, the tissue structure becomes less orderly and FA decreases as water diffuses more freely in multiple directions. While FA reflects the directionality of diffusion, MD reflects the magnitude of diffusion. AD corresponds to the diffusivity along the principal axis, whereas RD corresponds to the average of the diffusivities along the 2 minor axes.^{14,42}

The results of this study are consistent with those in prior studies showing

significant WM damage in patients with MS compared with HCs across measures of FA, MD, RD, and AD, by using both TBSS and global WM analysis.^{33,43} The results are also consistent with prior studies showing that subjects with MS perform significantly worse than HCs on cognitive tests assessing processing speed, working and visual-spatial processing/memory, sustained attention, and executive function.^{21,44-46}

The diffuse SLE syndromes such as anxiety disorders, mood disorders, headache, and cognitive impairment may be the result of diffuse damage, whereas focal SLE syndromes such as seizures, strokes, and transient ischemic attacks, result in high-attenuation focal lesions. Several studies have shown regionally-specific decreased FA and increased MD in patients with NPSLE compared with HCs.^{38,47} In our comparison of patients with diffuse NPSLE and HCs, we found significant differences in MD, AD, and RD in both the TBSS and global WM measures; however, we did not

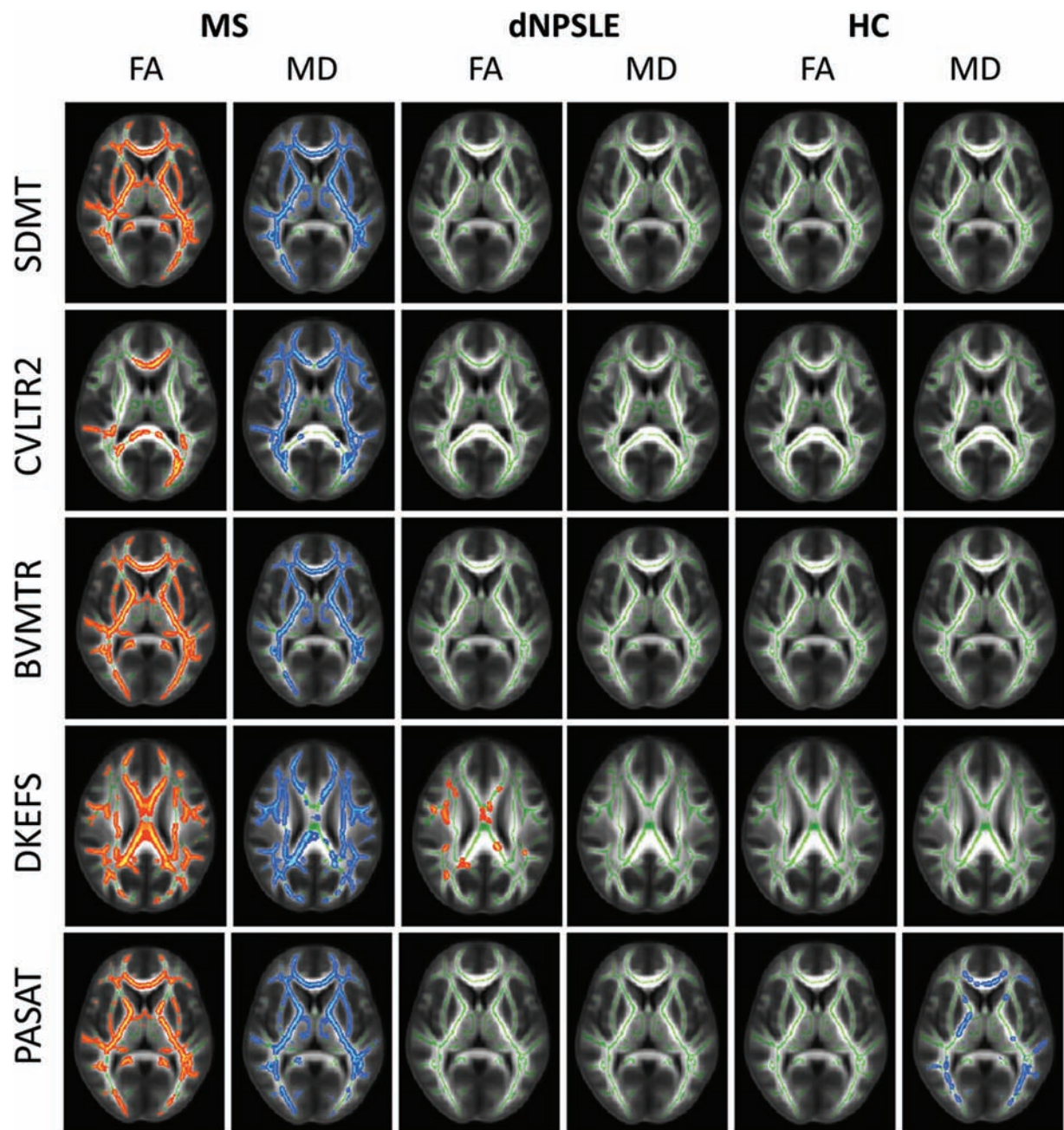


FIG 4. Highlighted tracts display significant correlations between TBSS differences and performance on neuropsychological tests ($P < .05$). Red-highlighted tracts represent positive correlations, and blue-highlighted tracts represent negative correlations. For patients with MS, decreased neuropsychological scores significantly correlated with decreased FA and increased MD for each of the neuropsychological tests. For patients with NPSLE, decreased Delis-Kaplan Executive Function System scores significantly correlated with decreased FA. For HCs, increased PASAT scores correlated significantly with decreased MD. CVLT2 indicates California Verbal Learning Test, 2nd ed; BVMTR, Brief Visuospatial Memory Test-Revised; D-KEFS, Delis-Kaplan Executive Function System; SDMT, Symbol Digit Modalities Test; dNPSLE, neuropsychiatric systemic lupus erythematosus with diffuse syndromes.

detect differences in FA in either of the analyses. These findings may be because the present study included only subjects with SLE with diffuse neuropsychiatric syndromes, unlike the previous studies, which included patients with focal neuropsychiatric SLE syndromes. Diffusivity changes in patients with NPSLE might be due to increased extracellular water, resulting in more isotropic WM changes affecting both RD and AD; this increased extracellular water would account for differences in MD, but not in FA, between patients with NPSLE and HCs.

No significant differences were found between patients with NPSLE and HCs in WM volume. This finding is consistent with a recent study by Zivadinov et al¹⁰ but contrary to the study of Appenzeller et al.¹² In addition, no differences were found between patients with NPSLE and HCs in GM volume, contrary to findings in our previously published study.¹⁰

Prior studies of cognitive impairment in SLE have most commonly found deficits in processing speed and working and verbal memory.^{3,8,48} Kozora et al⁴⁹ also found that subjects with SLE

showed impaired working memory on the PASAT, which inversely correlated to WM abnormalities. In this study, patients with NPSLE generally performed worse than HCs on all the administered cognitive tests, though the differences were only significant for auditory and verbal memory.

In the TBSS analysis comparing patients with MS with those with NPSLE, there was more diffuse damage in MS as evidenced by decreased FA throughout the central WM, including the corpus callosum and the inferior longitudinal and fronto-occipital fasciculi. However, no significant differences between patients with NPSLE and patients with MS were found for MD, AD, or RD; and the global WM measures failed to reveal differences in these diffusivity metrics.

It is possible that the positive findings of FA differences between MS and NPSLE and negative findings of MD, AD, and RD merely reflect insufficient statistical power. However, given the reasonably large group sizes involved, one should consider the true biologic mechanisms for this seemingly contradictory result. Increased RD has been shown to be a marker of decreased myelin content in postmortem MS brains.⁵⁰ Studies using MS mouse models have also established that changes in RD are attributed to myelin damage and additionally that AD characteristics are a strong predictor of axonal attenuation.^{51,52} Recent studies suggest that while axonal loss is characteristic of NPSLE pathology, demyelination is a less specific finding in patients with NPSLE.^{34,53} Although not significant between the disease groups, in MS versus HC, RD was increased by 9.2% compared with 4.8% for AD. In contrast, in NPSLE, RD was only increased by 6.1%, closer to the 4.9% difference in AD.

In patients with MS, it is likely that cognitive deficits are associated with the loss of WM integrity. However, in patients with NPSLE, the explanation for cognitive deficits was less clear. Executive function was the only domain that showed a significant association with decreased WM integrity. However, the lack of association between diffusivity and performance of other cognitive domains may be related to greater local anatomic heterogeneity of WM damage in the subjects. Most surprising, HCs also showed a correlation between MD and cognitive performance on the PASAT. It would be interesting in the near future to explore changes of diffusivity and attention and processing speed in relation to the age and sex of healthy individuals.

There are some limitations in the current study. Ideally, diffusion images can be corrected by field maps, which analytically remove distortion errors, or by the acquisition of 2 datasets with opposite phase-encoding directions, which can correct for both distortion errors and intensity artifacts. We were not able to acquire data in this way during clinical routine scanning and so used an ad hoc technique of nonlinearly aligning to FLAIR. While this corrects substantially for spatial distortions, it cannot recover lost intensity information near sinuses and other air/bone interfaces. Another limitation is that both MS and NPSLE had different clinical disease characteristics, so matching these 2 types of patients from the disease severity point of view is a difficult task. However, we matched the patients for disease duration and disease severity on the basis of the respective criteria for each condition, which certainly does not overcome the elimination of differences between the 2 disease states.

CONCLUSIONS

MS has provided an interesting comparison for the less studied disease, NPSLE. Our analyses confirmed the results of prior studies showing that patients with both MS and NPSLE experience significant decreases in WM tract integrity, compared with HCs. Global WM measures comparing patients with MS and those with NPSLE showed no significant differences, but more specific TBSS investigation indicated FA differences specifically in the central WM pathways between the groups. The decrease in WM tract integrity was associated with reduced cognitive function in all explored cognitive domains only in patients with MS, while the decline in verbal and auditory memory in patients with NPSLE was not associated with altered WM integrity. A larger and longitudinal study would be necessary to better evaluate how changes in MR imaging findings correlate with cognitive dysfunction in patients with NPSLE.

ACKNOWLEDGMENTS

We thank Ofer Pasternak for allowing us to use his free water elimination code.

Disclosures: Michael G. Dwyer—UNRELATED: Consultancy: EMD Serono, Claret Medical. Comments: Michael Dwyer has served as a consultant for Claret Medical and on a scientific advisory board for EMD Serono; Grants/Grants Pending: Novartis. Comments: Michael Dwyer has received research grant support from Novartis. Janet L. Shucard—RELATED: Grant: National Institutes of Health*; Support for Travel to Meetings for the Study or Other Purposes: National Institutes of Health.* Ralph H.B. Benedict—UNRELATED: Consultancy: Biogen, Genentech, Genzyme, Sanofi, Adamas; Grants/Grants Pending: Biogen, Genzyme, Acorda, Questcor; Payment for Lectures (including service on Speakers Bureaus): EMD Serono; Royalties: Psychological Assessment Resources; Other: Ralph H.B. Benedict received research support from Biogen Idec and Shire and serves on advisory panels for Bayer, Biogen, Novartis, and Actelion. Bianca Weinstock-Guttman—UNRELATED: Consultancy: Biogen Idec, Teva Neuroscience, EMD Serono, Novartis, Genzyme, Sanofi; Grants/Grants Pending: Biogen Idec,* Teva Neuroscience,* EMD Serono,* Novartis,* Genzyme, Sanofi*; Payment for Lectures (including service on Speakers Bureaus): Biogen Idec, Teva Neuroscience, EMD Serono, Novartis, Genzyme, Sanofi; Other: Bianca Weinstock-Guttman received honoraria as a speaker and as a consultant for Biogen Idec, Teva Pharmaceuticals, EMD Serono, Pfizer, Novartis, and Acorda. Dr Weinstock-Guttman received research funds from Biogen Idec, Teva Pharmaceuticals, EMD Serono, Pfizer, Novartis, Acorda, and Cyberonics. David W. Shucard—RELATED: Grant: National Institutes of Health—National Institute of Neurological Disorders and Stroke.* Comments: grant title: Neurological Indices of CNS Involvement in “Non CNS” SLE; Support for Travel to Meetings for the Study or Other Purposes: National Institutes of Health—National Institute of Neurological Disorders and Stroke.* Robert Zivadinov—UNRELATED: Consultancy: Teva, Genzyme, Biogen, Novartis, Claret Medical; Grants/Grants Pending: Teva, Genzyme, Biogen, Novartis, Claret Medical; Payment for Lectures (including service on Speakers Bureaus): Teva, Genzyme, Biogen, Novartis, Claret Medical. *Money paid to the institution.

REFERENCES

1. Rovaris M, Viti B, Ciboddo G, et al. **Cervical cord magnetic resonance imaging findings in systemic immune-mediated diseases.** *J Neurol Sci* 2000;176:128–30
2. Kozora E, Hanly JG, Lapteva L, et al. **Cognitive dysfunction in systemic lupus erythematosus: past, present, and future.** *Arthritis Rheum* 2008;58:3286–98
3. Benedict RH, Shucard JL, Zivadinov R, et al. **Neuropsychological impairment in systemic lupus erythematosus: a comparison with multiple sclerosis.** *Neuropsychol Rev* 2008;18:149–66
4. Fulford KW, Catterall RD, Delhanty JJ, et al. **A collagen disorder of the nervous system presenting as multiple sclerosis.** *Brain* 1972;95:373–86
5. Parmenter BA, Shucard JL, Shucard DW. **Information processing deficits in multiple sclerosis: a matter of complexity.** *J Int Neuropsychol Soc* 2007;13:417–23

6. Shucard JL, Lee WH, Safford AS, et al. **The relationship between processing speed and working memory demand in systemic lupus erythematosus: evidence from a visual n-back task.** *Neuropsychology* 2011;25:45–52
7. Kozora E, West SG, Kotzin BL, et al. **Magnetic resonance imaging abnormalities and cognitive deficits in systemic lupus erythematosus patients without overt central nervous system disease.** *Arthritis Rheum* 1998;41:41–47
8. Covey TJ, Shucard JL, Shucard DW, et al. **Comparison of neuropsychological impairment and vocational outcomes in systemic lupus erythematosus and multiple sclerosis patients.** *J Int Neuropsychol Soc* 2012;18:530–40
9. Kozora E, Arciniegas DB, Filley CM, et al. **Cognition, MRS neurometabolites, and MRI volumetrics in non-neuropsychiatric systemic lupus erythematosus: preliminary data.** *Cogn Behav Neurol* 2005;18:159–62
10. Zivadinov R, Shucard J, Hussein S, et al. **Multimodal imaging in systemic lupus erythematosus patients with diffuse neuropsychiatric involvement.** *Lupus* 2013;22:675–83
11. **The American College of Rheumatology nomenclature and case definitions for neuropsychiatric lupus syndromes.** *Arthritis Rheum* 1999;42:599–608
12. Appenzeller S, Bonilha L, Rio PA, et al. **Longitudinal analysis of gray and white matter loss in patients with systemic lupus erythematosus.** *Neuroimage* 2007;34:694–701
13. Jung RE, Chavez RS, Flores RA, et al. **White matter correlates of neuropsychological dysfunction in systemic lupus erythematosus.** *PLoS One* 2012;7:e28373
14. Smith SM, Jenkinson M, Johansen-Berg H, et al. **Tract-based spatial statistics: voxelwise analysis of multi-subject diffusion data.** *Neuroimage* 2006;31:1487–505
15. Liang MH, Socher SA, Larson MG, et al. **Reliability and validity of six systems for the clinical assessment of disease activity in systemic lupus erythematosus.** *Arthritis Rheum* 1989;32:1107–18
16. Smith A. *Symbol Digit Modalities Test: Manual.* Torrance: Western Psychological Services; 1982
17. Rao SM. *A Manual for the Brief, Repeatable Battery of Neuropsychological Tests in Multiple Sclerosis.* Washington, DC: National Multiple Sclerosis Society; 1991
18. Gronwall DM. **Paced auditory serial addition task: a measure of recovery from concussion.** *Percept Mot Skills* 1977;44:367–73
19. Delis D, Kramer JH, Kaplan E, et al. *California Verbal Learning Test Manual*, 2nd ed. San Antonio, TX: Psychological Corporation; 2000
20. Benedict RH. *Brief Visuospatial Memory Test-Revised: Professional Manual.* Odessa, FL: Psychological Assessment Resources; 1997
21. Roca M, Torralva T, Meli F, et al. **Cognitive deficits in multiple sclerosis correlate with changes in fronto-subcortical tracts.** *Mult Scler* 2008;14:364–69
22. Zhang Y, Brady M, Smith S. **Segmentation of brain MR images through a hidden Markov random field model and the expectation-maximization algorithm.** *IEEE Trans Med Imaging* 2001;20:45–57
23. Smith SM, Jenkinson M, Woolrich MW, et al. **Advances in functional and structural MR image analysis and implementation as FSL.** *Neuroimage* 2004;23(suppl 1):S208–19
24. Zivadinov R, Heininen-Brown M, Schirda CV, et al. **Abnormal subcortical deep-gray matter susceptibility-weighted imaging filtered phase measurements in patients with multiple sclerosis: a case-control study.** *Neuroimage* 2012;59:331–39
25. Behrens TE, Johansen-Berg H, Woolrich MW, et al. **Non-invasive mapping of connections between human thalamus and cortex using diffusion imaging.** *Nat Neurosci* 2003;6:750–57
26. Smith SM. **Fast robust automated brain extraction.** *Hum Brain Mapp* 2002;17:143–55
27. Basser PJ, Pierpaoli C. **Microstructural and physiological features of tissues elucidated by quantitative-diffusion-tensor MRI.** *J Magn Reson B* 1996;111:209–19
28. Pasternak O, Sochen N, Gur Y, et al. **Free water elimination and mapping from diffusion MRI.** *Magn Reson Med* 2009;62:717–30
29. Avants BB, Tustison NJ, Song G, et al. **A reproducible evaluation of ANTs similarity metric performance in brain image registration.** *Neuroimage* 2011;54:2033–44
30. Winkler AM, Ridgway GR, Webster MA, et al. **Permutation inference for the general linear model.** *Neuroimage* 2014;92:381–97
31. Smith SM, Nichols TE. **Threshold-free cluster enhancement: addressing problems of smoothing, threshold dependence and localisation in cluster inference.** *Neuroimage* 2009;44:83–98
32. Kurtzke JF. **Rating neurologic impairment in multiple sclerosis: An expanded disability status scale (EDSS).** *Neurology* 1983;33:1444–52
33. Rovaris M, Filippi M. **Diffusion tensor MRI in multiple sclerosis.** *J Neuroimaging* 2007;17(suppl 1):27S–30S
34. Magro Checa C, Cohen D, Bollen EL, et al. **Demyelinating disease in SLE: is it multiple sclerosis or lupus?** *Best Pract Res Clin Rheumatol* 2013;27:405–24
35. Ramage AE, Fox PT, Brey RL, et al. **Neuroimaging evidence of white matter inflammation in newly diagnosed systemic lupus erythematosus.** *Arthritis Rheum* 2011;63:3048–57
36. Bosma GP, Rood MJ, Zwinderman AH, et al. **Evidence of central nervous system damage in patients with neuropsychiatric systemic lupus erythematosus, demonstrated by magnetization transfer imaging.** *Arthritis Rheum* 2000;43:48–54
37. Appenzeller S, Vasconcelos Faria A, Li LM, et al. **Quantitative magnetic resonance imaging analyses and clinical significance of hyperintense white matter lesions in systemic lupus erythematosus patients.** *Ann Neurol* 2008;64:635–43
38. Hughes M, Sundgren PC, Fan X, et al. **Diffusion tensor imaging in patients with acute onset of neuropsychiatric systemic lupus erythematosus: a prospective study of apparent diffusion coefficient, fractional anisotropy values, and eigenvalues in different regions of the brain.** *Acta Radiol* 2007;48:213–22
39. Zivadinov R, Cox JL. **Neuroimaging in multiple sclerosis.** *Int Rev Neurobiol* 2007;79:449–74
40. Abda EA, Selim ZI, Radwan ME, et al. **Markers of acute neuropsychiatric systemic lupus erythematosus: a multidisciplinary evaluation.** *Rheumatol Int* 2013;33:1243–53
41. Cercignani M, Iannucci G, Rocca MA, et al. **Pathologic damage in MS assessed by diffusion-weighted and magnetization transfer MRI.** *Neurology* 2000;54:1139–44
42. Beaulieu C. **The basis of anisotropic water diffusion in the nervous system: a technical review.** *NMR Biomed* 2002;15:435–55
43. Yu HJ, Christodoulou C, Bhise V, et al. **Multiple white matter tract abnormalities underlie cognitive impairment in RRMS.** *Neuroimage* 2012;59:3713–22
44. Denney DR, Sworowski LA, Lynch SG. **Cognitive impairment in three subtypes of multiple sclerosis.** *Arch Clin Neuropsychol* 2005;20:967–81
45. Covey TJ, Zivadinov R, Shucard JL, et al. **Information processing speed, neural efficiency, and working memory performance in multiple sclerosis: differential relationships with structural magnetic resonance imaging.** *J Clin Exp Neuropsychol* 2011;33:1129–45
46. Vleugels L, Lafosse C, van Nunen A, et al. **Visuo-perceptual impairment in multiple sclerosis patients diagnosed with neuropsychological tasks.** *Mult Scler* 2000;6:241–54
47. Emmer BJ, Veer IM, Steup-Beekman GM, et al. **Tract-based spatial statistics on diffusion tensor imaging in systemic lupus erythematosus reveals localized involvement of white matter tracts.** *Arthritis Rheum* 2010;62:3716–21
48. Kozora E, Filley CM. **Cognitive dysfunction and white matter abnormalities in systemic lupus erythematosus.** *J Int Neuropsychol Soc* 2011;17:385–92
49. Kozora E, Arciniegas DB, Duggan E, et al. **White matter abnormalities and working memory impairment in systemic lupus erythematosus.** *Cogn Behav Neurol* 2013;26:63–72
50. Schmierer K, Wheeler-Kingshott CA, Tozer DJ, et al. **Quantitative**

- magnetic resonance of postmortem multiple sclerosis brain before and after fixation. *Magn Reson Med* 2008;59:268–77
51. Song SK, Yoshino J, Le TQ, et al. **Demyelination increases radial diffusivity in corpus callosum of mouse brain.** *Neuroimage* 2005;26:132–40
52. Budde MD, Kim JH, Liang HF, et al. **Axonal injury detected by in vivo diffusion tensor imaging correlates with neurological disability in a mouse model of multiple sclerosis.** *NMR Biomed* 2008;21:589–97
53. Bertsias GK, Boumpas DT. **Pathogenesis, diagnosis and management of neuropsychiatric SLE manifestations.** *Nat Rev Rheumatol* 2010;6:358–67

Cytotoxic Edema in Posterior Reversible Encephalopathy Syndrome: Correlation of MRI Features with Serum Albumin Levels

B. Gao, B.X. Yu, R.S. Li, G. Zhang, H.Z. Xie, F.L. Liu, and C. Lv



ABSTRACT

BACKGROUND AND PURPOSE: Posterior reversible encephalopathy syndrome is a clinicroadiologic entity with typical MR imaging showing predominant vasogenic and occasional cytotoxic edema. It is unclear whether MR imaging correlates with levels of serum albumin. We determined potential risk factors for development of cytotoxic edema in posterior reversible encephalopathy syndrome.

MATERIALS AND METHODS: Seventy-nine cases with typical clinical symptoms and characteristic neuroradiologic findings conformed to posterior reversible encephalopathy syndrome diagnostic criteria and were included in this study. FLAIR, DWI, and ADC maps were interpreted to evaluate the severity and type of edema. MR imaging was correlated with the levels of serum albumin, and cytotoxic edema was compared with the location and severity of brain edema.

RESULTS: Pure vasogenic edema was found in 53 cases (67.09%), and vasogenic edema complicated with cytotoxic components, in 26 patients (32.91%). There was no difference in serum albumin levels between patients with cytotoxic components and those with vasogenic edema ($P = .983$). There was a significant difference in the edema scale scores between patients with cytotoxic edema and those with vasogenic edema ($P = .006$). The percentage of cytotoxic edema located in the area with higher scale scores of edema was significantly larger than that in areas with lower scale scores of edema ($P = .002$).

CONCLUSIONS: Serum albumin may contribute to the development of edema in PRES but is not a decisive factor for edema type. Cytotoxic edema in posterior reversible encephalopathy syndrome is probably related to regional decreased perfusion and arteriopathy. Further work should be undertaken to discover the pathophysiologic mechanisms involved.

ABBREVIATIONS: COP = colloid osmotic pressure; PRES = posterior reversible encephalopathy syndrome

Posterior reversible encephalopathy syndrome (PRES) is a clinicroadiologic entity presenting with headache, visual blurring, alteration of mental state, and acute onset of seizures. MR imaging typically demonstrates evidence of vasogenic edema in the subcortical white matter and cortex, which predominantly involves the bilateral parieto-occipital lobes.^{1,2} DWI most com-

monly shows isointensities in the region of vasogenic edema as demonstrated by abnormalities on T2-weighted imaging or FLAIR images. However, although referred to as a reversible process, foci of reduced diffusion have been described in 17%–26% of patients with PRES.^{3,4} Cytotoxic edema in or outside the massive vasogenic edema was found in a relatively lower proportion of patients with PRES and could be differentiated from vasogenic edema by using DWI. Early detection of cytotoxic edema in PRES is critical to prevent vasogenic edema from progressing into irreversible insult.

Several theories exist as to why regions of reduced diffusion are seen in some cases of PRES.⁵ The most popular theory is hyperperfusion causing severe mass effect from vasogenic edema with compression of local microcirculation.^{6,7} Ay et al⁶ suggested that increased tissue pressure eventually impairs the microcirculation and leads to ischemia in areas of massive vasogenic edema. Covarrubias et al⁷ found that cytotoxic edema developed in the cortex immediately adjacent to the area with intensely elevated ADC values in subcortical white matter, which is consistent with a

Received January 9, 2015; accepted after revision February 28.

From the Department of Radiology (B.G., B.X.Y., R.S.L., G.Z., H.Z.X., F.L.L.), Yantai Yuhuangding Hospital, Qingdao University, Shandong Province, China; Department of Radiology (B.G.), Zhongda Hospital, Southeast University, Nanjing, China; and Department of Neurology (C.L.), Yantai City Yantai Hospital and Yantai Sino-France Friendship Hospital, Shandong Province, China.

B. Gao and B.X. Yu contributed equally to this article and are co-first authors.

This work was supported by National Natural Science Foundation of China (Grant No. 81471645).

Please address correspondence to Cui Lv, MD, Department of Neurology, Yantai City Yantai Hospital and Yantai Sino-France Friendship Hospital, Yantai 264001, Shandong Province, China; e-mail: ytbrian@126.com

Indicates open access to non-subscribers at www.ajnr.org

<http://dx.doi.org/10.3174/ajnr.A4379>

heavy burden of fluid in the interstitium. It has also been suggested that edema with resultant vasoconstriction or vasospasm (with or without subarachnoid hemorrhage) leads to cytotoxicity.^{8,9} Bartynski et al⁹ confirmed a high incidence of vascular abnormality in PRES (focal vasoconstriction, vasodilation, and string-of-beads appearance) at conventional angiography and demonstrated these observations and the reversibility at MRA. It remains unclear why vasogenic edema in PRES develops into cytotoxic edema. Unchecked vasogenic edema may develop into cytotoxic edema or irreversible insults. Pirker et al¹⁰ recently reported that vasogenic edema in PRES was much more frequent in patients with decreased levels of serum albumin, whereas cytotoxic components occurred more frequently in patients with normal levels. However, the extent to which vasogenic edema is associated with reduced serum albumin levels remains unclear, as does the cause of cytotoxic edema development.

Some studies have demonstrated that cytotoxic edema is more commonly seen in PRES. In the present study, we determined the association of edema type with the levels of serum albumin in patients with PRES. We hypothesized the following: 1) the level of serum albumin would correlate with edema type, 2) severe vasogenic edema could progress into cytotoxic edema, and 3) the location of cytotoxic edema would relate to the extent and location of vasogenic edema.

MATERIALS AND METHODS

Seventy-nine patients clinically diagnosed with PRES were identified during admission to Yantai Yuhuangding Hospital from January 1, 2008, to October 31, 2014, and were pooled with a data base containing complete electronic clinical records. Our institutional review board approved this study with a waiver of informed consent. The definition of PRES used in this study fulfills the following criteria: 1) presentation with acute clinical symptoms such as headache, altered mental status, seizures, or visual disturbance with or without elevated systemic blood pressure; 2) presence of known risk factors such as hypertension, eclampsia, renal failure, use of immunosuppressive drugs, or other known causes; 3) distributions of T2WI or T2-FLAIR hyperintensities compatible with typical PRES imaging patterns; 4) clinical and imaging abnormalities mostly or completely resolved after proper therapy; and 5) other possible causes of encephalopathy or vasogenic edema ruled out. Exclusion criteria included the inability to complete the imaging examination or severe motion degradation resulting in nondiagnostic images and known systematic factors that would affect the results of blood sampling.

The presence or absence of hypertension and evidence of endothelial injury and hemolysis (lactate dehydrogenase, liver function, kidney function) was recorded. Serial venous blood samples were collected at admission to our hospital at symptom onset. The time interval from symptom onset to the collection of blood samples was recorded in all patients. MR imaging was performed at our institution on 3T MR imaging equipment. Conventional axial T1WI, T2WI, FLAIR, and DWI sequences were acquired, and coronal and sagittal T2WI scanning was available for all patients. MR imaging was performed as soon as possible on the day of symptom onset, and the time interval from symptom onset to MR imaging examinations was recorded in all patients.

All MR imaging results were reviewed by 2 senior neuroradiologists (G.B., L.F.-I.) blinded to clinical data. Each reviewer thoroughly interpreted the location, distribution, and severity of the signal abnormality; the presence of hemorrhage; and reduced diffusion. The locations of hyperintensities were defined as frontal lobe, parieto-occipital region, temporal lobe, basal ganglia, cerebellum, brain stem, deep white matter, cortical zone, subcortical zone, or watershed zone. We scored 1 for any region with signal abnormality in the bilateral hemispheres. The sum of scores of all affected locations in an individual patient provided the score of brain edema. The severity of the abnormality was graded on a scale of 0–3 based on FLAIR images (0, normally appearing brain parenchyma; 1, subtle signal abnormalities that were only faintly visible; 2, larger confluent areas of hyperintense abnormalities that were easily perceptible; and 3, complete involvement of the brain region) modified from McKinney et al.³ Images of patients with multiple MR examinations were analyzed for resolution of imaging abnormalities.

The type of edema can be categorized as vasogenic or cytotoxic. Vasogenic edema was determined by T2WI hyperintensity without reduced diffusion, while cytotoxic edema was considered in cases of T2WI hyperintensity with reduced diffusion. When we measured molecular motion with DWI, only the ADC value could be calculated. Reduced diffusion was determined by the ADC value, which was calculated as follows: $ADC = \ln(S_0/S_1)/(b_1 - b_0)$, where S_0 and S_1 are the image intensities at b -values of b_0 and b_1 respectively.

The PASW statistical package (IBM, Armonk, New York) was used for all statistical analyses. Data normality was tested with the Shapiro-Wilk test. Normally distributed data are expressed as mean \pm SD, and data that are not normally distributed are presented as median (interquartile range). Intergroup comparison was performed by using the Student *t* test for normally distributed variables and the Mann-Whitney *U* test for variables not normally distributed.

RESULTS

Seventy-nine patients (34 male, 45 female; age range, 7–66 years; mean age, 32.1 ± 11.5 years) with complete in-hospital clinical records were included in this study. Thirty-five (44.3%) of all 76 cases were patients with eclampsia or pre-eclampsia, 25 cases (31.6%) were patients with chronic renal failure, 14 (17.7%) were patients with hypertension, and 5 (6.3%) had different clinical conditions (autoimmune disease in 3 and cancer chemotherapy in 2). Clinical symptoms included headache in 68 patients (86.07%), altered mental state in 59 (74.68%), seizures in 40 (50.63%), visual disturbances in 25 (31.64%), and focal neurologic deficit in 11 patients (13.92%).

All patients had typical clinical symptoms and characteristic MR imaging findings of PRES. The parietal and occipital regions were involved in all 79 (100%) patients; the frontal region, in 70 (88.61%); and the temporal region, in 36 (45.57%). The cerebellum was involved in 30 (37.97%) patients; the deep gray matter, in 22 (27.85%); the brain stem, in 15 (18.99%); the periventricular region, in 12 (15.19%); and the corpus callosum, in 10 (12.66%) patients. Hemorrhages were present in 16 (20.25%) patients. Nine had intraparenchymal hemorrhages, 5 had cerebral micro-

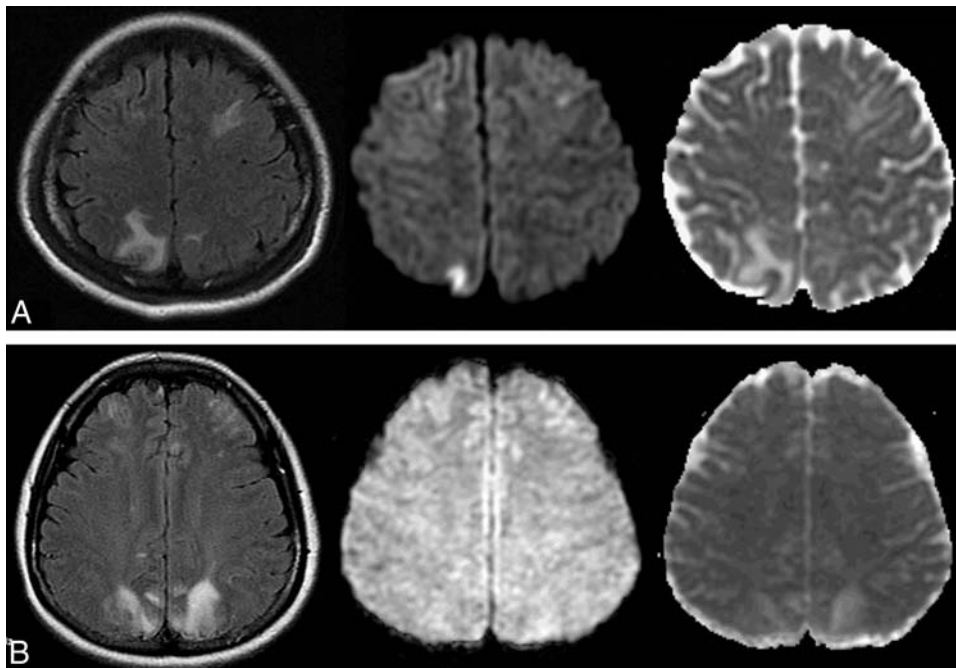


FIG 1. Comparison of serum albumin levels between patients with PRES with cytotoxic edema and those only with vasogenic edema. **A,** A 26-year-old pregnant woman presented with eclampsia, with a serum albumin level of 37 mg/dL. Hyperintense abnormalities are found in bilateral frontoparietal lobes on FLAIR (*left*), hyperintense on DWI (*middle*) and hypointense on ADC (*right*), and are also noted in the right parietal lobe, indicating cytotoxic edema. **B,** A 22-year-old woman with systemic vasculitis with a serum albumin level of 34.2 mg/dL and blood pressure of 175/110 mm Hg at onset. Symmetric hyperintensities are found in the bilateral frontoparietal lobes on FLAIR (*left*), isointense on DWI (*middle*) and hyperintense on ADC (*right*), indicating vasogenic edema.

leeds, and 2 had subarachnoid hemorrhages. MR venography examinations were performed in 56 patients (70.89%) and did not reveal an abnormality in any patient.

After analyzing all the study images including T1WI, T2WI, FLAIR, DWI sequences, and ADC maps, we found pure vasogenic edema in 53 cases (67.09%) and vasogenic edema complicated with cytotoxic components in 26 patients (32.91%). The type of edema was not associated with the interval between the onset of symptoms and MR imaging examinations ($P = .58$, Mann-Whitney U test) or with the interval between the onset of symptoms and blood sample collection ($P = .34$, Mann-Whitney U test). There was no difference in the time from presentation to imaging or to blood sample collection across subjects ($P = .61$, Mann-Whitney U test).

Serum albumin levels were normally distributed in all patients with PRES ($P = .059$, Shapiro-Wilk test), and a decrease of serum albumin concentration (<35 mg/mL) was observed in 67/79 patients (84.8%; mean, 23.6 ± 5.8 mg/dL). There was no difference in the serum albumin levels between patients with cytotoxic edema and those without ($P = .983$, Mann-Whitney U test) (Fig 1). There was no significant difference in the percentage of serum albumin decrease between patients presenting with cytotoxic edema (21/26, 80.77%) and those without (46/53, 86.79%) (Table). The scale scores of edema in all patients were not normally distributed ($P = .00$, Shapiro-Wilk test). The levels of serum albumin were not correlated with the scale scores of edema ($P = .267$). There was no statistically significant difference in serum albumin levels between the eclamptic group and the chronic renal failure group ($P = .23$), as well as the eclamptic

Comparison of clinical parameters in patients with present and absent cytotoxic edema

Parameters	Cytotoxic Edema Present (n = 26)	Cytotoxic Edema Absent (n = 53)	P Value
Age (y)	34.51 ± 11.42	33.21 ± 15.01	.74
Sex	11/15	21/32	.077
Cause ^a	4/33	5/46	.19
MAP (mm Hg)	138.51 ± 28.63	124.83 ± 30.22	.13
ALB (mg/mL)	522.00 ± 241.47	388.00 ± 191.18	.98
ALB decreased ratio	22/26	45/53	.12
SBE	20.36 ± 11.43	10.24 ± 7.20	.003 ^b

Note:—MAP indicates mean arterial pressure; ALB, albumin; SBE, score of brain edema.

^a Percentage of patients with eclampsia or pre-eclampsia.

^b Significant.

group and the hypertensive group ($P = .45$), and the chronic renal failure group and hypertensive group ($P = .17$).

Scores of brain edema in all patients were not normally distributed ($P = .037$, Shapiro-Wilk test), and serum albumin levels were not correlated with scores of brain edema ($P = .145$). There was a significant difference in scores of brain edema between patients with cytotoxic components and those without ($Z = 2.969$, $P = .003$, Mann-Whitney U test). The extent of edema in patients with cytotoxic components was significantly larger than that of patients without (Table). The percentage of cytotoxic edema located in the area with higher scale scores of edema ($= 3$) was significantly larger than that in those with lower scale scores (≤ 2) ($P = .002$, Fisher exact test) (Fig 2).

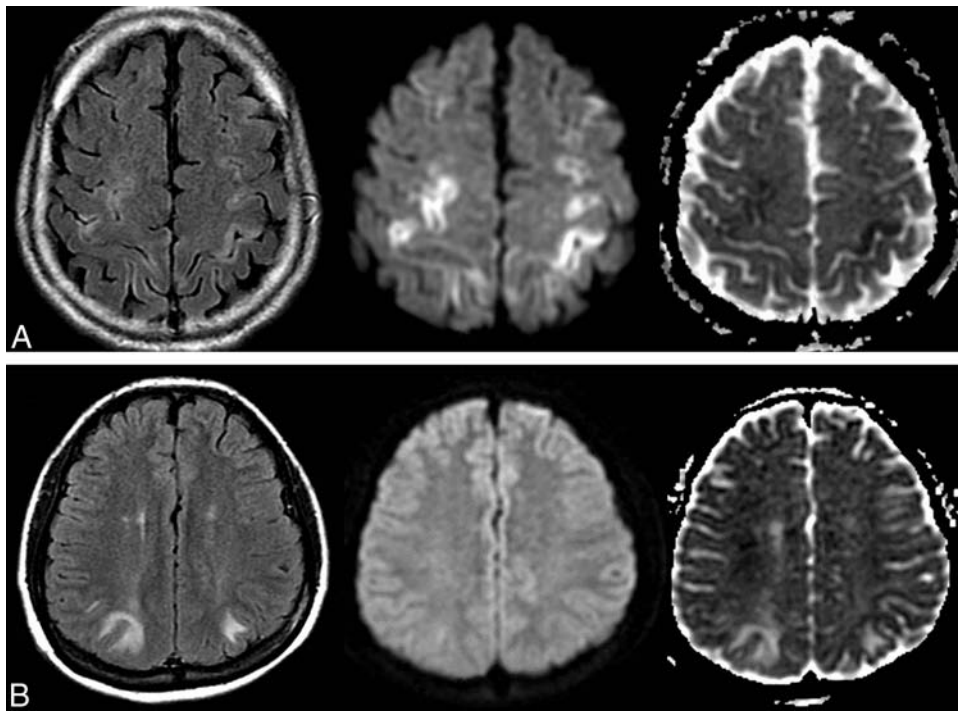


FIG 2. Comparison of the scores of brain edema between patients with PRES with cytotoxic edema and those only with vasogenic edema. *A*, A 25-year-old woman with eclampsia and seizures after cesarean delivery. FLAIR image shows symmetric confluent heterogeneous hyperintensities in the bilateral, frontal, and parietal lobes (*left*) with a scale score 3 of edema severity and marked hyperintensity in the adjacent cortex on DWI (*middle*), with hypointensity on the ADC map (*right*), indicating cytotoxic edema. *B*, A 27-year-old man with hypertension and nephritis had headache with blood pressure of 180/120 mm. Symmetric hyperintensities are found in the bilateral occipital lobes on FLAIR (*left*) with a scale score 1 of edema severity, isointense on DWI (*middle*) and hyperintense on ADC (*right*), indicating vasogenic edema.

DISCUSSION

In the present study, decreased levels of serum albumin were found in 84.8% of all patients, suggesting that a change in serum albumin levels may be one of the potential factors resulting in edema development in PRES. Serum albumin is a main contributor to colloid osmotic pressure (COP). Decrease of serum albumin levels would result in retention of intravascular fluid by reducing perfusion pressure.¹¹ In conditions with endothelial damage due to inflammatory processes, reduction of COP may facilitate fluid extravasation and edema development.¹⁰ Vasogenic edema can be aggravated by a marked decrease of COP, as shown by Pirker et al.¹⁰ However, we observed that serum albumin concentration was not associated with edema type and was decreased in patients with cytotoxic edema. Albumin contributes to up to 80% of COP in healthy subjects. However, its contribution toward COP is only 17% in critically ill individuals.¹² Reduction of COP alone would not cause edema in the normal brain tissue, which is largely due to the properties of capillary endothelium that constitute the BBB.¹³ The failure of autoregulatory mechanisms involved in the maintenance of CBF might also lead to hyperperfusion and vasogenic edema in the presence of excessive elevations in systemic blood pressure. Low serum albumin may be a surrogate marker of disease severity rather than an indicator of low COP. Therefore, when one treats patients with PRES with hypoalbuminemia, the underlying cause of hypoalbuminemia should probably be treated first. Two of our patients hardly improved with hypoalbuminemia treatment. While improving hypoalbuminemia may or may not help the patient, correction of

the underlying disorder is more critical than merely reversal of hypoalbuminemia.¹⁴

The pathogenesis of brain lesions in PRES is not fully understood, and 2 opposing theories have been proposed.¹⁵ Endothelial dysfunction seems to better account for the mechanisms of PRES, given that both vasogenic and cytotoxic edema could occur in PRES, as well as hypoperfusion or hyperperfusion.¹⁶ Forced dilation of cerebral arteries and disruption of the integrity of the BBB are considered the most important mechanisms underlying vasogenic edema observed in patients with PRES and hypertension. Alternatively, ischemia triggered by systemic inflammation, endothelial injury, and vascular dysfunction is also suggested to contribute to vasogenic edema observed in PRES, as well as active leakage of fluid due to other processes affecting the vascular wall. Parenchymal contrast enhancement, typically seen only with injury to the BBB, also supports this theory. Although most patients do not show any abnormal enhancement on postcontrast T1WI, it has been reported to occur in 21%–38% of patients with PRES.^{3,4} Typically, the enhancement is a mild, gyri form, and there is leptomeningeal or cortical enhancement within the lesions on postcontrast imaging studies. More commonly than in adults, contrast enhancement in children showed that pathophysiology was related to the BBB breakdown and also supported the theory of toxic endothelial injury.¹⁷ BBB dysfunction might not only be restricted to areas with apparent lesions but could also involve the normal-appearing cerebral tissue, and even the retinal circulation.¹⁸ Therefore, endothelial injury or injury to the BBB is

probably more likely than the other mechanism to account for the spectrum and variety of physiologic findings noted in PRES.

In this study, cytotoxic components in vasogenic edema were found in 33% of all patients, a slightly higher percentage compared with 17%–26% of patients with PRES with foci of reduced diffusion in prior studies of these patients.^{3,4} This slightly higher percentage may be attributable to either case selection criteria or case source.

Several studies have reported radiologic findings of cytotoxic edema or ischemia in PRES,^{3,4} which were associated with fibrinoid necrosis and microinfarction in pathologic studies.^{19,20} Cytotoxic edema manifests as DWI hyperintensity with decreased ADC values. Moreover, in patients with cytotoxic edema, there is partial reversal or nearly complete resolution of the abnormality, and even patients with cytotoxic edema would not show conversion to infarction or may have mild atrophy. Cytotoxic edema in the acute phase does by no means imply conversion to infarction, and DWI does not seem to be a valid prognostic marker.²¹ The value of DWI and ADC maps in predicting the clinical prognosis of PRES warrants further investigation.²² Cytotoxic edema in PRES may be attributable to cerebral vasospasm, with endothelial activation or injury leading to reduced CBF with consequent hypoxia, as described in several PRES studies using MR imaging or conventional angiography.⁹ Most interesting, a recent study reported that the high incidence of cerebral microbleeds was not correlated with edema severity/extent and the presence of DWI-positive findings.²³ Atypical neuroimaging appearances, such as intracranial hemorrhage, cytotoxic edema, and abnormal enhancement, may reflect endothelial injury or disruption and would contribute to early diagnosis and prognosis evaluation.²⁴ Vascular imaging and perfusion imaging would be helpful to further elucidate the mechanism of edema development in PRES.²⁵

We showed that the scale scores of edema in patients with cytotoxic components were significantly higher than those in patients with pure vasogenic edema, and the percentage of patients with cytotoxic edema in areas with higher scale scores was significantly higher than that in those areas with lower scale scores. The presence of ischemia within areas of vasogenic edema has been observed in several retrospective studies.^{3,4,6,7} However, to the best of our knowledge, the development of ischemia with an increasing degree of brain edema has not been well-described. A correlation between the presence of vasculopathy and ischemia was recently reported, suggesting a causal relationship between cytotoxic edema and larger areas of vasogenic edema.²⁶ The normally protective vasoconstrictive response can progress into vasospasm, leading to local hypoxia, BBB disruption, fluid extravasation, and subsequent edema.²⁷ Enhanced systemic endothelial activation (swelling) and leukocyte trafficking and vasoconstriction, alone or in combination, may result in brain and systemic hypoperfusion.¹⁵ Therefore, higher scale scores of brain edema often develop and progress into ischemia. We also found that most cytotoxic edema was superimposed on, or adjacent to, the larger areas of vasogenic edema. A larger area of edema is typically contiguous and crosses large vessel boundaries, rather than being a watershed pattern.²⁶ The mass effect induced by larger areas of vasogenic edema would compress or shift the vessels passing through or around the edema region, which may result in regional

hypoperfusion, elevation of tissue pressure, and reduction of CBF to ischemic levels, as well as vasoconstriction.^{5,28} Subsequently, the areas surrounding marked vasogenic edema may progress to cytotoxic edema. We agree with the proposal that cytotoxic edema in PRES is probably related to local decreased perfusion and arteriopathy.²⁸ However, further work should be performed to uncover the pathophysiologic mechanisms involved.

Eclampsia or pre-eclampsia is the primary clinical cause of PRES. During a normal pregnancy, the BBB adapts to prevent circulating permeable factors from entering the brain. Plasma from women with pre-eclampsia has been found to increase the permeability of the BBB; the latter would permit the passage of damaging antivasogenic and antiendothelial proteins into the brain and result in neurologic symptoms of eclampsia.^{29,30} A higher percentage (44.3%) of patients with eclampsia was also found in this study than was typically seen in past studies, which may be related to either our university hospital type or case-selection criteria. Ishikura et al³¹ even reported 7 pediatric patients with nephrotic syndrome who developed PRES and had low levels of serum albumin, implying a possible correlation between them. In these patients, PRES rapidly abated after the addition of albumin, despite further treatment with cytotoxic substances. Infusion of human serum albumin at early and reversible phases to increase oncotic pressure and restore antioxidative potential could theoretically prevent widespread oxidative and/or ischemic damage to vulnerable tissue in PRES.¹⁰ Many cases of acute toxic leukoencephalopathy may share common causes and pathophysiologic features with PRES. Reduced diffusion is typically seen in association with acute toxic leukoencephalopathy but less commonly in PRES, which could account for the differences of the mechanism and location in white matter involvement between the 2 processes.³²

Because clinical factors, imaging findings, and CSF laboratory results may influence the prognosis of PRES, a few limitations of this prospective study should be noted. First, selection bias toward the etiology of PRES may result in significant heterogeneity as to the relative proportion of patients for the study, and it is difficult to determine a single underlying etiology for PRES, often having multiple etiologies. Second, although vasculopathy is thought to play an important part in the pathophysiology of PRES, MR angiography was not routinely performed in our study. Additionally, the extent to which inflammatory changes contribute to vasculopathy has not been clarified. Third, because urine testing is not routinely performed at the onset in our patients with PRES, urine albumin concentrations could not be appreciated with serum albumin levels and neither could albumin concentration in CSF based on lumbar puncture.³³ Prospective exploration is warranted to establish the association of biochemical values with unfavorable outcome in patients with PRES, and this might prove useful to clinicians of various disciplines involved in the care of these patients.^{34,35}

CONCLUSIONS

Serum albumin may be a potential contributor to the development of edema in PRES, but it is not a decisive factor for edema type. Cytotoxic edema or ischemia is often seen in larger areas or to a higher extent of vasogenic edema, which is probably related to

local decreased perfusion and arteriopathy. Further work should be performed to uncover and understand the pathophysiologic mechanisms involved.

ACKNOWLEDGMENTS

The authors are grateful for the assistance of Dr Ri-ming Liu in the laboratory tests.

Disclosures: Bo Gao—RELATED: Grant: National Natural Science Foundation of China (Grant No. 81471645).

REFERENCES

- Hinchey J, Chaves C, Appignani B, et al. **A reversible posterior leukoencephalopathy syndrome.** *N Engl J Med* 1996;334:494–500
- Bartynski WS. **Posterior reversible encephalopathy syndrome, Part 1: fundamental imaging and clinical features.** *AJNR Am J Neuroradiol* 2008;29:1036–42
- McKinney AM, Short J, Truwit CL, et al. **Posterior reversible encephalopathy syndrome: incidence of atypical regions of involvement and imaging findings.** *AJR Am J Roentgenol* 2007;189:904–12
- Fugate JE, Claassen DO, Cloft HJ, et al. **Posterior reversible encephalopathy syndrome: associated clinical and radiologic findings.** *Mayo Clin Proc* 2010;85:427–32
- Rykkens JB, McKinney AM. **Posterior reversible encephalopathy syndrome.** *Semin Ultrasound CT MR* 2014;35:118–35
- Ay H, Buonanno FS, Schaefer PW, et al. **Posterior leukoencephalopathy without severe hypertension: utility of diffusion-weighted MRI.** *Neurology* 1998;51:1369–76
- Covarrubias DJ, Luetmer PH, Campeau NG. **Posterior reversible encephalopathy syndrome: prognostic utility of quantitative diffusion-weighted MR images.** *AJNR Am J Neuroradiol* 2002;23:1038–48
- Henderson RD, Rajah T, Nicol AJ, Read SJ. **Posterior leukoencephalopathy following intrathecal chemotherapy with MRA-documented vasospasm.** *Neurology* 2003;60:326–28
- Bartynski WS, Boardman JF. **Catheter angiography, MR angiography, and MR perfusion in posterior reversible encephalopathy syndrome.** *AJNR Am J Neuroradiol* 2008;29:447–55
- Pirker A, Kramer L, Voller B, et al. **Type of edema in posterior reversible encephalopathy syndrome depends on serum albumin levels: an MR imaging study in 28 patients.** *AJNR Am J Neuroradiol* 2011;32:527–31
- Quinlan G, Martin GS, Evans TW. **Albumin: biochemical properties and therapeutic potential.** *Hepatology* 2005;41:1211–19
- Blunt MC, Nicholson JP, Park GR. **Serum albumin and colloid osmotic pressure in survivors and nonsurvivors of prolonged critical illness.** *Anaesthesia* 1998;53:755–61
- Drummond JC. **Colloid osmotic pressure and the formation of posttraumatic cerebral edema.** *Anesthesiology* 2010;112:1079–81
- Pulimood TB, Park GR. **Debate: albumin administration should be avoided in the critically ill.** *Crit Care* 2000;4:151–55
- Bartynski WS. **Posterior reversible encephalopathy syndrome, Part 2: controversies surrounding pathophysiology of vasogenic edema.** *AJNR Am J Neuroradiol* 2008;29:1043–49
- Marra A, Vargas M, Striano P, et al. **Posterior reversible encephalopathy syndrome: the endothelial hypotheses.** *Med Hypotheses* 2014;82:619–22
- Donmez FY, Guleryuz P, Agildere M. **MRI findings in childhood PRES: what is different than the adults?** *Clin Neuroradiol* 2014 Oct 8. [Epub ahead of print]
- Ozkan E, Gocmen R, Topcuoglu MA, et al. **Blood-retina-barrier disruption accompanying blood-brain-barrier dysfunction in posterior reversible encephalopathy syndrome.** *J Neurol Sci* 2014;346:315–17
- Decker DA, Falchook AD, Yachnis AT, et al. **Radiographic and pathologic findings in an atypical brainstem variant of reversible posterior leukoencephalopathy syndrome.** *Neurologist* 2009;15:364–66
- Jacquot C, Glastonbury CM, Tihan T. **Is posterior reversible encephalopathy syndrome really reversible? Autopsy findings 4.5 years after radiographic resolution.** *Clin Neuropathol* 2015;34:26–33
- Kastrup O, Schlamann M, Moeninghoff C, et al. **Posterior reversible encephalopathy syndrome: the spectrum of MR imaging patterns.** *Clin Neuroradiol* 2015;25:161–71
- Gao B, Lv C. **Posterior reversible encephalopathy syndrome in 46 of 47 patients with eclampsia: beyond it.** *Am J Obstet Gynecol* 2014;211:83–84
- McKinney AM, Sarakiya B, Gustafson C, et al. **Detection of microhemorrhage in posterior reversible encephalopathy syndrome using susceptibility-weighted imaging.** *AJNR Am J Neuroradiol* 2012;33:896–903
- Lv C, Gao B. **Can clinical and MRI findings predict the prognosis of variant and classical type of posterior reversible encephalopathy syndrome (PRES)? Still a challenge.** *Acta Radiol* 2015;56:NP3–4
- Hinchey JA. **Reversible posterior leukoencephalopathy syndrome: what have we learned in the last 10 years?** *Arch Neurol* 2008;65:175–76
- Li Y, Gor D, Walicki D, et al. **Spectrum and potential pathogenesis of reversible posterior leukoencephalopathy syndrome.** *J Stroke Cerebrovasc Dis* 2012;21:873–82
- Williams KP, Wilson S. **Persistence of cerebral hemodynamic changes in patients with eclampsia: a report of three cases.** *Am J Obstet Gynecol* 1999;181:1162–65
- Tamaki K, Sadoshima S, Baumbach GL, et al. **Evidence that disruption of the blood-brain barrier precedes reduction in cerebral blood flow in hypertensive encephalopathy.** *Hypertension* 1984;6(2 pt 2):175–81
- Cipolla MJ, Bishop N, Chan SL. **Effect of pregnancy on autoregulation of cerebral blood flow in anterior versus posterior cerebrum.** *Hypertension* 2012;60:705–11
- Porcello Marrone LC, Gadonski G, de Oliveira Laguna G, et al. **Blood-brain barrier breakdown in reduced uterine perfusion pressure: a possible model of posterior reversible encephalopathy syndrome.** *J Stroke Cerebrovasc Dis* 2014;23:2075–79
- Ishikura K, Ikeda M, Hamasaki Y, et al. **Posterior reversible encephalopathy syndrome in children: its high prevalence and more extensive imaging findings.** *Am J Kidney Dis* 2006;48:231–38
- McKinney AM, Kieffer SA, Paylor RT, et al. **Acute toxic leukoencephalopathy: potential for reversibility clinically and on MRI with diffusion-weighted and FLAIR imaging.** *AJR Am J Roentgenol* 2009;193:192–206
- Alhilali LM, Reynolds AR, Fakhran S. **A multi-disciplinary model of risk factors for fatal outcome in posterior reversible encephalopathy syndrome.** *J Neurol Sci* 2014;347:59–65
- Gao B, Liu FL, Zhao B. **Association of degree and type of edema in posterior reversible encephalopathy syndrome with serum lactate dehydrogenase level: initial experience.** *Eur J Radiol* 2012;81:2844–47
- Lv C, Gao B. **Serum lactate dehydrogenase as a predictor of outcome in posterior reversible encephalopathy syndrome: imperative to unify.** *AJNR Am J Neuroradiol* 2015;36:E29–30

Seizure Frequency Can Alter Brain Connectivity: Evidence from Resting-State fMRI

R.D. Bharath, S. Sinha, R. Panda, K. Raghavendra, L. George, G. Chaitanya, A. Gupta, and P. Satishchandra



ABSTRACT

BACKGROUND AND PURPOSE: The frequency of seizures is an important factor that can alter functional brain connectivity. Analysis of this factor in patients with epilepsy is complex because of disease- and medication-induced confounders. Because patients with hot-water epilepsy generally are not on long-term drug therapy, we used seed-based connectivity analysis in these patients to assess connectivity changes associated with seizure frequency without confounding from antiepileptic drugs.

MATERIALS AND METHODS: Resting-state fMRI data from 36 patients with hot-water epilepsy (18 with frequent seizures [>2 per month] and 18 with infrequent seizures [≤ 2 per month]) and 18 healthy age- and sex-matched controls were analyzed for seed-to-voxel connectivity by using 106 seeds. Voxel wise paired *t*-test analysis ($P < .005$, corrected for false-discovery rate) was used to identify significant intergroup differences between these groups.

RESULTS: Connectivity analysis revealed significant differences between the 2 groups ($P < .001$). Patients in the frequent-seizure group had increased connectivity within the medial temporal structures and widespread areas of poor connectivity, even involving the default mode network, in comparison with those in the infrequent-seizure group. Patients in the infrequent-seizure group had focal abnormalities with increased default mode network connectivity and decreased left entorhinal cortex connectivity.

CONCLUSIONS: The results of this study suggest that seizure frequency can alter functional brain connectivity, which can be visualized by using resting-state fMRI. Imaging features such as diffuse network abnormalities, involvement of the default mode network, and recruitment of medial temporal lobe structures were seen only in patients with frequent seizures. Future studies in more common epilepsy groups, however, will be required to further establish this finding.

ABBREVIATIONS: DMN = default mode network; HWE = hot-water epilepsy; PCC = posterior cingulate cortex; FDR = false-discovery rate

Behind the unquestionable clinical and electroencephalographic manifestations of an epileptic seizure, there lie several molecular, metabolic, cellular, and hemodynamic events that alter the function of the brain in a complex manner. These alterations may be transient, but many such events can have a cumulative effect, resulting in psychological and memory deficits, personality changes, and reduced functioning in patients with epilepsy. Advances in neurophysiology, functional imaging, and

computational neurosciences have made it possible to derive models mathematically to describe such complex diseases.

Disease-state network analysis with resting-state fMRI is becoming increasingly popular because of its superior spatial resolution, nondependence on task, ease of acquisition, and ability to visualize whole-brain functional networks, which are amenable to long-term changes related to disease states.¹ Application of connectivity principles to these data has promoted research in various aspects of epileptic seizures, and there has been overwhelming report of decreased connectivity around the seizure-onset zone²⁻⁶ and the default mode network (DMN) by several groups.^{7,8} In 2012, Jehi⁷ and Morgan et al⁹ reported that connectivity patterns were different in patients with right and left mesial temporal sclerosis and that there was decreased connectivity between the regions of the DMN and the hippocampus and amygdala in patients with mesial temporal sclerosis. Similarly, hemispheric connectivity analysis in patients with unilateral mesial temporal sclerosis revealed decreased local and intrahemispheric connectivity and

Received September 16, 2014; accepted after revision February 25, 2015.

From the Departments of Neuroimaging and Interventional Radiology (R.D.B., R.P., L.G., A.G.) and Neurology (S.S., K.R., G.C., P.S.) and Advanced Brain Imaging Facility (R.D.B., R.P.), Cognitive Neuroscience Center, National Institute of Mental Health and Neuro Sciences, Bangalore, Karnataka, India

Please address correspondence to P. Satishchandra, DM, FRCP, National Institute of Mental Health and Neuro Sciences, Hosur Rd, Bangalore, Karnataka, India; e-mail: drpsatishchandra@yahoo.com; cns.researchers@gmail.com; @CNSresearchers



Evidence-Based Medicine Level 2.

<http://dx.doi.org/10.3174/ajnr.A4373>

increased interhemispheric connectivity.¹⁰ In contradistinction to the aforementioned results, there have been reports on increased hippocampal connectivity that was presumed to be a compensatory mechanism because it linearly correlated with a disease duration of >10 years.^{1-4,6} Graph-theory analysis of resting-state fMRI data from patients with epilepsy also revealed decreased functional nodal topologic properties of the DMN that were positively correlated with disease duration.^{8,11-14} Regional homogeneity analysis of resting-state fMRI data was even used as a presurgical tool for seizure identification in patients with MR-negative focal epilepsy.¹⁵ Thus, various models of data analysis have helped in understanding epilepsy further, and now there is increasing interest in using these models to reclassify epilepsy as a focal epileptogenic area^{10,15} or as a network of seizure-generating areas.¹⁶⁻¹⁸

Gower's clinical observation that "seizures beget seizures" in 1881 triggered several studies, especially animal models that addressed the genesis of epilepsy. Kindling is a phenomenon in which the repetition of subconvulsive electrical stimuli results in a progressive epileptic state and an increased frequency of seizures.^{19,20} Kindling is a continuous temporal process that remodels the mechanisms and circuits in the brain. Early changes, beginning with modulation of presynaptic and postsynaptic functioning in glutamate, *N*-methyl-D-aspartate, and α -amino-3-hydroxy-5-methyl-4-isoxazolepropionic acid receptors, and late changes, including mossy fiber sprouting, synaptogenesis/neurogenesis, and neurotrophic factor regulation, are known to occur as a result of kindling.²⁰⁻²² The increased risk for seizure recurrence with increasing numbers of seizures was first demonstrated clinically by Hauser and Lee.²³ The effects of seizure frequency and chronic epilepsy have been studied sparsely by using imaging techniques.¹ For example, Widjaja et al²⁴ found no significant correlation with seizure frequency, age of seizure onset, or duration of epilepsy in a group of children with medically refractory epilepsy.

Apart from other disease-related confounders such as type of seizure, duration of epilepsy, age of onset, family history of epilepsy, etc, each of which can induce connectivity differences independently, a major limitation of interpreting the results of functional connectivity in patients with epilepsy is the use of antiepileptic drugs. Patients with hot-water epilepsy (HWE) present with a history of complex partial seizures clinically suggestive of temporal lobe onset with or without secondary generalization. Most patients are drug naive at their first evaluation, which provided us an opportunity to study networks that were affected by seizure frequency and matched for other disease-related confounders but not antiepileptic drugs. On the basis of the phenomenon of kindling, we hypothesized that seizures can alter brain connectivity and that the frequency of seizures can influence the magnitude of this alteration. We predicted that patients with a higher seizure frequency would have widespread changes in comparison with patients with a lower seizure frequency. We used seed-to-voxel-based resting-state fMRI connectivity in 36 drug-naive patients with HWE who were comparable in terms of various factors such as age, sex, education, and epilepsy-related confounders. We hope that such quantifiable noninvasive *in vivo* evidence further enhances knowledge of the etiopathogenesis of HWE and, if applicable to refractory epilepsy, can identify such patients early to avoid time-consuming trial-and-error methods

of pharmacotherapy and facilitate early intervention to minimize cognitive deficits.

MATERIALS AND METHODS

This prospective study was conducted at a university hospital, a major tertiary care referral center for neurologic disorders. Written informed consent was obtained from each participant, and the study was approved by the institutional ethics committee of the National Institute of Mental Health and Neuro Sciences.

Participants. The participants were 36 drug-naive patients with HWE (male-to-female ratio, 3:1; mean age [\pm standard deviation], 28.86 \pm 10.07 years) who were categorized into 1 of 2 groups: 18 patients (mean age, 29.06 \pm 9.61 years; mean age at first seizure, 22.61 \pm 8.39 years; mean duration of epilepsy, 6.56 \pm 6.48 years) with a seizure frequency of >2 per month were assigned to the frequent-seizure group, and another 18 patients (mean age, 28.67 \pm 10.78 years; mean age at first seizure, 20.69 \pm 10.36 years; mean duration, 7.39 \pm 9.76 years) with a seizure frequency of \leq 2 per month were assigned to the infrequent-seizure group. The diagnosis of reflex HWE was based on criteria of the Commission of the International League Against Epilepsy.^{25,26} Recruitment and evaluation were carried out under the supervision of 2 epileptologists (P.S. and S.S.). The demographic and phenotypic details were recorded. Eighteen healthy controls (male-to-female ratio, 3:1; mean age, 29.1 \pm 9 years) matched in terms of age, sex, and years of education were recruited from the hospital staff. Only healthy participants who did not have any history of neurologic or psychiatric illnesses were enrolled in the study. Morphologic evaluation of brain MR imaging including the hippocampus revealed that none of the participants had any structural abnormalities. Patients with diffuse EEG abnormalities and frequent interictal epileptiform discharges were excluded from the analysis. Statistical analysis for the demographic variables using the independent-sample *t* test for continuous variables and the χ^2 test for categorical variables revealed no significant differences between the control and patient groups other than seizure frequency.

Image Acquisition. All the participants underwent resting-state fMRI and structural MR imaging by using a 3T Skyra MR scanner (Siemens, Erlangen, Germany) with a 20-channel head coil. Foam pads were used to reduce head motion. The acquisition parameters for EPI using blood oxygen level-dependent contrast were as follows: volumes, 185; TR, 3000 ms; TE, 30 ms; sections, 34; section thickness, 4 mm; FOV, 192 \times 192 mm; resolution, 64 \times 64; refocusing pulse, 90°; and voxel size, 3 \times 3 \times 4 mm. The total time of acquisition for resting-state fMRI was 9 minutes 24 seconds. Anatomic images were acquired by using a 3D T1-weighted MPRAGE sequence in 192 sections with a TR of 1900 ms, a TE of 2.43 ms, a TI of 900 ms, an FOV of 256 \times 256, a resolution of 256 \times 256, and a section thickness of 1 mm. Axial FLAIR, T2, and gradient sequences were used to rule out structural abnormalities.

Image Analysis

Preprocessing. The functional and structural MR imaging preprocessing was performed by using statistical parametric map-

Table 1: Demographic and clinical features of 2 groups (with frequent or infrequent seizures) of patients with HWE

Clinical Feature	Frequent-Seizure Group (>2/mo)	Infrequent-Seizure Group (≤2/mo)	P Value
Male/female ratio, <i>n</i>	14:4	13:5	.700
Mean (±SD) age at evaluation, <i>y</i>	29.06 ± 9.86	28.67 ± 10.78	.910
Mean (±SD) age at onset, <i>y</i>	22.61 ± 8.39	20.69 ± 10.36	.546
Mean (±SD) duration of illness, <i>y</i>	6.56 ± 6.48	7.39 ± 9.76	.546
HWE attacks per month			<.0001
Mean (±SD)	2.61 ± 0.69	0.62 ± 0.52	
Median (range)	2.5 (2–4)	0.43 (0.02–1.66)	<.0001
1:1 episodes, <i>n</i> (%) ^a	8 (44.4)	1 (5.6)	.717
Family history of any type of epilepsy, <i>n</i> (%)	6 (33)	5 (27)	.463
History of febrile convulsion, <i>n</i>	1	0	
Family history of HWE, <i>n</i> (%)	4 (22)	1 (5.6)	
Self-induction phenomena, <i>n</i> (%)	2 (11.1)	2 (11.1)	
Abnormal EEG, <i>n</i>	0	2 (11.1)	
Focal abnormalities in EEG, <i>n</i>	0	2	
Mean (±SD) time between last seizure and fMRI, days	10.6 ± 7.5	9.38 ± 6.9	.735
Complex partial seizures, <i>n</i>	12	10	
Generalized tonic-clonic seizures, <i>n</i>	6	8	

^a Patients who were having seizures every time they took a hot-water bath.

ping (SPM8; <http://www.fil.ion.ucl.ac.uk/spm/software/spm8/>). To maintain the magnetization equilibrium in the brain, the first 5 images were discarded. The data were realigned for motion correction by registration to the mean image. Each of the subjects' functional images were transformed to the Montreal Neurological Institute standard space by using the deformation field derived in the new segmentation procedure (voxel size, 3 × 3 × 3 mm) and smoothed with a Gaussian kernel of 6 mm at full width at half maximum. In addition to these steps, the structural data were segmented for gray matter, white matter, and CSF to remove the effects of head motion and WM and CSF noise reduction and for bias correction of magnetization in homogeneity.

Anatomic Parcellation. The fMRI data were segmented into 106 anatomic ROIs on the basis of a Talairach atlas for whole brain regions (47 Brodmann areas, cerebellar tonsils, pyramis, and the posterior and anterior thalami of both the hemispheres) by using the anatomically labeled template reported by Tzourio-Mazoyer et al²⁷ in 2002 and per several previous studies.^{28,29}

Functional Connectivity Analysis. A seed-to-voxel-based functional connectivity analysis was performed by computing the temporal correlation between the blood oxygen level-dependent signals to create a correlation matrix showing connectivity from the seed region to all other voxels in the brain by using the functional connectivity toolbox (CONN, version 13.L) implemented in SPM8 (<http://www.nitrc.org/projects/conn>; cited by Whitfield-Gabrieli and Ford, 2012)³⁰ and was used to create individual subject seed-to-voxel connectivity maps. The preprocessed images were used for seed-based connectivity analysis. Motion correction was performed by using rigid-body transformation. We used 3 translational and 3 rotational parameters as covariates. Because the spontaneous, coherent, and low-frequency fluctuations of the blood oxygen level-dependent signal are used for resting-state fMRI analyses, the blood oxygen level-dependent time-series for each subject was extracted and bandpass filtered

(0.009–0.09 Hz). Because neural activation is localized to gray matter, fluctuations in white matter and CSF regions should primarily reflect signals of non-neural origin, such as cardiac or respiratory fluctuations. Hence, WM- and CSF-related physiologic noise source reduction was carried out by using the CompCor algorithm.^{31,32} The seed ROIs consisted of 3-mm-radius spheres centered on Montreal Neurological Institute coordinates used to identify the corresponding networks. Bivariate analysis was performed between each pair of ROIs. The general linear modeling was designed with canonical hemodynamic response function to determine significant connections³⁰ at the individual level (first-level analysis). The connectivity maps were estimated for correlating seed region signals with voxel signals throughout the whole brain, thereby creating seed region-to-voxel Fisher-transformed connectivity maps. Second-level random-effects analysis was used to create within-group statistical parameter maps for each network and to examine connectivity differences between groups. The group mean effects were estimated for the 3 groups.

Statistical Analysis

Voxel wise paired *t*-test analyses between the 1) infrequent-seizure and control groups, 2) frequent-seizure and control groups, and 3) frequent-seizure and infrequent-seizure groups were performed to detect regions with significant intergroup differences. Between-group statistical parameter maps were thresholded at a whole-brain cluster-level-corrected α value of .05 for a voxel wise *P* value of <.005 with false-discovery rate (FDR) correction,³³ which was more stringent than the required adjusted *P* value of ≤.017.

RESULTS

The demographic and phenotypic details of the patients are provided in Table 1. At the time of recruitment, each patient was drug naive and had never been prescribed antiepileptic drugs. On average, there was a gap of 10.5 ± 7.5 days between the last seizure and MR imaging (frequent-seizure group, 10.6 ± 7.5 days; infrequent-seizure group, 9.38 ± 6.9 days). These differences between the groups were not statistically significant (*P* = .753). Only 2 patients in the infrequent-seizure group revealed focal EEG abnormalities as spike-and-wave epileptiform discharges over the right temporo-occipital region. A family history of seizures was present in 6 patients in the frequent-seizure group and 5 patients in the infrequent-seizure group. Most were complex partial seizures or secondarily generalized tonic-clonic seizures (Table 1). Among all the demographic variables, only the frequency of seizures was statistically significant when the independent-sample *t* test was used (*P* < .001). The seed-to-voxel-based connectivity analysis revealed that patients in the frequent-seizure group had a widespread decrease in connectivity, predominantly involving the

parietal lobes and the DMN, whereas those in the infrequent-seizure group had only a focal decrease in entorhinal connectivity. It is interesting to note that patients in the frequent-seizure group had increased visual cortex, entorhinal, and perirhinal connections, whereas those in the infrequent-seizure group had increased DMN connectivity compared to the healthy controls. The details of the various subgroup analyses are given below.

Frequent-Seizure Group versus Healthy Controls

In the analysis of healthy controls versus the frequent-seizure group, it was found that patients had significantly decreased connections of the posterior cingulate cortex (PCC) with the angular gyrus, temporopolar region, and medial prefrontal cortex ($P < .001$). Various seeds in the left parietal lobe also showed significantly (FDR-corrected $P < .001$) decreased connections with bilateral motor cortices, the dorsal frontal cortex, superior temporal lobes, and cerebellar tonsils. The right dorsal frontal cortex had significantly (FDR-corrected $P < .005$) decreased connections with the bilateral superior temporal gyrus. It was interesting to note that patients in the frequent-seizure group also had significantly ($P < .005$) increased connections of primary and secondary visual cortices to the precuneus. The mean images of the connectivity analyses of the most significant ROIs are presented in the composite Fig 1, and the areas are detailed in Table 2.

Infrequent-Seizure Group versus Healthy Controls

The patients in the infrequent-seizure group were similar to the healthy controls in most of the connections. Only the left posterior entorhinal cortex showed a significant (FDR-corrected $P < .005$) decrease in connectivity with the left fusiform gyrus. Patients in the infrequent-seizure group had increased connections of the DMN with the PCC and of the anterior prefrontal cortex. There was also increased connectivity of the anterior cingulate cortex with the superior temporal region. It should be noted that patients with infrequent seizures had no areas with decreased connections to the DMN. The mean image-of-connectivity analysis of these ROIs is presented in the composite Fig 1, and the most significant areas are listed in Table 3.

Frequent- versus Infrequent-Seizure Group

The patients in the frequent-seizure group were significantly (FDR-corrected $P < .001$) different from those in the infrequent-seizure group in their left parietal and PCC connections. The most significant (FDR-corrected $P < .001$) among these areas were the connections of the left angular gyrus, precuneus, and left parietal lobes with the PCC and medial prefrontal cortex. The left somatosensory cortex, bilateral premotor cortex, and left lower parietal lobe also showed significant (FDR-corrected $P < .005$) decreased connections. The bilateral prefrontal cortex, right superior frontal gyrus, and dorsal frontal cortex also revealed significant (FDR-corrected $P < .005$) decreased connections with the superior and middle temporal gyrus. The anterior cingulate showed significant decreased connections with the left piriform cortex. The patients with frequent seizures had a significant (FDR-corrected $P < .005$) increase in connections within the temporal lobes bilaterally involving the seizure-prone entorhinal, perirhinal with primary auditory cortex bilaterally. The mean image-of-connectivity analysis

of these ROIs is presented in the composite Fig 1, and the most significant areas are listed in Table 4.

DMN Connectivity

To assess the functional connectivity differences encompassing the DMN, seed-based connectivity analysis of the PCC (FDR-corrected $P < .001$) was performed for each of the 3 groups. Patients in the infrequent-seizure group revealed increased DMN connectivity with increased connections between the anterior prefrontal lobe, PCC, anterior cingulate cortex, and medial temporal lobe in comparison with those in the healthy controls. Patients in the frequent-seizure group had poor connections of the PCC seed with no connectivity to the anterior cingulate, medial frontal, bilateral parietal, or temporal lobes. These differences are highlighted in Fig 2.

DISCUSSION

The exact etiopathogenesis of hot-water epilepsy is not clear, but several factors, including genetic factors, environmental factors, consanguineous marriage, and a habit of taking baths in water at a high temperature, have been postulated as probable reasons.³⁴ We conducted a study to evaluate the functional connectivity in 2 groups of patients with HWE. Initially, we performed a seed-based analysis to understand connectivity patterns in 106 brain seeds of the Talairach coordinates with all the voxels in the brain to determine which of the seeds are significantly involved in patients with HWE and also to decipher how they differ between patients in the frequent-seizure group and those in the infrequent-seizure group. In patients with frequent seizures, we noted highly significantly reduced connectivity within several temporal and frontoparietal regions and increased temporal region connections. In patients with infrequent seizures, the disruptions were much less widespread and involved predominantly the temporal regions. Subsequent analysis of the DMN showed a grossly reduced connectivity of the DMN in the frequent-seizure group compared with increased connections in the infrequent-seizure group.

The connectivity differences could mean inherent differences between the groups. These differences could suggest disease focus, or could be indicators of disease progression and associated compensatory mechanisms. We found that there were several areas of decreased connectivity with associated decreased connectivity of the DMN, as found by many other researchers^{7-8,14,35,36} and as has been observed in children with refractory epilepsy,²⁴ which is known to correlate with disease duration.^{6,14} Decreased connectivity was limited to the temporal lobes in patients with infrequent seizures and was widespread and involved the frontal, parietal, and temporal lobes, thalamus, and cerebellum in patients with frequent seizures. Because evidence of decreased connectivity has also been associated with several neuropsychiatric diseases such as dementia, stroke, traumatic brain injury, depression, and schizophrenia, it is possible that decreased connectivity might be indicative of the cognitive and social deficits associated with the disease together with the disease burden. We found that patients in the frequent-seizure group had increased connections within the temporal lobes bilaterally involving the seizure-prone medial temporal structure and bilateral primary auditory cortex, and



FIG 1. Whole-brain cluster-correlation maps of seed-to-voxel-based resting-state functional connectivity (FDR-corrected $P < .001$) with seed regions in the medial prefrontal cortex (A and B), right anterior prefrontal cortex (C), left anterior prefrontal cortex (D), left primary somatosensory cortex (E), right middle temporal gyrus (F), left angular gyrus (G), left precuneus (H), left posterior entorhinal cortex (I), and right medial temporal gyrus (J). The columns represent the healthy controls (column 1), the infrequent-seizure group (column 2), the frequent-seizure group (column 3), the frequent-seizure group versus healthy controls (column 4), and the frequent-seizure group versus the infrequent-seizure group (column 5). The colors represent the significance of connectivity; red indicates an increase in connectivity, and blue indicates a decrease in connectivity.

Table 2: Seed-to-voxel–based connectivity results in the frequent-seizure and healthy control groups

Seed Region	Connectivity Region	P Value (FDR Corrected)	Cluster Size (No. of Voxels)	β Value ^a	T Value ^b
Posterior cingulate cortex	L angular gyrus (decreased)	.0003	381	−0.21	6.84
	L temporopolar region (decreased)	.0009	325	−0.24	7.11
	Medial prefrontal cortex (decreased)	.0009	247	−0.15	6.14
	L lateral parietal cortex (decreased)	.002	92	−0.15	4.96
	L inferior parietal cortex (decreased)	.002	52	−0.13	4.64
L superior temporal gyrus	L superior temporal cortex (decreased)	.005	37	−0.21	5.22
	R primary motor cortex (decreased)	.001	336	−0.22	8.70
L primary somatosensory cortex	L primary motor cortex (decreased)	.001	187	−0.17	6.51
	L precuneus (decreased)	.002	112	−0.11	5.79
L superior temporal gyrus	R dorsal frontal cortex (decreased)	.005	77	−0.11	5.82
	R premotor cortex (decreased)	.005	94	−0.17	6.87
L primary auditory cortex	R and L superior temporal gyrus (decreased)	.005	117	−0.12	5.86
R dorsal frontal cortex	R cerebellar tonsil (decreased)	.005	43	−0.09	5.13
L lateral parietal cortex	L and R dorsal posterior cingulate cortex (decreased)	.005	166	−0.11	5.52
Medial prefrontal cortex	L primary somatosensory cortex (decreased)	.005	137	−0.11	6.19
R medial temporal gyrus	R temporopolar region (increased)	.005	146	0.17	7.96
	R posterior entorhinal cortex (increased)	.005	108	0.17	6.28
L precuneus	L secondary visual cortex (increased)	.001	121	0.15	7.78
	L primary visual cortex (increased)	.003	83	0.13	5.49

Note:—L indicates left hemisphere; R, right hemisphere.

^a β values represent Fisher-transformed correlation coefficient values.

^b T values represent the strength of connectivity between the source seed region and correlated-voxels regions.

Table 3: Seed-to-voxel–based connectivity results in the infrequent-seizure and healthy control groups

Seed Region	Connectivity Region	P Value (FDR Corrected)	Cluster Size (No. of Voxels)	β Value ^a	T Value ^b
L posterior entorhinal cortex	L fusiform gyrus (decreased)	.004	140	−0.15	6.73
L anterior prefrontal cortex	L ventral posterior cingulate cortex (increased)	.003	136	0.12	7.34
	L dorsal posterior cingulate cortex (increased)	.005	74	0.10	6.17
R anterior cingulate cortex	R posterior superior temporal gyrus (increased)	.002	172	0.10	6.82

Note:—L indicates left hemisphere; R, right hemisphere.

^a β values represent Fisher-transformed correlation coefficient values.

^b T values represent the strength of connectivity between the source seed region and correlated-voxels regions.

Table 4: Seed-to-voxel–based connectivity results in the frequent- and infrequent-seizure groups

Seed Region	Connectivity Region	P Value (FDR Corrected)	Cluster Size (No. of Voxels)	β Value ^a	T Value ^b
Medial prefrontal cortex	Precuneus (decreased)	.00004	279	−0.19	9.76
	Posterior cingulate cortex (decreased)	.00004	347	−0.25	5.72
R anterior prefrontal cortex	R dorsal frontal cortex (decreased)	.005	284	−0.27	9.17
	R middle temporal gyrus (decreased)	.005	147	−0.18	6.13
L anterior prefrontal cortex	L middle temporal gyrus (decreased)	.005	92	−0.11	5.57
	Posterior cingulate cortex (decreased)	.005	110	−0.10	5.43
L primary somatosensory cortex	L pyramis (decreased)	.005	122	−0.14	6.02
	R premotor cortex (decreased)	.0001	192	−0.26	9.31
L angular gyrus	L premotor cortex (decreased)	.002	148	−0.18	8.66
	L superior temporal gyrus (decreased)	.002	108	−0.11	6.63
Anterior cingulate	L piriform cortex (decreased)	.005	56	−0.11	5.39
L lateral parietal cortices	Precuneus (decreased)	.0006	309	−0.18	8.17
	L somatosensory association area (decreased)	.003	164	−0.13	7.96
Posterior cingulate cortex	L angular gyrus (decreased)	.00006	321	−0.17	7.84
	L inferior parietal cortex (decreased)	.0009	191	−0.16	6.52
L thalamus	R somatosensory association cortex (decreased)	.009	78	−0.11	4.67
L posterior and anterior entorhinal cortex	R primary auditory cortex (increased)	.005	112	0.10	5.34
	L primary auditory cortex (increased)	.005	93	0.11	5.71

Note:—L indicates left hemisphere; R, right hemisphere.

^a β values represent Fisher-transformed correlation coefficient values.

^b T values represent the strength of connectivity between the source seed region and correlated-voxels regions.

those in the infrequent-seizure group had increased connections of the DMN. Observations of increased connectivity with other types of epilepsy, such as in the medial temporal lobes with mesial temporal sclerosis,^{8,10} the lateral orbitofrontal lobes with absence

seizures,³⁷ and frontal lobes with idiopathic generalized epilepsy,^{38,39} make us surmise that increased connections are probably more specific to understand epileptogenesis. Previous studies also pointed to a temporal lobe origin in 67%–100% of patients

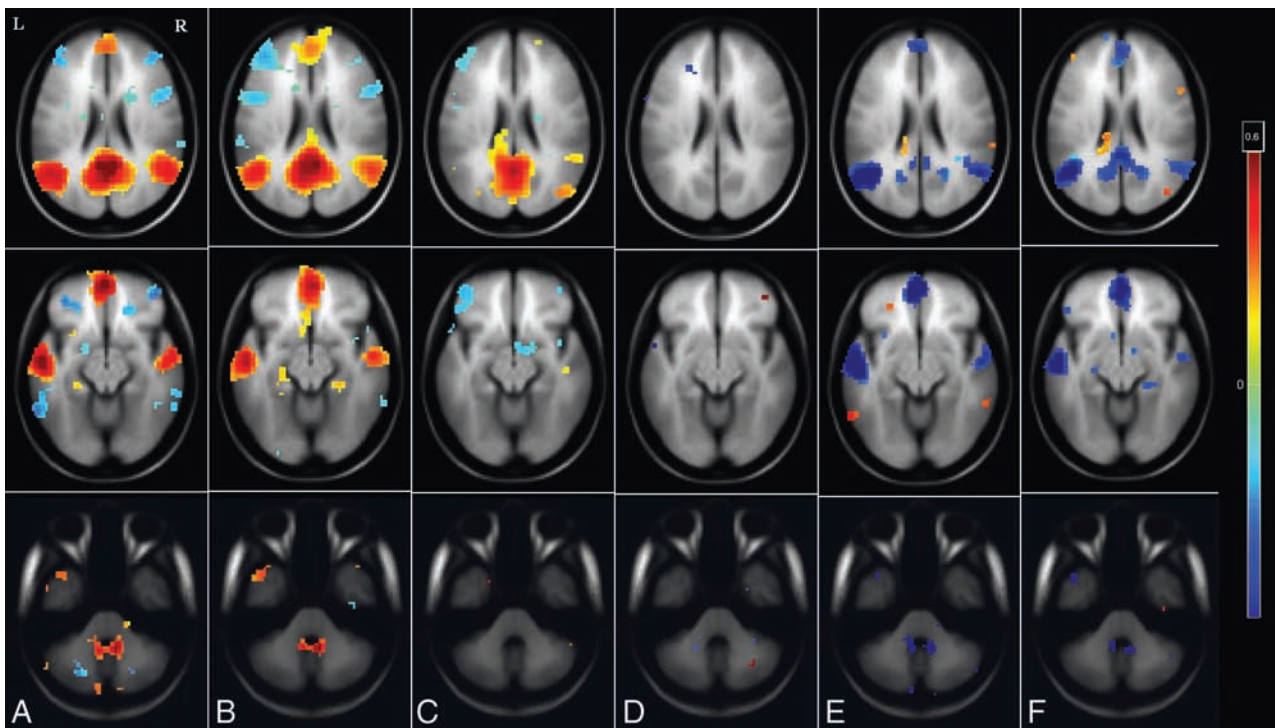


FIG 2. Whole-brain cluster-correlation maps of seed-to-voxel-based resting-state functional connectivity for the PCC seed region (FDR-corrected $P < .001$). Shown is DMN connectivity using PCC seed at 3 different axial levels: at the level of ventricles in the top row, midbrain in the middle row, and the cerebellum in the bottom row for healthy controls (A), the infrequent-seizure group (B), the frequent-seizure group (C), the infrequent-seizure group versus healthy controls (D), the frequent-seizure group versus healthy controls (E), and the infrequent-seizure group versus the frequent-seizure group (F). The colors represent the significance of connectivity; red indicates an increase in connectivity, and blue indicates a decrease in connectivity.

with HWE.^{40–42} Interictal EEG results are usually normal in most of the cases, but a few case studies showed localized temporal lobe discharges.^{41,43} Isolated case reports of associated hippocampal sclerosis have also been reported. In a recent study that involved 5 patients with HWE, 2 of 3 patients who underwent ictal SPECT had hyperperfusion in the temporal region,⁴⁴ and an fMRI-EEG study in 1 patient revealed frontoparietal occipital abnormalities.⁴⁵ Studies in rat models have found widespread kindling and hippocampal mossy fiber sprouting in hot-water-induced hyperthermic seizures at temperature ranges known to precipitate HWE in humans.⁴⁶ Thus, the evidence of increased connectivity of the temporal lobe in patients in the frequent-seizure group in this study supports the temporal lobe focus of HWE seen in the literature, and the absence of it in the infrequent-seizure group could indicate that this phenomenon is probably associated with disease progression. There have been few reports of increased DMN connectivity in patients with epilepsy.^{6,14} Our findings of differential DMN connectivity, which was increased in the infrequent-seizure group and decreased in the frequent-seizure group, directly supports the reports by Bettus et al² and Greicius et al⁴⁷ of increasing DMN connectivity as a compensatory mechanism. Hence, we presume that increasing DMN connectivity is a protective response and might indicate good seizure control in patients with epilepsy.

In this study, an attempt was made to overcome the widely accepted limitation of antiepileptic drugs on network connectivity, and it needs to be noted that the potential effect of interictal discharges on the network was not assessed because we did not record simultaneous EEG with fMRI. However, because only 2 patients in the infrequent-seizure group had 1–2 focal spike-and-

wave discharges in routine EEG, it might be of lesser significance in our study. Per the design of the study, we performed seed-based connectivity analysis in only certain regions of the brain. It is possible that there are many more areas that have been excluded because of the threshold and ranges applied. There was no attempt to overcome the limitations of parcellation algorithms, thresholding effects, or confounders caused by physiologic motion correction on resting-state fMRI. It is also possible that placing these patients into multiple lower- or higher-frequency groups rather than into 2 dichotomized groups might have revealed varying frequency-specific connectivity patterns. Additional studies should address these factors to detect early and potentially reversible connectivity abnormalities.

CONCLUSIONS

This network analysis of 36 patients with hot-water epilepsy revealed that repeated seizures affect brain connectivity and that patients with frequent seizures have widespread connectivity changes, involvement of the DMN, and recruitment of several seizure-prone areas in the medial temporal lobes bilaterally. Whether in the future one could predict the course of chronic epilepsy on the basis of these findings requires further studies on groups of patients with more common epilepsy types.

ACKNOWLEDGMENTS

We acknowledge the support of the Department of Science and Technology, Government of India, for providing the 3T MR imaging scanner exclusively for research in the field of neurosciences. We acknowledge that the data analysis was greatly bene-

fitted by our interactions with Bharat Biswal and his team at the New Jersey Institute of Technology. We thank all the patients who participated in this study without expecting anything in return. We are grateful to the staff, especially the radiographers (at the Neuroimaging and Interventional Radiology, National Institute of Mental Health and Neuro Sciences, India) for their odd-hour support during data collection.

REFERENCES

- Morgan VL, Rogers BP, Sonmez Turk HH, et al. **Cross hippocampal influence in mesial temporal lobe epilepsy measured with high temporal resolution functional magnetic resonance imaging.** *Epilepsia* 2011;52:1741–49 CrossRef Medline
- Bettus G, Guedj E, Joyeux F, et al. **Decreased basal fMRI functional connectivity in epileptogenic networks and contralateral compensatory mechanisms.** *Hum Brain Mapp* 2009;30:1580–91 CrossRef Medline
- Bettus G, Bartolomei F, Confort-Gouny S, et al. **Role of resting state functional connectivity MRI in presurgical investigation of mesial temporal lobe epilepsy.** *J Neurol Neurosurg Psychiatry* 2010;81:1147–54 CrossRef Medline
- Pereira FR, Alessio A, Sercheli MS, et al. **Asymmetrical hippocampal connectivity in mesial temporal lobe epilepsy: evidence from resting state fMRI.** *BMC Neurosci* 2010;11:66 CrossRef Medline
- Pittau F, Grova C, Moeller F, et al. **Patterns of altered functional connectivity in mesial temporal lobe epilepsy.** *Epilepsia* 2012;53:1013–23 CrossRef Medline
- Zhang Z, Lu G, Zhong Y, et al. **Altered spontaneous neuronal activity of the default-mode network in mesial temporal lobe epilepsy.** *Brain Res* 2010;1323:152–60 CrossRef Medline
- Jehi LE. **Functional connectivity in mesial temporal lobe epilepsy: a dynamic concept.** *Epilepsy Curr* 2012;12:238–40 CrossRef Medline
- Liao W, Zhang Z, Pan Z, et al. **Altered functional connectivity and small-world in mesial temporal lobe epilepsy.** *PLoS One* 2010;5:e8525 CrossRef Medline
- Morgan VL, Sonmez Turk HH, Gore JC, et al. **Lateralization of temporal lobe epilepsy using resting functional magnetic resonance imaging connectivity of hippocampal networks.** *Epilepsia* 2012;53:1628–35 CrossRef Medline
- Maccotta L, He BJ, Snyder AZ, et al. **Impaired and facilitated functional networks in temporal lobe epilepsy.** *Neuroimage Clin* 2013;2:862–72 CrossRef Medline
- van Dellen E, Douw L, Baayen JC, et al. **Long-term effects of temporal lobe epilepsy on local neural networks: a graph theoretical analysis of corticography recordings.** *PLoS One* 2009;4:e8081 CrossRef Medline
- Zhang Z, Lu G, Zhong Y, et al. **fMRI study of mesial temporal lobe epilepsy using amplitude of low-frequency fluctuation analysis.** *Hum Brain Mapp* 2010;31:1851–61 CrossRef Medline
- Vlooswijk MC, Jansen JF, Majoie HJ, et al. **Functional connectivity and language impairment in cryptogenic localization-related epilepsy.** *Neurology* 2010;75:395–402 CrossRef Medline
- Wang Z, Lu G, Zhang Z, et al. **Altered resting state networks in epileptic patients with generalized tonic-clonic seizures.** *Brain Res* 2011;1374:134–41 CrossRef Medline
- Weaver KE, Chaovalitwongse WA, Novotny EJ, et al. **Local functional connectivity as a pre-surgical tool for seizure focus identification in non-lesion, focal epilepsy.** *Front Neurol* 2013;4:43 CrossRef Medline
- Fahoum F, Lopes R, Pittau F, et al. **Widespread epileptic networks in focal epilepsies: EEG-fMRI study.** *Epilepsia* 2012;53:1618–27 CrossRef Medline
- Laufs H, Lengler U, Hamandi K, et al. **Linking generalized spike-and-wave discharges and resting state brain activity by using EEG/fMRI in a patient with absence seizures.** *Epilepsia* 2006;47:444–48 CrossRef Medline
- Moeller F, LeVan P, Muhle H, et al. **Absence seizures: individual patterns revealed by EEG-fMRI.** *Epilepsia* 2010;51:2000–10 CrossRef Medline
- Walker MC, White HS, Sander JW. **Disease modification in partial epilepsy.** *Brain* 2002;125:1937–50 CrossRef Medline
- Morimoto K, Fahnestock M, Racine RJ. **Kindling and status epilepticus models of epilepsy: rewiring the brain.** *Prog Neurobiol* 2004;73:1–60 CrossRef Medline
- Cavazos JE, Golarai G, Sutula TP. **Mossy fiber synaptic reorganization induced by kindling: time course of development, progression, and permanence.** *J Neurosci* 1991;11:2795–803 Medline
- Sutula T, Koch J, Golarai G, et al. **NMDA receptor dependence of kindling and mossy fiber sprouting: evidence that the NMDA receptor regulates patterning of hippocampal circuits in the adult brain.** *J Neurosci* 1996;16:7398–406 Medline
- Hauser WA, Lee JR. **Do seizures beget seizures?** *Prog Brain Res* 2002;135:215–19 CrossRef Medline
- Widjaja E, Zamyadi M, Raybaud C, et al. **Impaired default mode network on resting-state fMRI in children with medically refractory epilepsy.** *AJNR Am J Neuroradiol* 2013;34:552–57 CrossRef Medline
- Berg AT, Berkovic SF, Brodie MJ, et al. **Revised terminology and concepts for organization of seizures and epilepsies: report of the ILAE Commission on Classification and Terminology, 2005–2009.** *Epilepsia* 2010;51:676–85 CrossRef Medline
- Fisher RS, Acevedo C, Arzimanoglou A, et al. **ILAE official report: a practical clinical definition of epilepsy.** *Epilepsia* 2014;55:475–82 CrossRef Medline
- Tzourio-Mazoyer N, Landeau B, Papathanassiou D, et al. **Automated anatomical labeling of activations in SPM using a macroscopic anatomical parcellation of the MNI MRI single-subject brain.** *Neuroimage* 2002;15:273–89 CrossRef Medline
- Fornito A, Zalesky A, Bullmore ET. **Network scaling effects in graph analytic studies of human resting-state fMRI data.** *Front Syst Neurosci* 2010;4:22 CrossRef Medline
- Zalesky A, Fornito A, Harding IH, et al. **Whole-brain anatomical networks: does the choice of nodes matter?** *Neuroimage* 2010;50:970–83 CrossRef Medline
- Whitfield-Gabrieli S, Ford JM. **Default mode network activity and connectivity in psychopathology.** *Annu Rev Clin Psychol* 2012;8:49–76 CrossRef Medline
- Behzadi Y, Restom K, Liu J, et al. **A component based noise correction method (CompCor) for BOLD and perfusion based fMRI.** *Neuroimage* 2007;37:90–101 CrossRef Medline
- Whitfield-Gabrieli S, Nieto-Castanon A. **Conn: a functional connectivity toolbox for correlated and anticorrelated brain networks.** *Brain Connect* 2012;2:125–41 CrossRef Medline
- Woodward ND, Rogers B, Heckers S. **Functional resting-state networks are differentially affected in schizophrenia.** *Schizophr Res* 2011;130:86–93 CrossRef Medline
- Satishchandra P. **Hot-water epilepsy.** *Epilepsia* 2003;44:29–32 CrossRef Medline
- Luo C, Li Q, Lai Y, et al. **Altered functional connectivity in default mode network in absence epilepsy: a resting-state fMRI study.** *Hum Brain Mapp* 2011;32:438–49 CrossRef Medline
- Luo C, Li Q, Xia Y, et al. **Resting state basal ganglia network in idiopathic generalized epilepsy.** *Hum Brain Mapp* 2012;33:1279–94 CrossRef Medline
- Bai X, Guo J, Killory B, et al. **Resting functional connectivity between the hemispheres in childhood absence epilepsy.** *Neurology* 2011;76:1960–67 CrossRef Medline
- Killory BD, Bai X, Negishi M, et al. **Impaired attention and network connectivity in childhood absence epilepsy.** *Neuroimage* 2011;56:2209–17 CrossRef Medline
- Maneshi M, Moeller F, Fahoum F, et al. **Resting-state connectivity of the sustained attention network correlates with disease duration in**

- idiopathic generalized epilepsy.** *PLoS One* 2012;7:e50359 CrossRef Medline
40. Satishchandra P, Shivaramakrishana A, Kaliaperumal VG, et al. **Hot water epilepsy: a variant of reflex epilepsy in southern India.** *Epilepsia* 1988;29:52–56 CrossRef Medline
41. Satishchandra P, Ullal GR, Shankar SK. **Hot water epilepsy.** *Adv Neurol* 1998;75:283–93 Medline
42. Szymonowicz W, Meloff K. **Hot water epilepsy.** *Can J Neurol Sci* 1978;5:247–51 Medline
43. Meghana A, Sinha S, Sathyaprabha TN, et al. **Hot water epilepsy clinical profile and treatment—a prospective study.** *Epilepsy Res* 2012;102:160–66 CrossRef Medline
44. Patel M, Satishchandra P, Saini J, et al. **Eating epilepsy: phenotype, MRI, SPECT and video-EEG observations.** *Epilepsy Res* 2013;107:115–20 CrossRef Medline
45. Sandhya M, Bharath RD, Panda R, et al. **Understanding the pathophysiology of reflex epilepsy using simultaneous EEG-fMRI.** *Epileptic Disord* 2014;16:19–29 CrossRef Medline
46. Ullal GR, Satishchandra P, Kalladka D, et al. **Kindling & mossy fibre sprouting in the rat hippocampus following hot water induced hyperthermic seizures.** *Indian J Med Res* 2006;124:331–42 Medline
47. Greicius MD, Flores BH, Menon V, et al. **Resting-state functional connectivity in major depression: abnormally increased contributions from subgenual cingulate cortex and thalamus.** *Biol Psychiatry* 2007;62:429–37 CrossRef Medline

Meta-Analysis of CSF Diversion Procedures and Dural Venous Sinus Stenting in the Setting of Medically Refractory Idiopathic Intracranial Hypertension

S.R. Satti, L. Leishangthem, and M.I. Chaudry



ABSTRACT

BACKGROUND AND PURPOSE: In medically refractory idiopathic intracranial hypertension, optic nerve sheath fenestration or CSF shunting is considered the next line of management. Venous sinus stenosis has been increasingly recognized as a treatable cause of elevated intracranial pressure in a subset of patients. In this article, we present the results of the largest meta-analysis of optic nerve sheath fenestration, CSF shunting, and dural venous sinus stenting. This is the only article that compares these procedures, to our knowledge.

MATERIALS AND METHODS: We performed a PubMed search of all peer-reviewed articles from 1988 to 2014 for patients who underwent a procedure for medically refractory idiopathic intracranial hypertension.

RESULTS: Optic nerve sheath fenestration analysis included 712 patients. Postprocedure, there was improvement of vision in 59%, headache in 44%, and papilledema in 80%; 14.8% of patients required a repeat procedure with major and minor complication rates of 1.5% and 16.4%, respectively. The CSF diversion procedure analysis included 435 patients. Postprocedure, there was improvement of vision in 54%, headache in 80%, and papilledema in 70%; 43% of patients required at least 1 additional surgery. The major and minor complication rates were 7.6% and 32.9%, respectively. The dural venous sinus stenting analysis included 136 patients. After intervention, there was improvement of vision in 78%, headache in 83%, and papilledema in 97% of patients. The major and minor complication rates were 2.9% and 4.4%, respectively. Fourteen additional procedures were performed with a repeat procedure rate of 10.3%. Three patients had contralateral stent placement, while 8 had ipsilateral stent placement within or adjacent to the original stent. Only 3 patients required conversion to CSF diversion or 2.2% of patients with stents.

CONCLUSIONS: Patients with medically refractory idiopathic intracranial hypertension have traditionally undergone a CSF diversion procedure as the first intervention. This paradigm may need to be re-examined, given the high technical and clinical success and low complication rates with dural venous sinus stenting.

ABBREVIATIONS: BMI = body mass index; IIH = idiopathic intracranial hypertension; ONSF = optic nerve sheath fenestration

Idiopathic intracranial hypertension (IIH), previously referred to as pseudotumor cerebri and benign intracranial hypertension, is a syndrome defined by elevated intracranial hypertension without radiographic evidence of a mass lesion in the brain.¹ The overall prevalence of IIH in North America has been estimated to

be 0.9–1.07/100,000^{2,3}; however, in women with obesity between 20 and 44 years of age, the prevalence rises to 15–19/100,000.²

Although headache is the most common presenting symptom, seen in 92%–94% of patients,^{4,5} IIH also represents a significant cause of chronic headaches. In some patients, there may be vision changes,^{6–9} which, if not corrected, may progress to permanent visual loss.^{10,11}

The standard medical treatment includes weight loss, acetazolamide, diuretics, and repeat high-volume lumbar punctures. In patients with medically refractory IIH or progressive visual loss, a CSF-diversion procedure (lumboperitoneal shunt, ventriculoperitoneal shunts, or optic nerve sheath fenestration) is considered the next line of management.^{9,12}

CSF diversion procedures in the setting of medically refractory IIH have been described in the literature dating back to 1955, by

Received December 10, 2014; accepted after revision March 3, 2015.

From the Department of Neurointerventional Surgery (S.R.S., L.L.), Christiana Care Health Center, Wilmington, Delaware; and Department of Neuroradiology (M.I.C.), Medical University of South Carolina, Charleston, South Carolina.

Please address correspondence to Sudhakar R. Satti, MD, 4755 Oglethorpe-Stanton Rd, Newark, DE 19718; e-mail: ssatti@christianacare.org



Indicates article with supplemental on-line tables.



Evidence-Based Medicine Level 1.

<http://dx.doi.org/10.3174/ajnr.A4377>

Jackson and Snodgrass.^{13,14} These studies are level 3 evidence, comprising case series and individual case reports. There are no prospective randomized controlled studies on lumboperitoneal shunt, ventriculoperitoneal shunts, or optic nerve sheath fenestration, to our knowledge.

Venous sinus stenosis has been increasingly recognized as a treatable cause of elevated intracranial pressure. Venous sinus stent placement was first described by Higgins et al.¹⁵ During the past 20 years, an increasing number of case reports and larger case series have described dural venous sinus stent placement, and reported high rates of technical success and favorable clinical outcomes.^{6,7,16-21}

In this article, we present the results of the largest meta-analysis of optic nerve sheath fenestration, CSF diversion procedure, and venous sinus stent placement for medically refractory IIH from 1988 to present. We then compare these interventions with a focus on symptom improvement, complications, and the need for repeat procedures.

MATERIALS AND METHODS

Search Criteria

We performed a PubMed search of all peer-reviewed articles from 1988 to date with a combination of key words including “Idiopathic Intracranial hypertension,” “Pseudotumor Cerebri” and “Benign Intracranial Hypertension” and “Lumboperitoneal Shunts,” “Ventriculoperitoneal Shunts,” and “Optic Nerve Sheath Decompression” and “Intracranial Venous Shunts.” References from the articles that were identified in the initial search were also reviewed for extraction of additional studies.

Eligibility Criteria

Studies reporting patients with IIH and other secondary causes of increased intracranial pressure were separated into 2 groups, and only the patients with IIH who had undergone a procedure were included.

Because these studies were conducted with different aims and protocols, some data on visual acuity, visual fields, CSF pressure, and mean body mass index (BMI) were not available. We attempted to standardize the data as much as possible. The means, ranges, and percentages were calculated for the combined subset of patients with data available for each parameter or outcome. Patients without adequate data were excluded from the analysis to avoid bias and to produce reliable results. Symptom-resolution analysis was performed for only those patients with reported data. Symptom resolution and improvement are presented as improvement, except in the optic nerve sheath fenestration (ONSF) analysis, due to lack of homogeneity of the data. In dural venous sinus stenting and CSF flow-diversion articles, visual acuity and visual fields were combined and described as visual acuity changes.

Exclusion

All studies written before 1988; series with <9 patients for venous sinus stent placement, <6 for ONSF, and <7 for CSF flow diversion; non-English articles; and reports with inadequate information regarding patient selection and follow-up were excluded.

Data Extraction

Effort was made to standardize the data for ease of comparison among treatment modalities with a focus on the following end points:

- Presenting symptoms and patient characteristics (BMI and CSF opening pressure).
- Resolution of symptoms (including headache and visual loss).
- Resolution of papilledema.
- Revision rates of the CSF flow-diversion procedures.
- Complication rates.
- Technical success.

In the analysis of CSF-diversion procedures, patients needing revisions were considered as having complications because they needed repeat procedures, though indications were variable.

RESULTS

Optic Nerve Sheath Fenestration

ONSF (On-line Table 2)²²⁻³⁹ is usually the intervention of choice for patients with medically refractory IIH presenting with severe visual loss but minimal headache. The procedure has been shown to rapidly improve visual function (both visual acuity and visual fields) and stabilize the visual changes, thus preventing progression.^{9,28}

Our PubMed search identified 18 clinical studies with patients undergoing ONSF, including 712 patients and 1153 eyes. The mean age at presentation was 32.4 years (range, 4.4–74 years), and the mean follow-up period was 21 months (range, 0–160 months).

Sixty percent of patients presented with headaches, 92% presented with visual acuity changes, and 86% presented with visual field change. Females represented 82% (391/476 patients). Unilateral surgeries (53%, 252/476 patients) were slightly more common than bilateral surgeries. Eighty-nine percent of patients (389/439) had ONSF as their first surgical procedure for medically refractory IIH.

After optic nerve sheath fenestration, visual acuity improved in 59% (152/257 eyes) and improved or remained stable in 95% (1011/1066 eyes). Visual fields improved in 68% (470/688 eyes). Headache improved in 44% (56/127 patients), and papilledema improved in 80% (76/95 patients).

In the total 712 patients who underwent ONSF, there were 128 documented complications. Complications included diplopia (55; 43%), pupillary complications (32; 25%), late failure (13; 10%), and dellen (shallow excavations along the outer edge of the cornea caused by localized dehydration) (8; 6%).

The total average complication rate (including major and minor complications) was 18% (128/712). We defined major complications as esotropia, exotropia, retrolubar hemorrhage, orbital hematoma, orbital apex syndrome, orbital cellulitis, and traumatic optic neuropathy. The rate of major complications was 1.5% based on the total number of patients in the study group, 712. We defined minor complications as diplopia, late failure, dellen, synechia, atonic pupil, tonic pupil, anisocoria, pupillary dysfunction, perilimbal conjunctival bleb, peripapillary hemorrhages, disc hemorrhage, cyst formation, and conjunctival abscess. The rate of minor complications was 16.4%.

On the basis of the total number of procedures performed, 14.86% required a repeat procedure: 9.21%, repeat ONSF and 5.65%, CSF diversion. In the series of Spoor et al,²⁶ 31.4% (11 of 35) of patients with acute presentation required a second procedure (but a total of 16 procedures if both eyes were included in some patients).

Because all the data were not available for all the cases, denominators used in the calculation for percentages differed.

Unfortunately, BMI was only available for 1 study included in the analysis, Gupta et al,³⁵ with an average BMI of 24.4. Opening pressures were only available in 2 studies (Thuente et al³² and Gupta et al³⁵), with 30 patients and a mean opening pressure of 29.28 cm H₂O (range, 13–70 cm H₂O).

CSF Flow Diversion

Seventeen studies with a CSF-diversion (On-line Table 3)^{8,40–46,48,55–60} procedure meeting the inclusion criteria were analyzed, including 435 patients; 85% (310/363) were females. Sex was not reported in 3 studies (Abubaker et al,⁴⁶ Tulipan et al,⁴³ and Rosenberg et al⁴¹). The mean age was 31.9 years (range, 6 months to 68 years).

The mean follow-up time was 41 months (range, 1–278 months). Eighty-six percent (164/190) of patients had CSF diversion as their first surgery. The mean CSF opening pressure, reported in 120 cases, was 41.4 mm Hg (range, 29–60 mm Hg). After the procedure, headache improved in 80% (231/287) of cases. Papilledema improved in 70% (107/153) of cases. Visual acuity improved after treatment in 54% (104/193).

Forty-three percent of patients required at least 1 additional surgery. Most surprising, 154 of 435 patients undergoing CSF flow diversion underwent an additional 428 procedures (not reported in 2 studies: Thambisetty et al⁴⁷ and Tarnaris et al,⁴⁸) or 2.78 additional procedures for each failure. These additional procedures were mainly revisions of the shunt. The most common reason for the shunt revision was shunt obstruction (41%), followed by low-pressure headache (15%), shunt failure (11%), radicular pain (3%), and others (25%), which included abdominal pain, tonsillar herniation, valve dysfunction, shunt disconnection, shunt malposition, subdural hematoma, and CSF fistula.

The rate of major complications was 7.6% (33/435). We defined major complications as shunt infection, tonsillar herniation, subdural hematoma, and CSF fistula.

The rate of minor complications was 32.9% (143/435). We defined minor complications as abdominal pain, valve dysfunction, radicular pain, shunt disconnection, shunt malposition, low pressure headache and/or CSF leak, and catheter migration. In Rosenberg et al,⁴¹ operative complications (2/37 patients) were not clearly defined.

Venous Stent Placement

Our meta-analysis of dural venous sinus stent placement (On-line Table 4)^{6,7,16–21} included 8 studies with 136 patients. Eighty-eight percent were female (119/136 cases). The mean age was 34.5 years (range, 10–64 years), and the mean follow-up time was 22.9 months (range, 1–136 months). The mean BMI was 34 kg/m² (range, 22–73 kg/m²). The mean CSF pressure was 34.3 mm Hg

(range, 22–73 mm Hg). Seventy-three percent (88/121 cases) of patients who were medically refractory underwent venous stent placement as the first intervention.

Nearly all of the stents used were self-expanding nitinol stents; however, <5% of studies described placement of balloon-mounted stents. Stents included the following: Bridge X3 stent (Medtronic, Santa Rosa, California),¹⁶ S.M.A.R.T. stent (Cordis, Fremont, California),¹⁶ Complete SE stent (Medtronic),¹⁹ Zilver biliary stent (Cook Medical, Bloomington, Indiana),^{6,20,21} (Worthington Biochemical, Lakewood, New Jersey), Precise self-expanding stent (Cordis),²¹ or Acculink stent (Guidant, St. Paul, Minnesota).²¹

After the intervention, headache improved in 83% (101/121 cases) and papilledema improved in 97% of patients (104/108 cases). Visual acuity changes improved in 78% (40/51 cases) after treatment. The mean pre-stent pressure gradient was 20.6 mm Hg (range, 4–50 mm Hg), and the mean post-stent pressure gradient was 2.7 mm Hg (range, 0–23 mm Hg). Sixty-seven percent (*n* = 83) of stents were placed in the right transverse sinus, 29% (*n* = 36) of stents were placed in the left transverse sinus, and 4% were not specified. Stent location was not reported in 16 cases (Higgins et al¹⁷ and Ahmed et al¹⁹).

Of the 136 patients who underwent stent placement, 7.4% (10/136 cases) had complications, though no fatalities were reported. The major complication rate was 2.9% (4/136) and was defined as a subdural hematoma. The minor complication rate was 4.4% (6/136) and was defined as transient hearing loss, femoral pseudoaneurysm, retroperitoneal hematoma, urinary tract infection, and syncope.

Fourteen additional procedures were performed; therefore, the rate of repeat procedures was 10.3% (14/136). Additional procedures were performed in 8% of patients. Contralateral stent placement was performed in 3 patients, and additional ipsilateral stent placement at or near the original stent for restenosis, in 8 patients. Conversion to CSF diversion was seen in only 3 patients or 2.2% of total patients initially receiving stents.

Here again, similar to the ONSF studies, because all data were not available for all the cases, denominators used in calculation for percentages differed.

DISCUSSION

Idiopathic intracranial hypertension has been described dating back to 1893, by Quinke, who proposed the term “meningitis serosa.”^{49,50} The presenting symptoms included headache, blurred vision, and vomiting. The clinical syndrome was later described as “pseudotumor cerebri” by Nonne in 1904⁴⁹ and then “benign intracranial hypertension” by Foley in 1955.^{10,49,50} The inclusion of “benign” in the description was challenged in 1969 by Buchheit et al,^{49,51} who recognized that papilledema was present in almost 95% of the patients, which, if left untreated, could progress to optic atrophy and irreversible blindness. The term “idiopathic intracranial hypertension” was introduced in 2011⁵⁰ and may be increasingly used because the etiology and pathophysiology are poorly understood.

Idiopathic intracranial hypertension is currently defined by the Modified Dandy Criteria^{1,9} and includes an elevation of intracranial pressure with a normal composition of CSF and no intra-

cranial mass or venous sinus thrombosis. By using the Modified Dandy's Criteria, patients with a heterogeneous group may potentially be combined, confounding management and outcomes.

The underlying pathophysiology of elevated intracranial pressure can be divided into 2 groups, CSF overproduction and decreased CSF absorption. Some early hypotheses for IIH included serous meningitis resulting in decreased CSF outflow (Quinke), increased CSF in the subarachnoid space (Passot), hydrocephalus due to remote effects of bacterial toxins or otitis media (Warrington), and altered vasomotor control of the intracranial vascular bed (Dandy).⁵²

The mainstays of conservative therapy include weight loss, medications to reduce CSF production, and repeated high-volume lumbar punctures. Despite these measures, some patients may have progressive symptoms or develop visual changes. Patients who fail conservative measures are generally referred for CSF flow-diversion procedures such as lumboperitoneal shunting, ventriculoperitoneal shunting,^{13,14} or optic nerve sheath fenestration. More recently, dural venous sinus stent placement has been described in the literature.

ONSF appears to have the highest success rate in patients with visual field changes or vision loss, 86%–92% compared with CSF flow diversion or sinus stent placement, 58% and 65%, respectively. ONSF was associated with the lowest improvement of headache, 60%, compared with sinus stent placement (89%) or CSF flow diversion (80%). ONSF was also associated with a low major complication rate of 2%, a minor complication rate of 16%, and a revision rate of 15%. From a practical standpoint, ONSF may not be as readily available, and recovery from the procedure should be considered.

The most common indication for CSF flow-diversion procedures is severe headache or progressive visual change. There was a major complication rate of 8% and a minor complication rate of 33% in the 435 patients included. Considering this young population, with an average age of 31.9, the high reported repeat procedure rate of 43% is concerning. Most repeat procedures were shunt revisions. Forty-three percent of patients ultimately needed an additional procedure during the average follow-up period of 41 months. Of 358 patients (some patients were excluded in the denominator because of missing data), 154 patients underwent 428 additional procedures, or 2.78 additional procedures in >43% of patients undergoing CSF flow diversion.

There is limited but growing literature for dural venous sinus stent placement in the setting of elevated intracranial pressure and dural venous sinus stenosis. Dural venous sinus stenting may cause elevated intracranial pressure by 2 different mechanisms. The first is an increased gradient between the CSF space and the cerebral venous sinuses. A second is decreased CSF absorption by the arachnoid granulations, which are pressure-sensitive.^{3,12,16,17,20} Stent placement has been hypothesized to lower intracranial pressure by removing a Starling-like resistor, thereby removing the positive feedback loop.¹⁹

With noninvasive imaging, such as contrast-enhanced MRV, 3 patterns of dural venous sinus stenting may be amenable to sinus stent placement:

- Focal stenosis of the superior sagittal sinus.

- Bilateral transverse/sigmoid sinus stenosis.
- Unilateral transverse/sigmoid sinus stenosis with contralateral hypoplasia/aplasia.

Although most patients with stents included in this meta-analysis underwent stent placement as the first intervention for medically refractory IIH, 10.3% of patients underwent stent placement as a second procedure. Dural venous sinus stenting could be considered in patients who have failed the traditional CSF-diversion procedure.

Given the cost and morbidity of repeat procedures, CSF shunting as the criterion standard treatment should be re-evaluated. Ahmed et al⁵³ reported that in their health care system in Australia, the cost of the initial dural venous sinus stent placement was similar to the cost of the initial CSF flow-diversion procedure; however, when one took into account the cost of revisions, the total cost of CSF flow diversion was 5 times higher. Although CSF flow diversion is commonly performed, the literature regarding outcomes and high rates of revision does not compare favorably with recent data on venous sinus stent placement when using strict patient selection, dual antiplatelet therapy, and modern devices. We would argue that evaluation for underlying venous sinus stenosis should be undertaken with MRV (and confirmed, if present, with conventional catheter-based venography and pressure measurements) before any CSF flow-diversion procedure.

Limitations

Meta-analysis by definition is limited by a retrospective design; therefore, data collection was inconsistent and/or incomplete for both pre- and postoperative parameters. This was further compounded by inclusion of different surgical modalities and specialists. Ophthalmologists focused on vision, and most ONSF studies lacked CSF pressure and BMI. Neurosurgeons focused on headache, while neurointerventionalists focused on headaches and papilledema. All studies lacked consistent data on visual acuity and field changes. Different studies had different definitions for improvement, indications for surgery, and variable long-term follow-up (1–278 months). Although there were fewer patients included in the dural venous sinus stenting group than in the others, 136 patients who met inclusion should generate reliable data for comparison.

Despite these challenges, we summarized the available data as rigorously as possible, with an emphasis on presenting symptoms, resolution of presenting symptoms, repeat procedure rates, and complication rates.

In the CSF flow-diversion group, some pediatric patients were included because they could not be separated because individual data were not available.^{8,40,42,44,47,54–56} In the ONSF studies by Corbett et al²⁴ and Spoor et al,²⁶ complications were given in terms of eyes and not patients. We considered the number of eyes as the number of patients for calculation consistency. Nithyanandam et al³⁶ reported complications in terms of percentages, which we had to convert.

In studies in which values of certain parameters were marginally available (eg, CSF pressure >40 cm of H₂O in 73% of cases in the CSF diversion study by El-Saadany et al,³⁷), values were pre-

sented as “NR” or not reported in On-line 3 and excluded from the mean CSF pressure.

Future Directions

Surgery for medically refractory IIH is performed by different specialties; therefore, the data are inconsistent. Future CSF flow-diversion, ONSF, and dural venous sinus stenting studies for IIH should include documentation of the following:

- 1) Patient characteristics (age, comorbidities, BMI, symptoms, medications).
- 2) Formal ophthalmologic examination (pre- and post-intervention).
- 3) CSF studies (pre- and postintervention).
- 4) For dural sinus stent placement, angiography confirming stenosis and pressure gradients.
- 5) Long-term clinical follow-up and stent patency.

CONCLUSIONS

Patients with medically refractory idiopathic intracranial hypertension have traditionally undergone CSF flow-diversion procedures as the first intervention. On the basis of our meta-analysis comparing traditional CSF flow-diversion procedures with venous sinus stent placement, this paradigm may need to be re-examined, given high technical and clinical success with low complications and low repeat-procedure rates associated with stent placement compared with traditional surgical interventions.

ACKNOWLEDGMENTS

We would like to thank Ene O. Belleh, MLS, AHIP (Academy of Health Information Professionals), reference and instruction services librarian at the Christiana Care Medical Library, for her evidence-based research support.

Disclosures: M. Imran Chaudry—UNRELATED: Board Membership: Covidien Scientific Advisory Board; Consultancy: Covidien, MicroVenton, Penumbra, Codman and Shurtleff.

REFERENCES

1. Friedman DI, Jacobson DM. **Diagnostic criteria for idiopathic intracranial hypertension.** *Neurology* 2002;59:1492–95
2. Durcan FJ, Corbett JJ, Wall M. **The incidence of pseudotumor cerebri: population studies in Iowa and Louisiana.** *Arch Neurol* 1988;45:875–77
3. Puffer RC, Mustafa W, Lanzino G. **Venous sinus stenting for idiopathic intracranial hypertension: a review of the literature.** *J Neurointerv Surg* 2013;5:483–86
4. Francis CE, Quiros PA. **Headache management in idiopathic intracranial hypertension.** *Int Ophthalmol Clin* 2014;54:103–14
5. Wall M. **The headache profile of idiopathic intracranial hypertension.** *Cephalalgia* 1990;10:331–35
6. Fields JD, Javedani PP, Falardeau J, et al. **Dural venous sinus angioplasty and stenting for the treatment of idiopathic intracranial hypertension.** *J Neurointerv Surg* 2013;5:62–68
7. Donnet A, Metellus P, Levrier O, et al. **Endovascular treatment of idiopathic intracranial hypertension: clinical and radiologic outcome of 10 consecutive patients.** *Neurology* 2008;70:641–47
8. Eggenberger ER, Miller NR, Vitale S. **Lumboperitoneal shunt for the treatment of pseudotumor cerebri.** *Neurology* 1996;46:1524–30
9. Biousse V, Bruce BB, Newman NJ. **Update on the pathophysiology**

and management of idiopathic intracranial hypertension. *J Neurol Neurosurg Psychiatry* 2012;83:488–94

10. Ball AK, Clarke CE. **Idiopathic intracranial hypertension.** *Lancet Neurol* 2006;5:433–42
11. Friedman DI, Jacobson DM. **Idiopathic intracranial hypertension.** *J Neuroophthalmol* 2004;24:138–45
12. Galgano MA, Deshaies EM. **An update on the management of pseudotumor cerebri.** *Clin Neurol Neurosurg* 2013;115:252–59
13. Vander Ark GD, Kempe LG, Smith DR. **Pseudotumor cerebri treated with lumbar-peritoneal shunt.** *JAMA* 1971;217:1832–34
14. Jackson IJ, Snodgrass SR. **Peritoneal shunts in the treatment of hydrocephalus and increased intracranial pressure: a 4-year survey of 62 patients.** *J Neurosurg* 1955;12:216–22
15. Higgins JN, Owler BK, Cousins C, et al. **Venous sinus stenting for refractory benign intracranial hypertension.** *Lancet* 2002;359:228–30
16. Owler BK, Parker G, Halmagyi GM, et al. **Pseudotumor cerebri syndrome: venous sinus obstruction and its treatment with stent placement.** *J Neurosurg* 2003;98:1045–55
17. Higgins JN, Cousins C, Owler BK, et al. **Idiopathic intracranial hypertension: 12 cases treated by venous sinus stenting.** *J Neurol Neurosurg Psychiatry* 2003;74:1662–66
18. Bussière M, Falero R, Nicolle D, et al. **Unilateral transverse sinus stenting of patients with idiopathic intracranial hypertension.** *AJNR Am J Neuroradiol* 2010;31:645–50
19. Ahmed RM, Wilkinson M, Parker GD, et al. **Transverse sinus stenting for idiopathic intracranial hypertension: a review of 52 patients and of model predictions.** *AJNR Am J Neuroradiol* 2011;32:1408–14
20. Albuquerque FC, Dashti SR, Hu YC, et al. **Intracranial venous sinus stenting for benign intracranial hypertension: clinical indications, technique, and preliminary results.** *World Neurosurg* 2011;75:648–52; discussion 592–95
21. Kumpe DA, Bennett JL, Seinfeld J, et al. **Dural sinus stent placement for idiopathic intracranial hypertension.** *J Neurosurg* 2012;116:538–48
22. Alsuhaibani AH, Carter KD, Nerad JA, et al. **Effect of optic nerve sheath fenestration on papilledema of the operated and the contralateral nonoperated eyes in idiopathic intracranial hypertension.** *Ophthalmology* 2011;118:412–14
23. Brouman ND, Spoor TC, Ramocki JM. **Optic nerve sheath decompression for pseudotumor cerebri.** *Arch Ophthalmol* 1988;106:1378–83
24. Corbett JJ, Nerad JA, Tse DT, et al. **Results of optic nerve sheath fenestration for pseudotumor cerebri: the lateral orbitotomy approach.** *Arch Ophthalmol* 1988;106:1391–97
25. Sergott RC, Savino PJ, Bosley TM. **Modified optic nerve sheath decompression provides long-term visual improvement for pseudotumor cerebri.** *Arch Ophthalmol* 1988;106:1384–90
26. Spoor TC, Ramocki JM, Madion MP, et al. **Treatment of pseudotumor cerebri by primary and secondary optic nerve sheath decompression.** *Am J Ophthalmol* 1991;112:177–85
27. Kelman SE, Sergott RC, Cioffi GA, et al. **Modified optic nerve decompression in patients with functioning lumboperitoneal shunts and progressive visual loss.** *Ophthalmology* 1991;98:1449–53
28. Kelman SE, Heaps R, Wolf A, et al. **Optic nerve decompression surgery improves visual function in patients with pseudotumor cerebri.** *Neurosurgery* 1992;30:391–95
29. Acheson JF, Green WT, Sanders MD. **Optic nerve sheath decompression for the treatment of visual failure in chronic raised intracranial pressure.** *J Neurol Neurosurg Psychiatry* 1994;57:1426–29
30. Goh KY, Schatz NJ, Glaser JS. **Optic nerve sheath fenestration for pseudotumor cerebri.** *J Neuroophthalmol* 1997;17:86–91
31. Banta JT, Farris BK. **Pseudotumor cerebri and optic nerve sheath decompression.** *Ophthalmology* 2000;107:1907–12
32. Thuente DD, Buckley EG. **Pediatric optic nerve sheath decompression.** *Ophthalmology* 2005;112:724–27

33. Knapp CM, Sampath R. **Optic nerve sheath fenestration: a five year audit.** *Neuro-Ophthalmology* 2005;29:173–77
34. Chandrasekaran S, McCluskey P, Minassian D, et al. **Visual outcomes for optic nerve sheath fenestration in pseudotumour cerebri and related conditions.** *Clin Experiment Ophthalmol* 2006;34:661–65
35. Gupta AK, Gupta A, Kumar S, et al. **Endoscopic endonasal management of pseudotumor cerebri: is it effective?** *Laryngoscope* 2007;117:1138–42
36. Nithyanandam S, Manayath GJ, Battu RR. **Optic nerve sheath decompression for visual loss in intracranial hypertension: report from a tertiary care center in South India.** *Indian J Ophthalmol* 2008;56:115–20
37. Moreau A, Lao KC, Farris BK. **Optic nerve sheath decompression: a surgical technique with minimal operative complications.** *J Neuroophthalmol* 2014;34:34–38
38. Pineles SL, Volpe NJ. **Long-term results of optic nerve sheath fenestration for idiopathic intracranial hypertension: earlier intervention favours improved outcomes.** *Neuro-Ophthalmology* 2013;37:12–19
39. Sencer A, Akcakaya MO, Basaran B, et al. **Unilateral endoscopic optic nerve decompression for idiopathic intracranial hypertension: a series of 10 patients.** *World Neurosurg* 2014;82:745–50
40. Johnston I, Besser M, Morgan MK. **Cerebrospinal fluid diversion in the treatment of benign intracranial hypertension.** *J Neurosurg* 1988;69:195–202
41. Rosenberg ML, Corbett JJ, Smith C, et al. **Cerebrospinal fluid diversion procedures in pseudotumor cerebri.** *Neurology* 1993;43:1071–72
42. Burgett RA, Purvin VA, Kawasaki A. **Lumboperitoneal shunting for pseudotumor cerebri.** *Neurology* 1997;49:734–39
43. Tulipan N, Lavin PJ, Copeland M. **Stereotactic ventriculoperitoneal shunt for idiopathic intracranial hypertension: technical note.** *Neurosurgery* 1998;43:175–76; discussion 176–77
44. Maher CO, Garrity JA, Meyer FB. **Refractory idiopathic intracranial hypertension treated with stereotactically planned ventriculoperitoneal shunt placement.** *Neurosurg Focus* 2001;10:E1
45. McGirt MJ, Woodworth G, Thomas G, et al. **Cerebrospinal fluid shunt placement for pseudotumor cerebri-associated intractable headache: predictors of treatment response and an analysis of long-term outcomes.** *J Neurosurg* 2004;101:627–32
46. Abubaker K, Ali Z, Raza K, et al. **Idiopathic intracranial hypertension: lumboperitoneal shunts versus ventriculoperitoneal shunts—case series and literature review.** *Br J Neurosurg* 2011;25:94–99
47. Thambisetty M, Lavin PJ, Newman NJ, et al. **Fulminant idiopathic intracranial hypertension.** *Neurology* 2007;68:229–32
48. Tarnaris A, Toma AK, Watkins LD, et al. **Is there a difference in outcomes of patients with idiopathic intracranial hypertension with the choice of cerebrospinal fluid diversion site: a single centre experience.** *Clin Neurol Neurosurg* 2011;113:477–79
49. Pearce JM. **From pseudotumor cerebri to idiopathic intracranial hypertension.** *Pract Neurol* 2009;9:353–56
50. Degnan AJ, Levy LM. **Pseudotumor cerebri: brief review of clinical syndrome and imaging findings.** *AJNR Am J Neuroradiol* 2011;32:1986–93
51. Buchheit WA, Burton C, Haag B, et al. **Papilledema and idiopathic intracranial hypertension.** *N Engl J Med* 1969;280:938–42
52. Bandyopadhyay S. **Pseudotumor cerebri.** *Arch Neurol* 2001;58:1699–701
53. Ahmed RM, Zmudzki F, Parker GD, et al. **Transverse sinus stenting for pseudotumor cerebri: a cost comparison with CSF shunting.** *AJNR Am J Neuroradiol* 2014;35:952–58
54. Bynke G, Zemack G, Bynke H, et al. **Ventriculoperitoneal shunting for idiopathic intracranial hypertension.** *Neurology* 2004;63:1314–16
55. Abu-Serieh B, Ghassempour K, Duprez T, et al. **Stereotactic ventriculoperitoneal shunting for refractory idiopathic intracranial hypertension.** *Neurosurgery* 2007;60:1039–43; discussion 1043–44
56. Yadav YR, Parihar V, Agarwal M, et al. **Lumbar peritoneal shunt in idiopathic intracranial hypertension.** *Turk Neurosurg* 2012;22:21–26
57. El-Saadany WF, Farhoud A, Zidan I. **Lumboperitoneal shunt for idiopathic intracranial hypertension: patients' selection and outcome.** *Neurosurg Rev* 2012;35:239–43; discussion 243–44
58. Woodworth GF, McGirt MJ, Elfert P, et al. **Frameless stereotactic ventricular shunt placement for idiopathic intracranial hypertension.** *Stereotact Funct Neurosurg* 2005;83:12–16
59. Sinclair AJ, Kuruvath S, Sen D, et al. **Is cerebrospinal fluid shunting in idiopathic intracranial hypertension worthwhile? A 10-year review.** *Cephalalgia* 2011;31:1627–33
60. Huang LC, Winter TW, Herro AM, et al. **Ventriculoperitoneal shunt as a treatment of visual loss in idiopathic intracranial hypertension.** *J Neuroophthalmol* 2014;34:223–28

Changing Clinical and Therapeutic Trends in Tentorial Dural Arteriovenous Fistulas: A Systematic Review

D. Cannizzaro, W. Brinjikji, S. Rammos, M.H. Murad, and G. Lanzino



ABSTRACT

BACKGROUND AND PURPOSE: Tentorial dural arteriovenous fistulas are characterized by a high hemorrhagic risk. We evaluated trends in outcomes and management of tentorial dural arteriovenous fistulas and performed a meta-analysis evaluating clinical and angiographic outcomes by treatment technique.

MATERIALS AND METHODS: We performed a comprehensive literature search for studies on surgical and endovascular treatment of tentorial dural arteriovenous fistulas. We compared the proportion of patients undergoing endovascular, surgical, and combined endovascular/surgical management; the proportion of patients presenting with ruptured tentorial dural arteriovenous fistulas; and proportion of patients with good neurologic outcome across 3 time periods: 1980–1995, 1996–2005, and 2006–2014. We performed a random-effects meta-analysis, evaluating the rates of occlusion, long-term good neurologic outcome, perioperative morbidity, and resolution of symptoms for the 3 treatment modalities.

RESULTS: Twenty-nine studies with 274 patients were included. The proportion of patients treated with surgical treatment alone decreased from 38.7% to 20.4% between 1980–1995 and 2006–2014. The proportion of patients treated with endovascular therapy alone increased from 16.1% to 48.0%. The proportion of patients presenting with ruptured tentorial dural arteriovenous fistulas decreased from 64.4% to 43.6%. The rate of good neurologic outcome increased from 80.7% to 92.9%. Complete occlusion rates were highest for patients receiving multimodality treatment (84.0%; 95% CI, 72.0%–91.0%) and lowest for endovascular treatment (71.0%; 95% CI, 56.0%–83.0%; $P < .01$). Long-term good neurologic outcome was highest in the endovascular group (89.0%; 95% CI, 80.0%–95.0%) and lowest for the surgical group (73.0%; 95% CI, 51.0%–87.0%; $P = .03$).

CONCLUSIONS: Patients with tentorial dural arteriovenous fistulas are increasingly presenting with unruptured lesions, being treated endovascularly, and experiencing higher rates of good neurologic outcomes. Endovascular treatment was associated with superior neurologic outcomes but lower occlusion rates.

ABBREVIATIONS: DAVF = dural arteriovenous fistula; TDAVF = tentorial dural arteriovenous fistula

Intracranial dural arteriovenous fistulas (DAVFs) are abnormal direct shunts between the dural arteries and dural veins.¹ The shunt is located in the intracranial dura mater with venous drainage directed to the dural venous sinuses or cortical veins. Dural arteriovenous fistulas account for 10%–15% of all intracranial

vascular shunts.^{1,2} Tentorial dural arteriovenous fistulas (TDAVFs) constitute only 4% of DAVFs and are characterized by a high hemorrhagic risk. Because of this, these lesions are treated aggressively on diagnosis.^{3–5}

Traditionally, surgical resection was the only treatment available for these lesions. However, endovascular embolization, either alone or in combination with surgery, is increasingly used.⁶ Stereotactic radiosurgery is also increasingly used as an adjunct to surgical and endovascular treatment.⁷ We performed a systematic review of the literature on surgical and endovascular treatment of TDAVFs from 1980 to 2014. The purpose of our study was the following: 1) to determine whether there was a shift from primarily surgical treatments to endovascular and multimodality treatment during this time period, 2) to determine whether the proportion of patients presenting with ruptured TDAVFs during this

Received January 29, 2015; accepted March 5.

From the Departments of Neurosurgery (D.C., G.L.) and Radiology (W.B.) and Center for Science of Healthcare Delivery (M.H.M.), Mayo Clinic, Rochester, Minnesota; and Department of Neurosurgery (S.R.), Arkansas Neuroscience Institute, Little Rock, Arkansas.

Please address correspondence to Waleed Brinjikji, MD, Department of Radiology, Mayo Clinic, 200 1st St SW, Rochester, MN 55905; e-mail: brinjikji.waleed@mayo.edu; @WBrinjikji



Indicates article with supplemental on-line photo.



Evidence-Based Medicine Level 1.

<http://dx.doi.org/10.3174/ajnr.A4394>

time period has changed, 3) to determine whether the rate of good neurologic outcome has changed, and 4) to evaluate clinical and angiographic outcomes in endovascular, surgical, and combined treatments by performing a random-effects meta-analysis.

MATERIALS AND METHODS

A comprehensive literature search of the data bases (PubMed, Ovid MEDLINE, and Ovid EMBASE) was designed and conducted by an experienced librarian with input from the authors. The key words “endovascular,” “catheterization,” “percutaneous,” “embolization,” “coil,” “cerebral veins,” “intracranial,” “arteriovenous fistula,” “surgery,” “DAVF,” “resection,” and “tentorial” were used in both “AND” and “OR” combinations. The search was limited to articles published from 1980 to June 2014 in the English language only. All studies reporting patients treated with surgery or endovascular therapy for TDAVFs were selected. Inclusion criteria were the following: 1) series of >5 patients, with available data on clinical and/or angiographic outcomes. Studies with fewer than 5 patients were included only if they were published before 1995. Two reviewers selected the included studies. For each study, we extracted the following information: patient presentation (ruptured or unruptured), treatment technique (endovascular, surgical, or combined), long-term good neurologic outcome, long-term neurologic morbidity, angiographic occlusion status at last follow-up, resolution of symptoms for unruptured TDAVFs, and year of publication. Good neurologic outcome was defined as a modified Rankin Scale score of ≤ 2 . In cases in which a modified Rankin Scale score was not available, good neurologic outcome was determined if the study used terms such as “no morbidity” or “good recovery.”

The primary objective of this study was to determine the clinical and angiographic outcomes of patients with endovascular, surgical, or multimodality treatment. The secondary objective was to determine trends in patient presentations, treatment type, and clinical outcome following treatment of TDAVFs. For this secondary objective, studies were divided into 3 periods: 1) studies published from 1995 and earlier, 2) studies published from 1996 to 2005, and 3) studies published from 2006 to 2014. For this secondary objective, we performed the following analyses: 1) the proportion of patients presenting with ruptured TDAVFs in each period; 2) the proportion of patients receiving endovascular, surgical, and combined treatments; and 3) the proportion of patients with good neurologic outcome.

Study Quality

We modified the Newcastle-Ottawa Quality Assessment Scale for case-control studies to assess the quality of the studies included in this meta-analysis. The Newcastle-Ottawa score is designed for use in case-control-type studies; however, because none of the studies included in our analysis were of this type, we assessed study quality on the basis of the following: 1) The study included all patients or consecutive patients versus a selected sample, 2) the angiographic and clinical follow-up was satisfactory, thus allowing ascertainment of all outcomes, 3) the case definition was adequate (ie, the location and presen-

tation of the DAVF were clearly stated), 4) outcomes were clearly reported, and 5) the interventionalists/surgeons treating the patients were the same as those who assessed angiographic and clinical outcomes. High-quality studies were defined as those with ≥ 20 patients, high rates of clinical follow-up with clearly reported outcomes, and independent assessment of angiographic and clinical outcomes.

Statistical Analysis

All included studies were noncomparative. We estimated from each cohort the cumulative incidence (event rate) and 95% confidence interval for each outcome. Event rates for each intervention were pooled in a meta-analysis across studies by using the random-effects model.⁸ Anticipating heterogeneity between studies, we chose this model a priori because it incorporates within-study and between-study variances. We also extracted a 2×2 table for each studied outcome for interaction testing and calculated *P* values for the comparisons between endovascular and surgical groups, surgical and multimodality groups, and endovascular and multimodality groups. Heterogeneity of treatment effect across studies was evaluated by using the I^2 statistic.⁹

RESULTS

Literature Review

Studies included in our review are summarized in Table 1. Our literature search yielded 986 articles; 879 articles were excluded after reading the abstract alone, with a total of 107 articles reviewed. Of these, 78 were excluded for either not including TDAVFs in their patient population or not reporting patient presentation or angiographic outcomes. In total, 29 studies with 274 patients met our inclusion criteria. The search results are summarized in Fig 1.

Meta-Analysis Outcomes: All Patients

Meta-analysis outcomes are summarized in Table 2. Forest plots are provided as On-line Figs 1–5. The rates of complete occlusion at last follow-up were 71.0% (95% CI, 56.0%–83.0%) for the endovascular-only group, 81.0% (95% CI, 61.0%–92.0%) for the surgery-only group, and 84.0% (95% CI, 72.0%–91.0%) for the combined-treatment group. The combined-treatment group had a statistically significantly higher rate of complete occlusion ($P < .01$). The rate of long-term neurologic morbidity was 5.0% (95% CI, 2.0%–11.0%) for the endovascular group, 8.0% (95% CI, 2.0%–21.0%) for the surgery-only group, and 6.0% (95% CI, 2.0%–15.0%) for the combined-treatment group. There was no difference between groups in the rates of long-term neurologic morbidity. Perioperative morbidity occurred in 6.0% (95% CI, 3.0%–13.0%) for the endovascular group, 18.0% (95% CI, 8.0%–35.0%) for the surgery-only group, and 14.0% (95% CI, 8.0%–24.0%) for the combined-treatment group. Patients treated with endovascular therapy had significantly lower perioperative morbidity rates than those treated with surgery ($P = .03$) and combined treatments ($P < .01$). The long-term good neurologic outcome rates were 89.0% (95% CI, 80.0%–95.0%) for the endovascular group, 73.0% (95% CI, 51.0%–87.0%) for the surgical group, and 87.0% (95% CI, 71.0%–94.0%) for the combined-treatment group.

Table 1: Study characteristics

Authors, Year	Treatment Type	Clinical/Angiographic Follow-Up (mo)	Rupture Status	No. of Patients	Risk of Bias
Abud et al, 2011 ¹⁹	SE	6	NA	5	Medium
Bret et al, 1994 ²⁰	S	3	U	1	High
Byrne and Garcia, 2013 ³	SE	NA	RU	13	Medium
Fardoun et al, 1981 ²¹	S	12	R	1	High
Grisoli et al, 1984 ²²	S	10	RU	4	High
Gross and Du, 2013 ²³	S	25	RU	15	Medium
Hatano et al, 2013 ²⁴	S	6	U	9	Medium
Huang et al, 2009 ²⁵	E	13	RU	14	Medium
Ito et al, 1995 ²⁶	S	11	R	1	High
Kakarla et al, 2007 ²⁷	SC	21.2	RU	21	Medium
Lawton et al, 2008 ²⁸	C	50	RU	31	Medium
Lewis et al, 1994 ²⁹	S	12	RU	6	Medium
Lewis et al, 1997 ³⁰	E	30	RU	9	Medium
Liu et al, 2014 ³¹	E	33	U	26	Medium
Lucas Cde et al, 2005 ³²	SEC	3	NA	20	Medium
Lucas et al, 1997 ³³	EC	NA	U	1	High
Natarajan et al, 2010 ³⁴	EC	16.5	R	7	Medium
Ott et al, 1993 ³⁵	E	16	U	1	High
Pandey et al, 2011 ³⁶	S	NA	NA	6	High
Pierot et al, 1992 ³⁷	SEC	1	U	6	High
Piippo et al, 2013 ³⁸	SEC	NA	NA	7	High
Puffer et al, 2012 ¹⁶	C	4.6	RU	9	Medium
Rabinov et al, 2013 ³⁹	E	NA	NA	5	Medium
Tomak et al, 2003 ⁴⁰	SEC	60	RU	22	Medium
van Lindert et al, 2000 ⁴¹	C	30	RU	5	Medium
van Rooij et al, 2006 ⁴²	E	3	RU	6	Medium
Wachter et al, 2011 ⁴³	SE	NA	NA	9	Medium
Wajnberg et al, 2012 ⁴⁴	E	15.5	RU	9	Medium
Zhou et al, 2007 ⁶	SC	30	RU	5	Medium

Note:—S indicates surgery; E, endovascular; C, combined; R, ruptured; U, unruptured; NA, not available.

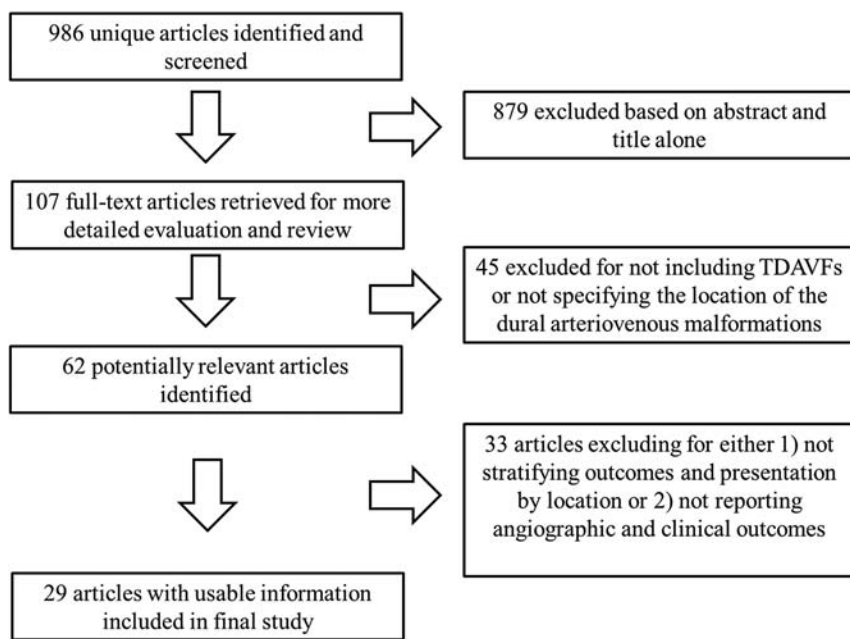


FIG 1. Literature search flow chart.

Long-term good neurologic outcome rates were significantly higher in the endovascular group than in the surgery group ($P = .03$).

Meta-Analysis Outcomes: Patients with Unruptured TDAVFs

Meta-analysis outcomes are summarized in Table 2. Forest plots are provided as On-line Figs 1–5. The rates of complete occlusion at last

follow-up were 76.0% (95% CI, 54.0%–89.0%) for the endovascular-only group, 89.0% (95% CI, 69.0%–97.0%) for the surgery-only group, and 78.0% (95% CI, 53.0%–92.0%) for the combined-treatment group. The rates of long-term neurologic morbidity were 10.0% (95% CI, 3.0%–27.0%) for the endovascular group, 11.0% (95% CI, 3.0%–31.0%) for the surgery-only group, and 10.0% (95% CI, 3.0%–28.0%) for the combined-treatment group. Perioperative morbidity occurred in 10.0% (95% CI, 3.0%–27.0%) for the endovascular group, 18.0% (95% CI, 5.0%–48.0%) for the surgery-only group, and 21.0% (95% CI, 8.0%–46.0%) for the combined-treatment group. The rates of resolution of symptoms were 82.0% (95% CI, 59.0%–94.0%) for the endovascular group, 50.0% (95% CI, 18.0%–82.0%) for the surgery-only group, and 73.0% (95% CI, 37.0%–92.0%) for the combined-treatment group. There were significantly higher

rates of symptom resolution in the endovascular group compared with the surgical group ($P = .03$). The long-term good neurologic outcome rates were 95.0% (95% CI, 91.1%–99.0%) for the endovascular group, 56.0% (95% CI, 20.0%–86.0%) for the surgical group, and 88.0% (95% CI, 68.0%–96.0%) for the combined-treatment group, with significantly better outcomes in the endovascular compared with surgical group ($P <$

Table 2: Outcomes of random-effects meta-analysis

	Endovascular	I ²	Surgical	I ²	Multimodality	I ²	P Value E vs S	P Value E vs M	P Value S vs M
Ruptured and unruptured									
Complete occlusion	71.0 (56.0–83.0)	43	81.0 (61.0–92.0)	33	84.0 (72.0–91.0)	14	.09	<.01	.63
Long-term neurologic morbidity	5.0 (2.0–11.0)	0	8.0 (2.0–21.0)	0	6.0 (2.0–15.0)	0	.66	1.00	1.00
Perioperative morbidity	6.0 (3.0–13.0)	0	18.0 (8.0–35.0)	0	14.0 (8.0–24.0)	0	.03	<.01	.76
Good long-term neurologic outcome	89.0 (80.0–95.0)	0	73.0 (51.0–87.0)	21	87.0 (71.0–94.0)	0	.03	1.00	.07
Unruptured									
Complete occlusion	76.0 (54.0–89.0)	0	89.0 (69.0–97.0)	50	78.0 (53.0–92.0)	9	.48	.95	.51
Long-term neurologic morbidity	10.0 (3.0–27.0)	0	11.0 (3.0–31.0)	0	10.0 (3.0–28.0)	0	.97	1.00	.95
Perioperative morbidity	10.0 (3.0–27.0)	0	18.0 (5.0–48.0)	0	21.0 (8.0–46.0)	0	.25	.45	.70
Good long-term neurologic outcome	95.0 (91.0–99.0)	55	56.0 (20.0–86.0)	0	87.0 (66.0–96.0)	0	<.01	.72	<.01
Resolution of symptoms (unruptured only)	82.0 (59.0–94.0)	0	50.0 (18.0–82.0)	48	73.0 (37.0–92.0)	0	.03	.57	.42
Ruptured									
Complete occlusion	78.0 (61.0–88.0)	0	88.0 (63.0–97.0)	0	82.0 (62.0–93.0)	0	.51	.65	.63
Long-term neurologic morbidity	7.0 (3.0–19.0)	0	12.0 (3.0–37.0)	0	9.0 (3.0–28.0)	0	.95	.93	.91
Perioperative morbidity	7.0 (3.0–19.0)	0	20.0 (6.0–49.0)	0	21.0 (10.0–38.0)	0	.14	.02	.76
Good long-term neurologic outcome	87.0 (71.0–94.0)	0	73.0 (44.0–90.0)	0	88.0 (68.0–96.0)	0	.44	.84	.22

Note:—M indicates multimodality; S, surgery; E, endovascular.

.01) and the combined-treatment compared with the surgical group ($P < .01$).

Meta-Analysis Outcomes: Patients with Ruptured TDAVFs

Meta-analysis outcomes are summarized in Table 2. Forest plots are provided as On-line Figs 1–5. The rates of complete occlusion at last follow-up were 78.0% (95% CI, 61.0%–88.0%) for the endovascular-only group, 88.0% (95% CI, 63.0%–97.0%) for the surgery-only group, and 82.0% (95% CI, 62.0%–93.0%) for the combined-treatment group. The rates of long-term neurologic morbidity were 7.0% (95% CI, 3.0%–19.0%) for the endovascular group, 12.0% (95% CI, 3.0%–37.0%) for the surgery-only group, and 9.0% (95% CI, 3.0%–28.0%) for the combined-treatment group. Perioperative morbidity occurred in 7.0% (95% CI, 3.0%–19.0%) for the endovascular group, 20.0% (95% CI, 6.0%–49.0%) for the surgery-only group, and 21.0% (95% CI, 10.0%–38.0%) for the combined-treatment group. The long-term good neurologic outcome rates were 87.0% (95% CI, 71.0%–94.0%) for the endovascular group, 73.0% (95% CI, 44.0%–90.0%) for the surgical group, and 88.0% (95% CI, 71.0%–94.0%) for the combined-treatment group. There were no significant differences among groups for any of the outcomes.

Secondary Outcomes

The proportion of patients treated with surgical treatment alone decreased from 38.7% to 20.4% between 1980–1995 and 2006–2014. The proportion of patients treated with endovascular therapy alone increased from 16.1% to 48.0% (Fig 2). The proportion of patients presenting with ruptured TDAVFs decreased from 64.4% to 43.6% (Fig 3). The rate of good neurologic outcome increased from 80.7% to 92.9% (Fig 4).

DISCUSSION

The results of this study confirm that contemporary treatment of TDAVF leads to a high percentage of both angiographic cure and favorable clinical outcomes. Successful treatment is achieved uniformly among ruptured and unruptured lesions, with comparable low morbidity, among endovascular, surgical, and combined-treatment modalities. Endovascular and multimodality approaches appear to be associated with a higher rate of symptom resolution in patients with nonhemorrhagic presentation, compared with stand-alone surgical approaches. Furthermore, our study reveals a sustained shift from surgery toward an endovascular approach as the preferred treatment technique of TDAVF in the past 2 decades. Advances in the understanding of the pathologic anatomy of TDAVFs coupled with significant improvement in microcatheter and embolic material technology and microsurgical technique are reflected in the achievement of improved neurologic outcomes in this period. Finally, an increasing number of TDAVFs are now diagnosed and treated before they present with hemorrhage, presumably due to wide availability and improved resolution of noninvasive angiography and the recognition of venous hypertension as a prominent cause of neurologic morbidity.

Dural arteriovenous fistulas of the tentorium have been traditionally considered among the most likely to present with hemorrhage or aggressive nonhemorrhagic neurologic dysfunction. In their review of 337 DAVF cases in 1990, Awad et al¹⁰ found that 97% of TDAVFs presented with either hemorrhage or symptomatic venous hypertension. In fact, the overwhelming majority of patients with DAVFs who present with hemorrhage have TDAVFs.⁵ It is now recognized that the presence of retrograde leptomeningeal drainage, not DAVF location, is the major determining factor of the mode of clinical presentation, and TDAVFs are universally associated with retrograde leptomeningeal drainage.¹¹ The natural history of symptom-

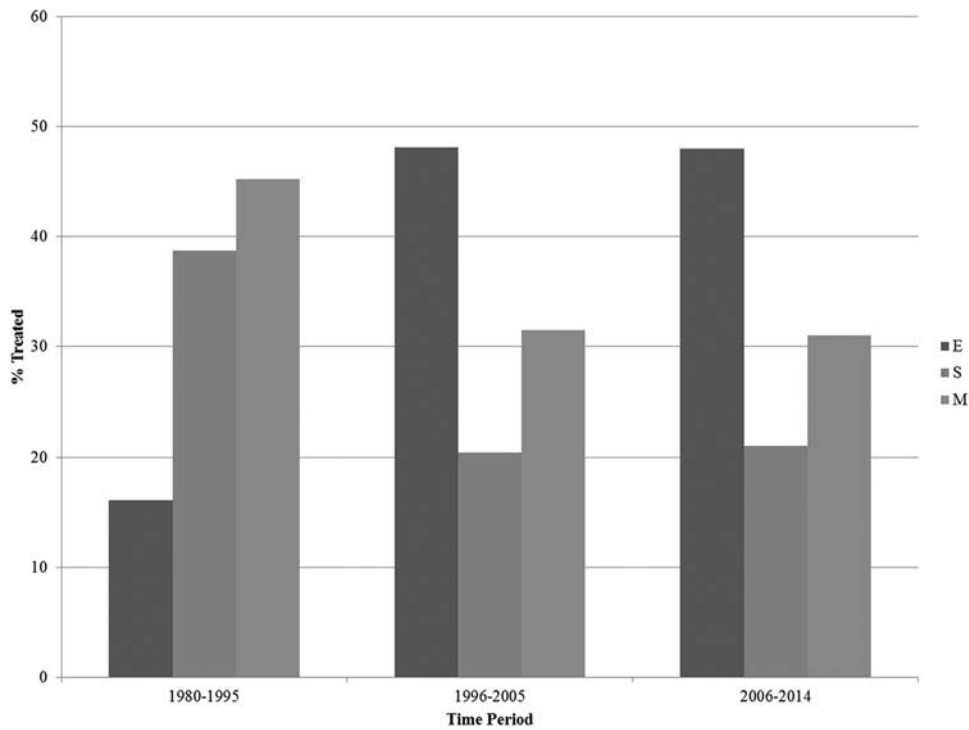


FIG 2. Treatment technique type by time period. E indicates endovascular; S, surgical; M, combined.

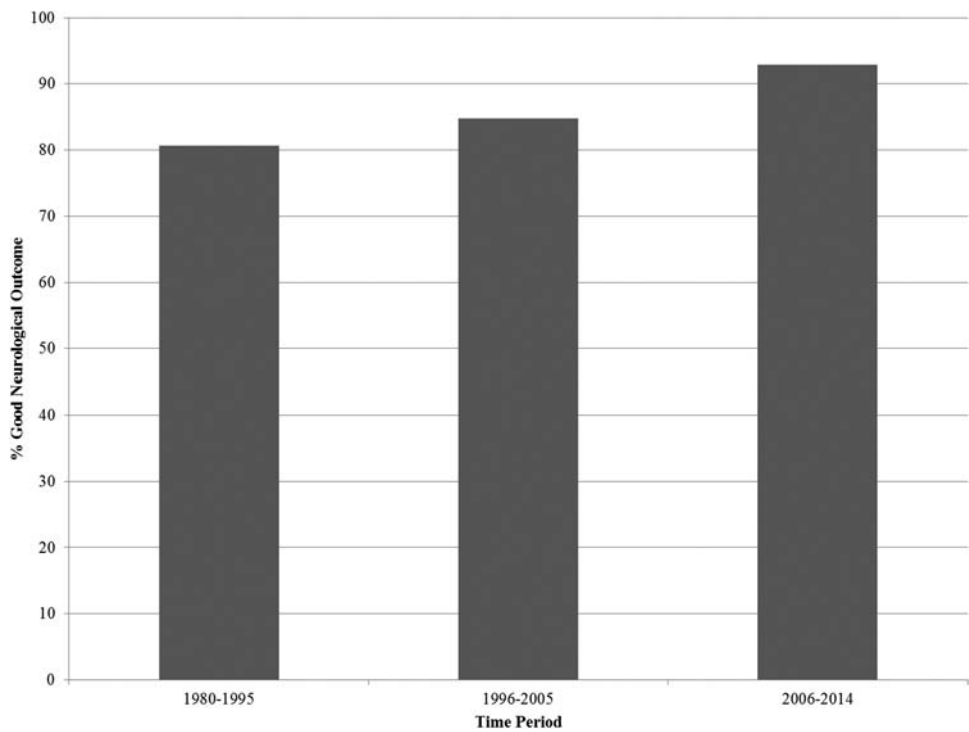


FIG 3. Rate of good neurologic outcome by time period.

atic DAVF with retrograde leptomeningeal drainage is particularly unfavorable. In 1 study of 20 patients who received either no or partial treatment for DAVFs with retrograde leptomeningeal drainage, the annual mortality rate was calculated at 10.4% and the annual risk for hemorrhage or nonhemorrhagic neurologic deficits after the first presentation were 8.1% and 6.9%, respectively. Five patients in this series had DAVFs of the tentorium, of whom 3 died and 1 had mod-

erate disability on follow-up.¹² On the other hand, recent studies have shown that asymptomatic DAVFs with retrograde leptomeningeal drainage may have a relatively benign natural course. Careful inspection reveals that this may not necessarily be valid in the case of TDAVFs, as evidenced in a series of 17 asymptomatic patients, in which only 1 patient had a DAVF of the tentorium and who, in fact, presented with subarachnoid hemorrhage after partial treatment.¹³

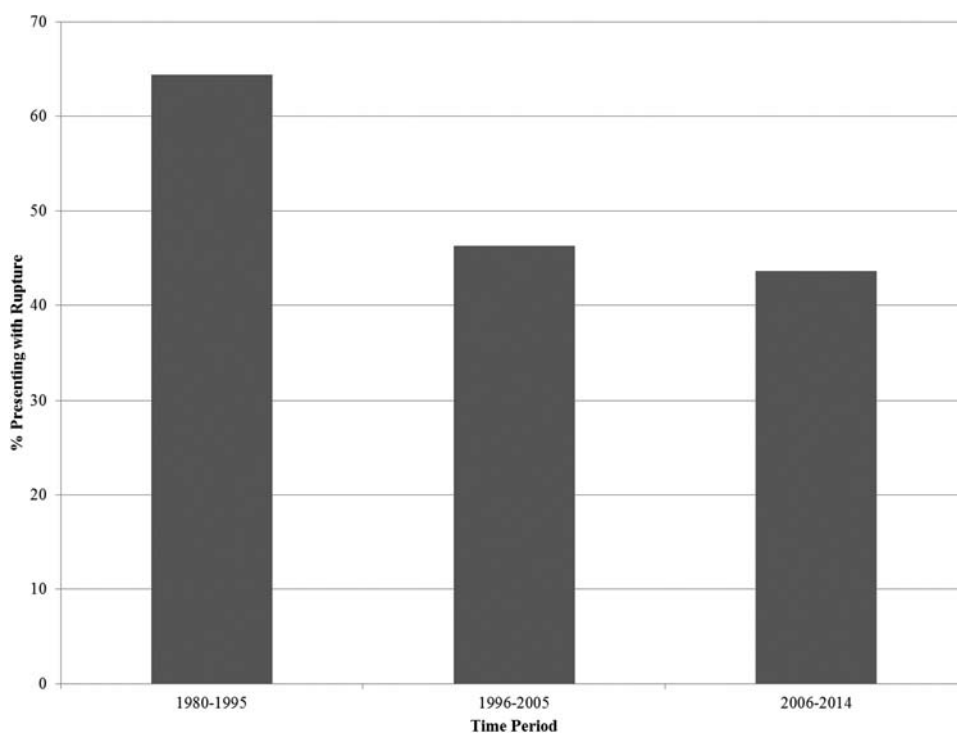


FIG 4. Proportion of patients presenting with ruptured TDAVs by time period.

Until recently, DAVFs of the tentorium were considered candidates only for surgical interruption in the form of microsurgical disconnection of the proximal leptomeningeal venous drainage.¹⁴ The introduction of ethylene-vinyl alcohol (Onyx; Covidien, Irvine, California), a permanent, nonadhesive, liquid embolic agent, has revolutionized DAVF treatment and may be the leading cause of the shift toward a predominantly endovascular treatment paradigm in TDAVs. In transarterial DAVF Onyx embolization, a proximal plug is created around the distal tip of the microcatheter to produce sufficient proximal flow arrest and allow distal penetration of ethylene-vinyl alcohol into the proximal venous outlet while allowing retrograde occlusion of contributing arterial feeders. More recently, dual-lumen balloon microcatheters are used that allow the unopposed forward penetration of Onyx, without the time-consuming effort of plug formation, while concurrently decreasing the risk of premature proximal reflux.¹⁵ The posterior branch of the middle meningeal artery almost always provides arterial supply to a TDAVF and provides a natural direct access to the venous collector system of the fistula. Furthermore, the middle meningeal artery and its branches run a relatively straight course and are anchored on the dura, making failed microcatheter retrieval rare despite substantial Onyx reflux. Although proximal Onyx reflux may occur with a high margin of safety in the middle meningeal artery, reflux should not be allowed in proximity to the level of the foramen spinosum to avoid inadvertent compromise of the arterial supply to the trigeminal and facial nerves.¹⁶

Even though we have attempted to summarize data on all published series of treated TDAVs, our study has certain limitations. The results of separate case series were published by multiple authors who reported independently assessed data and who determined different specific variables that are included in this article. However, the extracted data have been derived from a fairly ho-

mogeneous and strictly defined patient population. Furthermore, our study has publication bias, because patients who had either uneventful or poor outcomes may have been excluded from published results. Moreover, treatment modalities have varied during the time course of the published series; this variation makes standardization of treatment paradigms difficult. Last, uniform assessment and reporting of complications in a standardized fashion were lacking. On the basis of the Grading of Recommendations, Assessment, Development and Evaluation framework, the quality of evidence (confidence in estimates) is very low because of imprecision, heterogeneity, and methodologic limitations of the included studies.^{17,18} Nevertheless, this meta-analysis provides useful data to share with patients and families when assessing the risks of treatment of TDAVs and represents a benchmark against which future studies can be compared. With analysis of >270 patients, this is currently the largest study examining outcomes of surgical and endovascular treatment of TDAVs, to our knowledge.

CONCLUSIONS

During the past 35 years, patients with TDAVs have been increasingly presenting with unruptured lesions, receiving endovascular treatment, and experiencing higher rates of good neurologic outcomes. Endovascular treatment was associated with the best long-term neurologic outcomes but lower occlusion rates. Combined endovascular and surgical treatment was associated with high occlusion rates and low morbidity. Increasing use of Onyx may continue to shift the balance more and more toward increasing endovascular treatment as the sole mode of therapy.

Disclosures: Giuseppe Lanzino—UNRELATED: Consultancy: Covidien/ev3.**Money paid to the institution.

REFERENCES

1. Hiramatsu M, Sugi K, Hishikawa T, et al. **Epidemiology of dural arteriovenous fistula in Japan: analysis of Japanese Registry of Neuroendovascular Therapy (JR-NET2).** *Neurol Med Chir (Tokyo)* 2014;54:63–71
2. Söderman M, Pavic L, Edner G, et al. **Natural history of dural arteriovenous shunts.** *Stroke* 2008;39:1735–39
3. Byrne JV, Garcia M. **Tentorial dural fistulas: endovascular management and description of the medial dural-tentorial branch of the superior cerebellar artery.** *AJNR Am J Neuroradiol* 2013;34:1798–804
4. Cha KC, Yeon JY, Kim GH, et al. **Clinical and angiographic results of patients with dural arteriovenous fistula.** *J Clin Neurosci* 2013;20:536–42
5. Daniels DJ, Vellimana AK, Zipfel GJ, et al. **Intracranial hemorrhage from dural arteriovenous fistulas: clinical features and outcome.** *Neurosurg Focus* 2013;34:E15
6. Zhou LF, Chen L, Song DL, et al. **Tentorial dural arteriovenous fistulas.** *Surg Neurol* 2007;67:472–81; discussion 481–82
7. Yang HC, Kano H, Kondziolka D, et al. **Stereotactic radiosurgery with or without embolization for intracranial dural arteriovenous fistulas.** *Neurosurgery* 2010;67:1276–83; discussion 1284–85
8. DerSimonian R, Laird N. **Meta-analysis in clinical trials.** *Control Clin Trials* 1986;7:177–88
9. Higgins JP, Thompson SG, Deeks JJ, et al. **Measuring inconsistency in meta-analyses.** *BMJ* 2003;327:557–60
10. Awad IA, Little JR, Akarawi WP, et al. **Intracranial dural arteriovenous malformations: factors predisposing to an aggressive neurological course.** *J Neurosurg* 1990;72:839–50
11. Davies MA, Terbrugge K, Willinsky R, et al. **The validity of classification for the clinical presentation of intracranial dural arteriovenous fistulas.** *J Neurosurg* 1996;85:830–37
12. van Dijk JM, terbrugge KG, Willinsky RA, et al. **Clinical course of cranial dural arteriovenous fistulas with long-term persistent cortical venous reflux.** *Stroke* 2002;33:1233–36
13. Strom RG, Botros JA, Refai D, et al. **Cranial dural arteriovenous fistulae: asymptomatic cortical venous drainage portends less aggressive clinical course.** *Neurosurgery* 2009;64:241–47
14. Thompson BG, Doppman JL, Oldfield EH. **Treatment of cranial dural arteriovenous fistulae by interruption of leptomeningeal venous drainage.** *J Neurosurg* 1994;80:617–23
15. Rammos S, Bortolotti C, Lanzino G. **Endovascular management of intracranial dural arteriovenous fistulae.** *Neurosurg Clin N Am* 2014;25:539–49
16. Puffer RC, Daniels DJ, Kallmes DF, et al. **Curative Onyx embolization of tentorial dural arteriovenous fistulas.** *Neurosurg Focus* 2012;32:E4
17. Balshem H, Helfand M, Schünemann HJ, et al. **GRADE guidelines: 3. Rating the quality of evidence.** *J Clin Epidemiol* 2011;64:401–06
18. Guyatt GH, Oxman AD, Kunz R, et al. **GRADE guidelines 6. Rating the quality of evidence—imprecision.** *J Clin Epidemiol* 2011;64:1283–93
19. Abud TG, Nguyen A, Saint-Maurice JP, et al. **The use of Onyx in different types of intracranial dural arteriovenous fistula.** *AJNR Am J Neuroradiol* 2011;32:2185–91
20. Bret P, Salzman M, Bascoulergue Y, et al. **Dural arteriovenous fistula of the posterior fossa draining into the spinal medullary veins: an unusual cause of myelopathy—case report.** *Neurosurgery* 1994;35:965–68; discussion 968–99
21. Fardoun R, Adam Y, Mercier P, et al. **Tentorial arteriovenous malformation presenting as an intracerebral hematoma: case report.** *J Neurosurg* 1981;55:976–78
22. Grisoli F, Vincetelli F, Fuchs S, et al. **Surgical treatment of tentorial arteriovenous malformations draining into the subarachnoid space: report of four cases.** *J Neurosurg* 1984;60:1059–66
23. Gross BA, Du R. **Surgical treatment of high grade dural arteriovenous fistulae.** *J Clin Neurosci* 2013;20:1527–32
24. Hatano T, Bozinov O, Burkhardt JK, et al. **Surgical treatment of tentorial dural arteriovenous fistulae located around the tentorial incisura.** *Neurosurg Rev* 2013;36:429–35
25. Huang Q, Xu Y, Hong B, et al. **Use of Onyx in the management of tentorial dural arteriovenous fistulae.** *Neurosurgery* 2009;65:287–92; discussion 292–93
26. Ito M, Sonokawa T, Mishina H, et al. **Reversible dural arteriovenous malformation-induced venous ischemia as a cause of dementia: treatment by surgical occlusion of draining dural sinus—case report.** *Neurosurgery* 1995;37:1187–91; discussion 1191–92
27. Kakarla UK, Deshmukh VR, Zabramski JM, et al. **Surgical treatment of high-risk intracranial dural arteriovenous fistulae: clinical outcomes and avoidance of complications.** *Neurosurgery* 2007;61:447–57; discussion 457–59
28. Lawton MT, Sanchez-Mejia RO, Pham D, et al. **Tentorial dural arteriovenous fistulae: operative strategies and microsurgical results for six types.** *Neurosurgery* 2008;62(3 suppl 1):110–24
29. Lewis AI, Tomsick TA, Tew JM, Jr. **Management of tentorial dural arteriovenous malformations: transarterial embolization combined with stereotactic radiation or surgery.** *J Neurosurg* 1994;81:851–59
30. Lewis AI, Rosenblatt SS, Tew JM Jr. **Surgical management of deep-seated dural arteriovenous malformations.** *J Neurosurg* 1997;87:198–206
31. Liu C, Xu B, Song D, et al. **Clinical approach of using Onyx via transarterial access in treating tentorial dural arteriovenous fistula.** *Neurol Res* 2014;36:983–91
32. Lucas Cde P, Prandini MN, Caldas JG. **Analysis of the best therapeutic alternative for intracranial dural arteriovenous malformations.** *Arq Neuropsiquiatr* 2005;63:605–13
33. Lucas CP, Zabramski JM, Spetzler RF, et al. **Treatment for intracranial dural arteriovenous malformations: a meta-analysis from the English language literature.** *Neurosurgery* 1997;40:1119–30; discussion 1130–32
34. Natarajan SK, Ghodke B, Kim LJ, et al. **Multimodality treatment of intracranial dural arteriovenous fistulas in the Onyx era: a single center experience.** *World Neurosurg* 2010;73:365–79
35. Ott D, Bien S, Krasznai L. **Embolization of a tentorial dural arteriovenous fistula presenting as atypical trigeminal neuralgia.** *Headache* 1993;33:503–08
36. Pandey P, Steinberg GK, Westbroek EM, et al. **Intraoperative angiography for cranial dural arteriovenous fistula.** *AJNR Am J Neuroradiol* 2011;32:1091–95
37. Pierot L, Chiras J, Meder JF, et al. **Dural arteriovenous-fistulas of the posterior fossa draining into subarachnoid veins.** *AJNR Am J Neuroradiol* 1992;13:315–23
38. Piippo A, Niemela M, van Popta J, et al. **Characteristics and long-term outcome of 251 patients with dural arteriovenous fistulas in a defined population.** *J Neurosurg* 2013;118:923–34
39. Rabinov JD, Yoo AJ, Ogilvy CS, et al. **ONYX versus n-BCA for embolization of cranial dural arteriovenous fistulas.** *J Neurointerv Surg* 2013;5:306–10
40. Tomak PR, Cloft HJ, Kaga A, et al. **Evolution of the management of tentorial dural arteriovenous malformations.** *Neurosurgery* 2003;52:750–60; discussion 760–62
41. van Lindert E, Hassler W, Kühne D, et al. **Combined endovascular-microsurgical treatment of tentorial-incisural dural arteriovenous malformations: report of five cases.** *Minim Invasive Neurosurg* 2000;43:138–43
42. van Rooij WJ, Sluzewski M, Beute GN. **Tentorial artery embolization in tentorial dural arteriovenous fistulas.** *Neuroradiology* 2006;48:737–43
43. Wachter D, Hans F, Psychogios MN, et al. **Microsurgery can cure most intracranial dural arteriovenous fistulae of the sinus and non-sinus type.** *Neurosurg Rev* 2011;34:337–45; discussion 345
44. Wajnberg E, Spilberg G, Rezende MT, et al. **Endovascular treatment of tentorial dural arteriovenous fistulae.** *Interv Neuroradiol* 2012;18:60–68

Progressive versus Nonprogressive Intracranial Dural Arteriovenous Fistulas: Characteristics and Outcomes

S.W. Hetts, T. Tsai, D.L. Cooke, M.R. Amans, F. Settecasse, P. Moftakhar, C.F. Dowd, R.T. Higashida, M.T. Lawton, and V.V. Halbach



ABSTRACT

BACKGROUND AND PURPOSE: A minority of intracranial dural arteriovenous fistulas progress with time. We sought to determine features that predict progression and define outcomes of patients with progressive dural arteriovenous fistulas.

MATERIALS AND METHODS: We performed a retrospective imaging and clinical record review of patients with intracranial dural arteriovenous fistula evaluated at our hospital.

RESULTS: Of 579 patients with intracranial dural arteriovenous fistulas, 545 had 1 fistula (mean age, 45 ± 23 years) and 34 (5.9%) had enlarging, de novo, multiple, or recurrent fistulas (mean age, 53 ± 20 years; $P = .11$). Among these 34 patients, 19 had progressive dural arteriovenous fistulas with de novo fistulas or fistula enlargement with time (mean age, 36 ± 25 years; progressive group) and 15 had multiple or recurrent but nonprogressive fistulas (mean age, 57 ± 13 years; $P = .0059$, nonprogressive group). Whereas all 6 children had fistula progression, only 13/28 adults ($P = .020$) progressed. Angioarchitectural correlates to chronically elevated intracranial venous pressures, including venous sinus dilation (41% versus 7%, $P = .045$) and pseudophlebitic cortical venous pattern ($P = .048$), were more common in patients with progressive disease than in those without progression. Patients with progressive disease received more treatments than those without progression (median, 5 versus 3; $P = .0068$), but as a group, they did not demonstrate worse clinical outcomes (median mRS, 1 and 1; $P = .39$). However, 3 young patients died from intracranial venous hypertension and intracranial hemorrhage related to progression of their fistulas despite extensive endovascular, surgical, and radiosurgical treatments.

CONCLUSIONS: Few patients with dural arteriovenous fistulas follow an aggressive, progressive clinical course despite treatment. Younger age at initial presentation and angioarchitectural correlates to venous hypertension may help identify these patients prospectively.

ABBREVIATIONS: CVD = cortical venous drainage; DAVF = dural arteriovenous fistula

Intracranial dural arteriovenous fistulas (DAVFs) are rare arteriovenous shunts involving the epidural space and adjacent dura mater, which receive arterial supply from meningeal vessels and drain directly to dural venous sinuses or cortical veins.¹ In the early days of cerebral angiography, DAVFs were considered a subset of AVMs: Newton and Cronqvist² classified AVMs by arterial supply as pure dural, mixed pial-dural, or pure pial malformations. Unlike brain AVMs, however, DAVFs are most often

thought to be acquired (as opposed to congenital), and DAVFs lack a nidus of vessels in the brain parenchyma. DAVF is also distinguished from nongalenic pial arteriovenous fistula by its fistula location in the dura.

Management of a DAVF is based on its expected clinical course: Fistulas demonstrating cortical venous drainage (CVD) generally warrant curative therapy to prevent intracranial hemorrhage, and fistulas without CVD are managed for either symptom palliation or cure.³⁻⁶ Treatment modalities include transarterial or transvenous endovascular embolization to occlude the arteriovenous fistula site, microsurgical interruption of the fistula site, stereotactic radiosurgery, or multimodality therapy. Endovascular procedures are used to treat a most DAVFs and are the treatment of choice for lesions accessible to catheterization.^{5,6}

A small number of patients with DAVFs respond poorly to conventional therapies and demonstrate progressive neurologic and angiographic deterioration with enlargement of

Received October 10, 2014; accepted after revision February 5, 2015.

From the Departments of Radiology and Biomedical Imaging (S.W.H., T.T., D.L.C., M.R.A., F.S., P.M., C.F.D., R.T.H., V.V.H.), Neurological Surgery (C.F.D., R.T.H., M.T.L., V.V.H.), Neurology (C.F.D., R.T.H., V.V.H.), and Anesthesia and Perioperative Care (C.F.D., R.T.H., V.V.H.), University of California, San Francisco, San Francisco, California.

Please address correspondence to Steven W. Hetts, MD, 505 Parnassus Ave, L-349, San Francisco, CA 94143-0628; e-mail: steven.hetts@ucsf.edu

Indicates article with supplemental on-line tables.

<http://dx.doi.org/10.3174/ajnr.A4391>

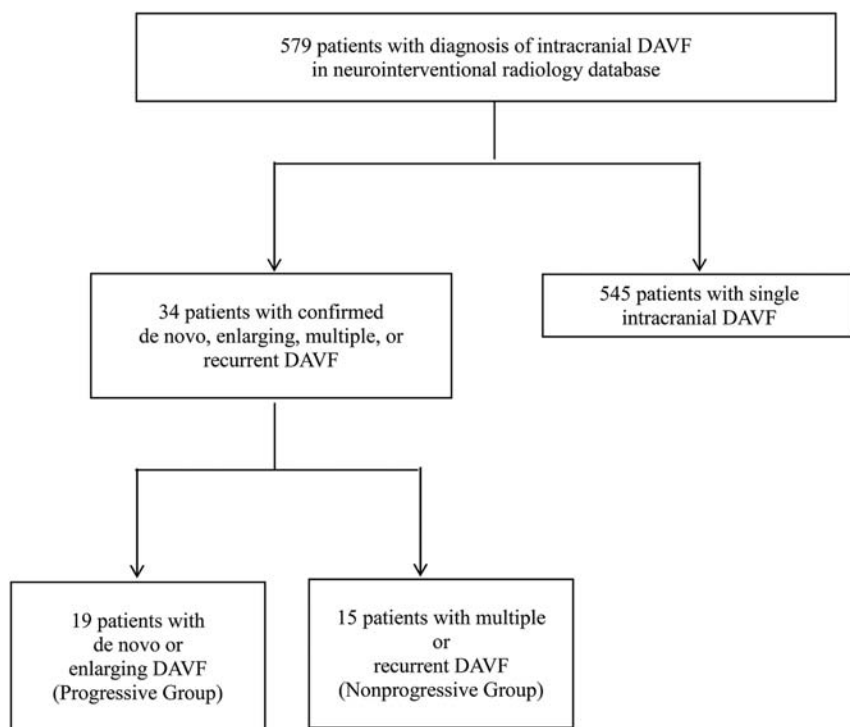


FIG 1. Cohort selection.

Table 1: UCSF intracranial dural arteriovenous fistula cohort with single fistulas versus subset with confirmed enlarging, de novo, multiple, or recurrent fistulas

	Enlarging, De Novo, Multiple, or Recurrent Fistulas (n = 34)	Remainder of UCSF Intracranial DAVFs (n = 545)	P Value ^a
Mean age at dx ± SD	45 ± 23 y	53 ± 20 y	.11 ^b
Median age (range)	52.5 y (0.2–77 y)	56 y (0–87 y)	
Male	35%	49%	.16 ^c

Note.—UCSF indicates University of California at San Francisco; dx, diagnosis.

^a Enlarging, de novo, multiple, or recurrent vs remainder of UCSF cohort.

^b Two-tailed t test.

^c Two-sided Fisher exact test.

existing fistulas, formation of de novo fistulas, and development of features that increase the risk of intracranial hemorrhage.⁷ Reports of such rapidly progressive “runaway” DAVFs are scarce. Only a few cases have been published in the past 15 years; therefore, the pathogenesis, presentation, clinical course, and treatment remain unclear.^{4,8–12} The purpose of this single-institution retrospective cohort study was to compare the clinical characteristics, angioarchitecture, and treatment outcomes of patients with progressive (enlarging fistulas or developing de novo fistulas) versus nonprogressive (recurrent original fistula or the presence of multiple unchanging fistulas) intracranial DAVFs.

MATERIALS AND METHODS

Subjects

In this institutional review board–approved study, a neurointerventional radiology data base was used to identify 579 subjects diagnosed with or treated for intracranial DAVFs at the University of California, San Francisco between 1986 and 2013 (Fig 1). Data were cross-referenced with a larger institutional brain AVM data

base for cases between 2000 and 2012. Imaging reports and medical records of 141 patients who underwent ≥ 2 cerebral DSAs were reviewed. Thirty-four patients with angiographically confirmed multiple, recurrent, enlarging or de novo DAVFs were identified. This search and classification approach was taken to be certain that fistula progression or nonprogression could be confirmed by angiographic images acquired at our institution by using selective DSA techniques that have been standard during a long period.

Medical Record and Imaging Review

Baseline demographic and clinical variables were recorded for each subject (Table 1). Angioarchitectural characteristics noted from initial pretreatment angiograms are outlined in On-line Table 1. Treatment and outcome variables are outlined in Table 2, and detailed information is included in On-line Table 2.

Preintervention diagnostic cerebral angiograms and accompanying reports were available for 32 of 34 patients. Angiographic images for these 32 patients were reviewed and scored (S.W.H., T.T., D.L.C.) according to a structured data-collection sheet previously developed for brain AVMs and nongalenic pial arteriovenous fistulas and modified to highlight features of DAVFs.^{13,14} Two patients were reviewed by using only structured angiography reports, which

are of the same format and authored by the same group of angiographers (S.W.H., D.L.C., C.F.D., R.T.H., V.V.H.) for the entire study period.

Individual DAVFs were graded according to the Borden-Shucart and Cognard scales.^{15,16} “Multiple” was defined as the simultaneous occurrence of ≥ 2 fistulas at anatomically different locations. “Recurrent” was defined as the recanalization of a fistula at its original location on follow-up DSA after apparent initial angiographic cure. “De novo” was defined as the development of ≥ 1 fistula during treatment or on follow-up DSA that was not detected on initial DSA. “Enlarging” was defined as the interval enlargement, increase in arterial flow, recruitment of new arterial feeders, or worsening of the venous drainage pattern of an existing fistula during treatment or on follow-up. When we combined these descriptions for analysis, the progressive fistula group included patients with enlarging and/or de novo fistulas and the nonprogressive group included patients with unchanging multiple or recurrent fistulas.

Intracranial venous pressures—as measured via microcath-

Table 2: Treatments and outcomes stratified by fistula progression

	All Subjects (n = 34)	Progressive (n = 19)	Nonprogressive (n = 15)	P Value
Treatments				
Median treatment procedures (25%, 75%)		5 (3, 9)	3 (2, 4)	.0068 ^a
Range treatment procedures		2–19	2–7	
Any surgical treatment		63%	33%	.17 ^b
Transarterial embolization		100%	80%	.076 ^b
Transvenous embolization		74%	67%	.72 ^b
Ethanol embolization		84%	67%	.42 ^b
Coil embolization		89%	80%	.63 ^b
PVA embolization		74%	53%	.29 ^b
Glue embolization		42%	13%	.13 ^b
Onyx embolization ^c		11%	20%	.63 ^b
Outcomes at last follow-up				
Mean follow-up duration	4.6 y	5.1 y	4.0 y	.70
Median (range) follow-up duration	2.5 y (56 d to 23 y)	3.9 y (58 d to 17 y)	1.4 y (56 d to 23 y)	.37 ^a
Death		16%	0%	.24 ^b
Median outcome (normal = 0, deficits/residual fistula = 1, death = 2)		1 (0, 1)	1 (0, 1)	.31 ^a
Median last mRS (25%, 75%)		1 (0, 3)	1 (0, 3)	.39 ^a
Range last mRS		0–6	0–3	
Good outcome (last mRS 0–2)		74%	73%	1.0
Median change in mRS (25%, 75%)		–0.5 (–1, 0)	–1 (–1, 0)	.83 ^a
Range change mRS		–3 to 1	–4 to 2	

Note:—PVA indicates polyvinyl alcohol.

^a Wilcoxon rank sum (Mann-Whitney) test.

^b Two-sided Fisher exact test.

^c Covidien, Irvine, California.

eters in situ during embolization procedures—were reviewed when available in DSA reports. Brain CT or MR imaging was reviewed for evidence of acute or prior hemorrhage, hydrocephalus, encephalomalacia, and intracerebral calcifications.

Treatment

Management of DAVFs at our institution is based on the expected clinical course of the lesion. Low-grade fistulas with antegrade dural sinus drainage and no CVD are managed conservatively, though endovascular repair is often considered for patients presenting with debilitating symptoms such as severe pulsatile tinnitus. DAVFs with CVD are treated in order to lower the risk of intracranial hemorrhage.^{12,17–19} Endovascular procedures are the treatment of choice for most lesions at our institution except in cases in which CVD cannot be eliminated by endovascular embolization, in which case an operation is undertaken.^{5,6} During the study period, patients were treated by endovascular intervention, a combination of endovascular and surgical intervention, radiosurgery, or observation. In the absence of clinical worsening, we typically perform DSA and clinical follow-up of DAVFs without CVD at 12 months following treatment and of DAVFs with CVD at 3 months following curative treatment.

Outcomes Assessment

Medical records from each patient's last clinical follow-up were assessed for neurologic or developmental disability by 2 investigators (T.T., S.W.H.). The mRS of neurologic disability was used for retrospective classification of initial clinical function and ultimate clinical outcome in all patients. Good clinical outcome was defined as an mRS of 0–2. At the time of last follow-up, records and images were assessed for evidence of change since initial presentation by 2 investigators (T.T., S.W.H.). Follow-up duration

was the time from clinical presentation to the last clinical or imaging report.

Statistical Analysis

In a descriptive analysis, subjects were stratified by DSA findings into those with progressive DAVFs compared with those with nonprogressive DAVFs. Student *t* tests were used to compare normally distributed continuous data, Wilcoxon rank sum tests were used to compare ordinal data, and Fisher exact tests were used to compare proportions. Descriptive statistics and Student *t* tests were calculated in Excel for Macintosh 2011 (Microsoft, Redmond, Washington). Risk ratios, 95% confidence intervals, odds ratios, and Wilcoxon rank sum and Fisher exact tests were performed in STATA SE, Version 12.1 (StataCorp, College Station, Texas).

RESULTS

Demographic Information

Multiple, recurrent, de novo, or enlarging DAVFs were present in 5.9% of the 579 patients diagnosed with intracranial DAVFs at our hospital during the study period. Patients with multiple DAVFs presented clinically at a mean age of 45 years (range, 2 months to 87 years), whereas patients with single fistulas presented at a mean age of 53 years (range, 0 days to 87 years, *P* = .11). Of the 34 patients included for further analysis, 12 (35%) were male and 22 (65%) were female. Patients with progressive DAVFs presented at a younger age compared with patients with nonprogressive fistulas (38 years versus 59 years, *P* = .0059). Whereas all 6 children (18 years of age or younger at time of initial presentation) in our cohort had fistula progression, only 13/28 adults (46%, *P* = .02) had fistula progression

(Fig 2). Baseline patient characteristics and clinical presentations are presented in Table 1.

Clinical Presentation

Initial clinical presentation did not differ significantly between subjects with progressive DAVFs and those with nonprogressive DAVFs. Headache and pulsatile tinnitus were the most common symptoms in both groups and occurred at similar rates. The likelihood of aggressive presentation, such as seizure or intracranial hemorrhage, did not differ between the 2 groups. Similarly, the median presentation mRS did not differ between subjects with

progressive DAVFs and those with nonprogressive DAVFs. Prior head trauma also occurred at similar rates in both groups.

Angioarchitecture

Angioarchitectural characteristics of the DAVFs are presented in On-line Table 1, and are illustrated in Figs 3–5. The initial venous drainage pattern in progressive fistulas did not differ from that of nonprogressive fistulas, as graded by the Cognard and Borden-Shucart classification systems. Venous sinus dilation was more common in patients with progressive fistulas (41%) than in patients with nonprogressive fistulas (7%, $P = .045$). The presence of a pseudophlebitic cortical venous pattern²⁰ was also more common in progressive fistulas than nonprogressive fistulas ($P = .048$). The median degree of sinus stenosis/occlusion (grouped ordinarily into 0%–24%, 25%–49%, 50%–74%, 75%–99% stenosis, and 100% occlusion categories) was higher in progressive fistulas (100%) compared with nonprogressive fistulas (0%–24%, $P = .091$), though this trend did not reach statistical significance. There was no significant difference in the presence of venous ectasia or in the median number of arteriovenous connections when progressive DAVFs were compared with nonprogressive DAVFs. The location of progressive fistulas also did not differ from that of nonprogressive fistulas. Venous pressures were provided in angiographic reports of 6 patients, all of whom had progressive fistulas. The mean venous pressure was markedly elevated: 53 mm Hg (range, 37–81 mm Hg, by using 8 mm Hg as the upper limit of normal).^{21–24}

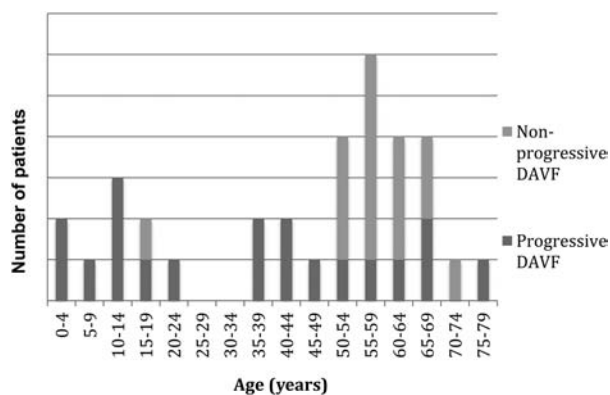


FIG 2. Age of diagnosis for patients with progressive-versus-nonprogressive fistulas.

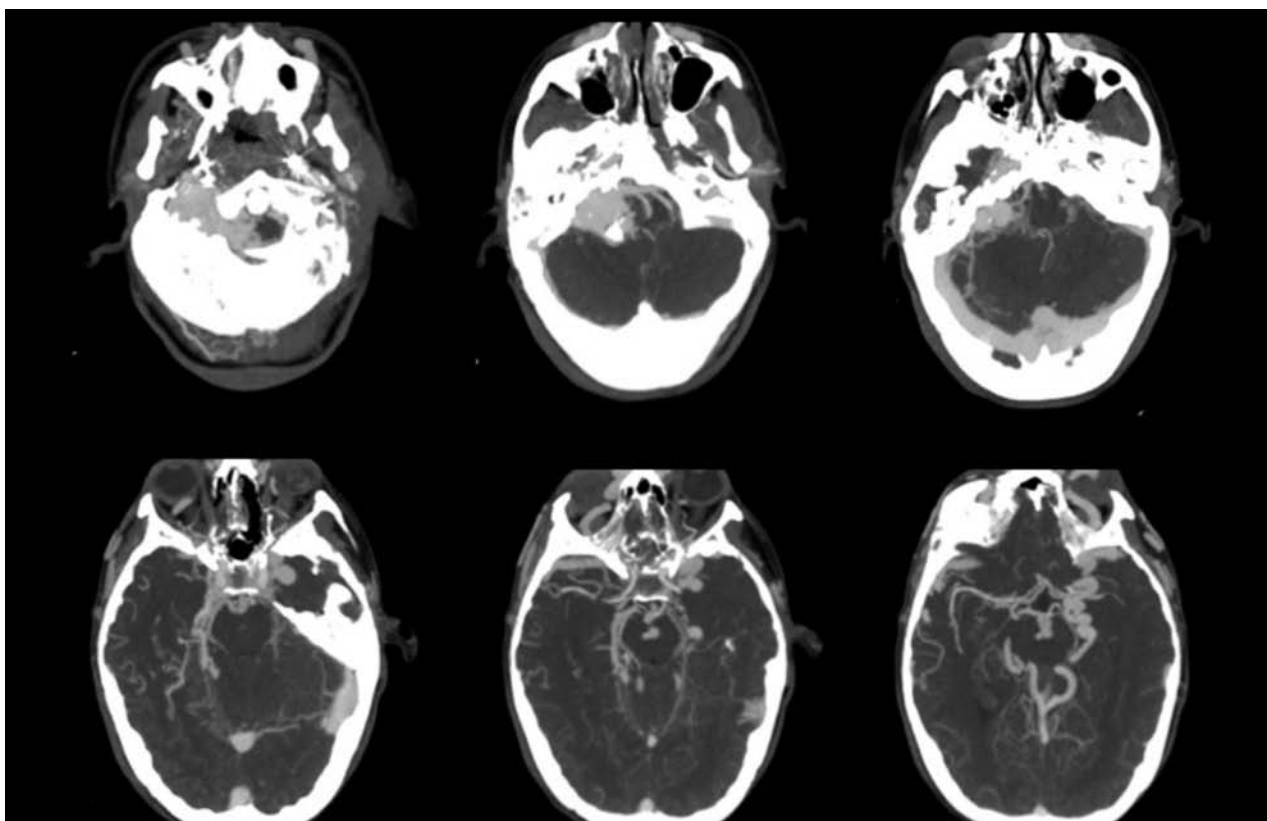


FIG 3. Multiple and progressive DAVFs. A 25-year-old female patient with large skull base DAVFs refractory to multiple endovascular treatments. She was initially diagnosed at 18 years of age and died of intracranial hemorrhage 6 years later in the setting of intractable intracranial venous hypertension. CTA images demonstrate an extensive skull base vascular abnormality with dilated cortical veins suggestive of intracranial venous hypertension.

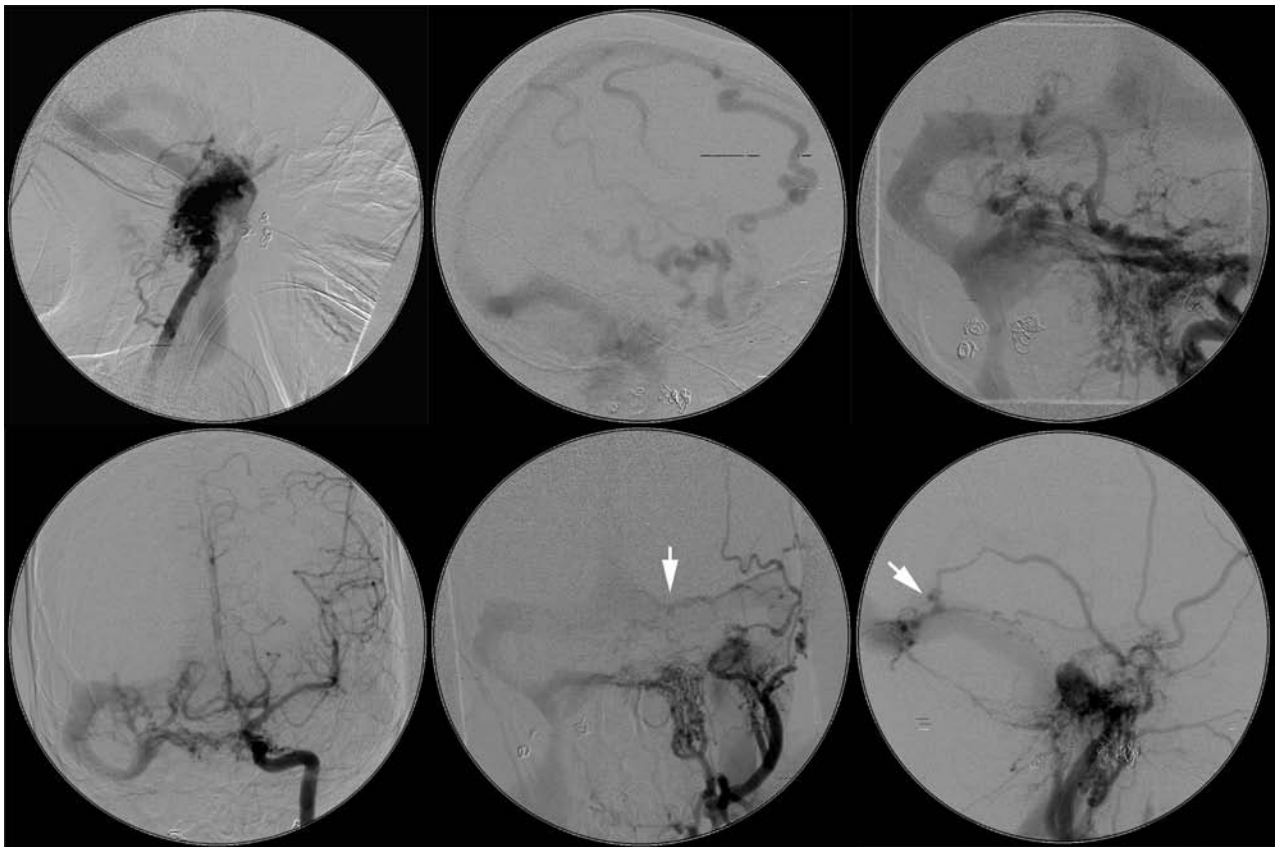


FIG 4. Multiple and progressive DAVFs. Same patient as in Fig 3. DSA images before treatment at our institution but 4 years after initial proximal coil embolization of external carotid artery feeders below the skull base at an outside institution demonstrate multiple skull base fistulas associated with venous hypertension, cortical venous reflux, venous sinus dilation, and a jugular bulb outflow stenosis (between white arrows). (Upper row: right vertebral artery lateral, right vertebral artery lateral, left vertebral artery anteroposterior; lower row: left ICA anteroposterior, left external carotid artery anteroposterior, left external carotid artery lateral). A middle meningeal artery to the torcular fistula indicated by the white arrows is shown in greater detail in Fig 5.

Treatment

Treatments are described in Table 2. Patients received between 2 and 19 endovascular, surgical, and/or radiosurgical treatments. Subjects with progressive DAVFs underwent more treatment procedures than did subjects with nonprogressive fistulas (median, 5 versus 3; $P = .0068$). There was no significant difference in the type of embolic materials used to treat progressive fistulas compared with those used for nonprogressive fistulas.

Clinical Outcomes

The median follow-up time was 2.5 years (range, 56 days to 23.3 years) for all patients. Median follow-up was longer in patients with progressive fistulas (3.9 years) than in those with nonprogressive fistulas (1.4 years), but this difference did not reach statistical significance ($P = .37$). Angiographic progression from lower risk to higher risk venous drainage on the basis of the Borden-Shucart or Cognard classification was noted in 9% of all patients. Good clinical outcome, defined as a last mRS of 0–2, was achieved in 74% of all patients. Median change in mRS did not differ between subjects with progressive fistulas compared with those with nonprogressive fistulas. Three deaths occurred in the progressive DAVF group (16%) due to intracranial hemorrhage, compared with no deaths among subjects with nonprogressive DAVFs ($P = .24$).

DISCUSSION

DAVFs are rare and present a variable clinical risk to patients.^{25,26} Although many DAVFs are curable by embolization,^{27–29} some DAVFs require surgery or a combination of embolization and surgery for effective treatment.³⁰ Despite the overall good success rates of treating even complex DAVFs by using modern techniques,³¹ progressive DAVFs, by definition, have eluded cure. Such lesions can often be palliated with stabilization or regression of clinical symptoms, but a minority of DAVFs progress and result in significant morbidity. As reported in the current study, a small number of progressive intracranial DAVFs are ultimately fatal.

Large series of DAVFs indicate that multiplicity is uncommon, with rates between 6.7% and 8.1%.^{19,28,31,32} The frequency of de novo or enlarging progressive DAVFs is difficult to assess due to the paucity of published data.^{33–35} In the present study, 19 (3.2%) of 579 patients had de novo or enlarging progressive fistulas, supporting the contention that such lesions are exceedingly rare. Our series may under-report the number of multiple DAVFs (15 of 579; 2.6%), given our approach requiring follow-up DSAs at our own institution with reviewable images.

Multiple synchronous DAVFs may be associated with a more aggressive clinical presentation compared with solitary lesions.^{19,28,32} In our cohort of patients with multiple, recurrent, de

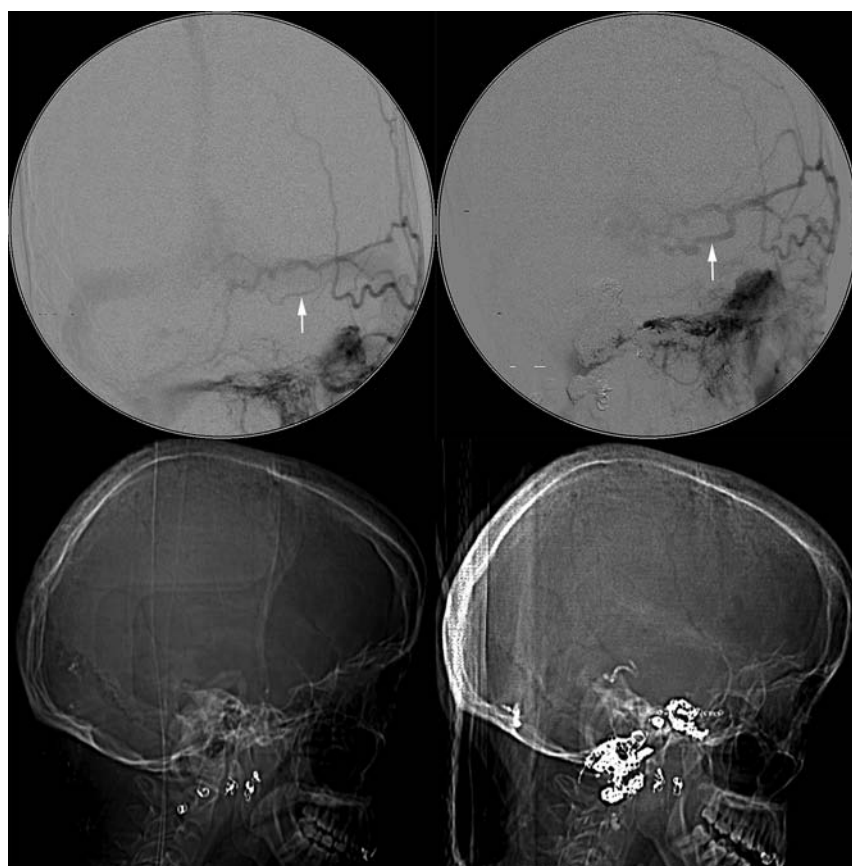


FIG 5. Multiple and progressive DAVFs. Same patient as in Figs 3 and 4. DSA demonstrates progression of a left middle meningeal artery to a torcular DAVF with interval enlargement of a feeding artery (arrow in upper left panel versus arrow in upper right panel) during 7 months. Lateral CT scanograms obtained at the same time as DSA provide an overview of treatment with interval deposition of embolic coils and *n*-BCA glue (lower left versus lower right panel).

novo, or enlarging DAVFs, we observed relatively high rates of intracranial hemorrhage (26%), cranial neuropathy (47%), and other focal neurologic deficits (32%). Fistulas that eventually progressed with enlargement or de novo fistula formation were not more likely to present initially with aggressive symptoms, suggesting that neurologic symptoms at presentation cannot necessarily be extrapolated to predict a malignant clinical course. A bias in our study, however, is that we would treat DAVFs with CVD at presentation aggressively at our institution, seeking prompt cure to reduce the risk of subsequent intracranial hemorrhage. Thus, one would expect that lesions with CVD at initial presentation would preferentially be extirpated and thus not persist to have progression in follow-up studies. Of course, the most complex lesions with CVD were not curable with embolization, surgery, or radiosurgery and thus did persist to show progression on follow-up.

Cortical venous drainage is a well-established risk factor for aggressive clinical presentation^{15,16,36,37} and is related to poor clinical outcome in untreated lesions: Venous hypertension can lead to not only cortical edema and seizures but, more seriously, vein rupture and intracranial hemorrhage.³⁸ Few studies to date have explored the prognostic significance of CVD in the setting of definitive management.³⁹ Our series demonstrates similar rates of CVD on initial angiography in nonprogressive DAVFs and lesions that ultimately progressed. The Cognard and Borden-Shucart

scales—and other scales that also rely primarily on the presence of CVD to stratify lesion risk—do not fully capture features of progressive DAVFs because new arteriovenous shunts can form and existing shunts can enlarge without necessarily changing venous drainage categories in the Cognard and Borden-Shucart systems.

There have been attempts to refine classification to improve stratification of neurologic risk in patients with DAVFs.⁴⁰ Geibprasert et al¹ proposed a different classification scheme based on 3 craniospinal epidural spaces, noting an aggressive clinical presentation in lateral epidural fistulas in contrast to the predominantly benign presentation in ventral epidural fistulas; the predictive validity of the scheme has not yet been established.

The pathophysiology of venous hypertension in DAVF genesis—in truly “runaway,” rapidly progressive malignant DAVFs in particular—likely involves a kindling effect of angiogenic factors, as supported by experimental and molecular data from small animal models.^{7,41,42} A positive feedback loop generates an increased number of arteriovenous shunts that result in arterIALIZED pressures within veins, thus substantially increasing the risk of intracranial hemorrhage and death. Progressive intracranial hypertension may also result from impaired resorption of CSF at the arachnoid granulations in the setting of intracranial venous hypertension. The relationship among thrombophilia, localized venous ischemia, and angiogenesis in progressive DAVF has yet to be elucidated.^{17,43,44} Young patient age at the time of fistula diag-

nosis also appears to play a role in the likelihood of fistula progression (Fig 2), perhaps because these patients are primed for angiogenesis as part of normal development in contrast to a more static angiogenic milieu in adults.⁴⁵

There are several important limitations to our study. This is a retrospective, single-center study during a 27-year time span. Treatment modalities and criteria for definitive management have evolved during this period. Although it is likely that embolization with a temporary agent such as polyvinyl alcohol leads to more fistula recurrences than embolization with a permanent agent such as *n*-BCA, the frequency of the use of particular embolic agents did not differ between progressive and nonprogressive groups in our small cohort. In addition, patients with exceptionally malignant DAVFs who did not survive the initial presentation and treatment or who refused or were ineligible for treatment would not have been identified from our data base in this series. Similarly, patients who underwent a single treatment session at our institution but had multiple prior or subsequent sessions at another hospital would have also been excluded from our retrospective review. Finally, because our institution is a quaternary care center, the duration of follow-up was highly variable; subsequent treatments and significant outcomes in the community may have been unavailable for analysis.

CONCLUSIONS

Intracranial DAVF is a heterogeneous disease. A small subset of young patients with intracranial DAVFs follow a malignant clinical course with progressive fistula formation and expansion, intractable intracranial venous hypertension, and recurrent intracranial hemorrhage, despite aggressive endovascular and surgical management. Better characterization of the molecular mechanisms underlying angiogenesis gone awry in runaway DAVFs is necessary and will potentially provide insight into new medical therapies for this rare and serious disease.

Disclosures: Steven W. Hetts—UNRELATED: Consultancy: Stryker Neurovascular, Silk Road Medical, Penumbra; Stock/Stock Options: ChemoFilter, Medina Medical. Christopher F. Dowd—UNRELATED: Other: MicroVention/Terumo.* Comments: Chief Adjunct, Flow Redirection Endoluminal Device Trial. *Money paid to the institution.

REFERENCES

- Geibprasert S, Pereira V, Krings T, et al. **Dural arteriovenous shunts: a new classification of craniocervical epidural venous anatomical bases and clinical correlations.** *Stroke* 2008;39:2783–94
- Newton TH, Cronqvist S. **Involvement of dural arteries in intracranial arteriovenous malformations.** *Radiology* 1969;93:1071–78
- Lalwani AK, Dowd CF, Halbach VV. **Grading venous restrictive disease in patients with dural arteriovenous fistulas of the transverse/sigmoid sinus.** *J Neurosurg* 1993;79:11–15
- Cognard C, Houdart E, Casasco A, et al. **Long-term changes in intracranial dural arteriovenous fistulae leading to worsening in the type of venous drainage.** *Neuroradiology* 1997;39:59–66
- Meyers PM, Halbach VV, Dowd CF, et al. **Dural carotid cavernous fistula: definitive endovascular management and long-term follow-up.** *Am J Ophthalmol* 2002;134:85–92
- Ng PP, Higashida RT, Cullen S, et al. **Endovascular strategies for carotid cavernous and intracerebral dural arteriovenous fistulas.** *Neurosurg Focus* 2003;15:ECP1
- Zhu Y, Lawton MT, Du R, et al. **Expression of hypoxia-inducible**

- factor-1 and vascular endothelial growth factor in response to venous hypertension.** *Neurosurgery* 2006;59:687–96; discussion 687–96
- Ha SY, Kwon YS, Kim BM, et al. **Clinical and angiographic characteristics of multiple dural arteriovenous shunts.** *AJNR Am J Neuroradiol* 2012;33:1691–95
- Dützmann S, Beck J, Gerlach R, et al. **Management, risk factors and outcome of cranial dural arteriovenous fistulae: a single-center experience.** *Acta Neurochir (Wien)* 2011;153:1273–81
- Pan HC, Sheehan J, Huang CF, et al. **Two consecutive dural arteriovenous fistulae in a child: a case report of successful treatment with gamma knife radiosurgery.** *Childs Nerv Syst* 2007;23:1185–90
- Kiyosue H, Tanoue S, Okahara M, et al. **Recurrence of dural arteriovenous fistula in another location after selective transvenous coil embolization: report of two cases.** *AJNR Am J Neuroradiol* 2002;23:689–92
- Hiu T, Horie N, Hayashi K, et al. **Recurrence of the cavernous sinus dural arteriovenous fistula at adjacent sinuses following repeated transvenous embolizations: case report and literature review.** *Radiat Med* 2008;26:431–37
- Atkinson RP, Awad IA, Batjer HH, et al. **Reporting terminology for brain arteriovenous malformation clinical and radiographic features for use in clinical trials.** *Stroke* 2001;32:1430–42
- Hetts SW, Keenan K, Fullerton HJ, et al. **Pediatric intracranial nongalenic pial arteriovenous fistulas: clinical features, angioarchitecture, and outcomes.** *AJNR Am J Neuroradiol* 2012;33:1710–19
- Borden JA, Wu JK, Shucart WA. **A proposed classification for spinal and cranial dural arteriovenous fistulous malformations and implications for treatment.** *J Neurosurg* 1995;82:166–79
- Cognard C, Gobin YP, Pierot L, et al. **Cerebral dural arteriovenous fistulas: clinical and angiographic correlation with a revised classification of venous drainage.** *Radiology* 1995;194:671–80
- Singh V, Smith WS, Lawton MT, et al. **Risk factors for hemorrhagic presentation in patients with dural arteriovenous fistulae.** *Neurosurgery* 2008;62:628–35; discussion 628–35
- Brown RD Jr, Flemming KD, Meyer FB, et al. **Natural history, evaluation, and management of intracranial vascular malformations.** *Mayo Clin Proc* 2005;80:269–81
- van Dijk JM, terBrugge KG, Willinsky RA, et al. **Clinical course of cranial dural arteriovenous fistulas with long-term persistent cortical venous reflux.** *Stroke* 2002;33:1233–36
- Willinsky R, Goyal M, terBrugge K, et al. **Tortuous, engorged pial veins in intracranial dural arteriovenous fistulas: correlations with presentation, location, and MR findings in 122 patients.** *AJNR Am J Neuroradiol* 1999;20:1031–36
- Ahmed RM, Wilkinson M, Parker GD, et al. **Transverse sinus stenting for idiopathic intracranial hypertension: a review of 52 patients and of model predictions.** *AJNR Am J Neuroradiol* 2011;32:1408–14
- Chimowitz MI, Little JR, Awad IA, et al. **Intracranial hypertension associated with unruptured cerebral arteriovenous malformations.** *Ann Neurol* 1990;27:474–79
- Little JR, Tomsak RL, Ebrahim ZY, et al. **Retinal artery pressure and cerebral artery perfusion pressure in cerebrovascular occlusive disease.** *Neurosurgery* 1986;18:716–20
- Miyasaka Y, Kurata A, Tokiwa K, et al. **Draining vein pressure increases and hemorrhage in patients with arteriovenous malformation.** *Stroke* 1994;25:504–07
- Söderman M, Pavic L, Edner G, et al. **Natural history of dural arteriovenous shunts.** *Stroke* 2008;39:1735–39
- van Dijk JM, Terbrugge KG, Willinsky RA, et al. **The natural history of dural arteriovenous shunts: the Toronto experience.** *Stroke* 2009;40:e412; author reply e413–14
- Kim DJ, terBrugge K, Krings T, et al. **Spontaneous angiographic conversion of intracranial dural arteriovenous shunt: long-term follow-up in nontreated patients.** *Stroke* 2010;41:1489–94
- Hu YC, Newman CB, Dashti SR, et al. **Cranial dural arteriovenous fistula: transarterial Onyx embolization experience and technical nuances.** *J Neurointerv Surg* 2011;3:5–13
- Shi ZS, Ziegler J, Feng L, et al. **Middle cranial fossa sphenoidal region**

- dural arteriovenous fistulas: anatomic and treatment considerations.** *AJNR Am J Neuroradiol* 2013;34:373–80
30. Barnwell SL, Halbach VV, Higashida RT, et al. **Complex dural arteriovenous fistulas. Results of combined endovascular and neurosurgical treatment in 16 patients.** *J Neurosurg* 1989;71:352–58
 31. Baltasvias G, Valavanis A. **Endovascular treatment of 170 consecutive cranial dural arteriovenous fistulae: results and complications.** *Neurosurg Rev* 2014;37:63–71
 32. Barnwell SL, Halbach VV, Dowd CF, et al. **Multiple dural arteriovenous fistulas of the cranium and spine.** *AJNR Am J Neuroradiol* 1991;12:441–45
 33. Bai Y, He C, Zhang H, et al. **De novo multiple dural arteriovenous fistulas and arteriovenous malformation after embolization of cerebral arteriovenous fistula: case report.** *Childs Nerv Syst* 2012;28:1981–83
 34. Paramasivam S, Toma N, Niimi Y, et al. **De novo development of dural arteriovenous fistula after endovascular embolization of pial arteriovenous fistula.** *J Neurointerv Surg* 2013;5:321–26
 35. Gupta R, Horowitz M, Tayal A, et al. **De novo development of a remote arteriovenous fistula following transarterial embolization of a carotid cavernous fistula: case report and review of the literature.** *AJNR Am J Neuroradiol* 2005;26:2587–90
 36. Awad IA, Little JR, Akarawi WP, et al. **Intracranial dural arteriovenous malformations: factors predisposing to an aggressive neurological course.** *J Neurosurg* 1990;72:839–50
 37. Davies MA, TerBrugge K, Willinsky R, et al. **The validity of classification for the clinical presentation of intracranial dural arteriovenous fistulas.** *J Neurosurg* 1996;85:830–37
 38. Davies MA, Ter Brugge K, Willinsky R, et al. **The natural history and management of intracranial dural arteriovenous fistulae. Part 2: aggressive lesions.** *Interv Neuroradiol* 1997;3:303–11
 39. Brown RD Jr, Wiebers DO, Nichols DA. **Intracranial dural arteriovenous fistulae: angiographic predictors of intracranial hemorrhage and clinical outcome in nonsurgical patients.** *J Neurosurg* 1994;81:531–38
 40. Strom RG, Botros JA, Refai D, et al. **Cranial dural arteriovenous fistulae: asymptomatic cortical venous drainage portends less aggressive clinical course.** *Neurosurgery* 2009;64:241–47; discussion 247–48
 41. Terada T, Higashida RT, Halbach VV, et al. **Development of acquired arteriovenous fistulas in rats due to venous hypertension.** *J Neurosurg* 1994;80:884–89
 42. Lawton MT, Jacobowitz R, Spetzler RF. **Redefined role of angiogenesis in the pathogenesis of dural arteriovenous malformations.** *J Neurosurg* 1997;87:267–74
 43. van Dijk JM, TerBrugge KG, Van der Meer FJ, et al. **Thrombophilic factors and the formation of dural arteriovenous fistulas.** *J Neurosurg* 2007;107:56–59
 44. Desal HA, Lee SK, Kim BS, et al. **Multiple de novo vascular malformations in relation to diffuse venous occlusive disease: a case report.** *Neuroradiology* 2005;47:38–42
 45. Kincaid PK, Duckwiler GR, Gobin YP, et al. **Dural arteriovenous fistula in children: endovascular treatment and outcomes in seven cases.** *AJNR Am J Neuroradiol* 2001;22:1217–25

Additional Value of Intra-Aneurysmal Hemodynamics in Discriminating Ruptured versus Unruptured Intracranial Aneurysms

J.J. Schneiders, H.A. Marquering, P. van Ooij, R. van den Berg, A.J. Nederveen, D. Verbaan, W.P. Vandertop, M. Pourquie, G.J.E. Rinkel, E. vanBavel, and C.B.L.M. Majoie



ABSTRACT

BACKGROUND AND PURPOSE: Hemodynamics are thought to play an important role in the rupture of intracranial aneurysms. We tested whether hemodynamics, determined from computational fluid dynamics models, have additional value in discriminating ruptured and unruptured aneurysms. Such discriminative power could provide better prediction models for rupture.

MATERIALS AND METHODS: A cross-sectional study was performed on patients eligible for endovascular treatment, including 55 ruptured and 62 unruptured aneurysms. Association with rupture status was tested for location, aneurysm type, and 4 geometric and 10 hemodynamic parameters. Patient-specific spatiotemporal velocities measured with phase-contrast MR imaging were used as inflow conditions for computational fluid dynamics. To assess the additional value of hemodynamic parameters, we performed 1 univariate and 2 multivariate analyses: 1 traditional model including only location and geometry and 1 advanced model that included patient-specific hemodynamic parameters.

RESULTS: In the univariate analysis, high-risk locations (anterior cerebral arteries, posterior communicating artery, and posterior circulation), daughter sacs, unstable inflow jets, impingements at the aneurysm body, and unstable complex flow patterns were significantly present more often in ruptured aneurysms. In both multivariate analyses, only the high-risk location (OR, 3.92; 95% CI, 1.77–8.68) and the presence of daughter sacs (OR, 2.79; 95% CI, 1.25–6.25) remained as significant independent determinants.

CONCLUSIONS: In this study population of patients eligible for endovascular treatment, we found no independent additional value of aneurysmal hemodynamics in discriminating rupture status, despite high univariate associations. Only traditional parameters (high-risk location and the presence of daughter sacs) were independently associated with ruptured aneurysms.

ABBREVIATIONS: CFD = computational fluid dynamics; 3DRA = 3D rotational angiography; PC = phase-contrast

The prevalence of intracranial aneurysms in the general population is approximately 1%–5%.^{1,2} Although most aneurysms remain asymptomatic, a minority rupture, and this scenario is associ-

ated with high morbidity and case fatality rates.² For unruptured aneurysms, the risk of treatment complications has to be carefully balanced against the future risk of rupture. At present, risk assessment of unruptured intracranial aneurysms and the decision to treat or observe are mainly based on patient age, family history, aneurysm size, and location.^{3–5} However, the predictive value of these characteristics is limited. For example, most ruptured aneurysms are smaller than the recommended minimum of 7 mm for treatment.⁶

Several researchers have attempted to better stratify rupture risk by assessments of the associations between local hemodynamic features and aneurysm formation, growth, and rupture by using computational fluid dynamics (CFD).^{7–10} In general, due to the difficulty of obtaining patient-specific velocity measurements, assumptions are made for the inflow boundary conditions. However, several studies have shown a large interpatient variation of intracranial artery flow.^{11,12}

The purpose of this study was to test whether estimation of local hemodynamics has additional value in discriminating ruptured and unruptured aneurysms. Thus, high-resolution 3D

Received September 10, 2014; accepted after revision March 3, 2015.

From the Departments of Radiology (J.J.S., H.A.M., P.v.O., R.v.d.B., A.J.N., C.B.L.M.M.), Biomedical Engineering and Physics (H.A.M., E.V.), and Neurosurgery (D.V., W.P.V.), Academic Medical Center, Amsterdam, the Netherlands; Department of Aero- and Hydrodynamics (M.P.), Delft University of Technology, Delft, the Netherlands; and Department of Neurology and Neurosurgery (G.J.E.R.), Rudolf Magnus Institute of Neuroscience, University Medical Centre Utrecht, Utrecht, the Netherlands.

H.A. Marquering and P. van Ooij contributed equally.

This study was supported by a grant from the Foundation Nuts Ohra, Amsterdam, the Netherlands, and the Gratama Foundation, the Netherlands.

Please address correspondence to J.J. Schneiders, MD, PhD, Department of Neuro-radiology, C1-425, Meibergdreef 9, 1105 AZ Amsterdam, the Netherlands; e-mail: jj.schneiders@amc.uva.nl



Indicates article with supplemental on-line tables.



Indicates article with supplemental on-line photo.



Evidence-Based Medicine Level 2.

<http://dx.doi.org/10.3174/ajnr.A4397>

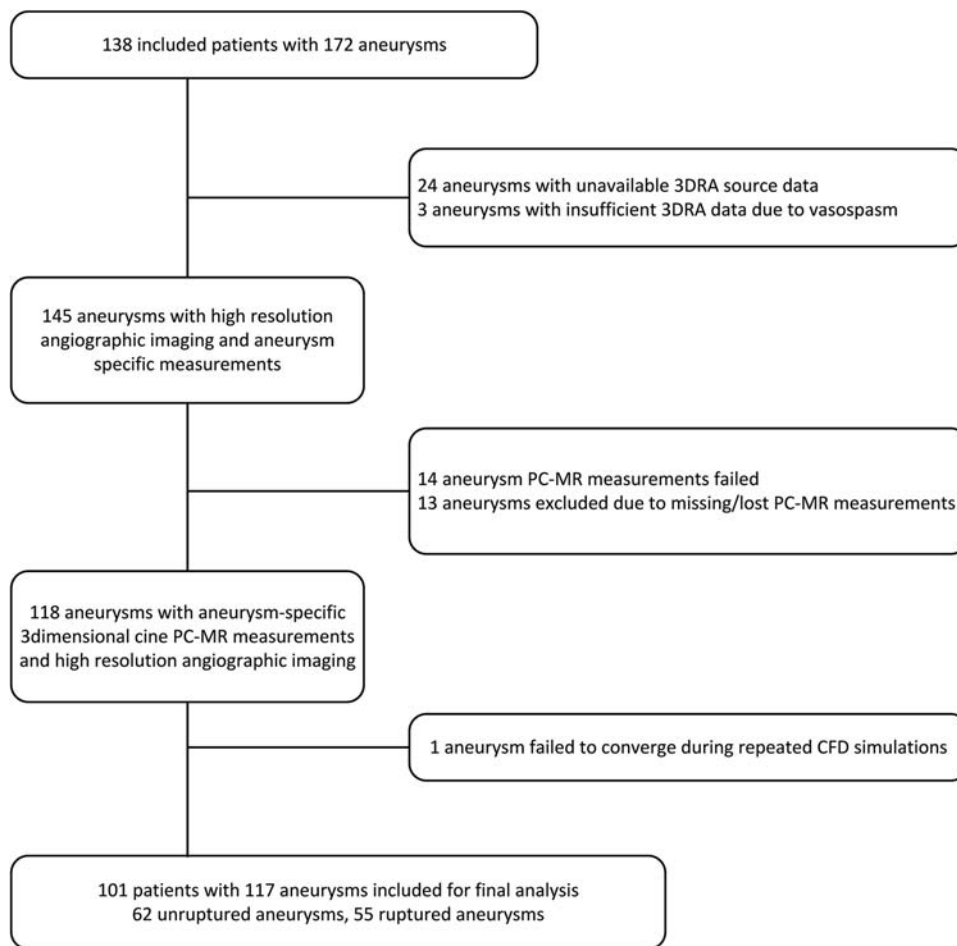


FIG 1. Flow chart of patient and aneurysm inclusion.

geometry and patient-specific measurements of local flow velocities in the afferent artery as boundary conditions for hemodynamic simulations were used.¹³⁻¹⁵

MATERIALS AND METHODS

Patients with intracranial aneurysms were invited to participate in this study by a consulting neurointerventionalist during a visit at the outpatient clinic in our tertiary care referral center from January 2009 to October 2011. Patients with ruptured aneurysms were invited to participate at their first consultation after discharge from the hospital. Patients with unruptured aneurysms were asked to participate during their work-up for aneurysm treatment. Inclusion criteria were the following: aneurysm size of >3 mm, 18–75 years of age, and the ability to give informed consent. Exclusion criteria were contraindications for 3T MR imaging and previous aneurysm clipping. One hundred thirty-eight patients (with 172 aneurysms) agreed to participate. The study was approved by the institutional review board. Written informed consent was obtained from all patients.

We excluded 55 aneurysms (37 patients) for the following reasons: missing 3D rotational angiography (3DRA) source data ($n = 24$); insufficient quality of 3DRA due to vasospasm ($n = 3$); missing ($n = 13$) or failed ($n = 14$) phase-contrast MR imaging (PC-MR imaging) measurements due to inaccurate cardiac gating; or failed CFD simulation ($n = 1$) (Fig 1).

The location of the ruptured or unruptured aneurysms was determined (Table). Because aneurysms located at the anterior cerebral arteries (anterior communicating artery, anterior cerebral artery, pericallosal artery), posterior communicating artery, and in the posterior circulation (basilar artery, vertebral artery, cerebellar arteries) are associated with a higher risk of rupture,⁴ dichotomization was performed by grouping these high-risk locations and comparing them with the other, lower risk locations.

In patients with multiple aneurysms with 1 rupture (6 patients), 2 experienced neuroradiologists (C.B.L.M.M., R.v.d.B., both with >10 years of experience) inspected all clinical and radiologic data in consensus to select the most likely source of hemorrhage. The other aneurysms were classified as unruptured.

Imaging Protocols

Acquisition of 3DRA was part of the standard clinical work-up. Images were acquired with either local (patients with unruptured aneurysms) or general anesthesia (during endovascular treatment in patients with ruptured aneurysms) by using a single-plane angiographic unit (Integris Allura Neuro; Philips Healthcare, Best, the Netherlands) following institutional protocol. 3DRA was acquired during a 6-second run, with 21 mL of contrast (iodixanol, Visipaque; GE Healthcare, Piscataway, New Jersey), which was administered at 3 mL/s, resulting in a 256^3 isotropic image volume. The 3DRA was started 3 seconds after contrast injection.

Location, aneurysm type, and rupture status of 117 aneurysms (101 patients)

Location ^a	No. of Cases	Total (n = 117)		Bifurcation (n = 90)		Sidewall (n = 27)	
		Unruptured	Ruptured	Unruptured	Ruptured	Unruptured	Ruptured
High-risk location							
PcomA	12 (10%)	4	8	3	3	1	5
BA	11 (9%)	8	3	8	2	0	1
VA	1 (1%)	0	1	0	0	0	1
ACA	8 (7%)	3	5	2	5	1	0
AcomA	28 (24%)	7	21	7	20	0	1
Subtotal	60 (51%)	22	38	20	30	2	8
Low-risk location							
MCA	36 (31%)	27	9	23	9	4	0
ICA	21 (18%)	13	8	3	5	10	3
Subtotal	57 (49%)	40	17	26	14	14	3
Total	117 (100%)	62	55	46	44	16	11

Note:—AcomA indicates anterior communicating artery; PcomA, posterior communicating artery; VA, vertebral artery.

^a ICA includes the internal carotid, ophthalmic, anterior choroidal arteries and the carotid tip; ACA includes the anterior cerebral and pericallosal arteries; BA includes the basilar, PICA, and superior cerebellar arteries.

MR imaging was performed at 3T (Intera; Philips Healthcare) and included a multiple overlapping thin-slab-acquisition 3D TOF MRA sequence and a 3D PC-MR imaging sequence with heart rate monitoring by electrocardiography or by a Peripheral Pulse Unit (Siemens, Erlangen, Germany) for velocity measurements in the afferent artery proximal to the aneurysm. The multiple overlapping thin-slab-acquisition 3D TOF had a scan resolution of $0.39 \times 0.6 \times 1$ mm. Other parameters were the following: TE/TR/flip angle, 4.2/21.4 ms/20°; parallel imaging factor, 2.5; scanning time, 6 minutes and 16 seconds.

3D PC-MR imaging (time-resolved measurement of velocity in 3 directions in a single plane perpendicular to the artery) was performed with a resolution of $0.64 \times 0.65 \times 3$ mm; TE/TR/flip angle, 5.7/8.5 ms/10°; receiver bandwidth, 172 kHz; parallel imaging factor, 2. Velocity-encoding was 100 cm/s and could be adjusted to 70 cm/s if needed. The velocity information was acquired in 23–36 cardiac phases. We ensured that the location of the 3D PC-MR imaging measurement was distal to any proximal branching artery (>1 mm) to obtain the most accurate velocity and flow information.

Patients with unruptured aneurysms were asked to undergo an additional PC-MR imaging study before endovascular treatment. In patients with ruptured aneurysms who were treated in an acute setting, it was not possible to perform PC-MR imaging velocity measurements before intervention, and these data were obtained at follow-up 6 months after coiling. All unruptured aneurysms were compared with previous imaging to detect possible geometric changes during the time interval of 3DRA and MR imaging. Postprocessing of the MR images was described in detail previously (On-line Fig).¹⁶

Vascular Models and Vascular Model Correction

A level set algorithm was used to segment the vascular tree in 3DRA image data.¹⁷ The segmentations were converted into a tetrahedral element mesh with >1,000,000 tetrahedral elements (± 3000 elements \times mm⁻³). Neck size overestimation was reviewed by 2 neuroradiologists, by comparing the segmentations with those in 2D DSA. Twenty-six of 117 aneurysm segmentations showed neck size overestimation and required modification according to a previously described method.¹⁸

Hemodynamic Modeling and Visualization

Fluent 6.3 (ANSYS, Canonsburg, Pennsylvania) was used to simulate hemodynamics. In-house-developed software was used to impose PC-MR imaging-measured spatiotemporal velocity profiles as inflow boundary conditions.¹⁶ In case of anterior communicating artery aneurysms, DSA images were reviewed by 2 neuroradiologists to determine the afferent artery. None of the anterior communicating artery aneurysms filled from both A1s.

The outflow ratio of the distal arteries was calculated by using the Murray law. A no-slip boundary was set at the vessel wall, and rigid walls were assumed.¹⁹ Density and dynamic viscosity were, respectively, $1060 \text{ kg} \times \text{m}^{-3}$ and $0.004 \text{ kg} \times \text{m}^{-1} \times \text{s}^{-1}$. Three complete cardiac cycles were calculated; the third cycle was used for analysis. The flow patterns resulting from the CFD simulations were visualized with streamlines and isosurfaces as movie clips by using Paraview 3.6 (Kitware; Los Alamos National Laboratory and Sandia National Laboratories, Los Alamos, New Mexico) (Fig 2).

Quantitative Parameter Assessment

The following geometric aneurysm parameters were determined from the 3D models by a research physician (J.J.S.): size (largest diameter in millimeters),²⁰ aspect ratio (height divided by the neck size),²¹ and spheric or nonspheric nature of the aneurysm (“spheric” defined as an aneurysm height within 80%–125% of its width).²⁰ Quantitative hemodynamic parameters (mean wall shear stress, maximum wall shear stress, and oscillatory shear index) were derived from the hemodynamic data provided by CFD by using in-house-developed software. The quantitative hemodynamic parameters were derived from the surface of the aneurysm sac. Time-dependent indices (oscillatory shear index) were calculated with a time-averaged method by using all the cardiac phases available.

Qualitative Parameter Assessment

Qualitative parameters were assessed by 2 interventional neuroradiologists (C.B.L.M.M., R.v.d.B.). Qualitative geometric parameters were assessed from the 3D model and included aneurysm type (sidewall or bifurcation) and the presence or absence of

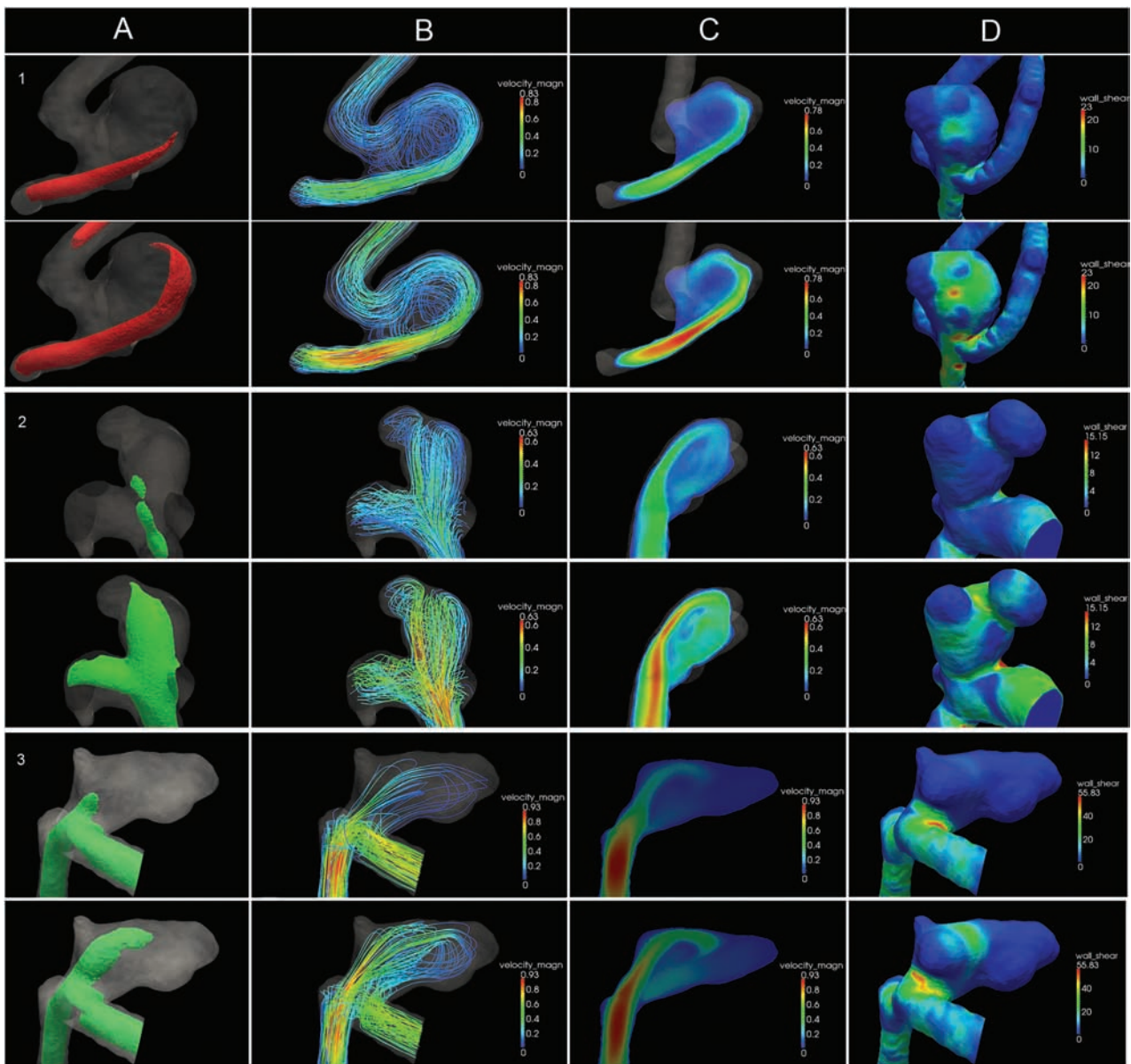


FIG 2. Intra-aneurysmal hemodynamics in 3 typical aneurysms. Diastole is depicted in the top row; systole, in the bottom row. The columns represent: A, Isosurface of the velocity. B, 3D streamlines colored by velocity magnitude. C, 2D slice of the velocity magnitude. D, Wall shear stress distribution displayed on 3D geometry. The rows represent cases 1–3. Case 1: Ruptured anterior communicating artery aneurysm with a concentrated inflow jet (A and C) and a stable-simple flow pattern: single vortex that is stable throughout the cardiac cycle (B). The impingement zone is located at the body (D). Case 2: Unruptured posterior communicating artery aneurysm with a concentrated inflow jet (A and C) and a stable-complex flow pattern: multiple flow structures that remain stable throughout the cardiac cycle (B). The impingement zone is located at the dome (D) and 2 daughter sacs (D). Case 3: Ruptured anterior communicating artery aneurysm with a concentrated inflow jet (A and C) and an unstable-simple flow pattern: a single flow structure that is unstable throughout the cardiac cycle. The primary direction of flow is different between systole and diastole (B). The impingement zone is located at the neck (D) and 2 daughter sacs (D).

daughter sacs. An aneurysm was classified as a sidewall aneurysm when it originated from a major vessel trunk with either no or a very small side branch (with a diameter of less than one-fifth of the parent vessel).¹⁰ All other aneurysms were classified as bifurcation aneurysms.

Qualitative hemodynamic parameters were assessed from movie clips and included the number of inflow jets (single or multiple), inflow jet concentration (concentrated or diffuse), inflow jet stability (stable or unstable), vortex complexity (simple or complex), vortex stability (stable or unstable) flow pattern category according to Cerebral et al,⁹ and location of the impingement zone.

The inflow jet was considered unstable if its main direction changed throughout the cardiac cycle. The inflow jet was considered concentrated if the inflow width was less than half the aneurysm neck. Vortices were assessed for complexity (simple/complex) and stability (stable/unstable). Vortices were considered complex if there was >1 major flow structure; they were categorized as unstable when ≥ 1 flow structure disappeared during a cardiac cycle. The stability and complexity of intra-aneurysmal flow were classified by assigning 1 of the following 4 flow types: 1) stable-simple: stable direction of the inflow jet with a single associated vortex, 2) stable-complex: stable direction of the inflow jet

with multiple associated vortices and no change in the number of vortices during the cardiac cycle, 3) unstable-simple: changing direction of inflow jet with the creation of a single vortex, and 4) unstable-complex: changing direction of the inflow jet associated with the creation or destruction of multiple vortices.⁹

Images of the wall shear stress magnitude were used to categorize the location of the impingement zone as neck, body, dome, or in a daughter sac.¹⁹ The “impingement zone” was defined as the area on the aneurysm sac where the inflow jet deflects.

Statistical Analysis

The Shapiro-Wilk test was used to assess the normality of the distribution of continuous variables (normally distributed if the *W* statistic was >0.9). The normally distributed variable (size) was expressed as mean with SD, whereas not normally distributed variables were presented as medians with interquartile ranges (interquartile range, 25%–75%).

To evaluate the relation between determinants and rupture status, we performed univariate and multivariate analyses by using logistic regression analysis. Variables that were significantly associated with rupture status in the univariate analysis were included in the multivariate analysis by using manual backward variable selection. To test for multicollinearity, we calculated the variance inflation factor. We generated 2 multivariate models: a “traditional” model including only the location and geometric determinants, and an advanced model including location and geometric and hemodynamic determinants. Interobserver agreement of all parameters was assessed by calculation of the intraclass correlation coefficient and the percentage of agreement. A *P* value < .05 was considered statistically significant in all analyses. All analyses were performed by using the SPSS, Version 20.0 (IBM, Armonk, New York).

RESULTS

In the analysis, 101 patients (63 women; mean age, 54.8 years) with 117 aneurysms (62 unruptured, 55 ruptured) were included (Fig 1). The distribution of aneurysm locations is depicted in the Table. The unruptured aneurysms had a mean size of 7.4 ± 3.7 mm; the ruptured aneurysms, 6.6 ± 2.8 mm (On-line Table 1). Eleven of the included patients had multiple aneurysms: 7 patients with 2 aneurysms, 3 with 3 aneurysms, and 1 with 4 aneurysms. Multiple aneurysms per patient were included if specific PC-MR imaging measurements were available for each aneurysm. None of the unruptured aneurysms showed geometric changes during the interval between 3DRA and MR imaging.

The univariate associations with aneurysm rupture status are depicted in On-line Table 1. There was no indication of severe multicollinearity. The interobserver agreement for qualitatively scored hemodynamic parameters is displayed in On-line Table 2. Aneurysms located at high-risk locations were more often associated with rupture compared with the aneurysms at other locations (OR, 4.06; 95% CI, 1.88–8.81). The only geometric parameter that was significantly associated with rupture status was the presence of a daughter sac (OR, 2.93; 95% CI, 1.37–6.29). Regarding the hemodynamic parameters, unstable inflow jet (OR, 13.56; 95% CI, 1.67–110), impingement zone location at the aneurysm body (OR, 2.49; 95% CI, 1.00–6.19), and complex vortices (OR,

2.34; 95% CI, 1.11–4.96) were significantly associated with ruptured aneurysms. In addition, an unstable-complex flow pattern was present significantly more often in ruptured aneurysms (OR, 2.59; 95% CI, 1.05–6.37) compared with a stable-simple flow pattern. The presence of stable-complex and unstable-simple flow patterns was not different in ruptured and unruptured aneurysms.

In the traditional multivariate model, both high-risk location (OR, 3.92; 95% CI, 1.77–8.68) and the presence of daughter sacs (OR, 2.79; 95% CI, 1.25–6.25) were independently associated with ruptured aneurysms (Nagelkerke *R*² of 0.21; area under the curve, 0.72; 95% CI, 0.63–0.82). The advanced multivariate model added (univariate significant) hemodynamic parameters: unstable inflow jet, vortex complexity, flow-pattern category, and location of the impingement zone. In this advanced model, high-risk location and the presence of daughter sacs were independently associated with ruptured aneurysms (OR values equal to the traditional model), resulting in exactly the same area under the curve (area under the curve, 0.72; 95% CI, 0.63–0.82; Nagelkerke *R*² of 0.21). Thus, hemodynamic parameters did not improve the traditional multivariate model.

DISCUSSION

In this study, which compared geometric and hemodynamic parameters in 117 aneurysms, no additional value of aneurysmal hemodynamics for the characterization of ruptured-versus-unruptured aneurysms was found. Rather, only the presence of daughter sacs and location at the anterior cerebral arteries, posterior communicating artery, or posterior circulation significantly characterized ruptured aneurysms, and this was the case for multivariate models with or without inclusion of hemodynamics.

Various hemodynamic aspects of aneurysms have been implicated as potential predictors of the risk of rupture, such as disturbed flow patterns, small impingement regions, narrow jets, wall shear stress, and oscillatory shear index.^{9,10,22} In addition, these complex and unstable flow patterns have been correlated with a clinical history of prior aneurysm rupture.⁸ This study does not address the causality of hemodynamics and aneurysm rupture and does not allow any statements considering causality. While univariate analyses in the current work and previous studies clearly argue for hemodynamic data as discriminators and candidate predictors for rupture, our multivariate models do not show additional value when we account for geometric data.

The independent association of location at the anterior cerebral arteries, posterior communicating artery, and posterior circulation with rupture is in accordance with a recently published pooled analysis based on 6 prospective studies with 8382 patients with unruptured aneurysms.⁴ That analysis, however, did not include hemodynamic parameters. Despite the evidence, several studies on hemodynamic risk factors for aneurysm rupture did not include location as a determinant in their analyses.^{8,10} A post hoc analysis of the findings of Xiang et al¹⁰ indicates that also in that study, location at the anterior cerebral arteries, posterior communicating artery, and posterior circulation is positively associated with rupture, with 84% in the ruptured group, as opposed to 33% in the unruptured group. It is not clear whether the

shear parameters would remain significantly involved if location had been included in their model.

Daughter sacs were present significantly more often in ruptured aneurysms compared with unruptured aneurysms. The importance of aneurysm shape for the risk profile has previously been acknowledged in a study comparing ruptured and unruptured cerebral aneurysms, in which 10% of unruptured aneurysms showed a multilobular appearance on DSA compared with 20% of ruptured aneurysms.²³ In the Unruptured Cerebral Aneurysm Study of Japan, daughter sacs were also associated with an increased rupture rate.²⁴ Aneurysm geometry and the presence of daughter sacs may change before, during, or after rupture. Two studies on 13 and 9 patients before and after rupture showed that indeed geometry after rupture may be different due to growth and displacements by hematoma.^{25,26} While rupture might have affected the percentage of aneurysms with visible daughter sacs, the Unruptured Cerebral Aneurysm Study of Japan underlines the view that the significant association in our study with ruptured aneurysms is not merely a consequence of rupture.

Aneurysm size did not significantly contribute to characterization of the rupture state, while it is a proved risk factor for aneurysm rupture in longitudinal follow-up studies.^{3,5,24} The reason for this finding is that in patients with ruptured aneurysms, 3DRA was routinely performed in the standard work-up protocol in all aneurysms regardless of size. However, patients with unruptured aneurysms were only scheduled for treatment when aneurysm size was >7 mm or when aneurysm growth was seen during follow-up. Unruptured MCA aneurysms were over-represented in our study compared with the patient population of the institution, though this number was comparable with that in a study by Morita et al.²⁴ This difference might have been related to the more frequent application of 3DRA imaging in relation to decisions for treatment.

In a recent study of Baharoglu et al,²⁷ rupture risk factors were assessed for sidewall and bifurcation aneurysms separately. This approach is promising for dealing with multicollinearity. The design and number of included patients in this study did not allow us to also compare all variables against these 2 aneurysm types.

Patient-specific inflow patterns for CFD, based on PC-MR imaging, were not always obtained within a short interval of 3DRA. Patients with unruptured aneurysms were asked to participate right before or after 3DRA, either in the pretherapeutic work-up or during an elective coiling procedure. Patients with a recent 3DRA (<1 year) were asked to participate during regular checkups at the outpatient clinic. For ruptured aneurysms, PC-MR imaging was performed 6 months after treatment. We do not believe that these timing differences biased the estimation of hemodynamic patterns. Cebral et al¹⁹ indicated that for variation of inflow within a ~25% range, calculated flow patterns remain unchanged. In the absence of major events such as rupture or stroke, no such variation is expected.

Data on flow changes after coiling are sparse. However, in a pilot study, we found that flow changes in inlet and outlet vessels before and after coiling are within this 25% range. These results, therefore, allow the PC-MR imaging flow measurements performed 6 months after coiling to serve as a boundary condition for CFD simulating pretreatment hemodynamics.

Several assumptions for the CFD simulations had to be made, including traction-free boundary conditions, rigid walls, and outlet boundary conditions. However, these assumptions are believed to have relatively limited influence on the predicted flow patterns.²⁸ The influence of mesh resolution is reported in an article by Valen-Sendstad and Steinman,²⁹ in which they have shown that lower resolution meshes can result in different oscillatory shear index values as opposed to higher resolution models. Not using the very-high-resolution models may have disguised the associations between oscillatory shear index and rupture status; however, this issue was beyond the scope of this study.

A limitation of this study is the absence of other established clinical risk factors for rupture, including multiple aneurysms,³⁰ a history of previous SAH,³¹ hypertension,⁴ female sex,⁵ and descent.⁵ Including such factors was not possible because it would have affected the power of tests for the hemodynamic parameters. It remains to be established whether such clinical factors interact with hemodynamics in risk prediction.

We reported the interobserver agreement for the classifications of our experts before consensus was reached. The agreement of the variables flow concentration, inflow stability, and flow complexity is, on average, 85%, compared with 99% in a previous study.⁸ The lower agreement and relatively low intraclass correlation coefficient for most variables may reduce the discriminating power of the analysis. Therefore, in the final analysis, we used the consensus of the 2 observers for all scored variables.

The current cross-sectional design does not allow straightforward estimation of rupture risk from the included parameters. For example, unruptured aneurysms included in this study may still have a high risk for future rupture, and this study cannot discriminate between aneurysms that have not yet ruptured and those that will never rupture.

The lack of additional value of hemodynamic parameters raises the question of whether and how such hemodynamics could be part of risk of rupture models. Larger longitudinal studies will provide more insight than could possibly be generated in the current cross-sectional design.

CONCLUSIONS

In this study population of patients eligible for endovascular treatment, we found no independent additional value of aneurysmal hemodynamics in discriminating rupture status, despite high univariate associations. Only traditional parameters (high-risk location and the presence of daughter sacs) were independently associated with ruptured aneurysms.

Disclosures: Ed vanBavel—UNRELATED: Grants/Grants Pending: Marie Curie Program of the European Union.* Charles B.L.M. Majoie—RELATED: Grant: Nuts Ohra Foundation,* Comments: SNO-T-0702-92; a research grant to evaluate the additional value of hemodynamics on the rupture risk assessment in intracranial aneurysms.* Gratama Foundation*; UNRELATED: Grants/Grants Pending: Dutch Heart Foundation*; Payment for Lectures (including service on Speakers Bureaus); Stryker.* *Money paid to the institution.

REFERENCES

1. Rinkel GJ, Djibuti M, Algra A, et al. **Prevalence and risk of rupture of intracranial aneurysms: a systematic review.** *Stroke* 1998;29:251–56
2. Brisman JL, Song JK, Newell DW. **Cerebral aneurysms.** *N Engl J Med* 2006;355:928–39

3. Wiebers DO, Whisnant JP, Huston J 3rd, et al; International Study of Unruptured Intracranial Aneurysms Investigators. **Unruptured intracranial aneurysms: natural history, clinical outcome, and risks of surgical and endovascular treatment.** *Lancet* 2003;362:103–10
4. Greving JP, Wermer MJ, Brown RD Jr, et al. **Development of the PHASES score for prediction of risk of rupture of intracranial aneurysms: a pooled analysis of six prospective cohort studies.** *Lancet Neurol* 2014;13:59–66
5. Wermer MJ, van der Schaaf IC, Algra A, et al. **Risk of rupture of unruptured intracranial aneurysms in relation to patient and aneurysm characteristics: an updated meta-analysis.** *Stroke* 2007;38:1404–10
6. Forget TR Jr, Benitez R, Veznedaroglu E, et al. **A review of size and location of ruptured intracranial aneurysms.** *Neurosurgery* 2001;49:1322–25; discussion 1325–26
7. Miura Y, Ishida F, Umeda Y, et al. **Low wall shear stress is independently associated with the rupture status of middle cerebral artery aneurysms.** *Stroke* 2013;44:519–21
8. Cebral JR, Mut F, Weir J, et al. **Association of hemodynamic characteristics and cerebral aneurysm rupture.** *AJNR Am J Neuroradiol* 2011;32:264–70
9. Cebral JR, Castro MA, Burgess JE, et al. **Characterization of cerebral aneurysms for assessing risk of rupture by using patient-specific computational hemodynamics models.** *AJNR Am J Neuroradiol* 2005;26:2550–59
10. Xiang J, Natarajan SK, Tremmel M, et al. **Hemodynamic-morphologic discriminants for intracranial aneurysm rupture.** *Stroke* 2011;42:144–52
11. Schneiders JJ, Ferns SP, van Ooij P, et al. **Comparison of phase-contrast MR imaging and endovascular sonography for intracranial blood flow velocity measurements.** *AJNR Am J Neuroradiol* 2012;33:1786–90
12. Radaelli AG, Augsburger L, Cebral JR, et al. **Reproducibility of haemodynamical simulations in a subject-specific stented aneurysm model: a report on the Virtual Intracranial Stenting Challenge 2007.** *J Biomech* 2008;41:2069–81
13. Venugopal P, Valentino D, Schmitt H, et al. **Sensitivity of patient-specific numerical simulation of cerebral aneurysm hemodynamics to inflow boundary conditions.** *J Neurosurg* 2007;106:1051–60
14. Marzo A, Singh P, Larrabide I, et al. **Computational hemodynamics in cerebral aneurysms: the effects of modeled versus measured boundary conditions.** *Ann Biomed Eng* 2011;39:884–96
15. Jansen IG, Schneiders JJ, Potters WV, et al. **Generalized versus patient-specific inflow boundary conditions in computational fluid dynamics simulations of cerebral aneurysmal hemodynamics.** *AJNR Am J Neuroradiol* 2014;35:1543–48
16. van Ooij P, Schneiders JJ, Marquering HA, et al. **3D cine phase-contrast MRI at 3T in intracranial aneurysms compared with patient-specific computational fluid dynamics.** *AJNR Am J Neuroradiol* 2013;34:1785–91
17. Piccinelli M, Veneziani A, Steinman DA, et al. **A framework for geometric analysis of vascular structures: application to cerebral aneurysms.** *IEEE Trans Med Imaging* 2009;28:1141–55
18. Schneiders JJ, Marquering HA, Antiga L, et al. **Intracranial aneurysm neck size overestimation with 3D rotational angiography: the impact on intra-aneurysmal hemodynamics simulated with computational fluid dynamics.** *AJNR Am J Neuroradiol* 2013;34:121–28
19. Cebral JR, Castro MA, Appanaboyina S, et al. **Efficient pipeline for image-based patient-specific analysis of cerebral aneurysm hemodynamics: technique and sensitivity.** *IEEE Trans Med Imaging* 2005;24:457–67
20. de Rooij NK, Velthuis BK, Algra A, et al. **Configuration of the circle of Willis, direction of flow, and shape of the aneurysm as risk factors for rupture of intracranial aneurysms.** *J Neurol* 2009;256:45–50
21. Dhar S, Tremmel M, Mocco J, et al. **Morphology parameters for intracranial aneurysm rupture risk assessment.** *Neurosurgery* 2008;63:185–96; discussion 196–97
22. Cebral JR, Raschi M. **Suggested connections between risk factors of intracranial aneurysms: a review.** *Ann Biomed Eng* 2013;41:1366–83
23. Beck J, Rohde S, el Beltagy M, et al. **Difference in configuration of ruptured and unruptured intracranial aneurysms determined by biplanar digital subtraction angiography.** *Acta Neurochir (Wien)* 2003;145:861–65
24. Morita A, Kirino T, Hashi K, et al; UCAS Japan Investigators. **The natural course of unruptured cerebral aneurysms in a Japanese cohort.** *N Engl J Med* 2012;366:2474–82
25. Schneiders JJ, Marquering HA, van den Berg R, et al. **Rupture-associated changes of cerebral aneurysm geometry: high-resolution 3D imaging before and after rupture.** *AJNR Am J Neuroradiol* 2014;35:1358–62
26. Rahman M, Ogilvy CS, Zipfel GJ, et al. **Unruptured cerebral aneurysms do not shrink when they rupture: multicenter collaborative aneurysm study group.** *Neurosurgery* 2011;68:155–60; discussion 160–61
27. Baharoglu MI, Lauric A, Gao BL, et al. **Identification of a dichotomy in morphological predictors of rupture status between sidewall- and bifurcation-type intracranial aneurysms.** *J Neurosurg* 2012;116:871–81
28. Dempere-Marco L, Oubel E, Castro M, et al. **CFD analysis incorporating the influence of wall motion: application to intracranial aneurysms.** *Med Image Comput Comput Assist Interv* 2006;9(pt 2):438–45
29. Valen-Sendstad K, Steinman DA. **Mind the gap: impact of computational fluid dynamics solution strategy on prediction of intracranial aneurysm hemodynamics and rupture status indicators.** *AJNR Am J Neuroradiol* 2014;35:536–43
30. Sonobe M, Yamazaki T, Yonekura M, et al. **Small unruptured intracranial aneurysm verification study: SUAVE study, Japan.** *Stroke* 2010;41:1969–77
31. Ishibashi T, Murayama Y, Urashima M, et al. **Unruptured intracranial aneurysms: incidence of rupture and risk factors.** *Stroke* 2009;40:313–16

Hemodynamic Differences in Intracranial Aneurysms before and after Rupture

B.M.W. Cornelissen, J.J. Schneiders, W.V. Potters, R. van den Berg, B.K. Velthuis, G.J.E. Rinkel, C.H. Slump, E. VanBavel, C.B.L.M. Majoie, and H.A. Marquering



ABSTRACT

BACKGROUND AND PURPOSE: Rupture risk of intracranial aneurysms may depend on hemodynamic characteristics. This has been assessed by comparing hemodynamic data of ruptured and unruptured aneurysms. However, aneurysm geometry may change before, during, or just after rupture; this difference causes potential changes in hemodynamics. We assessed changes in hemodynamics in a series of intracranial aneurysms, by using 3D imaging before and after rupture.

MATERIALS AND METHODS: For 9 aneurysms in 9 patients, we used MRA, CTA, and 3D rotational angiography before and after rupture to generate geometric models of the aneurysm and perianeurysmal vasculature. Intra-aneurysmal hemodynamics were simulated by using computational fluid dynamics. Two neuroradiologists qualitatively assessed flow complexity, flow stability, inflow concentration, and flow impingement in consensus, by using flow-velocity streamlines and wall shear stress distributions.

RESULTS: Hemodynamics changed in 6 of the 9 aneurysms. The median time between imaging before and after rupture was 678 days (range, 14–1461 days) in these 6 cases, compared with 151 days (range, 34–183 days) in the 3 cases with unaltered hemodynamics. Changes were observed for flow complexity ($n = 3$), flow stability ($n = 3$), inflow concentration ($n = 2$), and region of flow impingement ($n = 3$). These changes were in all instances associated with aneurysm displacement due to rupture-related hematomas, growth, or newly formed lobulations.

CONCLUSIONS: Hemodynamic characteristics of intracranial aneurysms can be altered by geometric changes before, during, or just after rupture. Associations of hemodynamic characteristics with aneurysm rupture obtained from case-control studies comparing ruptured with unruptured aneurysms should therefore be interpreted with caution.

ABBREVIATIONS: CFD = computational fluid dynamics; 3DRA = 3D rotational angiography; OSI = oscillatory shear index; WSS = wall shear stress

Intracranial aneurysms are found in 1%–5% of the adult population.^{1,2} For ruptured intracranial aneurysms, case morbidity and fatality rates are high.^{1,3} However, 50%–80% of all intracra-

nial aneurysms do not rupture during an individual's lifetime.¹ More commonly, unruptured aneurysms are incidentally found due to increasing use of imaging.^{4,5} The risk of rupture should be balanced against the risk of treatment when deciding whether an aneurysm should be treated. In clinical practice, the location and size of the aneurysm are the most important parameters for determining the risk of rupture.^{1,6} However, these geometric predictors are insufficient for optimal treatment selection. Therefore, the search for better predictors for rupture continues.^{7–9} Previous studies have associated intra-aneurysmal flow patterns and wall shear stress (WSS) distributions with aneurysm rupture status.^{7,8,10} However, these results are still controversial. For example, both high and low aneurysmal WSS were separately associated with aneurysm growth and rupture.^{11,12} In these risk-assessment studies, potential changes in hemodynamics due to the rupture itself were systematically neglected. Recently, 2 studies have shown changes in aneurysm geometry after rupture.^{13,14} These rupture-associated geometric changes may result in differences in hemodynamic characteristics as well.

Received October 24, 2014; accepted after revision March 3, 2015.

From the MIRA Institute for Biomedical Engineering and Technical Medicine (B.M.W.C., C.H.S.), University of Twente, Enschede, the Netherlands; Departments of Radiology (B.M.W.C., J.J.S., W.V.P., R.v.d.B., C.B.L.M.M., H.A.M.) and Biomedical Engineering and Physics (B.M.W.C., E.V., H.A.M.), Academic Medical Center, Amsterdam, the Netherlands; and Departments of Radiology (B.K.V.) and Neurology and Neurosurgery, Brain Center Rudolf Magnus (G.J.E.R.), University Medical Center Utrecht, Utrecht, the Netherlands.

C.B.L.M. Majoie and H.A. Marquering contributed equally to this work.

This work was supported by a grant from the NUTS-OHRA Foundation (grant no. SNO-T-0702-92) and a grant from the Dutch Technology Foundation STW (CARISMA 11629).

Please address correspondence to B.M.W. Cornelissen, MSc, Meibergdreef 9, 1105 AZ, Amsterdam, the Netherlands; e-mail: b.m.cornelissen@amc.uva.nl

Indicates open access to non-subscribers at www.ajnr.org

Indicates article with supplemental on-line table.

Indicates article with supplemental on-line video.

<http://dx.doi.org/10.3174/ajnr.A4385>

Table 1: Imaging modalities for all 9 patients before and after rupture, with the time between imaging before and after rupture and the days between hemorrhage and imaging after rupture^a

Pt	Imaging Modality before Rupture	Resolution (mm)	Imaging Modality after Rupture	Resolution (mm)	Time between Imaging before and after Rupture	Days between Hemorrhage and Imaging after Rupture
1	3D TOF MRA	0.49 × 0.49 × 1.2	3DRA	0.22 × 0.22 × 0.22	0 yr, 183 days	1
2	3D TOF MRA	0.31 × 0.31 × 1.0	CTA	0.31 × 0.31 × 0.45	0 yr, 72 days	1
3	CTA	0.33 × 0.33 × 1.0	CTA	0.35 × 0.35 × 0.33	2 yr, 323 days	2
4	3D PC MRA	0.78 × 0.78 × 1.0	3DRA	0.25 × 0.25 × 0.25	0 yr, 151 days	0
5	3D TOF MRA	0.45 × 0.45 × 1.0	3DRA	0.39 × 0.39 × 0.39	3 yr, 148 days	0
6	CTA	0.43 × 0.43 × 0.9	3DRA	0.22 × 0.22 × 0.22	0 yr, 34 days	0
7	3D TOF MRA	0.20 × 0.20 × 1.0	3DRA	0.17 × 0.17 × 0.17	4 yr, 1 day	3
8	3D TOF MRA	0.35 × 0.35 × 1.4	3DRA	0.17 × 0.17 × 0.17	0 yr, 14 days	9
9	CTA	0.33 × 0.33 × 1.3	3DRA	0.09 × 0.09 × 0.09	0 yr, 302 days	2

Note:—Pt indicates patient; PC, phase-contrast.

^a Table adapted from Schneiders et al.¹⁴

In this study, we had the opportunity to use high-quality 3D imaging data of 9 patients with intracranial aneurysms, obtained before and after rupture, to assess potential differences in hemodynamic characteristics associated with rupture.

MATERIALS AND METHODS

3D image data of intracranial aneurysms for 9 patients before (MRA [$n = 6$], CTA [$n = 3$]) and after (CTA [$n = 2$], 3D rotational angiography [3DRA, $n = 7$]) rupture were collected. The imaging parameters are shown in Table 1.¹⁴ Clinical data and aneurysmal geometric data are shown in the On-line Table. The image data were collected during 6 years in 3 different institutions. Four male and 5 female patients were included, with aneurysms located at the basilar artery ($n = 3$), posterior communicating artery ($n = 2$), middle cerebral artery ($n = 2$), anterior communicating artery ($n = 1$), and anterior choroidal artery ($n = 1$). The mean age at the time of rupture was 60 ± 12 years. The median time between imaging before and after rupture was 183 days, with a range of 14 days to 4 years 1 day. The median time between rupture and subsequent imaging was 1 day, with a range of 0–9 days. Informed consent was waived by the medical ethics committee because no diagnostic tests other than routine clinical imaging were used in this retrospective study.

Vascular Model Generation

To create a surface model of the aneurysm and perianeurysmal vasculature by using the available 3D imaging data, we used a level set algorithm of the Vascular Modeling Toolkit (<http://www.vmtk.org/>).^{15–18} For hemodynamic simulation, model accuracy and mesh quality are important.^{18–20} Therefore, inaccuracies due to imaging artifacts such as flow dispersion and saturation (in 3D time-of-flight MRA), partial voluming, beam hardening (in CTA), neck size overestimation,²¹ and inhomogeneous contrast agent distribution (in CTA and 3DRA) were corrected. Artificial narrowing results in overestimations of WSS and erroneous flow velocities²² and was, therefore, corrected by inflation by using Blender (<http://www.blender.org/>).²³ Vessel inflation was performed in the proximal arteries in 13 models and in the distal arteries in 12 models. Furthermore, the inflow jet and location of deflection may be sensitive to the segmentation of the neck area. To reduce this dependency, an experienced neuroradiologist (C.B.L.M.M.) carefully inspected the vascular models and corrected them for imaging artifacts. Imaging artifacts were distin-

guished from pathology by using additional DSA imaging. For the purpose of this study, manual corrections of the segmentation were performed by using ITK-SNAP 2.4.0 (www.itksnap.org).²⁴ In addition, the surface models were smoothed by using a built-in Taubin-smoothing algorithm of the Vascular Modeling Toolkit to remove high-frequency noise while preventing the surface models from shrinking.²⁵

Subsequently, all aneurysm models were inspected for apparent differences in visualized anatomy of perianeurysmal arteries before and after rupture. The vascular models agreed for all except 1 case. In case 8, we removed 2 outflow arteries from the ruptured model because in the before-rupture imaging, only 1 outflow artery was visible, while 3 outflow arteries were visible in the after-rupture imaging.

To decrease computational effort, we removed distant vessel branches located approximately 20 times the average radius distal to the aneurysm. Finally, the in- and outlet vessels were cut perpendicular to the vessel. To ensure fully developed flow entering the aneurysm model, we added cylindrical flow extensions, with a length of 12 times the radius of the afferent vessel, to the inlets of the models.^{18,26}

All surface models were converted into tetrahedral meshes by using the Vascular Modeling Toolkit.¹⁸ The element attenuation close to the wall was increased by adding a customized boundary layer. The median number of elements was 3,284,000 (range 2,101,000–5,248,000).

Computational Fluid Dynamics

Computational fluid dynamics (CFD) (Fluent 13.0; ANSYS, Canonsburg, Pennsylvania) was used to simulate hemodynamics in the vascular models. Transient Navier-Stokes equations were solved by using a pressure-based, 3D double-precision solver by following the SIMPLE Method.²⁷ Blood was modeled with an attenuation of 1060 kg/m³ and a dynamic viscosity of 0.004 Pa · s. A no-slip boundary was assumed at the rigid vessel wall.

Because patient-specific velocity data were not available for this patient selection, we calculated parent artery-specific velocity profiles for the basilar artery (cases 1, 6, and 9), internal carotid artery (cases 3, 7, and 8), middle cerebral artery (cases 4 and 5), and anterior cerebral artery (case 2). Median values for the maximum and minimum velocities were obtained from previous patient-specific 4D phase-contrast MR imaging velocity measure-

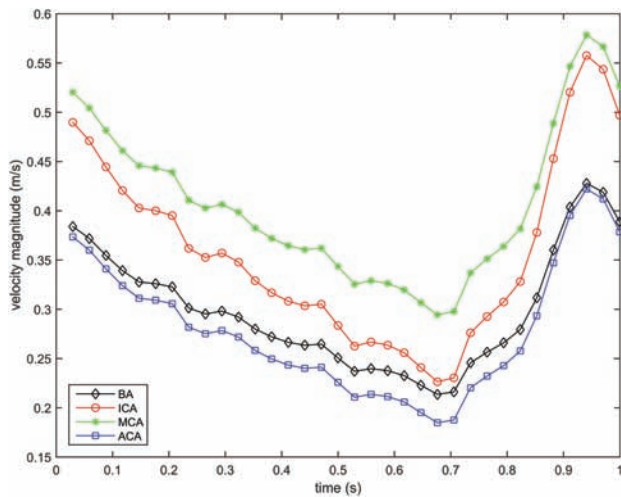


FIG 1. Velocity magnitude (m/s) waveforms for the basilar artery (BA), internal carotid artery, middle cerebral artery, and the anterior cerebral artery (ACA).

ments. A middle cerebral artery velocity profile was used as a reference waveform to reconstruct velocity profiles consisting of 34 interpolated time-steps for each location (Fig 1).

Murray's law was used to determine the outflow ratio of the distal arteries. The third of 3 cardiac cycles was used for analysis.²⁸

Qualitative Analysis

Flow-velocity magnitude streamlines and WSS distributions were visualized by using Paraview 3.6.2 (Kitware; Los Alamos National Laboratory, Los Alamos, New Mexico). The visualizations were qualitatively assessed by 2 experienced neuroradiologists (C.B.L.M.M., R.v.d.B.) for hemodynamic characteristics in consensus. Flow complexity, flow stability, and the inflow concentration were assessed on the basis of visualization of the streamlines.²⁹ The region and size of flow impingement were determined from the WSS distribution and streamlines.

Quantitative Oscillatory Shear Index Measurements

The mean and maximum oscillatory shear indices (OSIs)³⁰ were calculated to assess the directional change of WSS during the cardiac cycle. Differences in OSI values before and after rupture were determined.

RESULTS

Streamlines at peak systole and heart cycle-averaged WSS distributions of all 18 vascular models are shown in Figs 2 and 3, respectively. All vascular models had a single inflow jet, single or multiple vortices, and at least 1 clear impingement zone before and after rupture. The location of maximum WSS and the region of flow impingement agreed for all cases. Hemodynamic differences were observed in 6 of the 9 aneurysms (Table 2). For the 6 patients with hemodynamic changes, the median time between imaging before and after rupture was 678 days (range, 14–1461 days). For the 3 patients without hemodynamic changes, this was 151 days (range, 34–183 days). Flow complexity changed from simple to complex in 3 cases. Flow stability changed from stable to unstable in 3 cases. The inflow

concentration changed from diffuse to concentrated in 1 case and from concentrated to diffuse in another case. The region of flow impingement changed in 3 cases. These hemodynamic changes were associated with growth, aneurysm displacement, or newly formed lobulations.¹⁴ Changes in OSI after rupture ranged from -0.037 to $+0.034$ and from -0.030 to $+0.12$ for the spatially averaged and maximum values, respectively (Table 3).

Qualitative Characterization: Case-by-Case Description

For cases 1 and 6, aneurysmal geometry and hemodynamics did not change after rupture. In case 2, the aneurysm was displaced 8.9 mm after rupture, most likely due to mass effect from a large perianeurysmal hematoma (dimensions, $28 \times 22 \times 35$ mm). In this case, the region of flow impingement changed from the dome to the body. In the On-line Video, changes of WSS distributions before (A) and after (C) rupture with velocity magnitude streamlines before (B) and after (D) rupture of this case can be appreciated.

Case 3 showed a relative growth of 79% with 1 new lobulation after rupture. The flow profile changed from simple and stable to complex and unstable after rupture.

The aneurysm of case 4 was displaced 5.8 mm after rupture, most likely due to mass effect from a large perianeurysmal hematoma (dimensions, $46 \times 33 \times 38$ mm). However, there were no changes in hemodynamic characterizations.

In case 5, a volumetric increase of 176% and a displacement of 1.2 mm after rupture were found. For the hemodynamic characterization, a diffuse inflow pattern before rupture changed to a concentrated one after rupture.

In case 7, there was a relative growth of 832%, with a newly observed lobulation in the imaging after rupture. The simple flow changed to a complex flow pattern after rupture. Also, an additional impingement zone was observed in the body of the aneurysm at the border of the lobulation after rupture.

In case 8, there was a relative growth of 70% and a displacement of 2.5 mm after rupture. The flow pattern changed from stable to unstable. Before rupture, the inflow stream impacted the aneurysm at 2 regions: the aneurysm neck and body. After rupture, the neck of the aneurysm was the only region of impingement.

In case 9, a new lobulation was observed in the imaging after rupture. The flow changed from simple and stable to complex and unstable.

DISCUSSION

Most current rupture-risk identification studies compare models of ruptured aneurysms with unruptured models and ignore the possibility that the rupture itself may change aneurysm morphology and hemodynamics. However, our study shows that hemodynamic characteristics changed in 6 of the 9 aneurysms in the period between before and after imaging. Notably, we show changes in flow complexity, stability, and concentration, which have been associated with a risk of rupture.²⁹

The altered hemodynamics are the consequence of a change in morphology in the period between image acquisitions. Because of the large imaging time interval in some cases, we cannot relate the

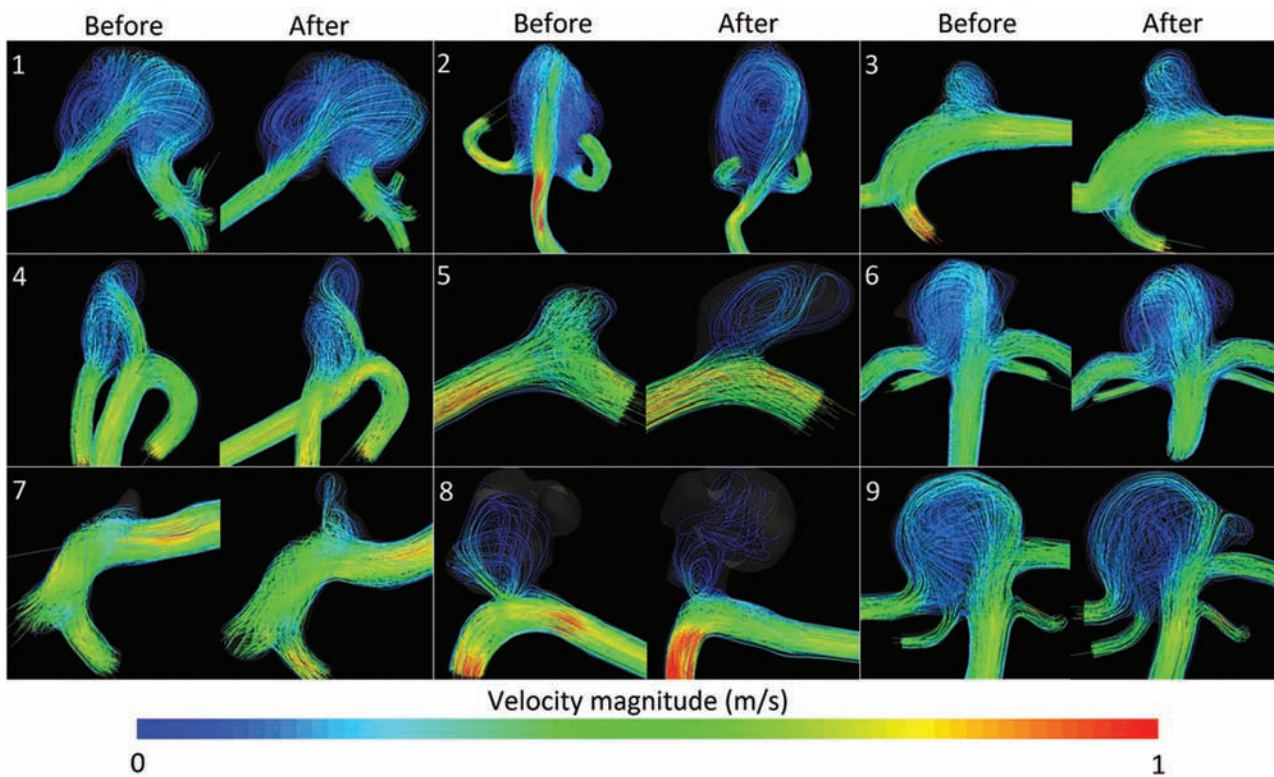


FIG 2. Flow-velocity streamlines (m/s) for all 9 aneurysms before and after rupture. For each aneurysm, the time-step with the peak velocity-magnitude of the inflow artery is shown.

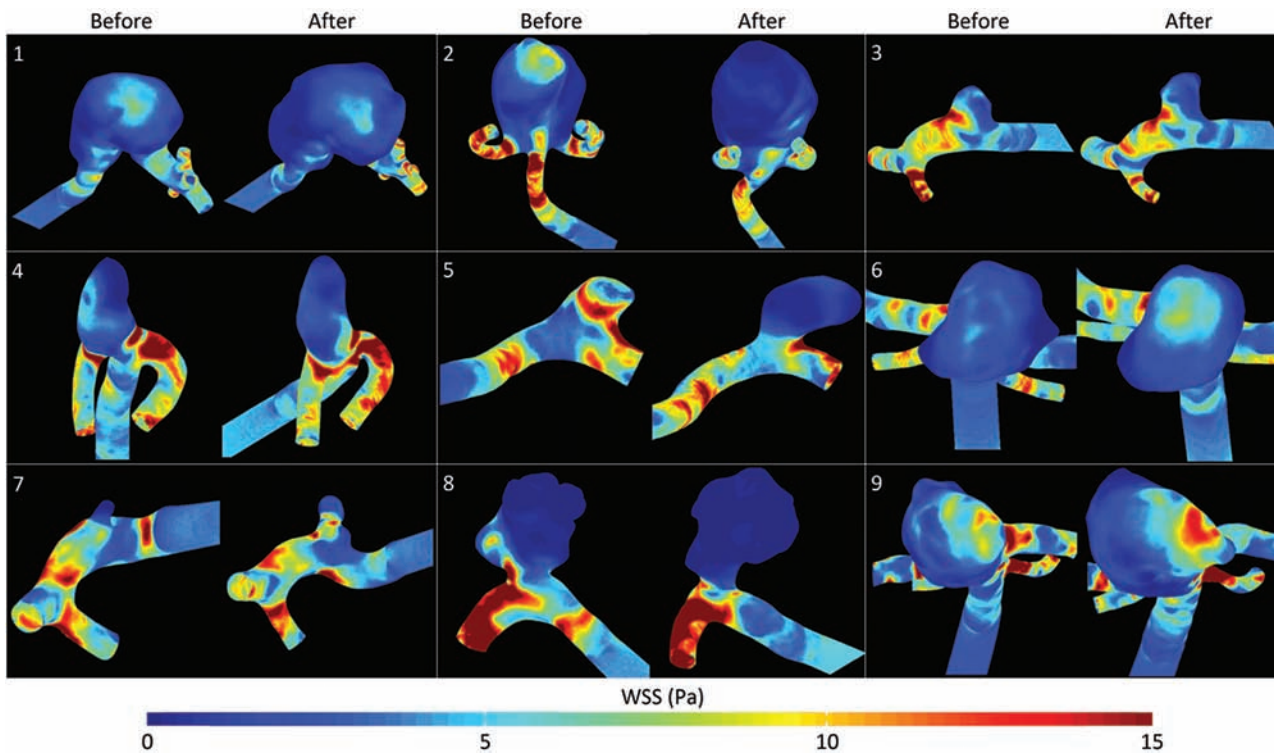


FIG 3. Heart cycle-averaged WSS (Pascal) distributions for all 9 aneurysms before and after rupture.

observed hemodynamic alterations to sudden, rupture-related morphologic changes alone. For instance, growth or lobulation formation may also have occurred more gradually during the whole time span. This scenario agrees with the median time be-

tween before and after rupture imaging, which was much larger for the cases with hemodynamic changes than for the cases without. Furthermore, all of the 3 cases in which flow patterns changed from simple to complex showed a newly formed lobulation. How-

Table 2: Hemodynamic characteristics of the aneurysm models before and after rupture^a

Pt	Location	Flow Complexity	Flow Stability	Inflow Concentration	Flow Impingement		Geometric Changes
					Region	Size	
1	Basilar	C-C	U-U	C-C	D-D	S-S	None ^b
2	AcomA	C-C	U-U	C-C	D-B ^c	S-S	Aneurysm displacement (8.9 mm)
3	PcomA	S-C ^c	S-U ^c	D-D	N-N	S-S	Growth (79%); 1 new lobulation
4	MCA	C-C	U-U	C-C	ND-ND	S-S	Aneurysm displacement (5.8 mm)
5	MCA	C-C	S-S	D-C ^c	ND-ND	S-S	Growth (176%)
6	Basilar	C-C	U-U	D-D	D-D	L-L	None ^b
7	PcomA	S-C ^c	U-U	C-D ^c	N-NB ^c	S-S	Growth (832%); 1 new lobulation
8	Anterior choroidal	C-C	S-U ^c	C-C	NB-N ^c	S-S	Growth (70%)
9	Basilar	S-C ^c	S-U ^c	C-C	BD-BD	L-L	1 New lobulation

Note:—AcomA indicates anterior communicating artery; PcomA, posterior communicating artery.

^a Flow complexity was characterized as simple (S) or complex (C); flow stability, as stable (S) or unstable (U); inflow concentration as diffuse (D) or concentrated (C); region of flow impingement, as dome (D), body (B), or neck (N); and size of the impingement zone, as small (S) or large (L).

^b Aneurysm displacement of ≤ 0.6 mm or not related to mass effect from hematoma; aneurysm growth of $\leq 40\%$.

^c Changed after rupture.

Table 3: Mean and maximum oscillatory shear index for all 9 aneurysms before and after rupture

Pt	Mean OSI			Maximum OSI		
	Before	After	Δ	Before	After	Δ
1	0.042	0.049	+0.007 (17%)	0.487	0.484	-0.003 (0.6%)
2	0.074	0.044	-0.029 (40%)	0.486	0.479	-0.007 (1.4%)
3	0.025	0.049	+0.024 (95%)	0.423	0.482	+0.059 (13.9%)
4	0.031	0.044	+0.013 (42%)	0.471	0.483	+0.012 (2.5%)
5	0.007	0.040	+0.034 (520%)	0.350	0.469	+0.119 (34.1%)
6	0.065	0.028	-0.037 (57%)	0.489	0.459	-0.030 (6.1%)
7	0.061	0.031	-0.029 (48%)	0.471	0.476	+0.005 (1.1%)
8	0.021	0.018	-0.003 (16%)	0.475	0.452	-0.023 (4.8%)
9	0.025	0.058	+0.034 (137%)	0.473	0.485	+0.011 (2.4%)
Mean	0.039 \pm 0.023	0.040 \pm 0.013		0.458 \pm 0.045	0.474 \pm 0.012	

ever, morphologic changes may also occur suddenly, shortly before, during, or just after rupture. This change can be illustrated by the large growth of case 8 within 14 days and by the aneurysm displacement in both cases (2 and 4) with a hematoma with mass effect.

Therefore, hemodynamics of ruptured models may still be valuable for gradually changing aneurysms, where the value seems more limited for models with rupture-related morphologic changes. In most cases, it is difficult to discriminate between sudden and gradual changes in morphology, except for cases with large perianeurysmal hematomas. We recommend excluding these cases in studies that compare hemodynamic characteristics in ruptured and unruptured aneurysms because hematomas may strongly influence hemodynamics.

Only a few studies assessed hemodynamics both before and after rupture. In 4 aneurysms of the posterior communicating artery, Chien and Sayre³¹ determined that only 1 hemodynamic parameter (pulsatility index) was not affected by rupture. This agrees with our observations that most hemodynamic characteristics changed. Duan et al³² examined hemodynamic and morphologic parameters by using a case-control study of 6 aneurysms on the posterior communicating artery with hemodynamic data within 7 days before rupture. However, they only compared parameters with those of matched controls and did not investigate the influence of the rupture itself. This was also the case in the study of Liu et al,³³ in which low WSS was associated with rupture in a case-control study of large internal carotid artery aneurysms, including 3 unruptured aneurysms just before rupture and 8 un-

ruptured controls. A recent case report of an aneurysm with imaging before and just after rupture demonstrated changes in WSS values between 20% and 30%, caused by a change in the aneurysm shape.³⁴

In a recent study by Bor et al,³⁵ aneurysm growth was studied in a large population of patients with unruptured and untreated intracranial aneurysms. In their study, >10% of the aneurysms grew during a mean follow-up time of <3 years. Growth is considered a marker for increased risk of rupture, and because growth may change hemodynamics, such a population allows improved characterization of hemodynamic rupture-risk factors.

A previous study by Xiang et al⁸ showed that high OSI values were associated with ruptured aneurysms. We indeed found high OSI values in all ruptured models. Most important, OSI was also high in all except 1 of the unruptured models. The exception was a case with >3 years between imaging, in which gradual progression from low-to-high shear stress oscillation might have been missed. These data therefore suggest that high OSI values may remain valuable for risk prediction.

Limitations

The current study has a number of limitations. Although this study is the largest comparing hemodynamic parameters within aneurysms before and after rupture, the number of patients was too small to perform statistical analysis. CFD is sensitive to the geometry and therefore image resolution, and neck size overestimation can affect the calculated hemodynamic parameters.¹⁹ Previous literature concluded that WSS calculations are strongly de-

pendent on segmentation and resolution.³⁶ Because of the large variation in resolution, the WSS estimations were not robust. Therefore, we used WSS distributions only for determining the impingement region, and no absolute WSS values were reported. Manual corrections for imaging artifacts were performed by a single neuroradiologist. These imaging artifacts were apparent in all cases; therefore, we do not expect large variations among different observers. Furthermore, common limitations for CFD studies, such as the generic pulsatile waveform, rigid wall assumption, limited accuracy of the algorithm, Newtonian fluid assumption, and CFD solution strategies may affect the accuracy of CFD results.^{37–39}

CONCLUSIONS

We have shown that morphologic changes before, during, or just after rupture may result in differences in hemodynamic characteristics between the ruptured and unruptured status of aneurysms. Hemodynamic differences were associated with aneurysm growth, lobulation formation, and displacement due to hematoma. Associations of hemodynamic characteristics with aneurysm rupture obtained from case-control studies comparing ruptured and unruptured aneurysms should, therefore, be interpreted with caution and not automatically used in risk models for aneurysm rupture.

Disclosures: Wouter Potters—RELATED: Other: Dutch Technology Foundation STW (Carisma 111629). * Comments: Salary was paid by a grant from a government granting agency (the Dutch Technology Foundation STW) for this submitted work. René van den Berg—UNRELATED: Consultancy: Codman/DePuy neurovascular consultancy in 2014. Birgitta Velthuis—UNRELATED: Payment for Lectures (including service on Speakers Bureaus): Philips Healthcare. * Ed VanBavel—UNRELATED: Grants/Grants Pending: European Union Marie Curie program. * Charles Majoie—RELATED: Grant: Nuts Ohra Foundation*. UNRELATED: Grants/Grants Pending: Dutch Heart Foundation. * *Money paid to the institution.

REFERENCES

- Brisman JL, Song JK, Newell DW. Cerebral aneurysms. *N Engl J Med* 2006;355:928–39
- Vlak MH, Algra A, Brandenburg R, et al. Prevalence of unruptured intracranial aneurysms, with emphasis on sex, age, comorbidity, country, and time period: a systematic review and meta-analysis. *Lancet Neurol* 2011;10:626–36
- Nieuwkamp DJ, Setz LE, Algra A, et al. Changes in case fatality of aneurysmal subarachnoid haemorrhage over time, according to age, sex, and region: a meta-analysis. *Lancet Neurol* 2009;8:635–42
- Gabriel RA, Kim H, Sidney S, et al. Ten-year detection rate of brain arteriovenous malformations in a large, multiethnic, defined population. *Stroke* 2010;41:21–26
- van Rooij WJ, Sprengers ME, de Gast AN, et al. 3D rotational angiography: the new gold standard in the detection of additional intracranial aneurysms. *AJNR Am J Neuroradiol* 2008;29:976–79
- Greving JP, Wermer MJ, Brown RD, et al. Development of the PHASES score for prediction of risk of rupture of intracranial aneurysms: a pooled analysis of six prospective cohort studies. *Lancet Neurol* 2014;13:59–66
- Cebral JR, Mut F, Weir J, et al. Quantitative characterization of the hemodynamic environment in ruptured and unruptured brain aneurysms. *AJNR Am J Neuroradiol* 2011;32:145–51
- Xiang J, Natarajan SK, Tremmel M, et al. Hemodynamic-morphologic discriminants for intracranial aneurysm rupture. *Stroke* 2011;42:144–52
- Backes D, Vergouwen MDI, Velthuis BK, et al. Difference in aneurysm characteristics between ruptured and unruptured aneurysms in patients with multiple intracranial aneurysms. *Stroke* 2014;45:1299–303
- Shojima M, Oshima M, Takagi K, et al. Magnitude and role of wall shear stress on cerebral aneurysm: computational fluid dynamic study of 20 middle cerebral artery aneurysms. *Stroke* 2004;35:2500–05
- Meng H, Tutino VM, Xiang J, et al. High WSS or Low WSS? Complex interactions of hemodynamics with intracranial aneurysm initiation, growth, and rupture: toward a unifying hypothesis. *AJNR Am J Neuroradiol* 2014;35:1254–62
- Xiang J, Tutino VM, Snyder KV, et al. CFD: computational fluid dynamics or confounding factor dissemination? The role of hemodynamics in intracranial aneurysm rupture risk assessment. *AJNR Am J Neuroradiol* 2014;35:1849–57
- Rahman M, Ogilvy CS, Zipfel GJ, et al. Unruptured cerebral aneurysms do not shrink when they rupture: multicenter collaborative aneurysm study group. *Neurosurgery* 2011;68:155–60; discussion 160–61
- Schneiders JJ, Marquering HA, van den Berg R, et al. Rupture-associated changes of cerebral aneurysm geometry: high-resolution 3D imaging before and after rupture. *AJNR Am J Neuroradiol* 2014;35:1358–62
- Manniesing R, Velthuis BK, van Leeuwen MS, et al. Level set based cerebral vasculature segmentation and diameter quantification in CT angiography. *Med Image Anal* 2006;10:200–14
- Cremers D, Rousson M, Deriche R. A review of statistical approaches to level set segmentation: integrating color, texture, motion and shape. *Int J Comput Vis* 2007;72:195–215
- Luboz V, Wu X, Krissian K, et al. A segmentation and reconstruction technique for 3D vascular structures. *Med Image Comput Comput Assist Interv* 2005;8(pt 1):43–50
- Antiga L, Piccinelli M, Botti L, et al. An image-based modeling framework for patient-specific computational hemodynamics. *Med Biol Eng Comput* 2008;46:1097–112
- Omodaka S, Inoue T, Funamoto K, et al. Influence of surface model extraction parameter on computational fluid dynamics modeling of cerebral aneurysms. *J Biomech* 2012;45:2355–61
- Hoi Y, Woodward SH, Kim M, et al. Validation of CFD simulations of cerebral aneurysms with implication of geometric variations. *J Biomech Eng* 2006;128:844–51
- Schneiders JJ, Marquering HA, Antiga L, et al. Intracranial aneurysm neck size overestimation with 3D rotational angiography: the impact on intra-aneurysmal hemodynamics simulated with computational fluid dynamics. *AJNR Am J Neuroradiol* 2013;34:121–28
- Moench T, Neugebauer M, Preim B. Optimization of vascular surface models for computational fluid dynamics and rapid prototyping. In: *Proceedings of the International Workshop on Digital Engineering*, Magdeburg, Germany. November 21–22, 2011:16–23
- Blender Foundation. Blender. *Free Open 3D Creat Softw*. 1995. <http://www.blender.org/>. Accessed October 9, 2013
- Yushkevich PA, Piven J, Hazlett HC, et al. User-guided 3D active contour segmentation of anatomical structures: significantly improved efficiency and reliability. *Neuroimage* 2006;31:1116–28
- Taubin G. Curve and surface smoothing without shrinkage. In: *Proceedings of the Fifth International Conference on Computer Vision*, Boston, Massachusetts. June 22–23, 1995
- Ortega J, Hartman J, Rodriguez J, et al. Post-treatment hemodynamics of a basilar aneurysm and bifurcation. *Ann Biomed Eng* 2008;36:1531–46
- Caretto LS, Gosman AD, Patankar SV, et al. Two calculation procedures for steady, three-dimensional flows with recirculation. In: Cabannes H, Temam R, eds. *Proceedings of the Third International Conference on Numerical Methods in Fluid Mechanics*. New York, NY: Springer-Verlag; 1973:60–68
- Cebral JR, Castro MA, Appanaboyina S, et al. Efficient pipeline for image-based patient-specific analysis of cerebral aneurysm

- hemodynamics: technique and sensitivity. *IEEE Trans Med Imaging* 2005;24:457–67
29. Cebal JR, Mut F, Weir J, et al. **Association of hemodynamic characteristics and cerebral aneurysm rupture.** *AJNR Am J Neuroradiol* 2011;32:264–70
 30. Ku DN, Giddens DP, Zarins CK, et al. **Pulsatile flow and atherosclerosis in the human carotid bifurcation. Positive correlation between plaque location and low oscillating shear stress.** *Arteriosclerosis* 1985;5:293–302
 31. Chien A, Sayre J. **Morphologic and hemodynamic risk factors in ruptured aneurysms imaged before and after rupture.** *AJNR Am J Neuroradiol* 2014;35:2130–35
 32. Duan G, Lv N, Yin J, et al. **Morphological and hemodynamic analysis of posterior communicating artery aneurysms prone to rupture: a matched case-control study.** *J Neurointerv Surg* 2014 Nov 17. [Epub ahead of print]
 33. Liu J, Fan J, Xiang J, et al. **Hemodynamic characteristics of large unruptured internal carotid artery aneurysms prior to rupture: a case control study.** *J Neurointerv Surg* 2015 Feb 4. [Epub ahead of print]
 34. Kono K, Tomura N, Yoshimura R, et al. **Changes in wall shear stress magnitude after aneurysm rupture.** *Acta Neurochir (Wien)* 2013; 155:1559–63
 35. Bor AS, Tiel Groenestege AT, terBrugge KG, et al. **Clinical, radiological, and flow-related risk factors for growth of untreated, unruptured intracranial aneurysms.** *Stroke* 2015;46:42–48
 36. Potters WV, van Ooij P, Marquering H, et al. **Volumetric arterial wall shear stress calculation based on cine phase contrast MRI.** *J Magn Reson Imaging* 2015;41:505–16
 37. Jansen IG, Schneiders JJ, Potters WV, et al. **Generalized versus patient-specific inflow boundary conditions in computational fluid dynamics simulations of cerebral aneurysmal hemodynamics.** *AJNR Am J Neuroradiol* 2014;35:1543–48
 38. Dempere-Marco L, Oubel E, Castro M, et al. **CFD analysis incorporating the influence of wall motion: application to intracranial aneurysms.** *Med Image Comput Comput Assist Interv* 2006; 9:438–45
 39. Valen-Sendstad K, Steinman DA. **Mind the gap: impact of computational fluid dynamics solution strategy on prediction of intracranial aneurysm hemodynamics and rupture status indicators.** *AJNR Am J Neuroradiol* 2014;35:536–43

Stent-Assisted Coiling of Wide-Neck Intracranial Aneurysms Using Low-Profile LEO Baby Stents: Initial and Midterm Results

K. Aydin, A. Arat, S. Sencer, M. Barburoglu, and S. Men



ABSTRACT

BACKGROUND AND PURPOSE: Low-profile self-expandable stents were recently introduced for the treatment of wide-neck intracranial aneurysms. This study investigated the initial and midterm clinical and angiographic results of LEO Baby stent–assisted coiling in the treatment of wide-neck intracranial aneurysms.

MATERIALS AND METHODS: A retrospective review was performed to identify patients who were treated with LEO Baby stent–assisted coiling. Eighty patients with 80 wide-neck intracranial aneurysms were included in the study. Eleven patients (13.8%) presented with subarachnoid hemorrhage. All patients were treated with LEO Baby stent–assisted coiling. Technical success and immediate postprocedural clinical and angiographic outcomes were evaluated. Seventy-three patients attended angiographic and clinical follow-up for a mean duration of 7.2 ± 3.8 months. Periprocedural and delayed complications were reviewed. Preprocedural and follow-up clinical statuses were assessed by using the modified Rankin Scale.

RESULTS: The technical success rate of the procedure was 97.5%. The immediate postprocedural angiography revealed a complete occlusion of the aneurysm in 75% of the 80 patients. The last follow-up angiograms showed complete occlusion in 85.7% of the 77 patients with an angiographic follow-up. Of the 77 patients with a follow-up angiography, 6.5% showed an increase in the filling status of the aneurysm and 5.2% required retreatment. The overall procedure-related complication rate, including asymptomatic complications, was 11.3%. The permanent morbidity rate was 3.8%. There was no mortality in this study.

CONCLUSIONS: This case series demonstrates the relative safety, efficacy, and midterm durability of the LEO Baby stent–assisted coiling procedure for the treatment of wide-neck intracranial aneurysms.

ABBREVIATIONS: AcomA = anterior communicating artery; SAC = stent-assisted coiling

Coiling has become the most common treatment for intracranial aneurysms since the results of the International Subarachnoid Aneurysm study were published.¹ However, treatment of wide-neck complex aneurysms remains challenging. The relatively high recurrence rates after coiling are another major limitation of the endovascular treatment of wide-neck and/or large aneurysms.^{2,3} The stent-assisted coiling (SAC) technique was developed to treat wide-neck intracranial aneurysms.⁴ Several self-expandable stents dedicated to intracranial use were introduced

in the past decade, and the availability of these self-expandable intracranial stents enabled the endovascular treatment of wide-neck complex aneurysms that were uncoilable previously.^{4,5} Stents create a mechanical scaffold that prevents coil protrusion into the parent artery. Stents also reduce the risk of recanalization because of their hemodynamic and biologic effects.⁶

Low-profile self-expandable intracranial stents (LEO Baby; Balt, Montmorency, France; and LVIS Jr; MicroVention, Tustin, California) were introduced recently.^{7,8} The designs of these stents enable their delivery into small arteries. These low-profile intracranial stents can be deployed into arteries with diameters as small as 1.5 mm to treat wide-neck aneurysms. Furthermore, these stents can be delivered through microcatheters with an internal diameter of 0.0165 inches, which facilitates navigation in small-sized vessels.

This multicenter retrospective study investigated the safety and efficacy of LEO Baby stent-assisted coiling treatment of wide-neck intracranial aneurysms. We also evaluated the midterm (6–12 months) durability of LEO Baby SAC treatment.

Received January 12, 2015; accepted after revision February 25.

From the Department of Radiology (K.A., S.S., M.B.), Neuroradiology Division, Istanbul Faculty of Medicine, Istanbul University, Istanbul, Turkey; Department of Radiology (A.A.), School of Medicine, Hacettepe University, Ankara, Turkey; and Department of Radiology (S.M.), Dokuz Eylul University, Izmir, Turkey.

Please address correspondence to Kubilay Aydin, MD, Istanbul University, Istanbul Faculty of Medicine, Department of Radiology, Neuroradiology Division, Istanbul 34340, Turkey; e-mail: dr.aydink@superonline.com

Indicates open access to non-subscribers at www.ajnr.org

<http://dx.doi.org/10.3174/ajnr.A4355>

MATERIALS AND METHODS

Patients

After approval of the study by the institutional review board, a retrospective review of interventional data base records of 3 university hospitals was performed to identify patients who were treated by using at least 1 LEO Baby stent between October 2012 and November 2014. Medical records and radiologic images of patients were gathered. Three neuroradiologists (K.A., M.B., and S.M.) assessed the surgery reports, medical charts, and radiologic images of the patients. Patient demographics and presenting symptoms, the location and size of aneurysms, previous treatment history, stent-deployment success, technical and clinical complications, and the degree of aneurysm occlusion were recorded.

Eighty-six patients received attempted treatment by using LEO Baby stents between October 2012 and November 2014. Only patients treated by using the SAC technique were included into the study; 6 patients who were treated by using stent monotherapy without coiling were excluded. LEO Baby stent-assisted coiling was performed in the treatment of aneurysms located in the parent arteries with a diameter of ≤ 3.5 mm and with a dome/neck ratio of < 2 or a neck diameter of > 4 mm, a morphology not suitable for primary coiling.

This study consisted of 80 aneurysms. Fifty of these aneurysms were treated in (Hacettepe University Medical School Hospital), 23 in (Istanbul Medical School Hospital), and 7 in (Dokuz Eylul University Hospital). There were 31 male and 49 female (61%) patients, with a mean age of 52.05 ± 10.17 years (range, 26–73 years). Eleven patients (13.8%) presented with subarachnoid hemorrhage in a subacute (2–4 weeks) phase, and the remaining 69 patients (86.2%) had unruptured aneurysms. No patient was stented during the acute phase of subarachnoid hemorrhage (< 2 weeks). Seventy-two of 80 aneurysms (90%) were incidental and had not received prior treatment. Eight aneurysms (10%) were recanalized aneurysms that were treated previously by using conventional coiling, balloon-assisted coiling, or open surgery (clipping). The mean dome size of the aneurysms was 7.26 ± 3.41 mm (range, 3–22 mm). The mean neck size was 4.44 ± 1.18 mm (range, 2.5–9 mm). The aneurysms were located in the middle cerebral artery bifurcation in 43 patients (53.8%), the anterior communicating artery (AcomA) in 27 patients (33.8%), the pericallosal artery in 1 patient (1.2%), the internal carotid artery bifurcation in 1 patient (1.2%), the basilar artery bifurcation/vertebrobasilar junction in 7 patients (8.6%), and the posterior inferior cerebellar artery in 1 patient (1.2%). The mean parent artery diameter was 2.35 ± 0.43 mm (range, 1.3–3.5 mm).

Preoperative patient conditions were evaluated by using the modified Rankin Scale. The preoperative mRS scores of all patients except 1 were 0. One patient was assigned a preprocedural mRS score of 3 because of a previous history of subarachnoid hemorrhage.

General Description of the Endovascular Procedure

Patients received 75 mg clopidogrel and 300 mg aspirin daily for at least 5 days before the procedure. Clopidogrel resistance was evaluated before the procedures (VerifyNow P2Y12 assay; Accumetrics, San Diego, California) to ensure a good response (platelet

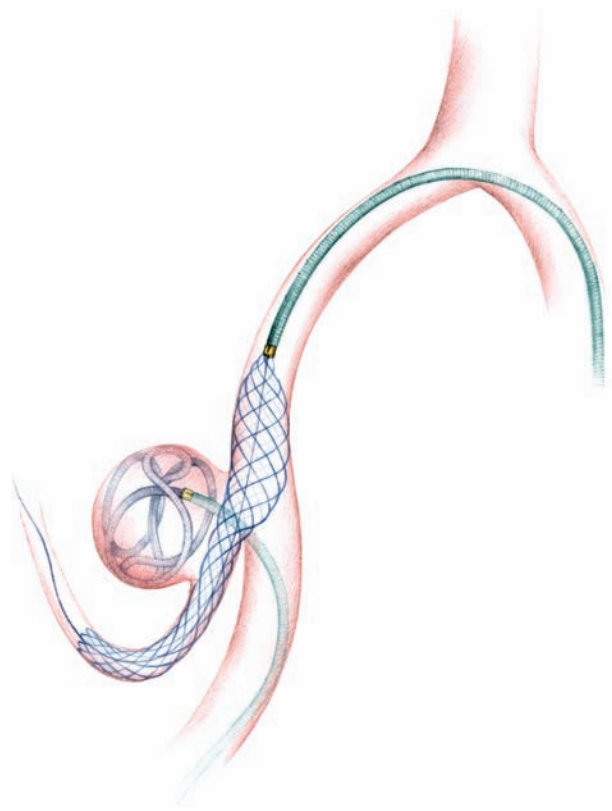


FIG 1. An illustration showing the LEO Baby stent-assisted coiling treatment of a PICA aneurysm. A microcatheter is jailed into the sac of aneurysm, while the LEO Baby stent is deployed to the parent artery through a second microcatheter.

aggregation inhibition $> 40\%$) to clopidogrel. Every endovascular procedure was performed by using a femoral approach with the patient under general anesthesia. Systemic anticoagulation was initiated immediately after the insertion of a femoral introducer sheath with a bolus dose of 5000 IU of IV heparin. The bolus dose was followed by a slow heparin infusion to maintain an activated clotting time of approximately twice the baseline value. A 6F guiding catheter or sheath was placed in the target artery. In patients with tortuous vascular anatomy, a distal access catheter (Fargomax; Balt; or Neuron 070; Penumbra, Alameda, California) was navigated through the guiding sheath into the petrous segment of the internal carotid artery or to the V2 segment of the vertebral artery. Aneurysm sacs were catheterized by using an Excelsior SL-10 (Stryker Neurovascular, Kalamazoo, Michigan) or Headway 17 (Microvention) microcatheter with a soft-tipped 0.014-inch microguidewire. A second microcatheter (Excelsior SL-10, Headway 17, or Vasco10; Balt) was navigated across the aneurysm for stent placement (Fig 1).

The same microcatheter was used for stent placement and coiling if the jailing technique was not performed. Stent sizes were chosen on the basis of the largest diameter of the parent artery and the length of the aneurysm neck. Coiling was performed by using bare platinum detachable coils after the stents were deployed. Aneurysms were coiled until complete occlusion was achieved or no further coils could be safely deployed within the aneurysm sac. Femoral puncture sites were sealed by using an arterial closure device. Postprocedural dual antiplatelet treatment, including 75

mg/day of clopidogrel and 300 mg/day of aspirin, was continued for 3 months. Dual antiplatelet therapy was switched to aspirin thereafter. Aspirin was continued life-long unless a contraindication existed. Dual antiplatelet treatment was prolonged to at least 6 months in patients who received >1 stent.

Stent-Placement Configurations

Sixty-six of 80 aneurysms (82.5%) were coiled with the assistance of a single LEO Baby stent. Fourteen aneurysms (17.5%) were coiled with the assistance of 2 stents in various configurations. Enterprise (Codman & Shurtleff, Raynham, Massachusetts) and LEO (Balt) stents were used as the first stent in the treatment of 3 aneurysms followed by the placement of a LEO Baby stent as the second stent. In the double LEO Baby cases, 6 aneurysms were treated by using Y-stent placement and 2 aneurysms received temporary Y-stent placement. T, X, and parallel stent placements were performed for the treatment of 8 aneurysms. Enterprise and LEO Baby stents were used as a bailout stent placement in 2 patients to treat complications.

Follow-Up

Immediate postprocedural angiograms were obtained to evaluate aneurysm occlusion according to the Raymond classification.⁹ Endovascular treatment was considered successful when stent deployment was successful and adequate angiographic occlusion by using coiling was achieved. The development of any technical complication was considered a technical failure, regardless of angiographic and clinical outcomes. Technical and clinical complications were recorded. Complications were “periprocedural” if they occurred within 48 hours postprocedure or “delayed” if they occurred later than 48 hours postprocedure. Postprocedural control cranial CT examinations were performed within 12 hours following the endovascular procedures. The first angiographic follow-up was performed at 3–6 months by using either MR angiography or conventional angiography, depending on the results of the endovascular procedure. The follow-up MR angiography examination included a 3D time-of-flight sequence performed before and after contrast material injection. The second and third angiographic follow-up DSAs were generally performed at 8–12 months and 18–24 months, respectively. Follow-up angiograms were assessed for the filling status of aneurysms and the development of in-stent stenosis or thrombosis. Progressive thrombosis on follow-up imaging was defined as an improvement in the Raymond class from sac or neck filling (class 3 or 2) toward total occlusion (class 1). Recanalization was defined as a deterioration in the Raymond class. Patient neurologic status was evaluated during discharge and during angiographic follow-ups by using the mRS score.

RESULTS

Technical Success and Immediate Angiographic Results

The endovascular procedure was successful in 78 of 80 patients (97.5%) (Fig 2). Technical complications developed during LEO Baby stent deployment in 2 patients, but the angiographic and clinical outcomes of these patients were successful. Among the patients with successful procedures, the LEO Baby stent was successfully deployed on the first attempt in 77 patients and on the

second attempt in 1 patient (Fig 3). Immediate postprocedural angiograms revealed a class 1 occlusion in 60 aneurysms (75%), class 2 occlusion in 17 aneurysms (21.3%), and class 3 occlusion in 3 aneurysms (3.7%) (Fig 4).

Complications

Complications, including asymptomatic technical and periprocedural thromboembolic events, developed in 9 patients (11.3%). Six patients (7.5%) remained asymptomatic. However, complications resulted in a permanent morbidity in 3 patients (3.8%). There was no mortality.

Technical complications without adverse clinical outcomes developed in 2 patients (2.5%). Stent migration without clinical adverse events developed during deployment in 1 patient. In this patient, the LEO Baby stent migrated into the sac of the aneurysm, and 2 other stents were implanted to complete the coil embolization. In another patient, the control procedural angiography immediately after deployment of a LEO Baby stent revealed an incomplete apposition of the stent. Telescopic implantation of an Enterprise stent resulted in complete stent apposition.

Periprocedural or delayed thromboembolic events developed in 6 patients (7.5%). Thromboembolic complications resulted in permanent neurologic deficits in 3 patients (3.8%). Thromboembolic complications were periprocedural in 5 patients and delayed in 1 patient.

In-stent thrombus formation was visualized during the endovascular procedures in 4 patients. Two of these patients were treated by using an intra-arterial infusion of tirofiban (Aggrastat), and 2 other patients were treated by using a continuous intravenous infusion of tirofiban. An MCA infarct developed in 1 patient who was treated by using intra-arterial tirofiban. The MCA infarct in this patient resulted in dysphasia and hemiparesis. This patient's mRS score both at discharge and at the final follow-up was 3. The other 3 patients who developed in-stent thrombi during the procedures remained asymptomatic.

One patient presented with ipsilateral ischemic stroke 4 hours after treatment of a right MCA bifurcation aneurysm by using a single LEO Baby stent. Emergent control angiography revealed an acute in-stent thrombosis. A proximal malpositioning of the stent was also observed. Telescopic implantation of an Enterprise stent successfully secured arterial flow in this patient. However, the patient developed a basal ganglia infarction and presented with hemiparesis. The mRS score of this patient at discharge was 4. This patient's symptoms resolved during several weeks, and her mRS score at the 6-month follow-up was 2.

One patient presented with hemiparesis 3 months after a single LEO Baby SAC to treat an AcomA aneurysm. This patient's control angiography revealed complete in-stent thrombosis; his final follow-up mRS score was 3.

One hemorrhagic complication (1.3%) developed during the treatment of an MCA bifurcation aneurysm. A mild extravasation from the aneurysm developed during coiling. Coiling was completed, and the patient awoke with a mild headache. The postprocedural cranial CT revealed that the contrast extravasation was confined to the Sylvian fissure. This patient did not develop any neurologic deficits.

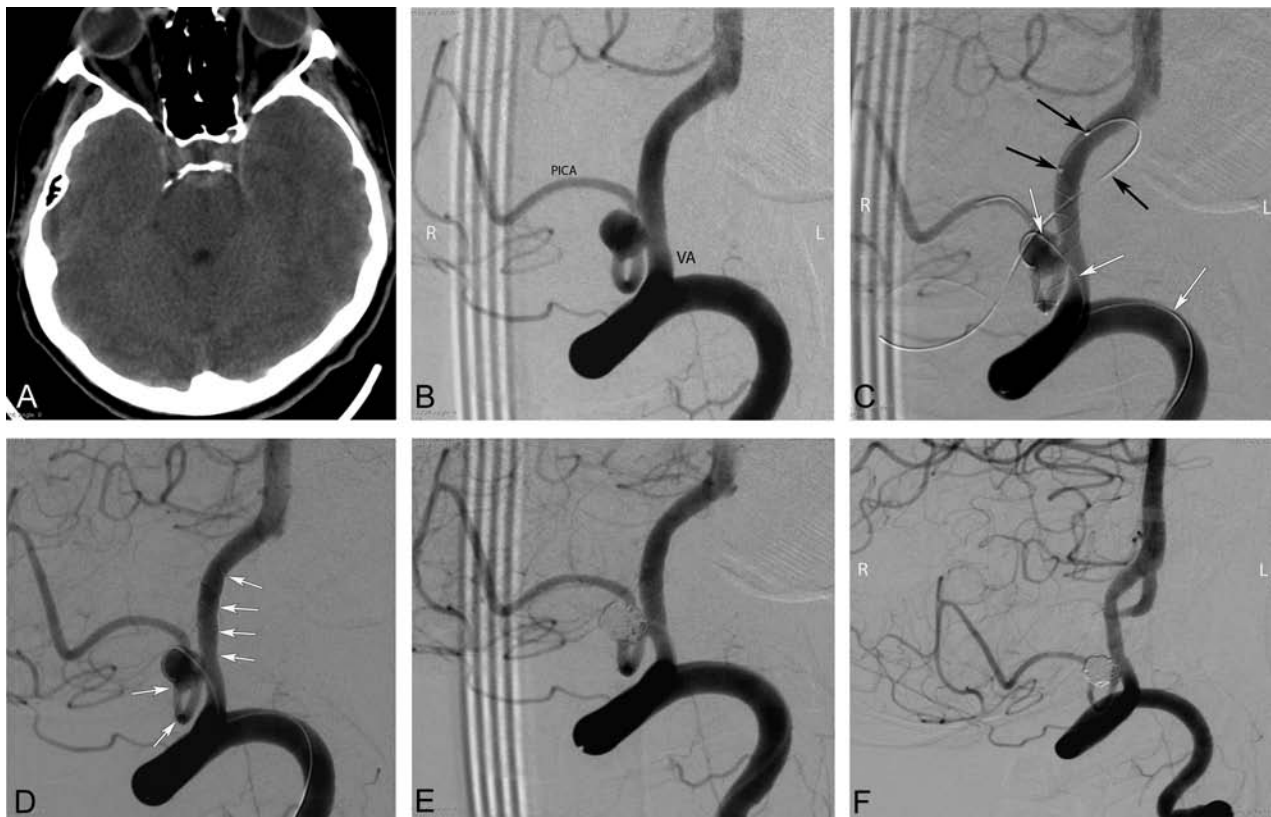


FIG 2. Preprocedural cranial CT and procedural and follow-up angiography images of a 44-year-old female patient with a ruptured PICA aneurysm. *A*, Cranial CT image obtained 9 days before the endovascular procedure (5 days following the rupture of aneurysm) shows the subarachnoid hemorrhage in the prepontine cistern. *B*, DSA image in a right anterior oblique projection reveals a 5-mm wide-neck aneurysm located on the medullary segment of the left PICA. *C*, DSA images obtained during the procedure show the catheterization of the parent artery for stent placement (*black arrows*) from the contralateral (*right*) vertebral artery and jailing of the coiling microcatheter (*white arrows*) through the ipsilateral (*left*) vertebral artery (the small filling defect in the aneurysm sac is a small air bubble introduced by the delivery of coil and trapped between the coil loops). *D*, DSA image obtained during the procedure shows the successful deployment of a LEO Baby stent (*arrows*) into the parent artery (PICA–vertebral artery). *E*, Immediate postprocedural DSA demonstrates the near-total occlusion of the aneurysm, with minimal filling in the neck. *F*, Six-month follow-up DSA shows complete occlusion of the aneurysm and a moderate degree of in-stent stenosis.

Follow-Up

Angiographic follow-ups were performed in 77 patients (96.2%). The mean length of follow-up was 7.2 ± 3.8 months (range, 3–22 months). The final angiographic follow-up was performed by using DSA in 64 cases (83.2%) and MR angiography in 13 patients (16.8%). The final follow-up angiograms revealed a class 1 occlusion in 66 patients (85.7%), class 2 in 9 patients (11.7%), and class 3 in 2 patients (2.6%). The follow-up of 16 aneurysms with a partial immediate occlusion (Raymond class 2 or 3) revealed 9 aneurysms (56.2%) with an improvement in the Raymond class (progressive occlusion) (Fig 5). Five aneurysms (6.5%) showed recanalization (deterioration of the Raymond class). Four of the 77 aneurysms with follow-up angiography (5.2%) required retreatment.

Follow-up angiography demonstrated incidental in-stent stenosis in 12 patients (15.6%). In-stent stenosis was anatomically mild (< 50%), not flow-limiting, and asymptomatic in all cases. Consequently, no further interventions were performed, but these patients continued clopidogrel instead of aspirin at follow-up.

The final follow-up mRS score was between 0 and 2 in 71 of 77 patients with a clinical follow-up. The final clinical follow-up in 2 patients with a 0 preprocedural mRS score revealed an mRS score

of 3. The mRS score of the patient with a preprocedural mRS score of 3 did not change during follow-up.

DISCUSSION

The first self-expandable stent was developed in 2002 for the treatment of wide-neck intracranial aneurysms.^{5,10} Several other self-expandable stents have been introduced since 2002, and SAC has become a widely applied method for the treatment of wide-neck intracranial aneurysms.¹¹ Self-expandable stents dedicated to intracranial use have enabled endovascular treatment in otherwise uncoilable aneurysms by providing a scaffold during coiling.

Until recently, the deployment of self-expandable stents necessitated the catheterization of the parent artery with 0.021- to 0.027-inch microcatheters. Low-profile, self-expandable stents (LEO Baby and LVIS Jr), deliverable through microcatheters with an internal diameter of 0.0165 inches, were developed in 2011.^{7,8,12} These low-profile stents allow easier catheterization and navigation in small-sized, delicate vessels and enable safer stent placement during the treatment of distal wide-neck aneurysms. Few articles have investigated the safety and efficacy of the treatment of intracranial aneurysms by using low-profile stents.^{7,8,12-14} The current study reports the retrospective experience of 3 university hospitals by using a low-profile stent system,

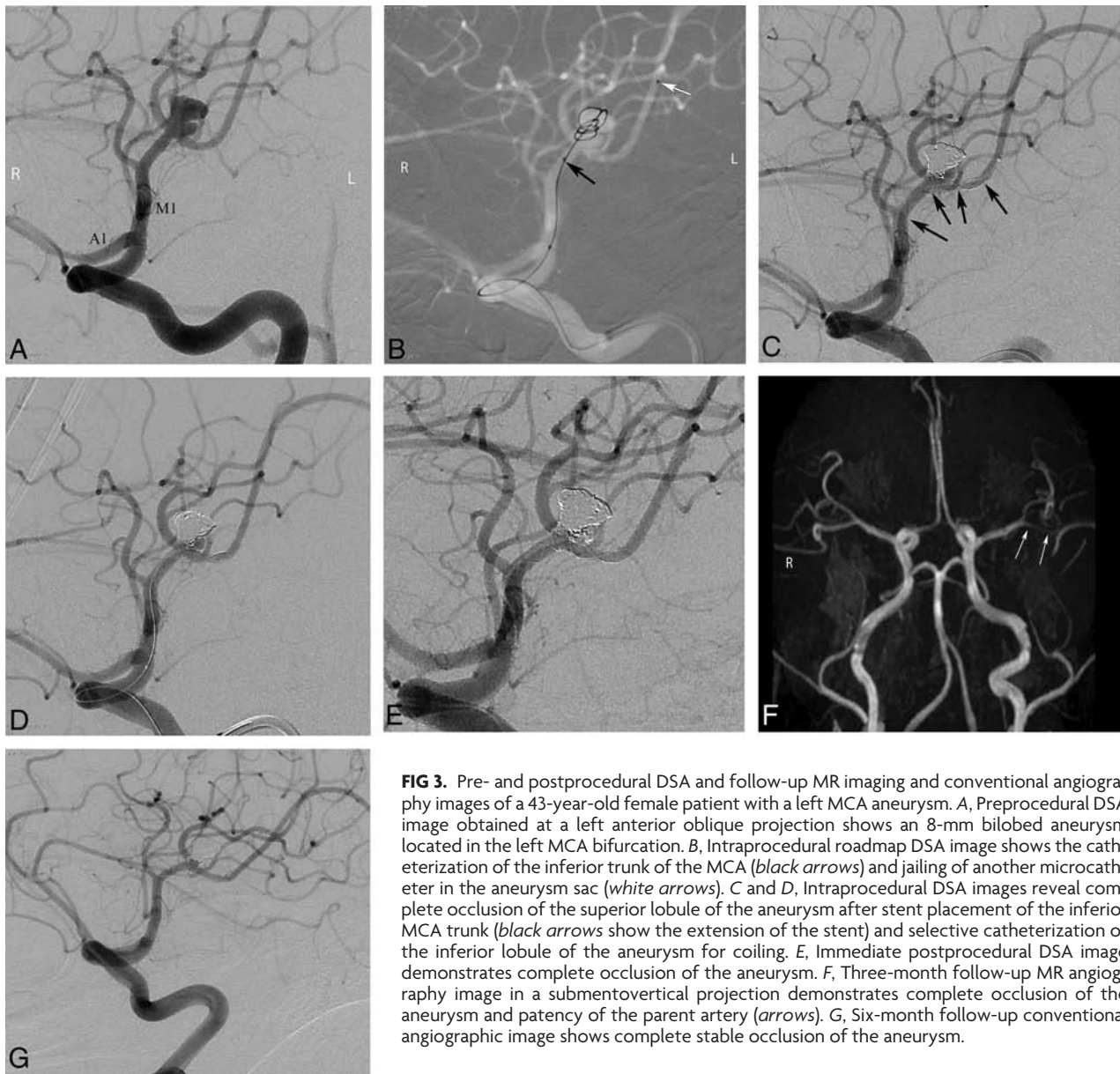


FIG 3. Pre- and postprocedural DSA and follow-up MR imaging and conventional angiography images of a 43-year-old female patient with a left MCA aneurysm. *A*, Preprocedural DSA image obtained at a left anterior oblique projection shows an 8-mm bilobed aneurysm located in the left MCA bifurcation. *B*, Intraprocedural roadmap DSA image shows the catheterization of the inferior trunk of the MCA (*black arrows*) and jailing of another microcatheter in the aneurysm sac (*white arrows*). *C* and *D*, Intraprocedural DSA images reveal complete occlusion of the superior lobule of the aneurysm after stent placement of the inferior MCA trunk (*black arrows* show the extension of the stent) and selective catheterization of the inferior lobule of the aneurysm for coiling. *E*, Immediate postprocedural DSA image demonstrates complete occlusion of the aneurysm. *F*, Three-month follow-up MR angiography image in a submentovertical projection demonstrates complete occlusion of the aneurysm and patency of the parent artery (*arrows*). *G*, Six-month follow-up conventional angiographic image shows complete stable occlusion of the aneurysm.

the LEO Baby stent, for SAC treatment of wide-neck intracranial aneurysms.

The LEO Baby stent is a self-expandable, low-profile stent composed of braided mesh nitinol wires.¹⁵ The LEO Baby stent is not approved by the FDA at the moment. It has received CE mark approval in Europe. LEO Baby stents, similar to LVIS Jr stents, have several advantages over laser-cut stents. First, LEO Baby stents have a sliding-strut design, and this hybrid design allows better wall apposition and scaffolding compared with open and closed cells. Second, LEO Baby stents are resheathable or repositionable up to approximately 95% of their length. LEO Baby stents have relatively small pore size compared with other self-expandable intracranial stents. This structural feature provides a tighter mesh, preventing coil protrusion during coiling. However, the small pore size may turn to a disadvantage in cases necessitating the catheterization of an aneurysm through the struts of the LEO Baby stent, though we did not experience such a disadvantage in our practice.

In the present study, the technical success rate of the procedures was high (97.5%). The flexibility of LEO Baby stents facilitates navigation even in small, tortuous arteries. We used distal-access catheters in cases with tortuous proximal vascular anatomy, which might contribute to successful stent navigation. At the moment, LEO Baby stents are available with diameters of 2.0 and 2.5 mm and lengths of 12, 18, 25, 30, and 35 mm. LEO Baby stents are labeled for deployment in arteries with diameters between 1.5 and 3.2 mm. Therefore, these are the only self-expandable stents that are labeled for deployment in arteries with diameters of <2 mm.¹⁵ LEO Baby stents were successfully deployed in arteries with diameters as small as 1.3 mm in our study. Furthermore, the LEO Baby stent could be deployed in branches having a diameter discrepancy of up to 60%. We observed technical complications in 2 cases, but they did not contribute to the angiographic or clinical outcomes of these patients.

Immediate complete occlusion rates after SAC showed vari-

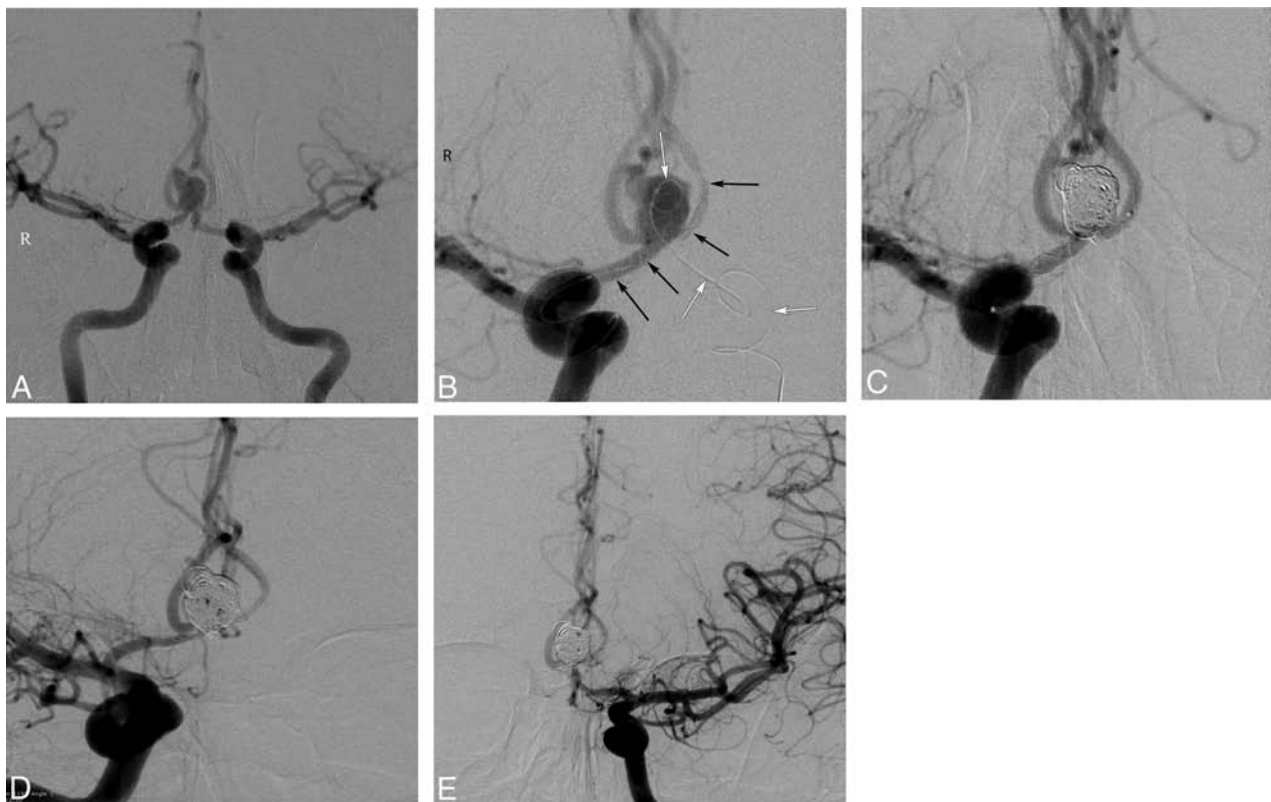


FIG 4. Procedural and follow-up angiographic images of a 42-year-old male patient with an AcomA aneurysm. *A*, Preprocedural DSA image obtained with bilateral internal carotid artery injections shows the wide-neck 8-mm AcomA aneurysm. *B*, DSA image obtained during the procedure demonstrates deployment of a LEO Baby stent extending from the left A2 to the right A1 (*black arrows*) and a jailed microcatheter in the aneurysm sac (*white arrows*). *C*, Postprocedural immediate DSA image shows complete occlusion of the aneurysm. *D* and *E*, Six-month follow-up DSA images demonstrate complete occlusion of the aneurysm and a mild degree of in-stent stenosis.

ability in the literature but are relatively low compared with coiling study results.^{6,11} A retrospective study by Maldonado et al¹⁶ reported that an immediate complete occlusion was achieved in 31.6% of aneurysms treated with Neuroform stents (Stryker Neurovascular). Lopes et al¹⁷ studied the long-term outcomes of 410 patients who were treated with SAC by using Neuroform or Enterprise stents and reported an immediate complete occlusion rate of 43.3%. Piotin et al⁶ compared the angiographic and clinical results of patients who were treated by using SAC, balloon remodeling, and conventional coiling. The immediate complete occlusion rate in the stented group was 46.3%, but 63.5% of the aneurysms in the group without stents were completely occluded in immediate postprocedural angiographs. A meta-analysis of the SAC literature by Shapiro et al¹¹ revealed an immediate complete occlusion rate of 45%. These relatively poor immediate complete occlusion rates may be because larger and more complex aneurysms are more likely to be treated with stents. Dual antiplatelet therapy in patients with stents might impede the immediate thrombosis of the aneurysm sac, and the difficulty in maneuvering coiling microcatheters between the struts of stents might contribute to the relatively low immediate occlusion rates. Möhlenbruch et al¹² recently published a prospective study in a relatively small patient group and reported the safety and efficacy of the LVIS Jr stent, which is one of the available low-profile stents. The immediate complete occlusion rate was 73%. Poncyjusz et al¹⁸ reported an immediate complete occlusion rate of 85% by using

either LVIS or LVIS Jr stents. The immediate total occlusion rate of 75% in our study is comparable with the results of previous studies.

Stent placement as a component of SAC treatment promotes the progressive occlusion of partially coiled aneurysms and more effectively impedes recanalization compared with conventional coiling or balloon-remodeling techniques.^{6,19} Stents have some hemodynamic and biologic effects on the parent arteries, which cause a progressive thrombosis of partially coiled aneurysms. Stent deployment across the orifice of an aneurysm redirects blood flow from the aneurysm sac toward the distal parent artery and decreases the hemodynamic stress that contributes to thrombosis of the aneurysmal sac.^{6,20,21} Furthermore, stent-induced neointimal overgrowth leads to healing of the aneurysm neck, promotes progressive thrombosis, and reduces the risk of recanalization.²² Gory et al²³ reported that 30.9% of aneurysms with partial immediate occlusion evolved into a complete occlusion during a 6-month follow-up, and the recanalization rate was only 14.5%. The progressive occlusion rate in another study was 69.7% after a mean follow-up of 8.2 months.²⁴ In our study, 56.2% of aneurysms with a partial immediate occlusion (Raymond classes 2 and 3) showed a progressive occlusion, which is comparable with the results of previous studies, and a complete occlusion (Raymond class 1) rate of 85.7% was achieved during a mean follow-up of 7.2 months. The filling status deteriorated in only

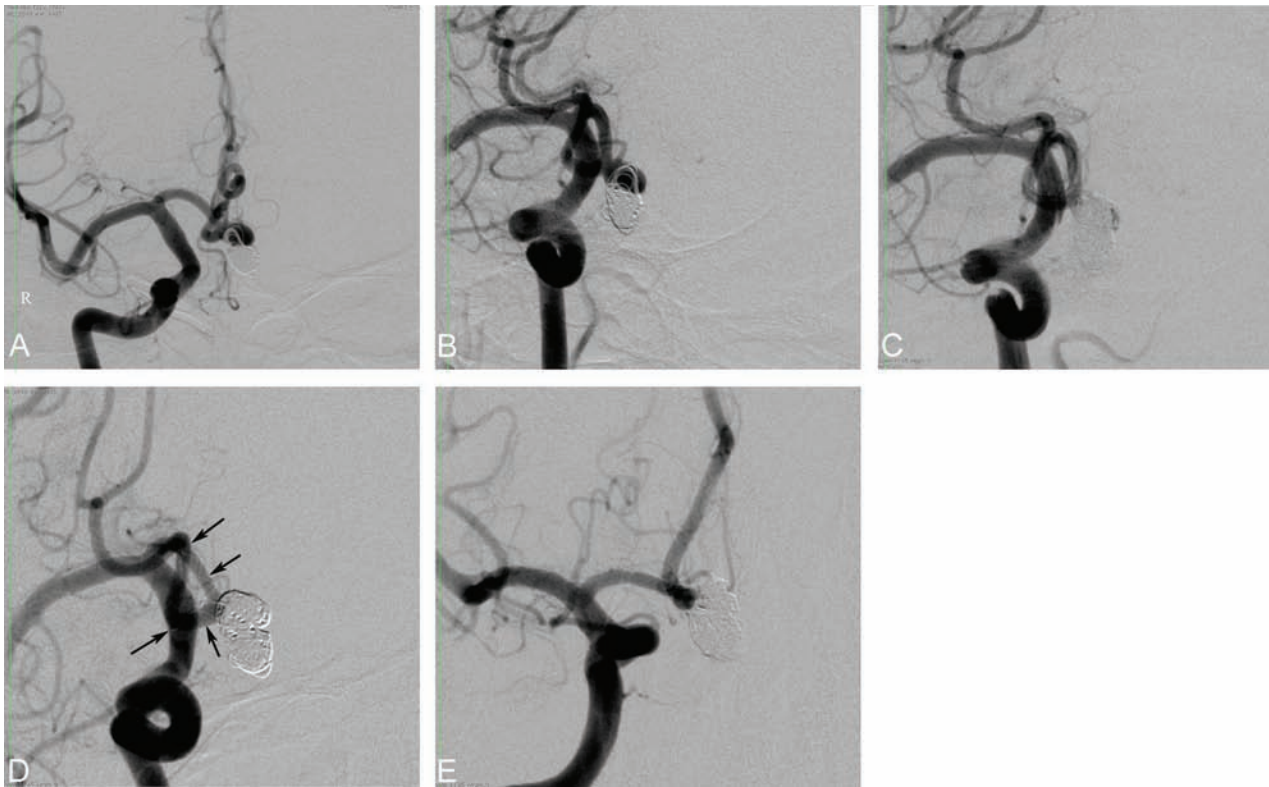


FIG 5. Procedural and follow-up angiographic images of a 53-year-old male patient with an AcomA aneurysm. *A* and *B*, Preprocedural DSA images show the recanalized AcomA aneurysm that was previously coiled. *C*, Postprocedural immediate DSA image reveals a partial filling of the aneurysm sac (Raymond class 3). *D* and *E*, Nine-month follow-up DSA images demonstrate complete occlusion (Raymond class 1) of the aneurysm as a result of progressive thrombosis during the follow-up period (*arrows* show the extension of the stent).

6.5% of aneurysms, and 5.2% of aneurysms required retreatment during follow-up.

Previous computational fluid dynamics studies demonstrated that stent placement caused a reduction of flow velocity in the aneurysm, and the flow-diversion effect was associated with the lower porosity of stents.²⁵ Enhanced flow-diversion capacity promotes the progressive thrombosis of the aneurysm and lowers the risk of recanalization.^{25,26} LEO Baby stents have a relatively high surface coverage ratio of approximately 18% and a small pore size, which create a relatively high flow-diversion capacity.²⁷ Therefore, the flow-diversion capacity of LEO Baby stents might contribute to the development of progressive thrombosis in partially coiled aneurysms by acting as a flow diverter. In support of this hypothesis, the successful treatment of dissecting wide-neck aneurysms by using telescopic implantation of LEO Baby stents without coiling was reported.¹⁰ The favorable midterm angiographic outcomes of this study suggest that LEO Baby SAC is a durable treatment for wide-neck intracranial aneurysms.

The overall complication rate, including asymptomatic minor events, was 11.3% in our study, which is consistent with that in previous studies. The procedure-related complication rate in a study of the Neuroform SAC of unruptured aneurysms was 12.1%.²⁸ A meta-analysis of the SAC literature conducted by Shapiro et al¹¹ revealed procedure-related complications in 19% of patients. Most of these complications in the current study remained asymptomatic, and only 3.8% of the patients had a permanent morbidity. Furthermore, the deficits in all patients with complications were mild to moderate,

with mRS scores of <3 at the last follow-up, and there was no mortality. Clajus et al²⁹ reported a morbidity of 3.9% and mortality of 2.9% for SAC treatment using Solitaire stents (Covidien, Irvine, California). Fiorella et al³⁰ reported that the rates of major ischemic stroke and neurovascular mortality were 8.8% and 2.8%, respectively, by using Neuroform SAC in 284 patients. A meta-analysis by Naggara et al³¹ showed that endovascular treatment of unruptured aneurysms was performed with a mortality rate of 1.2% and a morbidity rate of 4.8%. The morbidity and mortality rates of the current study are comparable with those reported in previous studies. The favorable clinical outcomes of patients in the current study suggest that LEO Baby SAC is a safe endovascular procedure for the treatment of wide-neck intracranial aneurysms.

In-stent stenosis is a previously defined late complication of stent-placement procedures. Fiorella et al³² reported that 5.8% of patients developed in-stent stenosis following the Neuroform SAC procedure. Another study reported that 3.4% of patients developed in-stent stenosis after Enterprise SAC on long-term follow-up.²¹ The in-stent stenosis incidence in the current study was quite high compared with those reported in previous studies. However, in-stent stenosis did not cause any symptoms or neurologic findings in our patients. The relatively high rate of progressive occlusion and the flow-diversion capacity of the LEO Baby stent suggest that in-stent stenosis is a consequence of the endothelial healing process that is induced by the stent.³⁰

There are some limitations to the current study: First, it was a nonrandomized retrospective study. Therefore, there was no

control group of potential alternative endovascular treatment methods. Second, follow-up angiography could not be performed in 3.7% of the patients until after the submission of this article.

CONCLUSIONS

We reported the results of the largest series of SAC by using a low-profile stent system, LEO Baby, for the treatment of wide-neck intracranial aneurysms. This study found that a high rate of complete aneurysm occlusion could be achieved by using LEO Baby SAC during the midterm, with an acceptable morbidity rate compared with the results of previous SAC studies. Although in-stent stenosis after LEO Baby SAC is a relatively common phenomenon, it appeared to remain asymptomatic during a midterm follow-up. The coiling of wide-neck intracranial aneurysms with the assistance of low-profile stents is a promising endovascular method.

REFERENCES

1. Molyneux AJ, Kerr RS, Yu LM, et al; International Subarachnoid Aneurysm Trial (ISAT) Collaborative Group. **International Subarachnoid Aneurysm Trial (ISAT) of neurosurgical clipping versus endovascular coiling in 2143 patients with ruptured intracranial aneurysms: a randomised comparison of effects on survival, dependency, seizures, rebleeding, subgroups, and aneurysm occlusion.** *Lancet* 2005;366:809–17
2. Crobeddu E, Lanzino G, Kallmes DF, et al. **Review of 2 decades of aneurysm-recurrence literature, part 2: managing recurrence after endovascular coiling.** *AJNR Am J Neuroradiol* 2013;34:481–85
3. Roy D. **Aneurysm recurrence after endovascular treatment** [in English, French]. *Neurochirurgie* 2012;58:97–102
4. Higashida RT, Smith W, Gress D, et al. **Intravascular stent and endovascular coil placement for a ruptured fusiform aneurysm of the basilar artery: case report and review of the literature.** *J Neurosurg* 1997;87:944–49
5. Akpek S, Arat A, Morsi H, et al. **Self-expandable stent-assisted coiling of wide-necked intracranial aneurysms: a single-center experience.** *AJNR Am J Neuroradiol* 2005;26:1223–31
6. Piotin M, Blanc R, Spelle L, et al. **Stent-assisted coiling of intracranial aneurysms: clinical and angiographic results in 216 consecutive aneurysms.** *Stroke* 2010;41:110–15
7. Behme D, Weber A, Kowoll A, et al. **Low-profile Visualized Intraluminal Support device (LVIS Jr) as a novel tool in the treatment of wide-necked intracranial aneurysms: initial experience in 32 cases.** *J Neurointerv Surg* 2015;7:281–85
8. Akmangit I, Aydin K, Sencer S, et al. **Dual stenting using low-profile LEO baby stents for the endovascular management of challenging intracranial aneurysms.** *AJNR Am J Neuroradiol* 2015;36:323–29
9. Roy D, Milot G, Raymond J. **Endovascular treatment of unruptured aneurysms.** *Stroke* 2001;32:1998–2004
10. Wanke I, Doerfler A, Schoch B, et al. **Treatment of wide-necked intracranial aneurysms with a self-expanding stent system: initial clinical experience.** *AJNR Am J Neuroradiol* 2003;24:1192–99
11. Shapiro M, Becske T, Sahlein D, et al. **Stent-supported aneurysm coiling: a literature survey of treatment and follow-up.** *AJNR Am J Neuroradiol* 2012;33:159–63
12. Möhlenbruch M, Herweh C, Behrens L, et al. **The LVIS Jr. microstent to assist coil embolization of wide-neck intracranial aneurysms: clinical study to assess safety and efficacy.** *Neuroradiology* 2014; 56:389–95
13. Cohen JE, Melamed I, Itshayek E. **X-microstenting and transmesh coiling in the management of wide-necked tent-like anterior communicating artery aneurysms.** *J Clin Neurosci* 2014;21:664–67
14. Conrad MD, Brasiense LB, Richie AN, et al. **Y stenting assisted coiling using a new low profile visible intraluminal support device for wide necked basilar tip aneurysms: a technical report.** *J Neurointerv Surg* 2014;6:296–300
15. LEO + & LEO + Baby [brochure]. Seoul: Mayabee Design Studio, Balt Extrusion; 2013
16. Maldonado IL, Machi P, Costalat V, et al. **Neuroform stent-assisted coiling of unruptured intracranial aneurysms: short- and midterm results from a single-center experience with 68 patients.** *AJNR Am J Neuroradiol* 2011;32:131–36
17. Lopes DK, Johnson AK, Kellogg RG, et al. **Long-term radiographic results of stent-assisted embolization of cerebral aneurysms.** *Neurosurgery* 2014;74:286–91
18. Poncyjusz W, Biliński P, Safranow K, et al. **The LVIS/LVIS Jr. stents in the treatment of wide-neck intracranial aneurysms: multicentre registry.** *J Neurointerv Surg* 2014 May 14. [Epub ahead of print]
19. Chalouhi N, Starke RM, Koltz MT, et al. **Stent-assisted coiling versus balloon remodeling of wide-neck aneurysms: comparison of angiographic outcomes.** *AJNR Am J Neuroradiol* 2013;34: 1987–92
20. Cantón G, Levy DI, Lasheras JC. **Hemodynamic changes due to stent placement in bifurcating intracranial aneurysms.** *J Neurosurg* 2005;103:146–55
21. Fargen KM, Hoh BL, Welch BG, et al. **Long-term results of Enterprise stent-assisted coiling of cerebral aneurysms.** *Neurosurgery* 2012;71:239–44
22. Lopes D, Sani S. **Histological postmortem study of an internal carotid artery aneurysm treated with the Neuroform stent.** *Neurosurgery* 2005;56:E416; discussion E416
23. Gory B, Klisch J, Bonafé A, et al. **Solitaire AB stent-assisted coiling of wide-necked intracranial aneurysms: mid-term results from the SOLARE study.** *Neurosurgery* 2014;75:215–19; discussion 219
24. Peng T, Qian Z, Liu A, et al. **Progressive occlusion of Enterprise stent-assisted coiling of ruptured wide-necked intracranial aneurysms and related factors on angiographic follow-up: a single-center experience with 468 patients.** *PLoS One* 2014;9:e92407
25. Kono K, Terada T. **Hemodynamics of 8 different configurations of stenting for bifurcation aneurysms.** *AJNR Am J Neuroradiol* 2013;34:1980–86
26. Chalouhi N, Jabbour P, Singhal S, et al. **Stent-assisted coiling of intracranial aneurysms: predictors of complications, recanalization, and outcome in 508 cases.** *Stroke* 2013;44:1348–53
27. Spiotta AM, Miranpuri A, Chaudry MI, et al. **Combined balloon stent technique with the Scepter C balloon and low-profile visualized intraluminal stent for the treatment of intracranial aneurysms.** *J Neurointerv Surg* 2013;5(suppl 3):iii79–iii82
28. Gentric JC, Biondi A, Piotin M, et al. **Safety and efficacy of Neuroform for treatment of intracranial aneurysms: a prospective, consecutive, French multicentric study.** *AJNR Am J Neuroradiol* 2013;34:1203–08
29. Clajus C, Sychra V, Strasilla C, et al. **Stent-assisted coil embolization of intracranial aneurysms using Solitaire AB neurovascular remodeling device: initial and mid-term follow-up results.** *Neuroradiology* 2013;55:629–38
30. Fiorella D, Albuquerque FC, Woo H, et al. **Neuroform stent assisted aneurysm treatment: evolving treatment strategies, complications and results of long term follow-up.** *J Neurointerv Surg* 2010;2:16–22
31. Naggara ON, Lecler A, Oppenheim C, et al. **Endovascular treatment of intracranial unruptured aneurysms: a systematic review of the literature on safety with emphasis on subgroup analyses.** *Radiology* 2012;263:828–35
32. Fiorella D, Albuquerque FC, Woo H, et al. **Neuroform in-stent stenosis: incidence, natural history, and treatment strategies.** *Neurosurgery* 2006;59:34–42; discussion 34–42

Single-Layer WEBs: Intrasaccular Flow Disrupters for Aneurysm Treatment—Feasibility Results from a European Study

J. Caroff, C. Mihalea, J. Klisch, C. Strasilla, A. Berlis, T. Patankar, W. Weber, D. Behme, E.A. Jacobsen, T. Liebig, S. Prothmann, C. Cognard, T. Finkenzeller, J. Moret, and L. Spelle



ABSTRACT

BACKGROUND AND PURPOSE: The safety and efficiency of the dual-layer Woven EndoBridge (WEB) device has already been published. However, this international multicenter study sought to evaluate the safety of single-layer devices, which are the newest generation of the WEB intrasaccular flow-disrupter family. They have been designed to offer smaller-sized devices with a lower profile to optimize navigability and delivery, which may, in turn, broaden their range of use.

MATERIALS AND METHODS: Data from all consecutive patients treated with a single-layer WEB device, in 10 European centers from June 2013 to May 2014 were included. Clinical presentations, technical details, intra- and perioperative complications, and outcomes at discharge were recorded. Clinical and angiographic data at last follow-up were also analyzed when available.

RESULTS: Ninety patients with 98 WEB-treated aneurysms were included in this study. In 93 cases (95%), WEB placement was possible. Complete occlusion at the end of the procedure was obtained in 26 instances (26%). Additional treatment during the procedure (coiling and/or stent placement) was necessary in 12 cases (12.7%). Procedure-related complications occurred in 13 cases, leading to permanent neurologic deficits in 4 patients (4.4%). Early vascular imaging follow-up data were available for 44 patients (57%), with an average time interval of 3.3 months. Treatment-related morbidity and mortality rates at last follow-up were 2.2% and 1.1%, respectively.

CONCLUSIONS: In this study, the feasibility and safety of the single-layer WEB device was comparable with that of the double-layer. However, further studies are needed to evaluate long-term efficacies.

ABBREVIATIONS: DL = dual-layer; WEB = Woven EndoBridge; SL = single-layer; SLS = single-layer sphere.

The Woven EndoBridge dual-layer device (WEB-DL; Sequent Medical, Aliso Viejo, California) is an intrasaccular flow-disruption device, initially developed to treat wide-neck bifurcation intracranial aneurysms. It has proved to be a highly feasible,

safe,¹⁻⁴ and efficient⁵ technique, particularly dedicated to the treatment of aneurysms challenging to treat with standard coiling.

The single-layer WEB (WEB-SL) device is the newest generation of the WEB family. Improved microbraiding technology allows a reduction in device size and profile, which optimizes navigability (through smaller catheters) and delivery. The purpose of this study was to evaluate the feasibility and safety of this new device, which has been available in Europe since 2013.

MATERIALS AND METHODS

Population

All patients with planned treatment with the WEB-SL device, in the 10 participating centers from June 2013 to May 2014, were consecutively included in this study. No exclusion criteria were used. The decision to use the WEB-single-layer device was made locally by the interventional teams and was based on aneurysm characteristics (size, wide-neck, bifurcation location, and so forth) in each case. It mostly corresponded to bifurcation aneurysms with aspect ratios of <1.2 , in which adjunctive techniques to coiling would have been required.⁶ Informed consent was obtained from all patients.

Received January 6, 2015; accepted after revision February 25.

From the Interventional Neuroradiology NEURI Center (J.C., C.M., J.M., L.S.), Beaujon Hospital, Clichy, France; Department of Neurosurgery (C.M.), University of Medicine and Pharmacy "Victor Babes," Timisoara, Romania; Department of Neuroradiology (J.K., C.S.), Helios General Hospital, Erfurt, Germany; Department of Diagnostic and Interventional Neuroradiology (A.B.), Klinikum Augsburg, Augsburg, Germany; MRI Department (T.P.), Leeds Teaching Hospitals National Health Service Trust, Leeds, UK; Interventional Neuroradiology (W.W.), Ruhr University Medical Center, Bochum, Germany; Departments of Radiology and Neuroradiology (D.B.), Klinikum Vest, Recklinghausen, Germany; Interventional Neuroradiology (E.A.J.), Oslo University Hospital, Oslo, Norway; Interventional Neuroradiology (T.L.), Universitätsklinik Köln, Köln, Germany; Abteilung für Diagnostische und Interventionelle Neuroradiologie (S.P.), Klinikum rechts der Isar, Technische Universität München, München, Germany; Interventional Neuroradiology (C.C.), Centre Hospitalier Universitaire Hôpital Purpan, Toulouse, France; and Interventional Neuroradiology (T.F.), Klinikum Nürnberg Süd, Nürnberg, Germany.

Please address correspondence to Jildaz Caroff, MD, Hôpital Beaujon, 100, Boulevard Général Leclerc, 92110 Clichy, France; e-mail: jildaz.caroff@bjn.aphp.fr; @jildaz

Indicates open access to non-subscribers at www.ajnr.org

<http://dx.doi.org/10.3174/ajnr.A4369>

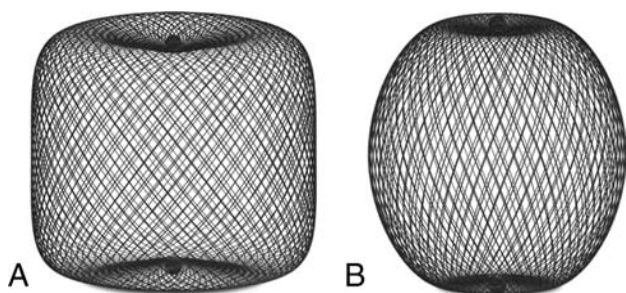


FIG 1. WEB-SL device family. A, The barrel-shaped WEB-SL, similar to the WEB-DL. B, The spheric WEB-SLS.

WEB Devices

The WEB-SL and WEB-single-layer sphere (SLS) are the latest generation of WEB devices and became available for use in 2013 (Fig 1). The WEB-SL is barrel-shaped (similar to the WEB-DL) and the WEB-SLS is spheric. They are available in various diameters, from 4 to 11 mm and heights from 3 to 9 mm. Unlike the WEB-DL, the WEB-SL and SLS devices can contain from 144 wires in the 4-mm-diameter devices to 216 wires in the 11-mm-diameter devices. They present a lower profile and were designed for use with the VIA-27 and VIA-33 catheters (Sequent Medical), which are 3F and 3.4F (outer diameter), respectively. The VIA-33 is dedicated to the WEB-SL and SLS devices with diameters of 10 mm and above.

Treatment Technique

Endovascular treatment was performed with the patient under general anesthesia and systemic heparinization. By the end of the procedure, the heparin therapy was discontinued but not reversed. Antiplatelet medications were used pre- and postoperatively, depending on local protocols and angiographic results. In 94% of cases, VIA catheters were used for WEB delivery. The use of antiplatelet agents in the pre- and postoperative periods was decided locally and for each case by the operator. Even if the use of an antiplatelet agent is not mandatory with the WEB device, depending on local habits, some patients were premedicated with aspirin and clopidogrel in case of a strategy shift to stent-assisted coiling.

Data Collection

For each aneurysm, we collected the following data retrospectively: age, sex, aneurysm location and biometry (maximum diameter, neck size, aspect ratio), rupture status, the modified Rankin Scale score at the time of admission and discharge, modalities of treatment (WEB type and size, associated medication and treatment), intraoperative complications (aneurysm rupture, thromboembolic events, deployment failure, WEB protrusion or migration), and postoperative complications (delayed bleeding, thromboembolic events). Immediate postoperative DSA, 3D rotational angiography, and VasoCT (Philips Healthcare, Best, the Netherlands)⁷ images were collected, along with any available follow-up imaging data (DSA, CTA, MRA).

Data Analysis

Data were self-reported by the different centers, but the principal investigators (J.C. and L.S.) performed a blinded review of the clinical and angiographic data, as an independent core laboratory not involved in patient care. Adverse events were adjudicated in-

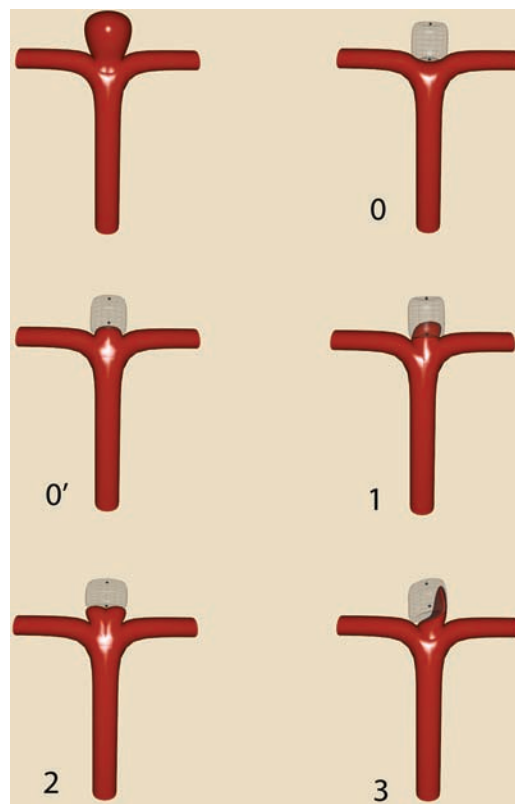


FIG 2. WEB occlusion scale. Grade 0 indicates complete occlusion. Grade 0' is similar but with opacification of the proximal recess, which may also be considered complete occlusion. Grade 1 signifies opacification inside the WEB. Grade 2 denotes a neck remnant. Grade 3 indicates an aneurysm remnant with contrast agent inside the sac between the wall and the WEB device.

dependently from operators. Permanent morbidity and mortality rates, subsequent to treatment, were evaluated at discharge and at follow-up when possible. Morbidity was defined as an mRS of >1 . When the preoperative mRS was >1 , morbidity was defined by any increase in the mRS score.

The principal investigators also independently assessed the degree of aneurysmal occlusion, by using a modified version of the Montreal 5-grade scale as previously published.⁸ The Beaujon Occlusion Scale Score is described as follows: 0 = no residual flow inside the aneurysm or the WEB, 0' = opacification of the proximal recess of the WEB, 1 = residual flow inside the WEB, 2 = neck remnant, 3 = aneurysm remnant, and 1 + 3 = contrast media depicted inside and around the device (Fig 2).

RESULTS

Population

Ninety patients (60 women and 30 men; age range, 26–83 years; median age, 55 years) with 98 WEB-treated aneurysms were included in this study. Of these, 65 aneurysms were unruptured (66%) (Fig 3). They were treated in 10 European centers with a median of 7.5 WEB implants per center.

It was determined that 38 aneurysms were located along the middle cerebral artery (38.8%); 21, along the anterior communicating artery (21.4%); 19, along the basilar artery (19.4%); and 15, along the supraclinoid internal carotid artery (15.3%). Aneurysm size varied from 3.7 to 39 mm (mean, 8.9 ± 5.5 mm), neck size

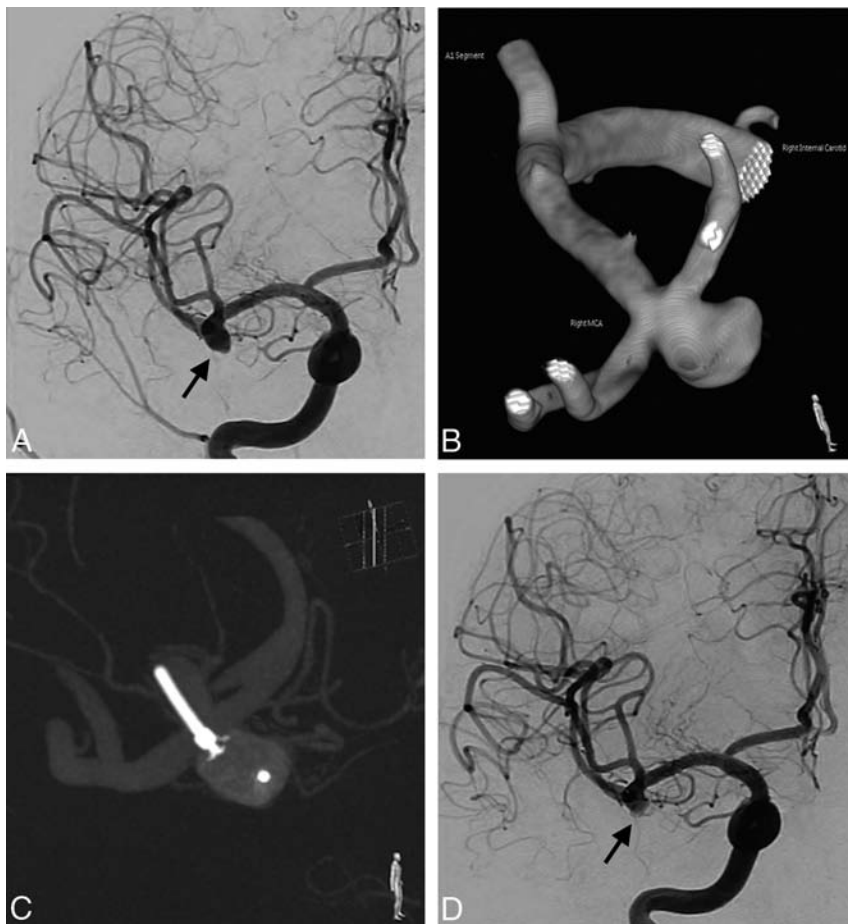


FIG 3. A 65-year-old man was admitted for the treatment of an asymptomatic aneurysm. Preoperative DSA showed a 6-mm right MCA bifurcation aneurysm (A). B, 3D rotational angiography before treatment. C, VasoCT before detachment confirmed the correct positioning of the WEB-SL. D, After WEB-SL deployment, postoperative DSA showed partial occlusion and stagnation of contrast agent inside the aneurysm. The Beaujon Occlusion Scale Score is 3.

varied from 2.0 to 12.3 mm (mean, 5.2 ± 2.1 mm), and the aspect ratio, defined as depth/neck, varied from 0.6 to 7.6 mm (mean, 1.6 ± 1.0 mm).

Treatment Feasibility

The WEB-SL device was successfully deployed inside the aneurysmal sac in 93 cases (95%). Deployment failures were attributed to device migration during detachment in 1 instance, while there were difficulties in achieving satisfactory positioning of the WEB before detachment in the other 4 cases. Of those 5 aneurysms, 3 were successfully treated with stent-assisted coiling, 1 case required a WEB-DL, and simple coiling was used in 1 case.

Additional Treatment

The necessity of additional coiling had been anticipated preoperatively, to manage large or giant aneurysms in 4 patients and to ensure immediate occlusion of a daughter bleb, in a fifth patient with a ruptured aneurysm. In 7 cases (8.2%), unplanned additional treatment had been required. In 5 of these cases, stent deployment was needed because of WEB protrusion into the parent artery (Fig 4). In the remaining 2 cases, additional coiling was performed to complete aneurysm occlusion after WEB deployment because of the presence of aneurysm remnants.

Protrusion

Postdelivery, major protrusion occurred in 14 cases. It required balloon remodeling in 5 and additional stent placement in 5. In 3 other cases, it led to clot formation, successfully treated with abciximab infusion in 2 cases and with mechanical thrombectomy in 1. In the last case, 1 branch occlusion occurred, resulting in an ischemic infarction. In 29 cases, a protrusion of only the proximal marker was depicted at the level of the bifurcation. In those situations, a postoperative antiplatelet regimen was prescribed at the physician's discretion.

Platelet Antiaggregation Therapy

One or 2 platelet antiaggregation agents were administered preoperatively to 27 patients (30%), while 60 patients (67%) were still given at least 1 antiplatelet therapy at discharge, mostly because of slight device protrusion in the parent artery.

Complication Rate

Procedure-related complications occurred in 13 cases. We observed 6 intraoperative thromboembolic complications, 4 of which were successfully managed (2 treated by intra-arterial infusion of abciximab; 1, by stent deployment; and another, by performing a thrombectomy by using a Solitaire stent [Covidien, Irvine, California]). The other 2 patients had arterial occlusion and hemiplegia. One recovered partially and was mRS 1 at last follow-up, and the

other was rated mRS 3.

We also observed 5 hemorrhagic complications. In 1 case, an aneurysmal rupture occurred due to a wire perforation but was immediately stopped after WEB delivery, and the patient remained asymptomatic. In another case, an occipital lobe parenchymal bleed occurred 4 days after the treatment of an anterior communicating artery aneurysm, and the patient still had hemianopsia at last follow-up. The patient had a history of uncontrolled hypertension and received double-antiplatelet therapy as a premedication.

The other 3 were ruptured cases, and early follow-up showed new parenchymal or subarachnoidal bleeding, which led to severe disability in 1 patient, seizures in the second patient, and death in the last patient. In the first one, an aneurysmal bleb was occluded by 1 coil, then the aneurysm itself was treated with a WEB, stagnation was obtained inside the sac, but 6 hours later a large parenchymal hematoma was depicted. In the second one, with a multilobulated anterior communicating artery aneurysm, only partial occlusion was obtained after WEB delivery. A nonoccluded part of the aneurysm, initially misjudged as a nonpotential source of bleeding, was secondarily coiled after rebleeding was revealed by seizures. The last case was one of major and diffuse SAH. Three potential ruptured aneurysms were discovered; 1 was treated with coils, and other 2, with the WEB-SL.



FIG 4. A 59-year-old woman was admitted for the treatment of an unruptured anterior communicating artery aneurysm. *A*, Preoperative DSA. *B*, After WEB-SL deployment, a protrusion occurred in the right A2 segment, leading to a significant stenosis (*black arrow*). The proximal marker is also depicted within the parent artery. *C*, A laser cut Enterprise stent (Codman & Shurtleff, Raynham, Massachusetts) was then delivered to restore the caliber of the artery. The Beaujon Occlusion Scale Score is 0. *D*, Final VasoCT confirmed satisfactory positioning of the stent without any protrusion of the WEB (*arrows* show the 2 radio-opaque markers of the WEB-SL).

Massive rebleeding predominantly located in the right Sylvian fissure occurred 3 hours after treatment, leading to death. The lesions that were most likely to be the cause of the recurrent fatal hemorrhage were probably 1 of the 2 right MCA aneurysms. One was treated with coils, and 1, with the WEB-SL. After treatment, those 3 patients were kept under at least 1 antiplatelet agent because of device protrusion.

A distal migration of the WEB device during removal, due to an incomplete detachment, was noted in 1 instance. It was impossible to recapture the device in the M1 segment. While we tried to

recapture it, it finally migrated into an M2 branch in a nondeployed fashion without flow repercussions. The patient remained asymptomatic under double antiplatelet therapy, and no ischemic lesions were observed on imaging follow-up.

One patient was mRS 1 at discharge due to a postoperative iliac artery occlusion.

Data from early clinical follow-ups were available for 52 patients (58%), with an average time interval of 3.8 months. Treatment-related morbidity and mortality rates at last follow-up were 2.2% and 1.1%, respectively.

Immediate Results

Immediate angiographic evaluation showed 27 cases (28%) of complete occlusion, 2 neck remnants, and a stagnation of iodine contrast agent in the aneurysm in all other cases.

Angiographic Follow-Up

Short-term vascular imaging follow-ups were available in 69 cases (70%), including DSA data in 54 cases, and the average time interval to follow-up was 3.3 months. Satisfactory results (complete occlusion or small neck remnants) were achieved in 45 patients (65%). In 8 cases, contrast opacification agent was still observed inside the device at that time.

DISCUSSION

The work presented here is the largest WEB study undertaken to date, wherein WEB-SL devices were used to treat aneurysms that would normally be considered difficult to treat with traditional endovascular approaches. Most of the treated aneurysms were wide-neck (average, 5.1 mm), with unfavorable anatomy (average aspect ratio, 1.6). Brinjikji et al⁶ defined 2 thresholds based on the aspect ratio value, to define the possible strategy of endovascular treatments. They reported that in cases with a value below 1.2 (39% of cases in our study), adjunctive techniques are almost always

necessary. Usually, an aspect ratio of >1.6 implied that adjunctive techniques were not required. In our study, 69% of cases presented a lower ratio than this.

Most lesions were bifurcation aneurysms (86%). Approximately 40% were middle cerebral artery aneurysms, 20% were anterior communicating artery aneurysms, and 20% were basilar tip aneurysms.

Within this study, 34% of cases were ruptured aneurysms, which is much higher than the percentage in other WEB series. In

contrast to our previous observations, from investigation of a smaller cohort,⁸ 3 patients had rebleeding after WEB treatment. At the end of the procedure, contrast agent stagnation was detected in the proximal part of those aneurysms, but complete occlusion was not yet achieved. After the endovascular treatment, those 3 patients were kept under at least 1 antiplatelet agent, and this could have influenced this relatively high rebleeding rate.

Despite the fact that aneurysm geometry was unfavorable in our study, the procedure-related complication rate was low (13%) and comparable with that obtained from the largest WEB-DL study (10.8%).¹ The rupture rate during treatment was low (1%) and was, in fact, unrelated to WEB delivery but was caused by guidewire perforation during catheterization of the sac. Bleeding was controlled by rapid WEB delivery, and the patient remained asymptomatic.

Treatment-related morbidity and mortality rates at last follow-up were 2.2% and 1.1%, respectively. Finally, safety results from this WEB-SL study are similar to those in other published WEB-DL studies. Indeed those authors reported morbidity (mRS of >2) rates between 1.3% and 6.7% and mortality rates between 0% and 2.2%.^{1,3,5} These results are also comparable with those obtained from neurosurgical clipping of unruptured aneurysms (6.7% overall morbidity, 1.7% mortality)⁹ and non-WEB endovascular treatment of unruptured aneurysms (2.5% morbidity, 1.8% mortality).⁹

An antiplatelet premedication was used in 30% of cases (aspirin and clopidogrel) because if during a procedure, WEB treatment appears to be unsuitable, another alternative therapy can be stent-assisted coiling for these wide-neck aneurysms. In 67% of cases, at least 1 antiplatelet agent was still used at discharge. It was given either in cases of device protrusion in the parent artery or sometimes only because of proximal marker protrusion, though the need for antiplatelets in those situations is not mandatory.

This study was not intended for the evaluation of anatomic results subsequent to WEB-SL treatment. Early follow-up vascular imaging was available in a large number of cases (70%), and it consisted of DSA data in half of these cases. These data demonstrated a low rate of satisfactory results (65%), which could probably improve during follow-up because in some cases, stagnation was depicted inside the WEB and patients were still kept under antiplatelet therapy at that time. In a WEB-DL article⁵ with a short-term imaging follow-up (average length, 5.0 months), authors reported complete occlusion in 57% of cases; in our series, it was obtained in only 38% of cases. However, as with flow-diverter stents, delayed thrombosis should be expected. Therefore, results must be reviewed after longer time intervals.

This study has several limitations. First the number of treated cases for each center is low and mostly corresponds to an initial experience for the operators with this new device. The complications were self-reported. Angiographic outcome is now still limited, but it appeared important for us to report these preliminary results before analysis of long-term follow-up imaging to evaluate the efficiency of the WEB-SL device.

CONCLUSIONS

In this study, the feasibility and safety of the single-layer WEB device was comparable with that of the double-layer device. However, further studies are needed to evaluate long-term efficacies.

ACKNOWLEDGMENTS

The authors thank Dr Francesco D'Argento from Policlinico A. Gemelli in Roma for his elegant work on the illustrations.

Disclosures: Joachim Klisch—RELATED: Consulting Fee or Honorarium: consultant to Sequent Medical.* Ansgar Berlis—RELATED: Consulting Fee or Honorarium: consultancy agreement for proctoring with Sequent Medical; UNRELATED: Consultancy: consultancy agreements for proctoring with Covidien and MicroVention; Payment for Lectures (including service on Speakers Bureaus): honorarium for lectures from Penumbra and Stryker. Tufail Patankar—UNRELATED: Travel/Accommodations/Meeting Expenses Unrelated to Activities Listed: travel expense paid by Sequent Medical to present Web data in Val d'Isère 2015; Other: proctor for Sequent Medical. Werner Weber—UNRELATED: Payment for Lectures (including service on Speakers Bureaus): Sequent Medical (lectures); Other: Sequent Medical (proctoring). Daniel Behme—RELATED: Consulting Fee or Honorarium: speaking honoraria, German Society of Neurosurgery meeting in Dresden 2014; Support for Travel to Meetings for the Study or Other Purposes: Sequent Medical; UNRELATED: Payment for Manuscript Preparation: Penumbra, Comments: Separator 3D Series; Travel/Accommodations/Meeting Expenses Unrelated to Activities Listed: Penumbra, Comments: Anatomy Biology Clinical correlations – Working group in Interventional Neuroradiology (ABC WIN) meeting in Val d'Isère 2014 and 2015. Eva Astrid Jacobsen—RELATED: Support for Travel to Meetings for the Study or Other Purposes: MicroVention, Comments: registration fee to Live Interventional Neuroradiology and Neurosurgery Course (LINNC) meeting in Paris 2014. Thomas Liebig—RELATED: Consulting Fee or Honorarium: proctoring and consulting for Sequent Medical; Support for Travel to Meetings for the Study or Other Purposes: Sequent Medical, Comments: reimbursement of traveling and meeting admission fees; UNRELATED: Consultancy: consulting for Acandis, MicroVention, and Stryker. Sascha Prothmann—UNRELATED: Consultancy: phenox, Bochum, Germany (proctor); Payment for Lectures (including service on Speakers Bureaus): Boston Scientific, Covidien, Comments: oral presentation (workshop) at Third Munich Aortic and Carotid conference 2013 (Boston Scientific), oral presentation (workshop) at European Society of Neuroradiology Annual Meeting, Frankfurt, 2013 (Covidien). Christophe Cognard—UNRELATED: Consultancy: Stryker, MicroVention, Codman, Covidien. Jacques Moret—UNRELATED: Board Membership: Covidien; Consultancy: Covidien, MicroVention. Laurent Spelle—UNRELATED: Consultancy: Stryker, Sequent Medical, Medtronic. *Money paid to the institution.

REFERENCES

1. Papagiannaki C, Spelle L, Januel AC, et al. **WEB intrasaccular flow disruptor—prospective, multicenter experience in 83 patients with 85 aneurysms.** *AJNR Am J Neuroradiol* 2014;35:2106–11
2. Pierot L, Liebig T, Sychra V, et al. **Intrasaccular flow-disruption treatment of intracranial aneurysms: preliminary results of a multicenter clinical study.** *AJNR Am J Neuroradiol* 2012;33:1232–38
3. Pierot L, Klisch J, Cognard C, et al. **Endovascular WEB flow disruption in middle cerebral artery aneurysms: preliminary feasibility, clinical, and anatomical results in a multicenter study.** *Neurosurgery* 2013;73:27–34; discussion 34–35
4. Lubicz B, Mine B, Collignon L, et al. **WEB device for endovascular treatment of wide-neck bifurcation aneurysms.** *AJNR Am J Neuroradiol* 2013;34:1209–14
5. Lubicz B, Klisch J, Gauvrit JY, et al. **WEB-DL endovascular treatment of wide-neck bifurcation aneurysms: short- and midterm results in a European study.** *AJNR Am J Neuroradiol* 2014;35:432–38
6. Brinjikji W, Cloft HJ, Kallmes DF. **Difficult aneurysms for endovascular treatment: overdue or undertall?** *AJNR Am J Neuroradiol* 2009;30:1513–17
7. Caroff J, Mihalea C, Neki H, et al. **Role of C-arm VasoCT in the use of endovascular WEB flow disruption in intracranial aneurysm treatment.** *AJNR Am J Neuroradiol* 2014;35:1353–57
8. Caroff J, Mihalea C, D'Argento F, et al. **Woven EndoBridge (WEB) device for endovascular treatment of ruptured intracranial wide-neck aneurysms: a single-center experience.** *Neuroradiology* 2014;56:755–61
9. Kotowski M, Naggara O, Darsaut TE, et al. **Safety and occlusion rates of surgical treatment of unruptured intracranial aneurysms: a systematic review and meta-analysis of the literature from 1990 to 2011.** *J Neurol Neurosurg Psychiatry* 2013;84:42–48

Combined Use of Mechanical Thrombectomy with Angioplasty and Stenting for Acute Basilar Occlusions with Underlying Severe Intracranial Vertebrobasilar Stenosis: Preliminary Experience from a Single Chinese Center

F. Gao, W.T. Lo, X. Sun, D.P. Mo, N. Ma, and Z.R. Miao



ABSTRACT

BACKGROUND AND PURPOSE: Acute basilar occlusions have a poor prognosis without recanalization. Many have underlying severe atherosclerotic intracranial stenosis coexisting with acute thrombosis, requiring treatment of both pathologies in the same session, though technical risks may be encountered. The purpose of this study was to evaluate the technical feasibility and safety of combined treatment by using stent retrievers for the thrombosis, together with angioplasty and stent placement for the underlying stenosis.

MATERIALS AND METHODS: This was a retrospective review of 13 patients with basilar occlusions treated with thrombectomy by the Solitaire stent retriever and angioplasty and intracranial stent placement for underlying severe vertebrobasilar stenosis in the same session. Reperfusion was assessed in terms of the TIC1 score. Perioperative complications were recorded. Clinical outcomes were assessed by the NIHSS at discharge and the mRS on follow-up at 90 days.

RESULTS: Of the 30 patients with acute basilar artery occlusions treated with stent retrievers during the study period, 18 had coexisting severe intracranial stenosis. Thirteen patients meeting the criteria for our study received combined mechanical thrombectomy and angioplasty with stent placement. The successful recanalization rate was 100%. Distal vessel embolizations occurred in 3 patients. There were 2 mortalities. On discharge, 10 patients (77%) had an improvement in NIHSS of ≥ 10 points. At 90 days, 6 patients (46%) had a good functional outcome with an mRS of ≤ 2 .

CONCLUSIONS: The combined use of mechanical thrombectomy with angioplasty and stent placement for acute basilar occlusions with underlying severe intracranial atherosclerotic stenosis is technically feasible and safe.

ABBREVIATIONS: BAO = basilar artery occlusion; PTA = percutaneous transluminal angioplasty

Acute basilar artery occlusion (BAO) carries a high morbidity and mortality. Among patients treated conventionally with antiplatelets or anticoagulation, the death and dependency rate was 80%.¹ Even with intravenous or intra-arterial thrombolysis, the overall death or dependency rate is not much improved. Without recanalization, the mortality can be up to 85%–95% and the likelihood of good outcome was only 2%.² The mechanism of occlusion includes acute local thrombosis over an underlying severe atherosclerotic stenosis and embolization from distant

sources. There has not yet been any epidemiologic data on the proportion of acute BAO attributed to atherosclerotic stenosis in Asians, though deducing from the higher prevalence of intracranial atherosclerosis observed in Asians, and especially in the Chinese population,³ the proportion of patients with BAO and underlying atherosclerotic stenosis may be higher than the 26%–36% reported on imaging studies from the white population.⁴ For the treatment of BAO, mechanical thrombectomy with stent retrievers has emerged in recent years as a promising method with a higher recanalization rate and better functional outcome.^{5,6} However, for those with underlying severe stenosis, there have been concerns over the feasibility and safety of these devices: Reperfusion may fail to be achieved by mechanical thrombectomy devices alone in patients with severe stenosis⁷; retrieval of the stent retrievers past the stenosis may damage the endothelium or the atherosclerotic plaque, leading to an increased risk of acute thrombosis and reocclusion; and the resistance posed by the stenosis may cause distortion of the natural course of the vessel during the tug of the retrievers past the stenosis, leading to tearing of

Received December 15, 2014; accepted after revision March 9, 2015.

From the Department of Interventional Neurology (F.G., X.S., D.P.M., N.M., Z.R.M.), Beijing Tiantan Hospital, Capital Medical University; China National Clinical Research Center for Neurological Diseases; Center of Stroke, Beijing Institute for Brain Disorders; Beijing, China; and Department of Medicine (W.T.L.), Queen Elizabeth Hospital, Hong Kong, China.

Please address correspondence to ZhongRong Miao, MD, Department of Interventional Neurology, Beijing Tiantan Hospital, Capital Medical University, 6 Tiantan Xili, Dongcheng District, Beijing 100050, China; e-mail: zhongrongm@163.com

Indicates article with supplemental on-line table.

<http://dx.doi.org/10.3174/ajnr.A4364>

the perforator vessels and intracerebral hemorrhage. We hereby report our experience with 13 patients treated with a combination of mechanical thrombectomy with the Solitaire device (Covidien, Irvine, California) for the thrombosis and angioplasty with stent placement for the underlying stenosis.

MATERIALS AND METHODS

Patients

This was a retrospective analysis of 30 patients with acute basilar artery occlusion who had undergone endovascular treatment with stent retrievers in our hospital from June 2012 to June 2014. Eighteen of these 30 patients were found to have underlying severe atherosclerotic intracranial vertebrobasilar stenosis. Thirteen patients fulfilling the following criteria were reviewed in this study: 1) an acute BAO presenting within 24 hours of symptom onset; 2) an NIHSS score of ≥ 8 on presentation; 3) no established large brain stem or cerebellar infarct on admission imaging studies, defined as involvement of more than two-thirds of the brain stem or cerebellum; 4) underlying severe stenosis of the intracranial vertebrobasilar artery of $\geq 70\%$ on DSA; 5) ≥ 1 vascular risk factor for atherosclerosis present (eg, diabetes, hypertension); and 6) a premorbid mRS of ≤ 2 . Five patients were excluded in our analysis: 3 due to presentation >24 hours from symptom onset with progressive deterioration and 2 due to large brain stem infarct size on admission imaging. The endovascular treatment for the latter 2 patients was performed in the initial phase of our acute stroke interventional service.

All patients had an assessment performed by a stroke neurologist on admission, and the NIHSS score was recorded. Multimodal MR imaging (including DWI, MRA, and MR perfusion studies) was performed on admission unless contraindicated, in which case cerebral CT, CTA, and CTP studies were performed. Baseline demographics, admission NIHSS and mRS scores, symptom-to-door time, needle-to-recanalization time, and door-to-recanalization time were documented. For patients with unknown symptom-onset time, the last known normal-to-onset time was taken as the symptom-to-onset time. The NIHSS score on discharge and the mRS score on follow-up at 90 days were recorded.

This study was approved by the institutional ethics committee, which also waived informed consent due to the retrospective nature of this study.

Interventional Procedure

With the patient under general anesthesia and by using transfemoral access, we advanced a 6F guiding catheter into the V2 segment of the vertebral artery. Intravenous heparin was given, aiming for an activated clotting time of 250–300 seconds. A microcatheter (Rebar microcatheter; Covidien) was carefully navigated through the basilar occlusion over a 0.014-inch microwire (Transend; Stryker, Kalamazoo, Michigan) under fluoroscopic guidance. Angiographic runs via the microcatheter were performed to confirm its location in the target artery with its tip distal to the thrombus. The Solitaire AB device was used for mechanical thrombectomy in our center. After advancement of the Solitaire via the microcatheter to the occluded segment, the stent retriever was unsheathed and allowed full expansion through the throm-

bus, acting as a transient endovascular bypass to restore flow across the occluded segment, and angiography was performed to assess the distal vessel flow. The fully deployed Solitaire device was then partially resheathed, and together with the delivery microcatheter, gently pulled back as a single unit, and recovered for thrombectomy. If this failed or recanalization was insufficient, further retrievals would be attempted. Angioplasty and stent placement would be considered if there was underlying severe vertebrobasilar stenosis causing inadequate distal perfusion, or new thrombus formation or reocclusion was noted at the site of residual stenosis on repeat angiography up to 30 minutes after thrombectomy. A loading dose of aspirin, 300 mg, and clopidogrel, 300 mg, was given via nasogastric tube to patients without prior use of antiplatelets once the decision to proceed to stent placement was made. Pantoprazole was given for gastric protection. Stent placement was done with either the balloon-mounted Apollo stent (MicroPort Medical [Shanghai], Shanghai, China) (Fig 1) or the self-expanding Wingspan stent (manufactured by Stryker for Boston Scientific, Natick, Massachusetts) (Fig 2). These stents have an advantage over detachment of the Solitaire AB device used as a stent because they provide a stronger radial force to overcome the underlying stenosis. Device selection depends on the vessel characteristics and lesion morphology, as previously described.⁸ For patients with tortuous arterial access and anticipated difficulty for stent passage, only percutaneous transluminal angioplasty (PTA) was performed. If patients were noted to have acute thrombosis over the stent or significant residual thrombosis impeding forward blood flow, glycoprotein IIb/IIIa inhibitor infusion (tirofiban) would be given.

Follow-up CT was performed immediately postoperatively to exclude intracerebral hemorrhage. Transcranial Doppler, CTA, MRA, or DSA would be performed within 24 hours postintervention to assess the patency of the basilar artery. Patients were maintained on dual-antiplatelet therapy of aspirin, 100 mg, and clopidogrel, 75 mg, for 3 months, followed by single-antiplatelet therapy life-long. Thromboelastography was arranged to check for platelet function, and CYP219 testing, to check for genetic resistance to clopidogrel. However, initial choice of antiplatelets was not based on these results because the interventions had been performed as an emergency operation and the results were not available before the operation. All patients were put on statins aiming for a low-density lipoprotein of <1.8 and on antihypertensives aiming for a systolic blood pressure of <140 mm Hg. Patients were followed up at 90 days by clinic visit or by phone if they could not attend follow-up. Follow-up imaging by CT angiography was arranged.

Outcome Measures

The primary outcome measure was the successful reperfusion rate, defined as a TICI grade 2b or 3 after endovascular treatment. The other outcome measures recorded were the intraoperative complications, including vessel perforation, arterial dissection, symptomatic intracerebral hemorrhage, and any other in-hospital neurologic complications. Clinical outcomes were the NIHSS score on discharge, functional outcome, and vascular-related mortality at 90 days. A good functional outcome was defined as an mRS of ≤ 2 .

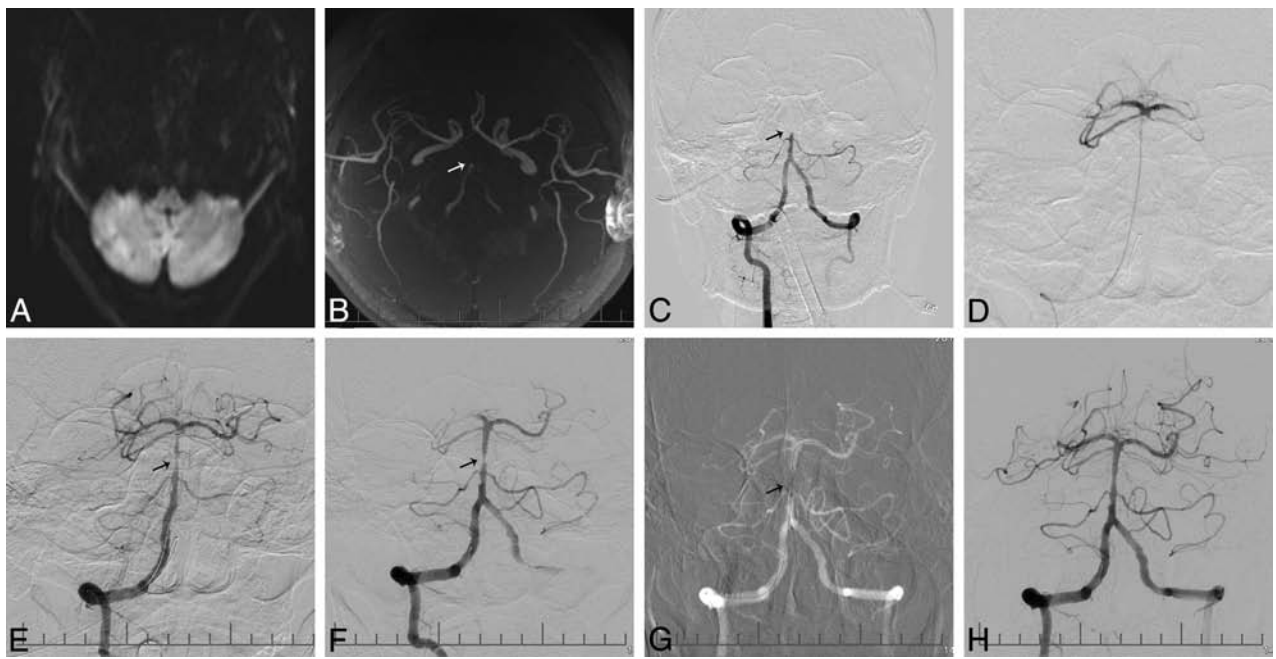


FIG 1. A 54-year-old male patient who presented with vertigo and decreased consciousness for 10 hours. *A*, MR imaging shows multiple infarcts over the bilateral cerebellar hemispheres on DWI. *B*, MRA shows basilar artery occlusion (*arrow*). *C*, A right vertebral angiogram shows occlusion of the basilar artery (*arrow*). *D*, An angiogram after crossing of the basilar artery occlusion with a microcatheter shows patent distal flow at the basilar artery tip, with opacification of both posterior cerebral arteries and superior cerebellar arteries. *E*, Angiogram after deployment of the Solitaire AB device shows restoration of flow in the basilar artery, with suspected thrombus and focal stenosis (*arrow*) in the mid-distal segment of the basilar artery. *F*, Angiogram post-mechanical thrombectomy shows underlying severe focal stenosis of the basilar artery (*arrow*). *G*, Deployment of an Apollo stent (*arrow*) at the site of the basilar artery stenosis. *H*, Final angiography shows a TIC1 flow of grade 3 in the basilar artery with good distal perfusion.

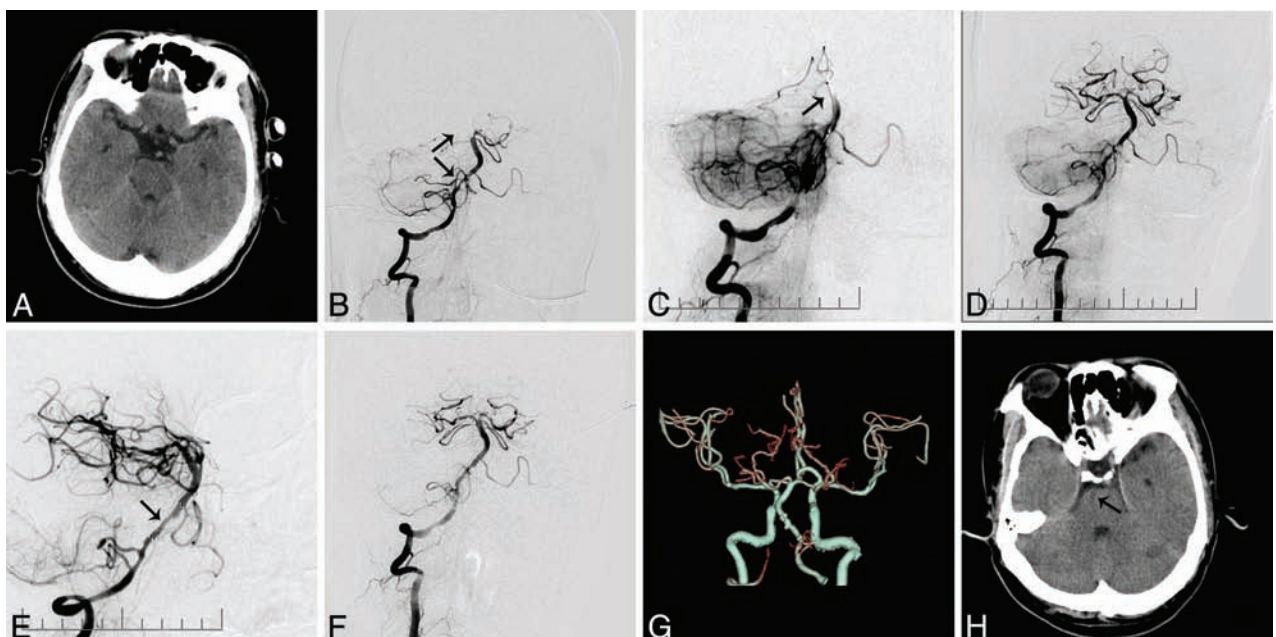


FIG 2. A 55-year-old male patient who presented with tetraparesis and decreased consciousness for 6 hours. *A*, Plain CT on admission does not reveal any large territory infarct. *B*, The right vertebral angiography shows occlusion at the tip of the basilar artery (*arrow*) and right posterior cerebral artery and severe stenosis of the right vertebrobasilar junction (*arrows*). *C*, Angiography postdeployment of the Solitaire AB device at the proximal right posterior cerebral artery shows no opacification of the distal basilar artery (*arrow*). *D*, Angiography post-mechanical thrombectomy shows opacification of the distal basilar artery and both posterior cerebral arteries and severe stenosis in the vertebrobasilar junction. *E*, Deployment of a Wingspan stent (*arrow*) at the vertebrobasilar junction. *F*, Right vertebral angiography after stent placement shows resolution of the proximal basilar artery stenosis and good contrast flow in the basilar artery (TIC1 grade 3). *G-H*, Follow-up CT and CTA at 24 hours show a patent basilar artery and a small right pontine infarct.

Summary of patient characteristics, treatment, and outcome

	No. of Patients (N = 13)
Male sex	11 (84.6%)
Age (mean \pm SD) (yr)	56 \pm 6.2
Pretreatment NIHSS (mean \pm SD)	26 \pm 4
Symptom-to-door time (mean \pm SD) (min)	587 \pm 341
Needle-to-recanalization (mean \pm SD) (min)	93 \pm 28
Door-to-reperfusion (mean \pm SD) (min)	301 \pm 117
Underlying site of stenosis	
BA	10 (76.9%)
V4	3 (13%)
Endovascular treatment for the stenosis	
PTA alone	3 (23.1%)
Apollo stent	3 (23.1%)
Wingspan stent	7 (53.8%)
Glycoprotein IIb/IIIa inhibitor	6 (46.2%)
Pre-PTA/stenting stenosis (mean \pm SD)	91.5 \pm 2.4%
Post-PTA/stenting stenosis (mean \pm SD)	24.6 \pm 12.6%
Pre-PTA/stenting TIC1 (post-mechanical thrombectomy)	
0	2 (5.4%)
1	7 (53.8%)
2a	4 (30.8%)
Post-PTA/stenting TIC1	
2b	3 (23.1%)
3	10 (76.9%)
Distal embolization to PCA/cerebellar arteries	3 (23.1%)
Outcome	
NIHSS score on discharge for surviving patients (mean \pm SD)	12 \pm 6
% of patients with NIHSS \geq 10-point improvement	10 (79.9%)
Mortality on discharge	2 (15.3%)
mRS at 90 days	
mRS 0–2	6 (46.2%)
mRS 0–3	9 (69.2%)
Ischemic events at 90-day follow-up	0 (0%)

Note:—BA indicates basilar artery; PCA, posterior cerebral artery; V4, vertebral artery V4 segment.

RESULTS

Eighteen of the 30 patients (60%) with acute BAO in our study who were treated with stent retrievers had underlying severe intracranial vertebrobasilar stenosis. Thirteen patients satisfied our study criteria. The mean age was 56 years. The mean baseline NIHSS score was 26 (range, 19–34). All patients presented outside the time window for intravenous thrombolysis, apart from 1 inpatient with known basilar stenosis deteriorating acutely during admission; hence, endovascular therapy was arranged immediately. The mean symptom onset-to-door, needle-to-recanalization, and door-to-recanalization times were 587, 93, and 301 minutes, respectively (Table and On-line Table).

After initial mechanical thrombectomy (average, 1.4 passes), all 13 patients had a TIC1 score of \leq 2a. Because satisfactory reperfusion was not achieved and underlying severe stenosis was noted, 10 patients had stent placement performed and 3 received PTA alone due to tortuous artery access. The site of the underlying severe stenosis was the basilar artery for 10 patients and the vertebral artery V4 segment for 3 patients. Six patients were given supplementary glycoprotein IIb/IIIa inhibitor for acute new thrombosis or significant residual thrombosis noted. The overall rate of successful reperfusion (final TIC1 2b to 3) was 100%. The mean residual stenosis was 24.6%. Three patients had distal em-

bolization to the posterior cerebral arteries or the cerebellar arteries on angiography during the procedure. No patient had vessel rupture or dissection. There were 2 mortalities. One patient developed a large-territory infarct and cerebral edema. Another patient died due to severe gastrointestinal bleeding possibly related to reactive gastritis aggravated by the use of dual antiplatelets. On discharge, an improvement of the NIHSS score of \geq 10 points was noted for 10 patients (76.9%). No patients were lost to follow-up. At 90 days, 6 patients had a good functional outcome with an mRS \leq 2, which represented 46% (6/13) of all patients and 54.5% (6/11) of the survivors. None of the patients developed recurrent ischemic attacks. Five patients had follow-up imaging by CT angiography at 90 days, with no restenosis or reocclusion demonstrated. All patients had CYP2C19 checked for clopidogrel resistance, and all had normal findings. Four patients had thromboelastography testing, and none showed aspirin resistance.

For the 5 patients who did not meet the inclusion criteria for our study, all had successful recanalization after thrombectomy and stent placement. One patient with a large brain stem infarct on admission imaging further deteriorated and died on day 2. Follow-up imaging of this patient showed cerebral edema with no hemorrhagic transformation. For the 4 patients who survived, 1 patient had an mRS of 2 and 3 patients had an mRS of $>$ 3 on follow-up at 90 days.

DISCUSSION

This case series selectively studied 13 patients with acute basilar occlusions, requiring combined mechanical thrombectomy for the thrombosis and stent placement for the underlying stenosis, performed in the same session. The prognosis of acute BAO in general is poor. Current studies have reported an improved outcome achieving a recanalization rate from 74% to 100% in recent years with the use of stent retrievers,^{9,10} but these studies were on acute BAO in general and the outcome of the patients had not been stratified according to whether there was underlying severe stenosis, probably due to the small absolute number of patients in the studies.^{9,11–14} The exact incidence of acute BAO with underlying severe stenosis is unknown. Extrapolation from case reports on patients with acute BAO treated by endovascular means requiring additional angioplasty or stent placement for underlying severe intracranial stenosis showed an approximate incidence of 14%–29% in studies of the white population.^{9,11–13} In our registry, having underlying stenosis was not uncommon; 60% (18/30) had severe intracranial stenosis requiring additional angioplasty or stent placement. We believe that other centers will also encounter similar patients, especially when treating patients from Asian countries where intracranial stenosis is more prevalent.³

Patients with combined thrombosis and underlying stenosis represent a distinct group in management, because they have a different technical risk profile and a good outcome is dependent on the treatment of both the thrombosis and the severe stenosis. All 13 patients in our analysis had the stent placement performed in the same session as the thrombectomy, rather than as a staged operation, because they could not achieve timely satisfactory reperfusion after thrombectomy alone without treatment of the stenosis. Possible reasons for failure to attain good reperfusion included flow limitation by the proximal stenosis or new thrombus

formation possibly aggravated by endothelial injury from the passage of the mechanical thrombectomy device through the stenosis. The negative Stenting vs Aggressive Medical Management for Preventing Recurrent Stroke in Intracranial Stenosis trial, which had raised concerns about the safety of intracranial stent placement,¹⁵ had been a study on secondary stroke prevention for a group of relatively more stable patients for whom a low operative risk was imperative to gain benefit over medical treatment. However, for our patients with BAO presenting acutely with severe neurologic deficits and a high risk of further deterioration and death if timely reperfusion could not be achieved, angioplasty and stent placement could be regarded as a brain- or life-saving attempt for this group with poor prognosis. Moreover, the potential immediate endothelial damage after the passage of the mechanical thrombectomy device past the stenosis might lead to an increased risk of early reocclusion if stent placement was not attempted or stalled.

For our patients, thrombectomy was first performed with stent retrievers, followed by angioplasty or stent placement for the residual severe stenosis. In contrast to those patients with purely thromboembolic occlusions, there were theoretic concerns that the retrieval of the thrombectomy devices may be impeded by the stenosis and forceful maneuvers to retrieve these devices would increase the risk of vessel rupture or tearing of perforator vessels.¹⁶ We did not encounter such difficulties in our study patients. Similarly, no retrieval difficulties or device complications were reported in the 4 patients with underlying severe stenosis in the study of Mordasini et al,¹² of whom 3 had stent placement and 1 patient had only PTA performed, and in the 5 patients with stent placement in the study of Espinosa de Rueda et al¹¹; but it is likely that publication bias existed.

In choosing stents for the underlying severe intracranial stenosis, 11 patients received the Wingspan stent after prior angioplasty or the Apollo stent according to lesion and vessel characteristics, which provided a relatively stronger radial force than a detached Solitaire AB stent.¹⁷ Deployment of these stents served several purposes: First, stent placement could improve distal perfusion, decreasing the risk of thrombosis induced by stagnant flow and facilitating the spontaneous thrombolysis of distal emboli. Second, the shear from the passage of the retrievers past the stenosis could potentially damage the endothelium or the unstable atherosclerotic plaque, increasing the risk of reocclusion related to the increased platelet activation and aggregation and vessel dissection. Stent placement over these vulnerable structures in the same session aimed to decrease the risk of thrombosis, recoil, restenosis, and dissection. Stent placement has advantages over angioplasty alone in reducing such risks because it can provide better coverage of the lesion and exposed endothelium. However, for some patients with tortuous access leading to a higher risk of complications if stent placement was attempted, angioplasty alone was performed.

In our study, the technical success rate for reperfusion was 100%. There was satisfactory resolution of the stenosis without recoil or dissection in all patients. In the case series of Möhlenbruch et al,⁹ in 24 patients treated with mechanical thrombectomy, the rate of successful reperfusion was 75% when only thrombectomy was performed; after stent placement was per-

formed for the 7 patients with underlying intracranial stenosis, the overall reperfusion rate improved to 87.5%. Other studies have reported technical success rates in the range of 74%–94%.^{11,12,14,18} No patients had procedure-related intracerebral hemorrhage on postoperative imaging; these results compared favorably with the 14% intracerebral hemorrhage rate in the endovascular treatment group from a recent meta-analysis.¹⁹ There were 2 mortalities, neither of which were procedure-related. On discharge, an improvement of NIHSS score of ≥ 10 points was noted for 10 patients (76.9%). This compared favorably with the 35.7% of patients having an NIHSS improvement at 24 hours in the study of Mordasini et al,¹² and the 54% with improvement on discharge in the study of Möhlenbruch et al⁹ on patients with BAO in general. At 90-day follow-up, a good functional outcome of mRS ≤ 2 was achieved in 6 of 13 patients (46.1%). Möhlenbruch et al reported an overall favorable clinical outcome of 33%, while Andersson et al¹³ reported an overall 57% favorable outcome for their 28 patients.

Other smaller case series reported a rate of 29%–50% on BAO treatment by using stent retrievers.^{11,12,14,18} However, it is difficult to do a reliable comparison of our results with those in other acute BAO series with mechanical thrombectomy performed due to the heterogeneity in patient characteristics, inclusion criteria, and types of adjuvant therapy used. The patients in our study were relatively young, with a mean age of 56 years. Younger age is a favorable prognostic factor because these patients have less challenging anatomy and are more likely to have better outcomes than older patients. However, our patients had a high NIHSS score on admission and a long symptom-to-recanalization time; this might account for the limited functional outcome in some patients. Compared with patients with good functional outcome, patients with poorer outcome of mRS of > 2 had a higher NIHSS score and longer symptom-to-door, needle-to-recanalization, and door-to-recanalization times. Reasons for the relatively long door-to-recanalization time included the acute interventional stroke service workflow in our institution being in the process of optimization during the initial stages and delay in receiving general anesthesia and intubation required by our patients for airway protection and aspiration prevention. Compared with patients with no underlying severe stenosis for whom sole mechanical thrombectomy was already successful in obtaining adequate distal perfusion, our patients with severe stenosis required additional time for the steps of angioplasty and stent placement to achieve reperfusion.

There were limitations to this study. This was a retrospective study with a small sample size of 13 patients providing preliminary experience of combined treatment, but further large-scale prospective studies with a longer follow-up are warranted. Because our patients could not achieve satisfactory reperfusion of the distal territories after the first stage of mechanical thrombectomy, revascularization by angioplasty or stent placement of the underlying stenosis in the same session was performed.

There was no control group of patients with just conservative treatment given for the stenosis, and there are currently sparse reports in the literature specifically on the outcome of patients with underlying severe stenosis for comparison. Only with randomized trials would we be able to directly compare the outcome of patients with acute BAO with or without stent placement per-

formed in the same session for the underlying stenosis. We recognized that intracranial stent placement with the use of the Wingspan stent would be regarded as off-label in some countries after the publication of the Stenting vs Aggressive Medical Management for Preventing Recurrent Stroke in Intracranial Stenosis results.¹⁵ However, there have been controversies over the study; with improved patient and device selection and increased technical experience, intracranial stent placement still holds a promising role for selected patients.^{8,20,21} The use of the Wingspan stent was not off-label in our center. Our choice of endovascular devices was based on lesion or vessel characteristics⁸; hence, we advise caution against overinterpretation of our data because our study was not meant to compare the efficacy among different vascularization methods by using the Apollo, the Wingspan stent, or sole angioplasty.

Conclusions drawn about which method conveyed a higher success rate would be difficult because the baseline vessel and lesion characteristics were different among patients, and our study was not adequately powered to perform a meaningful statistical interpretation. A previous study reported on the revascularization results of these 2 stents and angioplasty,⁸ though larger trials would be warranted. The use of glycoprotein IIb/IIIa inhibitor was not yet standardized in our hospital or according to international guidelines; more study results are awaited to guide its use. The Solitaire FR stent (Covidien) was not available in our center during the time of the study; instead the Solitaire AB device was used. Balloon occlusion catheters were not available in our center, but until now, there has been no conclusive evidence to prove that the balloon occlusion catheter can be of use in the posterior circulation to decrease the distal embolization rate significantly. The door-to-recanalization time for the patients in our study was relatively long. With more experience in acute stroke intervention gained from the previous years, our institution has streamlined our triage system and workflow to decrease our door-to-recanalization time.

CONCLUSIONS

Combined mechanical thrombectomy with stent retrievers and angioplasty and stent placement for the treatment of acute basilar occlusion with underlying severe intracranial vertebrobasilar stenosis was safe and feasible. No increased rate of arterial rupture or reocclusion was noted from this study. Further larger prospective clinical trials are needed to confirm our study results.

REFERENCES

- Schonewille WJ, Algra A, Serena J, et al. **Outcome in patients with basilar artery occlusion treated conventionally.** *J Neurol Neurosurg Psychiatry* 2005;76:1238–41
- Lindsberg PJ, Mattle HP. **Therapy of basilar artery occlusion: a systematic analysis comparing intra-arterial and intravenous thrombolysis.** *Stroke* 2006;37:922–28
- Wong LK. **Global burden of intracranial atherosclerosis.** *Int J Stroke* 2006;1:158–59
- Mattle HP, Arnold M, Lindsberg PJ, et al. **Basilar artery occlusion.** *Lancet Neurol* 2011;10:1002–14
- Saver JL, Jahan R, Levy EI, et al; SWIFT Trialists. **Solitaire flow restoration device versus the Merci retriever in patients with acute ischaemic stroke (SWIFT): a randomised, parallel-group, non-inferiority trial.** *Lancet* 2012;380:1241–49
- Nogueira RG, Lutsep HL, Gupta R, et al; TREVO 2 Trialists. **Trevo versus Merci retrievers for thrombectomy revascularisation of large vessel occlusions in acute ischaemic stroke (TREVO 2): a randomised trial.** *Lancet* 2012;380:1231–40
- Park JH, Park SK, Jang KS, et al. **Critical use of balloon angioplasty after recanalization failure with retrievable stent in acute cerebral artery occlusion.** *J Korean Neurosurg Soc* 2013;53:77–82
- Miao Z, Song L, Liebeskind DS, et al. **Outcomes of tailored angioplasty and/or stenting for symptomatic intracranial atherosclerosis: a prospective cohort study after SAMMPRIS.** *J Neurointerv Surg* 2015;7:331–35
- Möhlenbruch M, Stampfl S, Behrens L, et al. **Mechanical thrombectomy with stent retrievers in acute basilar artery occlusion.** *AJNR Am J Neuroradiol* 2014;35:959–64
- Mortimer AM, Bradley M, Renowden SA. **Endovascular therapy for acute basilar artery occlusion: a review of the literature.** *J Neurointerv Surg* 2012;4:266–73
- Espinosa de Rueda M, Parrilla G, Zamarró J, et al. **Treatment of acute vertebrobasilar occlusion using thrombectomy with stent retrievers: initial experience with 18 patients.** *AJNR Am J Neuroradiol* 2013;34:1044–48
- Mordasini P, Brekenfeld C, Byrne JV, et al. **Technical feasibility and application of mechanical thrombectomy with the Solitaire FR revascularization device in acute basilar artery occlusion.** *AJNR Am J Neuroradiol* 2013;34:159–63
- Andersson T, Kuntze Söderqvist Å, Söderman M, et al. **Mechanical thrombectomy as the primary treatment for acute basilar artery occlusion: experience from 5 years of practice.** *J Neurointerv Surg* 2013;5:221–25
- Mourand I, Machi P, Milhaud D, et al. **Mechanical thrombectomy with the Solitaire device in acute basilar artery occlusion.** *J Neurointerv Surg* 2014;6:200–04
- Chimowitz MI, Lynn MJ, Derdeyn CP, et al; SAMMPRIS Trial Investigators. **Stenting versus aggressive medical therapy for intracranial arterial stenosis.** *N Engl J Med* 2011;365:993–1003
- Kim TK, Rhim JK, Lee CJ, et al. **The limitations of thrombectomy with Solitaire AB as first-line treatment in acute ischemic stroke: a single center experience.** *J Cerebrovasc Endovasc Neurosurg* 2012;14:203–09
- Krischek O, Miloslavski E, Fischer S, et al. **A comparison of functional and physical properties of self-expanding intracranial stents [Neuroform3, Wingspan, Solitaire, Leo+, Enterprise].** *Minim Invasive Neurosurg* 2011;54:21–28
- Roth C, Mielke A, Siekmann R, Ferbert A. **First experiences with a new device for mechanical thrombectomy in acute basilar artery occlusion.** *Cerebrovasc Dis* 2011;32:28–34
- Kumar G, Shahripour RB, Alexandrov AV. **Recanalization of acute basilar artery occlusion improves outcomes: a meta-analysis.** *J Neurointerv Surg* 2014 Sep 30. [Epub ahead of print]
- Miao Z. **Intracranial angioplasty and stenting before and after SAMMPRIS: “from simple to complex strategy—the Chinese experience.”** *Front Neurol* 2014;5:129
- Yu SC, Leung TW, Lee KT, et al. **Angioplasty and stenting of intracranial atherosclerosis with the Wingspan system: 1-year clinical and radiological outcome in a single Asian center.** *J Neurointerv Surg* 2014;6:96–102

Clopidogrel Resistance in Neurovascular Stenting: Correlations between Light Transmission Aggregometry, VerifyNow, and the Multiplate

N. Flechtenmacher, F. Kämmerer, R. Dittmer, U. Budde, P. Michels, J. Röther, and B. Eckert

ABSTRACT

BACKGROUND AND PURPOSE: Clopidogrel resistance is blamed for thromboembolic complications in neurovascular stent placement. Platelet-function assays are weakly standardized. The aim of this study was to correlate the results of 3 different platelet-inhibition measurements (from light transmission aggregometry, the VerifyNow P2Y12 test, and the Multiplate analyzer) and their relation to periprocedural thromboembolic complications in elective neurovascular stent placement.

MATERIALS AND METHODS: Clopidogrel resistance was determined on the day of the intervention according to predefined platelet reactivity cutoff values. All 3 tests were performed in 103 consecutive neurovascular stent-placement procedures in 97 patients (extracranial, $n = 77$; intracranial, $n = 26$).

RESULTS: The clopidogrel resistance rates were 47.6% (light transmission aggregometry), 50.5% (VerifyNow), and 35.9% (Multiplate). In 67% of the patients, clopidogrel resistance was present according to at least one method. The correlations of qualitative results that classified a patient as responsive or resistant to clopidogrel were 67.9% for light transmission aggregometry with VerifyNow, 77.7% for light transmission aggregometry with the Multiplate, and 66% for VerifyNow with the Multiplate. Periprocedural thromboembolic complications ($n = 9$) occurred more frequently in patients who were determined by all 3 methods to be clopidogrel resistant. The difference was most pronounced with light transmission aggregometry (complication rates, 14.4% [clopidogrel-resistant patients] vs 3.7% [clopidogrel-responsive patients]). Sensitivity and specificity rates of clopidogrel resistance in relation to embolic complications were, respectively, 78% and 55% for light transmission aggregometry, 67% and 51% for VerifyNow, and 44% and 67% for the Multiplate.

CONCLUSIONS: Clopidogrel resistance is a frequent finding in patients who undergo neurovascular stent placement. The correlations among the different testing methods are only modest and differ considerably. Light transmission aggregometry results seem to correlate with thromboembolic complications more accurately than with VerifyNow and Multiplate point-of-care methods.

ABBREVIATION: LTA = light transmission aggregometry

In neurovascular procedures, especially the placement of a stent into an extracranial or intracranial artery, clopidogrel resistance is associated with an increased risk of thromboembolic complications.¹⁻⁵ In elective neurovascular stent placement, preprocedural testing of platelet inhibition is increasingly performed to identify patients with clopidogrel resistance. However, test result standards for clopidogrel resistance have not been established, and strong clinical evidence that supports the idea that the results of such tests definitively alter clinical outcomes is still

lacking. Light transmission aggregometry (LTA) is considered the criterion-standard test method, but standard values have not yet been established. LTA requires a preparation time of 2 hours, whereas point-of-care methods such as the VerifyNow P2Y12 assay (Accumetrics, San Diego, California) and impedance aggregometry using a Multiplate analyzer (Dynabyte, Munich, Germany) offer periprocedural test results within minutes in the operating suite.⁶

A study comparing LTA with point-of-care measurements in percutaneous coronary intervention has shown only modest agreement among the different tests.⁷ In neurovascular procedures, clopidogrel resistance has been investigated with various methods. However, a comparison of different test methods to determine the correlation of their results with the occurrence of embolic complications has not yet been performed in the clinical context of neurovascular stent placement.

Received December 22, 2014; accepted after revision March 3, 2015.

From the Departments of Neuroradiology (N.F., F.K., B.E.) and Neurology (P.M., J.R.), Asklepios Klinik Altona, Hamburg, Germany; and Department of Laboratory Medicine (R.D., U.B.), Medilys Laboratory Company, Hamburg, Germany.

Please address correspondence to B. Eckert, Prof Dr Med, Department of Neuroradiology Asklepios Klinik Altona, Abteilung für Neuroradiologie, Paul-Ehrlich-Str 1, 22763 Hamburg, Germany; e-mail: b.eckert@asklepios.com.

<http://dx.doi.org/10.3174/ajnr.A4388>

The purpose of this study was to determine the correlation of platelet inhibition with clopidogrel according to 3 different testing methods and the association of clopidogrel resistance with thromboembolic complications in elective neurovascular stent placement.

MATERIALS AND METHODS

Between September 2011 and August 2012, all consecutive patients who were undergoing elective intracranial or extracranial stent placement for atherosclerotic stenosis or stent-assisted coiling of intracranial aneurysms were included in this prospective study. Patients who underwent extracranial stent placement received local anesthesia, and those who underwent intracranial stent placement were intubated and received general anesthesia. Each patient received 100 mg of aspirin and 75 mg of clopidogrel daily for 5 days before the procedure ($n = 80$) or a loading dose of 600 mg of clopidogrel the day before the procedure ($n = 23$). Medication lists of the patients were reviewed before initiating clopidogrel to ensure that they were not taking any drugs that would potentially interact (eg, cytochrome P450 2C19 inhibitors, including proton-pump inhibitors), because that would have affected the results. The study was approved by the Ärztekammer Hamburg ethical review board, and written informed consent was obtained from each patient. Clopidogrel resistance was analyzed in each patient on the day of the procedure by using LTA (induced by 2 $\mu\text{mol/L}$ adenosine diphosphate), the VerifyNow P2Y12 assay, and impedance aggregometry using a Multiplate analyzer. LTA is a method that measures adenosine diphosphate-induced platelet aggregation in platelet-rich plasma by changes in light transmittance. Platelet-rich plasma is acquired by centrifuging citrate-anticoagulated whole blood, which requires a preparation time of 2 hours. The interpretation of the test results requires standardization and a trained laboratory staff. The VerifyNow system is a turbidimetric-based optical detection system that measures platelet-induced aggregation as an increase in light transmittance with citrate-anticoagulated whole blood. The VerifyNow P2Y12 assay is a fast, standardized, point-of-care test that does not require any special training for its performance. The Multiplate analyzer detects platelet aggregation by measuring impedance changes. Hirudin-anticoagulated whole blood is pipetted into a test cell. Aggregation starts by adding the agonist adenosine diphosphate. Pipetting is performed by an attached electronic pipette. No trained staff is needed to perform the test. Clopidogrel resistance was defined as follows: for the VerifyNow P2Y12 assay, >236 P2Y12 reaction units; for LTA, $>40\%$ of maximal aggregation and disaggregation curve; and for the Multiplate, >40 -U area under the curve value. If 2 of the 3 methods indicated resistance, the clopidogrel dose was increased to 150 mg daily after the procedure. Follow-up platelet-activity testing was not performed. Clopidogrel was maintained for 2 months after the extracranial procedures and 3 months after the intracranial stent-placement procedures; aspirin was continued long term. The stent-placement procedures were performed by 1 of 2 neurointerventionists (A.L. or B.E.) with >15 years' experience in neurointerventional procedures, both of whom were certified in the stent arm of the German Stent-Protected Angioplasty versus Carotid Endarterectomy (SPACE) study. Neurologic examination was performed on

Table 1: Incidence of clopidogrel resistance

Clopidogrel Status	n	%
Resistant according to:		
≥ 1 method	69	67
≥ 2 methods	43	41.9
All 3 methods	24	23.3
Clopidogrel responsive according to all 3 methods	34	33

each patient promptly after the intervention and before discharge by an independent neurologist. Each patient was monitored on a stroke unit certified by the German Stroke Society for at least 24 hours. In case of a new neurologic deficit, MR imaging was performed. A thromboembolic complication was defined as transient or persistent neurologic deficits associated with new DWI lesions found on MR imaging. NIHSS and the mRS were used to grade and follow up on neurologic deficits. After 3 months, clinical follow-up was accomplished by a structured telephone interview.

All statistical tests were performed with the use of SAS software version 9.3 (SAS Institute, Cary, North Carolina). For correlations between the continuous values of the 3 test methods, Spearman rank-order correlation (ρ) was used. A perfect monotonic relationship is represented by a ρ value of 1 or -1 . The clopidogrel resistance status in each method was entered in a multiple logistic regression model.

The sensitivity, specificity, positive predictive value, and negative predictive value of the 3 methods relating to the occurrence of thromboembolic events were calculated by building contingency tables.

Differences between categorical variables were evaluated with the χ^2 test or with the Fisher exact test in case of small expected cell frequencies. All P values were 2-sided. For all the statistical tests, a P value of $<.05$ was considered significant.

RESULTS

During the study period, 107 patients underwent neurovascular stent placement. Ten patients were excluded because of insufficient laboratory data or different antiplatelet therapy. The data analysis included 103 procedures in 97 patients. The procedures were stent placements for extracranial stenosis ($n = 77$) or intracranial stenosis ($n = 16$) and stent-assisted intracranial aneurysm coilings ($n = 10$). The mean patient age was 67.2 years; there were 64 male and 33 female patients.

Clopidogrel resistance was detected with LTA in 49 (47.6%) measurements, with VerifyNow in 52 (50.5%) measurements, and with the Multiplate in 35 (34%) measurements. The incidences of clopidogrel resistance in the 3 tests are listed in Table 1. In 33% of the measurements, all 3 tests indicated sufficient platelet inhibition; in the remaining two-thirds of the cohort, clopidogrel resistance was found in at least 1 of the 3 methods, and in 42%, clopidogrel resistance was found in 2 of 3 assays. Concordant clopidogrel resistance in all 3 methods was seen in 23% of the measurements. According to the study protocol, 39 patients (43 procedures) received 150 mg of clopidogrel after the procedure.

The individual test results for each method are shown in Fig 1.

Correlation scatter plots of the test results are shown in Fig 2. The statistical analysis revealed significant correlations among the quantitative values for LTA with the Multiplate ($\rho = 0.52$; $P =$

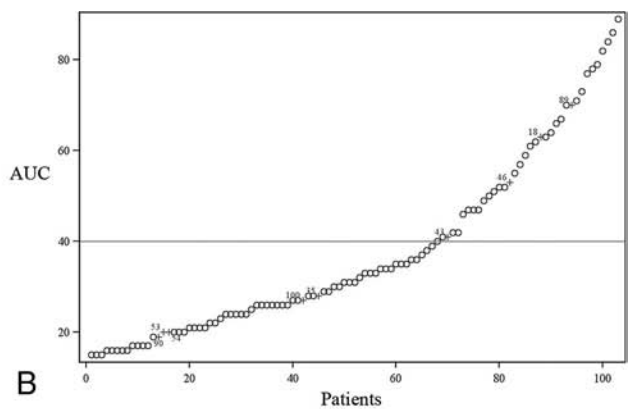
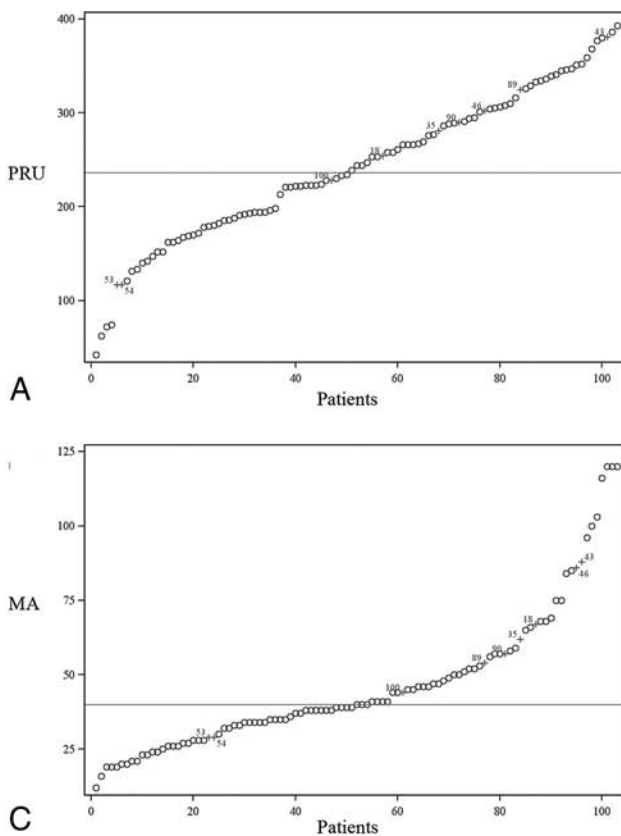


FIG 1. Individual test results of VerifyNow (A), the Multiplate (B), and LTA (C). The line parallel to the x-axis marks the particular cutoff value that has been used to discriminate between clopidogrel resistance and clopidogrel response. Procedures in which an embolic complication occurred are indicated by plus signs. Embolic complications Nr.53 and Nr.54 occurred in a single patient with 2 subsequent treatments of a symptomatic ICA and vertebral artery stenosis, respectively. PRU indicates P2Y12 reaction units; MA, maximal aggregation; AUC, area under the curve.

.0001), LTA with VerifyNow ($\rho = 0.33$; $P = .0008$), and VerifyNow with the Multiplate ($\rho = 0.28$; $P = .0041$). The correlations of the qualitative classification of a patient as clopidogrel responsive or resistant were 67.9% for LTA with VerifyNow, 77.7% for LTA with the Multiplate, and 66% for VerifyNow with the Multiplate.

Nine thromboembolic events that led to major stroke (1 patient), minor stroke (4 patients), or TIA (4 cases) occurred during the interventions. Thromboembolic complications occurred in 2 cases of stent-assisted aneurysm coiling, in 2 cases of extracranial vertebral stent placement, and in 5 cases of extracranial carotid stent placement. During the stent placements for intracranial stenosis, no thromboembolic complications occurred. In all 4 patients with transient symptoms, postprocedural MR imaging detected new DWI lesions. Additional TIAs without DWI lesions did not occur. No delayed thromboembolic complications (before discharge) occurred in any patient.

One patient who experienced thromboembolic procedural TIAs in 2 separate treatments of a symptomatic extracranial ICA stenosis and a vertebral artery–origin stenosis was classified as clopidogrel responsive by all 3 test methods in both stent-placement procedures (Nr.53 and Nr.54 in Figures). In this patient, no hematologic or anatomic abnormalities were found. In the remaining 7 complications, clopidogrel resistance was identified in all cases by LTA, in 6 cases by VerifyNow, and in 4 cases by the Multiplate. The correlations of the qualitative test results of each method with the occurrence of thromboembolic complications are listed in Table 2. Results of the statistical analysis of the qualitative test results in relation to thromboembolic complications (yes/no) are shown in Table 2.

Follow-up data were available after 3 months for 75 patients (81 stent-placement procedures), including all 39 patients whose dosage of clopidogrel was doubled. Follow-up telephone interviews did not reveal any medication-noncompliance issues. During the follow-up period, 1 ipsilateral stroke and 3 ipsilateral TIAs were detected. One postdischarge stroke occurred after ICA stent placement in a patient (Nr.100) who was identified as clopidogrel resistant by LTA alone and treated with 75 mg of clopidogrel after the procedure. Three postdischarge TIAs occurred after extracranial ICA stent placement. All 3 patients were identified as clopidogrel resistant according to all 3 tests and were treated with 150 mg of clopidogrel after the procedure. A symptomatic bleeding complication occurred in 1 patient suffering epistaxis and required embolization treatment; the patient recovered completely. Neither stent thrombosis nor intracerebral bleeding was detected in any patient.

DISCUSSION

To our knowledge, this is the first study to correlate 3 different clopidogrel-reactivity assays in the clinical context of elective neurovascular stent placement. In 67% of the patients, at least one test method revealed clopidogrel resistance. The clopidogrel-responsive status differed among the different methods for a considerable number of patients. Embolic complications occurred more frequently in patients with clopidogrel resistance determined by all 3 types of tests. The LTA results revealed a more accurate correlation of clopidogrel resistance and thromboembolic complications than the VerifyNow and Multiplate point-of-care methods.

The rates of clopidogrel resistance differed among the Multiplate (36%), LTA (48%), and VerifyNow (50%) methods. These

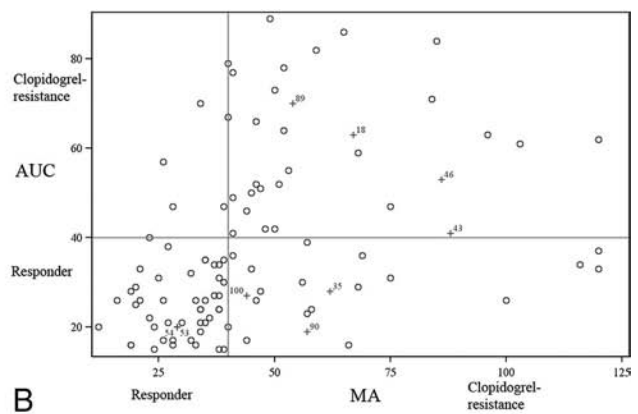
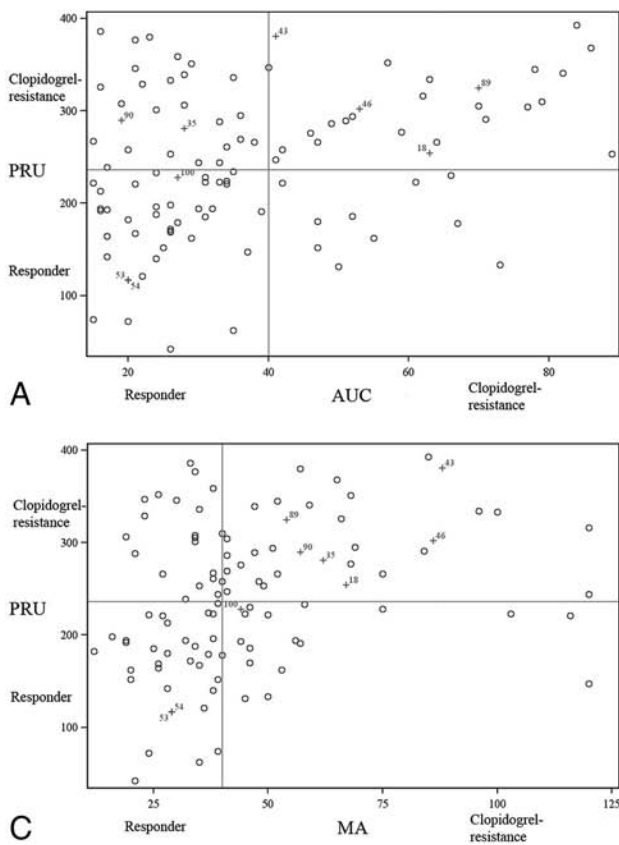


FIG 2. Correlation scatterplots of individual results obtained with VerifyNow versus the Multiplate (A), the Multiplate versus LTA (B), and VerifyNow versus LTA (C). Lines parallel to the axes mark the particular cutoff values. The upper-right and lower-left quadrants contain values with agreement in regard to the definition of clopidogrel resistance. Procedures in which an embolic complication occurred are indicated by plus signs.

data are in accordance with those of previous studies, which have indicated clopidogrel-resistance rates from 37% up to 52% in patients who were undergoing cerebrovascular stent placement.^{2,5} The clopidogrel dosing schedule in our study was 75 mg daily for 5–7 days before the intervention or a 600-mg loading dose on the day before the intervention. A loading dose of clopidogrel is usually given just 1 day before the procedure. Some centers, especially cardiology, recommend a loading dose of 300–600 mg of clopidogrel even 5 days before intervention. The relatively low doses may explain the high percentage of clopidogrel-resistant patients in comparison with that found in cardiology studies. Analysis of the correlation of different test methods was performed in one percutaneous coronary intervention study that compared LTA, VerifyNow, and a vasodilator-stimulated phosphoprotein phosphorylation assay. The incidence of clopidogrel resistance varied from 16% up to 39% in the patients. The level of agreement between the assays was in the moderate-to-poor range, with Spearman correlation coefficients between 0.60 and 0.86.⁷ Statistical analysis of the quantitative results in our study revealed significant but poor correlations between the different types of tests, with Spearman correlation coefficients between 0.28 and 0.52. In addition, the correlation of the qualitative classifications of a patient as clopidogrel responsive or resistant was poor in our study and ranged between 66% and 78% with the different measurements. In accordance with the percutaneous coronary intervention study by Gaglia et al,⁷ the results of our study underline the fact that results of the different tests do not agree in a notable number of patients.

Several studies have found a strong correlation of insufficient clopidogrel-related platelet inhibition and an increased risk of

thromboembolic events in supra-aortic stent placement and in cerebral aneurysm coiling.^{1,3–5,8} In line with the results of previous studies, we found increased complication rates in patients with clopidogrel resistance as determined by all 3 methods, but because of the small number of patients, the difference was not statistically significant. In patients who were deemed clopidogrel resistant by LTA, the complication rate was 14.3% (vs 3.7% of clopidogrel-responsive patients). The discrepancies in complication rates between clopidogrel-resistant and -responsive patients were less convincing with the VerifyNow (11.5% vs 5.9%, respectively) and Multiplate (11.4% vs 7.5%, respectively) methods. Hence, the statistical correlation of clopidogrel reactivity and the occurrence of embolic complications indicates a higher sensitivity for LTA (78%) than for VerifyNow (67%) and Multiplate (44%) testing.

In the present study, 1 patient who suffered a procedural thromboembolic TIA in 2 separate treatments of a symptomatic extracranial ICA stenosis and a vertebral artery–origin stenosis was classified as clopidogrel responsive by all 3 test methods in both stent-placement procedures, indicating that clopidogrel resistance is a major, but not the exclusive, factor of thromboembolic complications. In the remaining 7 thromboembolic complications, LTA identified clopidogrel resistance in all cases, VerifyNow in 6 cases, and the Multiplate in 4 cases.

The pharmacologic response of the P2Y₁₂ receptor antagonists such as clopidogrel strongly depends on cytochrome P450 genetic polymorphism. Carriers of reduced-function CYP2C19 alleles have significantly lower levels of active metabolite, resulting in diminished platelet inhibition.^{9,10} The pharmacodynamic process of converting the prodrug into the active metabolite dif-

Table 2: Correlation of clopidogrel test results and thromboembolic events

Method	Total (n)	No		Thromboembolic		P Value
		Complications (n [%])		Complication (n [%])		
VerifyNow						
Resistant	52	46	88.4	6	11.5	.6413
Responsive	51	48	94.1	3	5.9	
Multiplate						
Resistant	35	31	88.6	4	11.4	.5816
Responsive	68	63	92.7	5	7.5	
LTA						
Resistant	49	42	85.7	7	14.3	.0938
Responsive	54	52	96.3	2	3.7	

Table 3: Relationship of clopidogrel resistance and thromboembolic complications

Method	Sensitivity (%)	Specificity (%)	Positive Predictive Value (%)	Negative Predictive Value (%)
VerifyNow	66.7	51.1	11.5	94.1
Multiplate	44.4	67.0	11.4	92.7
LTA	77.8	55.3	14.3	96.3

fers between clopidogrel and the newer generations of antiplatelet agents such as the thienopyridine prasugrel. The conversion of prasugrel to its active metabolite involves cytochrome P450 subenzymes different than those involved by clopidogrel. The cyclopentyltriazolopyrimidine ticagrelor is not a prodrug and does not need cytochrome P450–dependent conversion at all. In contrast to clopidogrel, the common functional cytochrome P450 genetic variants did not affect active drug metabolite levels and platelet inhibition in patients treated with prasugrel in a cardiology study. The complication rate in percutaneous coronary intervention was not increased by any kind of cytochrome P450 gene variation in patients who were treated with prasugrel.¹¹

Because of the increased thromboembolic risk and unreliable test results for clopidogrel resistance, neurointerventionists have discussed the alternative application of these new antiplatelet agents. However, in patients with acute coronary syndromes and a history of stroke or TIA who were monitored over a time period of 15 months, the rate of intracranial bleeding was found to be 2.3% among patients on aspirin and prasugrel compared with 0% in the aspirin-plus-clopidogrel arm.¹² According to this study, prasugrel is contraindicated in patients with recent stroke or TIA and cannot be used as an alternative to clopidogrel as a periprocedural stent-placement medication for symptomatic extracranial or intracranial stenosis, regularly associated with TIA or stroke. In another recent study in which aspirin plus ticagrelor versus aspirin plus clopidogrel were compared in patients with acute coronary syndromes, a previous history of ischemic stroke or TIA was identified as a significant risk factor for impaired clinical outcome, but the bleeding rates in these high-risk patients who received ticagrelor were consistent with those of the overall trial population, and a favorable clinical benefit was found.¹³

In neurovascular stent placement, the alternative use of prasugrel or ticagrelor may be indicated for patients with clopidogrel resistance. Pilot studies have found contradictory results. In a study that included 16 patients, prasugrel was found to be effective and safe for neurointerventional procedures.¹⁴ In another

study that included 67 patients in various clinical conditions, including intracranial bleeding caused by arteriovenous malformation and aneurysm rupture, the use of aspirin and prasugrel in clopidogrel-resistant patients was associated with an increased risk of hemorrhagic complications over that of aspirin and clopidogrel therapy (19.4% vs 3.6%, respectively; $P = .02$).¹⁵ Additional studies in the setting of neurovascular stent placement with these alternative drug administrations and homogeneous study conditions, including postprocedural platelet-inhibition testing, are required.

Dose elevation to 150 mg of clopidogrel daily may be a treatment alternative. In a recent study, the stroke rate after dose adjustment in clopidogrel-resistant patients declined to 4.5% compared with the 10.3% stroke rate in those who received standard clopidogrel treatment.⁵ In our study, preprocedural clopidogrel treatment consisted of the standard 75-mg dosage. As a practical approach to preventing delayed complications, the study protocol dictated an increased dosage of 150 mg of clopidogrel after the procedure if clopidogrel resistance was evident in at least 2 of the 3 assays. Thirty-nine patients were treated with 150 mg of clopidogrel daily for 2 months after extracranial stent placement or for 3 months after intracranial stent placement. Follow-up platelet-inhibition testing was not performed. Three patients suffered recurrent ipsilateral TIAs despite the increased clopidogrel dosage during the follow-up period. Only one patient suffered epistaxis and required embolization treatment. Neither intracranial bleeding complications nor stent thrombosis occurred during the 3-month follow-up period. These observations provide a hint that a regimen of 150 mg of clopidogrel daily does not increase the bleeding risk but may not be effective in preventing delayed ischemic complications. However, our study was focused on periprocedural complications, and the follow-up data are not sufficient to draw any conclusions. Additional follow-up studies with alternative medication and continuous platelet-reaction measurements are needed.

There are several limitations to this study. Thromboembolic complications cannot be attributed only to insufficient platelet inhibition by clopidogrel but are the result of various risk factors, such as the degree of atherosclerosis, the configuration of the neurovascular access, the experience of the neurointerventionist, and low-aspirin-responder status. These factors were not analyzed separately in our study. In addition, we included different types of neurovascular stent-placement procedures with different risk profiles, such as stent placement for extracranial and intracranial stenoses and intracranial stent-assisted aneurysm treatment. A control group did not exist. Clopidogrel dosages were not completely homogeneous in the patient cohort, and postprocedural platelet-inhibition testing was not performed.

The strengths of our analysis were the consecutive assessment of all patients, the treatment by only 2 experienced neurointerventionists, and the comparison of 3 different test methods.

CONCLUSIONS

Clopidogrel resistance is a frequent finding in the clinical context of neurovascular stent placement and seems to be associated with an increased risk of thromboembolic complications. Different testing methods correlate poorly with regard to quantitative and

qualitative test results. LTA showed a better correlation between clopidogrel resistance and thromboembolic complications than the VerifyNow and Multiplate point-of-care methods.

Additional study with alternative periprocedural antiplatelet drug management involving prasugrel or ticagrelor and close clinical and continuous laboratory monitoring in neurointerventional procedures is warranted.

ACKNOWLEDGMENTS

We thank Peter Wohlmuth, Asklepios Proresearch, for statistical assistance.

Disclosures: Joachim Röther—UNRELATED: Consultancy: Boehringer Ingelheim, Pfizer, Bristol-Myers Squibb, Bayer, and Lundbeck; Payment for Lectures (including service on speakers bureaus): Boehringer Ingelheim, Pfizer, Bristol-Myers Squibb, Bayer, and Lundbeck. Bernd Eckert—UNRELATED: Payment for Lectures (including service on speakers bureaus): Codman and Covidien, Comments: travel expenses and honoraria for presentations to Congress or during workshops concerning neurointerventional therapies.

REFERENCES

1. Müller-Schunk S, Linn J. **Monitoring of clopidogrel-related platelet inhibition: correlation of nonresponse with clinical outcome in supra-aortic stenting.** *AJNR Am J Neuroradiol* 2008;29:786–91 CrossRef Medline
2. Prabhakaran S, Wells KR, Lee VH, et al. **Prevalence and risk factors for aspirin and clopidogrel resistance in cerebrovascular stenting.** *AJNR Am J Neuroradiol* 2008;29:281–85 CrossRef Medline
3. Lee DH, Arat A, Morsi H, et al. **Dual antiplatelet therapy monitoring for neurointerventional procedures using a point-of-care platelet function test: a single-center experience.** *AJNR Am J Neuroradiol* 2008;29:1389–94 CrossRef Medline
4. Kang HS, Kwon BJ, Kim JE, et al. **Preinterventional clopidogrel response variability for coil embolization of intracranial aneurysms: clinical implications.** *AJNR Am J Neuroradiol* 2010;31:1206–10 CrossRef Medline
5. Fifi JT, Brockington C. **Clopidogrel resistance is associated with thromboembolic complications in patients undergoing neurovascular stenting.** *AJNR Am J Neuroradiol* 2013;34:716–20 CrossRef Medline
6. Hussein HM, Emiru T, Georgiadis AL, et al. **Assessment of platelet inhibition by point-of-care testing in neuroendovascular procedures.** *AJNR Am J Neuroradiol* 2013;34:700–06 CrossRef Medline
7. Gaglia MA, Torguson R, Pakala R, et al. **Correlation between light transmission aggregometry, VerifyNow P2Y12, and VASP-P platelet reactivity assays following percutaneous coronary intervention.** *J Interv Cardiol* 2011;24:529–34 CrossRef Medline
8. Kim B, Kim K, Jeon P, et al. **Thromboembolic complications in patients with clopidogrel resistance after coil embolization for unruptured intracranial aneurysms.** *AJNR Am J Neuroradiol* 2014;35:1786–92 CrossRef Medline
9. Brandt JT, Close SL, Iturria SJ, et al. **Common polymorphisms of CYP2C19 and CYP2C9 affect the pharmacokinetic and pharmacodynamic response to clopidogrel but not prasugrel.** *J Thromb Haemost* 2007;5:2429–36 CrossRef Medline
10. Mega JL, Hochholzer W, Frelinger AL 3rd, et al. **Dosing clopidogrel based on CYP2C19 genotype and the effect on platelet reactivity in patients with stable cardiovascular disease.** *JAMA* 2011;306:2221–28 CrossRef Medline
11. Mega JL, Close SL, Wiviott SD, et al. **Cytochrome P450 genetic polymorphisms and the response to prasugrel: relationship to pharmacokinetic, pharmacodynamic, and clinical outcomes.** *Circulation* 2009;119:2553–60 CrossRef Medline
12. Wiviott SD, Braunwald E, McCabe CH, et al; TRITON-TIMI 38 Investigators. **Prasugrel versus clopidogrel in patients with acute coronary syndromes.** *N Engl J Med* 2007;357:2001–15 CrossRef Medline
13. James SK, Storey RF, Khurmi NS, et al; PLATO Study Group. **Ticagrelor versus clopidogrel in patients with acute coronary syndromes and a history of stroke or transient ischemic attack.** *Circulation* 2012;125:2914–21 CrossRef Medline
14. Stetler WR, Chaudhary N, Thompson BG, et al. **Prasugrel is effective and safe for neurointerventional procedures.** *J Neurointerv Surg* 2013;5:332–36 CrossRef Medline
15. Akbari SH, Reynolds MR, Kadkhodayan Y, et al. **Hemorrhagic complications after prasugrel (Effient) therapy for vascular neurointerventional procedures.** *J Neurointerv Surg* 2013;5:337–43 CrossRef Medline

A Comparison of 4D DSA with 2D and 3D DSA in the Analysis of Normal Vascular Structures in a Canine Model

C. Sandoval-Garcia, K. Royalty, B. Aagaard-Kienitz, S. Schafer,  P. Yang, and C. Strother



ABSTRACT

BACKGROUND AND PURPOSE: 4D DSA allows viewing of 3D DSA as a series of time-resolved volumes of a contrast bolus. There is no comparison of the accuracy of the anatomic information provided by 4D DSA with that available from conventional 2D and 3D DSA. Our purpose was to make this comparison by using a canine model.

MATERIALS AND METHODS: 2D, 3D, and 4D DSA acquisitions were performed in 5 canines from 3 catheter positions in the common carotid artery yielding 15 2D, 15 3D, and 15 4D datasets. For each territory, 3 vascular segments were chosen for comparison. Images were reviewed by 2 experienced neuroradiologists and were graded by the ability to visualize a segment, its filling direction, and preferred technique. Two visualization modes for 4D DSA were compared (volume-rendering technique and MIP).

RESULTS: 4D DSA was preferred in 73.9% of the image sets; 2D, in 22.7%; and 3D, in 3.4%. 4D DSA MIP rendering yielded superior visualization of very small vessel details; the 4D DSA volume-rendering technique offered superior depth and overlap information and better visualization of the surface details of the vasculature.

CONCLUSIONS: In this study, 4D DSA was preferred over 2D and 3D DSA for analysis of normal vasculature. The ability to provide any view of a vascular territory at any time during passage of a contrast bolus seems likely to reduce the need for many 2D acquisitions during diagnostic and therapeutic procedures. This then potentially translates into a reduction in radiation and contrast dose.

ABBREVIATION: VRT = volume-rendering technique

4D DSA provides the ability to create a series of time-resolved volumes of vasculature so that the passage of a contrast bolus may be viewed in 3D at any time and from any angle. Traditional 3D DSA acquisitions provide volumetric anatomic information but are not time-resolved. The overlap of vasculature in these 3D images often makes it difficult to analyze details (eg, angioarchitecture of an AVM nidus). To overcome this problem, multiple 2D DSA acquisitions at different angles are often necessary. The 4D algorithm applied to data from a rotational acquisition, obtained by using an injection protocol that starts the injection shortly after rotation of the C-arm rather than

simultaneous with its rotation, results in a series of 4D DSA volumes that provides a user with the ability to view both anatomic information and contrast dynamics.¹ The anatomic information provided by this technique has not, to our knowledge, been compared with that provided by conventional 2D and 3D DSA images. In this study, we aimed to assess the ability of 4D DSA to depict vascular anatomy. Our methods also aimed to acquire data that would allow us to make judgments as to whether the content was superior to and/or complementary to that of conventional DSA studies. We believed that this comparison was important because the ability to view relevant vasculature at any time and at any angle with a 4D reconstruction should result in less need to acquire multiple 2D series in both diagnostic and interventional procedures, thereby leading to reductions in both x-ray and contrast medium doses.

MATERIALS AND METHODS

2D, 3D, and 4D DSA images of 3 matching vascular territories from 5 canines were obtained by using a commercially available biplane angiography system (Artis zee; Siemens, Erlangen, Germany). All studies were performed under a protocol approved by the University of Wisconsin Animal Care Committee.

Received November 11, 2014; accepted after revision February 16, 2015.

From the Departments of Neurological Surgery (C.S.-G., B.A.-K.), Biomedical Engineering (K.R.), and Radiology (P.Y., C.S.), University of Wisconsin School of Medicine and Public Health, Madison, Wisconsin; Siemens (K.R., S.S.), Hoffman Estates, Illinois; and Department of Neurosurgery (P.Y.), Changhai Hospital, Second Military Medical University, Shanghai, China.

This work was supported by National Institutes of Health grant R01 144-PRJ68DN.

Please address correspondence to Charles Strother, MD, Department of Radiology, University of Wisconsin School of Medicine and Public Health, E3/366 Clinical Sciences Center, 600 N Highland Ave, Madison, WI 53792; e-mail: strother@wisc.edu

 Indicates open access to non-subscribers at www.ajnr.org

<http://dx.doi.org/10.3174/ajnr.A4359>



FIG 1. Example of the vasculature on anteroposterior 2D DSA projections for each catheter position: proximal (A), middle (B), and distal (C). These show the decrease in the vascular complexity as the injection site is moved from proximal to most distal. The magnification factor for the images increases, moving from proximal to most distal.

Table 1: Injection parameters used for the various acquisitions

	Proximal			Middle			Distal		
	2D DSA	3D DSA	4D DSA	2D DSA	3D DSA	4D DSA	2D DSA	3D DSA	4D DSA
Contrast volume (mL)	8–9	20	20	8–9	11	11	8–9	8	9
Concentration (%)	50	50	50	50	50	50	50	50	50
Flow rate (mL/s)	HI	3	3	HI	1.5–2.5	1.5–2.5	HI	1–1.5	1–1.5
Injection duration (s)	HI	6.6	6.6	HI	6	6	HI	7.3	7.3
Injection delay (s)	1	0	0	1	0	0	1	0	0
X-ray delay (s)	0	1	0	0	1	0	0	1	0

Note:—HI indicates hand injection.

Imaging Acquisition

After induction of endotracheal anesthesia, a 4F catheter was introduced into 1 common femoral artery. Under fluoroscopic guidance, the catheter was positioned first in one of the common carotid arteries, then more distally at a location just past the origin of the ICA, and finally still more distally at a location just beyond the superficial temporal artery. This sequence of locations for injections was chosen so that there would be a decrease in the complexity of the vasculature as the injection location was moved more distally. Figure 1 shows an example of these vascular territories on 2D DSA images.

The injection protocol rate, volume, contrast concentration, and timing were aimed at minimizing the reflux of contrast and optimizing enhancement of the vessels for a given acquisition. A dual-syringe power injector (Accutron; Medtronic, Saarbrücken, Germany) was used for all power injections. To mimic the bolus characteristics of a clinical study, we performed the 2D DSAs by using a hand injection of the contrast medium. Table 1 summarizes the injection protocols.

The 2D DSA images were acquired in standard anteroposterior and lateral projections. A conventional 3D DSA acquisition protocol was used to acquire a subtracted 3D dataset (5 seconds, 200°). For a typical 3D DSA clinical acquisition protocol, rotation of the C-arm is started 1–2 seconds after injection of the contrast to allow the contrast to reach a more steady-state of vascular opacification before the start of data acquisition. Because the

aim of the 4D technique is to capture both anatomic and temporal information of the contrast dynamics to capture the inflow of contrast, the C-arm rotation is started shortly (0.5–1 second) before injection of the contrast. To capture the steady-state and because of the rapid circulation time in the canine, we acquired the 4D datasets by using a 6-second 260° acquisition program.

Image Reconstruction

All 2D, 3D, and 4D DSA projection data were transferred to a research workstation running both commercial software (syngo X-Workplace VB21; Siemens) and 4D DSA prototype software. The 3D DSA reconstructions were performed by using the product software and standard reconstruction kernels (HU auto) with a projection-based motion-correction algorithm applied to minimize artifacts from any subject motion during the acquisition.

Once the 3D DSA reconstruction was complete, the 4D DSA reconstruction was performed. The 4D DSA reconstruction is a 2-step process; first, a conventional 3D DSA constraint volume is reconstructed by using the product software and the same reconstruction parameters used for the 3D reconstruction described above. Following this step, the temporal information contained in the rotational projection sequence is encoded into the constraint volume for every projection image. This process effectively creates a temporal volumetric representation of the contrast flow

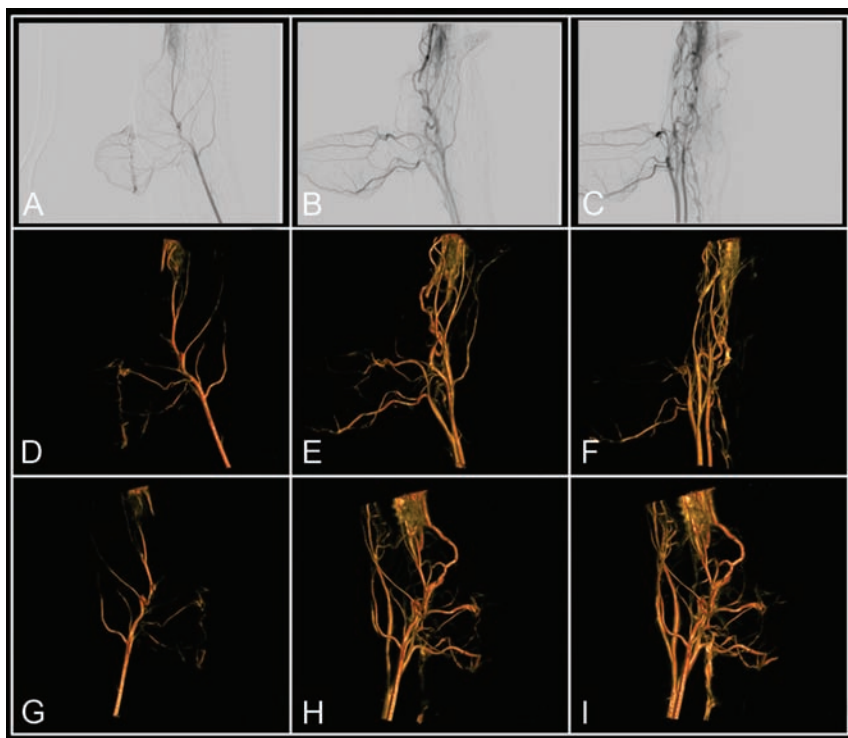


FIG 2. Illustration of 4D DSA reconstruction. No x-ray delay between contrast injection and rotational image acquisition results in contrast flow or inflow being visible in the rotational projections (A–C). Through a 2-step reconstruction process, this flow information is encoded into the 3D DSA for every projection, effectively creating a 4D DSA. This allows viewing of the contrast bolus passage at any desired angle at any time during the bolus passage. D–F, View of the bolus passage at 3 projection angles at 3 different time points. G–I, View of the bolus passage at 3 angles not present in the projections, again at 3 different time points. The figures correspond to sample angle projections selected to match the 2D acquisitions, even though once 4D images are reconstructed, views are available from any angle.

through the subject's vasculature at the frame rate of the rotational projection image acquisition (typically 30 frames/s).¹ Figure 2 shows an example of the contrast dynamics in the rotational projections along with a display of these dynamics as seen in the 4D reconstructions.

Image Evaluation

Three vascular segments were selected on each of the 2D image datasets. The same segments were used on the 2D studies from each of the 5 canines. Annotations were placed indicating the location of each segment. Scoring forms and labeled images were provided to the reviewers with a pictorial reference to clearly identify which vascular segments were to be evaluated. Figure 3A, -B shows an example of the material that was provided to the reviewers. The vessel characteristics that were evaluated included clarity of segment extent and margins, evidence of superimposed or adjacent vessels obscuring visualization, direction of filling, and individual rating of each of the available display modalities for 4D DSA and the choice of the overall preferred image. The Hinkmann rating scale (1–5) was used because it has been used for similar image evaluation tasks in previously published literature.² The reviewer was also asked to score the image quality of the 4D DSA (with respect to a given vascular segment) for 2 different rendering schemes (volume-rendering technique [VRT] and MIP), and a separate scale from 0 to 4 was used for this portion of the review. Both scales are shown in Fig 3B.

Each observer reviewed the image sets separately. All images were viewed on a workstation, and observers were allowed to manipulate all images (review, window, stop, magnify, and so forth) as they would do in clinical practice.

The reviewer was first presented with the 2D DSA image sequences and asked to score the 3 vascular segments from each territory (9 segments for each of the 5 canines). Next, the observer was shown the 3D DSA reconstructions of the corresponding territories and was asked to score the same 9 segments. Finally, the 4D DSA reconstruction was presented, and the same evaluation procedure was repeated. The reviewer was also asked to evaluate each of the 4D DSA studies when displayed either as a surface-rendered (VRT) volume or as an MIP and was allowed to make comments about any of the image datasets. The scoring schemes used for each of the evaluations are shown in Fig 3.

The 2 observers independently evaluated 44 vessel segments from the 5 canines (1 canine only had 8 vessel segments included for evaluation because 1 segment was not adequately visualized in any technique).

RESULTS

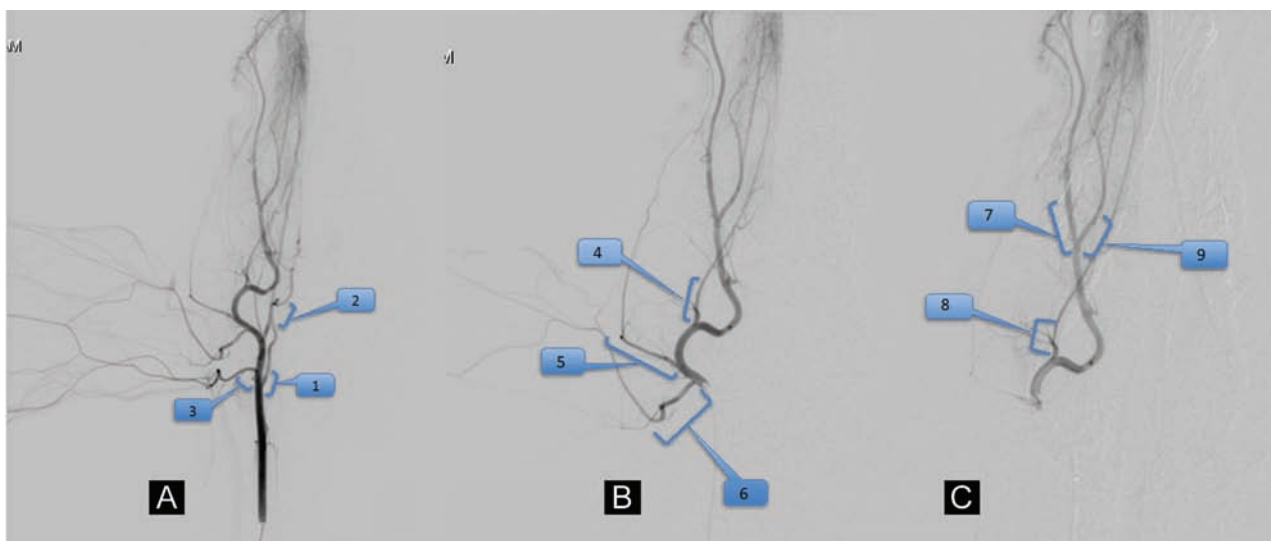
Overall, the 2 observers preferred the 4D DSA in 73.9% of the 88 image sets. The 2D DSA images were preferred in 22.7% of the image sets; the 3D DSA images were preferred in only 3.4%. Table 2 shows the raw data scores of each reviewer.

As can be seen from the raw data scores, one of the observers preferred the 4D images much more often than did the other (4D preferred in 40 of the 44 [91%] datasets by observer 2 compared with 25 of 44 [57%] by observer 1). These data also show that in 12 of the 28 (43%) image sets in which observer 1 preferred the 2D images, both the 2D and 4D images were, nonetheless, scored equally (ie, 4, excellent image quality).

Both 4D VRT and 4D MIP rendering yielded the same average rating of 1.9, in which 1 represented excellent image quality. In general, observers thought that the MIP rendering yielded superior visualization of very small vessel details, and the VRT offered superior depth and overlap information and better visualization of the surface details of the vasculature.

DISCUSSION

4D DSA provides a means to acquire a fully time-resolved 3D reconstruction of a vascular territory having superior spatial and temporal resolution to any other commercially available 4D imaging technique.¹ In this small study, we have shown that for the evaluation of the extracranial canine vasculature, 4D



SEGMENT 1: ICA origin				
	2D	3D	4D	
1. Is the segment present? Margins and full extent of the segment clearly seen?				Hinkmann scale (0) vessel not delimitable; (1) Poor image quality, blurring of the vessel contours; (2) Fair image quality, suboptimal arterial enhancement for confident diagnosis; (3) Good image quality and arterial enhancement, adequate for confident diagnosis; and (4) Excellent image quality and arterial enhancement.
2. Are there superimposed/adjacent arteries/veins that obscure visualization?				Yes/No
3. Is the segment filling in an antegrade or retrograde manner?				Antegrade/Retrograde
4. 4D DSA rating on 1 to 5 scale MIP				(1) Excellent cannot distinguish a difference in vascular filling from a corresponding 2D acquisition; (2) Good, looks almost like a 2D acquisition; (3) Useable but clearly different than a 2D acquisition; substandard; (4) Marginal for use, vascular filling does not look realistic; (5) Insufficient.
5. 4D DSA rating on 1 to 5 scale Golden				
6. Overall, which image do you prefer?				

FIG 3. A–C, Example of the pictorial reference form provided to the image reviewers identifying the vascular segments to be evaluated: proximal (A), middle (B), and distal (C) catheter positions on anteroposterior projections. D, Evaluation form and scales used for scoring of the images.

DSA frequently provided information that 2 experienced observers preferred over that provided by 2D or 3D studies. Although we did not explicitly ask whether the 4D dataset contained information equivalent to that in the combination of 2D and 3D series, we believe that this may be the case. All experience to date indicates that the 4D reconstruction contains the same information as a conventional 3D reconstruction and the time-resolved information contained in a full “library” of unlimited 2D acquisitions. The ability to view the vasculature at any desired angle and at any time during passage of a contrast bolus should allow elimination of most of the 2D acquisitions that now are often required in diagnostic and interventional procedures.

During an endovascular procedure, both the primary operator and the patient receive most of their x-ray exposure from DSA acquisitions.^{3,4} The use of 3D DSA results in a significant decrease in the need to perform 2D DSA acquisitions. This reduction translated into a significant decrease in patient x-ray exposure.⁵ While dose studies were not performed, it is estimated that the slight extension of acquisition time required for a 4D image acquisition (ie, 1 second) would result in an increase in radiation dose of approximately 20% compared with a conventional 3D acquisition. Because 3D image acquisitions represent, in general, only a minor fraction of the dose exposure during a conventional diagnostic or interventional procedure, this increase, when balanced against the potential reduc-

Table 2: Raw data from each of the 2 observers for all 44 vessel segments^a

2D	Reviewer 1			Reviewer 2			
	3D	4D	Preferred	2D	3D	4D	Preferred
3	4	4	4D	2	4	4	4D
3	3	4	4D	4	4	4	4D
4	2	4	4D	0	3	4	4D
4	2	4	2D	3	4	4	4D
4	2	4	4D	2	3	4	4D
4	2	4	4D	3	3	4	4D
4	3	4	2D	3	4	4	4D
4	3	3	2D	4	2	3	4D
4	2	4	4D	4	3	3	4D
4	4	4	4D	3	3	4	4D
4	4	4	4D	2	3	4	4D
4	4	4	4D	2	3	4	4D
4	3	3	2D	4	4	4	4D
4	3	4	2D	2	4	4	4D
4	3	4	4D	2	4	4	4D
4	3	3	2D	4	4	4	4D
4	4	2	3D	4	4	3	3D
4	3	4	4D	4	4	3	3D
4	2	4	2D	4	4	4	4D
4	1	3	4D	4	4	4	4D
4	3	4	2D	4	4	4	4D
4	4	4	2D	4	4	4	4D
4	3	4	2D	4	3	4	4D
4	3	4	4D	4	4	4	4D
4	4	4	2D	4	4	4	4D
4	3	4	2D	4	3	3	2D
3	2	2	2D	2	0	1	2D
4	4	4	4D	1	4	4	4D
4	2	4	4D	2	2	4	4D
4	3	4	4D	3	3	4	4D
4	4	4	4D	4	3	4	4D
4	4	4	4D	3	2	4	4D
4	3	4	4D	2	2	4	4D
4	4	4	4D	4	4	4	4D
4	3	4	4D	3	3	4	4D
3	3	4	4D	4	1	4	4D
4	3	4	2D	3	4	4	4D
4	2	4	4D	3	2	4	4D
4	4	4	2D	4	4	4	4D
4	3	4	2D	4	4	4	4D
4	4	4	4D	3	4	4	4D
4	3	4	4D	3	3	4	4D
3	4	4	2D	3	4	2	4D
4	4	3	2D	4	4	4	4D

^a The first 3 columns show the rating for each of the 3 modalities as described in the "Materials and Methods" and the scoring form (Fig 3B). The last column shows the preferred modality.

tion in exposure from 2D acquisitions is, in our opinion, acceptable.

This report represents a small series of animal studies and normal anatomy; we anticipate that the major advantages of 4D would be derived from the ability to delineate small-vessel abnormalities, particularly in areas where there is significant vascular overlap. In addition, more complex vascular anomalies with a significant flow-related component, such as arteriovenous malformations and arteriovenous fistulas, could be better evaluated because 4D allows for dissection of the angioarchitecture of early feeders and late venous drainage in several angles with 1 single acquisition.

The scales used for ranking the images and for the ratings of the display modes for the 4D-DSA images (MIP or surface-ren-

dered) are qualitative. This feature combined with the sample size limited our ability to perform meaningful statistical evaluations. For this initial validation study, we, therefore, present the raw data. Both rating scales have been previously used and reported for similar image-evaluation tasks.^{2,6} The cranial arteries in the canine are smaller than those of humans. This, as well as their overlap, posed significant challenges for all of the tested modalities. The observation that 4D DSA was preferred as the technique to accomplish the given task of evaluating a series of vascular segments gives us confidence that the technique will be valuable if made available in a clinical environment. Future studies will include a larger patient population of human subjects with normal and abnormal vasculature to further demonstrate the potential applications of the technique.

CONCLUSIONS

In this study, 4D DSA was preferred over 2D and 3D DSA for analysis of normal vasculature. The ability to provide any view of a vascular territory at any time during passage of a contrast bolus seems likely to reduce the need for many 2D acquisitions during diagnostic and therapeutic procedures. This then potentially translates into a reduction in radiation and contrast dose.

Disclosures: Carolina Sandoval-Garcia—RELATED: Grant: National Institutes of Health.* Comments: study performed under institutionally approved National Institutes of Health R01 grant. Beverly Aagaard-Kienitz—RELATED: Grant: National Institutes of Health.* Sebastian Schafer—RELATED: Other: I am an employee of Siemens USA. Kevin Royalty—UNRELATED: Employment: I am a full-time employee of Siemens. Charles Strother—RELATED: Grant: Siemens.* Comments: Imaging equipment and research support was provided under a Master Research Agreement between the University of Wisconsin Madison and Siemens; Support for Travel to Meetings for the Study or Other Purposes: support for travel to advisor meetings from Siemens under a Master Research Agreement between Siemens and University of Wisconsin School of Medicine and Public Health; Provision of Writing Assistance, Medicines, Equipment, or Administrative Support: Imaging equipment was provided under a Master Research Agreement between University of Wisconsin Madison and Siemens*; UNRELATED: Grants/Grants Pending: research support under a Master Research Agreement between University of Wisconsin Madison and Siemens*; Patents (planned, pending, or issued): I am coinventor on an issued patent for 4D DSA. Siemens has purchased a nonexclusive license for this intellectual property. *Money paid to the institution.

REFERENCES

1. Davis B, Royalty K, Kowarschik M, et al. **4D digital subtraction angiography: implementation and demonstration of feasibility.** *AJNR Am J Neuroradiol* 2013;34:1914–21
2. Hinkmann FM, Voit HL, Anders K, et al. **Ultra-fast carotid CT-angiography: low versus standard volume contrast material protocol for a 128-slice CT-system.** *Invest Radiol* 2009;44:257–64
3. Layton KF, Kallmes DF, Cloft HJ, et al. **Radiation exposure to the primary operator during endovascular surgical neuroradiology procedures.** *AJNR Am J Neuroradiol* 2006;27:742–43
4. Schueler BA, Kallmes DF, Cloft HJ. **3D cerebral angiography: radiation dose comparison with digital subtraction angiography.** *AJNR Am J Neuroradiol* 2005;26:1898–901
5. Abe T, Hirohata M, Tanaka N, et al. **Clinical benefits of rotational 3D angiography in endovascular treatment of ruptured cerebral aneurysm.** *AJNR Am J Neuroradiol* 2002;23:686–88
6. Yu S, Yan L, Yao Y, et al. **Noncontrast dynamic MRA in intracranial arteriovenous malformation (AVM), comparison with time of flight (TOF) and digital subtraction angiography (DSA).** *Magn Reson Imaging* 2012;30:869–77

Dynamic Angiography and Perfusion Imaging Using Flat Detector CT in the Angiography Suite: A Pilot Study in Patients with Acute Middle Cerebral Artery Occlusions

T. Struffert, Y. Deuerling-Zheng, S. Kloska, T. Engelhorn, S. Lang, A. Mennecke, M. Manhart, C.M. Strother, S. Schwab, and A. Doerfler

ABSTRACT

BACKGROUND AND PURPOSE: Perfusion and angiographic imaging using intravenous contrast application to evaluate stroke patients is now technically feasible by flat detector CT performed by the angiographic system. The aim of this pilot study was to show the feasibility and qualitative comparability of a novel flat detector CT dynamic perfusion and angiographic imaging protocol in comparison with a multimodal stroke MR imaging protocol.

MATERIALS AND METHODS: In 12 patients with acute stroke, MR imaging and the novel flat detector CT protocol were performed before endovascular treatment. Perfusion parameter maps (MTT, TTP, CBV, CBF) and MIP/volume-rendering technique images obtained by using both modalities (MR imaging and flat detector CT) were compared.

RESULTS: Comparison of MIP/volume-rendering technique images demonstrated equivalent visibility of the occlusion site. Qualitative comparison of perfusion parameter maps by using ASPECTS revealed high Pearson correlation coefficients for parameters CBF, MTT, and TTP (0.95–0.98), while for CBV, the coefficient was lower (0.49).

CONCLUSIONS: We have shown the feasibility of a novel dynamic flat detector CT perfusion and angiographic protocol for the diagnosis and triage of patients with acute ischemic stroke. In a qualitative comparison, the parameter maps and MIP/volume-rendering technique images compared well with MR imaging. In our opinion, this flat detector CT application may substitute for multisection CT imaging in selected patients with acute stroke so that in the future, patients with acute stroke may be directly referred to the angiography suite, thereby avoiding transportation and saving time.

ABBREVIATIONS: FD-CT = flat detector CT; FD-CTA = flat detector CT dynamic perfusion and angiographic imaging; FD-CTP = flat detector CT dynamic perfusion; MRP = MR perfusion imaging; MS-CT = multisection CT

Flat detector CT (FD-CT) equipped angiographic systems are now widely used in neurointerventional institutions. Recently, an application to perform imaging of the brain parenchyma (FD-CT), cerebral vasculature (flat detector CT dynamic perfusion and angiographic imaging [FD-CTA]), and cerebral blood volume has been described and was evaluated in patients with acute middle cerebral artery occlusions.^{1–3} However, this application

was limited due to the inferior FD-CT soft-tissue resolution of the brain parenchyma in comparison with multisection CT (MS-CT) or MR imaging. Additionally, there was a lack of temporal resolution so that calculation of dynamic (time-dependent) perfusion parameters was not possible.

Assessment of the impact of an ischemic stroke is best performed with physiologic criteria because especially in the acute phase, morphologic changes are only minimal and may be difficult to recognize by using MS-CT imaging.⁴ The use of perfusion and angiographic imaging increases the sensitivity of MS-CT and MR imaging in the acute phase of ischemic stroke. Thus, MS-CT angiography and MS-CT perfusion imaging are used to assess patients within a 0- to 4.5-hour time window of ischemic stroke. On the basis of the mismatch concept beyond 4.5 hours, multimodal MR imaging by using FLAIR, MR angiography, diffusion-weighted, and MR perfusion imaging (MRP) is used in many centers to identify patients eligible for recanalization therapies.⁵ MS-CT and MR imaging applications allow visualization of brain parenchyma and vessel occlusion (MS-CT angiogra-

Received September 2, 2014; accepted after revision February 16.

From the Department of Neuroradiology (T.S., S.K., T.E., S.L., A.M., M.M., A.D.), Pattern Recognition Lab (M.M.), and Department of Neurology (S.S.), University of Erlangen-Nuremberg, Erlangen, Germany; Siemens AG, Healthcare Sector (Y.D.-Z.), Forchheim, Germany; and Department of Radiology (C.M.S.), University of Wisconsin School of Medicine and Public Health, Madison, Wisconsin.

This work was supported by the Medical Valley National Leading Edge Cluster, Erlangen, Germany, diagnostic imaging network, subproject BD 16, research grant no. 13EX1212G.

Please address correspondence to Tobias Struffert, MD, Department of Neuroradiology, University of Erlangen-Nuremberg, Schwabachanlage 6, 91054 Erlangen, Germany; e-mail: tobias.struffert@uk-erlangen.de

<http://dx.doi.org/10.3174/ajnr.A4383>

phy, MRA); and calculation of the dynamic perfusion parameter maps (time-to-peak, mean transit time, cerebral blood flow, and cerebral blood volume) to assess the viability of the brain.⁶⁻⁹ The ability to obtain dynamic perfusion maps (FD-CTP) and angiographic images by using an intravenous contrast application within the angiography suite would seem to create a single ideal venue for both diagnosis and treatment of patients with an acute ischemic stroke. A FD-CT application replacing MS-CT or MR imaging would optimize the work flow, avoid transportation of the patient from one imaging location to the other, save time, and may allow periodic monitoring of brain viability during the endovascular treatment.

To date, dynamic perfusion imaging with the C-arm angiographic system has been limited by the slow gantry rotation time. However, recent studies in canines and swine models have now demonstrated the feasibility of dynamic perfusion imaging with the use of a flat detector angiographic system.¹⁰⁻¹² The aim of this pilot study was to test the feasibility of this novel application by comparing FD-CTP and FD-CTA with a multimodal MR imaging protocol in patients with acute ischemic stroke. Additionally, the effective patient dose was evaluated.

MATERIALS AND METHODS

Under an institutionally approved protocol (ethics committee approval was obtained), 12 patients were included in this study. According to institutional guidelines, patients seen beyond 4.5 hours after symptom onset are examined primarily by a multimodal stroke MR imaging protocol. If large-vessel occlusion and diffusion/perfusion mismatch are identified, intravenous thrombolytic therapy is initiated and patients are transferred to the angiography suite for subsequent endovascular treatment. In our practice, FD-CT is frequently used prior to and after endovascular treatment. This enables ruling out hemorrhage due to intravenous thrombolytic therapy prior to and iatrogenic hemorrhage after endovascular treatment. In this study, initial MRP and MRA images were compared with a novel FD-CT application that was applied before endovascular treatment.

Imaging Protocol

MR Imaging. In all patients, initial imaging was performed by using MR imaging (Magnetom Aera 1.5T; Siemens, Erlangen, Germany). We used standard applications including FLAIR, DWI, MRA (turbo time-of-flight), and MR perfusion imaging. MRP was performed by scanning the entire brain (gradient echo-planar imaging; 25 sections; 5-mm section thickness; TR, 2230 ms; TE, 50 ms; flip angle, 90°; FOV, 230 mm; 50 acquisitions) after injection of paramagnetic contrast material (gadobutrol, Gadavist; Bayer Schering Pharma, Berlin, Germany) by using a dual-syringe power injector (Accutron HP-D; Medtron, Saarbrücken, Germany). MRA was performed by using a time-of-flight technique (5 slabs; 0.5-mm section thickness; TR, 24 ms; TE, 7 ms; FOV, 200 mm). Postprocessing was performed by using a dedicated workstation and standard perfusion software (syngo MMWP; Siemens). We reconstructed TTP, MTT, CBF, and CBV parameter maps (5-mm section thickness and spacing). Additional volume-rendering technique and maximum intensity pro-

jection images (5-mm section thickness, 2.5-mm spacing) of the MRA were reconstructed.

FD-CT. A biplane flat detector angiographic system (Axiom Artis dBA; Siemens) was used both for FD-CT imaging and endovascular treatment. In FD-CT imaging, contrast was injected into a peripheral vein with the use of a dual-syringe angiographic power injector (Accutron HP-D). We used a contrast application protocol identical to that for MS-CT perfusion imaging (60 mL of contrast material, iomeprol, Iomeron 350; Bracco, Milan, Italy; injected at a rate of 5 mL/s followed by a 60-mL saline flush).¹¹ Technical details of this novel FD-CT perfusion application have been described and discussed in detail elsewhere.¹¹ Briefly, before the start of the contrast injection, 1 forward and 1 reverse high-speed baseline scan (rotation) were performed to obtain a baseline set of nonenhanced (mask) images. Five seconds after the start of the peripheral contrast injection, a bidirectional series of 7 high-speed FD-CT rotational acquisitions was initiated. Each rotation was 5 seconds in duration and covered a rotation angle of 200°. There was a 1-second pause between the rotations (4 forward rotations and 3 reverse rotations). During each rotation, the angiographic system acquires 160 projections (angulation step, 0.8°/frame). Each projection was acquired at 77 kV(peak) and 0.36- μ Gy/frame dose level. This acquisition protocol resulted in a sampling rate of approximately 6 seconds, with a total acquisition duration of 41 seconds (Fig 1).

Prototype perfusion software was used to calculate the FD-CTP parameter maps. The basic reconstruction represents a modified version of the algorithm reported previously, which uses the widely accepted deconvolution approach to calculate the dynamic perfusion parameters.^{11,12} The arterial input function was manually selected at the anterior cerebral artery. We reconstructed all parameters maps (eg, TTP, MTT, CBV, and CBF) by using a 5-mm section thickness and spacing. With standard FD-CT software (InSpace DynaCT, Siemens), it is possible to perform further reconstructions by using this FD-CTP dataset. A first reconstruction by using data obtained before contrast injection (mask images) was performed to visualize the brain parenchyma and was substituted for the FD-CT performed as a regular procedure in all our patients. Second, the 7 runs after contrast injection were reconstructed with standard parameters as described before to visualize the arterial vessels (ie, FD-CTA) (Fig 1A-E).¹ Briefly, reconstruction of the fill runs was performed by using the reconstruction-mode “native fill,” kernel-type “HU,” image-impression “normal,” and an FOV of 14 cm. Reconstruction of raw data resulted in 7 volume datasets with a batch of approximately 400 sections with a single section thickness of 0.2 mm. From the 7 datasets obtained after contrast injection, the one in the arterial phase was chosen for comparison with MRA. We used a matched volume-rendering technique and MIP reconstructions (section thickness, 5 mm; 2.5-mm spacing; axial orientation) to compare MRA with FD-CTA.¹

Dose Evaluation

We used a phantom-based method as described elsewhere to measure the effective dose to patients in this novel application.¹³

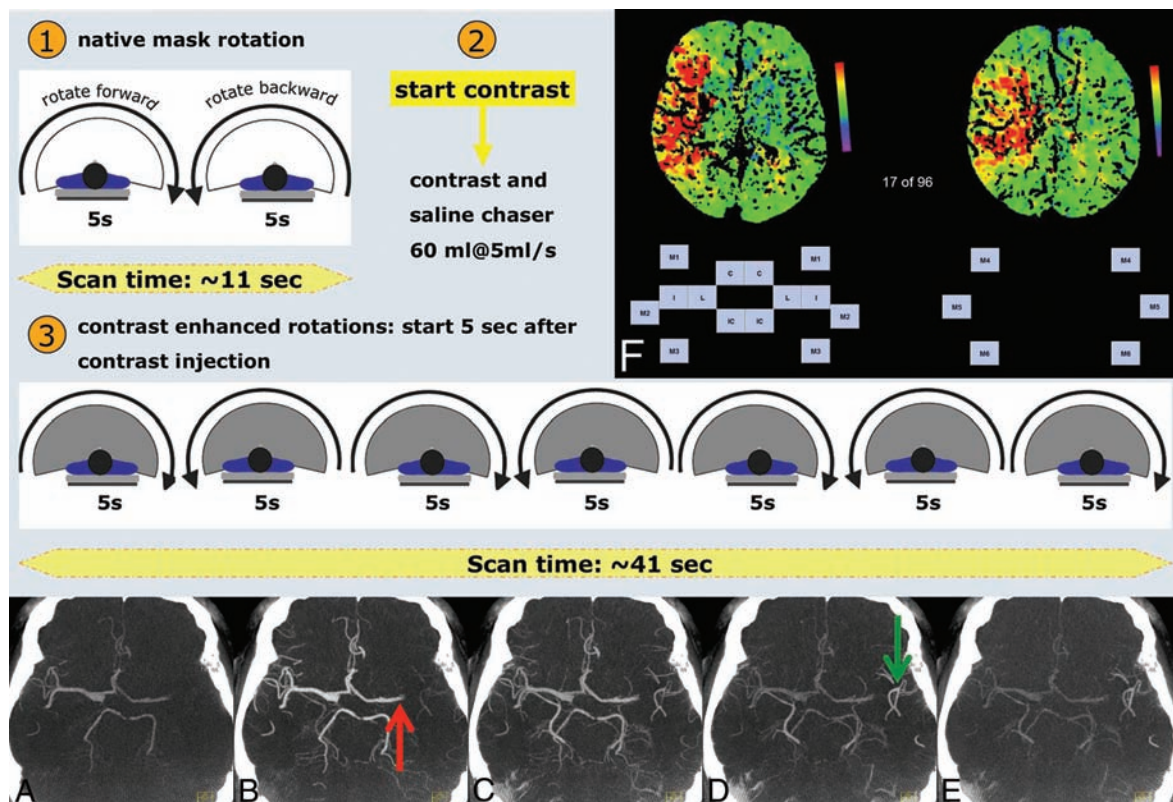


FIG 1. The FD-CT imaging protocol. The application is initiated (1) by 2 bidirectional mask runs. The contrast injection is started (2), and with a delay of 5 seconds, the acquisition of the dynamic fill runs (3) is initiated. Each fill run may be reconstructed as an FD-CTA (A–E), serving as “dynamic” contrast-enhanced angiography (4D CTA). In this example, 5 of 7 fill runs are displayed as MIP images (5-mm section thickness). Early arterial inflow is visible in A. During the arterial phase (B), left MCA occlusion (red arrow) is obvious. The late arterial phase (C) shows developing contrast attenuation increase in the left peripheral MCA branches, while during the venous phase (D), they are well-seen (green arrow). Filling is due to collateral flow. During the late venous phase (E), left peripheral MCA branches are still visible. Matlab software was used to display the parameter maps (F). Scaling is provided (color bar). Each ASPECTS region was represented by a button. By simply clicking on the desired button, the side and region of the assumed perfusion abnormality were recorded. C = caudate; L = lentiform; IC = internal capsule; I = insular ribbon; M1 = anterior MCA cortex; M2 = MCA cortex lateral to insular ribbon; M3 = posterior MCA cortex; M4, M5, and M6 are anterior, lateral, and posterior MCA territories immediately superior to M1, M2, and M3, rostral to the basal ganglia.

Image Analysis

Two experienced neuroradiologists blinded to clinical information randomly reviewed the perfusion studies separately. The Alberta Stroke Program Early CT Score was used for qualitative comparison of FD-CTP and MRP.^{14–17} For ASPECTS, the territory of the middle cerebral artery is allotted 10 points. One point is subtracted for any area of perfusion abnormality for each of the defined regions (Fig 1F). The standard ASPECTS section position at and immediately superior to the ganglionic level was identified for all datasets. These 2 images were displayed in anonymous random order by using Matlab software (MathWorks, Natick, Massachusetts) (Fig 1F). The type of the map (eg, TTP, MTT, CBV, or CBF) and the scaling (color bar) were displayed. There was no information on the technique used to obtain each single displayed map. The reviewers had to identify whether any perfusion abnormality was obvious on the 2 images. By a simple click on the region assumed to be affected by ischemic stroke, the side and ASPECTS region of the brain were recorded.

All vascular images (volume-rendering technique/MIP reconstructions of MRA and FD-CTA) were stored in anonymous random order on a dedicated workstation. Image evaluation was performed by the 2 neuroradiologists in consensus. Review was performed with the reviewers recording the presence of any vas-

cular occlusion (eg, internal carotid or middle cerebral artery occlusion).

Statistical analysis was performed by using the Statistical Package for the Social Sciences, Version 14.0 (IBM, Armonk, New York). The Pearson correlation coefficient was calculated for each reviewer in the comparison of the 2 different perfusion modalities. Additionally, interobserver correlation of the FD-CTP and MRP was calculated.

RESULTS

Between July 2012 and December 2013, 12 patients (5 men, 7 women; mean age, 72 ± 8 years) admitted for acute ischemic stroke were included. In all patients, the novel FD-CT application could be applied. In all patients, the time between MR imaging and FD-CT imaging was within 30 minutes, so we assume that relevant differences in the parameter maps were not present.

All 4 different parameter maps could be processed for both FD-CTP and MRP. Eight pairs of images per patient (initial MRP and FD-CTP before treatment), altogether 96 pairs, had to be evaluated. The ASPECTS correlation, FD-CTP versus MRP, of the 2 reviewers (reviewer A and B) revealed a high Pearson correlation coefficient in both reviewers for CBF, MTT, and TTP (0.95 to

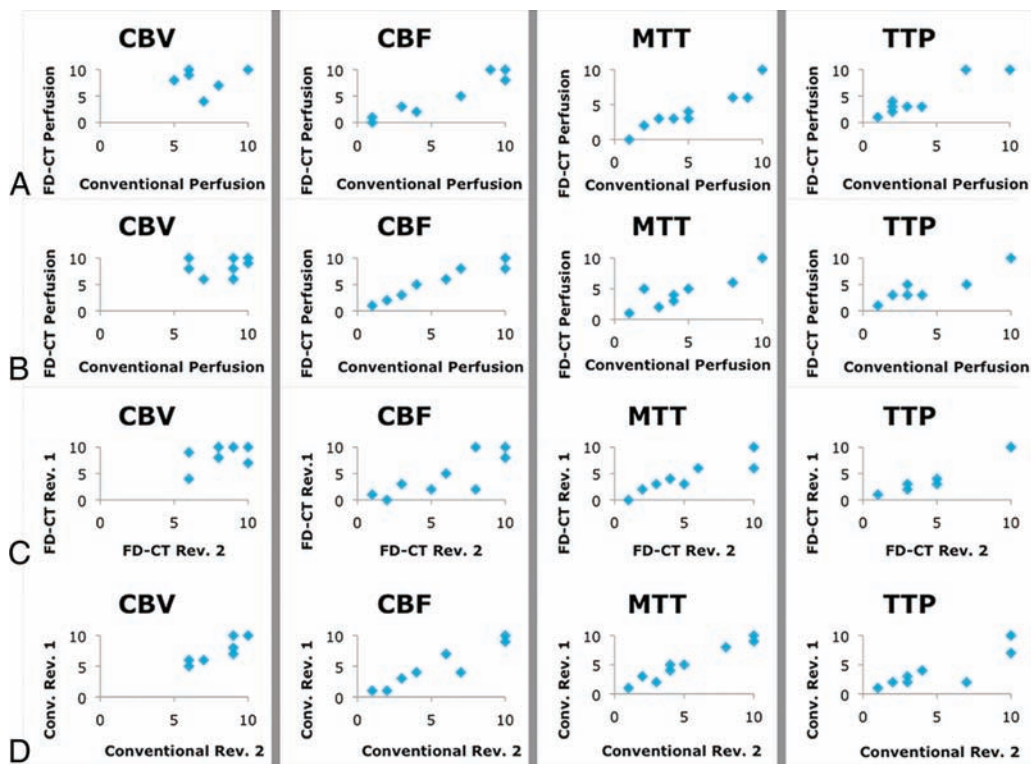


FIG 2. Pearson correlation coefficient calculation to compare FD-CTP with MRP (conventional perfusion). The correlations of the 2 reviewers (reviewers A and B) are given in A (Pearson: CBV, 0.49; CBF, 0.97; MTT, 0.96; TTP, 0.96) and B (Pearson: CBV, 0.40; CBF, 0.98; MTT, 0.95; TTP, 0.97). The correlation in CBV is limited in both reviewers. We believe this limitation is because most CBV lesions were small. Thus, the data points appear in the upper right part of the diagrams (A–D, left column). The correlation of the results of the 2 reviewers concerning FD-CTP (C, Pearson: CBV, 0.59; CBF, 0.87; MTT, 0.94; TTP, 0.99) and MR perfusion imaging (D, Pearson: CBV, 0.93; CBF, 0.96; MTT, 0.99; TTP, 0.91) was high. Scaling: x and y axis zero to a maximum of 10 ASPECTS points.

0.98). For CBV, the correlation coefficient was lower (0.49) (Fig 2A, -B). The interobserver correlation of the FD-CTP maps also revealed a high Pearson correlation coefficient for CBF, MTT, and TTP (0.87–0.99), while for CBV, it was 0.59 (Fig 2C). The interobserver correlation of the MRP maps showed a high correlation (0.91–0.99) (Fig 2D). In summary, the perfusion abnormalities could be recognized identically in FD-CTP and MRP parameter maps (Fig 3).

Review of the volume-rendering technique/MIP reconstructions of the vascular images from both FD-CTA and MRA revealed that all occlusions seen on MRA images could also be recognized in FD-CTA reconstructions. The reviewers identified MCA occlusions (5 right, 7 left MCA occlusions, all TIC1 3) in all cases (Figs 3F and 4F).

Considering patient safety, knowledge of the effective patient dose is necessary. According to the measurement method as described elsewhere, the effective dose of this novel application was 4.6 mSv.¹³

DISCUSSION

The aim of this study was to evaluate the feasibility of dynamic perfusion imaging by using a novel FD-CT application within the angiography suite. First, we described a scanning scheme analogous to MS-CT perfusion imaging (Fig 1). Contrary to MS-CT perfusion imaging, the number of acquired datasets and the duration of the entire scanning time are limited. However, the previously described prototype software allowed us to calculate and display all dynamic parameter maps. Using a qualitative evalua-

tion method, we demonstrated the comparability of the parameter maps obtained by MRP and FD-CTP. Because MRP does not provide the ability to calculate absolute values of the different parameters, absolute perfusion values were not considered. This does not represent a major drawback because in most institutions, qualitative evaluation of the maps is performed rather than measurement of absolute values in different regions of the affected tissue. It was our aim to show that the maps obtained by either MRP or FD-CTP may provide similar qualitative information. The analysis revealed high Pearson correlation coefficients except for CBV maps. We believe this limited Pearson correlation of CBV maps to be a bias caused by the fact that the CBV lesions in the patients examined were mostly small or absent (Fig 4). Visible in the diagrams, the average absolute ASPECTS numbers in the CBV evaluation were high (Fig 2). According to current literature, we only consider revascularization treatment beyond 4.5 hours if significant mismatch (small DWI and CBV lesion) is present.¹⁸ This “selection bias” is, in our opinion, why, in our series, the CBV lesion size was small. The patient example demonstrating the largest CBV lesion in our series is presented in Fig 3.

We performed additional postprocessing of the dataset by using standard software to reconstruct images to display the intracranial vessels.¹ We found that these reconstructions allowed us to visualize the intracranial arteries and occlusions with high image quality (Fig 3F and 4F). All occlusions were recognized as identical to those on MRA and FD-CTA images. This novel application performs a series of 7 bidirectional acquisitions, meaning that a

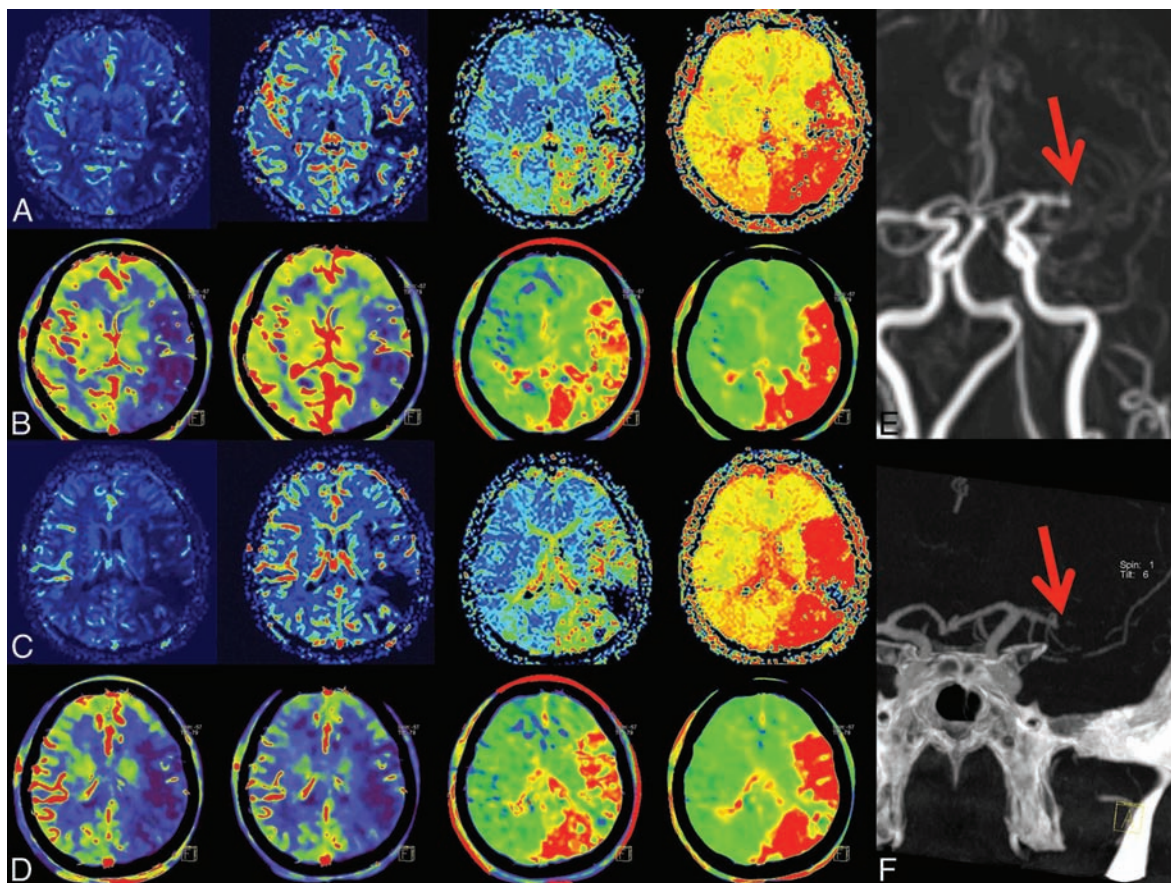


FIG 3. 1) Case example. In rows A and C, MRP; in B and D, FD-CTP parameter maps (left to right: CBF, CBV, MTT, and TTP) are displayed. A and B and C and D are corresponding MRP and FD-CTP images. Due to an MCA occlusion, there is a significant perfusion deficit in all parameter maps. The MCA occlusion was visible in either MRA (E, red arrow) or in FD-CTA (F, red arrow) volume-rendering technique reconstruction.

time-resolved “dynamic” FD-CTA may be reconstructed (Fig 1A–E). Recently, some articles described identical reconstructions conducted from MS-CT perfusion datasets (4D MS-CT angiography) to assess collaterals or thrombus length. As demonstrated in Fig 1A–E, this novel FD-CT application may also provide useful information concerning collateral flow and clot burden like that described for 4D MS-CT angiography.^{6–8,19} However, this evaluation may be subject to further assessment and was not the scope of this work.

Information on the effective dose of a novel application is crucial. In addition, we performed a dose measurement by using an Alderson Rando phantom, resulting in an effective dose of 4.6 mSv. The effective dose of this new FD-CT application is in line with MS-CT perfusion applications. In the literature, dose values of 3.6–5 mSv for MS-CT perfusion imaging are published. Additionally, as a second acquisition, a 3- to 5.5-mSv dose for angiographic MS-CT imaging is necessary, resulting in a total dose of approximately 8–9 mSv for the entire MS-CT evaluation.^{20–22} We believe that the new FD-CT application providing perfusion and angiographic evaluation with a single simultaneous acquisition and contrast is advantageous because contrast material volume and dose are less than those in MS-CT imaging.

There are some limitations. First, the number of patients included was small but sufficient to show the feasibility of this novel application. Only a qualitative comparison of the parameter maps

was performed. A subject of further studies should be to quantify absolute values in comparison with CT perfusion imaging. In all patients, general anesthesia was used. Movement may impair image quality. As a feasibility study, we did not evaluate the clinical outcome of our patients. This novel application is also limited by the total scanning time of 41 seconds and the temporal resolution of 5 seconds. A longer acquisition may further improve measurement of perfusion parameters (most CT and MR imaging applications use acquisition times of approximately 60 seconds). Additionally, a higher temporal resolution (faster rotation time than 5 seconds and less pause time between rotations) is desirable. This may improve the parameter maps and the evaluation of the dynamic FD-CTA to recognize the location of the occlusion and appearance of collateral flow. As described before, the image quality of the FD-CT needs further improvement to approach the quality level of regular MS-CT; therefore, detailed analysis of the FD-CT reconstructions was not performed. Ideally the time between the 2 imaging procedures should be equal to zero. We assume that there was no relevant change within 30 minutes.

The aim of this study was to show the feasibility and qualitative comparability of a new dynamic FD-CT perfusion and angiographic application with a standard method. Despite the necessity of further evaluation and improvement of this novel application, we have the impression that this FD-CT application is approaching MS-CT quality in terms of perfusion and

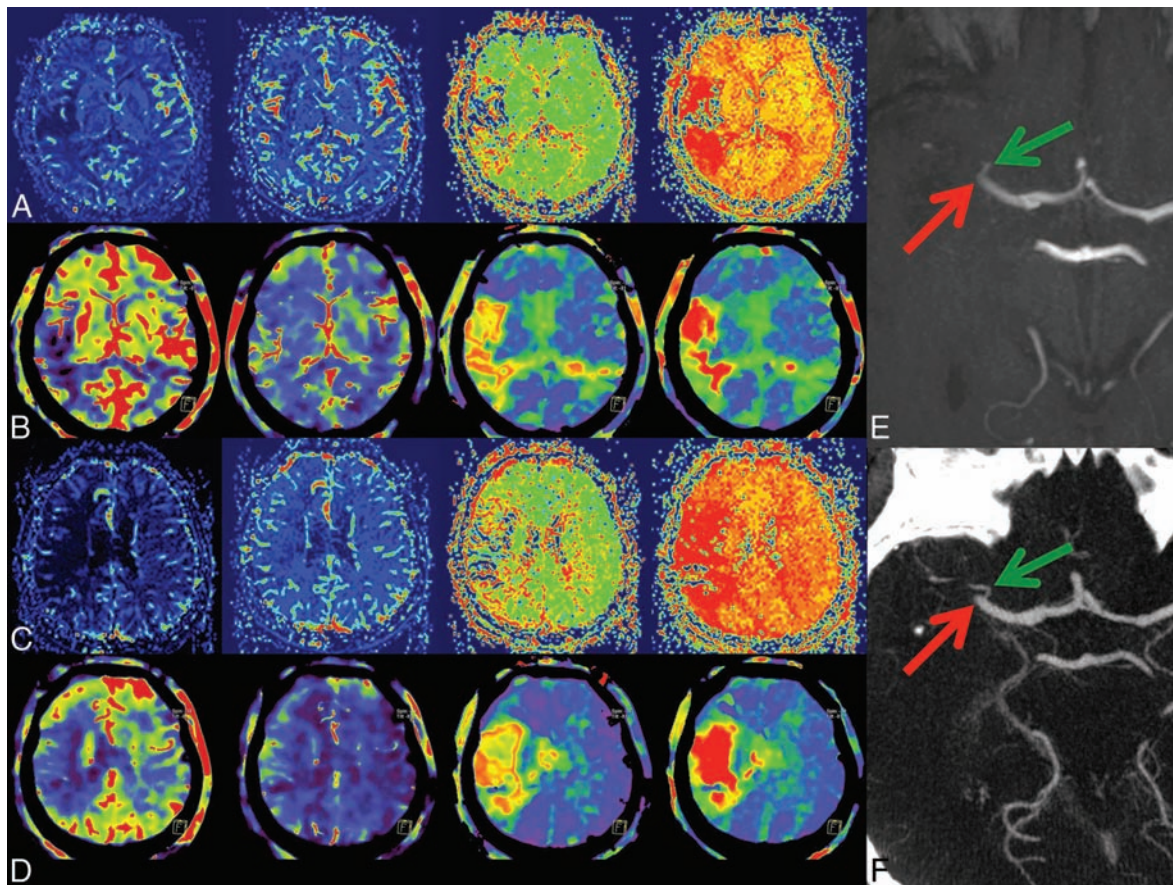


FIG 4. 2) Case example. In rows A and C, MRP; in B and D, corresponding FD-CTP parameters maps (left to right: CBF, CBV, MTT, and TTP) are displayed. A and B and C and D are corresponding MRP and FD-CTP images. Due to an MCA occlusion, there is a significant perfusion deficit in the CBF, MTT, and TTP maps. There is no significant CBV lesion in this patient. The MCA occlusion was visible in either the MRA (E, red arrow) or in FD-CTA (F, red arrow) MIP reconstruction. The green arrow indicates a small temporal branch.

angiographic imaging. Our idea is that in the future, this new application may modify the work flow of those caring for patients with stroke. To avoid time-consuming transportation of a patient from one imaging location to the angiography suite, in which the treatment is performed, direct referral will save time. In the identical environment, diagnostic imaging and treatment becomes feasible. Additional monitoring during the treatment may be possible. Further evaluation of this work flow with all its operational consequences is necessary but is beyond the scope of this work. We believe that physiologic data may be best to recognize the viability of brain tissue. Therefore, we believe that this new application is of high value. On the other hand, FD-CT quality in the visualization of brain tissue does, in our experience, not yet reach the level of MS-CT. Here further effort is necessary and ongoing so that FD-CT scanning may replace MS-CT.

CONCLUSIONS

We have shown the feasibility of a novel dynamic FD-CT perfusion and angiographic application in patients with acute stroke by using intravenous contrast application. The parameter maps and MIP/volume-rendering technique images compared well qualitatively with those of MR imaging. This FD-CT application may be substituted for MS-CT imaging in selected patients with acute

stroke so that in the future, patients may be directly referred to the angiography suite to save time and avoid transportation.

Disclosures: Tobias Struffert—RELATED: Grant: The authors gratefully acknowledge the funding of the Medical Valley National Leading Edge Cluster, Erlangen, Germany, diagnostic imaging network, subproject BD 16, research grant no. 13EX1212G.* Yu Deuerling-Zheng—OTHER RELATIONSHIPS: employment by Siemens. Michael Manhart—RELATED: Grant: Medical Valley National Leading Edge Cluster, Erlangen. Charles M. Strother—UNRELATED: Grants/Grants Pending: Research Support from Siemens.* *Money paid to the institution.

REFERENCES

1. Struffert T, Deuerling-Zheng Y, Kloska S, et al. Flat detector CT in the evaluation of brain parenchyma, intracranial vasculature, and cerebral blood volume: a pilot study in patients with acute symptoms of cerebral ischemia. *AJNR Am J Neuroradiol* 2010;31:1462–69
2. Struffert T, Deuerling-Zheng Y, Engelhorn T, et al. Feasibility of cerebral blood volume mapping by flat panel detector CT in the angiography suite: first experience in patients with acute middle cerebral artery occlusions. *AJNR Am J Neuroradiol* 2012;33:618–25
3. Struffert T, Deuerling-Zheng Y, Kloska S, et al. Cerebral blood volume imaging by flat detector computed tomography in comparison to conventional multislice perfusion CT. *Eur Radiol* 2011;21:882–89
4. Lees KR, Hankey GJ, Hacke W. Design of future acute-stroke treatment trials. *Lancet Neurol* 2003;2:54–61
5. Grigoryan M, Tung CE, Albers GW. Role of diffusion and perfusion MRI in selecting patients for reperfusion therapies. *Neuroimaging Clin N Am* 2011;21:247–57, ix-x

6. Saake M, Goelitz P, Struffert T, et al. **Comparison of conventional CTA and volume perfusion CTA in evaluation of cerebral arterial vasculature in acute stroke.** *AJNR Am J Neuroradiol* 2012;33:2068–73
7. Frölich AM, Wolff SL, Psychogios MN, et al. **Time-resolved assessment of collateral flow using 4D CT angiography in large-vessel occlusion stroke.** *Eur Radiol* 2014;24:390–96
8. Frölich AM, Schrader D, Klotz E, et al. **4D CT angiography more closely defines intracranial thrombus burden than single-phase CT angiography.** *AJNR Am J Neuroradiol* 2013;34:1908–13
9. Schramm P, Schellinger PD, Klotz E, et al. **Comparison of perfusion computed tomography and computed tomography angiography source images with perfusion-weighted imaging and diffusion-weighted imaging in patients with acute stroke of less than 6 hours' duration.** *Stroke* 2004;35:1652–58
10. Royalty K, Manhart M, Pulfer K, et al. **C-arm CT measurement of cerebral blood volume and cerebral blood flow using a novel high-speed acquisition and a single intravenous contrast injection.** *AJNR Am J Neuroradiol* 2013;34:2131–38
11. Ganguly A, Fieselmann A, Marks M, et al. **Cerebral CT perfusion using an interventional C-arm imaging system: cerebral blood flow measurements.** *AJNR Am J Neuroradiol* 2011;32:1525–31
12. Fieselmann A, Ganguly A, Deuerling-Zheng Y, et al. **Interventional 4-D C-arm CT perfusion imaging using interleaved scanning and partial reconstruction interpolation.** *IEEE Trans Med Imaging* 2012;31:892–906
13. Struffert T, Hauer M, Banckwitz R, et al. **Effective dose to patient measurements in flat-detector and multislice computed tomography: a comparison of applications in neuroradiology.** *Eur Radiol* 2014;24:1257–65
14. Aviv RI, Mandelcorn J, Chakraborty S, et al. **Alberta Stroke Program Early CT Scoring of CT perfusion in early stroke visualization and assessment.** *AJNR Am J Neuroradiol* 2007;28:1975–80
15. Lin K, Rapalino O, Law M, et al. **Accuracy of the Alberta Stroke Program Early CT Score during the first 3 hours of middle cerebral artery stroke: comparison of noncontrast CT, CT angiography source images, and CT perfusion.** *AJNR Am J Neuroradiol* 2008;29:931–36
16. Sillanpaa N, Saarinen JT, Rusanen H, et al. **CT perfusion ASPECTS in the evaluation of acute ischemic stroke: thrombolytic therapy perspective.** *Cerebrovasc Dis Extra* 2011;1:6–16
17. Psychogios MN, Schramm P, Frölich AM, et al. **Alberta Stroke Program Early CT Scale evaluation of multimodal computed tomography in predicting clinical outcomes of stroke patients treated with aspiration thrombectomy.** *Stroke* 2013;44:2188–93
18. Saake M, Breuer L, Göllitz P, et al. **Clinical/perfusion CT CBV mismatch as prognostic factor in intraarterial thrombectomy in acute anterior circulation stroke.** *Clin Neurol Neurosurg* 2014;121:39–45
19. Klingebiel R, Siebert E, Diekmann S, et al. **4-D imaging in cerebrovascular disorders by using 320-slice CT: feasibility and preliminary clinical experience.** *Acad Radiol* 2009;16:123–29
20. Cohnen M, Wittsack HJ, Assadi S, et al. **Radiation exposure of patients in comprehensive computed tomography of the head in acute stroke.** *AJNR Am J Neuroradiol* 2006;27:1741–45
21. Mnyusiwalla A, Aviv RI, Symons SP. **Radiation dose from multidetector row CT imaging for acute stroke.** *Neuroradiology* 2009;51:635–40
22. Diekmann S, Siebert E, Juran R, et al. **Dose exposure of patients undergoing comprehensive stroke imaging by multidetector-row CT: comparison of 320-detector row and 64-detector row CT scanners.** *AJNR Am J Neuroradiol* 2010;31:1003–09

MR Elastography Can Be Used to Measure Brain Stiffness Changes as a Result of Altered Cranial Venous Drainage During Jugular Compression

A. Hatt, S. Cheng,  K. Tan, R. Sinkus, and L.E. Bilston

ABSTRACT

BACKGROUND AND PURPOSE: Compressing the internal jugular veins can reverse ventriculomegaly in the syndrome of inappropriately low pressure acute hydrocephalus, and it has been suggested that this works by “stiffening” the brain tissue. Jugular compression may also alter blood and CSF flow in other conditions. We aimed to understand the effect of jugular compression on brain tissue stiffness and CSF flow.

MATERIALS AND METHODS: The head and neck of 9 healthy volunteers were studied with and without jugular compression. Brain stiffness (shear modulus) was measured by using MR elastography. Phase-contrast MR imaging was used to measure CSF flow in the cerebral aqueduct and blood flow in the neck.

RESULTS: The shear moduli of the brain tissue increased with the percentage of blood draining through the internal jugular veins during venous compression. Peak velocity of caudally directed CSF in the aqueduct increased significantly with jugular compression ($P < .001$). The mean jugular venous flow rate, amplitude, and vessel area were significantly reduced with jugular compression, while cranial arterial flow parameters were unaffected.

CONCLUSIONS: Jugular compression influences cerebral CSF hydrodynamics in healthy subjects and can increase brain tissue stiffness, but the magnitude of the stiffening depends on the percentage of cranial blood draining through the internal jugular veins during compression—that is, subjects who maintain venous drainage through the internal jugular veins during jugular compression have stiffer brains than those who divert venous blood through alternative pathways. These methods may be useful for studying this phenomenon in patients with the syndrome of inappropriately low-pressure acute hydrocephalus and other conditions.

ABBREVIATIONS: G' = shear storage modulus; G'' = shear loss modulus; MRE = MR elastography; PJVF = percentage jugular venous flow; SILPAH = syndrome of inappropriately low-pressure acute hydrocephalus

Changes in venous drainage from the cranium, such as reduction in internal jugular vein flow when moving from a supine to upright posture, can alter cerebral hemodynamics and CSF dynamics.¹ However, postural changes are difficult to study by

using brain MR imaging. There is recent clinical interest in understanding how cranial venous outflow affects the brain, in part due to the controversial chronic cerebrospinal venous insufficiency hypothesis.²

Reduction in venous outflow through the internal jugular veins, through the use of an elastic bandage (neck wrap), has also been used as a treatment for the syndrome of inappropriately low-pressure acute hydrocephalus (SILPAH),³ also known as negative or low-pressure hydrocephalus, rapidly reversing ventriculomegaly and restoring neurologic function.^{4–8} SILPAH is a rare and enigmatic condition in which patients exhibit ventricu-

Received October 8, 2014; accepted after revision March 3, 2015.

From Neuroscience Research Australia (A.H., S.C., K.T., L.E.B.), Randwick, New South Wales, Australia; School of Mechanical Engineering (S.C.), Macquarie University, North Ryde, New South Wales, Australia; School of Medical Sciences (S.C.) and Graduate School of Biomedical Engineering (K.T.), University of New South Wales, Kensington, New South Wales, Australia; British Heart Foundation Centre of Excellence (R.S.), Division of Imaging Sciences and Biomedical Engineering, King's College London, King's Health Partners, St. Thomas' Hospital, London, United Kingdom; and Prince of Wales Clinical School (L.E.B.), University of New South Wales, Randwick, New South Wales, Australia.

This research was supported in part by the Ronald Geoffrey Arnott Foundation. Lynne Bilston is funded by a National Health and Medical Research Council fellowship (No. 568610). Ralph Sinkus receives financial support from the UK Department of Health via the National Institute for Health Research Comprehensive Biomedical Research Centre award to Guy's and St Thomas' National Health Service Foundation Trust in partnership with King's College London and King's College Hospital National Health Service Foundation Trust.

Paper presented in part in abstract form at: Annual Meeting of the Australia and New Zealand Society of Magnetic Resonance, October 27–30, 2013; Brisbane, Queensland, Australia; and in poster form at: University of New South Wales Brain Sciences Symposium, October 18, 2013; Sydney, New South Wales, Australia.

Please address correspondence to Lynne E. Bilston, PhD, Neuroscience Research Australia, Barker St, Randwick, NSW 2031, Australia; e-mail: lbilston@neura.edu.au

 Indicates open access to non-subscribers at www.ajnr.org

<http://dx.doi.org/10.3174/ajnr.A4361>

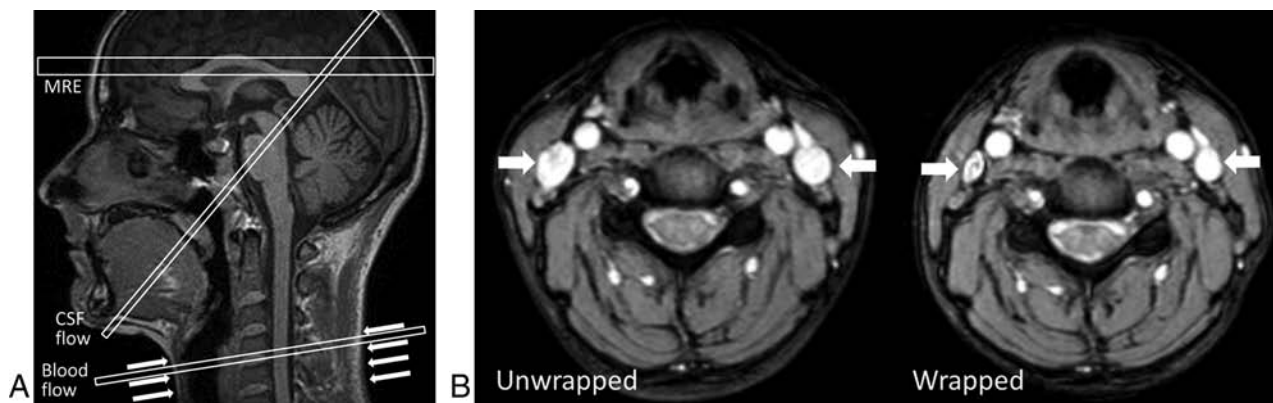


FIG 1. A, Sagittal view of imaging planes for the MRE study within and just above the ventricles, phase-contrast MR imaging CSF flow study of the cerebral aqueduct, and phase-contrast MR imaging flow study of the blood flow in the neck vessels at the level of the compression. The arrows denote the position of neck wrap. B, Images of neck vessels with and without the neck wrap, showing the reduction in internal jugular vein area. Internal jugular veins are indicated by white arrows.

omegaly and very low intracranial pressure⁹ associated with obstruction to the CSF pathways between the ventricles and the subarachnoid space. Despite low intracranial pressure, symptoms mirror those of high intracranial pressure.^{4-7,9-12} The pathophysiology for SILPAH remains unclear. However, changes in brain stiffness as a result of the loss of extracellular fluid^{4,8,9,11-13} combined with CSF leaks⁶ have been suggested. Jugular compression has also been observed to increase the amplitude of CSF waveforms in the cervical subarachnoid space in subjects whose venous drainage took place primarily through the internal jugular veins and to decrease the amplitudes in subjects with primarily extrajugular drainage.¹⁴ These changes may be related to alterations in intracranial pressure arising from increased dural venous pressure⁴ and stiffening of brain tissue.^{4,6,8} However, the relationships between cranial venous drainage routes, cerebral CSF flow, and brain tissue properties in the context of jugular compression have not been investigated, to our knowledge.

Viscoelastic tissue response to loading consists of a recoverable elastic component and a nonrecoverable viscous component. The response to shear loading comprises the shear storage (G') and loss (G'') moduli, representing elastic and viscous components, respectively. Increases in the shear moduli reflect higher stiffness.

MR elastography (MRE)¹⁵ is a noninvasive imaging technique that measures tissue stiffness by imaging the propagation of mechanical vibration with motion-sensitive gradients. Viscoelastic properties are quantified by analyzing the wave-propagation characteristics. MRE has been used to quantify the viscoelastic properties of healthy *in vivo* brain tissue¹⁶⁻¹⁸ and brain disorders such as normal pressure hydrocephalus.^{19,20} The shear moduli obtained depend on the vibration frequency, with lower values obtained at low frequencies.

In this study, we aimed to use MRE to determine the effect of restricting cranial venous outflow by using bilateral jugular compression on brain stiffness and CSF flow in healthy volunteers. We hypothesized that brain viscoelasticity and CSF velocity would increase with jugular compression.

MATERIALS AND METHODS

Nine healthy volunteers (3 women; mean age, 32.6 ± 10.9 years) were imaged supine with and without jugular compression. The

research was approved by the local Human Research Ethics Committee. Participants gave written informed consent.

Bilateral compression of the internal jugular veins⁴⁻⁸ was achieved by fastening an 8-cm wide elastic bandage around the neck (Fig 1) to apply a mild compression, but not impair breathing or comfort. After 1 scan acquisition, the wrap was released while maintaining the head position. After a short pause allowing normal flow to be restored, scans were repeated.

MR Imaging

Data were acquired by using a 3T MR imaging scanner (Achieva 3T TX; Philips Healthcare, Best, the Netherlands) and a 1-channel transmit-receive neurovascular coil.

Vascular and CSF Flow Studies. Phase-contrast MR imaging was used to measure blood flow through the internal jugular veins and carotid and vertebral arteries at the level of the neck wrap and CSF flow through the cerebral aqueduct. The imaging planes are shown in Fig 1. A single 5-mm-thick section was assessed over 30 cardiac phases and gated retrospectively by using a finger plethysmography sensor. For the vascular flow study, a phase-encoding velocity of 60 cm/s was used with FOV = 180×180 mm, matrix = 288×288 , TR/TE = 21/5.73 ms, flip angle = 10° . For CSF flow, a phase-encoding velocity of 4 cm/s was used, with FOV = 180×180 mm, matrix = 352×352 , TR/TE = 21/10.1 ms, flip angle = 10° .

MRE. MRE was performed on an axial imaging region within and just above the ventricles (Fig 1). Shear waves were produced in the brain via a purpose-built mechanical transducer consisting of a coaxial coil system and an individually molded polymer mouthguard,^{16,18} triggered by the MR spectrometer in synchrony with motion-sensitized gradients. A 30-Hz sinusoidal vibration frequency was used to maximize wave propagation into the deep regions of the brain. Tissue displacements were imaged in 3 directions at 8 time points during the sinusoidal vibration with a fast-field echo MRE sequence.²¹ Imaging parameters were the following: FOV = 192×192 mm, matrix = 96×96 , 9 sections, section thickness = 2-mm, TR/TE = 104.1/9.2 ms, flip angle = 20° , sensitivity encoding = 1.5 with no k -space reduction. Acquisition

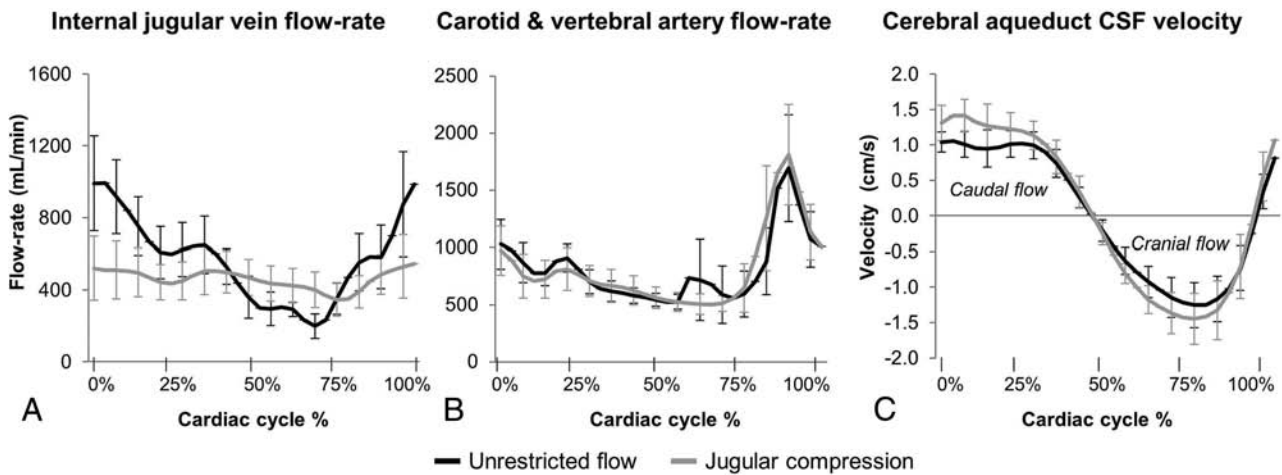


FIG 2. Group mean flow waveforms for internal jugular vein flow (A) and carotid and vertebral artery flow (B); and group mean CSF velocity waveforms through the cerebral aqueduct (C). Venous flow-rate peaks are suppressed with jugular compression; however, arterial flow waveforms are unaffected. Maximal caudally directed velocity of the CSF in the aqueduct increases with jugular compression.

Table 1: Blood flow parameters

	Internal Jugular Vein Flow		Arterial Flow	
	Unrestricted Flow	Jugular Compression	Unrestricted Flow	Jugular Compression
Mean vessel area (cm ²)				
Mean	1.17 ± 0.54	0.70 ± 0.35	1.0 ± 0.77	0.97 ± 0.68
Range	0.40–2.18	0.29–1.41	–0.99–1.53	–0.76–1.56
t test	t = 3.56, P = .005 ^a		t = 0.51, P = .604	
Mean flow rate (mL/min) (caudal flow for venous flow, cranial for arterial)				
Mean	572.2 ± 219.7	460.8 ± 202.4	814.7 ± 221.9	815.3 ± 290.6
Range	153.8–862.2	135–726.4	268–989.2	127.7–1070
t test	t = 2.85, P = .008 ^a		–0.01, P = .989	
Flow-rate amplitude (mL/min)				
Mean	974.1 ± 523.6	382.6 ± 312.7	1803.8 ± 490.1	1720.6 ± 688.4
Range	198.5–1838.8	56.8–1069.0	601.4–2290.2	282.8–2721.4
t test	t = 3.75, P = .002 ^a		t = 0.58, P = .558	

^a P < .05, paired t test.

time was 4 minutes. A high-resolution (matrix = 256 × 256) T2-weighted image set with matching geometry was acquired.

Analysis

Vascular and CSF Flow Studies. Vascular and CSF flows were analyzed by using Segment (Academic Research Version 1.9R2455; Medviso, Lund, Sweden) following eddy current effect compensation²² as follows:

- Mean vessel area: The mean cross-sectional area (square centimeters) of the left and right vertebral and carotid arteries, and left and right internal jugular veins.
- Mean flow rate and flow-rate amplitude: The mean blood flow rates (milliliter/minute) and the flow-rate amplitude (milliliter/minute) calculated as the difference between the maximum and minimum flow rates.
- Percentage jugular venous flow (PJVF): Flow in the internal jugular veins as a percentage of carotid and vertebral arterial inflow.
- CSF velocity maxima: The maximum velocity (centimeter/second) of CSF flowing in the caudal and cranial directions.
- Duration of caudal flow: The duration of caudally directed flow as a percentage of the cardiac cycle.

MRE. The shear storage and loss moduli, G' and G'', were estimated from the tissue displacements by numerically solving the governing equation for shear wave propagation through an isotropic viscoelastic material after applying the curl operator to remove the pressure term associated with compressional waves. Details of the theory and reconstruction have been described in depth previously.^{16,23,24}

ROIs covering the whole-brain parenchyma (gray and white matter) in each MRE section were manually defined on the anatomic images by using ImageJ software (National Institutes of Health, Bethesda, Maryland) and exported to Matlab (MathWorks, Natick, Massachusetts). Sulci, gyri, and regions of CSF, such as the ventricles and adjacent pixels that could have partial volumes of CSF, were excluded from the ROIs.

Statistical Analysis

The range, mean, and SD of the flow and brain viscoelastic parameters were calculated with and without jugular compression. A paired t test was used to evaluate the decrease in venous flow, increases in CSF flow, and viscoelastic parameters and to analyze differences in arterial flow and heart rate. Linear regression was used to analyze the relationships between PJVF and

the shear storage and loss moduli and between the intrasubject change in G' and G'' and the maximal velocity of caudally directed CSF.

Table 2: PJVF values for subjects

	PJVF	
	Unrestricted Flow	Jugular Compression
Subject 1	97.2%	53.0%
Subject 2	84.1%	70.6%
Subject 3	82.1%	81.5%
Subject 4	76.8%	69.5%
Subject 5	74.2%	44.3%
Subject 6	61.2%	27.0%
Subject 7	59.8%	63.8%
Subject 8	59.3%	60.0%
Subject 9	17.9%	13.7%
Mean	68.1 ± 22.7%	53.7 ± 21.9%
t test	$t = 2.33, P = .019^a$	
Predominantly jugular flow (between 50% and 100%) Subjects	8/9	6/9
Predominantly nonjugular flow (<50%) Subjects	1/9	3/9

^a $P < .05$, paired t test.

Table 3: CSF velocity parameters

	Aqueductal Flow	
	Unrestricted Flow	Jugular Compression
Maximum caudal velocity (cm/s)		
Mean	1.18 ± 0.33	1.53 ± 0.42
Range	0.81–1.85	1.04–2.36
t test	$t = -4.96, P = .0004^a$	
Maximum cranial velocity (cm/s)		
Mean	1.38 ± 0.57	1.62 ± 0.62
Range	0.73–2.47	0.66–2.48
t test	$t = 1.58, P = .066$	
Duration of caudally directed flow (% cardiac cycle)		
Mean	49.9 ± 5.2%	51.4 ± 5.3%
Range	40.7%–57.7%	42.1%–61.7%
t test	$t = -1.0, P = .160$	

^a $P < .05$, paired t test.

RESULTS

Blood Flow

Figure 2 shows the group mean flow waveforms for internal jugular venous flow (Fig 2A) and carotid and vertebral arterial flow (Fig 2B) with and without jugular compression. Jugular compression significantly reduced the mean internal jugular vein area ($t = 3.56, P = .005$), with suppression of the venous flow peak following systole and a significant reduction in the mean and peak venous flow rate ($t = 2.85, P = .008; t = 3.75, P = .002$). The mean arterial area, flow waveforms, and flow parameters were unaffected by jugular compression ($P > .05$). Blood flow parameters and statistical results are listed in Table 1.

Table 2 contains the values of PJVF for subjects with and without jugular compression. Without compression, the internal jugular veins carried most of the outflow of cranial blood (PJVF values of >50%) in 8 of 9 subjects. During jugular compression, PJVF was decreased (flow was diverted to nonjugular pathways) in 7 subjects, and 3 of these had predominantly nonjugular venous drainage (PJVF of <50%). PJVF was reduced with neck wrapping ($t = 2.33, P = .019$), indicating the redirection of venous blood to nonjugular vessels.

CSF Flow

Figure 2C depicts the group mean cerebral aqueduct CSF flow with and without jugular compression. Corresponding flow parameters and statistical analyses are listed in Table 3.

The maximal velocity of caudally directed CSF through the aqueduct increased significantly with jugular compression ($t = -4.96, P < .001$). Neither the maximal cranially directed velocity nor the duration of caudally directed flow was significantly changed ($P > .05$).

Heart rates calculated from vascular data were not significantly affected by the neck wrap ($t = -0.66, P = .528$).

Viscoelasticity

Figure 3 shows sample viscoelastic maps for shear storage and loss moduli. Table 4 contains the range, mean, SD, and statistics. Figure 4A depicts the change in G' and G'' between the unrestricted and jugular compression conditions for all subjects.

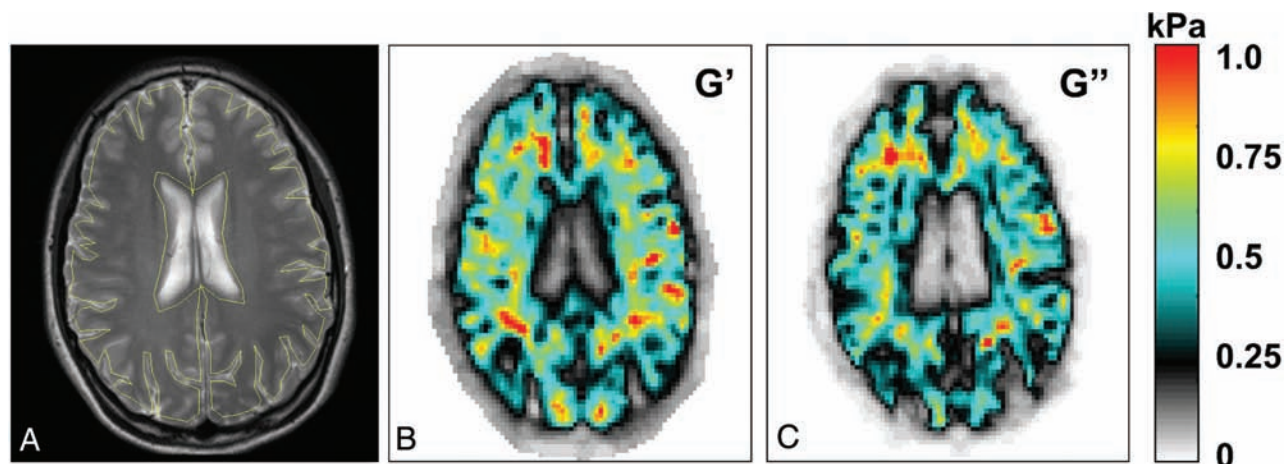


FIG 3. ROI and sample viscoelastic maps. A, Sample high-resolution anatomic image shows the ROI (yellow line). Viscoelastic property maps for G' (B) and G'' (C) in kilopascals. In the viscoelastic maps, the ventricles and large sulci have very low (near zero) shear moduli, indicating that they are filled with CSF, which has waterlike properties. Stiffer tissue is indicated by warmer colors, as indicated by the color bar (right).

Contrary to our hypothesis, jugular compression did not cause an overall significant increase in either the storage or loss moduli of the brain ($t = 0.167, P = .436; t = 0.227; P = .413$, respectively).

Linear regression results are in Table 5. There was no relationship between G' and G'' and the percentage of arterial blood draining through the internal jugular veins for unrestricted flow. However with jugular compression, both G' and G'' increased linearly with PJVF ($R^2 = 0.475, P = .04$; and $R^2 = 0.449, P = .048$, respectively) (Fig 5). There was no relationship between the change in the viscoelastic properties and the change in the peak caudal CSF velocity ($P > .05$).

Subject with the Lowest Initial Brain G'

Figure 4 (right) shows the CSF waveforms for 1 subject whose baseline brain stiffness (G') was lower than that of the other subjects (identified by the black line). Jugular compression in this subject resulted in a 17% increase in the brain shear storage modulus. This was accompanied by a 61% increase in the maximal peak caudal CSF velocity and an 11% increase in the duration of caudal CSF flow. These were the largest increases of these parameters seen in any subject. This pattern was, however, not uniform across all subjects.

DISCUSSION

This study shows that brain tissue stiffness during jugular compression varies depending on whether cranial venous blood flow is maintained or diverted from the internal jugular veins during jugular compression. Specifically, during jugular compression, brain tissue viscoelastic properties (shear storage and loss moduli) increase with the percentage of cranial blood draining through the

internal jugular veins—that is, brain tissue stiffness was greater in subjects who maintained jugular drainage paths despite jugular compression than in those who diverted venous blood through extrajugular pathways. CSF pulsations in the cerebral aqueduct are also affected by jugular compression, with an increase in the maximal velocity of caudally directed CSF during jugular compression. To our knowledge, this is the first study investigating the effect of jugular compression on the viscoelastic properties of the brain and intraventricular CSF dynamics.

Jugular compression is known to increase cerebral venous pressure and raise intracranial pressure due to increased resistance to outflow through the internal jugular veins.²⁵⁻²⁸ In this study, higher brain tissue shear storage and loss moduli were associated with the maintenance of predominantly jugular flow paths during jugular compression rather than diversion of blood flow to extrajugular pathways such as the vertebral, intraspinal, and deep cervical veins. Maintaining jugular venous flow during jugular compression suggests that the resistance to flow in the extrajugular pathways of these individuals was greater than that in their compressed internal jugular veins. Higher overall cerebral venous pressures likely result in these subjects having increased forces applied to the brain tissue. Conversely, internal jugular vein flow not decreasing as a proportion of total cranial outflow (in 2/9 subjects) suggests that even after compression, the internal jugular vein remained a low-resistance pathway. Because brain tissue stiffness increases with compression due to its nonlinear viscoelastic behavior,²⁹⁻³¹ it is probable that the increasing shear

Table 4: Elastic (G') and viscous (G'') mechanical properties of brain tissue

	Unrestricted Flow	Jugular Compression
G' (kPa)		
Mean	0.691 ± 0.067	0.688 ± 0.065
Range	0.567–0.805	0.606–0.798
t test	$t = 0.17, P = .436$	
G'' (kPa)		
Mean	0.587 ± 0.052	0.585 ± 0.046
Range	0.482–0.662	0.531–0.645
t test	$t = 0.23, P = .413$	

Table 5: Linear regression coefficients for the relationships between PJVF and G' and G'' with unrestricted flow and with jugular compression, and change in mean G' , G'' , and maximal caudal CSF velocity

	R^2	P
G' and PJVF, unrestricted flow	0.136	.330
G' and PJVF, jugular compression	0.475	.040 ^a
G'' and PJVF, unrestricted flow	0.151	.301
G'' and PJVF, jugular compression	0.449	.048 ^a
% Change G' and % change in max. caudal CSF velocity	0.412	.063
% Change G'' and % change in max. caudal CSF velocity	0.171	.268

Note:—max. indicates maximum.

^a $P < .05$, paired t test.

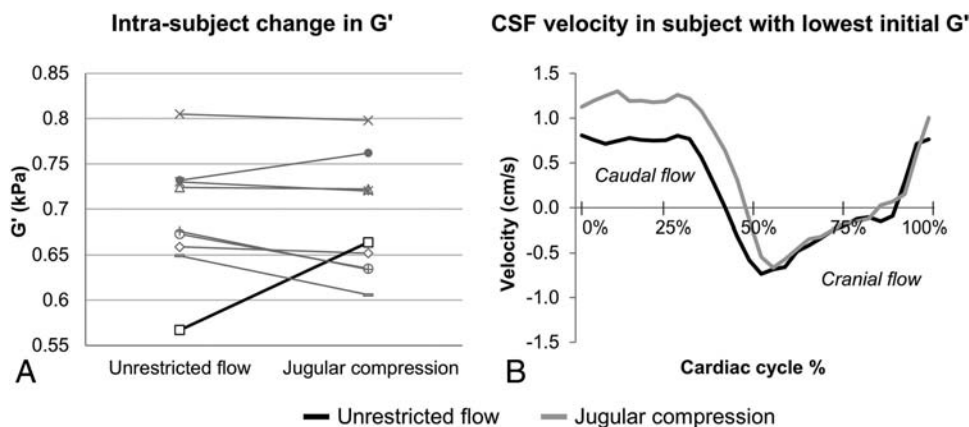


FIG 4. A, Individual subject change in G' in unrestricted and jugular compression conditions for all subjects. B, Cerebral aqueduct CSF velocity waveforms for a single subject are depicted by the black line in A. In this subject, the 17% increase in G' with jugular compression was related to a 61% increase in the maximal caudal CSF velocity and an 11% longer caudal-flow duration.

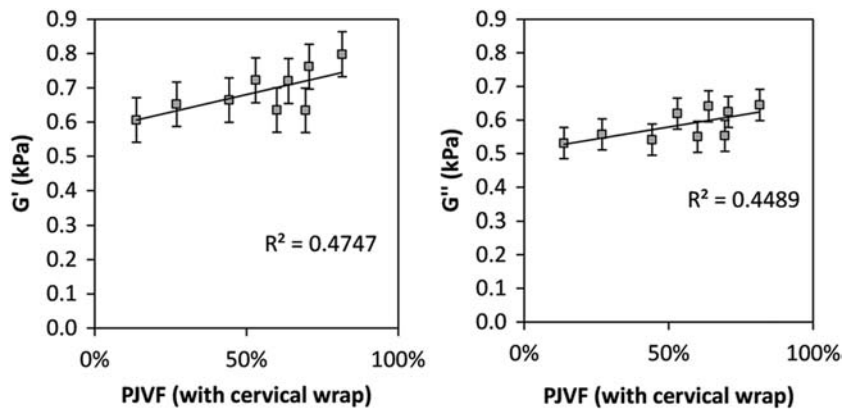


FIG 5. The relationship between shear moduli and the percentage of jugular vein flow with the cervical wrap in place. Storage modulus (G' , left) and loss modulus (G'' , right). Error bars are standard error of the mean in both panels. Both storage and loss moduli are significantly correlated with the percentage of jugular vein flow with the cervical wrap in place ($P < .05$).

storage and loss moduli measured with increasing jugular flow percentage are the result of higher pressure on the brain tissue from the cerebral veins. Note that the absolute changes in brain stiffness observed here in healthy volunteers are small and may not have clinical significance.

In this study, CSF was expelled more rapidly from the cerebral aqueduct with jugular compression. Similar findings have been reported in the cervical subarachnoid space in subjects with primarily jugular venous flow paths before compression.¹⁴ CSF pulsations in the brain are the result of the movement of cerebral blood within the rigid intracranial system.³² The influx of arterial blood following systole causes venous blood to be expelled from the cranium and CSF to flow into the spinal subarachnoid space. Jugular compression restricts venous outflow, limiting cranial space for arterial expansion and promoting more rapid expulsion of CSF from the ventricles.

Pang and Altschuler⁹ and ReKate⁸ describe SILPAH as resulting from changes to the viscoelastic properties of the brain. ReKate refers to the condition as “floppy brain syndrome,” describing jugular compression as a means of increasing brain “turgor,” defined as the ability of the brain tissue to resist distortion.⁸ While the hypothesis of lower brain tissue stiffness in patients with SILPAH^{4,6,8} has not been tested, 1 subject in our cohort who initially had lower brain stiffness than the rest of the group may lend support to the idea that jugular compression may “normalize” brain viscoelasticity. Jugular compression in this subject resulted in the largest increases in brain viscoelasticity and CSF velocity of any subject. If patients with SILPAH have lower brain stiffness than healthy subjects, it is possible that the stiffening of the brain tissue through the use of the neck wrap is enough to encourage expulsion of excess CSF from the ventricles, restoring normal ventricular size. This remains to be determined in patients with SILPAH, but this study suggests such research is feasible.

MRE has not been previously used to examine changes in brain stiffness in SILPAH or as a result of jugular vein compression. The lower absolute shear modulus values obtained in this study compared with previous studies^{16,19} are due to the lower vibration frequency, because brain tissue shear moduli increase with frequency.³¹ The lower frequency was chosen to maximize wave penetration into the deep brain because higher frequencies are more rapidly attenuated in brain tissue.

Limitations of this study include performing our measurements on healthy volunteers, who may not exhibit the same physiologic responses (such as cerebral vascular autoregulation) as patients with SILPAH. In addition, we did not measure intracranial or venous pressures, so we can only speculate about changes in these parameters with jugular compression. However, this study demonstrates the feasibility of using MRE in clinical studies to investigate the biomechanical mechanisms of brain disorders and its potential as an adjunct to phase-contrast MR imaging in assessing patients with CSF flow disorders.

CONCLUSIONS

In healthy subjects, those who do not divert venous blood through extrajugular pathways during jugular compression have higher brain stiffness than those who do, likely as a result of increased neurovascular pressure. While this study did not confirm our hypothesis that jugular compression increases brain viscoelasticity in all subjects, it has shown that the MRE technique can measure changes in brain tissue viscoelasticity in this context and suggests that MRE could be a useful tool to measure brain mechanical properties of patients with SILPAH, including during jugular compression. These findings may help elucidate the mechanisms of SILPAH and the means by which jugular compression improves symptoms, and they may also be useful for other conditions in which jugular flow is restricted.

ACKNOWLEDGMENTS

We thank the staff of the NeuRA Clinical Research Imaging Centre for their help in this study and also Dr Harold ReKate for stimulating discussions regarding this study.

Disclosures: Alice Hatt—RELATED: Grant: Ronald Geoffrey Arnott Foundation.* Lynne E. Bilston—RELATED: Grant: Ronald Geoffrey Arnott Foundation,* National Health and Medical Research Council of Australia*; UNRELATED: Consultancy: Linguaflex LLC; Grants/Grants Pending: National Health and Medical Research Council,* Australian Research Council,* Comments: I have research grant funding from these councils; Travel/Accommodations/Meeting Expenses Unrelated to Activities Listed: Université de Technologie de Compiègne, France, Comments: travel expenses and honorarium to attend the Scientific Advisory Committee for UTC Laboratory of Excellence in System of Systems, 2013 and 2014. *Money paid to the institution.

REFERENCES

- Alperin N, Lee SH, Sivaramakrishnan A, et al. Quantifying the effect of posture on intracranial physiology in humans by MRI flow studies. *J Magn Reson Imaging* 2005;22:591–96
- Laughlin S, Macgowan CK, Traubici J, et al. No evidence for impairment of venous hemodynamics in children or young adults with pediatric-onset multiple sclerosis. *AJNR Am J Neuroradiol* 2013;34:2366–72
- Hamilton MG, Price AV. Syndrome of inappropriately low-pressure acute hydrocephalus (SILPAH). *Acta Neurochir Suppl* 2012;113:155–59
- ReKate HL, Nadkarni TD, Wallace D. The importance of the cortical

- subarachnoid space in understanding hydrocephalus. *J Neurosurg Pediatr* 2008;2:1–11
5. Wait SD, Ponce FA, Killory BD, et al. **Neuroleptic malignant syndrome from central nervous system insult: 4 cases and a novel treatment strategy.** *J Neurosurg Pediatr* 2009;4:217–21
 6. Filippidis AS, Kalani MY, Nakaji P, et al. **Negative-pressure and low-pressure hydrocephalus: the role of cerebrospinal fluid leaks resulting from surgical approaches to the cranial base.** *J Neurosurg* 2011;115:1031–37
 7. Kalani MY, Turner JD, Nakaji P. **Treatment of refractory low-pressure hydrocephalus with an active pumping negative-pressure shunt system.** *J Clin Neurosci* 2013;20:462–66
 8. Rekatte HL. **Recent advances in the understanding and treatment of hydrocephalus.** *Semin Pediatr Neurol* 1997;4:167–78
 9. Pang D, Altschuler E. **Low-pressure hydrocephalic state and viscoelastic alterations in the brain.** *Neurosurgery* 1994;35:643–56; discussion 655–56
 10. Owlser BK, Jacobson EE, Johnston IH. **Low pressure hydrocephalus: issues of diagnosis and treatment in five cases.** *Br J Neurosurg* 2001;15:353–59
 11. Lesniak MS, Clatterbuck RE, Rigamonti D, et al. **Low pressure hydrocephalus and ventriculomegaly: hysteresis, non-linear dynamics, and the benefits of CSF diversion.** *Br J Neurosurg* 2002;16:555–61
 12. Clarke MJ, Maher CO, Nothdurft G, et al. **Very low pressure hydrocephalus: report of two cases.** *J Neurosurg* 2006;105:475–78
 13. Rekatte H. **Brain turgor (Kb): intrinsic property of the brain to resist distortion.** *Pediatr Neurosurg* 1992;18:257–62
 14. Bhadelia RA, Bogdan AR, Wolpert SM. **Cerebrospinal fluid flow waveforms: effect of altered cranial venous outflow—a phase-contrast MR flow imaging study.** *Neuroradiology* 1998;40:283–92
 15. Muthupillai R, Lomas DJ, Rossman PJ, et al. **Magnetic resonance elastography by direct visualization of propagating acoustic strain waves.** *Science* 1995;269:1854–57
 16. Green MA, Bilston LE, Sinkus R. **In vivo brain viscoelastic properties measured by magnetic resonance elastography.** *NMR Biomed* 2008;21:755–64
 17. Hamhaber U, Sack I, Papazoglou S, et al. **Three-dimensional analysis of shear wave propagation observed by in vivo magnetic resonance elastography of the brain.** *Acta Biomater* 2007;3:127–37
 18. Zhang J, Green MA, Sinkus R, et al. **Viscoelastic properties of human cerebellum using magnetic resonance elastography.** *J Biomech* 2011;44:1909–13
 19. Streitberger KJ, Wiener E, Hoffmann J, et al. **In vivo viscoelastic properties of the brain in normal pressure hydrocephalus.** *NMR Biomed* 2011;24:385–92
 20. Freimann FB, Streitberger KJ, Klatt D, et al. **Alteration of brain viscoelasticity after shunt treatment in normal pressure hydrocephalus.** *Neuroradiology* 2012;54:189–96
 21. Garteiser P, Sahebjavaher RS, Ter Beek LC, et al. **Rapid acquisition of multifrequency, multislice and multidirectional MR elastography data with a fractionally encoded gradient echo sequence.** *NMR Biomed* 2013;26:1326–35
 22. Heiberg E, Sjögren J, Ugander M, et al. **Design and validation of Segment—freely available software for cardiovascular image analysis.** *BMC Med Imaging* 2010;10:1
 23. Sinkus R, Lorenzen J, Schrader D, et al. **High-resolution tensor MR elastography for breast tumour detection.** *Phys Med Biol* 2000;45:1649–64
 24. Sinkus R, Tanter M, Xydeas T, et al. **Viscoelastic shear properties of in vivo breast lesions measured by MR elastography.** *Magn Reson Imaging* 2005;23:159–65
 25. Toung T, Ngeow YK, Long DL, et al. **Comparison of the effects of positive end-expiratory pressure and jugular venous compression on canine cerebral venous pressure.** *Anesthesiology* 1984;61:169–72
 26. Hulme A, Cooper R. **The effects of head position and jugular vein compression (JVC) on intracranial pressure (ICP): a clinical study.** In: Beks JW, Bosch DA, Brock M, eds. *Intracranial Pressure III*. Berlin: Springer-Verlag; 1976:259–63
 27. Grady MS, Bedford RF, Park T. **Changes in superior sagittal sinus pressure in children with head elevation, jugular venous compression, and PEEP.** *J Neurosurg* 1986;65:199–202
 28. Ho AM, Fung KY, Joynt GM, et al. **Rigid cervical collar and intracranial pressure of patients with severe head injury.** *J Trauma* 2002;53:1185–88
 29. Cheng S, Bilston LE. **Unconfined compression of white matter.** *J Biomech* 2007;40:117–24
 30. Bilston LE, Liu Z, Phan-Thien N. **Large strain behaviour of brain tissue in shear: some experimental data and differential constitutive model.** *Biorheology* 2001;38:335–45
 31. Cheng S, Clarke EC, Bilston LE. **Rheological properties of the tissues of the central nervous system: a review.** *Med Eng Phys* 2008;30:1318–37
 32. Greitz D, Wirestam R, Franck A, et al. **Pulsatile brain movement and associated hydrodynamics studied by magnetic resonance phase imaging: the Monro-Kellie doctrine revisited.** *Neuroradiology* 1992;34:370–80

Diagnostic Accuracy of 4 Commercially Available Semiautomatic Packages for Carotid Artery Stenosis Measurement on CTA

J. Borst, H.A. Marquering, M. Kappelhof, T. Zadi, A.C. van Dijk, P.J. Nederkoorn, R. van den Berg, A. van der Lugt, and C.B.L.M. Majoie



ABSTRACT

BACKGROUND AND PURPOSE: Semiautomatic measurement of ICA stenosis potentially increases observer reproducibility. In this study, we assessed the diagnostic accuracy and interobserver reproducibility of a commercially available semiautomatic ICA stenosis measurement on CTA and estimated the agreement among different software packages.

MATERIALS AND METHODS: We analyzed 141 arteries from 90 patients with TIA or ischemic stroke. Manual stenosis measurements were performed by 2 neuroradiologists. Semiautomatic measurements by using 4 methods (3mensio and comparable software from Philips, TeraRecon, and Siemens) were performed by 2 observers. Diagnostic accuracy was estimated by comparing semiautomatic with manual measurements. Interobserver reproducibility and agreement between different packages was assessed by calculation of the intraclass correlation coefficient and Bland-Altman 95% limits of agreement. False-negative classifications were retrospectively inspected by a neuroradiologist.

RESULTS: There was no significant difference in the diagnostic performance of the 4 semiautomatic methods. The sensitivity for detecting $\geq 50\%$ and $\geq 70\%$ degree of stenosis was between 76% and 82% and 46% and 62%, respectively. Specificity and overall diagnostic accuracy were between 92% and 97% and 85% and 90%, respectively. The interobserver intraclass correlation coefficient was between 0.83 and 0.96 for semiautomatic measurements and 0.81 for manual measurement. The limits of agreement between each pair of semiautomatic packages ranged from -18% – 24% to -33% – 31% . False-negative classifications were caused by ulcerative plaques and observer variation in stenosis and reference measurements.

CONCLUSIONS: Semiautomatic methods have a low-to-good sensitivity and a good specificity and overall diagnostic accuracy. The high interobserver reproducibility makes semiautomatic stenosis measurement valuable for clinical practice, but semiautomatic measurements should be checked by an experienced radiologist.

ABBREVIATION: ICC = intraclass correlation coefficient

Carotid endarterectomy in neurologically symptomatic patients with a 70%–99% stenosis results in a 16% decrease in the absolute risk for an ipsilateral stroke in 5 years. However, endarterectomy is only marginally beneficial for patients with a

50%–69% stenosis and has no positive effect in patients with a $< 50\%$ stenosis.¹ Therefore, the degree of carotid stenosis is crucial in clinical decision-making, and precise and accurate measurement of the degree of stenosis is mandatory. The stenosis measurements on which these thresholds are based were determined by using conventional angiography, which is considered as the original criterion standard.² Due to neurologic complications related to DSA³ and a good diagnostic accuracy of noninvasive tests, carotid stenosis measurement on CTA or MRA has become the standard in clinical practice.^{4,5} However, manual measurement of the degree of stenosis on CTA according to the NASCET method is prone to low interobserver reproducibility and requires experience.^{6,7} Semiautomatic methods increase the interobserver reproducibility and accelerate the measurement.^{8,9} Furthermore, semiautomatic methods require less observer experience compared with manual measurement.¹⁰ Multiple semiautomatic packages are currently available and used in clinical practice. Be-

Received December 17, 2014; accepted after revision February 26, 2015.

From the Departments of Radiology (J.B., H.A.M., M.K., R.v.d.B., C.B.L.M.M.), Biomedical Engineering and Physics (H.A.M.), and Neurology (P.J.N.), Academic Medical Center, Amsterdam, the Netherlands; and Department of Radiology (T.Z., A.C.v.D., A.v.d.L.), Erasmus University Medical Center Rotterdam, Rotterdam, the Netherlands.

This work was supported by the Information Technology for European Advancement (ITEA)2 project, label ITEA 10004: Medical Distributed Utilization of Services & Applications.

Please address correspondence to Jordi Borst, MSc. MD, Department of Radiology, GI-229, Academic Medical Center Amsterdam, Meibergdreef 9, 1105AZ Amsterdam, the Netherlands; e-mail: j.borst@amc.uva.nl

 Indicates article with supplemental on-line tables.

 Indicates article with supplemental on-line photo.

<http://dx.doi.org/10.3174/ajnr.A4400>

cause different vendors may use different algorithms,¹¹ the reliability of measurements with different software packages is unclear. To become a valuable clinical tool, the diagnostic accuracy must be further investigated. The goal of this study was to assess the agreement and diagnostic accuracy of 4 commercially available software packages for semiautomatic stenosis measurement compared with manual measurement on CTA and to estimate the interobserver reproducibility and the agreement among different semiautomatic packages.

MATERIALS AND METHODS

Patient Selection

Patients with a recent TIA or stroke suspected of having ICA stenosis were evaluated by duplex sonography. According to local guidelines, when the stenosis on duplex sonography was $\geq 30\%$ for a man and $\geq 50\%$ for a woman, CTA was performed to estimate the degree of stenosis more precisely. All consecutive patients ($n = 110$) who underwent a 64-section CTA with a 0.9-mm section thickness for carotid stenosis evaluation between April 2006 and December 2008 were retrospectively included in this analysis. This complete population was previously investigated to assess the performance of semiautomatic measurement of ICA stenosis on CTA by using Vitrea 2 version 4.1.2.0 (Vital Images, Plymouth, Minnesota).⁸ In the current study, we report the diagnostic accuracy and reproducibility of semiautomatic carotid stenosis measurement on CTA by using 4 other commercially available software packages and estimate the agreement among different software packages. Furthermore, this complete population was previously used to investigate the relation of calcium volume with carotid artery disease,¹² and it was also used to investigate the prevalence of intracranial carotid artery disease and quantify the intracranial stenosis,^{13,14} and to investigate the relation between intracranial carotid artery stenosis and poor outcome.¹⁵

Patients with a previous carotid intervention ($n = 16$) and those with CTA of insufficient quality ($n = 4$) were excluded; 90 patients remained for further analysis. The mean age was 66.8 years (range, 35–89 years), and 54 were men. Forty patients (44%) had ischemic stroke as a final diagnosis; 32 patients (36%), a transient ischemic attack; and 14 patients (16%), amaurosis fugax. Three patients (3%) were asymptomatic, and 1 patient (1%) had an ocular ischemic syndrome.

Because CTA was performed in the clinical setting, informed consent was waived by the local medical ethics committee.

CTA Protocol

CTA was performed as previously described⁸ with a 64-section scanner (Brilliance 64; Philips Healthcare, Best, the Netherlands). Eighty milliliters of contrast (iodixanol, Visipaque 320; GE Healthcare, Piscataway, New Jersey) was infused at 4 mL/s. Acquisition and reconstruction parameters were as follows: 120-kV tube voltage, 265 mAs, pitch of 0.765, and reconstructed section thickness of 0.9 mm with an increment of 0.45 mm. The scan ranged from the aortic arch up to 3 cm above the sella turcica. The in-plane grid was 512×512 pixels, with an FOV ranging from 128×128 mm² to 217×217 mm², with an average of 155×155 mm².

Stenosis Measurement

For both the manual and semiautomatic measurements, the observers were blinded to patient information and each other's findings. The degree of stenosis was defined according to the NASCET criteria² by using the minimal diameter at the stenosis and the maximum reference diameter at a healthy part of the artery well beyond (>30 mm) the stenosis.⁸ Because the cross-section of an artery is not round, there is no true diameter. Therefore, we defined the "minimal diameter" as the minimal cross-sectional distance of the artery from wall to wall and the "maximum diameter" as the maximum cross-sectional distance of the artery from wall to wall. The minimal diameter of the stenosis was determined by the observers within 3 cm proximal and distal to the bifurcation.¹⁶ Arteries with near-occlusion (collapsed or small distal artery) were identified according to the criteria described by Bartlett et al.¹⁷ For both the manual and semiautomatic measurements, occlusion of the arteries was reported. For all measurements, the processing time was recorded.

Manual Stenosis Measurements

Manual measurements were performed on CTA by 2 neuroradiologists both with >10 years of experience according to the method described by Bartlett et al.¹⁷ by using a workstation with MPR functionality (Impax, Version 5.2; Agfa-Gevaert, Mortsel, Belgium). Measurements were performed on a plane perpendicular to the centerline of the artery. The first observer measured all arteries, which were used as the reference, and a subset of 50 arteries a second time with a delay of 2 months. The second observer measured a subset of 48 arteries.

Semiautomatic Stenosis Measurements

Semiautomatic stenosis grading was performed with software packages from Pie Medical Imaging (3mensio Vascular 6.1; Pie Medical Imaging Maastricht, the Netherlands), Philips (Extended Brilliance Workspace, Version 4.1 Advanced Vessel Analysis), TeraRecon (Vessel Analysis 4.4.6.85; TeraRecon, San Mateo, California), and Siemens (syngo INspace4D Advanced Vessel Analysis 2009–2013; Siemens, Erlangen, Germany). One trained observer (2 years of experience) performed stenosis measurement by using all software packages with >2 months between measurements with different packages. A second trained observer (6 months of experience) performed the measurements by using Philips and 3mensio software, and a third trained observer (6 months of experience) performed the measurements by using Siemens and TeraRecon software, both with >2 months between measurements with different software packages. To prevent recall of measurements performed in previous studies on this population, we selected observers who were not involved in the previous studies.^{8,12–15}

Using the software from Philips, TeraRecon, and Siemens, we placed ≥ 2 seed points on the axial images: The first seed point was placed in the ICA close to the base of the skull, and the last seed point, in the common carotid artery below the bifurcation (>5 cm). Subsequently, software packages automatically segmented the ICA and determined the centerline of the ICA. Minimal and maximal lumen diameters of the arteries were automatically calculated and displayed together with

curved planar reformations of the artery. By dragging a slider along the curved planar reformation of the artery, observers were able to select the minimal stenosis diameter. For the 3mensio software, the ICA of interest was automatically segmented after placement of a single seed point. Subsequently, seed points were placed in the ICA, bifurcation, external carotid artery, and common carotid artery on a 3D representation, and the centerline was automatically determined. The 3mensio software fitted an ellipse on the segmented cross-sectional lumen area and presented the minimal and maximum diameters of the ellipse as the lumen diameters and displayed them together with curved planar reformations of the artery. The observer selected the region of the ICA containing the stenosis, and the software automatically determined the smallest diameter of the stenosis. For all software packages, the reference location was selected by dragging a slider on the curved planar reformation along the distal ICA well beyond the site of stenosis. The reference location was selected at a vertically running part with the largest diameter and the least variation in diameter. At the selected reference location, the minimal and maximal diameters were recorded. For all software packages, erroneous or incomplete segmentations and erroneous centerlines were manually corrected.

To evaluate potential improvements of the interobserver reproducibility, we performed an additional measurement with a second standardized reference location exactly 30 mm above the minimal stenosis diameter for a single software package (Siemens) and calculated the degree of stenosis.

Statistical Analysis

Diagnostic Accuracy. To determine the diagnostic accuracy of semiautomatic stenosis measurement, we used the manual stenosis measurements by the first observer as a reference. The agreement of the semiautomatic stenosis measurements with the manual reference was assessed by scatterplots, Bland-Altman analysis with 95% limits of agreement, and the calculation of the intraclass correlation coefficient (ICC) (agreement, 2-way-mixed, single measure). Diagnostic accuracy was determined for diagnoses of $\geq 50\%$ and $\geq 70\%$ stenoses. Sensitivity, specificity, positive predictive value, negative predictive value, and overall diagnostic accuracy were calculated. The extended McNemar test was used to compare the sensitivity, specificity, and overall diagnostic accuracy among the software packages. *P* values $< .05$ were considered statistically significant. Statistical analyses were performed by using SPSS, Version 21 (IBM, Armonk, New York).

Inter- and Intraobserver Reproducibility. Inter- and intraobserver reproducibility of the manual measurements and interobserver reproducibility of the semiautomatic measurements were assessed by scatterplots, Bland-Altman analysis, and the calculation of the ICC. A paired *t* test was used to determine whether the interobserver bias for semiautomatic measurements was statistically different from manual measurements. The Fisher Z-test was used to determine whether the interobserver ICC for semiautomatic measurements was statistically significantly different from manual measurements. The agreement of observers classifying a

Table 1: Average processing time

	Average Processing Time \pm SD (seconds)
Manual measurements	138 \pm 31
3mensio	86 \pm 42
Philips	115 \pm 77
TeraRecon	84 \pm 64
Siemens	89 \pm 86

stenosis equal to or higher than a cutoff of 50% and 70% was assessed by using κ statistics.

Agreement between Different Semiautomatic Software Packages.

The agreement between measurements with different semiautomatic software packages was assessed by Bland-Altman analysis and calculating the ICC. Instead of choosing a fixed observer per software package, we randomly selected 1 of the 2 observers for each measurement to avoid observer dependence. Thus, we aimed to simulate a clinical setting in which multiple users may use the software package.

Retrospective Error Analysis

Semiautomatic measurements classified as false-negative were retrospectively investigated by a neuroradiologist (10 years of experience) and trained observer (2 years of experience) to inspect whether the measurement was correctly performed by the observers and no erroneous centerlines or erroneous lumen segmentations were present. A measurement was classified as false-negative if the degree of stenosis was above the cutoff point (50% or 70%) according to manual measurement but below the cutoff for the semiautomatic measurement.

RESULTS

Ninety patients (180 arteries) were included in this study. Thirty-nine arteries were excluded because of near-occlusion ($n = 20$), occlusion ($n = 13$), dental artifacts at the bifurcation ($n = 3$), dissection ($n = 1$), and fibromuscular dysplasia ($n = 1$), or the bifurcation was not captured on the scan ($n = 1$). After exclusion, we ended up with 141 (180–39) arteries suitable for further analysis. A subset of 38 arteries that were manually measured a second time by the first observer and 37 arteries that were manually measured by the second observer were suitable for further analysis. According to the manual stenosis measurements, 47 arteries had a minimal stenosis (0%–29%); 29, a mild stenosis (30%–49%); 39, a moderate stenosis (50%–69%); and 26, severe stenosis (70%–99%).

As Table 1 shows, the average processing time of all semiautomatic measurements was faster than that for manual measurements. See On-line Fig 1 for examples of semiautomatic ICA stenosis measurement.

Diagnostic Accuracy

The agreement of semiautomatic measurements with manual measurements is illustrated in Fig 1 by scatterplots. The ICC and limits of agreement are shown in Table 2. All software packages showed a high correlation, with ICCs between 0.86 and 0.88. The mean paired difference between manual and semiautomatic measurements was small, ranging from $2.1\% \pm 13\%$ to $3.8\% \pm 14\%$ (Fig 2). However,

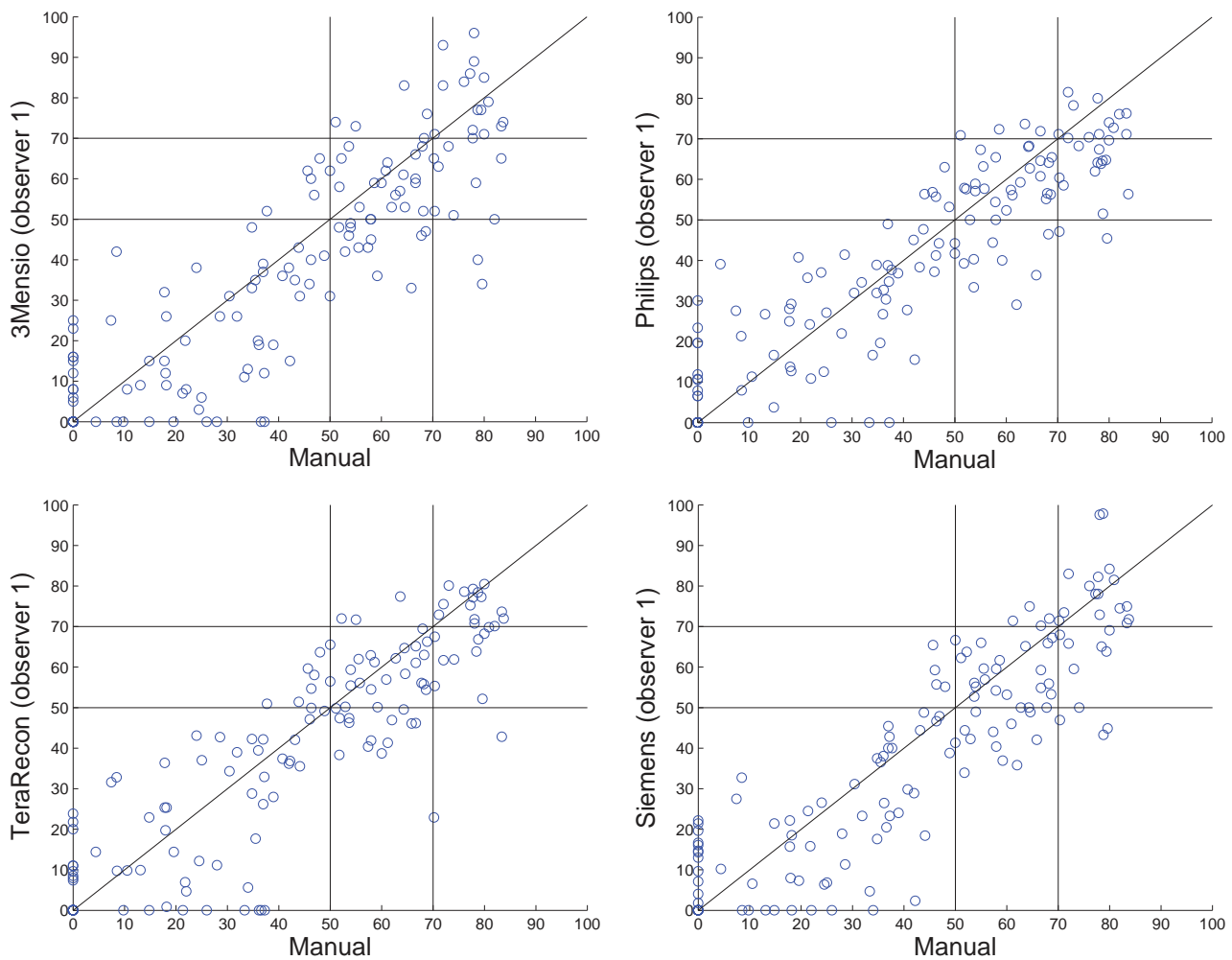


FIG 1. Scatterplots of the manual-versus-semiautomatic assessment of the degree of stenosis (percentage).

Table 2: Agreement manual vs semiautomatic stenosis measurement

	Average Difference Degree of Stenosis \pm SD (%) (Manual, Semiautomatic)	Bland-Altman 95% Limits of Agreement (%)	ICC for Degree of Stenosis (95% CI)
3mensio (observer 1)	3.8 \pm 14 ($P = .002$)	-24-31	0.86 (0.80-0.90)
Philips (observer 1)	2.1 \pm 13 ($P = .049$)	-23-27	0.88 (0.83-0.91)
TeraRecon (observer 1)	3.1 \pm 13 ($P = .007$)	-23-29	0.87 (0.82-0.90)
Siemens (observer 1)	3.5 \pm 13 ($P = .002$)	-22-29	0.88 (0.83-0.91)

the Bland-Altman limits of agreement were wide, ranging from -23%–27% to -24%–31% (Fig 2). The diagnostic performance is presented in Table 3. The semiautomatic measurements have a low sensitivity for detecting a $\geq 70\%$ stenosis, with sensitivity values between 46% and 62%. The specificity and overall diagnostic accuracy of detecting $\geq 70\%$ degree stenosis were good for semiautomatic measurements, ranging between 96%–97% and 87%–90%, respectively. The semiautomatic measurements showed a moderate-to-good sensitivity for detecting $\geq 50\%$ stenosis with values between 68% and 82%. The specificity and overall diagnostic accuracy for detecting $\geq 50\%$ stenosis were good, ranging between 93%–95% and 85%–88%, respectively. No statistically significant differences in the diagnostic performance among software packages were found. All occluded arteries were detected by the observers regardless of the semiautomatic method used.

Inter- and Intraobserver Reproducibility

Observer reproducibility is illustrated in Figs 3–5, and the results can be found in Tables 4 and 5. The Bland-Altman plots showed a small inter- and intraobserver reproducibility bias with wide limits of agreement for manual stenosis measurements (Fig 3). The manual measurements have a reasonable-to-good inter- and intraobserver reliability, with an ICC of 0.81 and 0.88, respectively. The Bland-Altman plots show that interobserver reproducibility bias was smallest for 3mensio and Philips (Fig 5). The semiautomatic measurements have a reasonable-to-excellent interobserver reproducibility with ICCs between 0.83 and 0.96. For 3mensio and Philips, the interobserver reproducibility was significantly better than the interobserver reproducibility of the manual measurements. With the Siemens software with a fixed reference location 3 cm above the minimal stenosis diameter, the average difference in degree of steno-

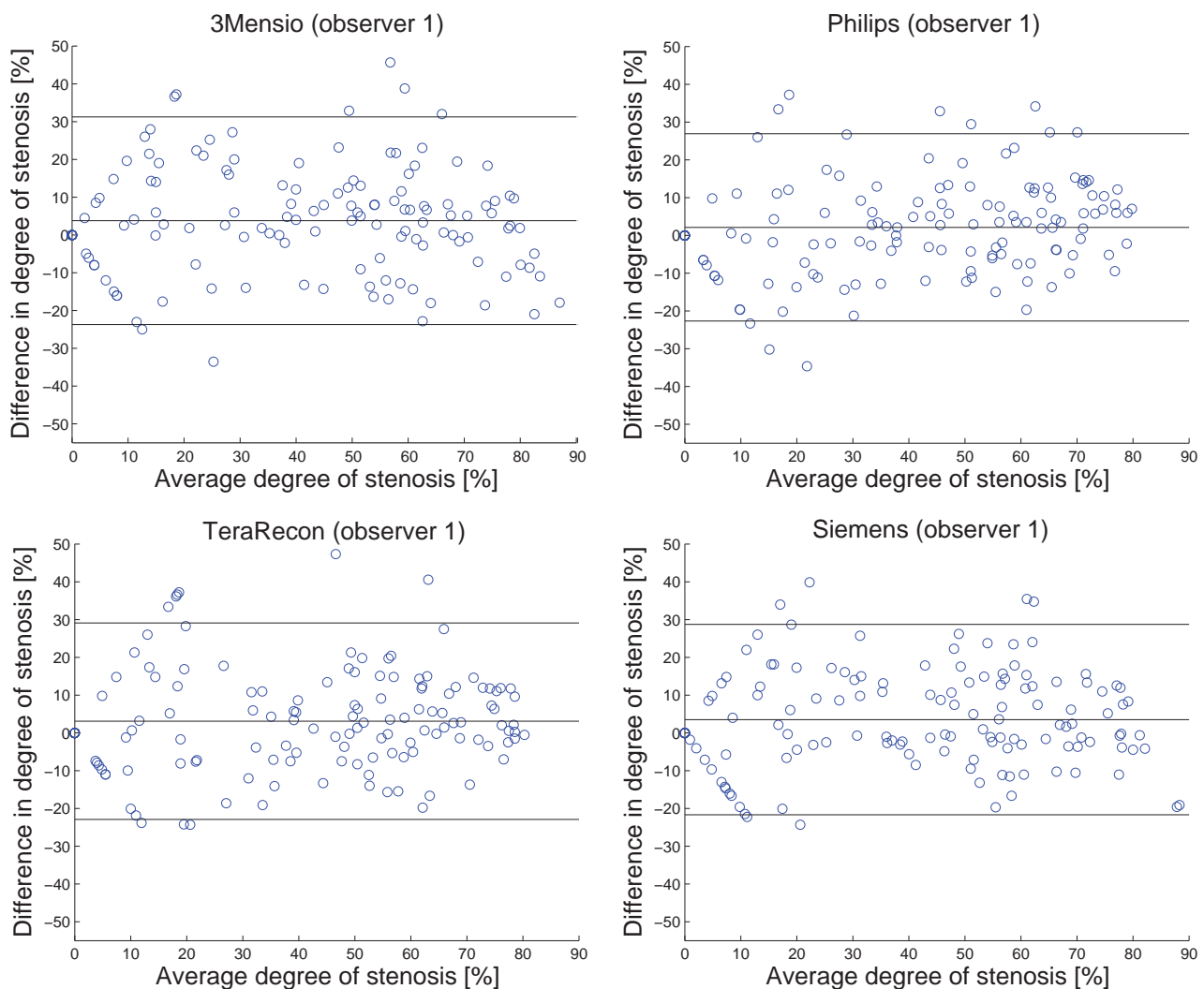


FIG 2. Bland-Altman plots of the degree of stenosis determined by manual and semiautomatic assessment. The *black lines* represent the mean paired difference and 95% limits of agreement. The characteristic V-shape in the Bland-Altman plot is caused by 1 of the 2 measurements being zero with the other measurement being nonzero. These measurements happened particularly when the degree of stenosis was small (<30%).

Table 3: Diagnostic performance of semiautomatic measurement in detecting a stenosis degree of $\geq 70\%$ and $\geq 50\%$

	Sensitivity (95% CI)	Specificity (95% CI)	PPV (95% CI)	NPV (95% CI)	Accuracy (95% CI)
70% Cutoff					
3mensio (observer 1)	62 (43–78)	96 (91–98)	76 (53–92)	92 (85–96)	89 (82–93)
Philips (observer 1)	46 (29–65)	96 (91–99)	75 (48–93)	88 (82–94)	87 (80–92)
TeraRecon (observer 1)	58 (37–77)	97 (93–99)	83 (59–96)	91 (85–95)	90 (84–94)
Siemens (observer 1)	62 (40–81)	97 (91–99)	80 (56–94)	92 (85–96)	90 (84–94)
50% Cutoff					
3mensio (observer 1)	77 (65–86)	93 (86–97)	91 (80–97)	83 (73–90)	86 (79–91)
Philips (observer 1)	82 (70–89)	93 (86–97)	91 (81–97)	86 (76–92)	88 (81–93)
TeraRecon (observer 1)	76 (65–86)	92 (84–97)	89 (78–96)	82 (73–90)	85 (78–90)
Siemens (observer 1)	77 (65–86)	95 (87–99)	93 (82–98)	83 (73–90)	87 (80–91)

Note:—PPV indicates positive predictive value; NPV, negative predictive value.

sis was $3.5\% \pm 15\%$ compared with $6.5\% \pm 12\%$ for the standard reference location ($P < .001$) and the interobserver reproducibility was slightly lower, with an ICC of 0.84 compared with 0.86 with a non-statistically significant difference ($P = .55$).

For detecting a stenosis of $\geq 50\%$, the κ statistics for the interobserver agreement were good for manual measurement and, depending on the software package, fair to excellent for the semiautomatic measurements (Tables 4 and 5). For detecting a stenosis of $\geq 70\%$,

the κ statistics for interobserver agreement were fair for the manual measurement and, depending on the software package, poor to excellent for the semiautomatic measurement packages.

Agreement among Semiautomatic Measurements

The agreement among measurements with different semiautomatic software packages can be found in the On-line Table. The correlation of measurements with different semiautomatic pack-

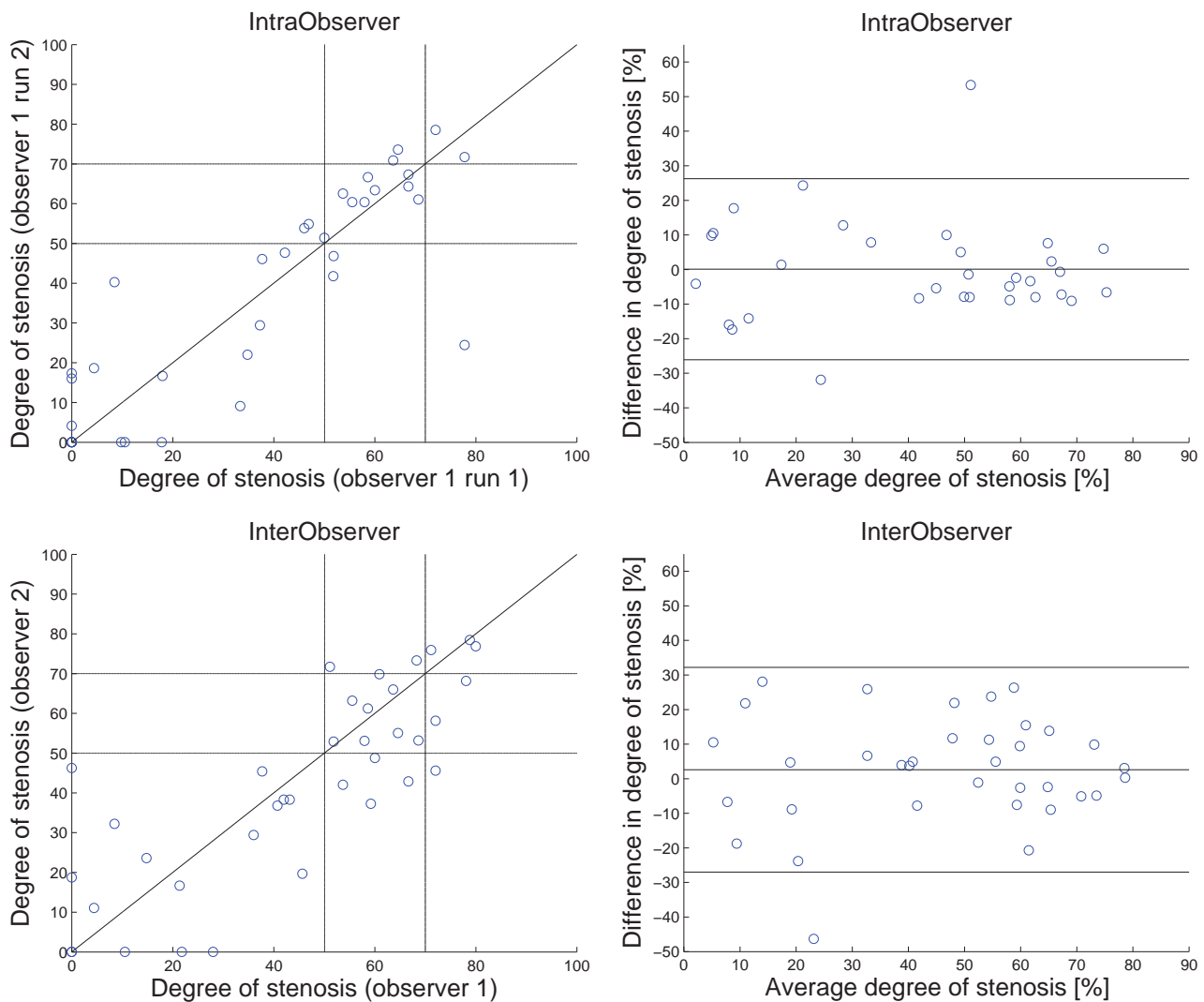


FIG 3. Scatterplot (*upper left corner*) and Bland-Altman plot (*upper right corner*) of the repeated manual stenosis measurement (percentage) (intraobserver). Scatterplot (*lower left corner*) and Bland-Altman plot (*lower right corner*) of the manual assessment of the degree of stenosis (percentage) measured by observer 1 and observer 2 (interobserver). The *black lines* in the right figures represent the mean paired difference and 95% limits of agreement.

ages is high, with ICCs ranging from 0.92 to 0.98. The mean paired differences between semiautomatic packages range from 0.49% to 5.7%, and the Bland-Altman limits of agreement are wide, ranging from -17%–18% to -33%–31%.

Retrospective Error Analysis

Most measurements classified as false-negative were because the semiautomatic method measured a larger stenosis diameter and/or a smaller reference diameter compared with manual measurements by the neuroradiologist (78% [36/46] for a stenosis of $\geq 70\%$ and 89% [51/57] for a stenosis of $\geq 50\%$). There were no apparent errors in the centerline, and only 4.3% (2/46) of the false-negatives for a stenosis of $\geq 70\%$ and 5.3% (3/57) for a stenosis of $\geq 50\%$ were caused by erroneous lumen segmentation due to calcium. An ulcerative plaque hampered semiautomatic measurements in 17.4% (8/46) for a stenosis of $\geq 70\%$ and 5.3% (3/57) for a stenosis of $\geq 50\%$ and resulted in severe overestimation of the stenosis diameter compared with manual measurement (Fig 6). 3mensio fits an ellipse on the segmented lumen and

uses the smallest diameter of the ellipse as a minimal stenosis diameter; this can result in a minimal stenosis diameter that is larger than the minimal stenosis diameter measured by a radiologist (Fig 6). This method caused 40% (4/10) of the 3mensio false-negatives for a stenosis of $\geq 70\%$ and 20.0% (3/15) for a stenosis of $\geq 50\%$. For 8.7% (4/46) of the false-negatives for a stenosis of $\geq 70\%$ and 12.3% (7/57) for a stenosis of $\geq 50\%$, the difference in the degree of stenosis with manual measurement was only 5% and the manual measurements were just above the cutoff point and the semiautomatic measurements were just below the cutoff.

DISCUSSION

In this study, we investigated the diagnostic performance of 4 commercially available semiautomatic software packages with manual measurement as a reference. All semiautomatic methods had a moderate-to-good sensitivity for detecting a stenosis of $\geq 50\%$ and low sensitivity for detecting a stenosis of $\geq 70\%$. All semiautomatic methods had a good specificity and overall diag-

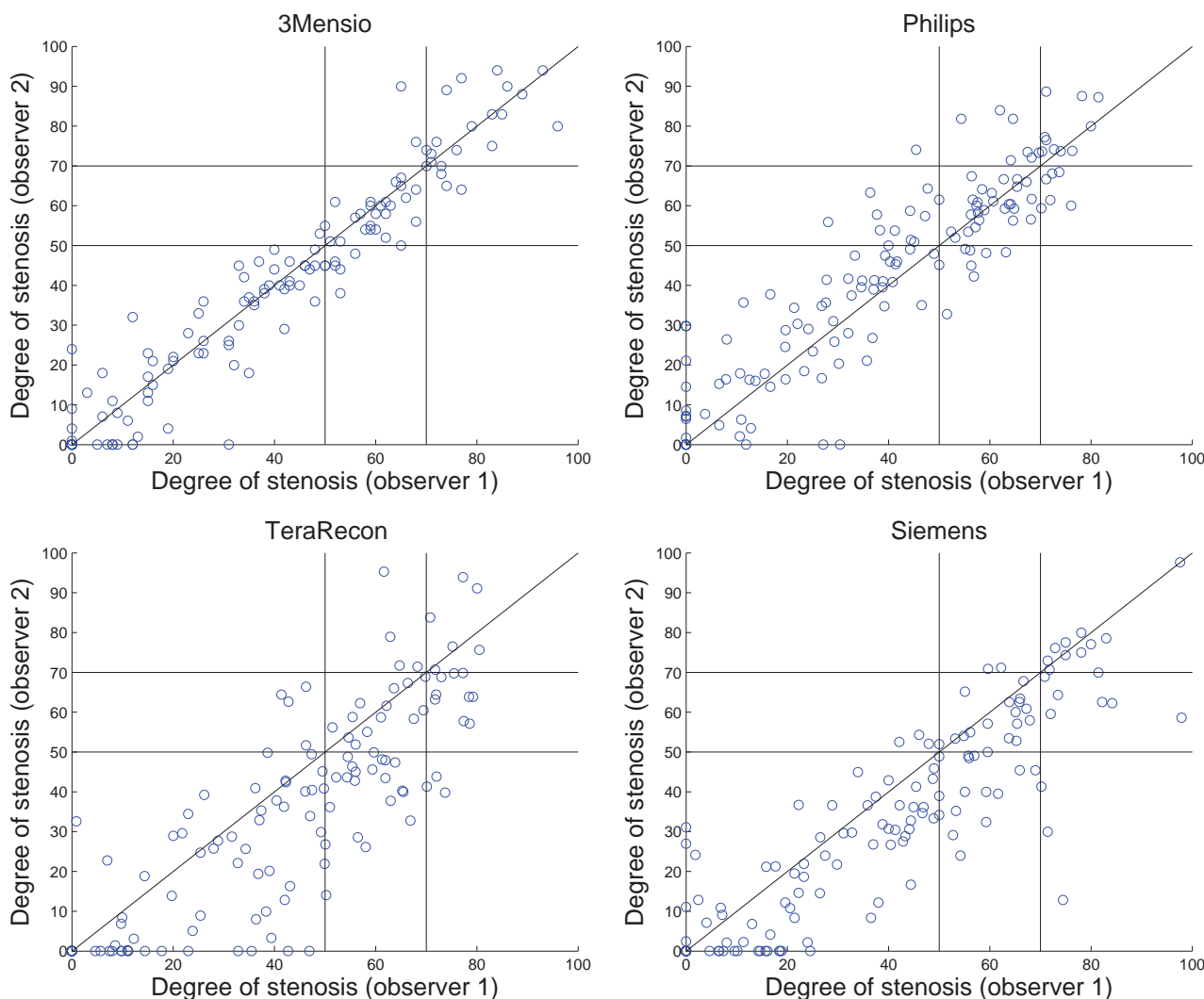


FIG 4. Scatterplots of the repeated semiautomatic assessment of the degree of stenosis (percentage) measured by observers 1 and 2.

nostic accuracy for detecting stenoses of $\geq 70\%$ and $\geq 50\%$. All semiautomatic stenosis measurement methods are 40% faster than manual measurements. For 3mensio, we found a much higher interobserver reproducibility compared with manual measurement. All semiautomatic methods had a good correlation with manual measurement.

Our results are in line with the previously reported sensitivity and specificity of 75% and 98% for detecting a stenosis of $\geq 70\%$ and 78% and 93% for detecting a stenosis of $\geq 50\%$.⁸ Our results are similar to the previously reported sensitivity and specificity of 44.2% and 97.7% for detecting a stenosis of $\geq 70\%$ and 86.2% and 93.1% for detecting a stenosis of $\geq 50\%$ in 46 patients with known cerebrovascular disease.¹⁸ The interobserver agreement for semiautomatic measurements is in line with previously reported κ statistics of 0.55 for detecting a stenosis of $\geq 50\%$, and 0.59 for detecting a stenosis of $\geq 70\%$ ¹⁹ and Pearson correlation coefficients of 0.89 and 0.90.^{9,19} As in previously reported studies,^{8,9} we found that semiautomatic stenosis measurement can increase observer reproducibility.

This study has a number of limitations. For pragmatic reasons, we used different observers for different software packages; this difference makes it more difficult to compare the

semiautomatic software packages. We used manual measurements on CTA as a reference, while the original NASCET classification is based on conventional catheter angiography. Due to the risks associated with conventional catheter angiography,³ it would be unethical to perform DSA. Bucek et al¹⁸ showed that the median difference between semiautomatic CTA and manual DSA stenosis measurement was smaller than the median difference between manual measurement on CTA and DSA, -2% versus 11% , respectively. This finding may imply that manual stenosis measurement tends to overestimate the degree of stenosis compared with measurement on DSA; this overestimation may have caused the low sensitivity found in this study. Due to the low observer reproducibility of manual stenosis measurement, one could question its value as a reference standard to determine the diagnostic accuracy of semiautomatic measurements. However, because manual stenosis measurement is standard in clinical practice, we believed that this measurement was the best choice to evaluate the accuracy of the automated methods.

Retrospective error analysis of the false-negatives showed that most false-negatives were due to the semiautomatic method measuring a larger stenosis diameter and/or a smaller reference diam-

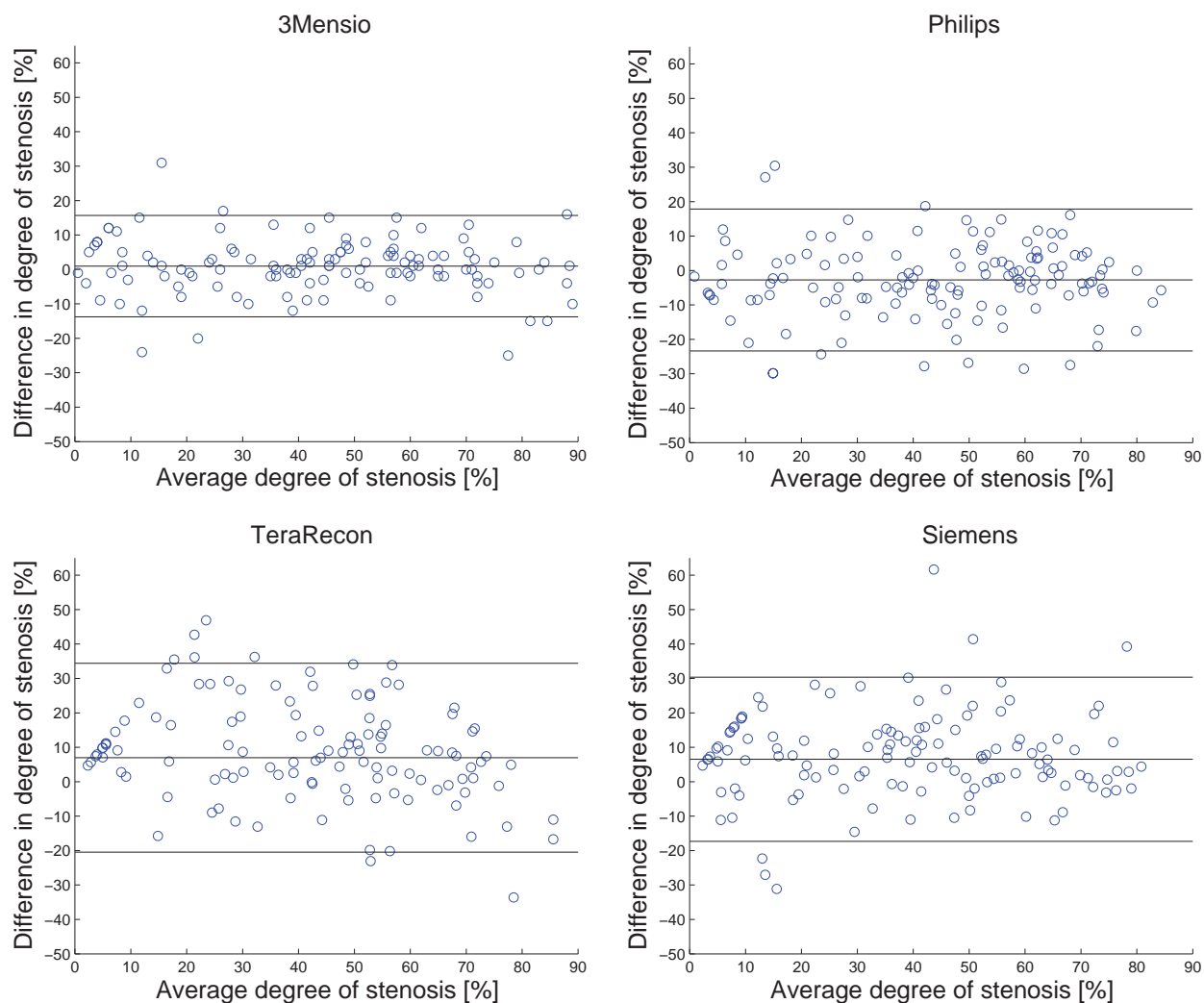


FIG 5. Bland-Altman plots of the repeated semiautomatic assessment of the degree of stenosis measured by observers 1 and 2. The black lines represent the mean paired difference and 95% limits of agreement.

Table 4: Observer reproducibility

	Average Difference Degree of Stenosis \pm SD (%)	Bland-Altman Limits of Agreement (%)	ICC (95% CI) for Degree of Stenosis
Manual intraobserver ($n = 38$)	0.083 ± 13	-26-26	0.88 (0.79-0.94)
Manual interobserver ($n = 37$)	2.6 ± 15	-28-32	0.81 (0.70-0.90)
3mensio interobserver ($n = 141$)	0.94 ± 7.5^a ($P = .007$)	-14-16	0.96 (0.95-0.97 ^a) ($P < .001$)
Philips interobserver ($n = 141$)	-2.8 ± 11	-23-18	0.90 (0.86-0.93) ^a ($P = .0041$)
TeraRecon interobserver ($n = 141$)	7.0 ± 14	-20-34	0.83 (0.70-0.90)
Siemens interobserver ($n = 141$)	6.5 ± 12	-17-30	0.86 (0.73-0.92)

^a Significant difference with manual interobserver measurements.

Table 5: Observer reproducibility by statistical κ values

	50% κ^a (95% CI)	70% κ^b (95% CI)
Manual intraobserver ($n = 38$)	0.73 (0.50-0.95)	0.53 (0.02-1)
Manual interobserver ($n = 37$)	0.73 (0.52-0.95)	0.47 (0.03-0.90)
3mensio interobserver ($n = 141$)	0.88 (0.80-0.96)	0.86 (0.73-0.98)
Philips interobserver ($n = 141$)	0.71 (0.60-0.83)	0.53 (0.30-0.77)
TeraRecon interobserver ($n = 141$)	0.56 (0.41-0.71)	0.37 (0.08-0.66)
Siemens Interobserver ($n = 141$)	0.67 (0.54-0.80)	0.63 (0.42-0.84)

^a κ values on 50% cutoff.

^b κ values on 70% cutoff.

eter compared with manual measurements by a radiologist. One-tenth of the false-negatives were caused by an ulcerative plaque that hampered correct semiautomatic measurement and was dif-

ficult for a nonradiologist to detect. To determine the agreement among different pairs of software packages, we randomly selected 1 of the 2 observers for each measurement instead of using the mean of the 2 observers. Averaging the measurements diminishes outliers and therefore might result in a too optimistic agreement between the different semiautomatic software packages.²⁰ Furthermore, in this manner, we aimed to simulate a clinical setting in which multiple users may use the software package.

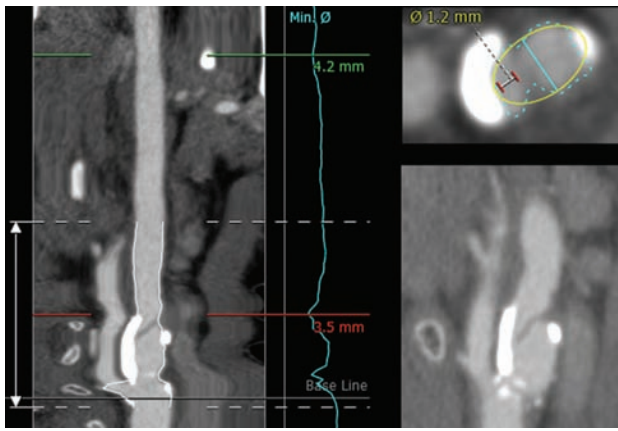


FIG 6. Example of ulcerative plaque. On the left side how 3mensio segments the artery is shown, and in the right upper corner how 3mensio segments the lumen and the ulcerative plaque is shown. The turquoise line is the minimal stenosis diameter as determined by 3mensio (3.5 mm); the white-with-red line is a measurement of the true lumen (1.2 mm). The right lower corner shows a sagittal view of the ulceration. This image also shows 3mensio fitting an ellipse (yellow) on the segmented lumen of the artery (turquoise).

Creating MPRs perpendicular to the artery, needed for manual stenosis measurement and manual measurement of the diameter of the artery lumen, is prone to observer variation and requires experience.^{7,8} This variation resulted in the lower interobserver reproducibility of manual stenosis measurement compared with semiautomatic measurement.

Semiautomatic methods ease stenosis measurements and can have a higher observer reproducibility compared with manual measurement, because manual creation of MPRs and manual lumen measurement are not needed. All 4 semiautomatic software packages are comparable in the ease of use and required observer skills. 3mensio was the only package that determined the minimal diameter of the stenosis automatically. This higher level of automation may have resulted in the superior observer agreement. Although the interobserver reproducibility can be higher for semiautomatic measurements, manual selection of the minimal stenosis diameter and reference diameter is still needed and is therefore a source of observer variability. Furthermore, manual correction of the center line and lumen segmentation are often needed to ensure accurate measurement, especially when the artery is very tortuous or the plaque is calcified.^{8,17} The manual selection of the minimal stenosis diameter and reference diameter and the manual corrections may have caused the wide Bland-Altman limits of agreement for the semiautomatic methods and the low observer reproducibility for some of the packages.

Endarterectomy is beneficial for patients with a stenosis degree of $\geq 50\%$ for men and $\geq 70\%$ for women.¹ Therefore accurate and reproducible measurement of the degree of stenosis is crucial for selecting patients for endarterectomy.

CONCLUSIONS

Most semiautomatic software packages have a higher observer reproducibility than manual measurements, which results in more consistent stenosis measurement and less observer dependency in treatment selection. Because of the necessity of manual corrections of semiautomatic measurements, training

of the observers and awareness of erroneous centerlines and lumen segmentations remain crucial. All 4 semiautomatic methods have a high positive predictive value and a good overall diagnostic accuracy for the detection of an ICA stenosis of $\geq 50\%$ and $\geq 70\%$. The potentially excellent observer reproducibility of semiautomatic measurements makes them suitable for clinical practice, but the poor sensitivity for a stenosis of $\geq 70\%$ should be taken into account and measurements should be checked by a radiologist.

Disclosures: Jordi Borst—RELATED: Grant: Information Technology for European Advancement (ITEA)2 project,* label ITEA 10004: Medical Distributed Utilization of Services & Applications,* Comments: <https://itea3.org>, <https://itea3.org/project/medusa.html>. Taihra Zadi—UNRELATED: Grants/Grants Pending: GE Healthcare. Paul J. Nederkoorn—UNRELATED: Grants/Grants Pending: 1) The Netherlands Organization for Health Research and Development (No. 171002302), 2) The Netherlands Heart Foundation (No. 2009B095), 3) NutsOhra fund, Comments: 3 grants for investigator-driven research: 1 and 2) The Preventive Antibiotics in Stroke Study, 3) Thrombolysis and Uncontrolled Hypertension study. Rene van den Berg—UNRELATED: Consultancy: agreement with DePuy Codman. Aad van der Lugt—UNRELATED: Grants/Grants Pending: GE Healthcare,* Comments: MRI vendor and provider of image analysis software; Payment for Lectures (including service on Speakers Bureaus): GE Healthcare,* Comments: MRI vendor and provider of image-analysis software. Charles B.L.M. Majoie—UNRELATED: Grants/Grants Pending: Dutch Heart Foundation,* NutsOhra Foundation.* *Money paid to the institution.

REFERENCES

- Rothwell PM, Eliasziw M, Gutnikov SA, et al. Analysis of pooled data from the randomised controlled trials of endarterectomy for symptomatic carotid stenosis. *Lancet* 2003;361:107–16
- Barnett HJ, Taylor DW, Eliasziw M, et al. Benefit of carotid endarterectomy in patients with symptomatic moderate or severe stenosis: North American Symptomatic Carotid Endarterectomy Trial Collaborators. *N Engl J Med* 1998;339:1415–25
- Willinsky RA, Taylor SM, Terbrugge K, et al. Neurologic complications of cerebral angiography: prospective analysis of 2,899 procedures and review of the literature. *Radiology* 2003;227:522–28
- Koelemay MJW, Nederkoorn PJ, Reitsma JB, et al. Systematic review of computed tomographic angiography for assessment of carotid artery disease. *Stroke* 2004;35:2306–12
- Wardlaw JM, Stevenson MD, Chappell F, et al. Carotid artery imaging for secondary stroke prevention: both imaging modality and rapid access to imaging are important. *Stroke* 2009;40:3511–17
- Bucek RA, Puchner S, Haumer M, et al. Grading of internal carotid artery stenosis: can CTA overcome the confusion? *J Endovasc Ther* 2006;13:443–50
- Howard P, Bartlett ES, Symons SP, et al. Measurement of carotid stenosis on computed tomographic angiography: reliability depends on postprocessing technique. *Can Assoc Radiol J* 2010;61:127–32
- Marquering HA, Nederkoorn PJ, Smagge L, et al. Performance of semiautomatic assessment of carotid artery stenosis on CT angiography: clarification of differences with manual assessment. *AJNR Am J Neuroradiol* 2012;33:747–54
- White JH, Bartlett ES, Bharatha A, et al. Reproducibility of semiautomated measurement of carotid stenosis on CTA. *Can J Neurol Sci* 2010;37:498–503
- Biermann C, Tsiflikas I, Thomas C, et al. Evaluation of computer-assisted quantification of carotid artery stenosis. *J Digit Imaging* 2012;25:250–57
- Hameeteman K, Zuluaga MA, Freiman M, et al. Evaluation framework for carotid bifurcation lumen segmentation and stenosis grading. *Med Image Anal* 2011;15:477–88

12. Marquering HA, Majoie CB, Smagge L, et al. **The relation of carotid calcium volume with carotid artery stenosis in symptomatic patients.** *AJNR Am J Neuroradiol* 2011;32:1182–87
13. Marquering HA, Nederkoorn PJ, Bleeker L, et al. **Intracranial carotid artery disease in patients with recent neurological symptoms: high prevalence on CTA.** *Neuroradiology* 2013;55:179–85
14. Bleeker L, Marquering HA, van den Berg R, et al. **Semi-automatic quantitative measurements of intracranial internal carotid artery stenosis and calcification using CT angiography.** *Neuroradiology* 2012;54:919–27
15. Steen WE Van Der, Vermeij J, Marquering HA, et al. **Intracranial carotid artery stenosis diagnosed with CTA in a western population: predictor for poor outcome.** In: Derricks, S ed., *Carotid Artery Disease: Risk Factors, Prognosis and Management. Cardiology Research and Clinical Developments.* Hauppauge, NY: Nova Science Publishers; 2014:33–48
16. Van Dijk AC, Fonville S, Zadi T, et al. **Association between arterial calcifications and nonlacunar and lacunar ischemic strokes.** *Stroke* 2014;45:728–33
17. Bartlett ES, Walters TD, Symons SP, et al. **Quantification of carotid stenosis on CT angiography.** *AJNR Am J Neuroradiol* 2006;27:13–19
18. Bucek RA, Puchner S, Kanitsar A, et al. **Automated CTA quantification of internal carotid artery stenosis: a pilot trial.** *J Endovasc Ther* 2007;14:70–76
19. Zhang Z, Berg MH, Ikonen AEJ, et al. **Carotid artery stenosis: reproducibility of automated 3D CT angiography analysis method.** *Eur Radiol* 2004;14:665–72
20. Maddox WT. **On the dangers of averaging across observers when comparing decision bound models and generalized context models of categorization.** *Percept Psychophys* 1999;61:354–74

Improved Image Quality in Head and Neck CT Using a 3D Iterative Approach to Reduce Metal Artifact

W. Wuest, M.S. May, M. Brand, N. Bayerl, A. Krauss, M. Uder, and  M. Lell

ABSTRACT

BACKGROUND AND PURPOSE: Metal artifacts from dental fillings and other devices degrade image quality and may compromise the detection and evaluation of lesions in the oral cavity and oropharynx by CT. The aim of this study was to evaluate the effect of iterative metal artifact reduction on CT of the oral cavity and oropharynx.

MATERIALS AND METHODS: Data from 50 consecutive patients with metal artifacts from dental hardware were reconstructed with standard filtered back-projection, linear interpolation metal artifact reduction (LIMAR), and iterative metal artifact reduction. The image quality of sections that contained metal was analyzed for the severity of artifacts and diagnostic value.

RESULTS: A total of 455 sections (mean \pm standard deviation, 9.1 ± 4.1 sections per patient) contained metal and were evaluated with each reconstruction method. Sections without metal were not affected by the algorithms and demonstrated image quality identical to each other. Of these sections, 38% were considered nondiagnostic with filtered back-projection, 31% with LIMAR, and only 7% with iterative metal artifact reduction. Thirty-three percent of the sections had poor image quality with filtered back-projection, 46% with LIMAR, and 10% with iterative metal artifact reduction. Thirteen percent of the sections with filtered back-projection, 17% with LIMAR, and 22% with iterative metal artifact reduction were of moderate image quality, 16% of the sections with filtered back-projection, 5% with LIMAR, and 30% with iterative metal artifact reduction were of good image quality, and 1% of the sections with LIMAR and 31% with iterative metal artifact reduction were of excellent image quality.

CONCLUSIONS: Iterative metal artifact reduction yields the highest image quality in comparison with filtered back-projection and linear interpolation metal artifact reduction in patients with metal hardware in the head and neck area.

ABBREVIATIONS: FBP = filtered back-projection; HU = Hounsfield unit; MAR = metal artifact reduction; IMAR = iterative MAR; LIMAR = linear interpolation MAR; NMAR = normalized MAR

Imaging plays a crucial role in the staging of oral cancers and is essential for determining tumor resectability, choosing suitable anatomic reconstruction, and planning radiation therapy. The imaging method of choice for evaluating the oral cavity and oropharynx is MR imaging because it provides higher soft-tissue contrast and is less susceptible to artifacts caused by dental hardware. Yet, the limited availability and higher costs of MR imaging, as well as individual patient conditions (breathing or swallowing disorders, claustrophobia, electronic implants such as pacemakers or ferromagnetic foreign bodies), make CT an important alternative option for many patients. Thus, CT is used frequently to

stage or follow-up patients because of its wide availability, relatively low cost, and very short scan time. In patients with dental fillings or implants, however, image quality can be degraded by photon starvation and beam hardening.¹ Due to these artifacts, tumors may be only partially visible or completely obscured, making it challenging to define tumor extent. Moreover, streak artifacts may obscure ipsilateral or contralateral lymph node metastases, which can potentially change the therapeutic approach.

The use of high-resolution kernels and extended CT-value ranges² improves image quality; evaluating the surrounding soft tissue, however, remains challenging or even impossible in many cases and can lead to missed findings. For metal artifact reduction (MAR),^{3,4} sinogram in-painting methods have been proposed. Areas affected by metal artifacts are regarded as missing data and are filled in by different interpolation techniques, such as linear interpolation metal artifact reduction (LIMAR). Because LIMAR is associated with algorithm-induced artifacts, normalized MAR (NMAR) was developed, and it has demonstrated the potential to

Received November 27, 2014; accepted after revision February 9, 2015.

From the Radiological Institute (W.W., M.S.M., M.B., N.B., M.U., M.L.), Friedrich-Alexander-University-Erlangen-Nuremberg, Erlangen, Germany; and Medical Imaging (A.K.), Siemens Healthcare, Erlangen, Germany.

Please address correspondence to Wolfgang Wuest, MD, Radiological Institute, Maximiliansplatz 1, 91054 Erlangen, Germany; e-mail: wolfgang.wuest@uk-erlangen.de

<http://dx.doi.org/10.3174/ajnr.A4386>

improve image quality in patients with artifacts from dental hardware and to improve the diagnostic accuracy of head and neck and of pelvic CT^{5,6} while minimizing algorithm-induced artifacts.

An extension of the MAR methods (ie, LIMAR and NMAR) is a frequency-split technique that also recovers noise texture and anatomic details in close proximity to metal. In a previous study of pelvic CT, this technique delineated adjacent bone and tissue next to metal implants more accurately than NMAR.⁶

The aim of this study was to evaluate a novel 3D iterative approach using normalized and frequency split metal artifact reduction in clinical routine head and neck imaging. The resulting image quality was compared with that of filtered back-projection (FBP) reconstructions and LIMAR.

MATERIALS AND METHODS

Study Population

From January to December 2013, consecutive patients scheduled for neck CT were screened for study participation. Each patient signed informed consent; the study protocol was approved by the local institutional review board. Raw datasets from 50 patients who met the inclusion criteria (no contraindication to contrast-enhanced CT and no motion artifacts) and whose testing resulted in impaired image quality caused by metallic dental hardware were enrolled. The study population consisted of 23 female and 27 male patients with a mean (\pm standard deviation) age of 61 \pm 15.1 years (range, 24–86 years). Each examination was performed on a single-source CT system (Definition AS+; Siemens, Erlangen, Germany) with the following parameters: 0.5-second gantry rotation time, 128- \times 0.6-mm section collimation using a z-flying focal spot, and 160 reference milliamperes-second tube current with automatic exposure control at a tube voltage of 120 kV. The contrast agent (350 mg of iodine/mL [Iomeron; Bracco, Milan, Italy]) was injected at a flow rate of 3 mL/s (volume, 90 mL) followed by a saline bolus (3 mL/s [volume, 30 mL]). A scan delay of 80 seconds was used for each patient. The raw data were transferred to an external workstation equipped with prototype LIMAR software, and 3 datasets (from FBP, LIMAR, and IMAR) were reconstructed with identical (anatomically adapted) fields of view, 2.5-mm section thicknesses, and standard soft-tissue (B35f) and bone (B70f) reconstruction kernels.

IMAR

IMAR combines 2 previously introduced MAR algorithms, NMAR⁷ and frequency-split MAR,⁸ in an iterative update scheme. NMAR replaces those parts of the sinogram that are affected by metal through normalized interpolation. The aim of NMAR is to avoid the introduction of new artifacts tangentially to high-contrast objects, which is often observed with other sinogram in-painting methods. This is achieved by removing high-contrast structures from the sinogram before interpolation and reinserting them afterward. A prior image is calculated from the initial image by assigning soft-tissue pixels (identified by thresholding) to 0 Hounsfield units (HU). The prior image is forward-projected, and the initial sinogram is divided pixel-wise with the prior sinogram. Linear interpolation is performed on the relatively flat normalized sinogram followed by denormalization with the prior sinogram. NMAR images are finally obtained by recon-

struction of the corrected sinogram and reinsertion of the metal pixels from the uncorrected images. Frequency-split MAR combines the low spatial frequencies of a metal artifact-corrected image with the high spatial frequencies of the corresponding initial image. Low- and high-frequency images are obtained by Gaussian filtering. The aim of frequency-split MAR is to preserve both the natural image impression and the edge information of the uncorrected image, which is often affected by pure sinogram in-painting methods, especially in the vicinity of the metal implants. The drawback of the frequency-split operation is the reinsertion of high-frequency streak artifacts into the corrected images. IMAR repeatedly performs the normalized sinogram interpolation and frequency-split operations by using the result of each iteration as input for the next iteration, which effectively reduces the remaining artifacts of the prior image and consequently improves the quality of NMAR in each iteration. The performance of IMAR depends on the choice of several user-selectable model parameters, such as the number of iterations, HU thresholds for metal segmentation and for prior image calculation, and the filter parameter of the frequency-split operation. Those parameters are vendor specific. However, the user can select from a list of parameter configurations that are optimized for several metal implant types, such as dental fillings, hip prostheses, spine implants, and cardiac pacemakers. All reconstructions in this study were performed with the dental-fillings parameter configuration.

Image Analysis

Images obtained by using FBP, LIMAR, and IMAR were displayed side by side on a dual-monitor 3D postprocessing platform (syn-go.via; Siemens) in random order for each acquisition after all identifying information had been removed. The images were reviewed in the soft-tissue window (window level, 50 HU; window width, 400 HU) and in the bone window (window level, 300 HU; window width, 2,500 HU).

To assess image quality, both subjective and objective parameters were evaluated. Subjective image quality of the FBP, LIMAR, and IMAR reconstructions was assessed by using a 5-point Likert scale (1, indicates severe artifacts, largely not diagnostic; 2, poor image quality, partly nondiagnostic; 3, moderate image quality, limited diagnostic confidence; 4, good image quality, sufficient for diagnosis; 5, excellent image quality, no artifacts). The structure with the least favorable diagnostic quality defined the rank for each category.

To obtain objective parameters of image quality, regions of interest were placed in the soft tissue of the tongue, cheeks, and muscles of the neck bilaterally. The standard deviation was measured for all the ROIs and regarded as an indicator of the presence of artifacts.

Statistical Analysis

Values are given as means \pm their standard deviation. One-way analysis of variance and nonparametric Friedman-ANOVA were performed for subjective and objective, respectively, image quality scores and values after the Kolmogorov-Smirnov test for normal distribution. Subsequent Bonferroni and Tamhane T2 post hoc tests, depending on variances in the Levene statistic, were performed for 1-way ANOVA. Pairwise post hoc tests, as pro-

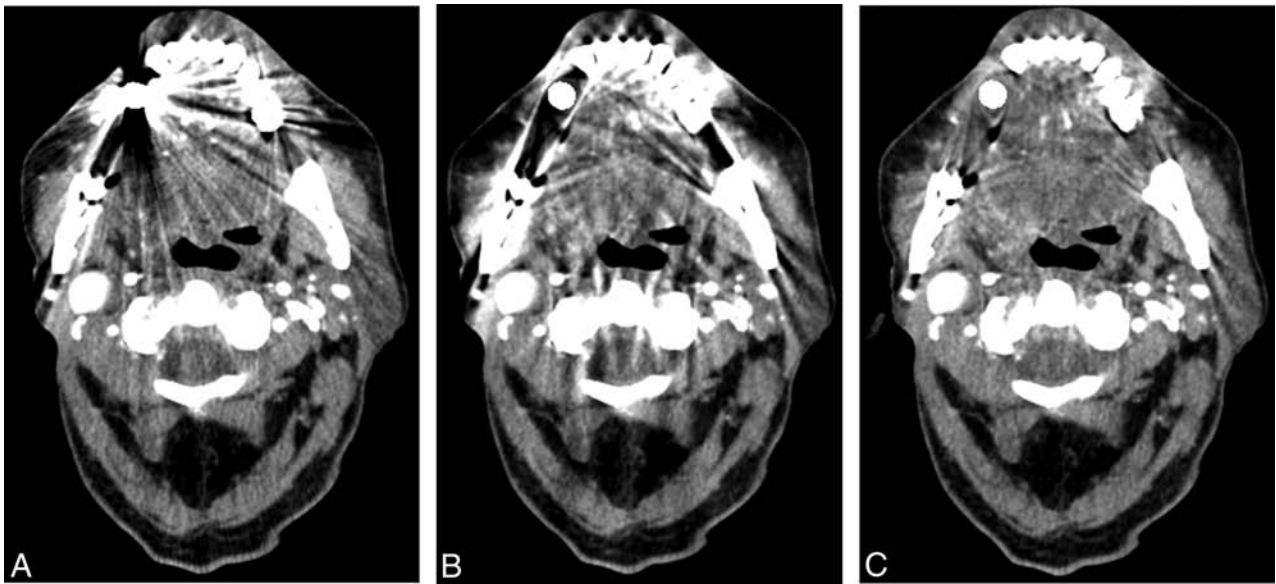


FIG 1. The effects of metal artifacts from dental hardware are highest with FBP (A), lower with LIMAR (B), and lowest with IMAR (C); a better visualization of the oral cavity was achieved with IMAR (C).

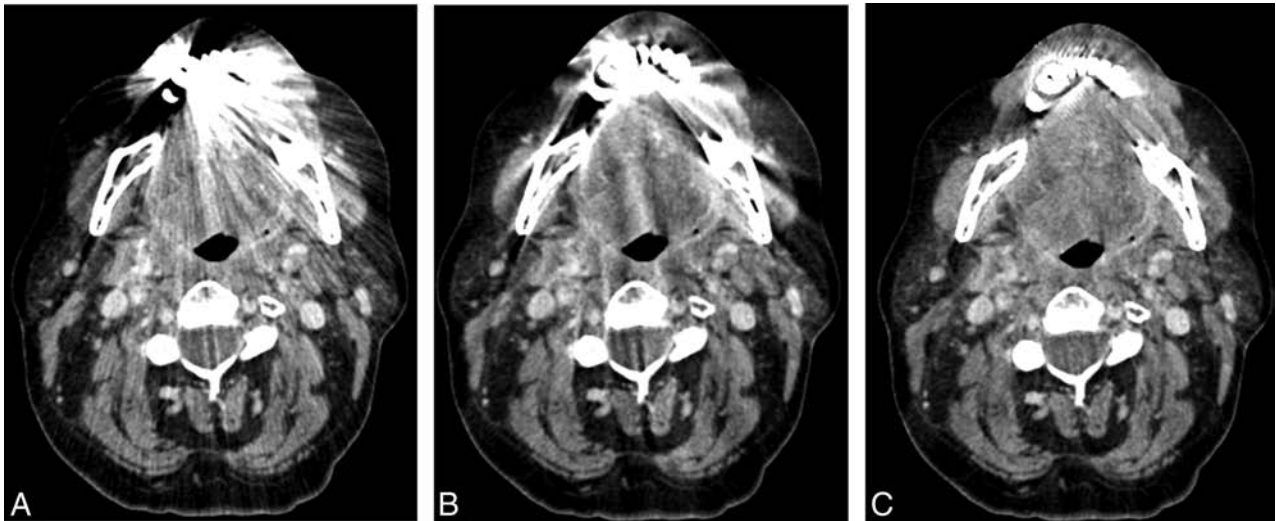


FIG 2. The effects of metal artifacts from dental hardware are highest with FBP (A), lower with LIMAR (B), and lowest with IMAR (C); a better visualization of the oral cavity was achieved with IMAR (C).

posed by Conover,⁹ were performed for the Friedman tests. A significance level of .05 was assumed. Statistical analysis was performed by using the software package SPSS Statistics version 19 (IBM, Armonk, New York).

RESULTS

Filtered back-projection, LIMAR, and IMAR reconstructions were performed successfully for each patient. A total of 455 sections (9.1 ± 4.1 sections per patient) contained metal artifacts and were evaluated with each reconstruction method. Sections without metal artifacts were not affected by the algorithms and had identical image quality.

IMAR significantly increased the subjective overall image quality compared with LIMAR and FBP ($P < .001$), and there was no significant difference between image quality after FBP and that after LIMAR ($P = .822$). The ratings were 2.1 ± 1.1 (FBP), 2 ± 0.9 (LIMAR), and 3.7 ± 1.2 (IMAR).

Of the sections, 38% were considered nondiagnostic with FBP,

31% with LIMAR, and only 7% with IMAR. Thirty-three percent of the sections had poor image quality with FBP, 46% with LIMAR, and 10% with IMAR. Moderate image quality was rated for 13% of the sections with FBP, 17% with LIMAR, and 22% with IMAR, good image quality was rated for 16% of the sections with FBP, 5% with LIMAR, and 30% with IMAR, and excellent image quality was rated for 1% of the sections with LIMAR and 31% with IMAR (Figs 1–3). These results are summarized in the Table.

The mean number of sections with severe artifacts was 3.5 ± 2.6 with FBP, 2.8 ± 2.2 with LIMAR, and 0.6 ± 1.1 with IMAR. With LIMAR, the mean number of sections with excellent image quality was 0.1 ± 0.3 , and with IMAR it was 2.8 ± 1.7 .

The mean standard deviation in the soft tissue of the tongue, the right cheek, and the left cheek were significantly higher with FBP than with LIMAR or IMAR ($P < .001$), and there was a significant difference between LIMAR and IMAR ($P < .001$):

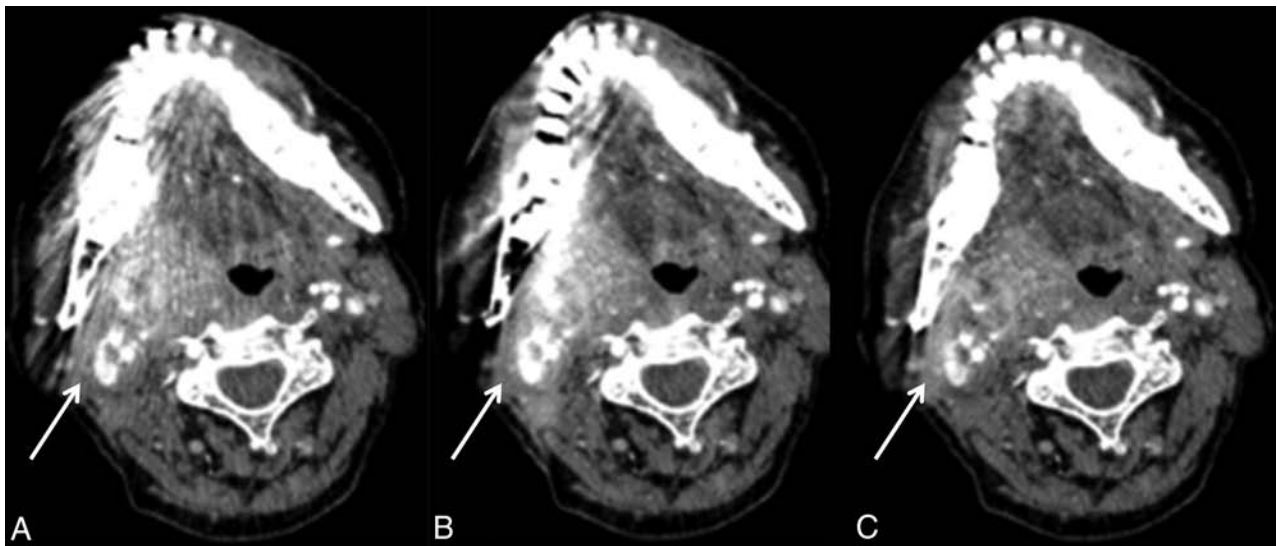


FIG 3. Imaging of oropharyngeal cancer on the right side with FBP (A), LIMAR (B), and IMAR (C). The effects of metal artifacts from dental hardware are highest with FBP (A), lower with LIMAR (B), and lowest with IMAR (C); full tumor extension is discernable only with IMAR (C, arrow).

Artifacts with FBP, LIMAR, and IMAR according to rating^a

Rating ^b	FBP	LIMAR	IMAR
1	174	140	31
2	150	211	47
3	61	78	100
4	71	22	135
5	0	4	142

^a Values shown are the number of sections with artifacts.

^b A rating of 1 indicates severe artifacts, largely not diagnostic; 2, poor image quality, partly nondiagnostic; 3, moderate image quality, limited diagnostic confidence; 4, good image quality, sufficient for diagnosis; and 5, excellent image quality, no artifacts.

162 ± 202 HU for FBP, 42 ± 19 HU for LIMAR, and 21 ± 6 HU for IMAR for the tongue; 73 ± 67 HU for FBP, 22 ± 10 HU for LIMAR, and 15 ± 5 HU for IMAR for the right cheek; and 63 ± 50 HU for FBP, 25 ± 14 HU for LIMAR, and 16 ± 5 HU for IMAR for the left cheek.

No significant difference was found between FBP and LIMAR in the muscles on either side of the neck ($P = .1$), but the IMAR mean standard deviation values were significantly lower than those of LIMAR and FBP ($P < .001$): 13 ± 4 for FBP, 12 ± 4 for LIMAR, and 11 ± 3 for IMAR on the left side and 14 ± 4 for FBP, 13 ± 4 for LIMAR, and 11 ± 3 for IMAR on the right side.

Cortical delineation of the alveolar process of the maxilla and mandible at the level of metal hardware improved with IMAR; however, IMAR induced some new artifacts next to metal hardware, which affected cortical delineation in 29 (58%) of 50 patients (Fig 4). Also, IMAR induced new artifacts in more remote areas, such as the spinal cord, in 9 (18%) of 50 patients (Fig 5).

DISCUSSION

Artifacts based on metallic implants and dental restorations are a frequently encountered obstacle in head and neck imaging, and advanced MAR algorithms might be a solution for this problem.⁵⁻⁷ Dental hardware affects not only CT imaging but also the attenuation correction in positron-emission tomography, dose calculation, and target definition for intensity-modulated radiation therapy.¹⁰

In our study, IMAR yielded objective and subjective image quality that was higher than that with FBP or LIMAR, and more than four-fifths of the sections that were not of diagnostic quality with FBP were evaluable with IMAR. Significantly more images were of diagnostic image quality with IMAR than with both FBP and LIMAR, which results in improvements in tumor detection and/or exclusion.

Tumor staging for squamous cell carcinoma of the oral cavity is based on size and extension into adjacent structures. The assessment of tumor infiltration depth is especially clinically challenging, and cross-sectional imaging is performed to gain that information. Yet, assessments of soft tissue in the oral cavity are often limited with CT and, to a lesser degree, MR imaging by metal artifacts. The first step for improving image quality and metal-streak artifacts is to remove all metal hardware from the scan range; however, that is not possible in many cases. In clinical routine, additional scans angulated to the mandible are often performed to increase diagnostic confidence for lymph node assessment and evaluation of the posterior neck. Parts of the oral cavity may still remain incompletely evaluated, however, and this approach increases radiation exposure and prolongs examination time. Application of an extended CT scale, thin-section collimation, a small FOV, dedicated reconstruction kernels,² and an increase of the tube voltage and current are options for reducing these artifacts; however, increasing the tube voltage and current increase patient radiation exposure, and none of these options have been dramatically successful. More elaborate strategies include monoenergetic processing of dual-energy CT data, which works nicely for surgical plates and implants,^{11,12} but its effect is limited with dental hardware. Sinogram in-painting methods^{8,13,14} and iterative,^{15,16} statistical,^{17,18} and filtering methods^{13,19} have been suggested, but for various reasons, they have not made their way into clinical practice. NMAR is an in-painting-based MAR method that is designed to reduce metal artifacts and to prevent the introduction of new artifacts by replacing raw data from the metal trace more reliably.⁷ Previously, the potential of NMAR to reduce artifacts from dental hardware was evaluated

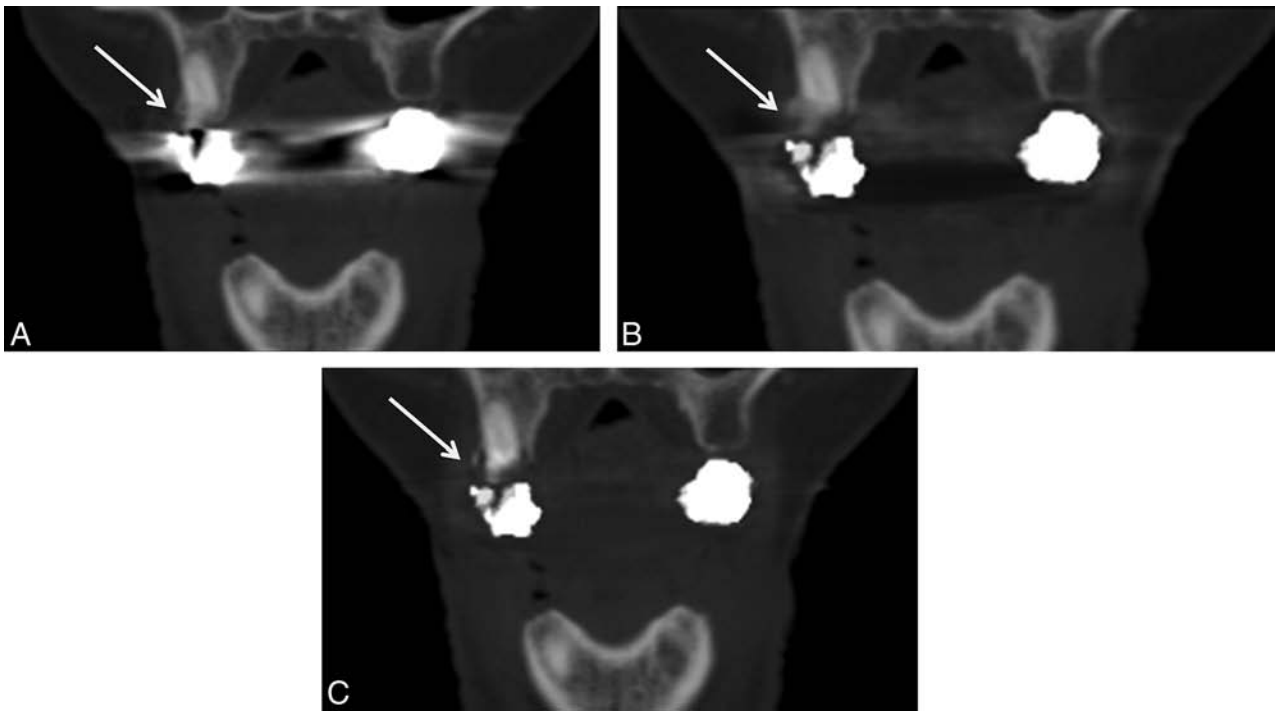


FIG 4. The effects of metal artifacts from dental hardware are highest with FBP (A), lower with LIMAR (B), and lowest with IMAR (C). Partial loss of cortical structures can be seen in B but is more pronounced in C (arrows).

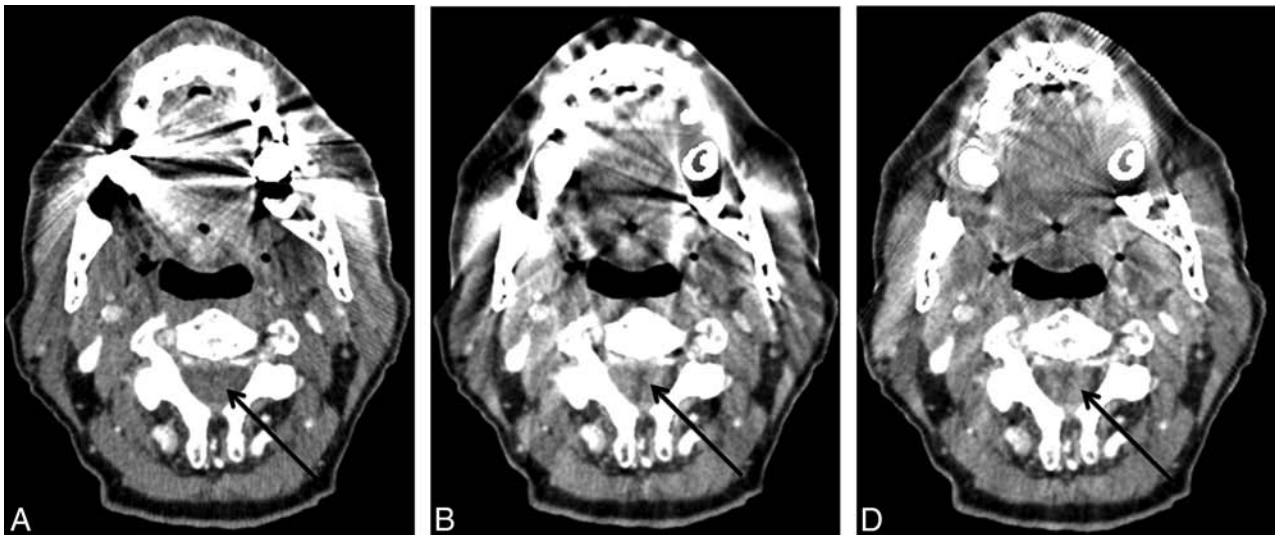


FIG 5. The effects of metal artifacts from dental hardware are highest with FBP (A), lower with LIMAR (B), and lowest with IMAR (C); however, LIMAR and IMAR induced new artifacts in the spinal cord (arrows).

in the head and neck region. The number of nondiagnostic sections with FBP was reduced by 50% with NMAR, which improved image quality and diagnostic accuracy. However, a drawback of LIMAR image reconstruction is that the tissues next to metal (eg, the bone trabeculae²⁰ or adjacent soft tissue) may be blurred and therefore not fully assessable. The frequency-split technique was introduced to address this problem of local blurring. With IMAR, anatomic information from the original images is recovered by high-pass filtering during the frequency-split iteration combined with multiple iterations in NMAR. This algorithm was evaluated in patients with hip prostheses. Image quality and the accuracy of pelvic abnormality assessments were compared in FBP,

LIMAR, and IMAR. IMAR reduced metal artifacts significantly and improved number measurements with CT and the confidence in depicting pelvic abnormalities.²¹

In our study, we found a significant improvement in soft-tissue delineation in the oral cavity and oropharynx, but we also found a degradation of bone delineation; artificial defects in the IMAR datasets of the bone abutting the metallic implants appeared in a number of cases (58%). Because of the reduction of streak artifacts, however, a better delineation of cortical bone at more remote areas in the sections containing metal hardware was achieved. Because the surgical approach is substantially influenced by tumor infiltration of the mandible or maxilla, which

leads to more extensive reconstruction methods to preserve function, the correct evaluation of bony structures is of high importance. Because of the imperfect bone delineation with IMAR, both FBP and IMAR images need to be reconstructed and evaluated to improve the overall diagnostic value in certain cases, which could be a significant limitation at the present time. Thus, detecting osseous involvement in tooth-bearing areas remains difficult with cross-sectional imaging (both CT and MR imaging). Additional limitations are that we did not investigate the clinical impact of our findings on treatment planning and prognosis, and only the metal artifact algorithm of one vendor could be evaluated, so no direct comparisons with other algorithms are possible.

CONCLUSIONS

In our patient population and with our specific CT scanner, IMAR yielded the highest image quality in comparison with FBP and LIMAR in patients with metal hardware in the head and neck area. We found significant improvement in the evaluation of soft tissue that was nondiagnostic with FBP and LIMAR.

Disclosures: Wolfgang Wuest—UNRELATED: Payment for Lectures (including service on speakers bureaus): Siemens AG, Healthcare Sector. Matthias Stefan May—UNRELATED: Payment for Lectures (including service on speakers bureaus): Siemens AG, Healthcare Sector; Payment for Development of Educational Presentations: Siemens AG, Healthcare Sector. Michael Brand—UNRELATED: Payment for Lectures (including service on speakers bureaus): Siemens Healthcare. Michael Lell—UNRELATED: Consultancy: Bracco and Guerbet; Grants/Grants Pending: Bayer,* Siemens,* and German Government (BMBF)*; Payment for Lectures (including service on speakers bureaus): Bayer and Siemens. Andreas Krauss—UNRELATED: Employment: Siemens AG; Patents (planned, pending or issued): Siemens AG; Stock/Stock Options: Siemens AG. *Money paid to the institution.

REFERENCES

1. Barrett JF, Keat N. **Artifacts in CT: recognition and avoidance.** *RadioGraphics* 2004;24:1679–91 CrossRef Medline
2. Lee MJ, Kim S, Lee SA, et al. **Overcoming artifacts from metallic orthopedic implants at high-field-strength MR imaging and multi-detector CT.** *RadioGraphics* 2007;27:791–803 CrossRef Medline
3. Kalender WA, Hebel R, Ebersberger J. **Reduction of CT artifacts caused by metallic implants.** *Radiology* 1987;164:576–77 CrossRef Medline
4. Glover GH, Pelc NJ. **An algorithm for the reduction of metal clip artifacts in CT reconstructions.** *Med Phys* 1981;8:799–807 CrossRef Medline
5. Lell MM, Meyer E, Kuefner MA, et al. **Normalized metal artifact reduction in head and neck computed tomography.** *Invest Radiol* 2012;47:415–21 CrossRef Medline
6. Lell MM, Meyer E, Schmid M, et al. **Frequency split metal artefact reduction in pelvic computed tomography.** *Eur Radiol* 2013;23:2137–45 CrossRef Medline
7. Meyer E, Raupach R, Lell M, et al. **Normalized metal artifact reduction (NMAR) in computed tomography.** *Med Phys* 2010;37:5482–93 CrossRef Medline
8. Meyer E, Raupach R, Lell M, et al. **Frequency split metal artifact reduction (FSMAR) in computed tomography.** *Med Phys* 2012;39:1904–16 CrossRef Medline
9. Conover WJ. *Practical Nonparametric Statistics.* New York: Wiley; 1980
10. Kennedy JA, Israel O, Frenkel A, et al. **The reduction of artifacts due to metal hip implants in CT-attenuation corrected PET images from hybrid PET/CT scanners.** *Med Biol Eng Comput* 2007;45:553–62 CrossRef Medline
11. Bamberg F, Dierks A, Nikolaou K, et al. **Metal artifact reduction by dual energy computed tomography using monoenergetic extrapolation.** *Eur Radiol* 2011;21:1424–29 CrossRef Medline
12. Zhou C, Zhao YE, Luo S, et al. **Monoenergetic imaging of dual-energy CT reduces artifacts from implanted metal orthopedic devices in patients with fractures.** *Acad Radiol* 2011;18:1252–57 CrossRef Medline
13. Abdoli M, Ay MR, Ahmadian A, et al. **Reduction of dental filling metallic artifacts in CT-based attenuation correction of PET data using weighted virtual sinograms optimized by a genetic algorithm.** *Med Phys* 2010;37:6166–77 CrossRef Medline
14. Prell D, Kyriakou Y, Kachelrie M, et al. **Reducing metal artifacts in computed tomography caused by hip endoprostheses using a physics-based approach.** *Invest Radiol* 2010;45:747–54 CrossRef Medline
15. De Man B, Nuyts J, Dupont P, et al. **An iterative maximum-likelihood polychromatic algorithm for CT.** *IEEE Trans Med Imaging* 2001;20:999–1008 CrossRef Medline
16. Zhang X, Wang J, Xing L. **Metal artifact reduction in x-ray computed tomography (CT) by constrained optimization.** *Med Phys* 2011;38:701–11 CrossRef Medline
17. Aootaphao S, Pintavirooj C, Sotthivirat S. **Penalized-likelihood reconstruction for metal artifact reduction in cone-beam CT.** *Conf Proc IEEE Eng Med Biol Soc* 2008;2008:2733–36 CrossRef Medline
18. Buzug T, Oehler M. **Statistical image reconstruction for inconsistent CT projection data.** *Methods Inf Med* 2007;46:261–69 Medline
19. Naranjo V, Lloréns R, Alcañiz M, et al. **Metal artifact reduction in dental CT images using polar mathematical morphology.** *Comput Methods Programs Biomed* 2011;102:64–74 CrossRef Medline
20. Liu PT, Pavlicek WP, Peter MB, et al. **Metal artifact reduction image reconstruction algorithm for CT of implanted metal orthopedic devices: a work in progress.** *Skeletal Radiol* 2009;38:797–802 CrossRef Medline
21. Morsbach F, Bickelhaupt S, Wanner GA, et al. **Reduction of metal artifacts from hip prostheses on CT images of the pelvis: value of iterative reconstructions.** *Radiology* 2013;268:237–44 CrossRef Medline

Standardized Brain Tumor Imaging Protocol for Clinical Trials

We would like to alert the neuroradiology community to a recent publication in *Neuro-Oncology*¹ that describes a standardized brain tumor MR imaging protocol, which is expected to gain widespread use in multicenter clinical trials of glioblastoma therapy.

Imaging is critical in the assessment of treatment response in glioblastoma, but its use faces a variety of challenges, including the morphologic complexity of these tumors, the confounding effects of therapies such as radiation and antiangiogenic agents, and the modest (at best) incremental benefits that new therapies generate. An important goal of imaging in clinical trials is to minimize assessment variability so that data can be pooled across sites to optimize the detection of treatment effects and provide accurate comparisons with prior trials.

The Imaging End Points in Brain Tumor Clinical Trials workshop, held in January 2014, involved patient advocates, device and pharmaceutical industry leaders, the FDA, the National Cancer Institute (NCI), and academic experts in neuro-oncology, neuro-radiology, and imaging physics, with the goal of improving the use of imaging end points in glioblastoma clinical trials. The workshop was predicated on the acknowledgment that large trials using survival end points are costly. Improving the use of imaging would allow smaller, less expensive clinical trials and help accelerate the development of new treatments.

A key recommendation that emerged from this meeting and that received the support of all participants, including the FDA, was the need to standardize the MR imaging acquisition and analysis for response assessment in glioblastoma trials. In response to this recommendation, the Jumpstarting Brain Tumor Development Coalition (consisting of several professional societies and patient advocacy groups) assembled a group of leading scientists, clinicians, and radiologists, who developed a standardized anatomic MR imaging protocol. This protocol permits response assessment according to established criteria (Response Assessment in Neuro-Oncology [RANO]) as well as emerging approaches (such as tumor volumetry and T1 subtraction). By minimizing variability, it allows trial results to be aggregated meaningfully across sites and across trials. It also facilitates the development of

robust automated segmentation methods on anatomic imaging and advanced applications such as diffusion and perfusion. The protocol balances these goals with practicality and widespread availability, by using sequences that are found on most MR imaging scanners as a result of the Alzheimer's Disease Neuroimaging Initiative.

The Standardized Brain Tumor Imaging Protocol (SBTIP) is based on the European Organisation for Research and Treatment of Cancer (EORTC) brain tumor imaging protocol that is being used successfully in clinical trials in Europe.² While the SBTIP parallels the methods already used in clinical practice in many centers, it is targeted for clinical trial use rather than for routine diagnostic imaging, because the latter may require other sequences for lesion detection and differential diagnoses. The protocol is similar to that recommended by the RANO group for assessment of metastatic disease and is already beginning to be implemented in several clinical trials funded by industry, the NCI, and cooperative groups.

The most significant difference from protocols in common clinical use is the acquisition of pre- and postcontrast 3D T1-weighted sequences. While some may not favor these volumetric acquisitions, compliance with the standardized protocol does not preclude the addition of other imaging sequences to local protocols. As the SBTIP is accepted by the FDA and becomes more widely adopted in clinical trials, it will be important for neuroradiologists to be aware of it and to make it available. This availability will ensure that their institutions will be eligible to participate in trials that require it and will be able to contribute data that can be meaningfully analyzed with those from other participating centers to help speed the development of novel therapies for this devastating disease.

Disclosures: Gregory V. Goldmacher—UNRELATED: Employment: ICON Plc. Whitney B. Pope—UNRELATED: Amgen, Roche, Celldex, Tocagen.

REFERENCES

1. Ellingson B, Bendszus M, Boxerman J, et al. **Consensus recommendations for a standardized Brain Tumor Imaging Protocol (BTIP) in clinical trials.** *Neuro Oncol* 2015;17:1188–98 CrossRef Medline
2. European Organisation for Research and Treatment of Cancer. **Bev-**

acizumab and lomustine for recurrent GBM. <http://clinicaltrials.gov/show/NCT01290939>. Accessed July 30, 2015

● **G.V. Goldmacher**

Department of Medical and Scientific Affairs
ICON Clinical Research
Warrington, Pennsylvania

● **B.M. Ellingson**

David Geffen School of Medicine
University of California, Los Angeles
Los Angeles, California

● **J. Boxerman**

Brown Alpert Medical School
Brown University
Providence, Rhode Island

D. Barboriak

Department of Radiology
Duke University School of Medicine
Durham, North Carolina

● **W.B. Pope**

Department of Radiology
UCLA Medical Center
Los Angeles, California

M. Gilbert

Center for Cancer Research
National Institutes of Health
Bethesda, Maryland

Please note that there is an error in Table 3 of the December 2013 article “Higher Rates of Decline for Women and *Apolipoprotein E* ϵ 4 Carriers” by Holland et al (*AJNR Am J Neuroradiol* 2013;34:2287–93, originally published on-line on July 4, 2013, doi:10.3174/ajnr.A3601). The *P* value for the whole brain “ b_{Sex} ” coefficient should be “.022” instead of “.22.” The Table is reproduced below with the corrected segment shown in bold. The Journal apologizes for the error.

<http://dx.doi.org/10.3174/ajnr.A4545>

Table 3: Effects of age, APOE ϵ 4, and sex on rates of change in MCI

MCI Measure	b_0	b_{Cog}	b_{Edu}	b_{Age} (SE; <i>P</i>)	b_{APOE} (SE; <i>P</i>)	b_{Sex} (SE; <i>P</i>)
Hippocampus	-1.83 ^a	-0.13 ^a	0.03	0.00 (.02; .8)	-0.40 ^a (.20; .045)	-0.29 (.20; .1)
Amygdala	-1.57 ^a	-0.15 ^a	0.01	0.03 (.02; .1)	-0.94 ^a (0.21; 7×10^{-6})	-0.98 ^a (.21; 2×10^{-6})
Entorhinal	-1.78 ^a	-0.12 ^a	0.00	0.04 ^a (.02; .006)	-0.44 ^a (.17; .011)	-0.54 ^a (.17; .002)
Inferior parietal	-0.91 ^a	-0.08 ^a	0.02	0.06 ^a (.01; 2×10^{-6})	-0.28 ^a (.14; .040)	-0.40 ^a (.14; .004)
Middle temporal	-1.40 ^a	-0.11 ^a	0.00	0.07 ^a (.02; 9×10^{-6})	-0.28 (.18; .1)	-0.52 ^a (.17; .003)
Med-orbito-frontal	-0.78 ^a	-0.04 ^a	0.04 ^a	0.02 ^a (.01; .023)	0.03 (.11; .8)	-0.24 ^a (.11; .026)
Whole brain	-0.74 ^a	-0.04 ^a	0.01	0.02 ^a (.01; 4×10^{-4})	-0.09 (.08; .2)	-0.17 ^a (.08; .022)
CDR-SB	0.46 ^a	–	0.01	0.01 (.01; .4)	0.38 ^a (.11; 6×10^{-4})	0.26 ^a (.11; .021)
ADAS-Cog	0.49 ^a	–	0.00	0.03 (.03; .3)	0.72 ^a (.31; .022)	1.40 ^a (.32; 2×10^{-5})
MMSE	-0.35 ^a	–	0.02	0.02 (.02; .4)	-0.81 ^a (.20; 4×10^{-5})	-0.34 (.20; .1)

Note:—See Table 2 for units and key.

^a Values significant at $P \leq .05$.

ROIs: *N* = 273; mean age = 76.65 years; mean ADAS-Cog = 11.68; mean years education = 15.61. Cognitive: *N* = 211; mean age = 76.84 years; mean years education = 15.63.